UNIVERSIDAD CARLOS III DE MADRID

TESIS DOCTORAL

Characterization and applications of new electrochromic devices. Comparison with other electrically controllable transmittance technologies

Autor:
David Barrios Puerto

Director/es:
Ricardo Vergaz Benito

DEPARTAMENTO DE TECNOLOGÍA ELECTRÓNICA

Leganés, Mayo de 2012

TESIS DOCTORAL

CHARACTERIZATION AND APPLICATIONS OF NEW ELECTROCHROMIC DEVICES. COMPARISON WITH OTHER ELECTRICALLY CONTROLLABLE TRANSMITTANCE TECHNOLOGIES

Autor: David Barrios Puerto

Director/es: Ricardo Vergaz Benito

Firma del Tribunal Calificador:

Firma

Presidente:	José Manuel Otón Sánchez
Vocal:	Gunnar A. Niklasson
Vocal:	Ana Viñuales
Vocal:	Vasko Jovanovski
Secretario:	María Carmen Vázquez García

Calificación:

Leganés, de de

If I were to suggest that between the Earth and Mars there is a china teapot revolving about the sun in an elliptical orbit, nobody would be able to disprove my assertion provided I were careful to add that the teapot is too small to be revealed even by our most powerful telescopes. But if I were to go on to say that, since my assertion cannot be disproved, it is intolerable presumption on the part of human reason to doubt it, I should rightly be thought to be talking nonsense. If, however, the existence of such a teapot were affirmed in ancient books, taught as the sacred truth every Sunday, and instilled into the minds of children at school, hesitation to believe in its existence would become a mark of eccentricity and entitle the doubter to the attentions of the psychiatrist in an enlightened age or of the Inquisitor in an earlier time.

Bertrand Russell

Si yo sugiriera que entre la Tierra y Marte hay una tetera de porcelana que gira alrededor del Sol en una órbita elíptica, nadie podría refutar mi aseveración, siempre que me cuidara de añadir que la tetera es demasiado pequeña como para ser vista aun por los telescopios más potentes. Pero si yo dijera que, puesto que mi aseveración no puede ser refutada, dudar de ella es de una presuntuosidad intolerable por parte de la razón humana, se pensaría con toda razón que estoy diciendo tonterías. Sin embargo, si la existencia de tal tetera se afirmara en libros antiguos, si se enseñara cada domingo como verdad sagrada, si se instalara en la mente de los niños en la escuela, la vacilación para creer en su existencia sería un signo de excentricidad, y quien dudara merecería la atención de un psiquiatra en un tiempo iluminado, o la del inquisidor en tiempos anteriores.

Bertrand Russell

Agradecimientos /Acknowledgements

Quisiera agradecer esta tesis doctoral a muchas personas que me han rodeado y apoyado para llegar a este punto.

En primer lugar a mi familia, mi padre Nicolás y mi madre Ascensión, que desde chico me han inculcado los valores del conocimiento y de la cultura, y a mis hermanas Paloma, Rosa, Vevi y Azahara, con las que he crecido en todos los aspectos, sin olvidarme de la primera sobrina, Violeta, que cuenta con sólo 5 meses y medio.

Este trabajo comenzó hace ya 8 años, cuando mi director de tesis, Ricardo Vergaz, me habló por primera la vez del término "electrocrómico". Quisiera agradecerle como consiguió atraer mi atención al mundo de la investigación, concretamente cuando me explicó por primera vez el monocromador, visualizando el color de la luz de una lámpara incandescente a través de una rendija, la cual fue variando de violeta a rojo durante el barrido del espectrómetro. También quiero agradecerle su gran dedicación y esfuerzo realizados en el campo de investigación de este trabajo, que han revertido directamente en mi investigación, ya que al ser un campo nuevo en nuestro grupo de investigación no era tarea fácil, al igual que tampoco era fácil tener la paciencia que ha tenido debido a que parecía que no llegaría el día en que yo terminase esta tesis, y no por que Ricardo no lo hubiera querido desde hace al menos un par de años. Ricardo, te estoy muy agradecido por haberme guiado tan bien en la tesis y algo muy curioso es que el título de esta tesis es y ha sido desde el principio el mismo, es decir, no han habido variaciones en cuanto a la dirección de mi investigación. Incluso acertaste en los trabajos futuros de la tesis, cuando hace ya más de tres años propusiste el estudio del scattering como línea de investigación a seguir, el cual me ha motivado y al que espero poder realizar nuevas aportaciones al campo del conocimiento.

Aparte de mi director de tesis, hay otras personas de mi grupo de investigación (GDAF) a las que quiero agradecer su apoyo, como a Pepe Sánchez Pena, quien en concreto para mi tesis de investigación supo adquirir las muestras de las ventanas SPD, las cuales me abrieron el camino para desarrollar el estudio del scattering. Quiero agradecer además a Ricardo y a Pepe por haberme financiado la posibilidad de asistir a una gran cantidad de congresos, nacionales e internacionales, y haber permitido la compra de equipos de medidas importantes para mi tesis, a cargo de los proyectos de investigación en los que participa GDAF.

En cuanto a las colaboraciones en el campo de investigación, quisiera agradecer a Cristina Pozo, Maitane Salsamendi, y Ana Viñuales, por su buena disponibilidad a la hora de proporcionarnos dispositivos, tanto EC como PDLC, para realizar las medidas oportunas, así como por la calidad de estos, que han ido mejorando con el tiempo. También quiero mostrarles mi gratitud por haberme recibido durante el mes de la estancia de investigación que realicé en CIDETEC en el verano de 2009.

According to the scientific collaborations, I also would like to show my gratitude to Claes G. Granqvist and Gunnar A. Niklasson for letting me profit already of four months in two research stays at the Angstrom Laboratory, in 2008 and 2010, which allowed me to learn about the optical scattering research topic. I want to thanks especially to Gunnar for spending the time and effort in advising and driving me about the results of hundreds of plots of the results that I sent him during the SPD fitting computations. I also would like to thank to Inger Ekberg for helping me in searching a place to live in Uppsala, to Arne Roos for teaching me integrating sphere theory, and to Bengt Götesson, who appears reflected with me in the photograph SPD3 sample of this work. I don't want to forget to say thank to Sara Green and Ilknur for their sympathy with me during these stays and the time spent together in conferences.

I also want to thank to Boris Orel for having invited to me to a research stay at the National Institute of Chemistry of Slovenia, during this year 2012, for starting a new collaboration regarding the inorganic EC devices. I also want to thank to Mohor for providing me several samples during this research time and Angela for helping me to start this research stay. I would like to thank to Vasko Jovanovski for friendship established after the several times we matched in conferences, research stays at CIDETEC and in Ljubljana, and visits to Madrid.

También agradecer a Javi Padilla por sus consejos científicos en los congresos de estos últimos años, a Alicia Pons por la colaboración en medidas de colorimetría, y al grupo de Xabi de la politécnica por cuando coincidimos en los optoeles.

En cuanto a los compañeros de trabajo, tanto del GDAF, como del propio departamento, de Tecnología Electrónica, quisiera agradecer en primer lugar a los "supervivientes" del mítico despacho 1.2.B16 al principio de mi investigación en la UC3M. A Juan Carlos Torres, porque tiene una risa muy fácil y contagiable, a Pedro Contreras, por ayudarme con la función "buscarv" de Excel, y además porque juega muy bien de portero y de defensa en los partidos de los miércoles, a David Sánchez Montero, "el pistachito", por sus famosos sándwiches tras venir de celebrar algo por cualquier excusa, y a Pablo Pedreira, por romper el cable de mi pantalla del ordenador y en especial por su gran apoyo este último año. Otros "supervivientes", ya no sólo del despacho, pero también del departamento, con los cuales he compartido muchos gratos momentos durante estos años y quiero agradecerles, como a Daniel Gallego, por dejarse hacerle un "cañito" en un partido de futbol reciente y por su ayuda en cuestiones científicas a parte de la wikipedia, a Carlos Marcos, por decirme siempre que he adelgazado aunque sea mentira, a Cristina de Dios, por haber sabido filtrar a Judith, por demostrar que era una amiga cuando la necesité, a Almudena, por darme de lo que le sobraba del "taper" que le hacía su madre cuando yo estaba a dieta, a Prefasi, por esas fiestecilla de la cerveza, a Oscar Miguel, Carlos González y Pedro el extremeño, como los nuevos compañeros de despacho, por aguantarme día a día desde hace ya unos 3 años. De los no tan antiguos, a Jesús "el cura", por llevarme la contraria en muchas cosas y por las recientes "partidillas" las

tardes de los viernes, a Guillermo Guarnizo, por cantarme siempre la canción de “mira que David danzaba…”, a Julio Posadas, por como imita el cantar del pájaro turpial, a Luis Jorge “mex”, por llevar mis restos de comida en su bandeja del comedor, a Delia, por ser mas chula que un ocho, a Carlos “chuche”, a Bruno, Robinson, Algorri, Plinio, Tapetado, Pedro Debora, Carmen Raga, Isa, Alberto Carrasco, Rubén, Marta Portela, y a un montón más de compañeros con los que he compartido estos años de investigación y que se fueron de la UC3M, como Angelillo, Miguel A., Roca, Manuel Sánchez, el cubano, David Piña, Noemí, María Mariño, Martin, Ana, Belen, Paloma, Cesar, Macías, Jesus el cachas, Aurora, Rui, Vincent, Linda, Dimitris (y Joana), Daniel, o incluso algunos que se fueron de la UC3M pero parece que nunca se fueron, como Julio Montalvo. También a Mercedes Chaparro, Víctor Montero, y Cristos por su amistad, y a Luca, Gocu, Jimmy, Quino, Sufi, Rachid, Efraín, Omar, Hugo, por los partidillos de futbol. A Diana por convencerme para hacer spinning, y a Susana, por llenarme el correo de forwards.

Quisiera agradecer al resto de mis compañeros del GDAF, como a Carmen Vázquez (por confiar en mí, ya que ella me hizo la 1ª entrevista), a Virginia (por dejarse que la subiera a un árbol en una fiesta del departamento en polvoranca), a Isabel (por haberle mareado tanto en la asignación docente), a Isidro (por hacer un salmorejo mas weno que el mío) , así como a los nuevos compañeros o algunos que dejaron el GDAF, como a Rodrigo (por comerse un donut de chocolate al lado de un huevo frito en un hotel de un congreso) y a Salva (por perdonarme tanto que me metiera con su Real Madrid). También agradecer a Marimar y Oscar por su disposición y apoyo en todo lo que he requerido para realizar las gestiones de investigación en cuanto a congresos y tesis. A los maestros de laboratorio Agustín, Cesar y Jesúses, y a Ernesto de oficina técnica, así como al resto de compañeros del departamento de Tecnología Electrónica. Como no, también agradecer a las camareras de cafetería, Yolanda, Paqui y Maricarmen, por todos los cafelitos que nos han puesto tan simpáticamente, además de alguna palmerita de chocolate que haya caído de regalo…

También quiero agradecer su apoyo a las amistades que he tenido en Madrid desde que llegué hace unos 10 años. A Gon, quien me ayudó mientras buscaba mi primer trabajo, y a Luis Mariano, con quien he compartido muchas experiencias y vivencias, así como viajes alrededor de todo el mundo. A mis colegas frikis Aitor y Juanjo, y no tan frikis (o a lo mejor más) Diego y Laura, por estar siempre ahí. A mis compañeros de piso de la calle luna, Tono, Valerie, Simone, Fas (y Araceli), Covi, Andrea, Enrico, Lorenzo, Teresa, María, Johannes, Momo… por ese año tan fabuloso que pasamos juntos. En especial a Tono por ser mi primer amigo desde que llegué a esta ciudad. A los coleguillas Erasmus de Uppsala, Javi, Alex, David Cayón, Andrés, Hans, María …

No quiero olvidarme de agradecer a mis amigos de Córdoba, algunos de ellos desde la infancia y otros algo menos, Toni caneloni, Emilioto, Aure, Sandra, Rafa, Rubén, Carlitros, Raigones, Eloy, David Chico, Alberto, Kike Palike, Medina, Carrillo, Dani

Perez, Alfonso, Belén, Rafa Chacón, María y Alvaro, a antiguos compañeros y amigos de la uni tanto en automática, Magda, Reme, Jose Manchego, Albendin, Legallic Loli, David, Mahillo, Fernando, el Santaella, Noelia y Pedro… como en peritos, Tomás, Juan de la Cruz, Concheso, Juan Ruiz, Mª Jose, …así como a mis compis de cole y de instituto Magda, Vero, Roldan, Enrique Jimenez, Merino, Guerrero, Domingo… y como no a todos mis prim@s, ti@s, y abuelos, Blas y Encarnación, Adolfo y Teodosia, Daniel y Milagros, Mila, Dani y Gema, Mari y Juanjo, Raúl, Sandra y Juanjo, Manolo y Maricarmen, Bárbara, Manolo y Joaquín, Rafael y Esperanci, Mariajesús y Genoveva,… así como a mis cuñaos.

Espero no haberme olvidado de nadie, y espero que si es así que me perdone y que comprenda el estrés que tiene escribir una tesis doctoral...

Por último, y sin ánimo de ofender, quiero agradecer a los equipos de futbol Juventus, Arsenal, Bayern de Munich x 2, Roma, Liverpool, y Olympique de Lyon, además del F.C. Barcelona, por haber eliminado al Real Madrid de la champions durante los años de investigación de mi tesis doctoral. También agradecer al movimiento 15M por preocuparse, entre otras cosas, en defender la calidad de la educación y de la investigación de mi país.

Contents

List of Figures Page

Chapter I: Introduction

Chapter II: Instrumental for characterization and techniques

Chapter III: New electrochromic devices under study

Section III.1: New all-plastic PEDOT EC devices

Section III.3: Dependence on thickness of new viologen EC devices

Chapter IV: Suspended particle devices (SPDs)

Chapter V: Polymer Dispersed Liquid Crystals (PDLCs)

Chapter VI: Developed applications

Section VI.1: New glasses with EC filter for people with low vision

Section VI.2: Variable optical attenuator (VOA) using EC devices

Section VI.3: Transparency domotic control of PDLC based smart windows

Section VI.4: Electro-optic Characterizer of Electrochromic Devices (CEODEC)

Chapter VII: Brief discussion and conclusions

List of Tables

Acronyms list/ Lista de Acrónimos

Acronym (Acrónimos)	English Term (Término en Inglés)	Spanish Term (Término en Castellano)
ΔA	Absorptance Contrast	Contraste de Absorbancia
ΔQ_{redox}	Effective Charge Density	Densidad de Carga Efectiva
ΔT_{600nm}	Transmittance Contrast at 600 nm	Contraste de Transmitancia
α	Intrinsic Scattering Coefficient	Coeficiente de Dispersión Intrínseco
β	Intrinsic Absorption Coefficient	Coeficiente de Dispersión Intrínseco
δ	Thickness	Espesor
ω	Interface Reflectance	Reflectancia de la Interfaz
ω_c	Collimated Interface Reflectance	Reflectancia Colimada de la Interfaz
ω_d	Diffuse Interface Reflectance	Reflectancia Difusa de la Interfaz
ω_0	Reflectance of the Bottom Interface	Reflectancia de la Interfaz Inferior
ω_δ	Reflectance of the Top Interface	Reflectancia de la Interfaz Superior
A	Absorptance	Absorbancia
AC	Alternating Current	Corriente Alterna
ACP	Average Crossing Parameter	Parámetro de Camino Medio
AZO	Aluminium-doped Zinc Oxide	Óxido de Aluminio y Zinc
bipm	Bipiridium Salts	Sales de Bipiridilo
$bipm^{2+}$	Dicationic Form of Viologen	Forma Dicatiónica de Viológeno
$bipm^{+\bullet}$	Radical Cation Form of Viologen	Forma Radical Catión de Viológeno
$bipm^{0}$	Neutral Form of Viologen	Forma Neutra de Viológeno
BV	Benzyl Viologen	Bencil Viológeno
Cdl	Double Layer Capacitor	Condensador de Doble Capa
CE	Counter Electrode/Coloration Efficiency	Electrodo Contador/Eficacia de Coloración
CEODEC	Electro-Optic Characterizer of EC Devices	Caracterizador Electro-Óptico de Dispositivos Electrocrómicos
ChLC	Cholesteric LC	LC colestérico
ChrA	Chronoamperometry	Cronoamperometría
ChrC	Chronocoulometry	Cronocoulometría
ChrP	Chronopotentiometry	Cronopotenciometría
CIE	International Commission on Illumination (Commission Internationale de l'Eclairage)	Comisión Internacional de Iluminación
CNT	Carbon Nanotubes	Nanotubos de Carbono
CPE	Constant Phase Element	Elemento de Fase Constante
CPEdiff	Diffusion CPE	CPE de Difusión
CPEdl	Double Layer CPE	CPE de Doble Capa
CPQ	Cyanophenyl Paraquat	Cianofenil Paracuat
CRI	Continuous Refractive Index	Índice de Refracción Continuo
CV	Cyclic Voltammetry	Voltametría Cíclica
CYM	Cyan, Yellow and Magenta	Cian, Amarillo y Magenta
DC	Direct Current	Corriente Continua
DM-CSIC-IFA	Metrology Department of Applied Physics Institute Scientific Research High Council	Departamento de Metrología del Instituto de Física Aplicada del Consejo Superior de Investigaciones Científicas
DoE	Department of Energy	Departamento de Energía
EC	Electrochromic	Electrocrómico
E	Extinction Coefficient	Coeficiente de Extinción
ECD	Electrochromic Device	Dispositivo Electrocrómico
EEC	Equivalent Electric Circuit	Circuito Eléctrico Equivalente
EIS	Electrochemical Impedance Spectroscopy	Espectroscopía de Impedancia Electroquímica
EMI	Electromagnetic Interference	Interferencia Electromagnética
EMRS	European MRS	MRS Europeo
E-PAD	Electronic Paper Display	Pantalla de Papel Electrónica
ESCA	Electron Spectroscopy for Chemical Analysis	Espectroscopía de Electrón para Análisis Químico

ESR	Electron Spin Resonance	Resonancia del Spin del Electrón
CCT	Correlated Color Temperature	Temperatura de Color Correlacionada
FWHM	Full Width at Half Maximum	Anchura a Media Altura
FRA	Frequency Response Analyzer	Analizador de Respuesta en Frecuencia
FSR	Forward Scattering Ratio	Fracción de Dispersión Hacia Adelante
FTO	Fluor-doped Tin Oxide	Oxido de Flúor y Estaño
GDAF	Group of Displays and Photonic Applications	Grupo de Displays y Aplicaciones Fotónicas
GSVD	Glass Supports Violet Device	Dispositivo Violeta de Soporte en Cristal
GSBD	Glass Supports Blue Device	Dispositivo Azul de Soporte en Cristal
GZO	Gallium-doped Zinc Oxide	Oxido de Galio y Zinc
HP	Hewlett Packard	Hewlett Packard
H-PDLC	Holographic PDLC	PDLC Holográfico
HV	Heptyl Viologen	Heptil Viológeno
HVAC	Heating Ventilation and Air Conditioning	Calefacción, Ventilación y Aire Acondicionado
IME	International Meeting on Electrochromism	Congreso Internacional de Electrocromismo
i	Downwelling Light Beam	Haz de Luz Descendente
IR	Infrared	Infrarrojo
ITO	Indium Tin Oxide	Oxido de Indio y Estaño
j	Upwelling Light Beam	Haz de Luz Ascendente
K	Extensive Absorption Coefficient	Coeficiente de Absorción Extensivo
KM	Kubelka-Munk Theory	Teoría de Kubelka-Munk
LBNL	Lawrence Berkeley National Labs	Laboratorio Nacional Lawrence Berkeley
LC	Liquid Crystals	Cristales Líquidos
LCD	Liquid Crystal Display	Pantalla de Cristal Líquido
LCOS	LC on Silicon	LC en Silicio
Low-e	Low Emittance	Baja Emitancia
MEPA	Poly 3 methyl aniline	Poli 3 metil anilina
MRS	Materials Research Society	Sociedad de Investigación de Materiales
MV	Methyl Viologen	Metil Viológeno
NCAP	Nematic Curvilinear Aligned Phase	Nemático Curvilineal Alineado en Fase
NCD	NanoChromic Display	Pantalla Nanocrómica
NIR	Near Infrared	Infrarrojo cercano
NiO	Nyquel Oxide	Óxido de Niquel
NM_{PDLC}	Normal Mode PDLC	PDLC en Modo Normal
NREL	National Renewal Energy Laboratory	Laboratorio Nacional de Energía Renovable
NVS	Night Vision System	Sistema de Visión Nocturna
OLED	Organic Light Emitting Diode	Diodo Emisor de Luz Orgánico
OPTOEL	Spanish Meeting of Optoelectronics	Reunión Española de Optoelectrónica
P3MPy	Poly(3-methyl-pyrrole)	Poli(3-metil-pirrol)
P3MT	Poly(3-methyl-thiophene)	Poli(3-metil-tiofeno)
PANI	Polyaniline	Polianilina
PB	Prussian Blue	Azul Prusiano
PbS	Lead Sulfide	Sulfuro de Plomo
Pc	Phthalocyanine	Ftalocianina
PDLC	Polymer Dispersed Liquid Crystal	Cristal Líquido Disperso en Polímero
PEDOT	Poly(3,4-ethylenedioxy-thiophene)	Poli(3,4-etilenodioxi-tiofeno)
PET	Polyethylene-terephthalate	Polietileno teraftalato
PhC	Photochromic	Fotocrómico
PIPS	Polymerization-Induced Phase Separation	Separación de Fase Inducida por Polimerización
PNLC	Polymer Network LC	LC en Red de Polímero
PPy	Polypyrrole	Polipirrol
PSBD	Plastic Supports Blue Device	Dispositivo Azul de Soporte en Plástico
PSLC	Polymer stabilized LC	LC Estabilizado en Polímero
PSS	Poly(styrene sulfonate)	Poli(estireno sulfonato)
PT	Polythiophene	Politiofeno

q_0	Diffuse Fraction at the Bottom Interface	Fracción Difusa en la Interfaz Inferior
q_δ	Diffuse Fraction at the Top Interface	Fracción Difusa en la Interfaz Superior
R	Reflectance	Reflectancia
r_c	Collimated Interface Reflectance	Reflectancia Colimada de la Interfaz
R_{CRI}	CRI Reflectance	Reflectancia CRI
Rct	Charge Transfer Resistance	Resistencia de Transferencia de Carga
r_d	Diffuse Interface Reflectance	Reflectancia Difusa de la Interfaz
R_{diff}	Diffuse Reflectance	Reflectancia Difusa
redox	Reduction/Oxidation	Reducción/Oxidación
RFI	Research Frontiers Inc	Corporación Fronteras de la Investigación
R_g	Bottom Interface Reflectance of Two Flux Model Downwelling Light Beam	Reflectancia del Haz de Luz Descendente en la Interfaz Inferior del Modelo de Dos Flujos
RGB	Red, Green and Blue	Rojo, Verde y Azul
R_{lum}	Luminous Reflectance	Reflectancia Luminosa
RM_{PDLC}	Reverse Mode PDLC	PDLC en Modo Reverso
Rs	Contacts Resistance	Resistencia de los Contactos
R_{sol}	Solar Reflectance	Reflectancia Solar
R_{spec}	Specular Reflectance	Reflectancia Especular
R_{tot}	Total Reflectance	Reflectancia Total
S	Extensive Scattering Coefficient	Coeficiente de Dispersión Extensivo
S & K	Scattering and Absorption Coefficients	Coeficientes de Dispersión y Absorción
SCSC	SPD Control Systems Corporation	Corporación Sistemas de Control SPD
SEM	Scanning Electron Microscopy	Microscopía Electrónica de Barrido
SEM&SC	Solar Energy Materials and Solar Cells	Materiales de Energía Solar y Células Solares
SP	Suspended Particle	Partículas Suspendidas
SPD	Suspended Particle Device	Dispositivo de Partículas Suspendidas
SPIE	International Society of Optics and Photonics	Sociedad Internacional de Óptica y Fotónica
T	Transmittance	Transmitancia
T_{600nm}	Transmittance at 600 nm	Transmitancia a 600 nm
tb	Bleaching Time	Tiempo de Aclarado
tc	Coloring Time	Tiempo de Coloreado
TC	Transparent Conductor	Conductor Transparente
TCO	Transparent Conductive Oxide	Óxido Conductor Transparente
T_{CRI}	CRI Transmittance	Transmitancia CRI
T_{dir}	Direct Transmittance	Transmitancia Directa
T_{diff}	Diffuse Transmittance	Transmitancia Difusa
TFT	Thin Field Transistor	Transistor de Capa Delgada
ThC	Thermochromic	Termocrómico
TIR	Total Internal Reflection	Reflexión Interna Total
T_{lum}	Luminous Transmittance	Transmitancia Luminosa
TMO	Transition Metal Oxide	Oxido de Metal de Transición
TNO	Niobium-doped Titanium Oxide	Oxido de Titanio y Niobio
TO	Tin Oxide	Oxido de Estaño
T_{sol}	Solar Transmittance	Transmitancia Solar
T_{tot}	Total Transmittance	Transmitancia Total
UC3M	University Carlos III of Madrid	Universidad Carlos III de Madrid
UV	Ultraviolet	Ultravioleta
VEECD	Variable EC Emittance Device	Dispositivo EC de Emitancia Variable
VIS	Visible	Visible
V_{TH}	Threshold Voltage	Voltaje de Umbral
Wo	Open-circuit Warburg Impedance	Impedancia de Warburg en circuito abierto
WO_3	Tungsten Oxide	Óxido de Wolframio
Ws	Short-circuit Warburg Impedance	Impedancia de Warburg en cortocircuito

Abstract

Characterization and applications of new electrochromic devices.
Comparison with other electrically controllable transmittance technologies.

by

David Barrios Puerto
PhD of Electrical, Electronic and Automatic Engineering

University Carlos III of Madrid, Electronic Technology Department,
Group of Displays and Photonic Applications (GDAF)

Electrochromic (EC) materials are able to change their optical properties, such as color, in a persistent and reversible way under the action of a voltage pulse or a small constant value. Nowadays, electrochromic devices (ECD) are, with suspended particle devices (SPD), polymer dispersed liquid crystals (PDLC) and micro-blinds, the four electrically controllable smart windows technologies. Not only used for optical appearance purposes, the use of such technologies could reduce the cost of heating, air-conditioning and lighting by the energy savings that can be accomplished in buildings and vehicles, places where modern people use to spend around 90% of their time.

These variable transmittance technologies allow the optical switching from a transparent or bleached state to a colored, darken or in another case to translucent state by different operation principles. In all the cases these technologies require the use of transparent conductors. Other applications of these technologies, besides windows are found on mirrors and displays.

ECDs for architectural applications incorporate solid EC films and consist of a thin multi-layer assembly that is typically sandwiched between two panes of glass. Coloration of solid anodic films rely on upon electrochemical oxidation or cathodic films upon electrochemical reduction, involving transfer of ions into and out of the EC films, which requires a component where ions can be stored. Among the materials showing electrochromism effect it can be found transition metal oxides (TMOs), Prussian Blue (PB) systems, viologens, conductive polymers and rare earth metals. Regarding the 2nd smart windows technology in the list, SPD incorporates an active layer that contains needle-shaped dipole particles that are uniformly distributed in an organic fluid or film. The active layer is laminated of filled between two transparent conductors on polyester. The change in the optical properties is caused by the motion and orientation of dispersed particles relative to a fluid under the application of an AC electrical potential of high amplitude. Smart windows LC technology has already been used in buildings and several LC glass products are available in the market. PDLC, the LC glazing, consists of two outer layers of polyester that are coated with a transparent conductor and a polyester matrix that contains the LCs. When no voltage is applied, the LC molecule chains are

randomly scattered and LC system is translucent opal white, showing a milky appearance. When a voltage is applied, the molecules align with the lines of the electric field and the film appears almost transparent.

In this work, different samples of new ECDs, SPDs and PDLCs were electro-optically characterized. ECD and PDLC samples were developed by CIDETEC, the Center of Electrochemical Research and Development of San Sebastian (Spain). SPD samples were supplied by Cricursa S.A. Cristales Curvados Company from Barcelona (Spain).

Optical characterization was performed by means of spectral and time domain transmittance measurements in the visible wavelength region when applying or not the appropriated electrical voltage required for each controllable transmittance technology. CIE 1931 chromaticity coordinates and sRGB space color values were obtained from optical measurements applying colorimetric techniques. Visual appearance of the samples was simulated by RGB values and the human eye sensitivity curve. Irradiance and correlated color temperature of the lamp used in the spectrometer was measured in the Metrology Department of CSIC-IFA, Applied Physics Institute Scientific Research Superior Center. The calibrated light source is useful for obtaining absolute measurements.

An equivalent electrical circuit (EEC) model was derived for the different devices from the impedance characterization by means of electrochemical impedance spectroscopy (EIS) technique. Since a small DC value of voltage is required for coloration process in the case of ECD samples, EEC model were determined by fitting process for bleached, colored and intermediate coloration states by means of impedance measurements while applying to the ECD different DC bias voltage levels. Resistance of the contacts (Rs), double layer capacitance (Cdl), charge transfer resistance (Rct) and diffusion Warburg element (W) were used in the Randles circuit based EEC model. The evolution of the components of the EEC model with the coloration was related to the physical and chemical principles of ECDs.

Electrochemical techniques such as chronoamperometry (ChrA), chronocoulometry (ChrC), cyclic voltammetry (CV) were simultaneously measured with optical transmittance for the ECD samples, revealing information of the redox reaction and the consumed electrical charge required for the colored state. Several parameters useful for the criteria of evaluation of ECDs such as coloration efficiency, write-erase efficiency, effective charge density, response times for coloring and bleaching process, transmittance contrast and redox peak potentials and currents, were analyzed.

Two types of ECD organic samples, based on PEDOT and based on viologens, were characterized in this work. Symmetrical optical operation for both polarities of applied voltage DC signals was analyzed for different samples of plastic supports PEDOT based EC devices, with less number of layers than the normally observed in the sandwich structure of an ECD. Optical characterization of glass supports and plastic supports

viologen based ECD samples showing a high transmittance contrast from uncolored to blue-purple colors was carried out. Thickness dependence of glass supports blue viologen based ECD samples was also studied. The results of ChrA, ChrC, CV and EIS experiments were related with the optical spectral transmittance at the different levels of coloration for each thickness and hence for the different amount of color centers formed in each sample. For SPD and PDLC samples, since a high amplitude AC voltage signal is required for switching to the transparent state, the EEC model was only determined for the dark and translucent appearance states for SPD and PDLC samples respectively.

Regarding SPD sample, since the scattering effect is intrinsically present in this technology, it was consider relevant to develop a new method for approximating the scattering and absorption coefficients, being carried out in collaboration with the Division of Solid State Physics at the Department of Engineering Sciences, at the Angstrom Laboratory of Uppsala (Sweden). Total and diffuse transmittance and reflectance (T and R) measurements in the visible and near infrared region by means of a three ports integrating sphere based spectrophotometer. The method,computed in Matlab , was based on the four flux and the two flux models, together with Saunderson correction for refractive index discontinuities and spectral interface reflectances derived from refractive index fitted by collimated components of T and R. Total and diffuse T and R, and hence the direct T and specular R, were estimated for different thicknesses of the SPD sample. Optimum thickness as well as optimum level of haze, defined as the diffuse to total components ratio, were determined from the approximated extensive scattering and absorption coefficients (S and K) derived from two flux Kubelka-Munk (KM) model.

CIDETEC developed PDLC samples with different active areas and thicknesses of the internal layers, operating in both normal and reverse mode (i.e. more translucent without applied voltage and more transparent with applied voltage and vice versa). Total and diffuse transmittances were measured using the spectrometer based on a two ports integrating sphere (for measuring total T and R and diffuse T) available at the lab of CIDETEC. These measurements were compared with the measurements carried out using a one port integrating sphere (for measuring total T) available at GDAF-UC3M labs. Diffuse T was obtained by subtracting the direct T measured without integrating sphere to total T. Besides, total and diffuse T and R were measured for eight PDLC samples with two different active areas and four different internal layer thicknesses using the three ports integrating sphere based spectrometer at the Angstrom Laboratory.

The developed method of scattering characterization and new future improvements over such method will be considered as future research lines on the SPD and PDLC devices studied in this work. Among the future works it can be found, for instance, the difficult task of decoupling the extinction or attenuation coefficients (derived from Lambert-Beer law) into the intrinsic scattering and absorption coefficients This model and new improvements, for obtaining intrinsic scattering and absorption coefficients (α and β),

obtaining the spectral values of the forward scattering ratio (FSR) and average crossing path (ACP) parameters derived from Maheu, Le Toulouzan and Gouesbet (MLG) four flux model. Also as a future work and in collaboration with Angstrom Laboratory, it will be studied the determination of S and K from the optical constant of herapathite (material present at the SPD devices) as well as from the geometry of scatter particles. As the result of other collaboration with a foreign research group, in this case the Laboratory for Spectrometry of Materials of the National Institute of Chemistry in Ljubljana (Slovenia), electro-optical characterization of inorganic EC devices developed by this group, using WO_3 and NiO for the cathodic and anodic EC layers switching from an uncolored appearance to blue and brown colorations respectively, will be carried out. By using these layers together in a device, the observed appearances change from an uncolored state to a grey colored state. The level of coloration rises when increasing the thickness of the two active layers, causing the increment of the undesired scattering effect. The optimum thicknesses of such layers will be studied by means of determining the scattering and absorption coefficients S and K for each layer switching coloration.

As a future research lines for PDLC samples, the scattering and absorption coefficients will be determined using the developed method applied for the SPD sample in this work. Future improvements on such method could also be applied for the PDLC samples. Also, a tandem EC-PDLC device was developed by CIDETEC and electro-optically characterized allowing transparency and coloration control. Four different states were mainly observed: uncolored translucent state, transparent uncolored state, transparent colored state and translucent colored state. The EEC model was determined for each separated part (PDLC and EC) by means of EIS technique.

Among the developed applications of chromogenic technologies, four different cases were studied. New glasses with EC filter for people with low vision were studied as a first application by mixing the EC filters with the photochromic ophthalmologic lenses recommended by IOBA, University Institute of Applied Ophthalmology of Valladolid (Spain), in order to determine the best possibilities for patients with low vision. The second application consist of a variable optical attenuator (VOA) using EC devices for attenuation control in optical communication systems at the different wavelength of the optical transmission windows (850, 1310 and 1550 nm). The third application, based on the Project of Engineering of the author in 2002, is a transparency domotic control of PDLC based smart windows using Zigbee domotic standar. A software for remote control by internet was developed for checking and switching by sockets communication of a Macromedia Flash client and java server application. Finally, the fourth developed application consisted of an electro-optic characterizer prototype for EC devices based on a data acquisition card of National Instrument and programmed in Labview, including a pair of RGB photodiodes, all packaged in a small size box. The system is able to measure simultaneously electrical current and optical transmittance in the three wavelengths (for RGB), when different voltage signals are applied, such as the triangular or square shape required for CV and ChrA experiments.

Different conclusions can be extracted for each chromogenic technology studied in this work. For PEDOT EC devices, the symmetrical optical operation for positive and negative polarities of the applied voltage was tested and an EEC model was determined for the different coloration levels for each DC bias voltage applied. Increasing the coloration in these devices resulted in an increment of the charge transfer resistance and in the diffusion impedance, accompanied with a decrement of the double layer capacitance. Sealing problems and bubbles, represented in the EEC model by means of a resistance and capacitor parallel shunt, as well as the contacts resistance, showed an independent from coloration state. This could be useful for checking manufacturing errors in larger devices.

In the case of Viologen EC devices in plastic and glass substrates, the parameters useful for the evaluation criteria used in EC devices showed different results for the different studied devices. For the glass supports devices, the best results in direct transmittance contrast at 600 nm (ΔT_{600nm}), around 72% (switching to blue color), were not corresponded with the best results of the response times, which were obtained for the lower ΔT_{600nm} (switching to purple color), around 57%, with 7 and 8 seconds for coloring and bleaching times processes (t_c and t_b), respectively. The best result for the coloration efficiency (CE), or colored area per absorbance unit per consumed coulomb, was for the blue device with higher ΔT_{600nm}, which showed a value of 136 cm^2/C (versus the 80 cm^2/C for the purple device), which corresponded with the higher effective charge density (ΔQ_{redox}) with a value of 8.92 C/cm^2 (versus 6.82 C/cm^2 for the purple device), parameter related with the coloration level and the applied voltage, showing a linear increment from the threshold value, from which the coloration change in the devices starts. The plastic supports device showed a value of 64% for ΔT_{600nm} with 13 and 18 seconds for t_c and t_b respectively, with CE of 122 cm^2/C and ΔQ_{redox} of 7.35 C/cm^2.

The variation of the thickness of the internal layer resulted directly to a variation of ΔT_{600nm}, due to the different amount of color centers formed upon the electrochemical redox reaction. The EEC model derived from fitting process of the results of the EIS experiments was applied for the different thicknesses devices. As a difference with the PEDOT based EC devices, where the impedance of the colored states increased with the coloration state, respect to the bleached state, in the viologen based EC devices, the impedance of the colored states decreased, respect to the bleached state. This difference is due to the different electrical properties of the different materials. The PEDOT based devices are conductor polymers losing part of their conductivity when coloring. The viologen based device, more conductive in the colored state, corresponding to their radical cation form, loss the part of their conductivity in their bleached state, corresponding to their dication form. An increment of the double layer capacitance and a decrement of the charge transfer resistance, together with the charge diffusion impedance, are observed in these viologen based EC devices with the coloration state. Voltammograms revealed peak voltages matching with a peak in the diffusion

impedance. The electrical current measured in the CV shows a decrement related with a slight increment of the diffusion impedance, at voltages close to the peak voltages.

Regarding the SPD samples, the prediction of the optical behavior in these devices, simulated for different thicknesses, once obtained the scattering and absorption coefficients by means of the new developed method, showed that the used thickness was close to the optimum thickness, being possible to slightly enhance the darken and bleached states by means of a slight decrement of the internal layer thickness. This method can also be used for other smart windows technologies such it is the case of the PDLC devices.

In the case of the PDLC devices, the parameters derived from the EEC mode, such as the dipolar displacement resistance (Rd) or the double layer capacitance (Cdl), showed respectively an increment and a decrement with the internal layer thickness and with the active area size. The electrical current consumption was lower, with the same level of applied AC voltage signal, for the lower size and lower thickness PDLC device, concluding that it should be necessary to perform new total and diffuse transmittance contrast with higher amplitudes of the feeding signal for the thicker devices, in order to improve the transparent transmission state, currently with too much scattering.

Eight JCR journal publications, and another in revision process, have been the research result developed in this work. Four of them were published in the journal "Solar Energy Materials and Solar Cells" (SEM&SC), placed in the first quart by impact factor order. The other journals were "Optical Engineering", "Optoelectronic Review", "Microwave and Optical Technology Letter" and "Displays". From the eight publications, four of them are referred to PEDOT based EC devices, two for viologen based EC devices, and two for SPD devices. The other publication, currently in revision process in SEM&SC, is referred to the collaboration with Angstrom Laboratory concerning to the S and K determination for a SPD sample. Besides to the journal publications, different contributions of the author to different international conferences can be found, such as the 6^{th}, 7^{th}, 8^{th} and 9^{th} International Meeting on Electrochromism (IME) from 2004 (Brno, Czech Republic), 2006 (Istanbul, Turkey), 2008 (Seoul, South Korea) and 2010 (Bordeaux, France) respectively, Microtechnologies for the New Millenium Symposium of Photonics and Optoelectronics (SPIE) in 2005 (Seville, Spain), International Commission for Illumination (CIE) Expert Symposium on Advances in Photometry and Colorimetry in 2008 (Turin, Italy), Electrochromic Materials and Devices Symposium of Material Research Society (MRS) in 2011 (San Francisco, USA) and New Trends in Chromogenic Materials and Devices Symposium of European MRS in 2011 (Warsaw, Poland). Among the national contributions, the author contributed to the 4^{th}, 5^{th}, 6^{th} and 7^{th} Spanish Meeting of Optoelectronics (OPTOEL) in 2005 (Elche), 2007 (Bilbao), 2009 (Malaga) and 2011 (Santander), respectively, the 7^{th} National Conference of Color in 2007 (Madrid) and the 6^{th} Spanish Conference of Electronic Devices (CDE) in 2007 (El Escorial). Some of these contributions derived to publications.

Resumen

Caracterización y aplicaciones de nuevos dispositivos electrocrómicos. Comparativa con otras tecnologías de transmitancia controlable eléctricamente

por

David Barrios Puerto
PhD de Ingeniería Eléctrica, Electrónica y Automática

Universidad Carlos III de Madrid, Departamento de Tecnología Electrónica,
Grupo de Displays y Aplicaciones Fotónicas (GDAF)

Los materiales electrocrómicos (EC) son capaces de cambiar sus propiedades ópticas, como el color, en una forma persistente y reversible bajo la acción de un pulso de pequeño valor de voltaje constante. Actualmente, los dispositivos electrocrómicos (ECD) son, junto a los dispositivos de partículas suspendidas, los cristales líquidos dispersos en polímero (PDLC) y las micro-persianas, las cuatro tecnologías de ventanas inteligentes eléctricamente controlables. No siendo únicamente utilizadas con la finalidad de apariencia óptica, el uso de estas tecnologías podría reducir el coste de calefacción, aire acondicionado y de iluminación, debido al ahorro energético que se puede llevar a cabo en edificios y vehículos, lugares donde la gente de hoy en día suele emplear alrededor del 90% de su tiempo.

Estas tecnologías de transmitancia variable permiten la conmutación óptica desde un estado transparente o aclarado, a un estado coloreado, oscuro o, en otros casos, translúcido, mediante diferentes principios de operación. En todos los casos estas tecnologías requieren la utilización de conductor transparente. Entre otras aplicaciones de estas tecnologías se pueden encontrar espejos y pantallas.

Los ECDs para aplicaciones arquitectónicas incorporan capas EC sólidas y consisten en una delgada estructura de sándwich de multicapas rodeadas de dos paneles de cristal. La coloración de las capas anódicas y catódicas tiene lugar debido a un proceso electroquímico de oxidación y de reducción, respectivamente, en el cual existe una transferencia de iones hacia dentro y hacia fuera de las capas EC, las cuales requieren de un componente donde los iones son almacenados. Entre los materiales que muestran el efecto de electrocromismo se pueden encontrar los óxidos de metales de transición, tales como los complementarios WO_3 (óxido de wolframio) y NiO (óxido de níquel), catódico y anódico respectivamente, los sistemas de Azul Prusiano, viológenos, polímeros conductores y metales de tierras raras dentro de la Tabla Periódica. Dentro de la segunda tecnología de ventanas inteligentes, los SPDs incorporan una capa activa que contiene partículas bipolares con forma de aguja uniformemente distribuidas en un fluido o película orgánica. La capa activa es laminada entre dos conductores transparentes y poliéster. El cambio de las propiedades ópticas es causado por el

movimiento y orientación de las partículas dispersas relativo al fluido, bajo la aplicación de una señal alterna de potencial eléctrico de gran amplitud. La tecnología de ventanas inteligentes basada en cristales líquidos (LC) ha sido ya utilizada en edificios, estando algunos productos actualmente disponibles en el mercado. Los PDLCs, o acristalamientos de LC, consisten en dos capas exteriores de poliéster que están cubiertas de un conductor transparente y una matriz de poliéster que contiene los LCs. Cuando no se aplica voltaje, las cadenas de moléculas de LC están aleatoriamente dispersadas y el sistema muestra una apariencia opaca translúcida blanquecina. Cuando se aplica una señal alterna de potencial eléctrico de mediana amplitud, las moléculas se alinean con las líneas del campo eléctrico y la apariencia de la película se muestra casi transparente.

En este trabajo, diferentes muestras de nuevos ECDs, SPDs y PDLCs han sido caracterizadas electro-ópticamente. Las muestras de ECDs y PDLCs fueron desarrolladas por CIDETEC, un Centro de Investigación y Desarrollo Electroquímico situado en San Sebastian (España). Las muestras de SPDs fueron suministradas por la empresa Cricursa S.A. Cristales Curvados de Barcelona (España).

La caracterización óptica se realizó mediante medidas de transmitancia directa espectral y en el dominio temporal en la región de longitud de onda visible de la luz, aplicando o no el voltaje eléctrico requerido para cada tecnología de transmitancia controlable. Las Coordenadas de Cromaticidad e Iluminancia CIE 1931 Yxy y los valores del el espacio de color sRGB fueron obtenidos a través de las medidas ópticas aplicando técnicas de colorimetría. La apariencia visual de las muestras fue simulada mediante los valores RGB calculados y la curva de sensibilidad del ojo humano. La irradiancia y la temperatura de color correlacionada de la lámpara utilizada en el espectrómetro fueron medidas en el Departamento de Metrología del Instituto de Física Aplicada del Consejo Superior de Investigaciones Científicas CSIC-IFA. La fuente de luz calibrada fue útil para medidas absolutas.

Se propuso un modelo de circuito eléctrico equivalente (EEC) para los diferentes dispositivos mediante la caracterización de impedancia eléctrica utilizando la técnica de espectroscopía de impedancia electroquímica (EIS). Debido a que para la coloración de las muestras de ECDs se requiere de una pequeña señal continua de voltaje, el modelo de EEC fue propuesto para los estados aclarados, coloreados e intermedios, aplicando diferentes niveles de señal de voltaje continua. Un modelo de EEC, basado en el circuito de Randles, fue determinado mediante un proceso de ajuste en el cual se identificó la resistencia de los contactos (Rs), la capacidad de doble capa (Cdl), la resistencia de transferencia de carga (Rct) y una impedancia de Warburg (W), esta última representando al proceso de difusión de las cargas. La evolución de los componentes del modelo de EEC fue relacionada con los principios físico-químicos que afectan a los ECDs en el proceso coloración.

Técnicas electroquímicas de cronoamperometría (ChrA), cronocoulometría (ChrC) y voltametría cíclica (CV) fueron llevadas a cabo de manera simultánea a la medición de la

transmitancia óptica de las muestras de ECDs, revelando información de las reacciones redox y de la carga eléctrica consumida requerida para el estado coloreado. Se analizaron algunos parámetros útiles para el criterio de evaluación de los ECDs, tales como la eficacia de coloración, la eficacia de escritura-borrado, la densidad de carga efectiva, tiempos de respuesta para los procesos de coloración y aclarado, el contraste de transmitancia y las corrientes y tensiones de pico.

Dos tipos de muestras orgánicas de ECD, basadas en PEDOT y basadas en viológenos, fueron caracterizadas en este trabajo. Se analizó la simetría del comportamiento óptico, al aplicar señales de tensión continua de ambas polaridades, para diferentes muestras de dispositivos EC basados en PEDOT en un soporte de plástico y con un número de capas menor que el normalmente usado en la estructura de sándwich de un ECD. Se llevó a cabo la caracterización óptica de dispositivos en soporte de cristal y en soporte de plástico, basados en material EC viológeno, que mostraron un gran contraste de transmitancia y conmutación desde un estado incoloro a un tono de coloración azul y púrpura. Se estudió además la dependencia de los parámetros con el espesor de la capa interna de distintas muestras de dispositivos en soporte cristal en material EC viológeno con conmutación a color azul. Los resultados de los experimentos de ChrA, ChrC, CV y EIS fueron relacionados con las medidas de transmitancia espectral a los distintos niveles de coloración para cada espesor de los dispositivos, y por tanto para cada cantidad diferente de centros de color formados en cada muestra. Para las muestras de SPDs y PDLCs, como se requiere de una señal alterna de gran amplitud para conmutar al estado transparente, el modelo de EEC fue determinado solamente para el estado oscuro de las muestras de SPD, y para el estado translúcido de las muestras de PDLC.

Con respecto a la muestra de SPD, como el efecto de dispersión está presente intrínsecamente en esta tecnología, se consideró relevante el desarrollo de un método para aproximar los coeficientes de dispersión y absorción, el cual fue desarrollado en colaboración con la División de Física de Estado Sólido del Departamento de Ciencias de la Ingeniería del Laboratorio Angstrom de Uppsala (Suecia). Se realizaron medidas totales y difusas de transmitancia y reflectancia (T y R) en la región solar de longitudes de onda, comprendiendo principalmente la región visible y la de infrarrojo cercano, mediante la utilización de un espectrómetro que incorpora una esfera integradora. El método, desarrollado en Matlab, se basó en los modelos de dos y cuatro flujos, junto a la corrección de Saunderson para las discontinuidades del índice de refracción, y utilizando valores espectrales de la reflectancia a las distintas interfases que se obtuvieron mediante el ajuste del índice de refracción a las componentes colimadas de T y R. Mediante el ajuste de los coeficientes de dispersión y de absorción, se pudieron estimar, para distintos espesores, los valores totales y difusos, y por tanto las componentes directa y especular, de T y R respectivamente. Además se determinó el valor óptimo del espesor así como la proporción de componente difusa sobre el total, a partir de los valores extensivos de los coeficientes de dispersión y absorción (S y K) derivados del modelo de dos flujos de Kubelka-Munk (KM).

Diferentes muestras de PDLCs con diferentes áreas activas y diferentes espesores de la capa interna, con modos de funcionamientos normal y reverso (es decir, estado translúcido sin tensión y transparente con tensión y viceversa), fueron desarrolladas por CIDETEC. La transmitancia total y difusa fue medida en ambos estados de apariencia óptica utilizando un espectrómetro basado en esfera integradora de dos puertos disponible (para medida de T y R total y de T difusa) en los laboratorios de CIDETEC. Estas medidas fueron comparadas con las realizadas utilizando una esfera integradora de un solo puerto (para medida de T total), disponible en los laboratorios de GDAF-UC3M. La medida de T difusa se obtuvo restando a la T total la medida de T directa realizada sin la esfera integradora. Además se realizó las medidas de T y R total y difusa de ocho muestras de dos distintos tamaños y cuatro distintos espesores, utilizando el espectrómetro basado en esfera integradora de tres puertos disponible en el Laboratorio Angstrom.

El método de caracterización de scattering desarrollado y nuevas futuras mejoras sobre dicho método serán considerados como futuras líneas de investigación sobre los dispositivos SPD y PDLC caracterizados en este trabajo. Entre los trabajos futuros se encuentran por ejemplo, la difícil tarea de desemparejar los coeficientes de extinción o atenuación (derivados de la ley de Lambert-Beer) en los coeficientes intrínsecos de dispersión y absorción (α y β), obteniendo los valores espectrales de los parámetros "proporción de dispersión hacia delante" (FSR) y "promedio del camino cruzado" (ACP), derivados del modelo de cuatro flujos de Maheu, Le Toulouzan y Gouesbet (MLG). También como trabajo futuro y en colaboración con el Laboratorio Angstrom, se estudiará la obtención de S y K a partir de las constantes ópticas de la herapatita (material presente en los dispositivos SPD) así como de la geometría de las partículas dispersas. Como resultado de otra colaboración con un grupo de investigación extranjero, en este caso el Laboratorio de Espectroscopía de Materiales del Instituto Nacional de Química de Eslovenia, situado en Liubliana, se realizará la caracterización electro-óptica de dispositivos EC inorgánicos desarrollados por dicho centro utilizando WO_3 y NiO para las capas EC catódica y anódica respectivamente, las cuales conmutan desde una apariencia incolora hasta un tono de coloración azulado y marrón respectivamente. Al usarlas de forma conjunta en un dispositivo, la apariencia de los estados observados varía desde una apariencia incolora, de los estados aclarados, a un tono de coloración grisáceo, en los estados coloreados. El nivel de coloración aumenta con el espesor de las dos capas activas, pero a su vez también aumenta la dispersión de la luz, parámetro no deseado. El espesor óptimo de dichas capas será estudiado mediante la determinación de los coeficientes de dispersión y absorción S y K para cada una de las capas que cambian de color.

Como líneas de investigación futuras para los PDLC, se determinarán los coeficientes de dispersión y absorción mediante el método desarrollado en el presente trabajo para la muestra de SPD. Futuras mejoras de dicho método también podrán ser objeto de estudio para las muestras de PDLCs. Así mismo, un dispositivo tándem de tecnologías PDLC y

EC, fue desarrollado por CIDETEC y electro-ópticamente caracterizado en este trabajo, permitiendo un control de transparencia y de coloración. Cuatro distintos estados fueron principalmente observados: estado translúcido incoloro, estado transparente incoloro, estado transparente coloreado y estado translúcido coloreado. El modelo de EEC fue determinado para cada parte de forma separada (PDLC y EC), mediante la técnica EIS.

Entre las aplicaciones desarrolladas para las tecnologías cromogénicas estudiadas, cuatro casos distintos fueron aplicados. La primera aplicación consistió en el desarrollo de unas nuevas gafas con filtros EC para personas con baja visión, mezclando los filtros EC estudiados en este trabajo, con las lentes fotocrómicas oftalmológicas recomendadas por IOBA, Instituto de Oftalmobiología Aplicada de la Universidad de Valladolid (España), con la finalidad de determinar las mejor posibilidad entre los distintos casos de conmutación entre los colores logrados para cada paciente con baja visión. La segunda aplicación consiste en un atenuador óptico variable (VOA) basado en dispositivos EC para control de atenuación en sistemas de comunicaciones ópticas a las distintas longitudes de onda de las ventanas de transmisión (850, 1310 y 1550 nm). Como tercera aplicación, y basada en el Proyecto de Fin de Carrera del autor de este trabajo, realizado en el año 2002, se desarrolló un software de control domótico de forma local o remota, de la transparencia de ventanas inteligentes de tecnología PDLC. El control remoto, de chequeo y conmutación, se desarrolló mediante una aplicación cliente servidor basada en "sockets". La aplicación cliente fue programada en Macromedia Flash y la aplicación servidor fue programada en java, la cual utilizó el estándar de domótica Zigbee. Finalmente, la cuarta aplicación desarrollada consistió en un caracterizador electro-óptico de dispositivos EC basado en una tarjeta de adquisición de datos de National Instruments y programadao en Labview, incluyendo un par de fotodiodos RGB y una caja de pequeño tamaño para su manejabilidad y portabilidad. El sistema es capaz de medir simultáneamente la corriente eléctrica y la transmitancia óptica en los tres rangos de longitud de onda correspondientes a los fotodiodos RGB, a la vez que el mismo sistema aplica diferentes señales de voltaje, como las señales triangular o cuadrada requeridas para los experimentos de CV o de ChrA respectivamente.

Distintas conclusiones pueden extraerse para cada tecnología cromogénica estudiada en este trabajo. Para los dispositivos EC basados en material PEDOT, se comprobó la simetría del comportamiento óptico para niveles de tensión positivos y negativos, así como se determinó un modelo de EEC para los distintos niveles de coloración correspondientes a cada nivel de tensión continua aplicada. En estos dispositivos se pudo comprobar que al aumentar la coloración, se producía un aumento de la resistencia de la transferencia de carga y de la impedancia de difusión, acompañado de un decremento de la capacidad de doble capa. Los problemas de sellado y burbujas, reflejados en el modelo de EEC mediante un conjunto resistencia en paralelo con un condensador, así como la resistencia de los contactos, mostraron un comportamiento independiente del estado de coloración. Esto puede servir como comprobación de errores de fabricación en dispositivos mayores.

En el caso de los dispositivos EC basados en material viológeno, con soporte cristal o de plástico, los diferentes parámetros de evaluación mostraron distintos resultados para los distintos dispositivos estudiados. Para los dispositivos de soporte en cristal, los mejores resultados de contraste de transmitancia directa a 600 nm (ΔT_{600nm}), en torno al 72% (conmutando a color azul), no se correspondieron con los mejores resultados de tiempos de respuesta, que se obtuvieron para dispositivos de menor ΔT_{600nm} (conmutando a color púrpura), en torno al 57%, con 7 y 8 segundos para los procesos de coloración y aclarado (t_c y t_b) respectivamente. El mejor resultado para la eficacia de coloración (CE), o área coloreada una unidad de absorbancia por cada culombio consumido, fue para el dispositivo azul con mayor ΔT_{600nm}, el cual mostró un valor de 136 cm^2/C (frente a 80 cm^2/C para el púrpura) que se correspondió con el de mayor densidad de carga efectiva (ΔQ_{redox}) con un valor de 8.92 C/cm^2(frente a 6.82 C/cm^2 para el púrpura), parámetro que se relacionó con el nivel de coloración y el nivel de voltaje aplicado, mostrando un aumento lineal a partir de la tensión de umbral a partir de la cual se empezó a observar cambio de coloración en los dispositivos. El dispositivo de soporte de plástico obtuvo un valor de ΔT_{600nm} del 64% con 13 y 18 segundos de t_c y t_b respectivamente, con CE de 122 cm^2/C y ΔQ_{redox} de 7.35 C/cm^2.

La variación del espesor de la capa interna se reflejó directamente en la variación del ΔT_{600nm} debido a la cantidad de centros de color formados bajo la reacción electroquímica de oxidación reducción. El modelo de EEC derivado del proceso de ajuste de los resultados de los experimentos EIS fue aplicado para los distintos dispositivos de distintos espesores. A diferencia de los dispositivos EC basados en PEDOT, donde la impedancia de los estados coloreados aumentó con el estado de coloración, con respecto al estado aclarado, en los dispositivos EC basados en viológenos la impedancia de los estados coloreados disminuyó con el estado de coloración, con respecto al estado aclarado. Esta diferencia se debe a las distintas propiedades eléctricas de los distintos materiales. Los basados en PEDOT son polímeros conductores que al colorearse pierden parte de su conductividad, frente a los basados en viológenos, que son más conductores en su estado coloreado, correspondiente a su forma radical catión, frente a su estado aclarado, correspondiente a su forma dicatión. En estos dispositivos basados en viológenos se observa un aumento de la capacidad de doble capa y un decremento de la resistencia de transferencia de carga, así como de la impedancia de la difusión de cargas, con el aumento del estado de coloración. Los voltamogramas revelaron unas tensiones de pico en las cuales se observa un pico de la impedancia de difusión. La corriente eléctrica medida en CV muestra un decremento relacionado con un ligero aumento de la impedancia a la difusión, cercano a las tensiones de pico.

Con respecto a las muestras de SPD, la predicción del comportamiento óptico de estos dispositivos, simulada para distintos espesores, una vez obtenidos los coeficientes de dispersión y de absorción por el nuevo método desarrollado, reveló que el espesor utilizado estaba cercano al espesor óptimo, pudiendo ser ligeramente mejorados los estados aclarados y oscurecidos, mediante una ligera disminución del espesor de la capa

interna. Este método también puede ser utilizado para otras tecnologías de ventanas inteligentes, tal como es el caso de los dispositivos PDLC.

En el caso de los dispositivos PDLC, los parámetros derivados del modelo de EEC, tales como la resistencia al desplazamiento bipolar o la capacidad de doble capa, muestran respectivamente un incremento y un decremento con el espesor de la capa interna y con el tamaño del área activa. El elemento de difusión muestra un aumento capacitivo para mayor tamaño y menor espesor, siendo la resistencia de los contactos independiente del tamaño y del espesor. Con el mismo nivel de tensión alterna aplicada, el consumo de corriente fue mayor para el dispositivo de menor tamaño y de menor espesor, concluyendo que es necesario realizar nuevas medidas de contraste de transmitancia total y difusa para mayores amplitudes de la señal de alimentación en los dispositivos de mayor espesor, a fin de mejorar el estado de transmisión transparente, aún con demasiada dispersión.

Ocho publicaciones en revistas de alto impacto JCR, más otra en proceso de revisión, han sido el resultado de la investigación desarrollada en el presente trabajo. Cuatro de ellas han sido publicaciones en la revista "Solar Energy Materials and Solar Cells" (SEM&SC), situada en el primer cuarto por orden de factor de impacto. Las otras revistas JCR son "Optical Engineering", "Optoelectronic Review", "Microwave and Optical Technology Letter" y "Displays". De las ocho publicaciones, cuatro de ellas se refieren a dispositivos EC basados en PEDOT, dos en viológenos y otras dos en dispositivos SPD. La otra publicación, actualmente en revisión en SEM&SC, se refiere a la colaboración realizada en el Laboratorio Angstrom referente a la determinación de S y K para un dispositivo SPD. Aparte de las publicaciones en revista JCR, distintas contribuciones a congresos, como el 6º, 7º, 8º y 9º IME ("International Meeting on Electrochromism") o Congreso Internacional de Electrocrómicos, celebrados en 2004 (Brno, República Checa), 2006 (Estambul, Turquía), 2008 (Seúl, Corea del Sur) y 2010 (Burdeos, Francia), respectivamente, Microtechnologies for the New Millenium Symposium of Photonics and Optoelectronics (SPIE) en 2005 (Sevilla, España), Comisión Internacional de Iluminación (CIE) Expert Symposium on Advances in Photometry and Colorimetry en 2008 (Turín, Italia), Electrochromic Materials and Devices Symposium of Material Research Society (MRS) en 2011 (San Francisco, USA) y New Trends in Chromogenic Materials and Devices Symposium del MRS Europeo en 2011 (Varsovia, Polonia). Entre las contribuciones a congreso nacional, el autor participó en la 4ª, 5ª, 6ª y 7ª Reunión Española de Optoelectrónica (OPTOEL) celebradas en 2005 (Elche), 2007 (Bilbao), 2009 (Málaga) y 2011 (Santander), respectivamente, el 7º Congreso Nacional de Color en 2007 (Madrid) y el 6º Congreso de Dispositivos Electrónicos (CDE) celebrado en 2007 (El Escorial).

Chapter I: Introduction

This chapter is divided in two parts, being the first part a detailed state of the art of electrically controllable transmittance materials and electrochromic (EC) devices, and a second part including the motivation, objectives and outline of this thesis.

I.1 A state-of-the-art: Electrically controllable transmittance materials and electrochromic devices

Some 'smart' materials, known as chromogenic materials, allow the variation of the transmitted, reflected or scattered light passing through them by the application of an external stimulus. The main application of these materials is found for windows in large area glazing in buildings, automobiles and planes. Switchable mirrors, displays and other applications are also considered [Lam04].

I.1.1 Glazing and coatings

The energy consumption for heating, cooling and lighting of buildings (which is around 30-40% of the primary energy used in the world) can be reduced by using 'smart' windows technologies [Gra99]. Thus, considerable energy savings can be achieved by using chromogenic technologies, nowadays necessary due to the problem of the global warming [Gra11a]. Around 19-26% in solar heat gain and 48-67% in lighting energy would be saved by using smart windows [Gra10a], instead of the conventional windows, which are the less energy efficient component in buildings [Bae10]. In this regard, low-emittance (low-e) windows have been considered a first solution in winter periods, since they let passing the short-wave solar radiation (from 0.3 to 3 μm wavelength) and cut the long-wave radiation (from 3 to 50 μm wavelength), corresponding to the heated objects in the Earth, such as the warm inside of a house achieved by heating systems (Figure I.1 [Gra01]). However, low-e windows are not energy efficient in summer periods since objects inside buildings are heated by warm solar rays rather than by heating systems, being air-cooling systems necessary in this case (Figure I.2, [ios]).

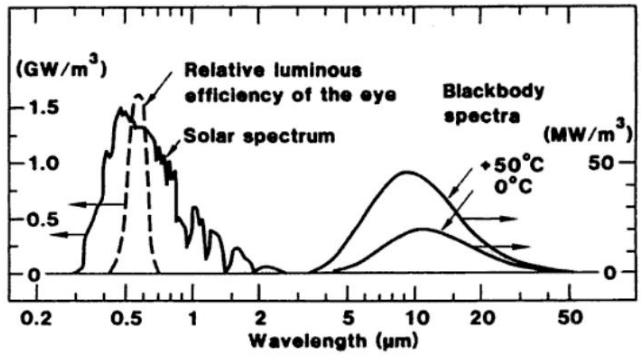

Figure I.1: Spectra for black-body radiation at two temperatures, the solar radiation that passed through the Earth's atmosphere, and the sensitivity of the human eye [Gra01].

Since ambient radiations are spectrally selectable, angular dependent and time variable [Gra07, Gra11a and Gra11b], a transparent 'long-wave' insulator coating (such as in static low-e windows) is not enough since glazing must be also energy-efficient. A 'smart' window must control the flow of light and heat into and out of a glazing in order to improve the comfort of the occupants. Transmission, absorption and infrared (IR) emission must be selective in coatings and surface treatments for static or dynamic energy efficient windows [Gra89]. To the ends mentioned above, control of visible radiation (for lighting energy savings) and control of IR radiation (for cooling and heating energy savings) could be accomplished by chromogenic technologies [Gra10b]. Chromogenic materials can increase above 30% energy savings over conventional glazing [Lam98].

Figure I.2: Low-e windows insulating 'long-wave' radiation [ios].

I.1.2 Chromogenic materials

According to the relationship of energy conservation (R+A+S+T=1), also known as Kirchhoff's law, when an electromagnetic radiation, as it is the case of solar radiation, strikes a surface (Figure I.3), it may be reflected (R), scattered (S), absorbed (A) or transmitted (T). Chromogenic materials are able to control any of these four parameters by means of different external stimulus. Hence, measurements of reflectance, transmittance and scattering must be carried out in order to characterize these materials, being the magnitude of the absorptance derived from the previous relationship.

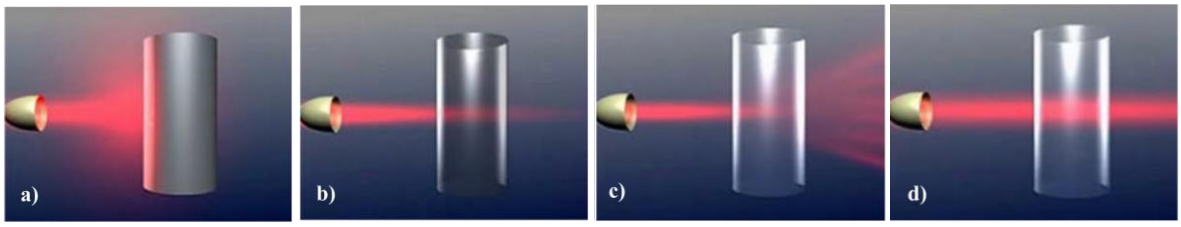

Figure I.3: Reflection (a), Absorption (b), Scattering (c) and Transmission (d) [Men08].

Four different chromogenic technologies with external stimulus triggering signal are commonly known for this purpose and indeed are or start to be available at the market:

- Chromic materials (Electrochromic (EC) materials)
- Electrophoretic or suspended particle devices (SPD)
- Liquid crystals (LC) (Polymer dispersed liquid crystals (PDLC))
- Micro-blinds

- Chromic materials change their color in a reversible way by the application of an external stimulus. Color change is caused by a transition of electrons to a higher energy orbital in the region of the molecule called chromophore, which is the part of the molecule responsible of its color, since it absorbs certain wavelengths of visible light and transmits or reflects others. EC materials are electrically controlled chromic materials, where the optical properties changes are caused by a small electrical DC voltage or charge in an electrochemical reduction-oxidation (redox) reaction (Figure I.4). EC materials change their opacity from a transparent bleached state to a transparent/translucent colored state when applying a small DC voltage signal.

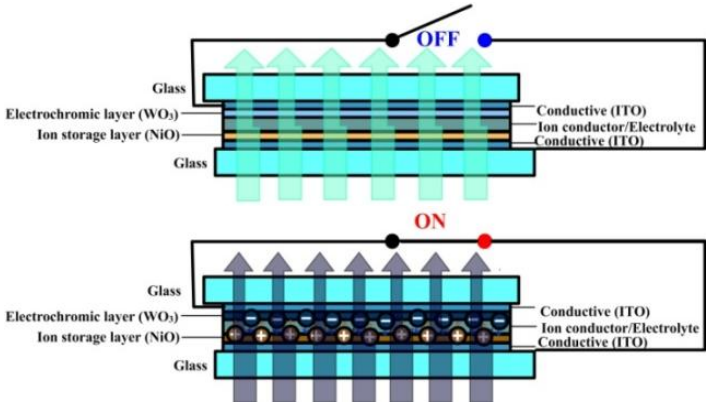

Figure I.4: Sandwich structure and principle of operation of an EC smart window in bleached OFF (up) and colored ON (down) states.

- Electrophoretic SPD technology uses the movement up and down of bluish-black colored absorption particles that are suspended in a cross linked polymer matrix to control light transmission when applying an AC voltage signal (Figure I.5).

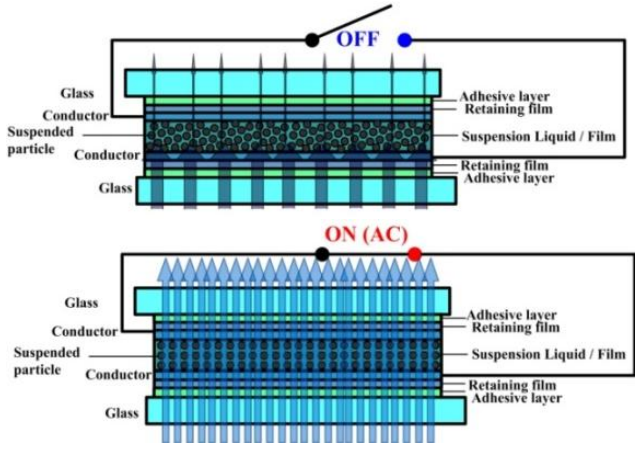

Figure I.5: Sandwich structure and principle of operation of a SPD smart window in darken OFF (up) and clear ON (down) states.

- The amount and spectrum of light crossing the LC is controlled using its molecular axis orientation to turn the polarization of the incoming light. By changing the orientation of the LC molecules placed between two conductive electrodes with the electric field it is possible to vary the intensity of transmitted light, as it is the case of switchable devices based on LC. A PDLC consists of microscopic nematic LC spheres, known as droplets, dispersed in a polymer matrix (Figure I.6). These droplets scatter incoming light resulting in a milky white appearance. LC molecules are oriented allowing light transmission instead of scattering when applying an AC voltage signal.

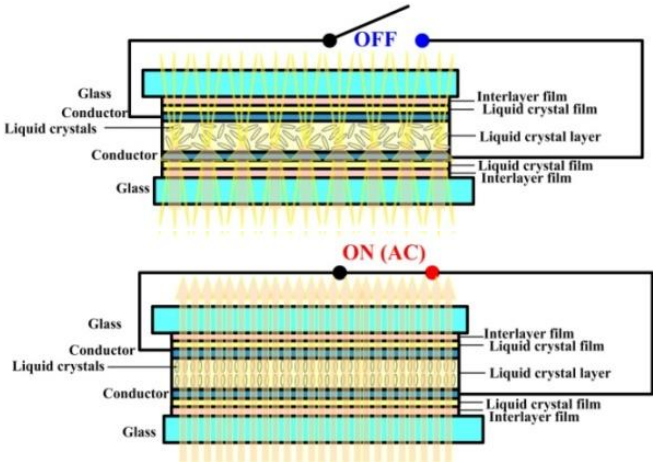

Figure I.6: Sandwich structure and principle of operation of a PDLC smart window in translucent OFF (up) and transparent ON (down) states.

- Micro-blinds are composed of very small rolled thin metal blinds on conductive glass practically invisible to the eye (Figure I.7). With no applied potential they are rolled and let light pass through, stretching out and thus blocking light when a potential difference is applied between the curling electrodes blinds and the transparent conductive oxide (TCO) of the glass.

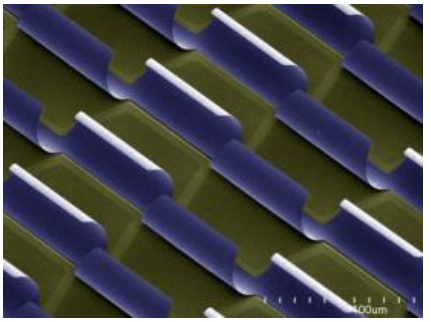

Figure I.7: Scanning Electron Microscope (SEM) of micro-blinds [nrc].

To mention two examples of the possibilities of chromogenic materials in glazing applications, a study of EC windows in warm climates showed a better energy saving strategy if the EC remains in the bleached state during the heating season, being controlled according to daylight illuminance during the cooling season [Sul96]. On the other hand, in accordance with Lawrence Berkeley National Labs, in California, which is part of the US Department of Energy (DoE), a 20% is the difference of annual energy savings achieved (30% in peak demand) by using dynamic windows compared to low-e glass (currently used to control solar heat gain through windows into buildings) [ESL06, ESL11 and SVB11]. Three of these four chromogenic technologies use transparent conductors (being micro-blinds the exception).

I.1.3 Transparent conductors

Chromogenic technologies use transparent conductive coatings or transparent conductors (TCs) to achieve the electrical control for many applications, such as flat panel displays (like plasma displays, liquid crystal displays (LCDs) and organic light-emitting diodes (OLEDs) displays), touch panels, electronic ink, solar cells, antistatic coatings and electromagnetic interference (EMI) shielding [Lam90], as well as for 'smart' windows or IR reflecting coating to reflect heat energy in low-e windows, improving the thermal properties of modern fenestration [Gra07a]. The high transparency and the low resistivity of the TCs make them useful as current collector in solar cells and for inserting and extracting electrical charge in EC 'smart' windows, being this lower resistivity less necessary for PDLCs and electrophoretic SPDs than for EC devices. Simultaneous solar cells and 'smart' windows applications are photovoltaic powered EC windows [Deb00], where TCs are double used. Electrodes on both sides of the cell gap of TFT (thin field transistor) LCDs and touch screen displays are also made from TCs.

Currently, the best combination of transparency and conductivity is tin-doped indium oxide In_2O_3:Sn or more commonly known as ITO, a mixture by weight of 90% indium oxide (In_2O_3) and 10% tin oxide (SnO_2). Belonging to the inorganic TC oxides (TCOs), ITO is the most widely used TC in all kind of devices, showing very low value of resistivity (0.0001 Ω cm), high level of transmittance (>90%) and IR reflectance. The main drawback of ITO is its expensive price since indium is rare. Among the TCOs (replacing indium with heavily doped conductors, wide band gap and thickness of ~200 nm [Gra11b]) some examples are SnO_2:F (FTO), ZnO:Al (AZO)or ZnO:Ga (GZO) and TiO_2:Nb (TNO). It is expected that the 90% of the market of capacitive touch screens and smart phones would use ITO or other TCOs by 2016 [Nan09]. The alternatives to ITO and TCOs are organic polymers and nanomaterials.

Among the organic polymers, poly(3,4-ethylenedioxy-thiophene) or PEDOT has several advantages over ITO such as its flexibility, easily printed and the lower price cost. With better transmittance but higher resistivity than TCOs, PEDOT can improve their properties by doping with poly(styrene sulfonate) or PSS, resulting in a water soluble

PEDOT:PSS, which is the leader in transparent conducing polymers, with a resistivity from 0.0017 to 0.0025 Ω cm and transmitting around 80% of visible light. Other polymers, such as PEI-LiTFSI with SiO_2 nanoparticles, obtain an increment of the ion conductivity without increment of light scattering [Gra11b]. Among the nanomaterials, one-dimensional conducting polymers nanostructures of conjugated polyaniline (PANI), polypyrrole (PPY) and PEDOT shows good physical properties for this end [Yun11]. Carbon nanotubes (CNTs) layers are also a promising option due to their high conductivity and transmittance over 90% in the range 400 nm - 22 µm. As hybrids of the renowned one atom thick planar *graphene* (Nobel Prize in Physics for 2010, Figure I.8), CNTs are good TCs with transparency and absence of haze in NIR region and they have been already used in some EC devices instead of ITO, improving electrochemical stability, optical contrast and better switching times [Zha09 and Dee10]. Since a single sheet of *graphene* is a zero-band gap semiconductor with extremely high carrier mobility that only absorbs 2.3% of visible light, it may be a viable candidate for applications as a TC [Was10].

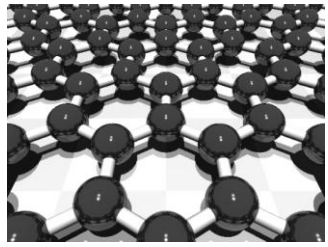

Figure I.8: "for groundbreaking experiments regarding the two-dimensional material graphene", Nobel Prize in Physics for 2010, Andre Geim and Konstantin Novoselov [Gei09].

I.1.4 Electrochromism

Electrochromism is defined as the reversible change in optical properties when a material is electrochemically oxidized or reduced. This phenomenon is known since 1968 [Deb69] and it is not only referred to visible color changes but also in the NIR, thermal IR and microwave regions and `color' can mean response of detectors of these wavelengths, not just for the human eye. Commercial interest in electrochromism is mainly centered on windows, mirrors and displays. EC devices (ECDs) use to have a two terminal electrochemical cell configuration and at least one optically transparent electrode is used [Rau99]. A certain charge of mC/cm^2 is required for achieve an appreciable change in the optical state. In order to decrease the power consumption to the order of LCDs and light modulators ($\mu C/cm^2$), ECDs should use materials with very high coloration efficiencies [Rau00].

To show the advantage of EC technology on glazing, Figure I.9 shows a study of cooling versus electric lighting energy of ‘smart’ windows technologies was carried out by Madison Gas and Electric Company comparing three chromic technologies by the improvement of the energy consumptions with other three static options [Gra09 and Gra10a]. Static clear glass is more efficient for lighting than thermal insulation. On the

other hand, static reflective glass improves thermal efficiency with a cost of lighting energy increment. However, dynamic technologies improve both lighting and thermal efficiencies. Photochromic (PhC) and thermochromic (ThC) technologies are good in lighting and thermal efficiencies respectively. Among other chromic technologies [Gre94] used for solar control EC technology results to be the most efficient in both thermal and lighting efficiencies, reducing static tinted glass energy consumption.

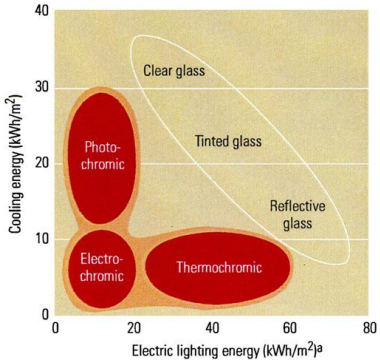

Figure I.9: Lighting and thermal energy efficiencies of static and dynamic technologies [Gra09].

I.1.4.1 Electrochromic devices

EC devices usually consist of seven layers in a sandwich structure, as it is shown in Figure I.10 [Gra06]. Three internal active layers (ion storage or counter electrode, ion conducting layer or electrolyte and EC film or working electrode) are placed between two transparent and electronically conductor electrode layers. Other two glasses or plastic substrates are placed externally in order to protect these five layers. All these layers must be as much transparent as possible, for visible EC applications. A redox reaction between two electroactive materials (ion storage and EC film layers) with at least one of them presenting a reversible change in optical properties at oxidation or reduction is needed for EC effect to appear. Electrons or ions moving from or towards the EC film layer must be interchanged with the counter electrode layer crossing the electrolyte layer.

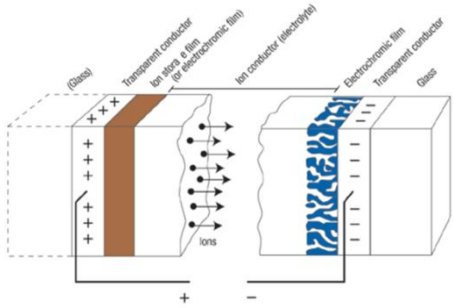

Figure I.10: Sandwich structure of an EC device [Gra06].

The multilayer assembly of a typical EC window requires good electrical contact between the layers. The ion storage or counter electrode layer can be a non-coloring

redox material or a complementary EC film. Other devices, such as displays, show a different or modified construction. The electrolyte may be a polymer adhesive in which the salt is dissolved. The salt can be NaCl, $LiClO_4$ or another salt. For flexible devices, in the place of glass, the ITO coated polymer PET (polyethylene-terephthalate) can be used [Ros01]. The principle of four different applications of ECDs for information display, variable reflectance mirror, smart window and variable emittance surface, is shown in Figure I.11 [Gra95].

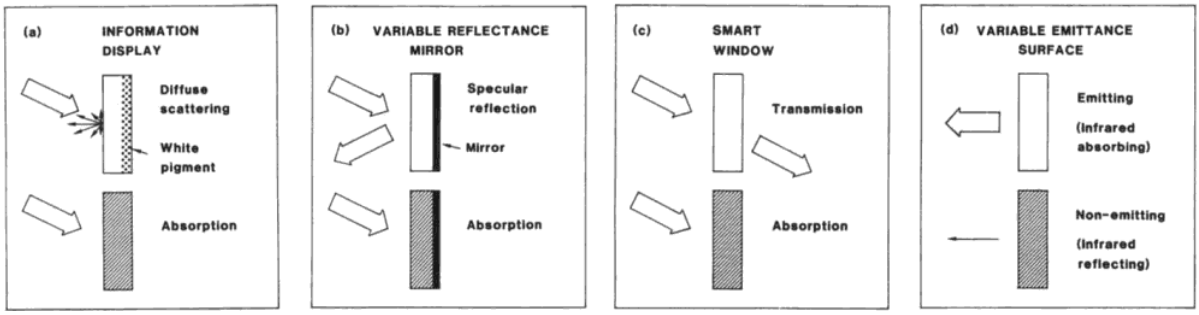

Figure I.11: The principle of four different applications of ECDs, as information display, variable reflectance mirror, smart window and variable emittance surface [Gra95].

I.1.4.2 Configuration of EC windows

Three different types EC windows were classified in terms of the phases present initially and formed electrochemically and directly related to the current-time and coloration-time relationships [Cha75 and Cha81]. There are presently three major EC window configurations that have been demonstrated, as shown in Figure I.12 [Rau99]; solution phase (type I), hybrid structures (type II) and battery-like (type III) [Nik07 and Gra12].

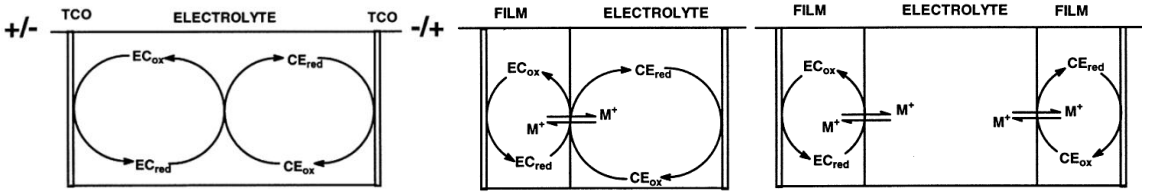

Figure I.12: Schematic illustration of EC window configurations [Rau99]. (left) Type I: Solution, (center) Type II: Hybrid and (right) Type III: Battery-like.

All-liquid electrochromes, liquid/solid and all –solid systems are also references to these three types of configurations [Ros01]. Optically transparent front and back electrodes for delivering current are common to all configurations. A charge balance between the electrodes is required for the stoichiometry of EC windows operation, like for all ECDs. Charge inserted during the cathodic half reaction must be exactly balanced by charge extracted from the anodic side of the device.

The general reaction can be written as:

$$EC^{n} + yCE^{m}\ \text{(bleached)} \leftrightarrow EC^{n-a} + yCE^{m+a/y}\ \text{(colored)}$$

Where EC and CE are primary EC and counter electrode layers, respectively. In complementary EC windows, CE is an anodically coloring EC layer [Rau99].

Type I: Solution.

$$MV^{2+}(aq) + e\ \text{(colorless)} \rightarrow MV^{+\bullet}\ (aq)\ \text{(intense blue)}$$

Type II: Hybrid.

$$CPQ^{2+}(aq) + e^{-} + X^{-}(aq)\ \text{(colorless)} \rightarrow [CPQ^{+\bullet}X^{-}](s)\ \text{(olive green)}$$

Type III: Battery Like.

$$MO_y + x(H^{+} + e^{-})\ \text{(colorless)} \rightarrow H_xMO_y\ \text{(intense color)}$$

- Type I solution configuration EC materials are in solution form in both bleached and colored states. An example is methyl viologen (MV, l,10-dimethyl-4,4'-bipyridinium, being pyridinium=C_5H_6N) in water [Mon97]. Other examples are any viologen in organic solution [Mon98] or phenothiazine ($C_{12}H_9NS$) [BG80] in nonaqueous solution.

- Type II hybrid configuration EC materials are in solution form in the bleached state and in solid form in the colored state. An example is cyanophenyl paraquat (CPQ, 1-1'cyanophenyl-4,4'-bipyridinium, being paraquat = $C_{12}H_{14}C_{l2}N_2$ another way to name viologens, due to the name of an herbicide) in water [Ros90 and Ros92]. Other examples are aqueous viologen systems, such as heptyl or benzyl viologen (HV or BzV), or methoxyfluorene $C_3H_4Cl_2F_2O$ compounds in acetonitrile (C_2H_3N) solution. There are also some inorganic examples of type II EC materials.

- Type III battery like configuration EC materials are in solid form in both bleached and colored states. They follow the sandwich structure of Figure I.10. Practically all inorganic EC materials are type III, such as the metal oxides, being the metal a d-block element like Co, Mo, Ni, V, or W, being Li^{+} the mobile counter ion. Other inorganic type III EC materials are phthalocyanine (Pc=$C_{32}H_{18}N_8$) complexes and metal hexacyanometallates such as Prussian blue (PB=$C_{18}Fe_7N_{18}$). Organic type III systems are typified by electroactive conducting polymers such as polypyrrole (PPy), polythiophene (PT), or polyaniline (PANI) [Mon95a].

Solution type I and hybrid type II EC window configurations are the self-erasing types since a continuous current is required to maintain the coloration in these ECDs. On the other hand, battery-like type III EC window configuration shows an open-circuit memory. The specific conductivity of the electrolytes could be further increased by adding ionic liquids, which can be used in a wide range of electrochemical applications where high ionic mobility is required [Jov04]. For instance, by the addition of lithium salt [Sur08] or using iodine ionic liquid electrolyte [Jov07]. The liquid electrolyte is substituted by polymer electrolyte in other works, not only used for ECDs but also for lithium batteries and super capacitors [Von04 and Tre05]. For large window applications, coloration efficiencies of complementary EC materials must be higher than for mirrors, displays or small area window applications such as optical filters and eyewear [Rau99].

I.1.4.3 Electrochromic materials

EC materials are classified in three categories: metal oxide films, molecular dyes and conducting polymers. The most important compounds that exhibit electrochromism are: transition metal oxides (TMOs), Prussian blue (PB) systems, viologens (1,1'-disubstituted-4,4'-bipyridinium salts), conducting polymers, transition metal and lanthanide coordination complexes and metallopolymers, and metal phthalocyanines [Row02].

Examples and applications of the large number of materials that exhibit electrochromism are shown in Table I.1 [Row02].

Class of EC materials:	Examples	Potential uses
Transition metal oxides (TMOs)	WO_3, MoO_3, V_2O_5, Nb_2O_5, $Ir(OH)_3$ and NiO_xH_y.	Smart windows, thermal control of satellites and EC writing paper.
Prussian blue (PB) systems	Prussian blue ($C_{18}Fe_7N_{18}$), Prussian brown ($C_6Fe_2N_6$), Prussian green (C_3FeN_3) and Prussian white ($C_6Fe_3N_6$).	Displays.
Viologens	1,1′-Disubstituted-4,4′-bipyridinium salts (being pyridinium=C_5H_6N).	Car rear view mirrors (already used) and displays.
Conducting polymers	PEDOT (being EDOT=$C_6H_6O_2S$), PPy (being Py=Pirrole=C_4H_5N), PT (being =thiophene=C_4H_4S), PANI (being anyline=ANI=$C_6H_5NH_2$)	Smart windows and displays.
Transition metal and lanthanide	Y , 'symmetric GdMg', $[Ru^{II}(vbpy)_3]^{2+}$ (being vbpy = 4-vinyl-4′-methyl-2,2′- bipyridine where vinyl=−CH=CH_2) and poly-$[Ru^{II}(vbpy)_2(py)_2]Cl_2$ (being py=pyridine =C_5H_5N)	Switchable mirrors and NIR switching.
Metal phthalocyanines (Pc)	$[Lu(Pc)_2]$ being Pc= $C_{32}H_{18}N_8$	Displays.

Table I.1: Summary of EC materials, examples and potential uses [Row02].

I.1.4.3.1 Transition metal oxides (TMOs)

Two types of electrochromism (cathodic and anodic) are observed in oxides of transition metal elements of Periodic Table, depending if the material is colored under injection or extraction of ions respectively, i.e. by a reduction or by an oxidation process (Figure I.13, [Gra95]). Cathodic coloration (in blue color) is found in oxides of Ti, Nb, Mo, Ta and W, being by far tungsten oxide (WO_3) the first reported and the most extensively studied one. Anodic coloration (in red color) is found in oxides of Cr, Mn, Fe, Co, Ni, Rh and Ir, being nickel oxide (NiO) and iridium oxide (Ir_2O) the most investigated.

In 1994 Asashi Glass (Japan) developed prototypes of inorganic EC windows (1 x 1.5 cm^2 or 1.5 x 2 cm^2) based on Li_xWO_3/metal oxide/NiO_x for testing and evaluation, with optical properties of T_{lum}=73-18% and T_{sol}=55-11%, showing good repeatability in transmission between 25-60ºC [Lam98]. Figure I.14 shows the typical sandwich structure of inorganic EC glazing (battery-like type III), as the ones of Asashi Glass, and its spectral transmittance in both colored and bleached states.

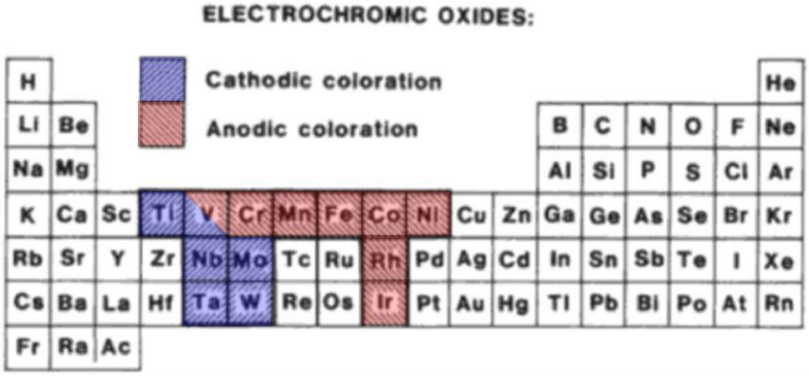

Figure I.13: Transition metal elements of The Periodic Table which oxides (TMOs) show cathodic (blue) and anodic (red) electrochromism [Gra95].

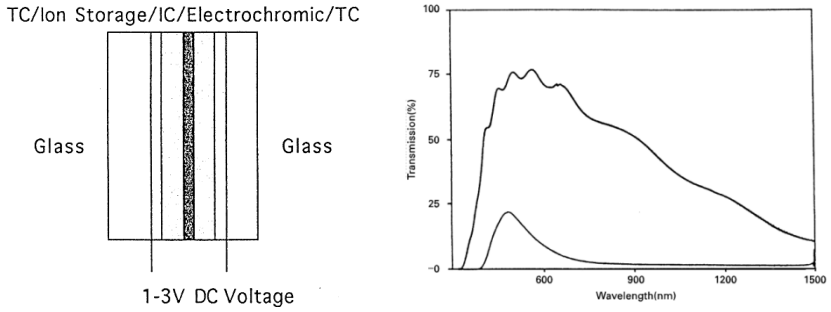

Figure I.14: (left) Schematic of a typical inorganic EC glazing [Lam94, Lam95 and Lam98]. (right) Transmission properties of inorganic TMOs EC windows prototypes developed by Asashi (Japan) in the bleached OFF and the colored ON states [Lam98 and Nag94].

I.1.4.3.1.1 Tungsten oxide

Tungsten oxide WO_3 was the first discovered and most studied EC material. A high-efficiency blue color is observed in amorphous WO_3 films, which switches reversibly from transparent to dark blue upon electrochemical redox reactions. The characteristics of coloration depend on the constitution and the composition of the film as well as on the atomic structure and the size of the nanoparticles, pores and adsorbed substances [Lus03 and Cui05]. The insertion / extraction process can be represented by:

$$WO_3 + x(M^+ + e^-)\ \text{(transparent)} \leftrightarrow M_xWO_3\ \text{(deep blue)}$$

$$WO_3 + x(M^+ + xe^-) \leftrightarrow M_xW^{VI}_{(1-x)}W^{V}_{x}O_3$$

where M^+ can be H^+, Li^+, Na^+ or K^+, $0<x<1$ and e^- denoting electrons. The transparent oxidized state of WO_3 has all W^{VI} tungsten sites while colored reduced state of WO_3 has x W^V tungsten sites, being the colored state an intense blue for low values of x and a metallic bronze for higher values of x.

During the charge injection an intervalence charge transfer transition between W^{VI} and W^V are accompanied of a lattice distortion forming small polarons (quasi-particles composed of a charge and its accompanying polarization field) causing the absorption of light in the film, which is related to the W^V density. This phenomenon can be observed by X-ray photoelectron spectroscopy (XPS) [Tem90] and electron spin resonance (ESR) [Gab84]. WO_3 shows a strong absorption peak in the NIR due to polaron absorption [Nik01]. The oxygen vacancies with one trapped electron cause the coloration, which was explained by Deb's first color-centre model [Deb73], showing no coloration in fully oxidized samples. The electrical characterization of WO3 was explained by a Randles cell [Ran82]. The response times are around one minute for a 1 m^2 WO3-based EC layer, being of one second for a small display element. Bleaching times increase with the temperature [Vie82]. Coloration efficiency (change in optical absorption per unit of charge) can be improved in mixed EC oxides, like hydrated nickel oxide [Gra89]. Solar transmittance (T_{sol}) can be modulated between 86% and 12% [Sve84].

I.1.4.3.1.2 TMOs color reactions

From the many reports of research into the EC properties of TMOs, WO_3 and NiO, (cathodically and anodically colored respectively) are commonly used together in a single device as working and counter electrodes since they have complementary reactions and hence coloration processes. Other TMOs are also found to switch from oxidized transparent state to colored reduced state such as Nb, V or Mo oxides (cathodic EC elements) or from a transparent reduced state to a colored oxidized state such as IrO_2 (anodic EC element).

The reactions and colors of bleached and colored states for different TMOs are:

- Tungsten oxide: (cathodic), as commented above.
- Nickel oxide: (anodic)

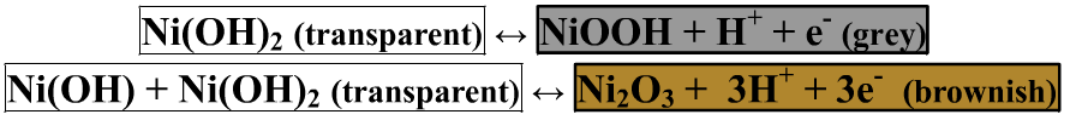

- Niobium oxide: (cathodic)

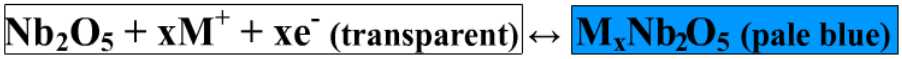

- Vanadium oxide: (cathodic)

- Molybdenum oxide: (cathodic)

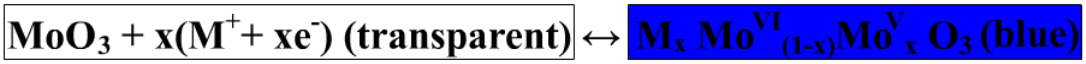

- Iridium oxide: (anodic)

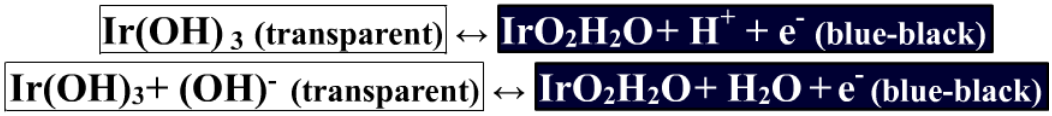

I.1.4.3.2 Prussian blue systems

Several compounds with the general formula $M'_A[M''(CN)_6]_B$ are known as Prussian blue (PB) systems. Typically, M' and M'' are Fe^{III} and $Fe^{III}(CN)_6$ ions respectively (the prototype of PB systems) although it can be other transition metals [Row02].

- Prussian Brown to Prussian Blue and Prussian Blue to Prussian Brown:

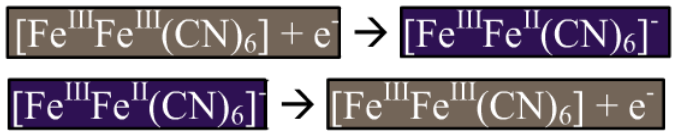

- Prussian Blue to Prussian White (Everitt's salt):

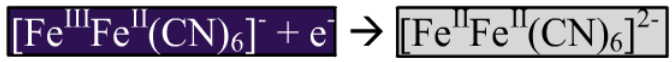

- Prussian Blue to Prussian Green:

Prussian brown can be one electron reduced to produce Prussian Blue, which also can be oxidized to produce again Prussian Brown. Prussian White and Prussian Green are produced by one and two electrons reduction from Prussian Blue, respectively. It is possible to use PB and WO_3 together in a single device since they have complementary EC reactions [LCC01] and PB with viologen for a matrix paper application [Mor99b].

I.1.4.3.3 Viologens (1,1'-disubstituted-4,4'-bipyridinium salts)

Viologens are a type of organic EC materials formed by the diquaternizing of 4,4'-bipyridine to form 1,1'disubstituted-4,4'-bipyridilium salts (being bipyridine a chemical compound with the formula $(C_5H_4N)_2$ usually formed by the coupling of two pyridine rings). The name of viologen derives from the violet color observed in the colored state [Mic33], although they are also known as paracuat, since the famous herbicide, which active component is MV. Viologens are solids (as crystals or powder), although liquid-crystalline viologens with long-chain substituents are also known.

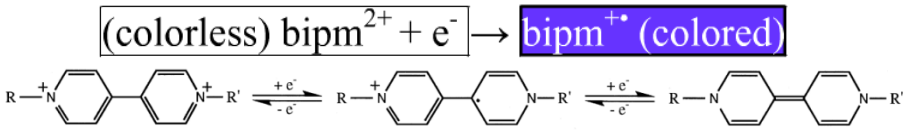

Figure I.15: Three common redox states of viologens undergoing two successive electron transfer reaction: dication ($bipm^{2+}$), radical cation ($bipm^{+\bullet}$) and neutral species ($bipm^{0}$).

Viologens are colorless in the dicationic form ($bipm^{2+}$) and colored, after one electron reduction, in the radical cation form ($bipm^{+\bullet}$), which color depends on the substituents R and R' (Figure I.15). If they interact with the bipyridine core, a red black color is obtained if R=R'=phenyl, and an olive green if the two substituents are *p*-cyanophenyl. The radical cation is blue in all cases where the substituents R = R' are not in conjugation with the bipyridine core, which is the case for R = R' = alkyl (consisting in single bonded carbon and hydrogen atoms) [Mon01a]. Short alkyl chains are blue or blue-purple color in concentrated solution, changing to crimson color as alkyl chains length increases because of the red color of the dimer (two identical monomers). Most of viologen EC materials studied are solution type I MV. A third neutral form ($bipm^{0}$) is observed after a one electron reduction from dicationic form ($bipm^{+\bullet} + e^- \rightarrow bipm^0$) or by a two-electron reduction of the dication ($bipm^{2+} + 2e^- \rightarrow bipm^0$). Their color is red-brown for viologens with simple alkyl substituents. A viologen-modified nanoporous-nanocristalline TiO_2 electrode used in an ECD showed improvements over viologen ECDs in EC parameters such as coloration efficiency, response times and long-term stability [Cin99]. Viologen ECDs are a good candidate for display applications [God83 and Mor08].

I.1.4.3.4 Conducting polymers: PANI, PPy, PT and PEDOT

Various aromatic monomer compounds with conjugated ring structures, as thiophene, aniline, furan, carbazole, azulene and indole, can undergo chemical or electrochemical oxidation producing doped conducting polymer films of polypyrrole (PPy), polythiophene (PT) or polyaniline (PANI), poly 3 methyl aniline (MEPA), poly(3-methyl-thiophene) (P3MT), poly(3-methyl-pyrrole) (P3MPy), etc., doped with counter anions. The highly conducting oxidized (doped) and the electrically insulating reduced (undoped) or neutral states exhibit different colors due to substantial changes in optical absorption spectra in the visible and NIR regions [Row02 and Jen05], which varies

continuously with the degree of oxidation or reduction, being possible multiple colors. Some works demonstrate how the color of the polymers and the solar-cell performance can be controlled by the molecular design of the polymers [Bea08 and Sub10]. The full completion of the color palette including the entire visible spectrum with polymers that have neutral colored states, with range from yellow to orange, red, magenta, blue, green, cyan and even black, switching from these vibrantly colored states to highly transmissive, near colorless in the oxidized state; necessary for both window and display applications, was recently presented in a meeting [Tho11 and Rey11]. Typical conjugated polymers that have been explored as EC materials are shown in Figure I.16. All have conjugated ring structures. High levels of transparency of the bleached state are achieved using conducting polymers, with high EC contrast and coloration efficiency, such as the hybrid EC coating material described in [Coc10]. These hybrids organic-inorganic materials have been reported for several applications[Gom01].

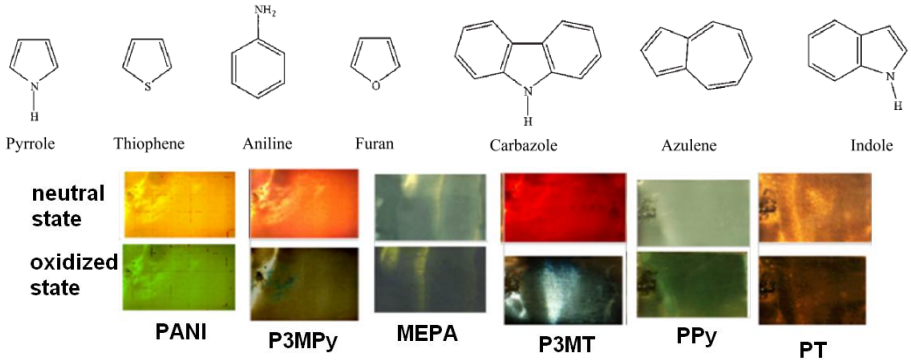

Figure I.16: (up) Conducting polymers are produced by oxidation of aromatic monomer compounds [Row02]. (down) Different EC conductor polymers in their neutral and oxidized states [Pad06].

PANI:

yellow (leucoemeraldine) → green (emeraldine salt-conductor) → blue (emeraldine base) → black (pemigraniline)

PANI & PB:

Doped (oxidized) state deep blue oxidized polyaniline + Prussian blue → Undoped (reduced) state green emeraldine polyaniline + Prussian green

PPy:

Doped (oxidized) state blue/violet (λ_{max} = 670 nm) → Undoped (reduced) state yellow/green (λ_{max} = 420 nm)

PT:

Doped (oxidized) state blue (λ_{max} = 730 nm) → Undoped (reduced) state red (λ_{max} = 470 nm)

PEDOT:

Doped (oxidized) state sky blue transparent (highly transmissive) → Undoped (reduced) state deep blue (highly absorbing to visible light)

There are advantages of conducting polymers versus inorganic materials, such as the previous mentioned color adjustment capability, but also the ease of processing, the operation at low voltages and the great capacity to modify the chemical structures [Arg04]. Their mechanic properties allow constructing flexible devices [Rey03]. Besides, all conducting polymers are potentially EC in thin-film form [Mor99a]. Conducting polymers are used in commercial and proposed ECDs as many parts of the devices, such as solution thickeners, matrix or solid phase gels, solid polymers electrolytes and sealants [Byk00].

PANI ECDs allow only the yellow and green stable colorations doping with Cl^- [Gur99]. Combined with PB, PANI changes from green to blue coloration. Doping PPy with BF_4^- changes from green to violet coloration [Gur99] and doping PT with ClO_4^- [Gur99] changes from red to blue coloration (a "custom" ECD can be achieved, being the neutral polymers yellow, orange, red, or purple, turning either blue or violet on oxidation [Mon95b] with both liquid electrolyte and solid-state configurations [Mor97]). PEDOT and its derivatives (such as PEDOT:PSS) show long term stability, a low oxidation potential, high contrast ratios and fast switching times, being also researched to be used for both the working and the counter electrodes of an ECD, as it will be seen in Chapter III of the present document.

I.1.4.3.5 EC polymers based on transition metal coordination complexes

EC materials based on transition metal coordination complexes show an intense coloration and redox activity. Among this type of EC materials there are reductive and oxidative electropolymerization of polypyridyl complexes, including the $[M^{II}(bipy)^3]^{2+}$ series (being M^{II}=Fe, Ru or Os elements and bipy=2-2'-.bipyridine), and the methallophthalocyanine EC films, mainly rare earth elements, being the first discovered of the $[Lu(Pc)_2]$, where Pc=phthalocyanine (which molecular formula is $C_{32}H_{18}N_8$), that shows an intense blue-green coloration [Mor06, Mor11 and Row02].

I.1.4.4 Complementary EC devices

A complementary EC device is a transparent electrochemical battery which consists of three main components: EC working electrode, EC counter-electrode, and electrolyte (see Figures I.10 and I.12). Such EC devices show reversibly adjustable light transmittance induced by an applied, low-voltage DC electrical current. Complementary solid-state ECDs could cause problems of discoloration when cycling due to the charge imbalance on one of the electrodes [Kuo99a]. The range of optical attenuation can be optimized balancing the electrode capacities, i.e. matching the charge capacities of the two complementary EC layers. For instance, the prediction of the charge capacity ratio was studied for complementary ECDs for WO_3-PB system [Kuo99b and LCC01], PANI and PEDOT [THL06], PB thin film and HV solution [CFL11] or PB and poly(ProDOT-Et2) [Kuo11, KCC11]. For complementary WO_3-NiO EC window [SHL95], a larger

optical modulation is observed than for a single WO_3 film [Hua11]. Other works of complementary EC windows with different materials are also found in the literature [NLe92 and Oze99], such as WO_3 with organic polymers in a single device [Rau01] due to the high coloration efficiency observed in organic polymers [Sap98].

However, some research on the optical contrast of a dual EC system, computed as a function of the redox charge density of the constituent materials, showed and proved mathematically that the maximum values obtainable for several dual systems obeying the Beer-Lambert law were lower than those obtained by one of them independently (Figure I.17-left). Also, the optical contrast of a system depends on the thicknesses of the electrodes (Figure I.17-right) [Pad07, Pad08, Pad09, Pad10 and Pad11].

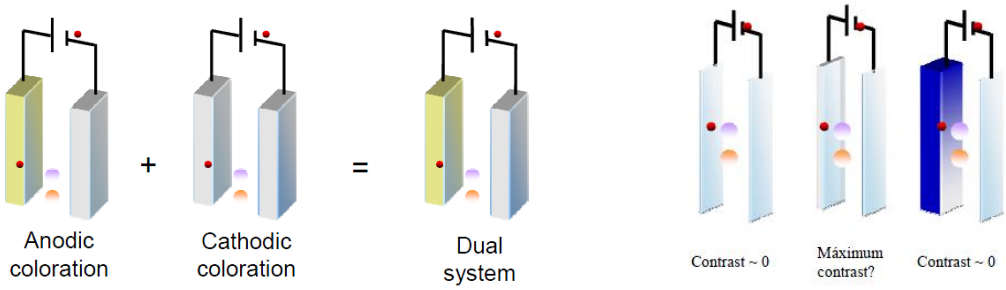

Figure I.17: (left) For complementary EC devices with anodic and cathodic colorations, the maximum contrast achievable for a dual system is always lower than that achievable for one of its components alone [Pad10]. (right) Contrast of a single layer as a function of the thickness [Pad10].

I.1.4.5 Electrochromic devices applications

An outline of both the most extended applications and the new possibilities of the ECDs will be presented next. From 'smart' windows, for reducing heating ventilation and air conditioning (HVAC) and lighting costs [NREL10], to rear view mirrors in cars, sunglasses, visor helmets, textile, and thermal control of satellites or logic flip flops.

I.1.4.5.1 Cost-effective smart windows to reach the market in 2012

The Flabeg company showed in 1999 several ''E-Control'' switchable glazing units of 0.8 x1.6 m^2 installed in buildings (Figure I.18-left) with a transmittance range of T_{lum}=50-15% [Lam03 and Bec99]. Some problems related to the contact layers appeared causing degradation. The same year, Lawrence Berkeley National Laboratory (LBNL) installed large-area EC double-pane window with a transmittance range of T_{lum}=51-14% mounted on the interior side of the building's existing monolithic green-tinted glazing (T_{lum}=75%). The overall composite T_{lum} range was therefore 38-11% (Figure I.18-right), and operated from November 1999 through February 2000 [ELe00].

Twelve years later, some companies are developing smart window products that can be at the market in 2012. Switch Materials in Canada (Photochromic and EC hybrid film) and Pleotint's film in USA (Thermochromic reaction), Soladigm in California (which long-term durability was measured by the National Renewal Energy Laboratory

(NREL)) or Sage Electrochromics (Figure I.19-left) are some examples in USA. ChromoGenics AB in Sweden manufactured ECDs (Figure I.19-right) used for large area windows (0.8 x 1.8 m^2) applications, showing gray coloration of the darken state, response times, after 750 cycles, of 40 and 120 seconds, for coloring and bleaching times respectively, and transmittance range from 70% in the bleached state to 37% in the colored state (after 1400 cycles becomes around 41%). Towards the ideal window, both electrochromism and thermochromism functionalities should be considered (being VO_2 is a good option from the ThC materials among the TMOs).

Figure I.18: (left) EC E-Control™ glass made by Flabeg installed in Dresden (Germany) [Lam03 and Bec99]. (right) LBNL test rooms in the Federal Building, Oakland, California (USA) [ELe00].

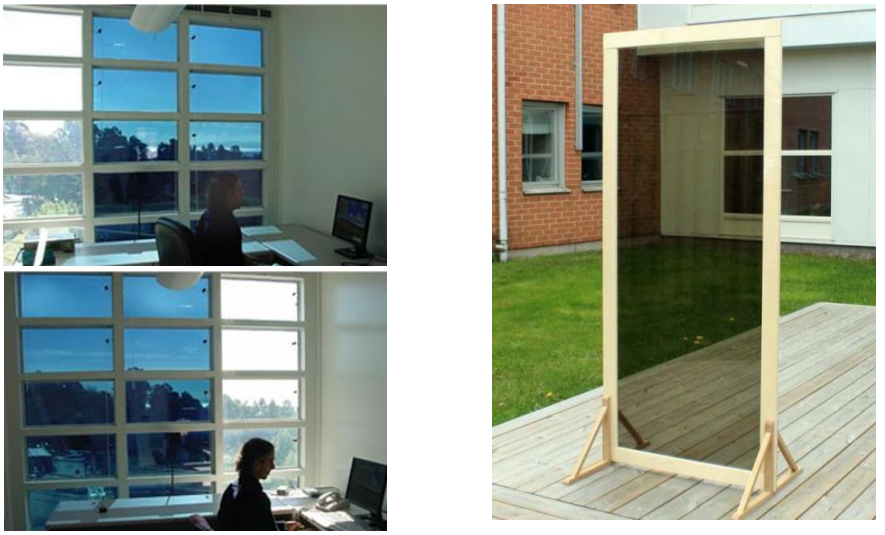

Figure I.19: (left) SageGlass EC windows at LBNL reducing glare [SVB11]. (right) Smart window prototype developed by ChromoGenics of 0.8 x 1.8 m^2 area [Gra08].

I.1.4.5.2 Commercial EC car rear view mirrors

An already commercialized application of electrochromism can be found in EC car rear view mirrors (Figure I.20). In order to avoid the dazzle of lights of following vehicles on reflection from the driver's or door mirror, Gentex Corporation [Byk90] developed the EC automatic dimming mirror interior or night vision system (NVS) that detect and eliminate rearview mirror glare by the formation of an optically absorbing EC color over the reflecting surface. At the bleached state the EC device acts as a straightforward mirror. For the dark state the EC device must be only with a moderate opacity, in order to allow the mirror still reflects some light, retaining its function as a mirror.

Figure I.20: Gentex Corporation EC mirrors [aut].

Many millions of these mirrors have been purchased to date. As smart windows, EC mirrors do not necessarily require such short response times of displays applications. Two photosensitive detectors are used, the first one to detect any dazzling incident light and the second one to detect daylight and turn off the first one. In operation, the color in a commercially available NVS mirror is an intense green-blue [Mon01a]. The only mass-produced ECD presently available uses self-erasing type I solution-phase EC cathodic material: viologens. This type of ECD requires the application of a continuous small current. Basically, each NVS mirror incorporates a front electrode of ITO-glass and a metallic rear electrode which surface is reflective [Byk94a, Byk94b and Byk94c].

I.1.4.5.3 EC displays and paper

EC displays, as LCDs and contrary to OLED technologies, are nonemissive and require external illumination. The main advantages of EC displays over these other technologies are the low power consumption, due to the observed EC memory effect in some EC materials. However, the slow response times is the main drawback, making EC displays only suitable for some types of specific applications, such as long term information displays like as transport termini, reusable price labels or advertisement boards. For large area displays the color formation could be irregular since the voltage near the electrode contacts is larger [Mon01a].

As some examples of EC displays, in Figure I.21-left, a flexible EC display using conducting polymers is shown [Che05]; and in Figure I.21-right, a transistor is attached to each pixel in order to retain charge inside its updated display cell and also for suppressing cross-talk between neighboring addressing lines and columns [And07].

Figure I.22 shows a work related to electronic paper display with catenanes (molecular architecture consisting in two interlocker macrocyles) capable of show RGB colors in response to the applied voltage [Tai08]. Another possibility is to use CYM colors (Cyan, Yellow and Magenta), as the EC display of Figure I.23. Although EC response times are usually long, the PEDOT nanotubes based EC display of Figure I.24 shows switching times of 8.8 and 3.5 ms for coloration and bleaching processes respectively. Variable color EC polymers films on ITO/glass of The Reynolds Research Group of University of Florida are shown in Figure I.25 [Mor06]. Figure I.26 shows, from left to right, Acreo's printed ECD technology into Paper-Display products, Aveso paper-thin (250 µm) ECD used in smart cards for reducing fraud in financial transactions, based on reflective EC technology for blue digits on a yellow background, NanoChromic Display (NCD) technology using EC viologen molecules in ECD simulating ink or paper with a pure white background with very high contrast ratios, and flexible modified bipyridium salts based EC display of Siemens.

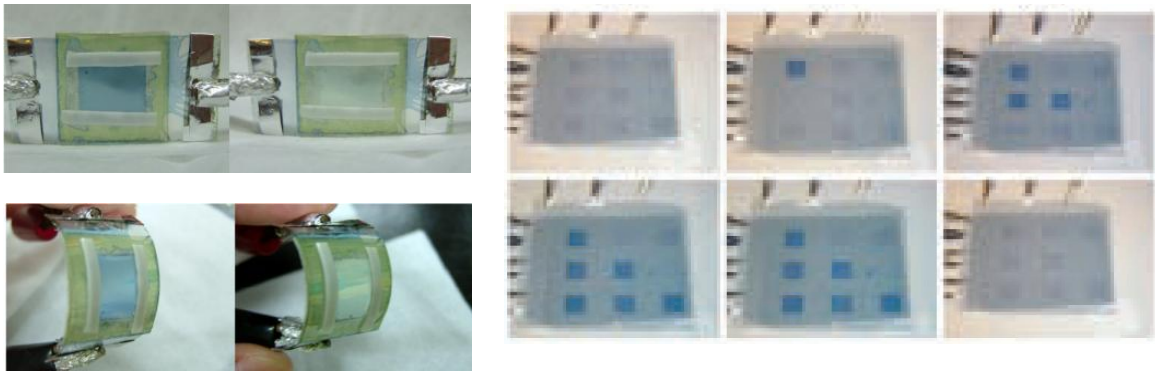

Figure I.21: (left) PES-ITO/PANI-PSS||PEO-PC-LiClO$_4$||PEDOT-PSS/ITO-PES device at normal and bending states, applying -0.5 V bias for bleaching state, transparent, and 2.5 V for coloring state, dark blue [Che05]. (right) 3x3 active matrix PEDOT:PSS ECD. Potentials required of 2V for ON state and 0 V for OFF state [And07].

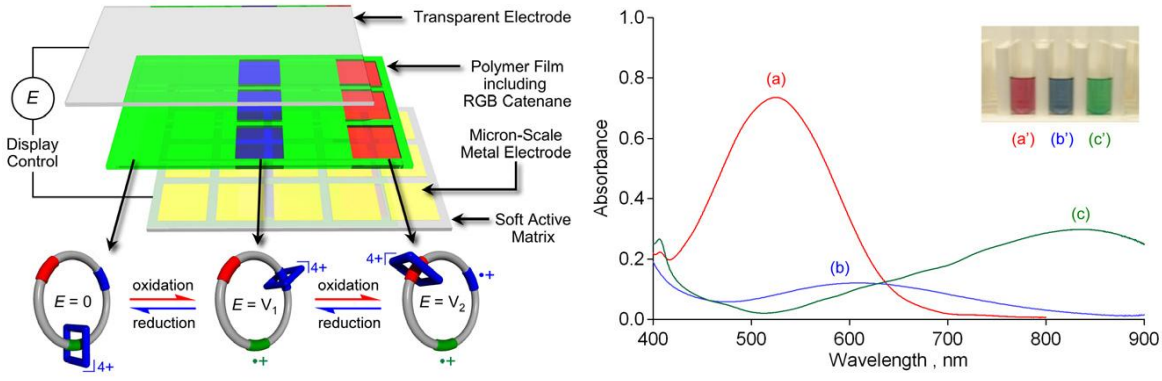

Figure I.22: Electronic paper display (E-PAD) based on EC materials [Tai08]

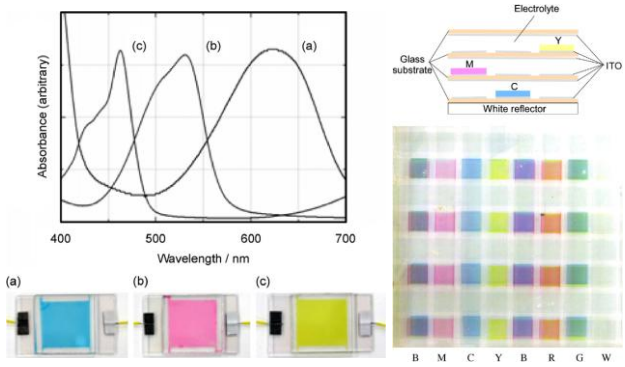

Figure I.23: Cyan Yellow Magenta ECD using terephthalate derivatives for EC paper-display developed by Chiba University of Japan [Kob08, STa09 and Wat11].

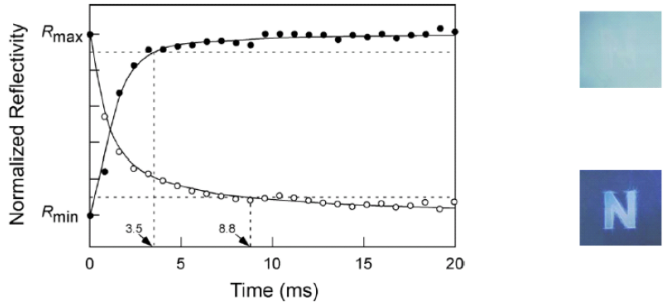

Figure I.24: Reflectivity of PEDOT nanotubes 4 cm^2 EC window at 530 nm upon voltage-switching between -1.0 V and 1.5 V. [SHK04].

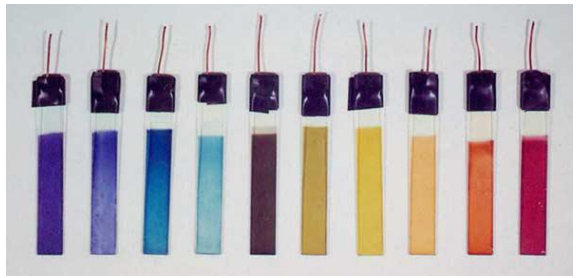

Figure I.25: Range of colors available of a series of neutral EDOT and BEDOT-arylene variable color EC polymer films on ITO/glass [Mor06].

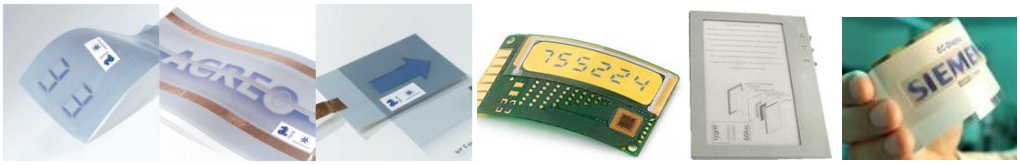

Figure I.26: (from left to right) Acreo's printed ECD technology into Paper-Display products, Aveso paper –thin ECD, NCD technology and EC display of Siemens [epa].

I.1.4.5.4 Sunglasses and helmets

A prototype version of "smart" sunglasses (Figure I.27-up) was developed by researchers of University of Washington using polymer EC materials [ChXu07]. Figure I.27-downd-left shows a variable transmission vision system integrated ECD developed by researchers of two research groups, Sotzing research group (Institute of Materials Science of University of Connecticut (UCONN, USA) and and Otero research group Electrochemical and Smart Materials Center of Polytechnic University of Cartagena (UPCT, Spain) [Pad06]. As it will be seen in Chapter VIII of this document, the author has also contributed to the state of the art of this technique (kind of systems). Figure I.27-downd-right shows a variable-tint visor for motorcycle helmets applications with transmittance range from 70% to 25% developed by ChromoGenics [Gra08].

Figure I.27: (left) Polymer EC sunglasses in bleached and colored states [ChX07]. (center) Variable transmission vision system integrated ECD [Pad06]. (right) Variable tint-visor ECD developed by ChromoGenics for motorcycle helmets applications.

I.1.4.5.5 Switchable mirrors

Switchable optical properties of metal hydrides involve a metallic state that, on hydrogenation, transform to transparent or strongly absorbing states [Ric03]. Some examples are shown in Figure I.28.

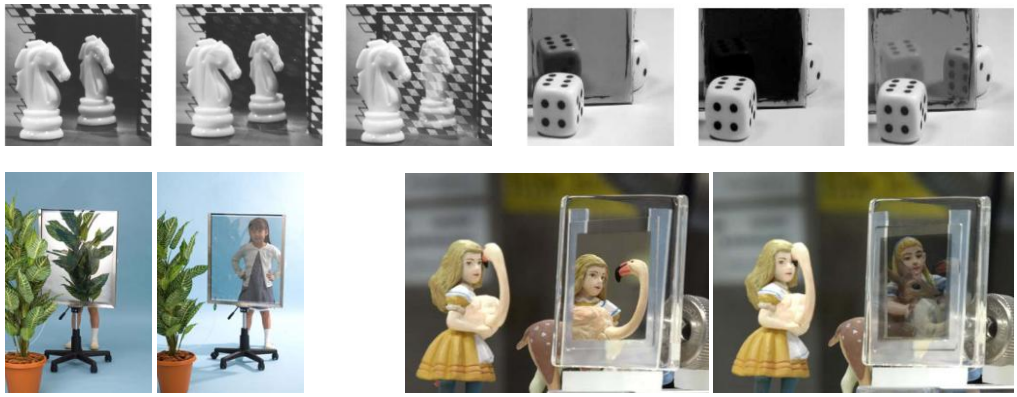

Figure I.28: (up left) Reflecting, weak transmitted and transparent states of YH_2 films [ACG06]. (up right) Metallic, absorbing and transparent states of RE-Mg hydride films [Koo02] (down left) Development of a switchable mirror that turns into a color-neutral transparent state [Yos07]. (down right) Mg-Ca switchable mirror (metal state) and transparent (hydride state) [Yam07 and Yam10].

The four pictures of Figure I.29 show the four states of a smart window combining an EC mirror and a light source, switching from a transparent, reflective and uniform white emission states [And05]. However, the transparent state shows a non negligible level of haze.

Figure I.29: The first integrated window technology that combines an EC mirror and a light source that is transparent in the off-state [And05].

I.1.4.5.6 Thermal control of satellites

A variable EC emittance device (VEECD) was considered for thermal control in space, modulating the IR emittance of the satellite, which could be affected by the large temperature variations as a result of changes in orbital conditions, which is not only referred to the radiation from the sun and sunlight reflected from the earth's surface (earth's albedo) but also to IR radiation emitted from the earth (earthshine) in the case of low earth orbit (Figure I.30). The modulation of the emittance can be achieved by reversibly changing the optical properties (such as refractive index and extinction coefficients) of the EC layer upon insertion or extraction of ions. The VEECDs were found to modulate mid IR emittance from 0.55 in a low reflective state to 0.30 in a high reflective state [Kis02, Kis04 and KLe07].

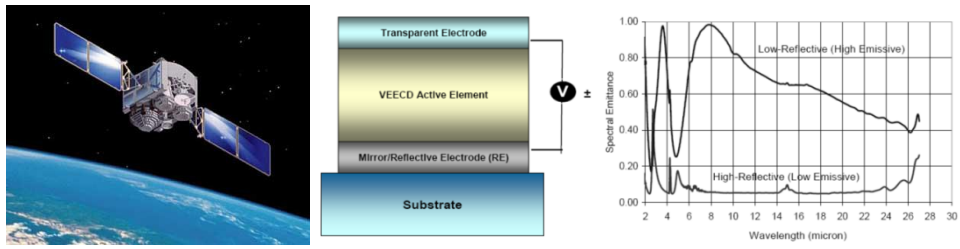

Figure I.30: Reflective and emissive states of a variable EC emittance device (VEECD) developed by Eclipse Energy Systems, Inc for thermal control in space [Kis02, Kis04 and KLe07].

I.1.4.5.7 EC textile

EIC Laboratories initiated a program for developing a fully printable multicolor EC textile technology in the visible and even IR spectral regions using conductive polymers [Wan03]. Organic electronics (based on PEDOT) on microfiber were found suitable for electronic textiles in an approach embedding electrolyte gated transistors and devices, including light emitting electrochemical cells and EC fibers, directly on textile microfibers (Figure I.31). The addition of these devices could allow for the design of active matrix displays integrated in textiles [Ham08]. PEDOT:PSS nanoparticles, rather

than a film, were observed in the EC textile [Din10]. EC textile as wearable displays is the goal of a PEDOT:PSS spandex stretchable researched by University of Connecticut (USA), being adaptive camouflage with pixilated fabric one of its application, or even women underwear famous company (Victoria Secret) involved in the contract for developing this EC textile [Sot11]. An example of 6 cm^2 motif with two layer fabric structure changing from blue to red in 10 seconds is shown in the Figure I.32. More vibrant colors affected the observed color through a subtractive mixing effect, as expected, but no adverse contrast effects between the two states of the EC system was observed [Inv11].

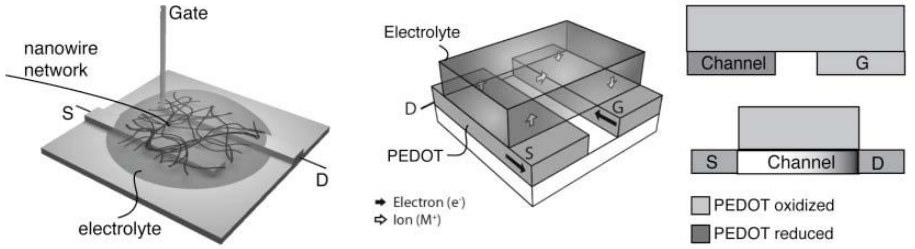

Figure I.31: EC PEDOT nanowires used for a FET electrochemical transistor [Ham08].

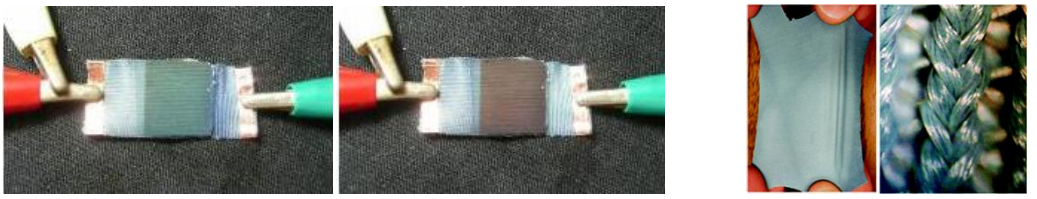

Figure I.32: (left) Spandex fabric changing from blue to red color [Sot].
(right) Conducting Spandex [Sot].

I.1.4.5.8 EC Sequential logic circuits and memory elements

Systems behaving according to various logic schemes are currently in development, since it was first suggested that molecules could be used for information processing. Various approaches in order to construct a (bio)-molecular flip-flop (Figure I.33), using polymeric materials, ranges from all photonic systems to transition metal complexes and hybrid nanoparticle/protein-based systems on solid supports [Rui10, Rui11 and Boo11].

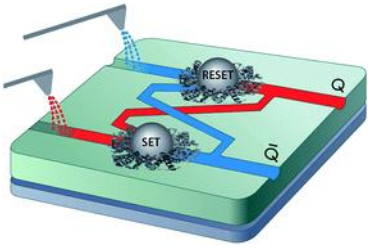

Figure I.33: A molecular approach of sequential logic flip-flop [Rui11].

I.1.5 Electrophoretic suspended particle devices

Initially developed for displays, because of their fast answer, suspended particle devices (SPDs) are an electrically powered chromogenic technology, as ECDs, but with a different principle of operation. The first device based on SPD technology was invented by Edwin Land of Polaroid in 1934. However, its development was slow due to problems of stability and durability when cycling [Lam93].

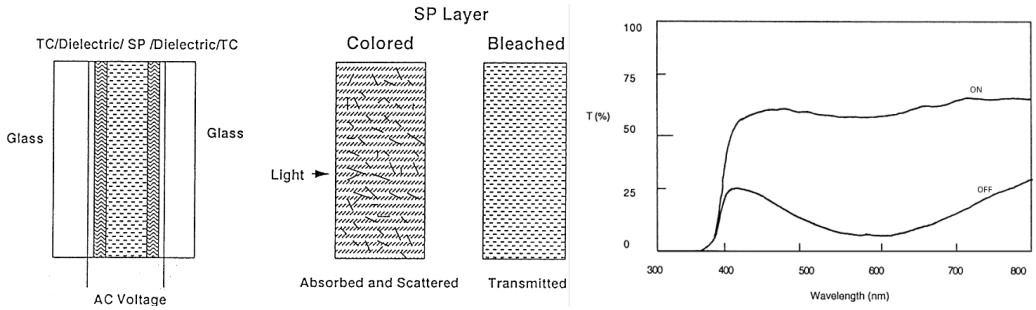

Figure I.34: (left) Schematic of a dispersed particle glazing [Lam03]. (center) Suspended particle (SP) layer in the absorbing OFF state and transmitting ON state [Lam03]. (right) Spectral transmittance of a SPD glazing made by Hankuk Glass Industries (Korea) [Lam98].

A SPD consists of 3-5 layers. The active layer has millions of black needle shaped dipole particles of (dihydrocinchonidine bisulfate polyiodide) or heraphathite (<1 μm long) suspended in a polymer. This layer is laminated between two dielectric layers, which are filled between two electrical conductors (such as ITO) and placed between two glass layers. As it was done for ECDs in Figure I.14, a schematic of the SPD is shown in Figure I.34-left [Lam03]. In the off state the SP droplets are randomly oriented, absorbing and scattering visible light. The SPD window shows a bluish-black dark color since most of the light is not passing through the SPD film [Dou00], and the scattering effect is mainly due to small particles, more effective at short wavelengths. When the electric field is applied, the particles line up and become perpendicular to the window, allowing more light crossing and hence increasing the transmission (Figure I.34-center). Typical transmittance ranges are 6-75% to 15-60% and fast switching times are around 100-200 miliseconds. The voltage required for the transmitted state depends on the thickness of the device, being usually in between 20 and 150 V rms (root mean square). Contrary to type III ECDs, which show memory effect, the electric field must be maintained for keep the film transparent. The transmittance of the SPD glazing developed by Hankuk Glass Industries is shown in Figure I.34-right [Lam98].

Currently, the SPD window is a film patented technology developed and licensed by Research Frontiers Inc (RFI) (NY, USA) and their licensees (Hitachi, Pilkington, PGW/PPG, Nippon Sheet Glass, Asahi, Isoclima, AGP Group, SPD Control Systems Corporation (SCSC),…). The sandwich structure of a SPD film developed by Hitachi is shown in Figure I.35-up [Hit]. Microcapsules containing oriented particles dispersed in the matrix resin is shown in a cross sectional view of the film (Figure I.35-down)

[Mat09]. The lighting efficiency of SPD glazing for potential energy savings was determined of around 35 to 60% from the 10 to 20% of the total energy consumed for lighting in US [GSo09].

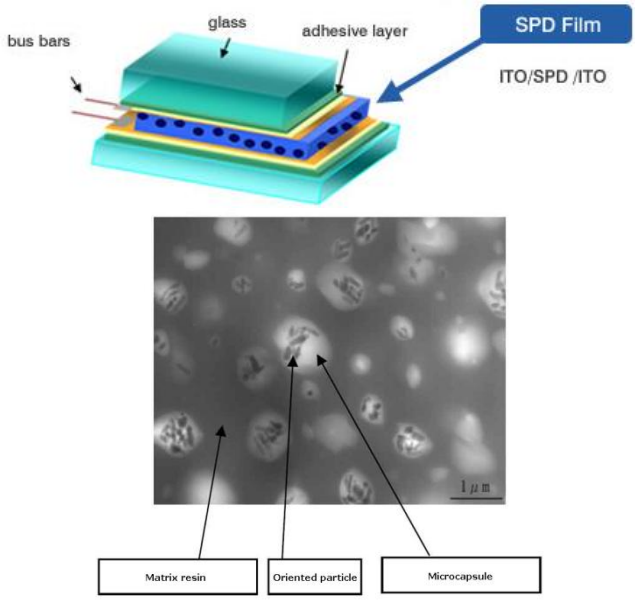

Figure I.35: (up) Sandwich structure of a SPD developed by Hitachi [Hit]. (down) Microcapsules containing oriented particles dispersed in the matrix resin [Mat09].

I.1.5.1 Electrophoretic SPD glazing

Some examples of electrophoretic SPD glazing can be found, such as the SPD windows installations of Figure I.36 (which price starts around $2,000) [Cer11], the SPD films developed by Hitachi of Figure I.37 (with light transmittance modulation from 0.4% to 52%) [SCSC], the rear view SPD windows of Figure I.38 [Iso08] and the glass roof SPD panels in cars (tested for temperature range from -30 to 50º C) of Figures I.39 and I.40 [RFI11a]. Besides Mercedes, other car companies, such as Audi, are also considering the use of this technology [RFI11b].

Figure I.36: SPD-Smartglass installations in Boca Raton, FL in the clear (left) and darker (right) states [Cer11].

Figure I.37: Automotive controller demo setup at the 2008 RFI Annual Meeting [SCSC].

Figure I.38: Fiat Croma Smartglass Isoclima's Cromalite side window in darker and clear states [Iso08].

Figure I.39: (right) Mercedes SLK with SPD-SmartGlass technology (RFI) in the clear state. (left) Mercedes SLK with Magic Sky Control (Daimler AG) in the darker (up) and clear (down) states [RFI11].

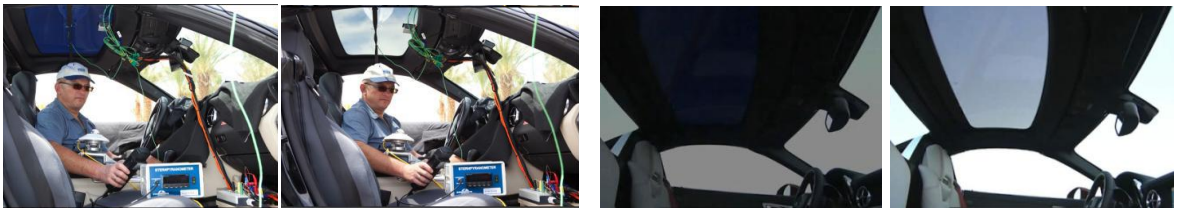

Figure I.40: (left) SPD-SmartGlass being tested in Mercedes-Benz SLK (Death Valley, California). (right) Magic Sky Control in the darker and clear states [Mer11].

I.1.5.2 Electrophoretic displays and electronic paper (e-paper) based on SPD

Electrophoresis is not only used for 'smart' windows applications, but also for displays and electronic paper (e-paper), where various backplane technologies are used to power the e-paper front-plane. One of such backplane technology, also used in active matrix LCDs, is the TFT. In an electrophoretic front-plane, charged micro size particles are suspended in a dielectric fluid that is enclosed into a microcapsule [epa]. The backlight used to retro illuminate conventional flat panel displays is not required in e-paper since the external light is reflected as in ordinary paper. A method of improving the contrast by using two different types of pigment particles, one black and one white (with opposite charge), was developed in several works [Com98, Her02 and Her06]. When an electric field is applied across this cell or capsule, the ink particles move towards the electrode with the opposite charge (Figure I.41). E-paper with other colors is also being considered [Ber10]. As a passive display, e-paper requires external power only when the image changes. The refreshing rate is however not as fast as the required for animated movies. As examples of e-paper, nano-size cationically charged particles of TiO_2 were used for electrophoretic paper and display works in Figure I.42-left [LSP06 and JHP07]. Figure I.42-right Amazon kindle and Sony Reader are examples of e-paper already available at the market,

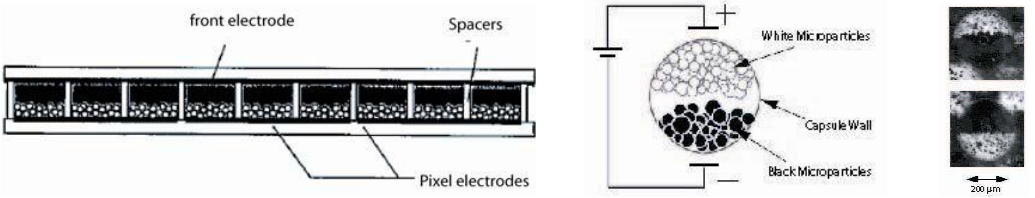

Figure I.41: (left) Cross-section schematic of spacers, (center) schematic of electrophoretic ink capsule and (right) charged microparticles within a single capsule reacting to a positive (top) and a negative field (bottom) in electrophoretic e-paper [epa and Com98].

Figure I.42: (left) Photographs of electrophoretic displays in power-off and power-on (30 V) [LSP06]. (right) Amazon Kindly and Sony Reader, e-paper available at the market [Abd11].

I.1.6 Liquid crystals

Liquid-crystal (LC) based systems offer another approach to chromogenic electrically activated devices. As an intermediate state of matter between solid and liquid, LCs show characteristics of these two phases, such as the molecular organization of solids but being at the same time a fluid. Their molecules are often shaped like rods or plates in order to be aligned collectively along a certain direction, thus the LC properties are anisotropic, i.e. depending on the direction. The mechanism of optical switching in LCs is changing the orientation or twist of LC molecules between two conductive electrodes, by means of an applied electric field. Reflectance and transmittance of the window or display is directly related to the orientation of the LCs. The voltage required to switch LC between bright and clear states (typically between 24 and 100 V in PDLC and between 3 and 15 V in LCDs) could be decreased by the development of a new class of LC with an electric dipole that over twice the existing LCs [Rin10 and Cox10].

The properties of LC show large temperature dependence, being distinguished three phases, from lower temperature and solid condition to higher temperature and liquid condition: smectic (A, B, C and D, ferroelectric, antiferroelectric and V-shape crystals), cholesteric, and nematic. These types are shown in Figure I.43, being n the refractive index [JTZ09]. The nematic phase is close to the liquid phase, where the molecules flow around but ordered in their orientation. When the molecules are chiral, showing strongly twisted structures, the LCs are in the cholesteric phase and reflect visible light in different bright colors which depend on the temperature. The smectic phase is close to the solid phase, where the molecules are ordered in layers, floating around freely but without moving freely between the layers. From the smectic LCs, chiral V shape LCs show the fast response times of the ferroelectric LCs and the possibility of generation of an analog gray scale with voltage lower than that of the nematic LCs. The V-shape smectic LCs can be used for micro displays of LC on silicon (LCOS) for projection [Urr03].

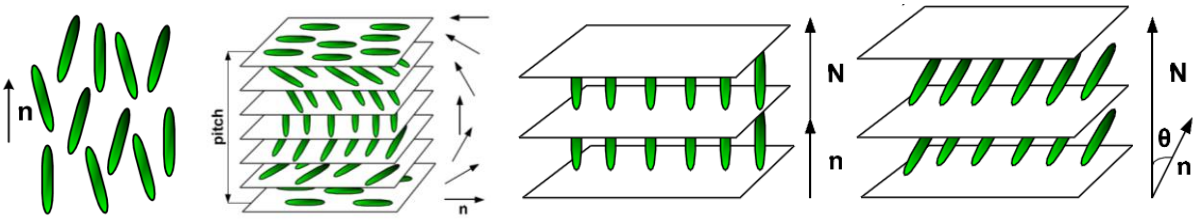

Figure I.43: (from left to right) Nematic, cholesteric and smectic A and C LC phases [JTZ09].

Guest-host LCs are applied in commercial switchable glazing or windows since the 1990s, of which polymer-dispersed liquid crystals (PDLC) and encapsulated nematic curvilinear aligned phase LC (NCAP) are the most common [Fer85]. For applications in displays, twisted nematics are the most commonly used LCs. Cholesteric LCs (ChLCs) are used in electronic paper applications.

I.1.6.1 Liquid crystal display (LCD)

A LCD usually consists of a twisted nematic LC material between two crossed polarizers (Figure I.44-left). When no voltage is applied the cell appears bright. When an electric field is applied, the twist is destroyed since all the LC molecules arrange parallel and all the light is absorbed by the crossed polarizers, the cell appearing black. A LCD contains a matrix of a large number of pixels, including a TFT and color filters for each pixel [LCs12].

I.1.6.2 Liquid crystal glazing: Polymer dispersed liquid crystals (PDLCs)

PDLCs consist of thin films with electrically controllable scattering obtained by phase separation methods. The LC droplets, usually with a size comparable to an optical wavelength (5 µm), are encapsulated within an index matched polymer matrix (22 µm). The LC droplets produce a random scattering of light, appearing milky white. However, if an electric field is applied, it is possible to reorient the LC molecules in the droplets. A sufficiently strong field aligns these molecules along the field direction (Figure I.44-right). Then if the ordinary refractive index of the LC closely matches the polymer index, the film becomes optically clear. This switching from opaque white (depending on the author it is also called translucent) to transparent states is the result of LC orientation. The polymer should be highly transparent, and do not scatter light.

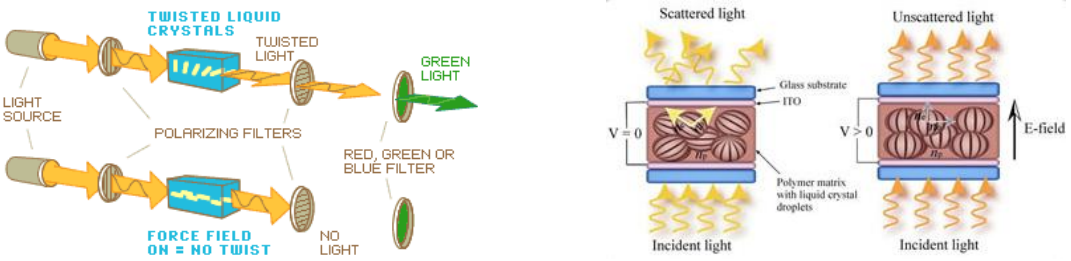

Figure I.44: (left) Twisted nematic LCD configuration [LCs12].
(right) Sandwich structure of a PDLC OFF (scattering) and ON (transparent) states [CMM07].

First examples of PDLC preparation was reported in 1985 [Doa86, Doa87 and Doa88]. Epoxy resin was mixed with the LC to form an isotropic solution PDLC in a heterogeneous, two-phase material with the polymer serving as the host and the LC serving as the dispersed phase. An important class of these systems is formed by a process known as polymerization-induced phase separation (PIPS) [Wes88 and Muc03]. As it was seen in Figures I.14 and I.34 for ECDs and SPDs, the sandwich structure of a PDLC is shown in Figure I.45 (Lam94, Lam95 and Lam98]. The PDLC is placed between two sheets of TC coated polyester or glass, serving as electrodes. In the off state, the device appears translucent white. When an electric field is applied the LC droplets align with the field and the device becomes transparent [Lam03]. Open circuit memory is not possible in PDLCs, which is a drawback since the transparent state requires energy consumption (5 up to 20 W/m^2). Long-term UV stability and high cost

are also disadvantages of PDLC 'smart' windows technology [Bae10]. The total visible transmittance for a PDLC device is T_{lum} (OFF–ON)=50–80%. Dying the film can result in a better control of Tvis and also for improving contrast ratio ion LCDs [Hei68 and Blo77]. PDLCs are also dyed leading to different optical texture at different concentration [Mal06].

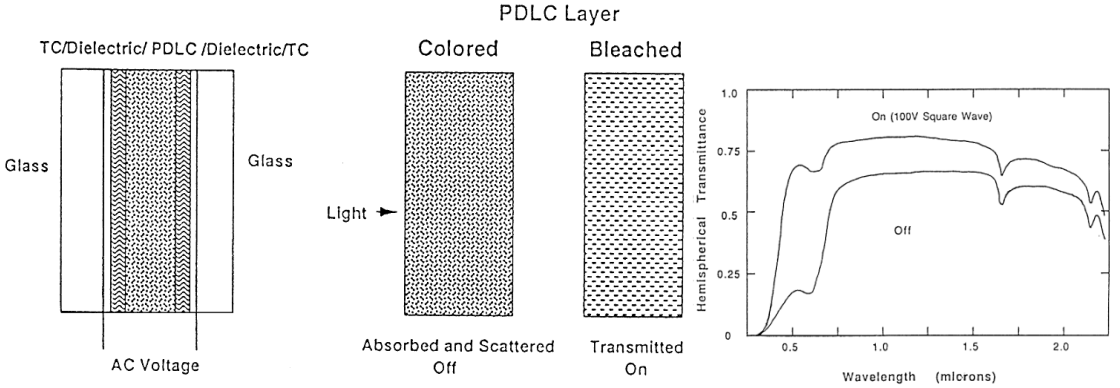

Figure I.45: (left) (left) Schematic of a PDLC [Lam03]. (center) PDLC layer in the scattering off state and transmitting on state [Lam03]. (right) Spectral total transmittance of a dyed NCAP Taliq LC glazing made by Raychem (Varilite^{TM}) [Lam98].

New optical properties can be observed by varying the rate and temperature at which the polymer curing occurs, determining the size an d shape of the LC and polymer, being divided in optically scattering PDLCs, nano PDLC or holographic PDLCs (H-PDLC) and polymer stabilized LC (PSLCs) or polymer network LCs (PNLCs). Some examples of works with H-PDLCs are found in [Tan94, Nat03, All06, Wol07, YJL08, Zhe09 and Hos12]. Optically scattering PDLCs are the most common variety of PDLC with a 30-50% of concentration of polymer within the PDLC, and which droplets are of the micron size scale. Chemical dyes can also be added to the PDLC mixtures, scattering red, green or blue light, which could be applied for RGB pixels in flexible displays. Approximately from 2 to 10 V/µm is the voltage required to switch PDLC devices, higher than the required for conventional LCs such as nematics (from 1 to 5 V/µm). This type of PDLC is suitable for 'smart' windows, mainly for switchable privacy windows application (Figure I.46) and also for projection displays [Nag98].

Figure I. 46: Private window SGG-Priva-Lite® by Saint Gobain Glass Vision, based in PDLC technology in translucent OFF (left) and in transparent ON states (right) [ide].

I.1.7 Micro-blinds and Power-blinds 'smart' windows technologies

Another kind of 'smart' windows technology is the micro-blinds, being developed by the National Research Council Canada. Not in a micron scale, power-blinds can also be included into the electrically controlled transmittance technologies.

I.1.7.1 Power-blinds

Power-blind system uses static electricity in a switch-operated set of horizontal window blinds [But06 and Sil98]. Electromechanical and thermal analyses confirmed the functionality and validity of the system as an energy saving design [Kie01]. Figure I.47 shows the assembly ladder/slat/tab used, the schematic side view of slats and glass in closed and open positions and a the film of the first generation developed at Talley Student Center at North Carolina State University. Figure I.48 shows two examples of power-blinds system in both, closed and open positions. With power on, the slats are open, with power off, the slats are closed due to gravity [Gal01].

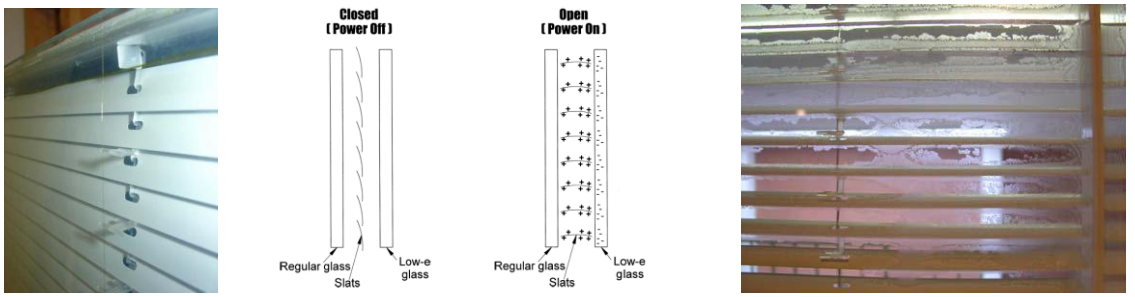

Figure I.47: (left) Ladder/Slat/Tab Assembly. (center) Side view of slats and glass in closed and open positions. (right) Film on First Generation Glass [Gal01, But06].

Figure I.48: Boardroom power-blind units in the closed and open positions [Gal01]

I.1.7.2 Micro-blinds

The micro-blinds are really similar to power blinds but of micrometer size, making them less visible for the human eye. They are curling electrodes activated by voltage. Micro-blinds use voltage to unroll curled electrodes blocking the light transmission.

As advantages of micro-blinds over other 'smart' windows technologies it can be found the switching speed, UV durability, customized appearance and transmission, and the not requirement of using ITO, as the currently other smart windows technologies, ECDs, SPDs and PDLCs. Figure I.49 shows such curled electrodes: micro-blinds and a schematic view of a micro-blind cross-section [BL09]. Two photographs obtained from screenshots of a video showing the operation of a sample of micro-blind technology window are shown in Figure I.50 [nrc]. The scattering observed in the bleached state is a drawback of this 'smart' windows technology.

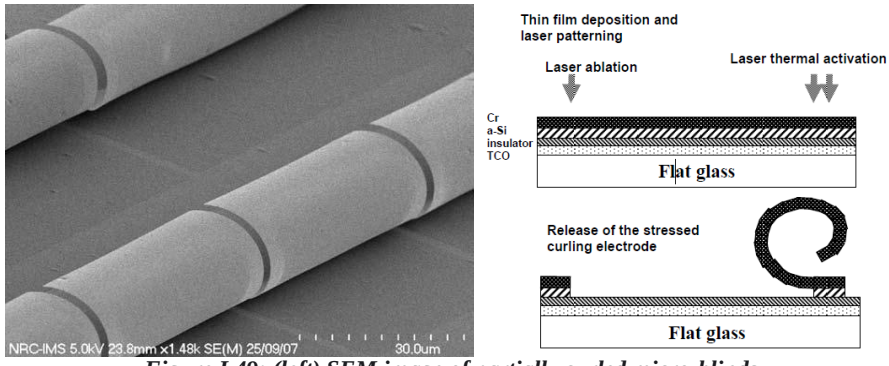

Figure I.49: (left) SEM image of partially curled micro-blinds (right) Schematic views of a micro-blind's cross-section [BLG09].

Figure I.50: A 'smart' windows technology based on micro-blinds in OFF and ON states [nrc].

I.1.8 New Smart Window using total internal reflection: TIR window

As at the beginning of this chapter was mentioned, spectral transmittance control can be accomplished by low-e glass windows in order to reflect and insulate long wave radiation (being transparent to shortwave radiation). However, a time control needs the switching of EC or other 'smart' windows technology. Another kind of control, able to avoid undesired glare inside buildings, is the angular control that can be used to reject the entry of unwanted radiation by means of total internal reflection (TIR) windows [Yos11].

The TIR window consists of an optical wedge arrangement of a configuration such that undesirable radiant energy is blocked from crossing it. Optical window formed from two wedges, with an air gap between them, can be used as an energy saving 'smart' window. In that way, energy from within a desired field of view can pass through such window, while unwanted energy, coming in from a different angle, strikes the internal surfaces between the wedges, such that the critical angle is exceeded. This undesired energy is totally reflected internally and absorbed by the outer wall of the window. A TIR window consists of two triangularly shaped wedges of optical material (Figure I.51). The first wedge reject incoming radiation from a direction below the base plane [Amo00].

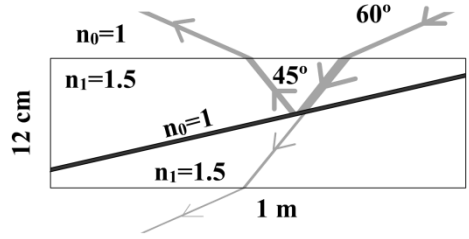

Figure I.51: Sketch of the structure of a TIR window rejecting radiation of a determined direction.

The present work of thesis discusses over devices such as the described in this Chapter I, including EC, SPD and PDLC technologies.

I.2 Motivation, objectives and outline of this work

I.2.1 Motivation of this work

GDAF, Group of Displays and Photonic Applications, is a research group of Electronic Technology Department of University Carlos III of Madrid (Spain) consisting of a team of experts in telecommunications, photonics and advanced electronic instrumentation with a long trajectory of recognized work on providing solutions to requirements from industrial sector related to three research branches:

- Optic communication systems (displays, filters, switchers, multiplexors).
- Domotics (smart windows and environment control)
- Assistive supporting technologies (mobility, communication and perception aids for disabled people).

The present work has been carried out in the research framework of GDAF, which started in 2002 a research collaboration with CIDETEC, a Center for Electrochemical Research and Development of San Sebastian (Spain). At the beginning, the collaboration was mainly based on the area of ECDs (PEDOT and viologen based organic types), and lately in the area of PDLC. Two different technologies of electrically controlled variable transmittance devices were studied in order to develop applications according to the three research branches of the group. Thus, new organic EC devices and PDLC devices developed and manufactured by CIDETEC were electro-optically characterized by the author of this work by means of different techniques. Among the optical techniques, optical transmittance, response times, or colorimetry, (useful for deriving the chromaticity coordinates and the RGB values), were studied over the different samples. The visual appearance of the different samples was simulated from RGB calculated values and considering the human eye sensitivity curve. The irradiance and the correlated color temperature (CCT) of the lamp of a monochromator based spectrophotometer were measured in the Metrology Department of CSIC-IFA (Applied Physics Institute at the Scientific Research High Council) placed in Madrid (Spain), in order to perform absolute measurements from the spectrometer by means of a calibrated source. Impedance characterization involving EIS (Electrochemical Impedance Spectroscopy), a useful technique for deriving the equivalent electric circuit (EEC) model of the measured samples, and electrochemical methods, such as cyclic voltammetry (CV), chronoamperometry (ChrA) or chronocoulometry (ChrC) experiments, required for computing parameters such as coloration efficiency or effective charge density, were carried out using commercial characterization instrumentals, such as impedance analyzer or potentiostat, acquired by GDAF. Besides, an electro-optic characterizer prototype of EC devices based on a data acquisition card was developed in this work.

EC and PDLC samples were further studied for using them in applications such as displays, variable optical attenuator (VOA) for optical fiber optic communications, smart windows domotic system with local and internet control, and different kind of technologies developed for optical glasses and vision systems adequate for impaired people in glare environments, being this last application carried out since 2007 in collaboration with IOBA, University Institute of Applied Ophthalmology of Valladolid (Spain).

A year later, two samples of a suspended particle device (SPD) smart window technology were acquired by GDAF, being optically and electrically characterized by the author. The acquired SPD technology favored a research collaboration with the Division of Solid State Physics at the Department of Engineering Sciences, at the Angstrom Laboratory of Uppsala (Sweden), regarding optical characterization including the study of the scattering and absorption (S & K) coefficients, derived from diffuse transmittance and reflectance measurements, which were performed with integrating sphere based spectrophotometers. The S & K coefficients were computed in Matlab by a fitting process using two flux Kubelka-Munk and four flux Maheu models, Saunderson correction for refractive index discontinuities, spectral interface reflectances and diffuse fractions of light at the top and at the bottom interfaces. Angle dependence transmission and electrical current consumption measurements on the SPD were also performed.

The knowledge and development of such optical methods, useful for prediction of the optimum thickness of active layers of transmittance variable technologies, led to the start of a new collaboration framework this current year with the Laboratory for Spectrometry of Materials of the National Institute of Chemistry in Ljubljana (Slovenia), which develops inorganic EC devices and black coatings for solar absorbers applications. These two research areas are not included in the current work of thesis, but considered for near future research lines of the author. Optical constants of materials and particle geometry is the next step of the future research lines in collaboration with Angstrom Laboratory, in order to compare with scattering and absorption coefficients derived from two flux and four flux models.

The author contributed also to the biannual International Meeting on Electrochromism (IME) conferences since 2004 and to the biannual Spanish Meeting of Optoelectronics (OPTOEL) since 2005. Other international meeting contributions of the author can be found, such as the International Society of Optics and Photonics (SPIE), International Commission of Illumination (CIE), and Materials Research Society (MRS and EMRS) and national meeting, such as National Congress of Color in 2007 and Spanish Conference in Electronic Devices. Several publications were derived from such contributions.

I.2.2 Outline of the Thesis

I. A state of the art of electrically controllable transmittance materials and electrochromic devices is widely covered in this Chapter I, including how chromogenic technologies can be used in applications for glazing and coatings for satisfying the requirements of energy savings in heating, cooling and lighting systems. The use of transparent conductors in the different types of EC, SPD and PDLC devices, and other smart windows technology such as micro blinds are seen in this chapter. Besides the state of the art, Chapter I also deals of an introduction of the document, including the motivation and the outline of the thesis, the present work has been written according to the following structure:

II. Instrumental and techniques, such as transmittance, colorimetry, scattering and angle dependence for optical characterization, and fundamentals of EIS, studies of EEC models, including Warburg and constant phase elements, for electrical impedance characterization, and CV, ChrA and ChrC experiments performed for electrochemical characterization, are covered in Chapter II.

III. The characterization of new PEDOT and viologen based EC devices, developed by CIDETEC, and their dependence with the thickness, is covered in Chapter III. Parameters of the EEC model of Impedance EIS characterization are related with the optical coloration levels and the parameters derived from CV experiments. The internal layer thickness dependence is studied for optical, electrical impedance and electrochemical characterization of viologen based EC devices.

IV. SPD technology samples are electro-optically characterized in Chapter IV, including a new method developed for computing S & K coefficients from diffuse transmittance and reflectance components measured in the Angstrom Laboratory for different levels of coloration observed in these devices.

V. New PDLC samples with different size and thicknesses and a new PDLC-EC tandem device, developed by CIDETEC, are characterized in Chapter V. Diffuse transmittance and reflectance of these samples were measured in the Angtrom Laboratory.

VI. Several applications developed using chromogenic technologies are described in Chapter VI, including new glasses with EC filter for people with low vision, VOA using EC devices, transparency domotic control of PDLC based smart windows and the design and development of an electro-optic characterizer of EC devices (CEODEC).

VII. Conclusions and future research lines of the results obtained with the characterized PEDOT and viologen based EC devices, SPD and PDLC samples, and relative to the developed applications. Finally, appendix A deals with the procedure followed for deriving the two flux transmittance and reflectance equations by using the S & K coefficients.

References

[Abd11] Abdul Vahid," Amazon Kindle Touch 3G vs. Sony Reader Wi-Fi PRS-T1, e-Reader to wait for?" (2011) http://www.gizmowatch.com/entry/amazon-kindle-touch-3g-sony-reader-wi-fi-prs-t1-reader-wait/

[ACG06] A.C. van Geest-Lokhorst, "Reflections on switchable mirror devices", PhD. Thesis, Vrije University Amsterdam, The Netherlands (2006).

[All06] Robert Allan Ramsey, "Holographic patterning of polymer dispersed liquid crystal materials for diffractive optical elements", PhD. Thesis, University of Texas (USA) (2006).

[Amo00] Max Amon, Clifford J. Luty, "TIR window", U.S. Patent No. 6,116,740, (2000).

[And05] Brian D'Andrade, "Novel Smart Windows Based on Transparent Phosphorescent OLEDs", Universal Display Corporation Report (2005).

[And07] Peter Andersson, "Charge Transport Modulation and Optical Absorption Switching in Organic Electronic Devices Switching in Organic Electronic Devices", PhD Thesis, Linköpings university, Sweden (2007).

[Arg04] A.A. Argun, P-H. Aubert, B.C. Thompson, I. Schwendeman, C.L. Gaupp, J. Hwang, N.J. Pinto, D.B. Tanner, A.G. MacDiarmid, and J.R. Reynolds, "Multi-colored electrochromism in polymers: Structures and devices", Chemistry of Materials 16 (2004) 4401-4412.

[aut] http://www.autoaccessoriesgarage.com/Rear-View-Mirrors/Gentex-Auto-Dimming-Rear-View-Mirror

[Bae10] R. Baetens, B. Jelle, A. Gustavsen, "Properties, requirements and possibilities of smart windows for dynamic daylight and solar energy control in buildings: A state-of-the-art review". Solar Energy Materials & Solar Cells, 94 (2) (2010) 87-105.

[Bea08] P. M. Beaujuge, S. Ellinger, and J. R. Reynolds, "Spray processable green to highly transmissive electrochromics via chemically polymerizable donor-acceptor heterocyclic pentamers," Advanced Materials 20 (2008) 2772–2776.

[Bec99] H. Becker, H. Wittkopf, "Variable solar control glazing - an outstanding application for electrochromics", Proceedings of the Third International Meeting on Electrochromics, London, UK, Proceedings Electrochimica Acta 44 (1999) 3259-3268.

[Ber10] Michael Berger, "Nanotechnology drives electronic paper displays", (2010) http://www.nanowerk.com/spotlight/spotid=14546.php

[BG80] Barbara Grant, N. J. Clecak, Michael Oxsen, Annette Jaffe, G. S. Keller, "Study of the electrochromism of methoxyfluorene compounds",The Journal of Organic Chemistry 45 (4) (1980) 702–705.

[BL09] Boris Lamontagne, Pedro Barrios, Christophe Py and Suwas Nikumb "The next generation of switchable glass: the Micro-Blinds", Glass Performance Days (2009) 637–639.

[Blo77] Allen Bloom and E. B. Priestley, “Criteria for evaluating pleochroic dye liquid-crystal displays”, IEEE Transactions on Electron Devices, 24 (7) (1977) 823-826.

[Boo11] Milko van der Boom, “From Monolayer-based Sensors to Sequential Logic Circuits and Memory Elements”, Materials Research Society MRS Spring Meeting, Symposium H: Electrochromic Materials and Devices, San Francisco, USA (2011).

[But06] Matthew Paul Butterfield, “Design and Manufacture of a Second Generation Switch-Operated Window Wall”, (2006) North Carolina State University (USA).

[Byk90] Harlan J. Byker, Gentex Corporation, "Single-compartment, self-erasing, solution-phase electrochromic devices, solutions for use therein, and uses thereof”, U.S. Patent No.4,902,108, (1990).

[Byk94a] Harlan J. Byker, “Bipyridinium salt solutions”, U.S. Patent No. 5,294,376, (1994).

[Byk94b] Harlan J. Byker, “Electrochromic devices with bipyridinium salt solutions” U.S. Patent No. 5,336,448, (1994).

[Byk94c] Harlan J. Byker, “Variable reflectance mirror” U.S. Patent No. 5,282,077, (1994).

[Byk00] Harlan J. Byker, "Electrochromics and polymers", Electrochimica Acta 46 (2001) 2015–2022.

[Cer11] Rachel Cericola, "Could SPD-Smartglass Replace Shades?" Electronic House Magazine (2011).

[CFL11] Chiao-Fen Lin, Chih-Yu Hsu, Hwa-Chiang Lo, Cheng-Lan Lin, Lin-Chi Chen, Kuo-Chuan Ho, "A complementary electrochromic system based on a Prussian blue thin film and a heptyl viologen solution", Solar Energy Materials and Solar Cells 95 (2011) 3074–3080.

[Cha75] I. F. Chang, B. L. Gilbert, and T. I. Sun, "Electrochemichromic Systems for Display Applications Journal of The Electrochemical Society 122 (7) (1975) 955-962.

[Cha81] I.F. Chang, "Electrochromic and electrochemichromic displays", Displays 2 (6) (1981), 275-278.

[Che05] Cheng-Hou Chen, “Flexible Electrochromic Devices Employing Conducting Polymers”, Master Thesis, National Cheng Kung University, Taiwan (2005).

[ChX07] Chunye Xu, Chao Ma, "Smart sunglasses feature lenses that change color on demand", 233rd American Chemical Society National Meeting, Chicago, USA (2007).

[Cin99] Rachel Cinnsealach, Gerrit Boschloo, S. Nagaraja Rao, Donald Fitzmaurice, "Coloured electrochromic windows based on nanostructured TiO2 films modified by adsorbed redox chromophores", Solar Energy Materials and Solar Cells 57 (1999) 107-125.

[CMM07] Research at CMMPE — Materials — Polymer dispersed liquid crystals (PDLCs), Centre of molecular materials for photonics and electronics, University of Cambridge (2007) http://www-g.eng.cam.ac.uk/CMMPE/res_mat_pdlc.html.

[Coc10] Ayse Cochet, Uwe Posset, Gerhard Schottner, Giorgio Pagani, Ricardo Ruffo, Luca Beverina, Claudio Maria Mari, Giorgio Patriarca, Alessandro Abbotto, “Highly

transparent electrochromic coating material, method for producing the same and use of the material" US. Patent 2010/0189918 A1.

[Com98] Comiskey, B., Albert, J.D., Yoshizawa, H. and Jacobson, J. "An electrophoretic ink for all-printed reflective electronic displays." Nature 394 (1998) 253-255.

[Cox10] Ben Coxworth, "Electronic displays could benefit from new class of liquid crystals", gizmag (2010) http://www.gizmag.com/new-class-of-liquid-crystals/16614/

[Cui05] Hai-Ning Cui, "Preparation and characterization of optical multilayered coatings for smart windows applications", University of Minho, School of Sciences, PhD. Thesis, Braga and Guimarães, Portugal (2005).

[Deb69] S. K. Deb, "A Novel Electrophotographic System", Applied Optics 8 S1 (1969) 192-195.

[Deb73] S. K. Deb, "Optical and photoelectric properties and colour centres in thin films of tungsten oxide", Philosophical Magazine 27 (4) (1973) 801-822.

[Deb00] Satyen K. Deb, "Photovoltaic-Integrated Electrochromic Device for Smart-Window Applications", World Renewable Energy Congress VI, Brighton, U.K., (2000).

[Dee10] M. Deepa, A.P. Saxena, A.G. Joshi, A.K. Srivastava, "Poly(3,4ethylenedioxythiophene) doped by ionic liquid / acid functionalized graphene: Syntheses, electrochromism and electrochemistry", 9th International Meeting on Electrochromism (I.M.E.9), Bordeaux, France (2010).

[Din10] Y. Ding, M.A. Invernale, G.A. Sotzing, "Conductivity Trends of PEDOT-PSS Impregnated Fabric and the Effect of Conductivity on Electrochromic Textile", ACS Applied Materials & Interfaces 2(6) (2010) 1588-1593.

[Doa86] Doane JW, Vaz NA, Wu BG, Zumer S., "Field controlled light scattering from nematic microdroplets", Applied Physics Letter 48 (1986) 269-271.

[Doa87] Doane JW, Chidichimo G, Vaz NA., " Light modulating material comprising a liquid crystal dispersion in a plastic matrix". US Patent 4,688,900 (1987).

[Doa88] Doane JW, Golemme A., West JL, Whitehead JB, Jr., B.-G. Wu, "Polymer Dispersed Liquid Crystals for Display Applications," Molecular Crystals and Liquid Crystals 165 (1988) 511.

[ELe00] Eleanor Lee, Dennis DiBartolomeo, and Stephen Selkowitz, "Electrochromic Window Tests in U.S. Office Show Promise", Environmental Energy Technologies Division News, Lawrence Berkeley National Laboratory (2000).

[epa] http://www.epapercentral.com/epaper-technologies-guide

[ESL06] Eleanor S. Lee, Stephen E. Selkowitz, Robert D. Clear, Dennis L. DiBartolomeo, Joseph H. Klems, Luis L. Fernandes, Greg J. Ward, Vorapat Inkarojrit, Mehry Yazdanian, "A Design Guide for Early-Market Electrochromic Windows", Lawrence Berkeley National Laboratory (2006).

[ESL11] Eleanor S. Lee "On Characterizing the Energy-efficient Potential of Electrochromic Windows in Buildings: Measured and Simulated Data", Materials Research Society MRS Spring Meeting, Symposium H: Electrochromic Materials and Devices, San Francisco, USA (2011).

[Fer85] Fergason, J. L. "Polymer encapsulated nematic liquid crystals for display and light control applications". Symposium of Technical Digest of the Society for Information Display 16 (1985) 68-70.

[Gab84] J.V. Gabrusenoks, P.D. Cikmach, A.R. Lusis, J.J. Kleperis, G.M. Ramans, "Electrochromic colour centres in amorphous tungsten trioxide thin films", Solid State Ionics 14 (1) (1984) 25-30.

[Gal01] Gallion, Franklin Cordell, "Manufacture and Field Test of a New Adaptive Shading Product: A Case Study", Master's Thesis, North Carolina State University, USA (2001).

[Gei09] A. K. Geim, "Graphene: Status and Prospects", Science 324 (2009) 1530-1534.

[God83] N.J. Goddard, A.C. Jackson, M.G. Thomas, "Spectrelectrochemical studies of some viologens used in electrochromic display applications", Journal of Electroanalytical Chemistry and Interfacial Electrochemistry 159 (2) (23) (1983) 325-335.

[Gom01] Pedro Gomez-Romero, "Hybrid organic-inorganic materials. In search of synergic activity", Advanced Materials 13 (3) (2001) 163-174.

[Gra89] Claes-Göran Granqvist "Spectrally selective surfaces for heating and cooling applications", SPIE Optical Engineering Press, Bellingham, Wash., USA (1989).

[Gra92] Claes-Göran Granqvist, "Electrochromism and smart window design", Solid State Ionics 53-56 Part 1 (1992) 479-489.

[Gra95] Claes-Göran Granqvist, Handbook of Inorganic Electrochromic Materials, Elsevier, Amsterdam, (1995).

[Gra01] K. G. Terry Hollands, J.L. Wright, C. G. Granqvist, Solar Energy - the State of the Art – International Solar Energy Society (ISES) Position Papers. (2) Glazing and Coatings. London: James & James (2001).

[Gra06] Claes-Göran Granqvist, "Electrochromic materials: Out of a niche", Nature Materials 5, (2006) 89-90.

[Gra07a] Claes G. Granqvist, "Transparent conductors as solar energy materials: A panoramic review", Solar Energy Materials and Solar Cells 91 (2007) 1529-1598.

[Gra07b] C.G. Granqvist,"Electrochromics: Why, How, and Whither", 7th International Meeting on Electrochromism (I.M.E.7), Istanbul, Turkey (2006).

[Gra08] C. G. Granqvist, "Electrochromic foil devices with variable optical transmittance", Active, functional and nanostructured coatings, 4th Mikkeli International Industrial Coating Seminar MIICS, Mikkeli, Finland (2008).

[Gra09] C. G. Granqvist, P. C. Lansaker, N.R. Mlyuka, G. A. Niklasson, E. Avendaño, "Progress in chromogenics: New results for electrochromic and thermochromic materials and devices", Solar Energy Materials and Solar Cells 93 (2009) 2032-2039.

[Gra10a] C.G. Granqvist, S. Green, G.A. Niklasson, N.R. Mlyuka, S. von Kræmer, P. Georén, "Advances in chromogenic materials and devices", Thin Solid Films 518 (2010) 3046-3053.

[Gra10b] C.G. Granqvist, "Oxide Electrochromics: An Introduction", 9th International Meeting on Electrochromism (I.M.E.9), Bordeaux, France (2010).

[Gra11a] C. G. Granqvist, I. Bayrak Pehlivan, S. V. Green, P. C. Lansaker and G. A. Niklasson, "Oxide-Based Electrochromics: Advances in Materials and Devices", Proceedings of Materials Research Society MRS Spring Meeting, Symposium H: Electrochromic Materials and Devices, San Francisco, USA, (2011).

[Gra11b] C. G. Granqvist, "Advances in chromogenics: Toward superfenetration", European Materials Research Society EMRS Fall Meeting, Symposium L: Towards lightweight, flexible and self sustained ion-based devices, Warsaw, Poland (2011).

[Gra12] C.G. Granqvist, "Oxide electrochromics: An introduction to devices and materials", Solar Energy Materials and Solar Cells 99 (2012) 1-13.

[Gre94] Charles B. Greenberg, "Optically switchable thin films: a review", Thin Solid Films 251 (2) (1994) 81-93.

[GSo09] Gregory M. Sottile, "Daylight harvesting using SPD-SmartGlass and advanced control systems", Research Frontiers Inc. (2009).

[Gur99] K. Gurunathan, A. Vadivel Murugan, R. Marimuthu, U.P. Mulik, D.P. Amalnerkar, "Electrochemically synthesized conducting polymeric materials for applications towards technology in electronics, optoelectronics and energy storage devices", Materials Chemistry and Physics 61 (1999) 173-191.

[Ham08] Mahiar Hamed, "Organic electronics on micro and nano fibers from e-textiles to biomolecular nanoelectronics", PhD Thesis, Linköpings University, Sweden (2008).

[Hei68] G. H. Heilmeier and L. A. Zanoni, "Guest-host interactions in nernatic liquid crystals. A new electro-optic effect" Applied Physics Letter 13 (1968) 91-92.

[Her02] Herb, C. A., Zhang, L. "Electrophoretic ink composed of particles with field dependent mobilities" U.S. Patent No.7,038,655, (2002).

[Her06] Erik Herz, "Electrophoretic Display Technology: The beginnings, the improvements, and a future in flexible electronics", MSE 542 (2006) Materials Science and Engineering Cornell University, Ithaca, NY (USA).

[Hit] http://www.hitachi-chem.co.jp/english/products/arp/018.html

[Hos12] Nahid Hosein Nataj, Ezeddin Mohajerani, Hossein Jashnsaz, and Ali Jannesari,"Holographic polymer dispersed liquid crystal enhanced by introducing urethane trimethacrylate", Applied Optics 51 (6) (2012) 697-703.

[Hua11] H. Huang, J. Tian, W.K. Zhang, Y.P. Gan, X.Y. Tao, X.H. Xia, J.P. Tu, "Electrochromic properties of porous NiO thin film as a counter electrode for NiO/WO3 complementary electrochromic window", Electrochimica Acta 56 (2011) 4281-4286.

[ide] Asunción Josefa Galvan, Ana Sanchez, Cristina Casellas, Nuria Guilera, Laura López, Cristina Pozo, Ana Viñuales, "Plastic Electronics and Its Introduction Into the Toy Sector", http://www.ides.com/articles/design/2010/plastic-electronics.asp

[Inv11] Michael A Invernale, Yujie Ding, Gregory A Sotzing, "The effects of coloured base fabric on electrochromic textile", Coloration Technology 127 (3) (2011)167-172.

[ios] http://www.iossisidingandwindows.com/low-e.html

[Iso08] Fiat Croma automobile and BMW armored glass window debut at Security Essen 2008 featuring Isoclima's Cromalite® brand of SPD-Smartglass.

[Jen05] S. A. Jenekhe, D. J. Kiserow, "Chromogenic Effects in Polymers: An Overview of the Diverse Ways of Tuning Optical Properties in Real Time," American Chemical Society Symposium Series 888 (2005) 2-15.

[JHP07] Jeong Hyun Park, Mi Ah Lee, Bong Jun Park, Hyoung Jin Choi , "Preparation and electrophoretic response of poly(methyl methacrylate-co-methacrylic acid) coated TiO2 nanoparticles for electronic paper application", Current Applied Physics 7 (2007) 349–351.

[Jov04] V. Jovanovski, A. Surca Vuk, R. Jese, B. Orel, P. Lianos, "Synthesis and properties of R' R'' $Im^{+}I^{-}$ ionic liquids based redox electrolytes and their performance in hybrid electrochromic cells", 6th International Meeting on Electrochromism (I.M.E.6), Brno, Czech Republic (2004).

[Jov07] V. Jovanovski, B. Orel, I. Jerman, S.B. Hocevar, B. Ogorevc, "Electrochemical and in-situ Raman spectroelectrochemical study of 1-methyl-3-propylimidazolium iodide ionic liquid with added iodine", Electrochemistry Communications 9 (2007) 2062-2066.

[JTZ09] Juan Carlos Torres Zafra, "Characterization, electrical modeling and development of new applications of liquid crystals based devices", PhD. Thesis, Carlos III University of Madrid, Spain (2009).

[Kie01] Kiefer, Scott F., Larry M. Silverberg, and Manoel L. Gonzalez "Electrostatically actuated window blinds" Journal of Electrostatics 50 (2001) 229-248.

[Kob08] Norihisa Kobayashia, Shohei Miura, Mami Nishimura, Hikaru Urano, "Organic electrochromism for a new color electronic paper", Solar Energy Materials and Solar Cells 92 (2008) 136-139.

[Koo02] E.S. Kooij, J.H. Rector, D.G. Nagengast, J.W.J. Kerssemakers, B. Dama, R. Griessen, A.Remhof, H.Zabel, "Growth and hydrogenation of epitaxial yttrium switchable mirrors on CaF_2", Thin Solid Films 402 (2002) 131-142.

[Kis02] Nikolai Kislov, "Electrochromic Variable Emissivity Devices for Thermal Control, Electrochromic Variable Emissivity Devices for Thermal Control", National Aeronautics and Space Administration (NASA) Award (2002)

[Kis04] Nikolai Kislov, "Space related applications of electrochromics", 6th International Meeting on Electrochromism (I.M.E.6), Brno, Czech Republic (2004).

[KLe07] Kenny Lee, "Satellite thermal control with variable emittance electrochromic devices", Mechanical and Aerospace Engineering (MAE) 221A (2007).

[Kuo99a] Kuo-Chuan Ho, "The influence of charge capacity ratio on the performance of a complementary electrochromic system", Solar Energy Materials and Solar Cells 56 (1999) 271-280.

[Kuo99b] Kuo-Chuan Ho, "Cycling and at-rest stabilities of a complementary electrochromic device based on tungsten oxide and Prussian blue thin films" Electrochimica Acta 44 (1999) 3227-3235.

[Kuo11] Kuo-Chuan Ho, "Optimal Design for Complementary Electrochromic Devices: Application to the Prussian Blue and Poly(ProDOT-Et2) System", European Materials Research Society EMRS Fall Meeting, Symposium G: New trends in chromogenic materials and devices, Warsaw, Poland (2011).

[KCC11] Kun-Chieh Chen, Chih-Yu Hsu, Chih-Wei Hu, Kuo-Chuan Ho, "A complementary electrochromic device based on Prussian blue and poly(ProDOT-Et2) with high contrast and high coloration efficiency", Solar Energy Materials and Solar Cells 95 (2011) 2238-2245.

[Lam90] Carl M. Lampert, C.G. Granqvist, " Large-Area Chromogenics: Materials and Devices for Transmittance Control", Optical Engineering Press-SPIE, Bellingham, WA (1990).

[Lam94] Carl M. Lampert, "Glazing Materials for Solar and Architectural Applications", International Energy Agency Solar Heating and Cooling Program Task 10-Solar Materials R&D Subtask C-Glazing Materials (1994).

[Lam95] Carl M. Lampert, "Chromogenic Switchable Glazing: Towards the Development of the Smart Window", Conference Proceedings of WINDOW INNOVATIONS '95 (1995), Toronto (Canada).

[Lam98] Carl M. Lampert, "Smart switchable glazing for solar energy and daylight control", Solar Energy Materials and Solar Cells 52 (1998) 207-221.

[Lam03] C.M. Lampert, "Large-area smart glass and integrated photovoltaics", Solar Energy Materials and Solar Cells 76 (2003) 489-499.

[Lam04] Carl M. Lampert, "Chromogenic smart materials", Materials Today 7 (3) (2004) 28-35.

[LCC01] Lin-Chi Chen, Kuo-Chuan Ho, "Design equations for complementary electrochromic devices: application to the tungsten oxide–Prussian blue system", Electrochimica Acta 46 (2001) 2151–2158.

[LCs12] "Liquid Crystals". Nobelprize.org. 13 Apr 2012 http://www.nobelprize.org/educational/physics/liquid_crystals/history/

[LSP06] Lee Soon Park, Jin Woo Park, Hae Yun Choi, Yoon Soo Han, Younghwan Kwon, Hyung Suk Choi, "Fabrication of charged particles for electrophoretic display", Current Applied Physics 6 (2006) 644-648.

[Lus03] Andrejs Lusis, Janis Kleperis and Evalds Pentjuss, "Model of electrochromic and related phenomena in tungsten oxide thin films", Journal of Solid State Electrochemistry 7 (2003) 106-112.

[Mal06] Praveen Malik, Pankaj Kumar and K.K. Raina, Guest-Host Polymer Dispersed Liquid Crystal Display Device: Role of Dichroic Dye, Proc. of ASID'06.

[Mat09] Chiho Matsuda, Nikkei Monozukuri, "Hitachi Chemical Rolls Out Voltage-controlled Dimming Film" (2009).

[Men08] Santi Mensa, "Optimización y extracción de parámetros ópticos de estructuras multicapas", Proyecto final de carrera de Enginyeria Automática i Electrónica Industrial (2008) Universitat Rovira i Virgili, Tarragona (Spain).

[Mer11] Mercedes-Benz Unveils Viano Vision Pearl Luxury Van Using SPD-SmartGlass Technology at 2011 Frankfurt Auto Show.

[Mic33] L. Michaelis and E. S. Hill, "The viologen indicators", The Journal of General Physiology 16, 859-873 (1933).

[Mon95a] P. M. S. Monk, R. J. Mortimer, and D. R. Rosseinsky, "Electrochromism: Fundamentals and Applications." VCH, Weinheim, (1995).

[Mon95b] Paul Monk, Roger Mortimer and David Rosseinsky, "Through a glass darkly", Chemistry in Britain, (1995), 31,380.

[Mon98] P. M. S. Monk, "The Viologens: Physicochemical Properties, Synthesis and Applications of the Salts of 4,4'-Bipyridine." Wiley, Chichester (1998).

[Mon01a] P.M.S. Monk, "Electrochromism and Electrochromic Materials for Displays", Handbook of Advanced Electronic and Photonic Materials and Devices 7 (3), H.S. Nalwa, (2001).

[Mon01b] Paul M.S. Monk, Frederic Delage, Sara Maria Costa Vieira, "Electrochromic paper: utility of electrochromes incorporated in paper", Electrochimica Acta 46 (2001) 2195-2202.

[Mor97] Roger J. Mortimer, Electrochromic materials, Chemical Society Reviews 26 (1997) 147-156.

[Mor99a] Roger J. Mortimer, "Organic electrochromic materials", Electrochimica Acta 44 (1999) 2971-2981.

[Mor99b] Roger J. Mortimer, Christopher P. Warren, "Cyclic voltammetric studies of Prussian blue and viologens within a paper matrix for electrochromic printing applications", Journal of Electroanalytical Chemistry 460 (1999) 263-266.

[Mor06] Roger J. Mortimer, Aubrey L. Dyer, John R. Reynolds, "Electrochromic organic and polymeric materials for display applications", Displays 27 (2006) 2-18.

[Mor08] Roger J. Mortimer, John R. Reynolds, "An in situ colorimetric measurement study of electrochromism in the di-n-heptyl viologen system", Displays 29 (2008) 424-431.

[Mor11] Roger J. Mortimer, Thomas S. Varley, "Synthesis, characterisation and in situ colorimetry of electrochromic Ruthenium purple thin films", Dyes and Pigments 89 (2011) 169-176.

[Muc03] M. Mucha, “Polymer as an important component of blends and composites with liquid crystals”, Progress in Polymer Science 28 (2003) 837-873.

[Nag94] J. Nagai, G. McMeeking, T. Seike, Y. Noutomi, “Smart electrochromic glazing”, Glazing Today (1994) 34.

[Nag98] T. Nagata et al., "Silicon chip based reflective PDLC light valve for projection display", SID Symposium Digest 29 (1998) 37.

[Nan09] “Indium Tin Oxide and Alternative Transparent Conductor Markets”, NanoMarkets study (2009).

[Nat03] Lalgudi LV. Natarajan, Christina K. Shepherd, Donna M. Brandelik, Richard L. Sutherland, Suresh Chandra, Vincent P. Tondiglia, David Tomlin,and Timothy J. Bunning, "Switchable Holographic Polymer-Dispersed Liquid Crystal Reflection Gratings Based on Thiol−Ene Photopolymerization", Chemistry of Materials 15 (2003) 15 (12) 2477-2484.

[Nik01] Gunnar A. Niklasson, Josefin Klasson, Eva Olsson, “Polaron absorption in tungsten oxide nanoparticle aggregates”, Electrochimica Acta 46 (2001) 1967-1971.

[Nik07] G. A. Niklasson and C. G. Granqvist, “Electrochromics for smart windows: Thin films of tungsten oxide and nickel oxide, and devices based on these”, Journal of Material Chemistry 17 (2007) 127-156.

[NLe92] Nicholas Leventis, Young C. Chung, “New complementary electrochromic system based on poly(pyrrole)-Prussian blue composite, a benzylviologen polymer, and poly(vinylpyrrolidone)/potassium sulfate aqueous electrolyte”, Chemistry of Materials 4 (6) (1992) 1415-1422.

[nrc] Micro-blinds, New smart glass, National Research Council Canada, Institute for Microstrutural Sciences, http://www.youtube.com/watch?v=RqwL2egaqYY

[NREL10] “NREL researchers: Dynamic windows could cut building energy use by one-eighth” (2010).

[Oze99] N. Ozer, C.M. Lampert, "Electrochromic performance of sol-gel deposited WO_3-V_2O_5 films", Thin Solid Films 349 (1999) 205-211.

[Pad06] Javier Padilla Martínez, “Characterization and optimization of conducting polymer based dual electrochromic devices”, PhD. Thesis, Polytechnic University of Cartagena, Spain (2006).

[Pad07] J. Padilla, V. Seshadri, T.F. Otero, G.A. Sotzing, "Electrochemical study of dual conjugated polymer electrochromic devices", Journal of Electroanalytical Chemistry 609 (2007) 75-84.

[Pad08] J. Padilla, T.F. Otero, "Contrast limitations of dual electrochromic systems", Electrochemistry Communications 10 (2008) 1-6.

[Pad09] J. Padilla, "A theoretical investigation on the contrast limitations of dual electrochromic systems", Thin Solid Films 517 (2009) 5580–5583.

[Pad10] J. Padilla, N. Espinosa, R. Garcia Valverde, A. j. Fernández Romero, A. Urbina, "The role of counter electrodes in electrochromic devices: necessary, but, beneficial or damaging?", 9th International Meeting on Electrochromism (I.M.E.9), Bordeaux, France (2010).

[Pad11] J. Padilla, "Increasing performance of electrochromic devices by modifying surface and charge ratio between electrodes", Solar Energy Materials and Solar Cells 99 (2012) 56-61.

[Ran82] J.-P. Randin and R. Viennet, "Proton diffusion in tungsten trioxide thin films", Journal of The Electrochemical Society 129 (10) (1982) 2349-2354.

[Rau99] R. David Rauh, "Electrochromic windows: an overview",Electrochimica Acta 44 (1999) 3165-3176.

[Rau01] R.D. Rauh, F. Wang, J.R. Reynolds, D.L. Meeker, "High coloration efficiency electrochromics and their application to multi-color devices", Electrochimica Acta 46 (2001) 2023–2029.

[Rey11] John R. Reynolds, Aubrey L. Dyer, Chad Amb, David Y. Liu, Michael R. Craig, Emily J. Thompson, Eric P. Knott, Justin A. Kerszulis, Andrew D. Chilton and Joseph E. Babiarz, "Completing the Color Palette With Conjugated Electrochromic Polymers", Materials Research Society MRS Spring Meeting, Symposium H: Electrochromic Materials and Devices, San Francisco, USA (2011).

[RFI11a] http://www.spdcontrolsystems.com/Docs/Research_Frontiers_Press_Release-_February_7_2011.pdf

[RF11b] Audi Premieres A2 Concept Car With Research Frontiers' SPD-SmartGlass Technology at 2011 Frankfurt Auto Show. SPD Control Systems Corporation (2010).

[Ric03] Thomas J. Richardson, "New electrochromic mirror systems", Solid State Ionics 165 (2003) 305-308.

[Rin10] Bryan Ringstrand and Piotr Kaszynski, "Electronic displays could benefit from new class of liquid crystals High D3 nematic liquid crystals: fluxional zwitterions of the [closo-1-CB_9H_{10}]$^-$ cluster", Journal of Materials Chemistry 21 (2010) 90-95.

[Ros90] D.R. Rosseinsky, P.M.S. Monk, R.A. Hann, "Anion-dependent aqueous electrodeposition of electrochromic 1,1′-bis-cyanophenyl-4,4′-bipyridilium(cyanophenyl-paraquat) radical cation by cyclic voltammetry and spectroelectrochemical studies", Electrochimica Acta 35 (7) (1990) 1113-1123.

[Ros92] David R. Rosseinsky, Paul M.S. Monk, "Electrochromic cyanophenylparaquat (CPQ: 1,1′-bis-cyanophenyl-4,4′-bipyridilium) studied voltammetrically, spectroelectrochemi-cally and by ESR", Solar Energy Materials and Solar Cells 25 (3-4) (1992), 201-210.

[Ros01] David R. Rosseinsky and Roger J. Mortimer, "Electrochromic Systems and the Prospects for Devices", Advanced Materials 13 (11) (2001) 783-793.

[Row02] Natalie m. Rowley and Roger J. Mortimer, "New electrochromic materials", Science Progress 85 (3) (2002) 243-262.

[Rui10] Graham de Ruiter, Yair H. Wijsboom, Noa Oded, and Milko E. van der Boom, "Polymeric Memory Elements and Logic Circuits that Store Multiple Bit States", ACS Applied Materials and Interfaces 2 (12) (2010) 3578–3585.

[Rui11] Graham de Ruiter and Milko E. van der Boom, "Sequential logic and random access memory (RAM): a molecular approach" Journal of Materials Chemistry (2011).

[Sap98] S. Sapp, G.A. Sotzing, J.R. Reynolds, "High contrast ratio and fast switching dual polymer electrochromic devices", Chemistry of Materials 10 (1998) 2101-2108.

[SCSC] http://www.spdcontrolsystems.com/AutoDemo.htm

[SHK04] Sang-Ho Kim, Sang-Bok Lee, "Electrochromism of conducting polymer nanotubes", 6th International Meeting on Electrochromism (I.M.E. 6), Brno, Czech Republic (2004).

[SHL95] S.-H. Lee, S.-K. Joo, "Electrochromic behavior of Ni-W oxide electrodes", Solar Energy Materials and Solar Cells 39 (1995) 155-166.

[Sil98] Silverberg, Larry M. "Electrostatically Positioned Blind Insert for Insulated Glass." U.S. Patent No. 5,850,861, (1998).

[Sot] http://chemistry.uconn.edu/sotzing.html.

[Sot11] G.A. Sotzing, Y. Ding, M.A. Invernale, "Electrochromic Spandex and Other Fabrics for Adaptive Camouflage", Program No. *H1.8 (2011) Abstract Viewer, San Francisco, CA; Materials Research Society.

[STa09] Satomi Tanaka, Yuichi Watanabe,Takeshi Nagashima,Norihisa Kobayashi, "Phthalate-derivative/TiO2-modified electrode for electrochromic application", Solar Energy Materials and Solar Cells 93 (2009) 2098-2101.

[Sub10] Jegadesan Subbiah, Kaushik Roy Choudhury, Stefan Ellinger, John R. Reynolds, and Franky So, "Color Tunable π-Conjugated Polymers for Solar-Cell Applications: Engineering of Bandgap, Interface, and Charge Transport Properties", IEEE Journal of Selected Topics in Quantum Electronics 16 (6) (2010) 1792-1799.

[Sul96] R. Sullivan, E.S. Lee, M. Rubin, S. Selkowitz, "The Energy Performance Of Electrochromic Windows in Heating-Dominated Geographic Locations", SPIE International Symposium on Optical Materials Technology for Energy Efficiency and Solar Energy Conversion XV, Freiburg, Germany (1996).

[Sur08] A. Surca Vuk, V. Jovanovski, A. Pollet-Villard, I. Jerman, B. Orel, "Imidazolium-based ionic liquid derivatives for application in electrochromic devices, Solar Energy Materials and Solar Cells 92 (2008) 126-135.

[SVB11] Sara Ver-Bruggen, "Cost-effective smart windows to reach the market in 2012", +Plastic Electronics magazine (2011).

[Sve84] J.S.E.M. Svensson, C.G. Granqvist, "Electrochromic tungsten oxide films for energy efficient windows", Solar Energy Materials and Solar Cells 11 (1-2) (1984) 29-34.

[Tai08] Taichi Ikeda and James Fraser Stoddart, "Electrochromic materials using mechanically interlocked molecules", Science and Technology of Advanced Materials 9 (2008)

[Tan94] Tanaka K, Kato K, Tsuru S, Sakai S, " Holographically formed liquid crystal/polymer device for reflective color display", Journal of the Society for Information Display 2 (1994) 37-40.

[Tem90] A. Temmink, O. Anderson, K. Bange, H. Hantsche, X. Yu, "Optical absorption of amorphous WO3 and binding state of tungsten", Thin Solid Films 192 (2) (1990) 211-218.

[Tho11] Emily J. Thompson, Eric P. Knott, David Y. Liu, Andrew D. Chilton, Michael R. Craig, Chad M. Amb, Justin A. Kerszulis, Pengjie Shi, Joseph E. Babiarz, Aubrey L. Dyer and John R. Reynolds, "A Completed Color Palette: Electrochromic Polymers and Colorimetric Characterization Methods", Materials Research Society MRS Spring Meeting, Symposium H: Electrochromic Materials and Devices, San Francisco, USA (2011).

[THL06] Tzung-Hua Lin, Kuo-Chuan Ho, "A complementary electrochromic device based on polyaniline and poly(3,4-ethylenedioxythiophene)", Solar Energy Materials & Solar Cells 90 (2006) 506–520.

[Tre05] S, M. Tretera, J. Reiter, J. Vondrák, M. Sedlaříková, "Ionic conductance of Lithium salts in PMMA gel electrolyte", 6th Advanced Batteries and Accumulators A.B.A, Brno, Czech Republic (2005).

[Urr03] Virginia Urruchi, "Liquid crystals on silicon microdisplays based on chiral V-shaped smectic materials, PhD. Thesis, Polytechnic University of Madrid, Spain (2003).

[Vie82] R. Viennet, J.-P. Randin, I. D. Raistrick, "Effect of Active Surface Area on the Response Time of Electrochromic and Electrolytic Displays", Journal of The Electrochemical Society 129 (11) (1982) 2451-2453.

[Von04] J. Vondrák, J. Reiter, J. Velicka, B. Klapste, M. Sedlaříková, M. Tretera, "Ion conductive PMMA gel electrolytes", 6th International Meeting on Electrochromism (I.M.E.6), Brno, Czech Republic (2004).

[Wan03] Fei Wang, "Electrochromic Textiles Using Star Polymers", EIC Laboratories, Inc., Department of Defense (DoD), Army Award (2003).

[Was10] Jonathan K. Wassei and Richard B. Kaner, "Graphene, a promising transparent conductor", Materials Today 13 (3) (2010).

[Wat11] Yuichi Watanabe, Kinji Imaizumi, Kazuki Nakamura, Norihisa Kobayashi, "Effect of counter electrode reaction on coloration properties of phthalate-based electrochromic cell", Solar Energy Materials and Solar Cells 99 (2012) 88-94.

[Wes88] West JL, "Phase separation of liquid crystals in polymers," Molecular Crystals and Liquid Crystals 157 (1988) 427.

[Wol07] Scott J. Woltman and Gregory P. Crawford, "Patterned liquid-crystal laser film for multi-dimensional multi-color emissive film technology", Journal of the Society for Information Display 15 (8) (2007) 559-564.

[Yam07] Yasusei Yamada, Kazuki Tajima, Shanhu Bao, Masahisa Okada, and Kazuki Yoshimura, "Toward Solid-State Switchable Mirror Devices Using Magnesium-Rich Magnesium–Nickel Alloy Thin Films", Japanese Journal of Applied Physics 46 (2007) 5168-5171.

[Yam10] Y. Yamada, H. Sasaki, K. Tajima, M. Okada, K. Yoshimura, "Optical Switching Properties of Switchable Mirrors Based on Mg Alloyed with Alkaline-earth Metals", 9th International Meeting on Electrochromism (I.M.E. 9), Bordeaux, France (2010).

[YJL08]]Y. J. Liu and X.W. Sun, "Holographic Polymer-Dispersed Liquid Crystals:Materials, Formation, and Applications", Advances in OptoElectronics (2008).

[Yos07] Kazuki Yoshimura, "Successful Development of a Thin Film for a Switchable Mirror That Can be Switched Between Reflective and Transparent States", (2007) National Institute of Advanced Industrial Science and Technology (AIST), http://www.aist.go.jp/aist_e/latest_research/2007/20070129/20070129.html

[Yos11] Kazuki Yoshimura, Kazuki Tajima, Yasusei Yamada, "New Smart Window using Total Internal Reflection", European Materials Research Society EMRS Fall Meeting, Symposium L: Towards lightweight, flexible and self sustained ion-based devices, Warsaw, Poland (2011).

[Yun11] Yun-Ze Longa,f, Meng-Meng Li, Changzhi Gub, Meixiang Wanc, Jean-Luc Duvaild, Zongwen Liue, Zhiyong Fanf, "Recent advances in synthesis, physical properties and applications of conducting polymer nanotubes and nanofibers", Progress in Polymer Science 36 (2011) 1415-1442.

[Zha09] Lu Zhao, Liang Zhao, Yuxi Xu, Tengfei Qiu, Linjie Zhib, Gaoquan Shia, "Polyaniline electrochromic devices with transparent graphene electrodes", Electrochimica Acta 55 (2009) 491 -497.

[Zhe09] Jihong Zheng, Songlin Zhuang, "Electrically-controlled, variable focal length H-PDLC optical imaging apparatus and method", US patent application 20090174918 (2009).

Chapter II: Instrumental for characterization and techniques

This chapter will detail the optical, electrical impedance and electrochemical characterization instrumentals and experimental techniques used for the measurements of EC, SPD and PDLC devices described in this work. Optical characterization in section II.1 includes transmittance measurement, colorimetry fundamentals, scattering measurement with integrating sphere for diffuse transmittance and reflectance measurements, angle of incidence dependence and spectrometer used as instrumentals. Electrical impedance characterization in section II.2 includes EIS technique and impedance analyzer instrumentals. Electrochemical characterization in section II.3 includes CV, ChrA and ChrC techniques and potentiostat instrumental. Finally, section II.4 consists on the electrical feeding systems for SPD and PDLC devices and a photograph of the instrumental available at GDAF-UC3M lab.

II.1 Optical characterization

The transmittance measurement system, the simulation of color appearance by using colorimetry technique and the fundamentals of the scattering measurement using integrating sphere, by means of the computation of the diffuse transmittance and reflectance, will be detailed in the optical characterization section.

II.1.1 Transmittance: measurement system

Optical transmittance is defined as the fraction of incident light (or other electromagnetic radiation) at a specified wavelength that passes through a sample (Figure II.1-left). Its mathematical expression is given by Equation II.1, where I_0 is the intensity of light incident to the sample, and I is the intensity of the light crossing the sample. Transmittance is usually given as percentage, using equation II.2. Transmittance T is related by equation II.3 with Absorbance A (not Absorptance, from the energy conservation relationship of Figure I.3).

$$T_\lambda = \frac{I}{I_0} \qquad \text{(Eq.II.1)} \qquad T_\lambda(\%) = \frac{I}{I_0} \times 100 \qquad \text{(Eq.II.2)}$$

$$A_\lambda = -Log_{10} T_\lambda = -Log_{10}(\frac{I}{I_0}) = 2 - Log_{10} T_\lambda(\%) \qquad \text{(Eq. II.3)}$$

For a transmittance measurement, a radiation source or illuminant, which provides enough radiation energy at the wavelength range of the measurement, and a radiation detector, in the same wavelength range, are needed. Two steps are followed in a transmittance measurement. First, a reference measurement is carried out by measuring directly the intensity of light from the illuminant to the detector (I_0 in Equation II.1).

Then, a second measurement is carried out placing the sample in the path between the illuminant and the detector (I in Equation II.1).

The color temperature describes the level of warmth or coldness of a light source based on the color of its light emitted, changing from red to sky blue as the color temperature increases (Figure II.1-right). From the different types of illuminants, CIE (Commision Internacional de l'Eclairage) recommends using the standard illuminant D65 or also called daylight illuminant, with a correlated color temperature (CCT) of 6500 K, which approximately corresponds to a mid-day sun in the west-north of Europe (Figure II.2-left).

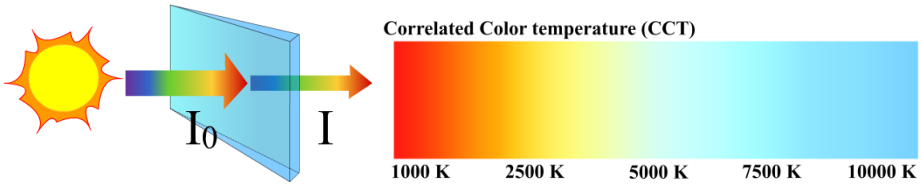

Figure II.1: (left) Solar energy transmittance of a sample calculated as the ratio of crossing intensity I and incident intensity I_0. (right) Correlated color temperature (CCT) depending on the heating of a blackbody.

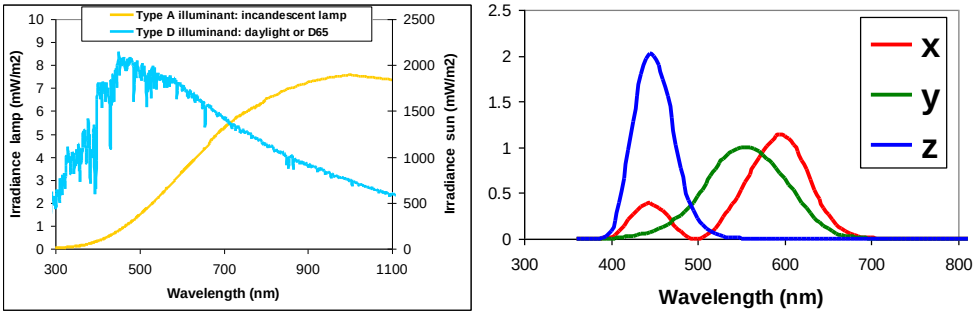

Figure II.2: (left) Spectrums of illuminants A and D65.
(right) CIE 1931 standard observer color matching functions for 2 degree.

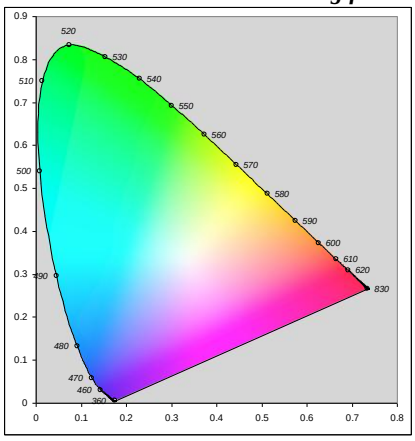

Figure II.3: CIE 1931 color space chromaticity diagram for Y=100.

II.1.2 Colorimetry: Fundamentals

All along this document, computations based in the measurements and in the colorimetry theory have been made to paint the color achieved in the studied devices in order to show to the reader. Equations II.4, II.5 and II.6 have been used in this work for computing the CIE Tristimulus Values (XYZ) by means of using the CIE 1931 color matching functions x_λ, y_λ and z_λ of Figure II.2-right for a 2 degree standard observed, being E_λ the illuminant function, T_λ is the transmittance (or reflectance) of the object at a given wavelength λ [Hun96a, Hun96b and Wys00]. The CIE Chromaticity Coordinates Yxy have been used for representing the CIE 1931 Chromaticity Diagram of Figure II.3, being x=X/(X+Y+Z) and y=Y/(X+Y+Z). This diagram must be considered as a cone shaped in a three dimensional way and perpendicular to the plane of the paper, being Y the lightness. For Y=100 the Chromaticity Diagram matches with the one shown in Figure, being Y=0 the vertex of black color. The perfect white is considered at coordinates (x,y)=(0.33, 0.33). However, for Y=50 it should be imagined a gray color for this coordinates. The horseshoe shape is formed by the pure spectral color corresponding to the monochromatic radiations. Finally, in order to obtain the color in RGB values, the forward transformation matrix CIE XYZ to sRGB was used (Equation II.7), being sRGB a color space created cooperatively by Hewlett Packard and Microsoft in 1996 for using on monitors, printers, and the Internet. Once the sRGB values have been calculated, in order to simulate in this work the real appearance of a transmissive device using Macromedia Flash, a property of transparency called "Alpha" was applied to the obtained color. Since the transparency "Alpha" is a number between 0 and 100, being 0 opaque and 100 full transparent, the average transparency of a plot was calculated multiplying the spectral transmittance measurements by the human eye sensitivity curve, which is the CIE 1931 standard observer color matching function "y" for 2 degree (Figure II.3-right). The simulation of the real appearance was done in this work for the EC, PDLC and SPD samples, using these computations.

$$X = 100 \times \frac{\int E_\lambda T_\lambda \bar{x}_\lambda d\lambda}{\int E_\lambda \bar{y}_\lambda d\lambda} \qquad \text{(Eq. II.4)}$$

$$Y = 100 \times \frac{\int E_\lambda T_\lambda \bar{y}_\lambda d\lambda}{\int E_\lambda \bar{y}_\lambda d\lambda} \qquad \text{(Eq. II.5)}$$

$$Z = 100 \times \frac{\int E_\lambda T_\lambda \bar{z}_\lambda d\lambda}{\int E_\lambda \bar{y}_\lambda d\lambda} \qquad \text{(Eq. II.6)}$$

$$\begin{bmatrix} R_{linear} \\ G_{linear} \\ B_{linear} \end{bmatrix} = \begin{bmatrix} 3.2406 & -1.5372 & -0.4986 \\ -0.9689 & 1.8758 & 0.0415 \\ 0.0557 & -0.2040 & 1.0570 \end{bmatrix} \times \begin{bmatrix} X \\ Y \\ Z \end{bmatrix} \qquad \text{(Eq. II.7)}$$

$$Csrgb = \begin{cases} 12.92 \times Csrgb & C_{linear} \le 0.0031308 \\ (1+a) \times C_{linear}^{\,1/2.4} - a & C_{linear} > 0.0031308 \end{cases}$$

II.1.3 Scattering measurement using integrating sphere based spectrometer: Fundamentals. Diffuse transmittance and reflectance

Diffuse components of transmittance and reflectance (T_{diff} and R_{diff}) represent the scattering component of the energy conservation relationship (Figure I.3). Integrating sphere based spectrometer is used for such measurements. Scattering process takes place when there is a deviation of the light from the straight trajectory, which can be caused by non uniformities or small scale density fluctuations in the medium where the light passes through. Scattering includes the diffuse reflection deviated from the angle predicted by the Snell's law, being the reflections obeying that law defined as unscattered reflections or also called specular (mirror-like) reflections [Ker69 and Koh04]. An integrating sphere is an optical device used for measuring the optical flux, such as the one of light emitting diodes (LEDs), or the scattering of a surface, by measuring total and diffuse transmittance and reflectance components [Roo93]. Direct transmittance (T_{dir}) and specular reflectance (R_{spec}) are calculated subtracting the diffuse ones to the total ones.

The light scattering is the sum of the T_{diff} and R_{diff} components, which can be measured by using the integrating sphere. The inside of an integrating sphere is coated with a white diffuse coating (usually $BaSO_4$) that hypothetically scatters 100% of incident light uniformly distributed over the sphere surface (Lambertian surface). Several ports appear to detect light, The surface of the integrating sphere ports cannot be higher than the 2% of the total (Figure II.4).Three scans are required for measuring T_{tot} and T_{diff} components [Roo91]. A first reference scan is performed without the sample in the T port and closing the sample R port with a white $BaSO_4$ cover. For T_{tot} measurement, the sample is placed in T port, being the light transmitted in all angles able to reach the detector after several reflection in the inside of the sphere. For T_{diff} measurement, the only difference with the T_{tot} measurement is the substitution of the white cover with a black cone shaped trap, in order to absorb all the transmitted light which has not been deviated from the straight trajectory after passing through the sample in sample T port, i.e., the T_{dir} component.

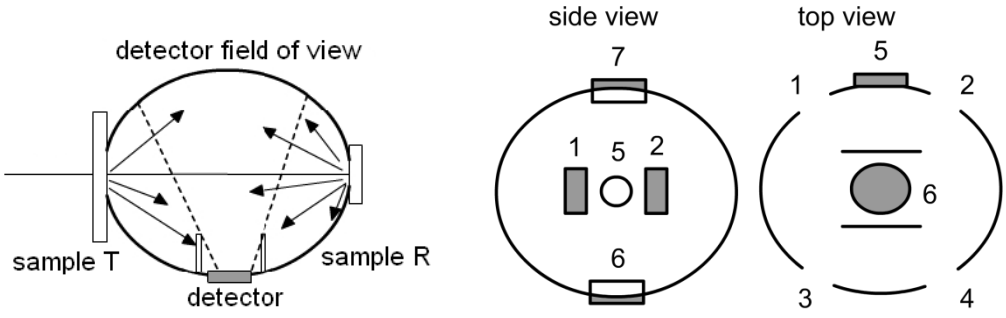

Figure II.4: (left) Schematic picture of an integrating sphere. (right) Design of a double beam integrating sphere. (1) entrance port reference beam, (2) entrance port-sample beam, (3) sample port, (4) reference port, (5) specular exit port, (6) PbS detector, (7) PM detector [Roo91].

For measuring R_{tot} and R_{diff} components, again three scans are required, being the first reference measurement the same one performed for the transmittance case. Since the spectrometer used for scattering measurements is usually a double beam one, ports 1 and 4 of Figure II.4-right are used for the reference beam. For R_{tot} measurement, the sample is placed in port 3 of Figure II.4-right (R port of Figure II.4-left), being the port 2 and the T port the same port in both figures. The black cone shaped trap must be placed after the sample in order to avoid reflected light after the sample from entering back again into the sphere. For R_{diff} measurement, the port 5 should be open in order to allow the light reflected in the straight direction from the sample to escape. This port 5 communicates with the black compartment of the spectrometer, which is covered in the instrumental avoiding entering undesired outside light (stray light).

This instrumental, available at the Angstrom Laboratory of Uppsala, was used in this work for measuring T_{tot}, T_{diff}, R_{tot} and R_{diff} of the SPD at different levels of coloration.

II.1.4 Angle dependence

A single beam integrating sphere spectrophotometer set-up allowing reflectance and transmittance measurements versus angle of incidence is shown in Figure II.5 [Nos99]. Two integrating spheres of 20 cm of diameter are used for diffuse transmittance and reflectance measurements. The transmittance sphere can be turned around an axis through the sample to vary the angle of incidence. The reflectance sphere uses a center mounted sample and a special feature is the position of the detector, which is mounted on the sample holder, both at the center of the sphere.

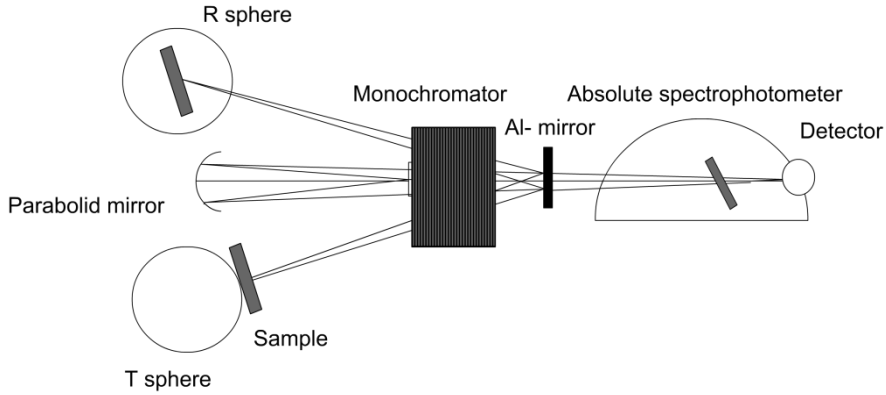

Figure II.5: Schematic top view of a single integrating sphere spectrophotometer setup for Ttot and Rtot measurements versus the angle of incidence [Nos99].

This set-up, available at the Angstrom Laboratory of Uppsala, was used in this work for measuring the T_{tot} of the SPD in three different levels of coloration, versus the angle of incidence. For R_{tot}, due to the dimensions of the SPD sample, which should be introduced into the sphere, it was not possible to measure the reflectance versus the angle of incidence.

II.1.5 Instrumental

A spectrophotometer is a device that can measure intensity as a function of the light source wavelength. Important features of spectrophotometers are spectral bandwidth and linear range of absorption or reflectance measurement.

II.1.5.1 Spectrophotometer based on an Acton Research SpectraPro 300i-P Scanning monochromator + Hamamatsu photomultiplier tube

The spectrophotometer based on an Acton Research SpectraPro 300-iP Scanning monochromator, available at the GDAF-UC3M lab, was used in this work for T_{dir} measurements in the visible wavelength range on EC, PDLC and SPD samples. This spectrophotometer, with a slit opening which allows a resolution of 5 nm between 300 and 1100 nm, and a Hamamatsu photomultiplier tube are shown in Figure II.6 [act and pmt]. The lamp used is a type A illuminant with a CCT of 2791 K measured by Dr. Alicia Pons at the Metrology Department of Applied Physics Institute of Scientific Research High Center of Madrid (DM-IFA-CSIC), which irradiance spectrum was shown in Figure II.2.

Figure II.6: (left) Acton Research SpectraPro® 300-i-P monochromator [act] and (right) Hamamatsu Photomultiplier [pmt].

II.1.5.2 Ocean Optics USB2000 Fiber Optic Spectrophotometer + FOIS-1 integrating sphere

Ocean Optics USB2000+ spectrometer in the 400 to 800 nm range is a system measuring up to 1000 spectra per second, a signal to noise ratio of 250:1, and a FWHM under 10 nm in the specified wavelength range (Figure II.7). This portable spectrophotometer, available in the GDAF-UC3M lab, was used in this work for direct and total transmittance measurements on PDLC devices.

Figure II.7: (left) Ocean Optics Fiber Optic USB2000 Spectrophotometer [oce1] and (right) FOIS-1 integrating sphere [oce2].

II.1.5.3 Jasco V 570 UV-Vis-NIR Spectrophotometer equipped with an integrating sphere

JASCO V-570 UV-VIS-NIR Spectrophotometer (Figure II.8- left) is a double beam system with single monochromator in the wavelength range between 190 and 2500 nm, which light source is an halogen lamp in the wavelength range 330 - 2500 nm, with 0.5 nm resolution, and equipped with a JASCO ILN-472 Integrating Sphere of 15 cm diameter for diffuse reflectance and transmittance. This spectrophotometer, available at CIDETEC lab in San Sebastian, was used in this work for T_{tot}, T_{diff} and R_{tot} measurements on PDLCs. Also available at CIDETEC lab, a Leica DM 4000M optical microscope with cross polarizers (Figure II.8-right) was used in this work to study the morphology of the composites in PDLC samples.

Figure II.8: (left) Jasco V 570 UV-Vis-NIR Spectrophotometer equipped with an integrating sphere [jas]. (right) Leica DM 4000M optical microscope [lei].

II.1.5.4 Perkin Elmer Lambda 900 Spectrophotometer

Perkin Elmer Lambda 900 is a double beam, double monochromator, ratio recording UV/Vis/NIR spectrophotometer using a light source with pre-aligned tungsten-halogen and deuterium in the wavelength range between 175 and 3300 nm with UV/Vis resolution lower than 0.05 nm and NIR resolution lower than 0.20 nm. The spectrometer, based on a monochromator and a photomultiplier, includes a a 15 cm diameter Spectralon integrating sphere.

This spectrophotometer, available at Angstrom Laboratory of Uppsala (Sweden), was used in this work for T_{tot}, T_{diff}, R_{tot} and R_{diff} measurements on SPD and PDLC samples. Since the size of the SPD sample (22 x 28 cm^2) was higher than the permitted by the characterization instrumental, a setup for avoiding outside light to enter into the sphere was followed by using black bags, for both transmittance and reflectance measurements (Figure II.9). The noise of such system was measured and observed to be lower than 0.1% (of course, light in the lab was turned off). As explained above, a light trap is placed at the reflectance port, protecting undesired light from outside the instrumental to enter the sphere. However, reflectance of the light trap is not completely zero, being necessary to use a black cone shaped trap for T_{diff}, R_{diff} and R_{tot} measurements. Since the multiple reflections of the light over the cone will be added, the black cone would be considered as a perfect absorbing, with a final characterized reflectance of 0.3%

throughout the spectrum. The back reflectance of the compartment lid, for the R_{diff} measurement, is measured between 0.1 and 0.2%, which is considered negligible for most measurements.

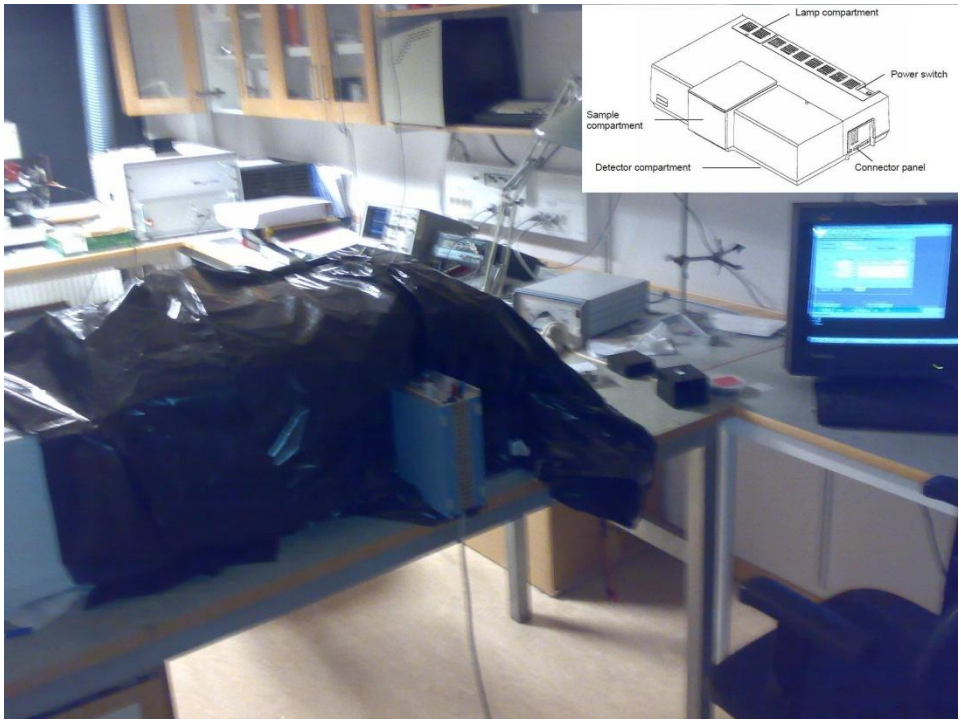

Figure II.9: Photogram of the Perkin Elmer Lambda 900 Spectrophotometer available at Angstrom Laboratory of Uppsala (Sweden) with a setup made of black bags for avoiding undesired light to enter the sphere for transmittance and reflectance measurements of a SPD.

II.1.5.5 Infrared photometers

A laser diode (Advanced Fiber Solutions) emitting at 850 and 1300 nm is used as light source for the transmittance measurement in the infrared wavelength range by means of the power meter Equitel 201. This instrumental, available at GDAF-UC3M lab, was used for measurements in PEDOT ECDs for variable optical attenuator (VOA) applications.

II.2 Electrical Impedance characterization

Electrochemical Impedance Spectroscopy (EIS) is the technique used for fitting the measured impedance to an equivalent electric circuit (EEC) model. The measurements were carried out using two different impedance analyzers, HP4194A and Solartron 1260.

II.2.1 Electrochemical Impedance Spectroscopy (EIS): Fundamentals

Measuring the electrical current circulating through a sample and plotting together with the small amplitude sinusoidal electrical voltage signal applied at different frequencies derives to gain and phase (in polar coordinates) or imaginary and real parts (in Cartesian coordinates) of the impedance, which can be represented by the Bode (magnitude and phase) and the Nyquist diagrams respectively (Figure II.10).

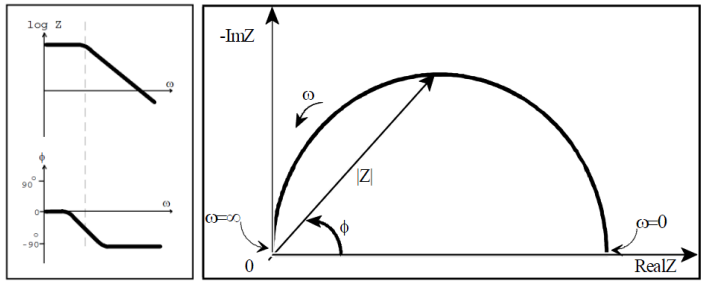

Figure II.10: Impedance diagrams. (left) Bode magnitude (up) and phase (down) and (right) Nyquist diagram [gam].

The elements used in the EEC models used in this work are presented in Table II.1. Equations for impedance are given for each element [zvi].

Element	Symbol	Impedance Equation		
R: Resistor	R	$Z = R$	$Z' = R$	$Z'' = 0$
C: Capacitor	C	$Z = \frac{1}{j\omega C}$	$Z' = 0$	$Z'' = \frac{1}{\omega C}$
L: Inductor	L	$Z = j\omega L$	$Z' = 0$	$Z'' = \omega L$
Constant Phase Element (CPE)	CPE	$Z = \frac{1}{T(j\omega)^P}$ Parameters CPE-T & CPE-P		
Finite Length Warburg Short Circuit Terminus (Ws)	Ws	$Z = \frac{R\tanh((jT\omega)^P)}{(jT\omega)^P}$ Parameters Ws-R, Ws-T & Ws-P		
Infinite Length Warburg Open Circuit Terminus (Wo)	Wo	$Z = \frac{Rctnh((jT\omega)^P)}{(jT\omega)^P}$ Parameters Wo-R, Wo-T & Wo-P		

Table II.1: Circuit elements used in the models [zvi].

Besides the common electrical circuits, i.e. resistors, capacitors and inductors, distributed elements such as a constant phase element (CPE), short-circuit Warburg impedance (Ws) or open circuit Warburg impedance (Wo), are used for fitting the Nyquist and Bode magnitude and phase impedance measurements to a proposed EEC model.

The CPE is defined by two parameters, CPE-T and CPE-R. If CPE-P=1 the equation is identical to that of a capacitor. If CPE-P=0.5, a 45 degree line is observed in the Nyquist diagram which can be used in Wo or Ws elements related to charge diffusion process, depending on the diffusion length (L_{diff}) , i.e., if it is lower or higher than the thickness (δ) of the sample respectively. The high frequency part of a CPE matches with the one of a W element if CPE-T = $(W\text{-}T)^{1/2}$ / W-R, being the parameters Ws-P and Wo-P fixed to a value of 0.5 for diffusion. In the Ws case ($L_{diff} > \delta$) Ws-T=L^2/D, being L the effective diffusion thickness and D is the effective diffusion coefficient of the particle. For Ws, at very low frequencies, Z' approaches Ws-R and Z" goes to zero. For Wo, at very low frequencies, Z' approaches Wo-R and Z'' continues increasing. If the data exhibit only the high frequency (45 degree slope) behavior and not the transition to low frequency behavior, a CPE can be used for simulation for both Ws and Wo.

EIS data is analyzed by fitting to an EEC model whose impedance matches with the measured data. Each of the EEC model components represents a physical process in the measured device, such as a small value for contacts resistance R_s, a charge transfer resistance R_{ct}, a diffusion process element W or a double layer capacitive element C_{dl} or CPE_{dl}, with a semicircle (depressed for CPE_{dl}) observed in the Nyquist diagram. A Levenberg-Marquart algorithm will be used to minimize the electrical response of the EEC model to the measured impedance response of the sample [Lev44]. In order to evaluate the goodness of the fit between the EEC model amd the measured impedance, besides of matching the best possible, the element errors and the parameters Chi-Squared χ^2 (the square of the standard deviation between the original data and the calculated spectrum) and the Weighted Sum of Squares (Sum χ^2) are used.

II.2.2 Instrumental: Impedance gain phase analyzer instrumental

Two impedance gain phase analyzers were used in this work (Hewlett Packard 4194A and Solartron 1260). Both allowed measurements of impedance with a DC bias voltage applied, useful for the EC samples characterization, in order to appreciate the electrical impedance behavior with the coloration. However, almost all the electrical impedance measurements of this work were carried out using Solartron 1260, due to the different features of both instrumentals.

III.2.2.1 Hewlett Packard 4194A

The features of the impedance analyzer HP 41941A are the accuracy 0.1 mΩ to 1.6 MΩ, 0.17% in the frequency range from 100 Hz to 40 MHz. Since lower frequencies than the lowest available with this instrumental (100 Hz) are required for electrical impedance characterization of EC, PDLC and SPD samples studied in this work, the HP4194A impedance analyzer (Figure II.11-left), available at GDAF-UC3M lab, was only used for the first series of PEDOT EC devices, when the analyzer Solartron 1260 was still not available in the group.

II.2.2.2 Solartron 1260

The Solartron 1260 impedance / gain phase analyzer is a frequency response analyzer (FRA) (Figure II.11-right) with a frequency range of 10 μHz to 32MHz, being the higher measured impedance of 100 MΩ, and the bias voltage up to ± 40.95 V [sol].

Figure II.11: (left) HP4194A impedance analyzer [hp]. (right) Solartron 1260 impedance analyzer [sol]

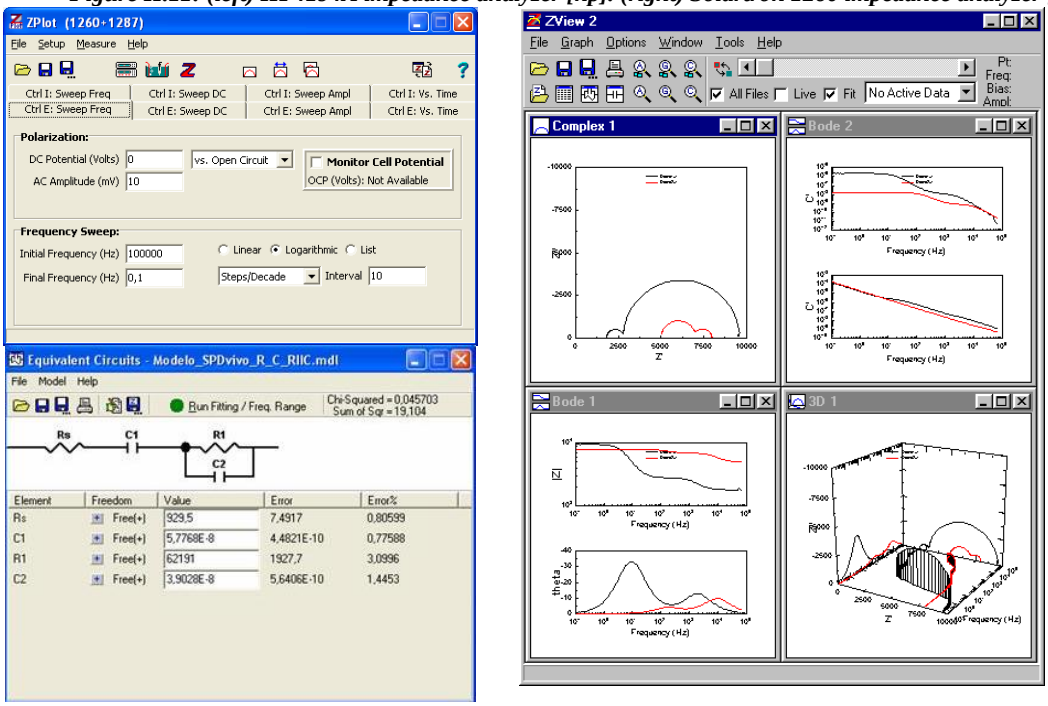

Figure II.12: Control and visualization Zplot and Zview of Solartron 1260 [sol].

For measuring the impedance of a material, the impedance analyzer can act as a potentiostat or galvanostat, i.e., applying a voltage the current is measured in the case of potentiostat or, for the case of the galvanostat, by applying an electric current the voltage is measured. The software for EIS measurement instrument used by Solartron 1260 is a dual program: ZPlot / ZView (Figure II.12).

It is also possible to make adjustments based on EEC models, some implemented in software, or designed and drawn by the user. This is the case used in this work for EC, PDLC and SPD devices. This instrumental is available both at GDAF-UC3M lab and at Angstrom Laboratory of Uppsala.

II.3 Electrochemical characterization

The instrumental used for electrochemical characterization of EC devices was the potentiostat FAS2 Gamry, available at GDAF-UC3M lab, which includes the software PHE200 for CV, ChrA and ChrC experiments, described in next subsections. Since electrochemical processes are not taking place for PDLC neither SPD devices, these measurements were only carried out on EC devices.

II.3.1 Cyclic Voltammetry (CV): Fundamentals

Cyclic voltammetry (CV) is a type of potentiodynamic electrochemical measurement, a technique used to measure potential at an electrode in an electrochemical cell, such as the EC samples in this work. CV is based on a potential waveform where potential is changed as a linear function of time. The EC material is scanned in a potential range, starting at the initial potential and ending at the final potential. Then, the potential range is reversed scanning back from the final potential to the initial potential. These two scans (forward and reverse) can be applied during several cycles. The scan rate used must be very slow (around 10 mV/s or slower), in order to find the redox potentials, for both cathodic and anodic redox reactions. In an electrochemical cell used for electroanalytical measurements there are three electrodes used, the reference electrode, the counter electrode, and the working electrode. Current is determined and plotted as a function of the potential applied to the working electrode (plot defined as a voltammogram), and the electrode potential ramp linearly, versus time. In EC devices, the hysteretic behavior between the forward and back scans will be related to the coloration changes induced on the devices. The area enclosed in the voltammogram obtained from the CV measurements will be caused by the different behavior of the electrical current in the coloration and bleaching processes. Hence in this work it has been considered interesting to measure, simultaneously with CV experiments, the optical transmittance of the EC devices during the time required (in the present work at 600 nm wavelength).

Figure II.135 shows an example of the CV experiments using the PHE200 software of FAS2 Gamry instrumental. A double ramp or triangle potential signal is applied

selecting initial and final potentials values and the slope of the signal or scan rate, in mV/s. For the case of a simple one-electron transfer reaction, the resulting current vs. voltage plot (voltammogram) will give the familiar to EC devices "duck shape" waveform shown below, with the peaks of redox reactions.

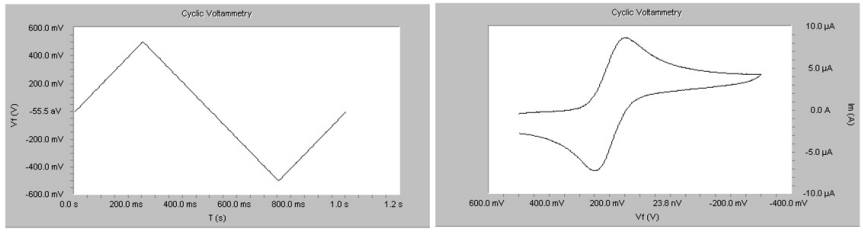

Figure II.13: CV experiment examples using Gamry FAS2 PHE200 software [phe].

II.3.2 Chronoamperometry/Chronocoulometry: Fundamentals

Chronoamperometry (ChrA) experiments were carried out in this work to EC samples in order to observe the electrical current measured when a double potential step is applied to the electrode and the resulting current vs. time is observed. The memory effect of EC devices can be determined with this method by simultaneously measuring the optical transmittance. This method is also useful for measuring other parameters such as the diffusion coefficients or concentrations of electro active material.

Figure III.14 shows an example of the ChrA experiments using the PHE200 software of FAS2 Gamry instrumental. A double step potential signal is applied selecting initial and final potentials values and the time required for each step. For the case of the solution-phase type I EC devices, where a constant electrical current is required for coloration maintenance on the EC devices, the double peak waveform for current is usually observed for both coloring and bleaching processes.

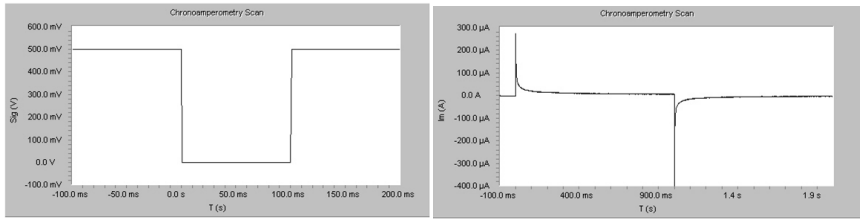

Figure II.14: ChrA experiment using example using Gamry FAS2 PHE200 software [phe].

Chronocoulometry (ChrC) experiments were carried out in this work to EC devices in order to observe the electrical charge measured when a double potential step is applied to the electrode and the resulting charge vs. time is observed. As charge can be obtained by time integrating of electrical current, both ChrA and ChrC results are obtained from a single experiment, which is simultaneously measured with the optical transmittance. In

the present work this ChrC experiments were carried out in order to obtain both the injected charge density (required for obtaining the coloration efficiency parameter) and effective charge density (a parameter directly related to the color centers formed in the EC layer, and hence to the transmittance contrast). Figure III.15 shows an example of the ChrC experiments using the PHE200 software of FAS2 Gamry instrumental.

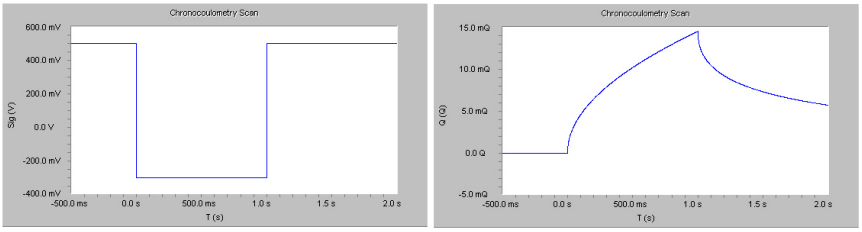

Figure II.15: ChrC experiment using example using Gamry FAS2 PHE200 software [phe].

II.3.3 Instrumental: Gamry FAS2 Femtostat / Potentiostat / Galvanostat / Zero Resistance Ammeter (ZRA)

The instrumental used for measuring chronopotentiometry experiments (ChrA), cronocoulometry (ChrC) and cyclic voltammetry (CV) was a femtostat / potentiostat / galvanostat / zero resistance ammeter FAS2 Gamry which includes the software PHE200 [fas]. Gamry FAS2 potentiostat (Figure II.16) is an instrumental available at GDAF-UC3M lab, and it was used for CV, ChrA and ChrC experiments on EC samples.

Figure II.16: Gamry FAS2 Femtostat/Potentiostat/Galvanostat/Zero Resistance Ammeter used for ChrA, ChrC and CV experiments [gam].

II.4 Signal waveform generation and powering systems used for SPD and PDLC devices

Three different ways for electrically powering the SPD samples were used. A single phase autotransformer or variac (model Verilec) supplying intermediate AC sinusoidal voltage signals from 0 to 220 V rms and 50 Hz, was used to optically characterize the sample SPD1 while switching (Figure II.17-left). Since a higher clearance was expected for a higher applied voltage, measurements were carried out at the maximum voltage. Unfortunately, despite the datasheet of the samples included as electrical current admitted from 80 to 220 V rms AC, 50 Hz, the sample SPD1 stopped its optical switching after no more than 50 cycles. Due to the short lifetime of the first sample, and the possible peaks of voltage that could damage the optical operation of the SPD devices when using the variac for electrical feeding, other options were taken into account in

order to switch the rest of SPD samples. A FPGA-based customized electronic driver was designed and implemented for addressing the sample SPD2 (Figure II.17-right, Gom07). This driver could be used, in principle, with devices of arbitrary size, except for the output power stage which largely depends on panel consumption. This has been measured to be about 5 Wm^{-2} in our current working conditions. Since none appreciable extra bleaching was observed for applied voltage signals higher than 100 V peak, a function generator in series with a broadband linear amplifier, model F10A of FLC Electronic AB with an amplification of 10 times and maximum input voltage of ±10 V, were used for the samples SPD2 and SPD3, in order to achieve electrical control signals of 50 Hz frequency with amplitude values from 0 to 100 V peak (Figure II.18).

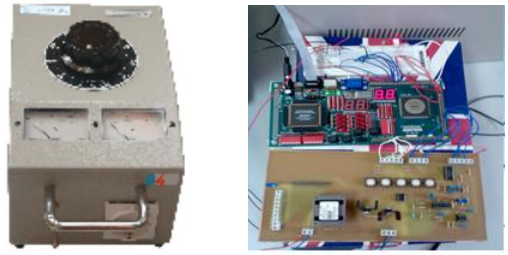

Figure II.17: Instrumentals used for electrical feeding of samples. SPD1: (left) A single phase auto-transformer (Variac) model Verilec. SPD2: (right) A FPGA setup with a local control + actuator.

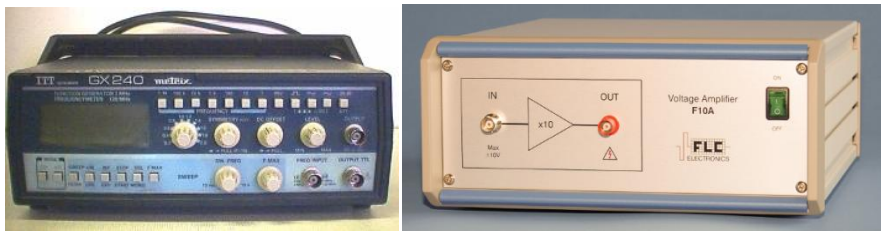

Figure II.18: Instrumentals used for electrical feeding the samples SPD2 and SPD3: An ITTGX240 Metrix function generator (left) in series with a broadband linear amplifier model F10A of FLC Electronic AB (right) with amplification of 10 times and maximum input voltage of ±10 V.

II.5 Electrical current and capacitance systems used for SPD devices

The electrical current during switching of the sample SPD3 (see Chapter IV) was measured with a digital multimeter model Keithley 197A of Figure II.19-left. A first and fast capacity measurement on the devices was carried out using the LCR instrumental of Figure II.19-right. Values of the capacitive components of the fitted EEC model obtained with EIS experiments using the impedance analyzers were related to the measured values with the LCR instrumental.

Figure II.19: Instrumentals used for the sample SPD3. Digital multimeter model Keithley 197A used for measuring electrical current during switching (left) and LCR 400 Precision LCR Bridge of Thurlby Thandar Instruments (right).

Figure II.20 shows a photograph of the instrumental available at GDAF-UC3M lab for electro-optical characterization of the different samples studied in this work.

Figure II.20: Photograph of Solartron 1260 impedance analyzer and Acton Research monochromator with Hamamatsu photomultiplier tube used in GDAF-UC3M lab.

References

[act] Acton Research SpectraPro i300 datasheet.

[fas] FAS2 Femtostat Datasheet, Gamry Instruments.

[gam] Tutorial of Gamry FAS2.

[hp] Hewlett Packard, Component meaurement, Impedance/Gain-Phase Analyzer Model 4194" Datasheet.

[Hun96a] HunterLab, "XYZ - CIE Tristimulus Values", Insight on Color 8 (1) 1996.

[Hun96b] HunterLab, "Yxy CIE Chromaticity Coordinates", Insight on Color 8 (2) 1996.

[jas] Jasco V 570 datasheet.

[Ker69] Milton Kerker, "The scattering of light and other electromagnetic radiation", Academic Press (1969) ISBN-10: 0124045502 ISBN-13: 978-0124045507

[Koh04] Michael Kohl, Bo Carlsson, S.E. Jorgensen, Alvin W Czanderna, "Performance and durability assessment: optical materials for solar thermal systems", Elsevier Science (2004), ISBN-10: 0080444016 ISBN-13: 978-0080444017

[lei] Leica DM 4000M optical microscope datasheet.

[Lev44] Kenneth Levenberg, "A Method for the Solution of Certain Non-Linear Problems in Least Squares". Quarterly of Applied Mathematics 2 (1944) 164–168.

[Nos99] Per Nostell, Arnee Roos Daniel Rönnow, "Single-beam integrating sphere spectrophotometer for reflectance and transmittance measurements versus angle of incidence in the solar wavelength range on diffuse and specular samples", Review of Scientific Instruments 70 (5) (1999) 2481-2494.

[oce1] USB2000 Fiber Optic Spectrometer Installation and Operation Manual

[oce2] http://www.oceanoptics.com/products/fois.asp

[phe] PHE200 Physical Electrochemistry Software, Gamry Instruments.

[pmt] http://cdms.physics.ucsb.edu/bunker/shield/VetoII/pics/pmt.gif

[Roo91] Arne Roos, "Interpretation of integrating sphere signal output for nonideal transmitting samples", Applied Optics 30 (4) (1991) 468-474.

[Roo93] Arne Roos, "Use of an integrating sphere in solar energy research", Solar Energy Materials and Solar Cells 30 (1993) 77-94.

[sol] Solartron 1260 Impedance/gain-phase Analyzer Datasheet.

[Wys00] Wyszecki & Stiles, Color Science, Concepts and Methods, Quantitative Data and Formulae, Wiley-Interscience (2000) ISBN: 0471399183.

[zvi] Tutorial of Zview Solartron 1260.

Chapter III: New electrochromic devices under study

Several samples of different kind of ECDs were manufactured using different techniques. These devices represent the main object of study in this work, being this study detailed in this chapter. New organic polymer- based ECDs, manufactured with PEDOT and viologens, using both all-plastic or glass supports technologies, were developed by CIDETEC and provided to GDAF-UC3M, in order to be electro-optically and electrochemically characterized. The chapter is divided in PEDOT and viologen based ECDs, and this is also a chronological way to present the information. The measurements that will be presented were performed during five years to the different samples of ECD in a chronologic order, i.e. as instrumental and knowledge were being acquired, and also depending on the availability of the CIDETEC supplied ECD samples, which operated within a finite lifetime. In Chapter III, new all-plastic PEDOT based ECDs will be covered in section III.1, new viologen based ECDs will be covered in section III.2 and dependence on thickness of new viologen based ECDs will be covered in section III.3.

III.1 New all-plastic PEDOT ECDs

New all-plastic ECDs were developed by CIDETEC and described in [Mec04, Ver03 and Ver04a]. The devices are based on PEDOT, which acts as both EC layer and counter electrode, changing its coloration from transparent-blue when oxidized to dark-blue when reduced. The low resistivity of the polymer, which value is in the order of 0.1 Ω m, makes it suitable as a transparent conductor electrode, replacing the traditionally used ITO.

The devices were manufactured with the sandwich structure of Figure III.1 using commercial PEDOT foils and classical polymer electrolyte electro-deposition techniques. This configuration avoids the use of a conductor layer to make a contact electrode, because it is taking advantage of PEDOT conductivity to assign it a role of contact layer. Several devices with different areas were optically characterized [Ver04b], by using a micro controlled electro optic system for online transmission control [Ver06a], and also electrically characterized [Ver04c], by using EIS technique. An EEC was proposed for modeling purposes [Ver06b]. Due to the symmetrical sandwich structure, bipolar DC bias voltages were applied in order to increase the lifetime of the devices [Ver06c]. The voltage dependence of the circuit parameters were analyzed [Ver07a]. Some changes on the previous EEC model [Ver08a] were considered in a new approach [Bar07]. All these works show a brief description of the manufacturing process followed by a discussion about optical and electrical properties and their dependence with the size of the device. Visible transmittance spectra, switching times and CIE

chromaticity coordinates were obtained for optical characterization. On the other hand, Bode diagrams and Nyquist diagrams were obtained for electrical characterization. In this section, a resume of the measurements and some interesting conclusions derived from Nyquist and Bode plots are detailed. Some improvements in EEC models and manufacturing process of this kind of devices are also proposed.

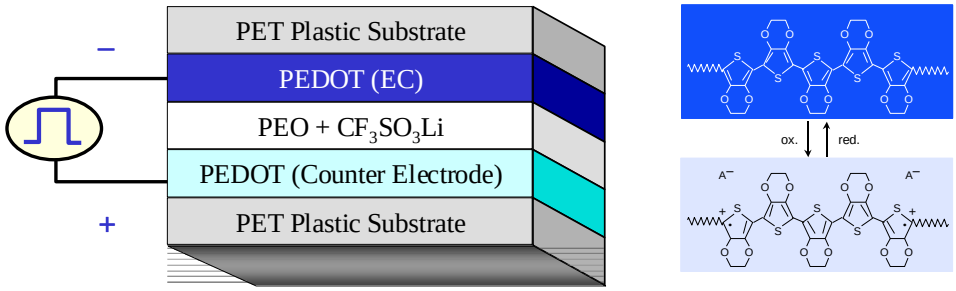

Figure III.1: Sandwich structure of a PEDOT based ECD.

III.1.1 Introduction: the former works

The classical research on EC materials is focused mainly on solid devices in which glass is used as a transparent substrate. Other investigations are focused on plastic substrates due to its flexibility, which can be used for applications such as flexible displays and switchable optical filters. However, no industrially all-plastic ECDs existed until 2004, due to a number of drawbacks such as low quality of the TC layer onto plastic substrates. Nevertheless, several samples of new all-plastic ECDs based on PEDOT were manufactured in the research line of this work after the work of Di Paoli and coworkers [Pao99]. Figure III.2 shows pictures of the PEDOT devices in the transparent and colored states for 0 and 2 V applied respectively.

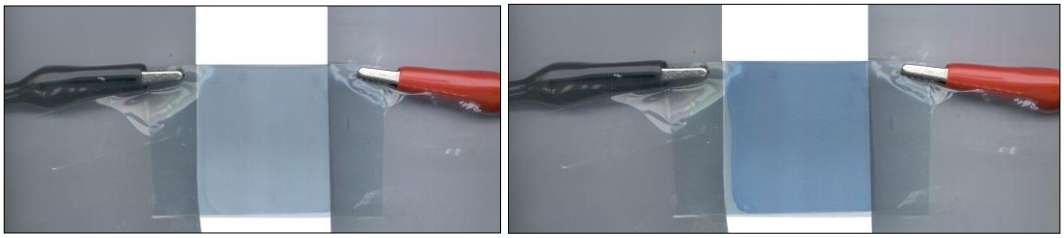

Figure III.2: Photographs of the 1st series of PEDOT based ECDs. (left) Transparent state with 0 V applied or high impedance. (right) Colored state with 2 V applied.

Repetitive optical measurements after a reduced number of cycles (under 100) leaded to different results, due to a short lifetime of the devices. Once the devices are deteriorated, their appearance in the bleached state was observed to be the same as in the colored state (Figure III.3), only bleaching again after several days, and not homogeneously (leading to a 0% of Write-Erase Efficiency after even one day) [Ver05 and Poz06]. Lately, tailor-

made polymers electrolytes based upon ionic liquids were developed for the internal layer of these ECDs in order to improve their cycle life [Mar06].

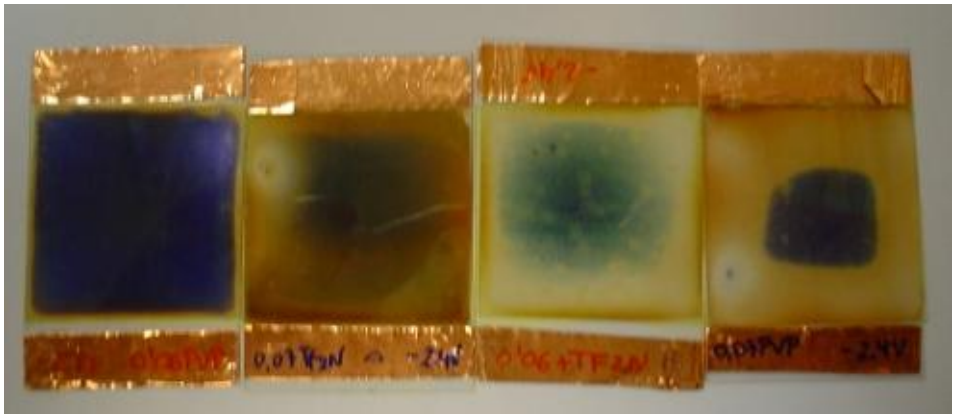

Figure III.3: PEDOT based ECDs deteriorated after being characterized with a short number of cycles in chronologic order from left to right.

III.1.2. Experimental: device series and manufacturing

Three series of PEDOT based ECDs were developed (Table III.1):

PEDOT series	Name	Area (mm^2)	Work
First series	PEDOT1a PEDOT1b PEDOT1c	92 419 1538	[Ver04a, Ver04b, Ver04c, Ver06a and Ver06v]
Second series	PEDOT2a PEDOT2b PEDOT2c	100 500 1500	[Ver06c and Ver08a]
Third series	PEDOT3a PEDOT3aa PEDOT3b PEDOT3bb PEDOT3c PEDOT3cc	128 150 235 275 427 434	[Ver07a and Bar07]

Table III.1: PEDOT based ECDs characterized.

The first series were manufactured by means of the same fabrication method described in [Mec04] (Figure III.4): Over one PET foil covered by PEDOT, commercialized by AGFA under the trademark of ORGACON, a tetrahydrofurane solution of a poly(ethylene oxide-lithium triflate) polymer electrolyte is deposited by casting. Once the solvent is evaporated, a second ORGACON EL-350 foil is glued on top of the polymer electrolyte layer. One of the PEDOT layers is the EC material and the other one

acts as counter electrode, being able to reverse their roles with reverse polarization voltage, because of the symmetrical construction.

The second and third series of PEDOT based ECDs were manufactured by means of a slightly different method than the previous series, also developed by CIDETEC (see Figure III.5). PEDOT dispersions in alcoholic medium were prepared as electroactive materials for both EC layer and ion storage layer purpose. PET foils covered with Indium Tin Oxide (PET/ITO) (20 Ω/□) was delivered by Sheldahl. Thin films of conducting polymers were prepared on ITO plastic using spin-coater (Chemat technology KW-4A) leading to homogeneous layers. The films were baked at 110 ºC for 15 min. After the baking process, the EC films were ready for assembly. A mixture based on the ionic liquid 1-butyl-3-methylimidazolim bis(trifluoromethanesulfonimide) and an ionic liquid based polymer, poly(1-vinyl-3-methylimidazolium bis(trifluoro-methanesulfonimide)), in ratio 50:50 was dissolved in THF. The polymeric electrolyte mixture was deposited by casting on the PEDOT EC films, which were prepared by spin-coating. The electrolyte mixture, which was over the EC film, was allowed to evaporate for 2 hours at room temperature. After the drying process, a second layer of EC film was placed on top of the electrolyte mixture. Such assembly was facilitated by the stickiness of the electrolyte mixture, which operates as glue.

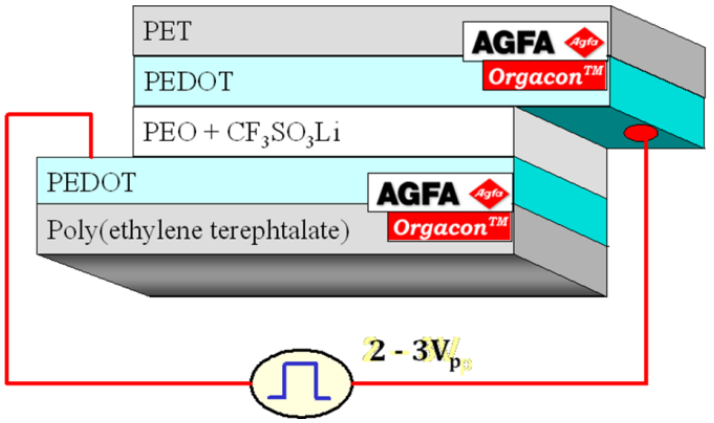

Figure III.4: Sandwich structure of 1st series of PEDOT based ECDs.

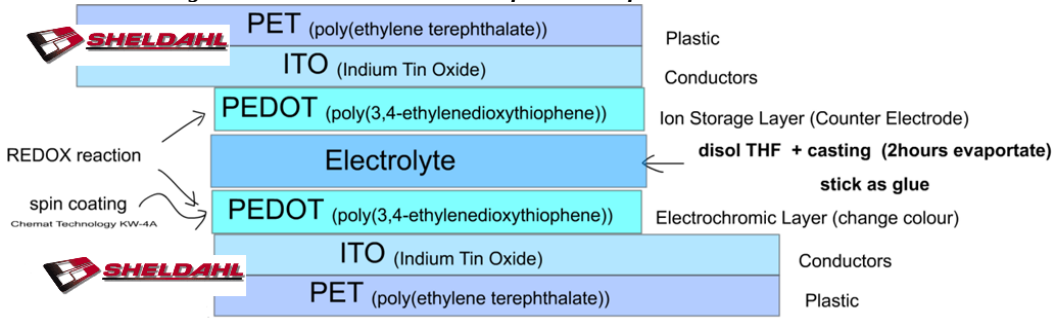

Figure III.5: Sandwich structure of the 2nd and 3rd series of PEDOT based ECDs.

III.1.3 Optical characterization

The optical response of the devices was analyzed by means of the spectrometer available at GDAF-UC3M, based on the Acton Research monochromator. Several spectral measurements in the visible range at different DC voltages were carried out in order to achieve the maximum coloration on the devices. Once no appreciable coloration increment is observed when increasing the DC applied voltage, the voltage for the maximum optical contrast (V_{moc}) achieved is selected. Several time-domain optical measurements were carried out at different selected wavelengths while applying square voltage signal from 0 V to V_{moc}.

III.1.3.1 Spectral transmittance contrast: operation in the visible range

Spectral transmittance ($T_{spectral}$) measurements were carried out for PEDOT1a device, in the wavelength range from 300 to 850 nm, applying a step voltage signal from 0 to 3 V with 0.5 V steps (Figure III.6). The voltage is applied at least during 60 seconds before each measurement in order to ensure the stability of the achieved color. Figure III.7 shows the $T_{spectral}$ of PEDOT1b and PEDOT1c devices with 0 and 3 V applied for bleached and colored states respectively. Transmittance contrast (ΔT) is observed to decrease as the effective area of the device increases.

The plots show that the highest transparency takes place at 0 V or high impedance (HZ) state. Two main absorption bands usual of PEDOT can be found: the device cuts mainly the UV radiation without an appreciable optical change for the different voltage levels, while the switching changes take place mainly in the red interval (600 to 700 nm) being it the reason of the bluer coloration of the device at 3 V (red interval is more absorbed). A variation on the contrary trend is observed in the NIR interval (over 780 nm). For PEDOT1a device, values of 56, 34 and 32% for T_{600nm}, the most varying wavelength (T_{600nm}), are obtained for 0, 2 and 3 V applied respectively. Plots show also that the main transmittance changes take place from 0.5 V to 2 V, with a 22% of transmittance contrast at 600 nm (ΔT_{600nm}), leaving the remnant 1.5% transmittance change for the 2 to 3 V switch.

Because of the symmetry of the device construction, $T_{spectral}$ of PEDOT2a and PEDOT2b devices is shown in Figure III.8 when applying 0 and ±2 V [Ver08a]. Again, the bleached state is obtained for 0 V applied, which optical appearance matches with the one at HZ state, showing a slight transparent blue appearance. A darker blue coloration is observed in the device for both positive and negative voltage levels, corresponding to ±2 V applied. A small difference between two voltage polarities appears at the NIR. Values of 38 and 25% for T_{600nm} are obtained when applying 0 and ±2 V for the PEDOT2a device. A slight darkening of the bleached and colored states is observed for the 500 mm^2 active area PEDOT2b device, with values of 36 and 20% respectively.

Measurements of $T_{spectral}$ of the PEDOT3c and PEDOT3cc devices are shown in Figure III.9 for different DC bias voltages, leading to different coloration levels. As it was the case of the two previous series, a blue transparent appearance with 0 V applied or HZ state and a darker blue coloration are observed in the devices when increasing from 0 to 2.25 V applied. A threshold voltage value V_{TH} of 0.75 V, from which the ECD changes its coloration, is observed for the PEDOT3c and PEDOT3cc devices. Values of 52 and 33% of T_{600nm} are obtained for 0 and 2.25 V applied respectively for PEDOT3c device. Bleached state is enhanced for the PEDOT3cc device with values of 60 and 38% respectively.

Summarizing, a 24%, 13%, 16%, 19% and 22% of ΔT_{600nm} is observed for PEDOT1a, PEDOT2a, PEDOT2b, PEDOT3c and PEDOT3cc devices respectively. Same spectral absorption bands are observed in the devices since same PEDOT mixture is used in their manufactured process. CIE 1931 color space chromaticity diagram for a 2 degree observer and a D65 illuminant for each PEDOT based ECD is shown in Figure III.10. Chromaticity coordinates CIE 1931 xy are observed in Table III.2. As it was seen in section II.1.2, from CIE Yxy luminance and chromaticity coordinates, sRGB values are obtained by means of the CIE XYZ to sRGB forward transformation matrix.

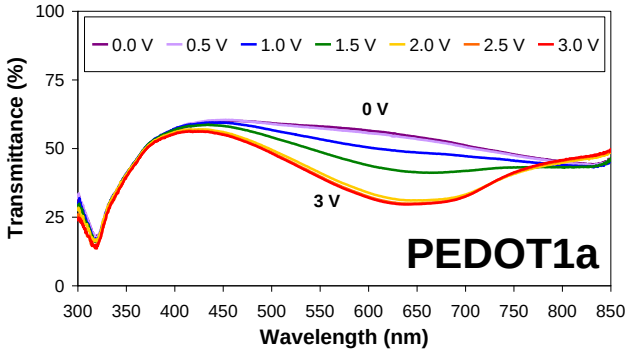

Figure III.6: Spectral transmittance of the PEDOT1a device from 0 to 3 V with 0.5 V steps.

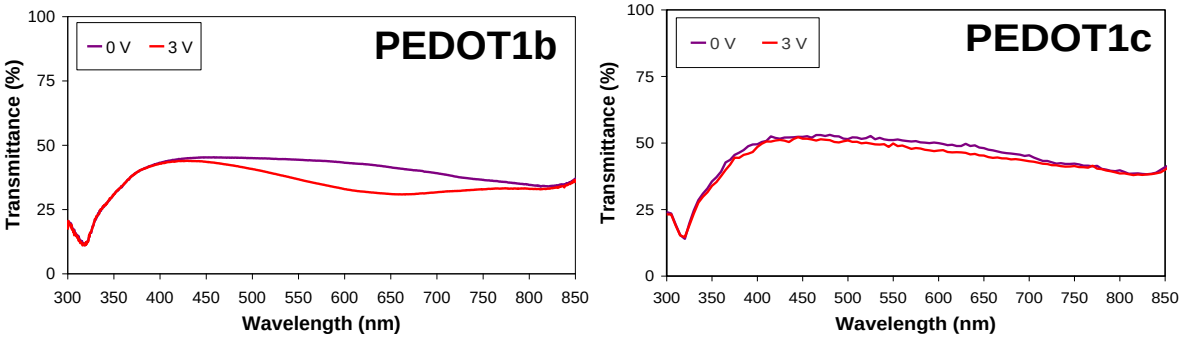

Figure III.7: Spectral transmittance of the PEDOT1b and PEDOT1c devices in the bleached and colored states, with 0 and 3 V respectively.

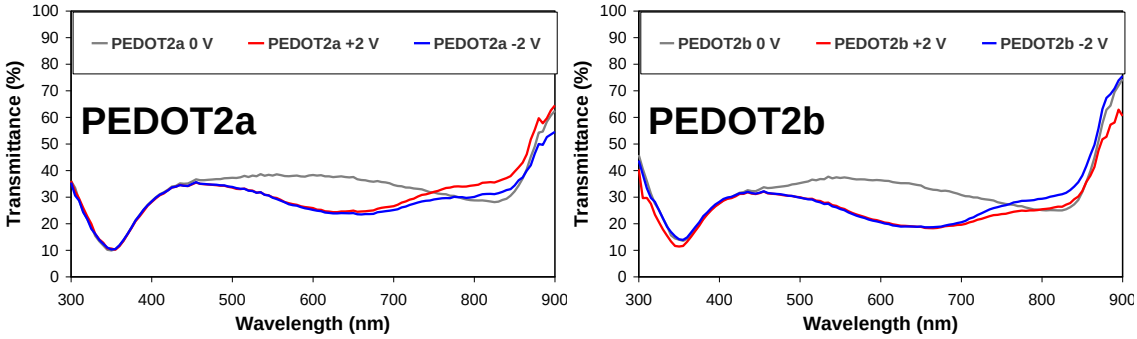

Figure III.8: Spectral transmittance of PEDOT2a and PEDOT2b devices in the bleached and colored states, with 0 and ±2 V respectively.

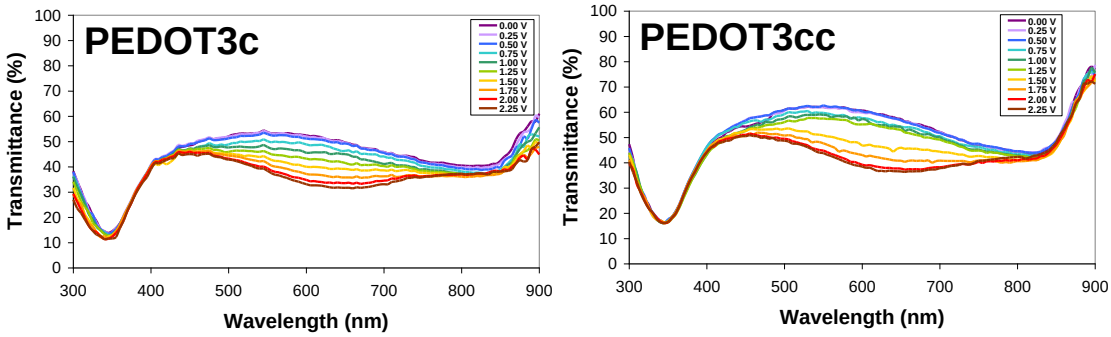

Figure III.9: Spectral transmittance of PEDOT3c and PEDOT3cc devices from 0 to 2.25 V with 0.25 V steps. Coloration changes at a 0.75 V threshold value.

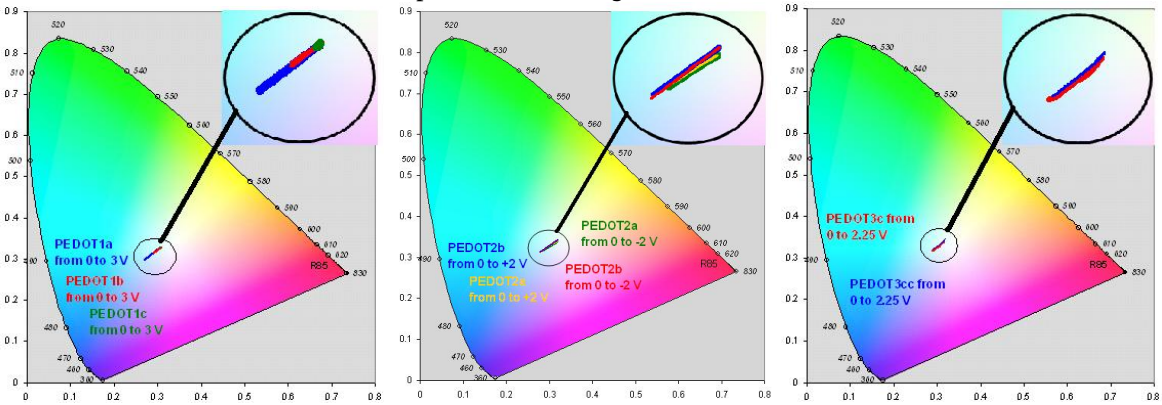

Figure III.10: CIE 1931 color space chromaticity diagram for a 2 degree observer and a D65 illuminant for 1st, 2nd and 3rd series of PEDOT based ECDs: (left) PEDOT1a, PEDOT1b and PEDOT1c from 0 to 3 V. (center) PEDOT2a and PEDOT2b from 0 to ±2 V. (right) PEDOT3c and PEDOT3cc from 0 to 2.25 V.

1st series PEDOT1			2nd series PEDOT		3rd series PEDOT	
PEDOT1a	PEDOT1b	PEDOT1c	PEDOT2a	PEDOT2b	PEDOT3c	PEDOT3cc
(0.3083, 0.3287) 0V	(0.3093, 0.3296) 0V	(0.3086, 0.3291) 0V	(0.3185, 0.3393) 0V	(0.3201, 0.3443) 0V	(0.3182, 0.3425) 0V	(0.3200, 0.3462) 0V
(0.2691, 0.2971) 3V	(0.2898, 0.3144) 3V	(0.3057, 0.3267) 3V	(0.2872, 0.3185) +2V (0.2858, 0.3178) -2V	(0.2776, 0.3128) +2V (0.2759, 0.3103) -2V	(0.2879, 0.3166) 2.25V	(0.2899, 0.3185) 2.25V

Table III.2: Chromaticity coordinates CIE 1931 xy for each PEDOT ECD in bleached and colored states obtained from Figure III.10.

Figure III.11 shows the simulated aspect of each PEDOT device at the different coloration levels for the different potentials applied with a photograph of the Mosque of Córdoba (Spain) as background.

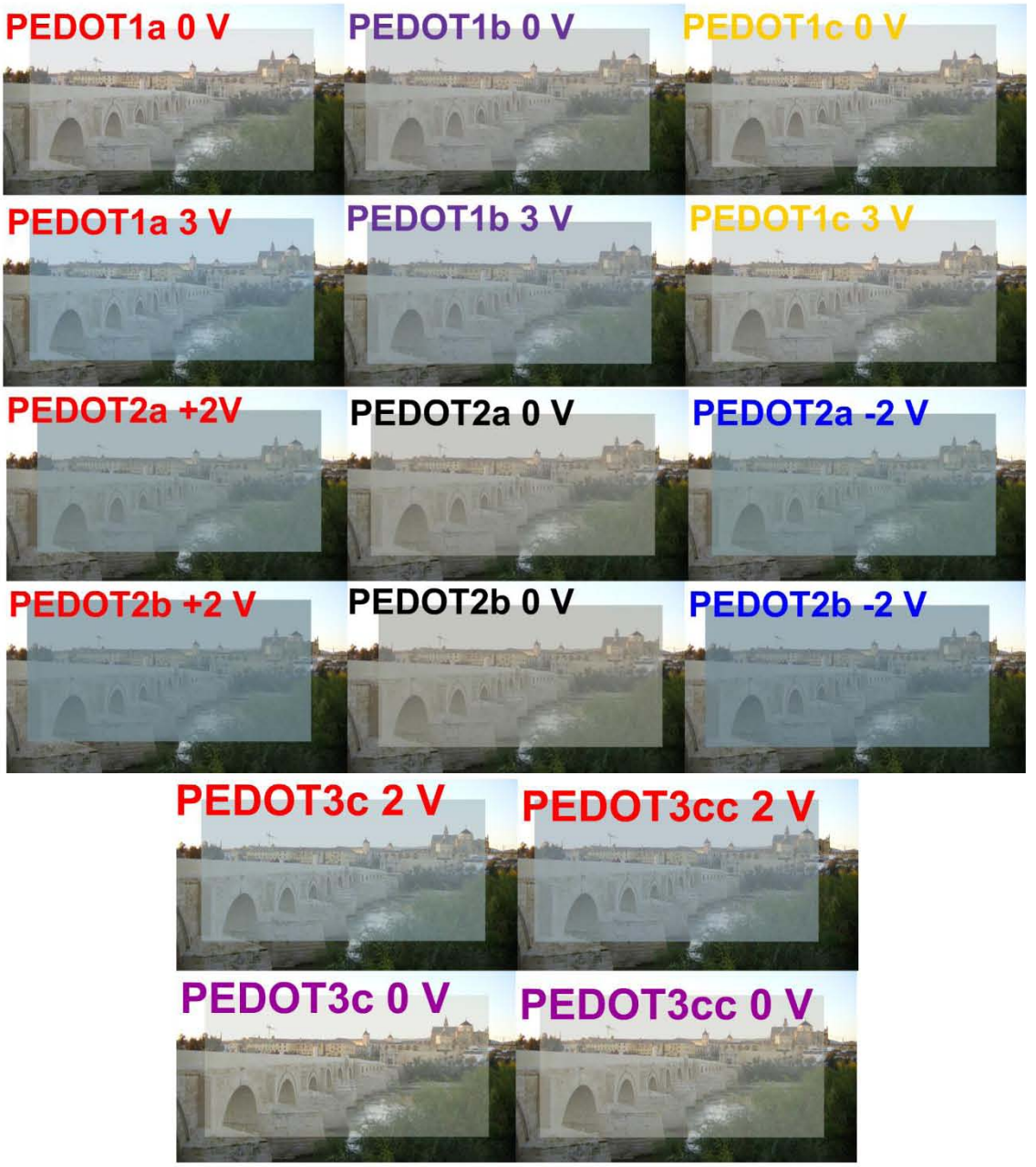

Figure III.11: PEDOT1a, PEDOT1b &PEDOT1c (up), PEDOT2a & PEDOT2b (center) and PEDOT3c & PEDOT3cc (down) simulations over a background photograph of the Mosque of Córdoba (Spain).

III.1.3.2 Response times: coloring and bleaching

Temporal evolution of the optical transmittance at the interval from 400 to 800 nm with 50 nm steps is shown in Figure III.12 for the PEDOT1 series when applying a square voltage signal from 0 to 3 V with a 40 seconds period. The fastest response time is observed for the smallest active area device (PEDOT1a), with a coloring process faster than the bleaching process. The largest device shows the slowest response, being necessary longer periods of the square voltage signal than the here used for a properly appreciation of the optical switching.

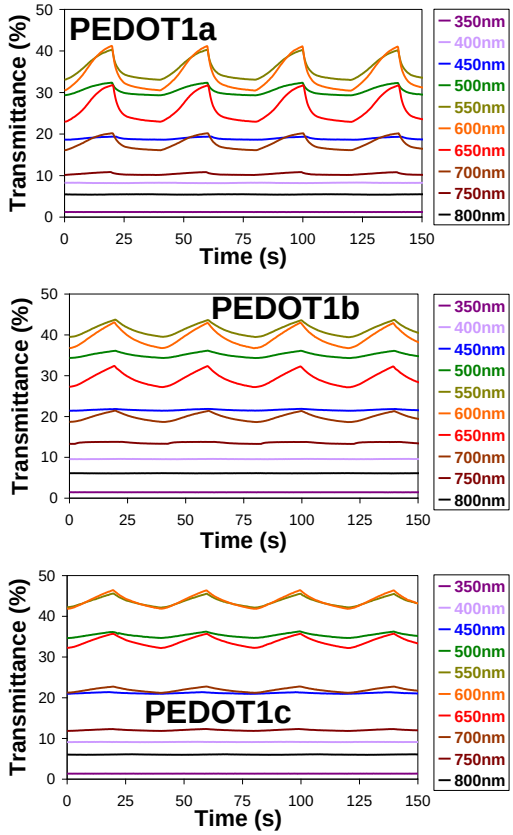

Figure III.12: Transmittance evolution at different wavelengths for square voltage signal from 3 V to 0 V with 40 seconds of period of the 1st series of PEDOT based ECDs with active areas of 92 mm^2, 419 mm^2 and 1538 mm^2.

T_{600nm} and the electrical current crossing PEDOT1c device were simultaneously measured when applying a slower square voltage signal, with a period of 300 seconds, in order to achieve stabilized bleached and colored states (Figure III.13). For the sake of characterization measurements, an electronic circuit with an I-V converter, an A/D converter and an 8-bit microcontroller was used to monitor the current injected to the

device. The calibration of this system was made using conventional passive components and at the same voltage values as will be applied to the ECDs, i.e., from 0 to 3 V.

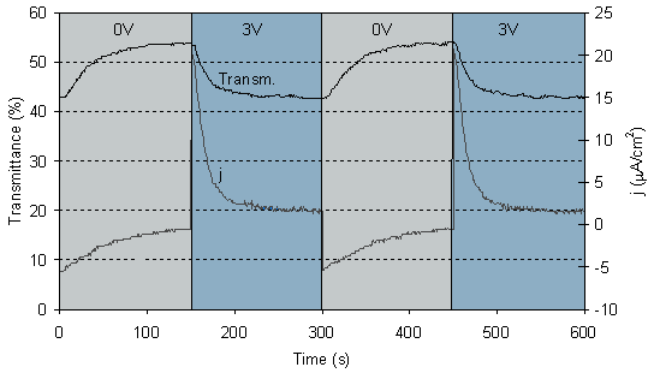

Figure III.13: Electro-optical characterization of a PEDOT1c device: T_{600nm} and current density in the device while applying a square waveform of 3 V with a period of 300 seconds.

The current peaks observed at the rising edge for t=150 s and t=450 s in the Figure III.13 are related with the speed at which the device coloration is changing. The more color centers formed, the more redox reactions in the PEDOT molecules take place and hence the more electrical current is consumed. I.e., coloring process takes place with the reduction of the molecules that gain electrons, in a faster way than bleaching process, being the electrons now released from PEDOT reduced molecules. The exponential decay of the electrical current, when transmittance decreases, looks like the curve of the discharge of a capacitor. A small residual value of electrical current is observed for the device to keep coloration. This is due since the PEDOT device is a self erasing type I solution ECD, as it was seen in section I.4.4.

T_{600nm} was measured for the PEDOT2 series while applying square voltage signals from 0 V and ±2 V, in order to compare the optical operation of the symmetrical constructed device for both polarizations [Ver08a]. Periods of 80 seconds were used for the square voltage signals in order to achieve measurements with stabilized bleached and colored states. A slight asymmetry is observed between the two optical responses (Figure III.14). Bleaching process, with response times of 3 and 4 seconds, is faster than coloration process, with response times of 4 and 10 seconds, being these times obtained for positive and negative applied square voltage signal, respectively, for PEDOT2a device (Figure III.14-up-left). PEDOT2b device shows deeper coloration but similar response times (Figure III.14-up-right). The discrepancies of T_{600nm} at the bleached state between both voltage polarities are caused by the non stability of the transmittance evolution in the time domain. Symmetry in optical contrast for both polarities is not perfect.

T_{600nm} was measured for the PEDOT3 series [Bar07]. Figure III.14-down-left shows an undesired slightly progressive increment on the coloration of devices in both, bleached and colored states, increasing the number of cycles. Figure III.14-down-right shows that

the bleaching process is faster than the coloring process (4 and 9 seconds respectively), being $\Delta T_{600nm} \approx 20\%$ with $T_{600nm\text{-bleached state}} = 51.43\%$ and $T_{600nm\text{-colored state}} = 31.87\%$.

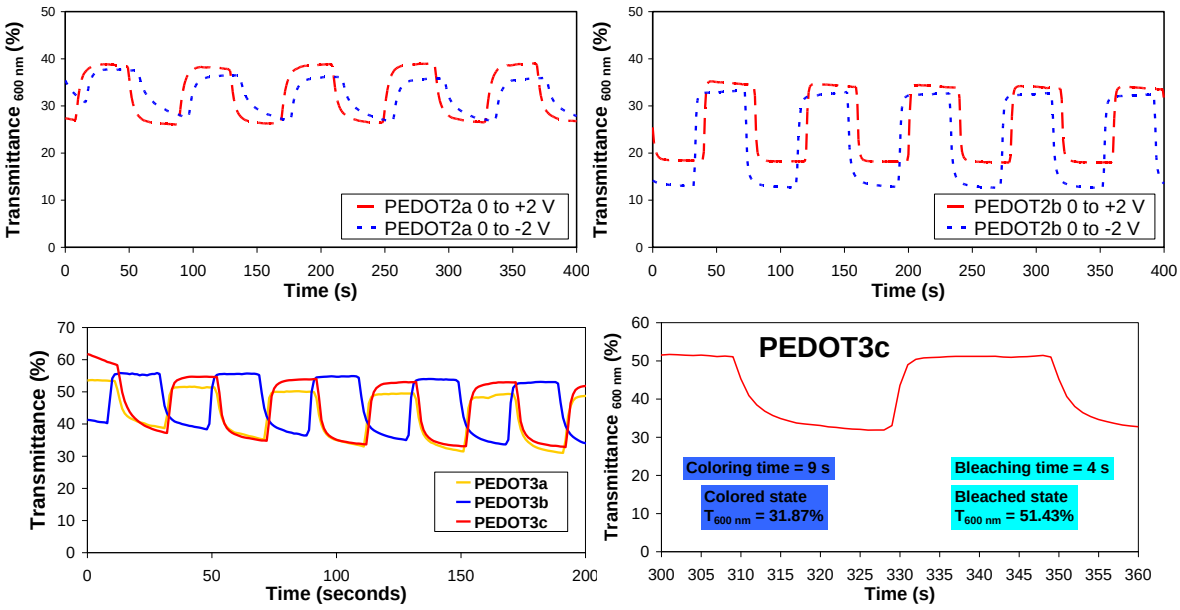

Figure III.14: (up) T_{600nm} evolution of PEDOT2a (left) and PEDOT2b (right) for an 80 seconds period square voltage signal from 0 to ±2 V. (down) T_{600nm} evolution PEDOT3a, PEDOT3b and PEDOT3c for a 40 seconds period square voltage signal from 0 to 2 V (left). Optical contrast and switching times of PEDOT3c device (right).

III.1.4 Impedance characterization

The 3 series of PEDOT based ECDs were electrically characterized, by means of EIS method, for different DC bias voltage levels (corresponding to different coloration states) and frequency ranges (depending on the chronologically used impedance analyzer), as it is shown in Table III.3. Bode magnitude and phase plots, as well as Nyquist diagrams, were derived. Some models for EEC were proposed. The evolution of the relevant electric parameters fitted to the proposed EEC models and its physical consistency were finally studied for the different DC bias voltage levels applied, and hence for the different coloration states of the devices.

Device	Impedance Analyzer	Frequency range	DC bias voltage levels	DC voltage steps
PEDOT1a PEDOT1c	HP 4194A	1 MHz – 100 Hz	0 - 3 V	0.50 V
PEDOT2b	Solartron 1260	1 MHz – 0.1 Hz	0 – 2 V	0.25 V
PEDOT3c	Solartron 1260	1 MHz – 0.01 Hz	0 – 2 V	0.25 V

Table III.3: Impedance measurements of PEDOT ECDs.

III.1.4.1 Bode and Nyquist diagrams

Bode magnitude and phase impedance measurements were carried out for the PEDOT1a and PEDOT1c devices while applying different DC bias voltage levels from 0 to 3 V with 0.5 V steps and after 60 seconds for coloring process, in the frequency range from 1 MHz to 100 Hz (Figure III.15). Impedance measurements of frequencies slower than 100 Hz were not possible to obtain because of the limitations of the used impedance analyzer (HP 4194A). Nyquist diagrams are shown in Figure III.16 for PEDOT1a and PEDOT1c devices from 0 to 3 V DC bias voltage levels applied. The higher active area device shows the lower the impedance magnitude but also the lower the ΔT.

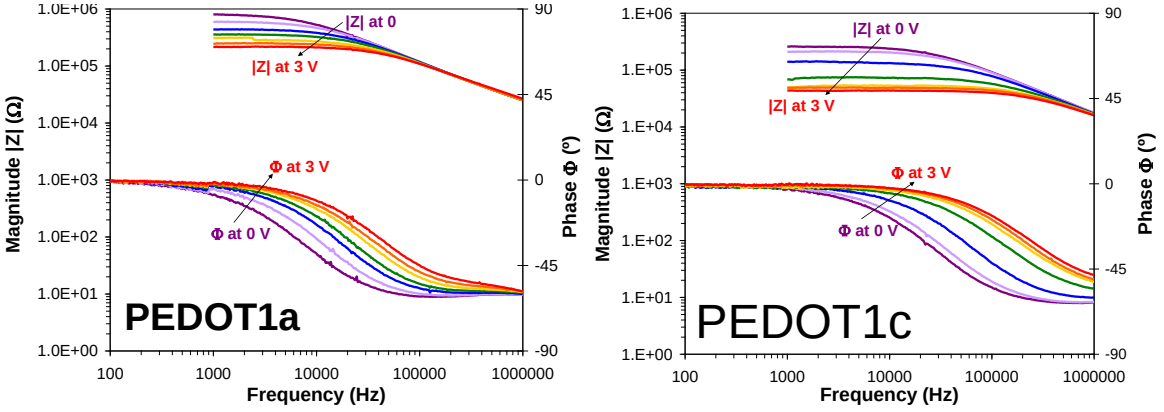

Figure III.15: Bode magnitude (left axis & upper plot) and phase (right axis & lower plot) impedance plots for different DC bias voltage applied from 0 to 3 V with 0.5 V steps of devices PEDOT1a (left) and PEDOT1c (right) using HP 4194A impedance analyzer.

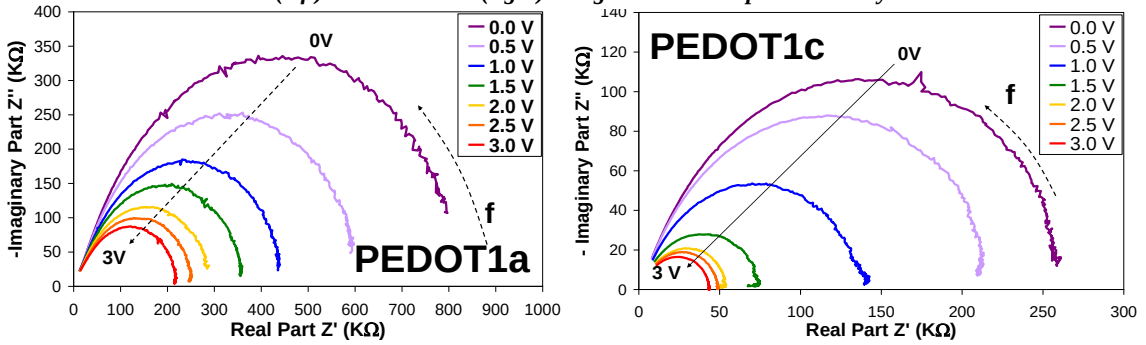

Figure III.16: Nyquist plots for PEDOT1a (left) and PEDOT1c (right) devices when switching, with 0.5 V steps, from 0 to 3 V.

Similar measurements were carried out for PEDOT2 and PEDOT3 series using Solartron 1260 impedance analyzer, which allow impedance measurements at frequencies lower than 100 Hz. The results of PEDOT1 series were used as a starting point for further discussion on EEC, which will be explained in section III.1.4.3 for the 2nd and 3rd series of PEDOT ECDs.

III.1.4.2 Equivalent electric circuit (EEC): A Randles circuit as a first attempt

These models can be used to interpret simple EIS data. The simplified Randles cell is one of most common cell models which use to be the starting point for other more complex models. A Randles cell circuit consists on a resistance R_1 in series with a shunt set formed by a capacitor C and a resistance R_2. In this case, the EEC of Figure III.17 fits perfectly to the impedance results of PEDOT1 series, being the Nyquist plot of a Randles cell a semicircle [EBa05]. Hence, a first interpretation of the results [Ver04c] led to a low value of the series resistance R_1 (standing for the contacts resistance), a variable value of the parallel resistance R_2 (standing for the charge transfer process), and a parallel capacitor C (standing for a double layer capacitance). The value of R_1 is found by reading the real axis value at the high frequency intercept, near the origin of both axis of the plot. The real axis value at the other intercept, at low frequency, is the sum of the series and parallel resistances R_1 and R_2. The diameter of the semicircle is therefore the value of resistance R_2. Checking in Figure III.16, the value of the charge transfer resistance R_2 for PEDOT1a is equal to 800 kΩ and 200 kΩ, for 0 and 3 V DC bias voltage levels respectively, being of 250 kΩ and 30 kΩ for the case of PEDOT1c.

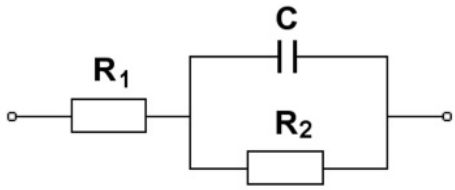

Figure III.17: Randles cell as starting point for other more complex models of EEC. Contacts resistance R_1, charge transfer resistance R_2 and double layer capacitance C of the EEC model of the 1st series of PEDOT based ECDs.

As it will be seen in the following sections, these first results of impedance and EEC were not complete because the influence of more parameters is observed at frequencies lower than 100 Hz. However, as it is above mentioned, due to limitations of the used impedance analyzer (the only one available in the research group at the moment of the measurements), when the PEDOT1 series were characterized, the author could only measure its impedance at frequencies over 100 Hz.

III.1.4.3 Extra coloration and over exposition to high DC bias voltage levels

As it was mentioned in the previous section, a Solartron 1260 impedance analyzer was used for measuring the magnitude and phase of the impedance at the range of frequencies from 0.1 Hz to 1 MHz for the PEDOT2b device. Because of the importance of low frequencies in order to obtain relevant information about the rest of the parameters of the EEC model, the lowest frequency selected for the PEDOT3c device was decreased, with respect to the PEDOT2b device, from 0.1 to 0.01 Hz.

Lower frequencies impedance measurements at the higher DC bias voltage levels could be a cause of deterioration observed in the optical operation of the devices. As long times of exposure to coloration voltages are required for measuring impedance at the lower frequencies, and taking into account that each impedance measurement is carried out with DC bias voltage applied (being the device in colored state), the memory effect and the long periods of high coloration on the devices could affect to the repeatability of the color appearance and hence to their electrical properties. A hysteresis in the impedance measurements is observed for increasing and decreasing coloration, at the up and down senses of the DC bias voltage levels applied. This hysteresis will be observed for the PEDOT2b device, where around 19 minutes are required for each impedance measurement (since the lowest frequency of 0.1 Hz). However, a higher hysteresis would be expected for the PEDOT3c device, since more time (28 minutes) was required for each impedance measurement (since the lowest frequency of 0.01 Hz).

Bode magnitude and phase plots on PEDOT2b and PEDOT3c devices, for increasing and decreasing DC bias voltage applied, from 0 to 2 V (*up sense* or coloring process) and from 2 to 0 V (*down sense* or bleaching process) with 0.25 V steps, are shown in Figures III.18 and III.19, respectively. Main changes take place at frequencies lower than 100 Hz. The bleached state of the device shows an impedance of lower magnitude and a more resistive behavior, being the phase close to zero. Impedance magnitude increases with coloration in the device (i.e., for higher values of DC bias voltage), showing a more capacitive behavior, as it can be observed in the phase plots with higher values of negative phase, due to the accumulation of charges at the electrode, causing a double layer capacitance effect between the electrolyte and the electrode interfaces.

Both magnitude and phase of PEDOT2b device increase while coloring in the up sense of the impedance measurements, i.e. increasing DC bias voltage levels from 0 to 2 V with 0.25 V steps (Figure III.18). Phase shows a lobule with a minimum peak moving from -10º at 9 Hz to around -45º at 3 Hz frequency. A slight undesired memory effect on the device is observed when bleaching in the down sense of the impedance measurements, i.e. decreasing DC bias voltage levels from 2 to 0 V with 0.25 V steps. Both magnitude and phase show an opposite behavior when decreasing the DC bias voltage from 2 to 1.75 V respect with when increasing from 1.75 to 2 V. This could be caused by a supposed increment of coloration at 1.75 V in the down sense, which should be instead decreased. This non desired coloration increment could be explained due to an over exposition of the device to coloration voltage levels.

Same behavior in coloring DC bias voltage levels or up sense of impedance measurements is observed for PEDOT3c device (Figure III.19). Phase shows a lobule with a minimum peak moving from close to -50º at 9 Hz to close to -70º at 3 Hz frequency.

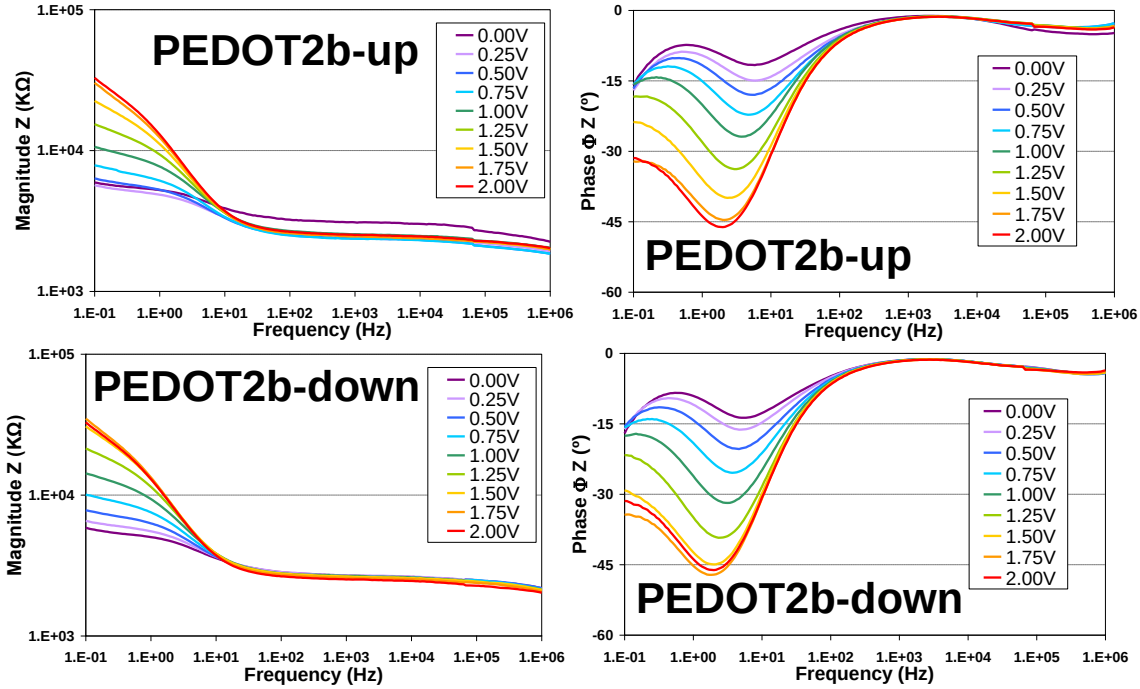

Figure III.18: Bode magnitude (left) and phase (right) impedance plots PEDOT2b ECD, increasing from 0 to 2 V (up) in the coloring process and decreasing from 2 to 0 V (down) in the bleaching process, with 0.25 V steps.

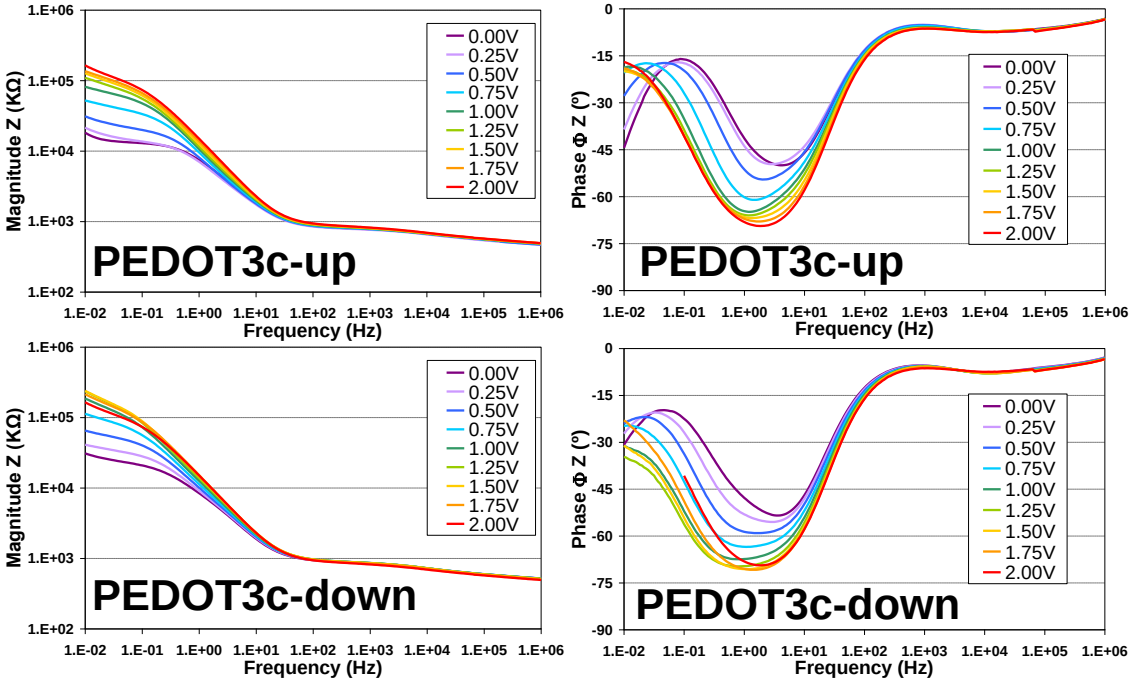

Figure III.19: Bode magnitude (left) and phase (right) impedance plots for PEDOT3c ECD, increasing from 0 to 2 V (up) in the coloring process and decreasing from 2 to 0 V (right) in the bleaching process, with 0.25 V steps.

The previously mentioned non desired coloration of PEDOT2b device, which is the possible cause of non logical impedance behavior for some DC bias voltage levels, seems to be much responsible for PEDOT3c device impedance measurements for bleaching impedance processes, i.e. when decreasing the DC bias voltage levels from 2 to 0 V with 0.25 V steps. Bode plots do not give much information, except of this strange behavior of impedance, when decreasing from 0.1 to 0.01 Hz with respect to PEDOT2b. However, more relevant information is obtained with Nyquist diagrams plotted in Figure III.20.

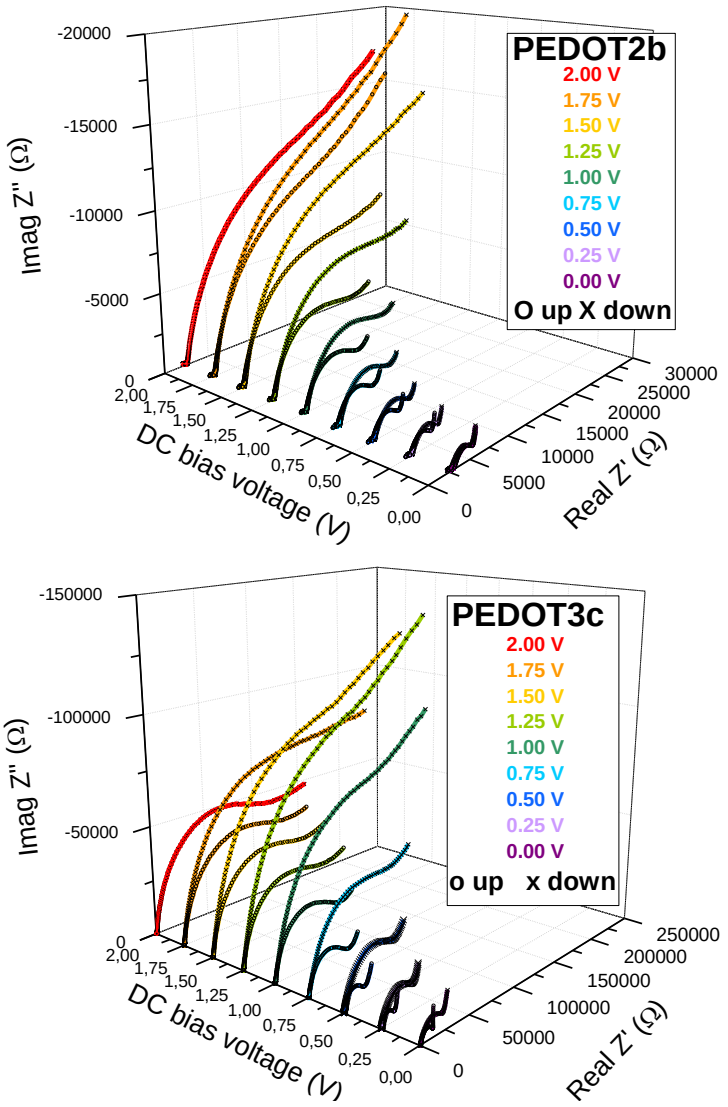

Figure III.20: Hysteresis of Nyquist plots applying different DC bias voltage levels increasing from 0 to 2 V (up sense) and decreasing from 2 to 0 V (down sense) with 0.25 V steps for coloring and bleaching processes respectively. Frequency ranges: (up) PEDOT2b: 100 mHz to 1 MHz. (down) PEDOT3c: 10 mHz to 1 MHz.

Impedance results of the devices depend on their coloration state, which depend on the DC bias voltage level applied, and also depend, unfortunately, on the time during which the device is exposed to the highest DC bias voltage levels. Since different ranges of frequencies were considered for both devices, a higher hysteresis of the impedance measurements can be clearly observed for PEDOT3c rather than PEDOT2b devices, due to the required longer time of exposure to each DC bias voltage level corresponding for each coloration level.

The differences between up and down senses show a hysteresis that is caused by the extra coloration related to the over exposition of devices to high DC bias voltage levels. Nyquist plots of PEDOT2b device almost perfectly match at 0 V for up and down senses in Figure III.20-up. However, the hysteresis is observed to be higher for PEDOT3c device in Figure III.20-down, which impedance results depends more on the coloration of the device than on the DC bias voltage level applied.

III.1.4.4 Warburg impedance

Just like the differences with the results of the 1st series of PEDOT based ECDs, measured with HP4194A impedance analyzer, the results at lower frequencies obtained by using Solartron 1260 show another shapes different than the previously obtained semicircle (that regarded a Randles cell). Some new elements should be introduced in the EEC model in order to simulate the electrical properties of the device. Among the differences, the main one is that the magnitude of impedance, and hence the coloration, increases with the DC bias voltage, the contrary trend than in Figure III.16. This different electrical behavior is due to the different manufacturing process of the first and the other PEDOT series, such as the different ionic liquids based polymer electrolytes.

Different EEC models, based on the EEC model of Figure III.21, have been proposed for the impedance results of the 2nd and 3rd series of PEDOT ECDs. As a difference with the EEC model of Figure III.17, a Warburg impedance Z_W modeling the diffusion process towards the electrode is associated in series to the charge transfer resistance R_{ct} and shunted to the double layer capacitance C_{dl} of the Randles cell, as it is shown in Figure III.21. Impedance control of measurements and treatment of results were carried out using two software packages provided with the impedance analyzer. Solartron 1260 Zplot software, with different options as frequency range, DC bias voltage level or AC signal amplitude, was used for the set up, control and acquisition of impedance experiments data. On the other hand, Solartron 1260 Zview software was used for displaying results in the required format for a later analyzing. The non linear programming and least squares method based Levenberg–Marquardt algorithm is used for each impedance curve fitting, once an EEC model is proposed. Figure III.23 shows

impedance results and fitting of the PEDOT3c device at 0 V DC bias voltage level, plotted using Solartron 1260 Zview software.

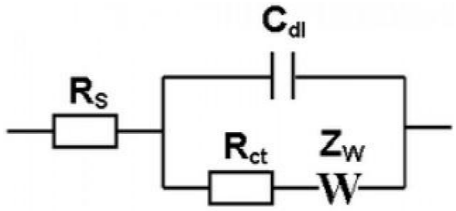

Figure III.21: Warburg impedance Z_W standing or diffusion effects in a Randles cell of the EEC model of the 2nd and 3rd series of PEDOT based ECDs.

Diffusion of charge, detected at the lower frequencies of the Nyquist plots, is represented by a Warburg impedance in the EEC model. For low frequencies the diffusion is deeper into the device. For thin devices, the diffusion crosses the entire thickness, being represented by a Ws element. If the device is thick enough that the diffusion process does not cross the entire thickness, a Wo element is used [EBa05 and gam]. If Z" tends to infinite the open-circuit Wo is used. However, if Z" tends to 0, the short-circuit Ws is used. As it was seen in section II.2.1, Equations III.1 and III.2 describe the Warburg impedance elements:

$$W_O = R\frac{\coth(T\omega j)}{(T\omega j)^P} \quad \text{(Eq. III.1)} \qquad W_S = R\frac{\tanh(T\omega j)}{(T\omega j)^P} \quad \text{(Eq. III.2)}$$

R, T and P are parameters: R is a resistance, T a time constant related with the effective diffusion coefficient and length, and P an exponent to describe the capacitive character of the impedance. Figure III.22 shows the two Warburg impedance elements, Wo and Ws, simulated for the same values of the parameters (i.e Ws-R=Wo-R, Ws-T=Wo-T and Ws-P=Wo-P).

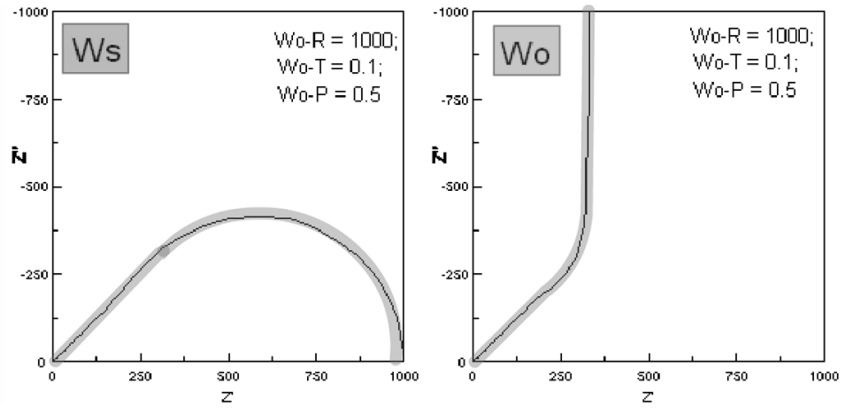

Figure III.22: Nyquist plots of short-circuit (left) and open-circuit (right) Warburg impedances (Ws and Wo) with parameters Ws-R, Ws-T, Ws-P and Wo-R, Wo-T, Wo-P.

EIS technique is followed for analyzing the impedance results. Nyquist plot of Figure III.23 shows a double lobule that can be modeled as two Randles cells circuits in series. The resistance of the contacts is modeled again as R_s. The smaller semicircle is modeled with a parallel resistance (R_p) - capacitor (C_p) set and represents problems in the construction of the device, such as bubbles, bad adhesion to the contacts, non homogeneity of the materials, etc [EBa05]. The second semicircle is modeled by a series resistance (R_{ct}) that reflects the charge transfer insertion reaction, and shunted with a capacitor that stands for the double layer capacitance (C_{dl}) associated with the interfaces. A tail related to the ionic diffusion is observed at the lowest frequencies of the bigger semicircle, which behavior was modeled using the Warburg impedance element (Z_W or W), an element with distributed parameters and dependent on the frequency. As the measured impedance result of Figure III.23 is not clearly divergent at low frequencies, a Ws element is introduced in the EEC model.

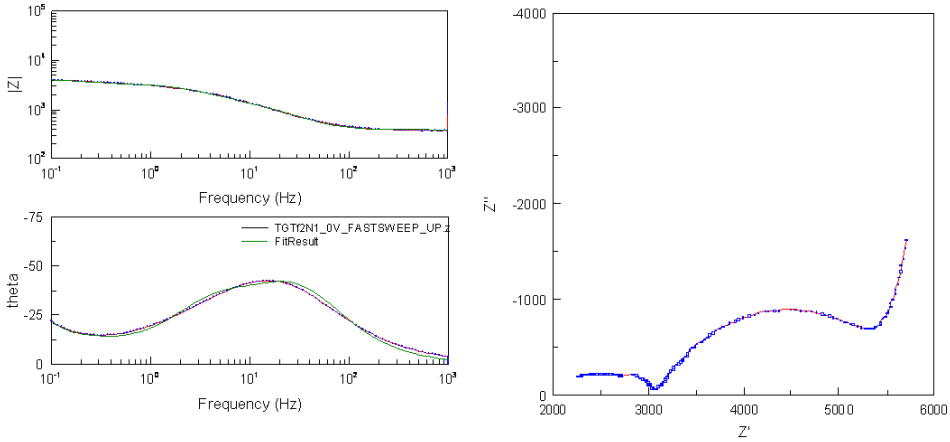

Figure III.23: Bode magnitude and phase and Nyquist impedance plots for the PEDOT3c device at 0 V DC bias voltage level. The green line is the EEC model fitting.

Hence a first attempt of an EEC model for the impedance results of the PEDOT3c device with 0 V DC bias voltage level (shown in Figure III.22) is proposed in Figure III.24.

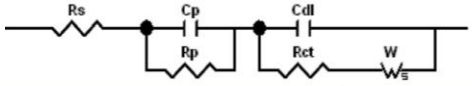

Element	Freedom	Value	Error	Error%
Rs	Free(+)	385,5	0,45342	0,11762
Cp	Free(+)	1,5231E-5	1,5402E-7	1,0112
Rp	Free(+)	2204	13,942	0,63258
Cdl	Free(+)	1,9414E-5	3,2607E-7	1,6796
Rct	Free(+)	212,5	9,3364	4,3936
W-R	Free(+)	3660	177,66	4,8541
W-T	Free(+)	7,039	0,42044	5,973
W-P	Free(+)	0,60846	0,0094092	1,5464

Figure III.24: Data fitting obtained for each impedance measurement at the 0 V DC bias voltage level for the PEDOT3c device.

Values of fitted parameters and its errors of fittings are in the data fitting box inset of the figure. To resume and to interpret components of the EEC model with their source, Table III.4 is shown.

Component	Source	Component type
Rs	**Contacts**	**Resistance of the contacts**
Cp	**Sealing problems, bubbles**	**Capacitor**
Rp	**Sealing problems, bubbles**	**Resistance**
Cdl	**Active layers**	**Double-layer capacitance**
Rct	**Active layers**	**Charge transfer resistance**
Ws	**Ionic diffusion**	**Warburg impedance**

Table III.4: Components of the 1st proposed EEC model of Figure III.24 for PEDOT2 and PEDOT3 ECDs.

III.1.4.5 Relevant electric parameters: 1st EEC model

The so named 1st EEC model shown in Figure III.25 was proposed for the PEDOT3a, PEDOT3b and PEDOT3c devices [Ver06b, Ver06c, Ver07 and Ver08a]. Data fitting is obtained for each component of the 1st EEC model at the different DC bias voltage levels applied to the devices from 0 to 2 V for coloring process or up sense, and from 2 to 0 V for bleaching process or down sense. The variations of the relevant parameters (R_s, R_p, C_p, R_{ct}, C_{dl}, W-R, W-T and W-P) for the PEDOT3c device have been plotted with different colors which stand for the errors of fittings (Figure III.26). The arrows stand for the coloring or bleaching processes. Errors of fittings were very high for some parameters mainly in the colored states, as it is the case of Rp, Cp or Ws. The most relevant information in these kind of plots, from now on, will not be the exact quantity of the value of the parameter, but the fitting error and the differences for up and down senses related to coloring and bleaching processes respectively, in order to detect the cause of the non reversibility in optical spectral transmittance measurements, which is translated as an hysteresis in electrical measurements.

Fitting errors below 1% are achieved for the contact resistance Rs, which is observed to decrease with the size of the active area from 4 KΩ to 400 Ω for 128 and 427 mm^2 devices respectively. In principle, the value of this resistance should be constant and it should not depend on the DC bias voltage applied. Depending on the active area of the devices, the shunt of capacitor and resistance, standing for sealing problems and bubbles Cp and Rp (with fitting errors below 10%), shows different fitted values that could be related to independent problems derived from their manufacturing process. Despite the veracity of its physical interpretation, Cp and Rp show fitting errors in some cases that cannot be accepted to validate the EEC model, as those ones in red or violet colors in Figure III.26. The fitting errors of Ws-T component could be due to the needed of more points for low frequencies. The behavior of the resistive parameter of Warburg element

Ws-R shows and increment with the applied potential. Low diffusion impedance for ECDs is required for coloration and bleaching processes.

Figure III.25: 1st proposed EEC model for the 2nd and 3rd series of PEDOT based ECDs. Warburg impedance at low frequencies is related to diffusion.

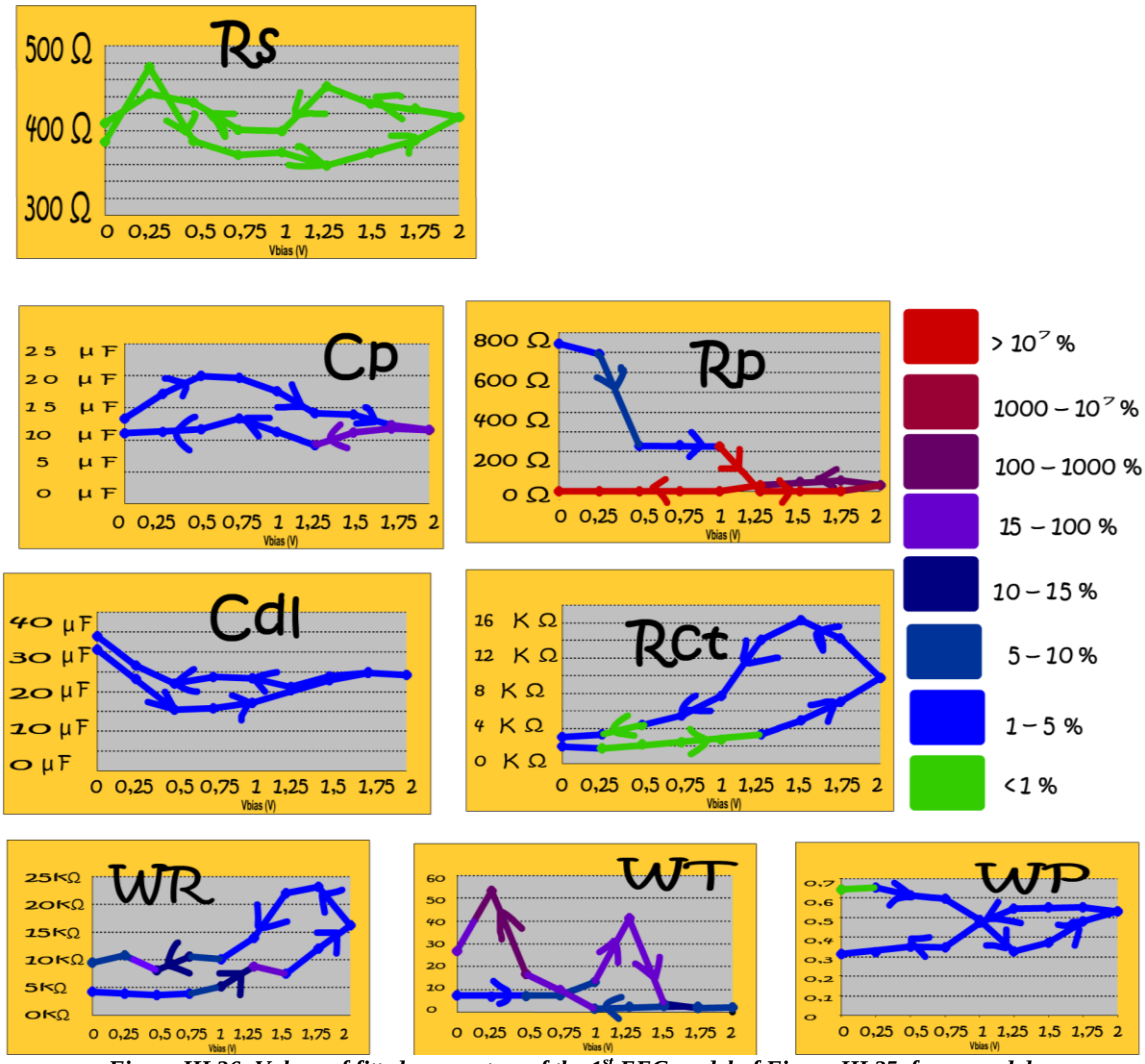

Figure III.26: Values of fitted parameters of the 1st EEC model of Figure III.25, for up and down senses, of the 427 mm² active area PEDOT3c device. Fitting errors are indicated with colors.

III.1.4.6 Constant Phase Element (CPE): 2nd EEC model

The double layer capacitance Cdl of the 1st EEC model (shown in Figure III.25) is now changed by a double layer constant phase element CPEdl, which is used instead of the capacitor in order to compensate the non-homogeneity in the system, as it can be a rough or porous surface, with a CPE-P value between 0.9 and 1. Equation III.3 describes is impedance:

$$CPE = \frac{1}{(T\omega j)^P} \qquad \text{(Eq. III.3)} \qquad CPE - T = \frac{\sqrt{W - T}}{W - R} \qquad \text{(Eq. III.4)}$$

Note that, as it was also seen in section II.2.1, if CPE-P=1 the equation corresponds to a capacitor. The Nyquist plot of a CPE is a straight line that can be modeled using an infinite network of resistances and capacitances [Sek09]. The Nyquist diagram of a CPE matches with the one of the high frequency part of a Warburg impedance when CPE-P=0.5 (Figure III.27), being CPE-T calculated from Equation III.4.

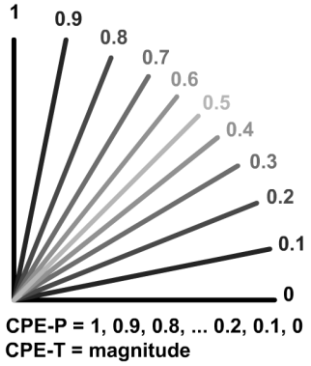

Figure III.27: Nyquist plots of a Constant Phase Element with parameter CPE-P varying from 0 to 1 and for the same value of the parameter CPE-T.

Another EEC model is proposed in Figure III.28 [Bar07] called 2nd EEC model. This EEC model changes depending on the DC bias voltage applied. For low DC voltage values, a CPEs standing for the non-homogeneities of the contacts is added in series with the set. At DC bias voltage levels over the potential of redox reaction (1.5 V), a short-circuit Warburg element Ws is added in series with the charge transfer resistance Rct.
Figure III.29 is obtained for PEDOT3c device by plotting the data into the same form than Figure III.26. In this case, the parameter Ws-P was selected as fixed, with a value of 0.5, for the high frequency range of the Nyquist diagram of the Warburg impedance element. Errors of fittings are significantly decreased by using this 2nd EEC model, being higher for CPEs-P and CPEs-T parameters at potentials over 1.5 V, which requires the introduction of the Warburg element in order to decrease the fitting errors to lower than 10%. However, some values of the obtained parameters, such as the capacitance of the CPEs (in the order of mF and standing for too much charge to store in the non-homogeneities of the contacts), make this circuit not to be valid for the ECDs in study. A

new EEC model is proposed in next sections which improve both fitting errors and physical meaning of the parameters involved. Comparing the 1st and the 2nd EEC model, it can be observed that Rs is the same in both models. Cdl and CPEdl show similar capacities, around 20 µF, in the colored states. The parameter Rct in the 2nd EEC model shows the same tendency than the parameter Rct of the 1st EEC model. Also, for potentials lower than 1.5 V, $Rct^{2nd} \approx Rct^{1st} + Ws\text{-}R^{1st}$. This is logic if the shunt Cp^{1st} in parallel with Rp^{1st} of 1st EEC model is substituted by $CPEs^{2nd}$ of the 2nd EEC model.

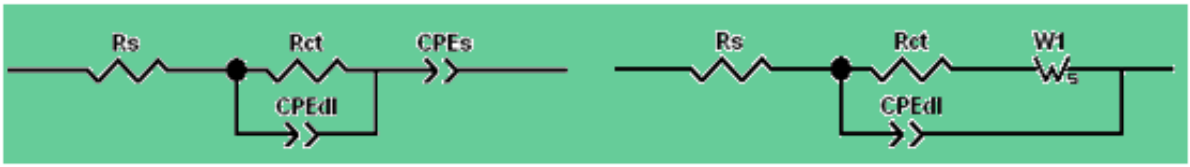

Figure III.28: 2nd Proposed EEC model for the 3rd series of PEDOT based ECDs. Low DC bias voltage levels (left). DC bias voltage levels over redox potential (right).

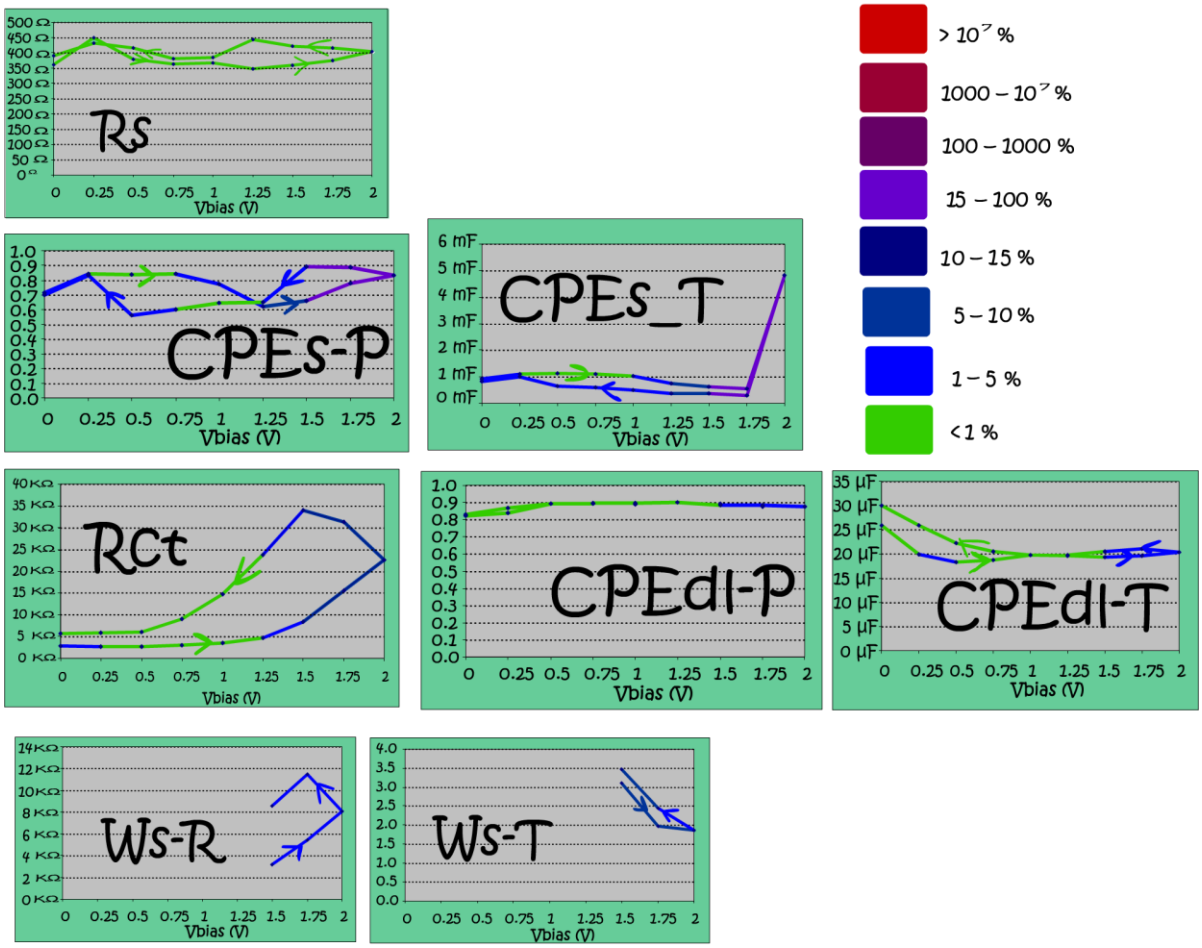

Figure III.29: Values of fitted parameters of the 2nd EEC model of Figure III.28, for up and down senses, of the 427 mm² active area PEDOT3c device. Fitting errors, lower than 10%, are indicated with colors.

III.1.4.7 Relating coloration states with impedance elements: 3rd EEC model

A new work has been carried out over the impedance measurements of the PEDOT based ECDs, once adquired the knowlegde of EEC models for the ECDs, which was sucesfully obtained for the viologens based ECDs as it will be exposed in sections III.2 and III.3. Since this model is available only since the writing of the present document, once the 2nd and 3rd series of PEDOT based ECDs are no longer optically switching because of degradation, a 3rd EEC model is proposed, which most of errors of fittings are below 1% and the rest of them not above 5%.

Figure III.30 shows the 3rd EEC model proposed for the PEDOT3c device, as a mixture of the 1st and 2nd EEC models proposed in Figure III.25 and III.28, replacing the capacitors with CPE elements, and using an open-circuit Warburg element Wo instead of the short-circuit Warburg element Ws, since the real values of the impedance measurements at low frequencies are not tending to zero (Figure III.23). Figure III.31 shows the Nyquist impedance results of PEDOT3c device and the fittings to the 3rd EEC model of Figure III.30, for coloring and bleaching DC bias voltage levels in up and down senses respectively.

Following the same style for plotting the results, Figure III.32 shows the values of the obtained parameters and the errors of fittings in different colors, as well as the arrows for coloring and bleaching senses, giving relevant information such as that most of the fitting errors are under 1%. On the contrary to the 2nd EEC model, in this case the parameter Wo-P was not selected as fixed to 0.5, leading to improvements in the fitting errors. The parameters Rs, Rp, CPEp-P, CPEp-T, CPEdl-P and CPEdl-T (i.e , all of them but Wo and Rct), have approximately the same values for coloring and bleaching processes, with slight differences. Hence, differences of Nyquist impedance results for up and down senses of Figure III.20-down (which should be due to a non desired memory effect and long periods of coloration voltage levels applied to the device) can now be linked in the model to the diffusion and charge transfer processes. Comparing with the 1st and 2nd EEC model, the 3rd EEC model shows that the huge fitting errors observed for Rp^{1st} parameter were caused by the high difference of the $CPEp^{3rd}$ parameter from behaving as a capacitor, since from fittings $CPEp^{3rd}$-P≈0.3. As it can be observed in Figure III.22, this shunt Rp||CPEp stands for the first and smaller lobule of the Nyquist diagram, taking place at high frequencies, with flatened semicircle shape. The $CPEdl^{3rd}$ parameter shows a behavior close to a capacitor, which decreases with the coloration observed in the device since redox reaction has taken place. Hence, the second lobule of the Nyquist diagram of Figure III.22 shows a closer shape to a semicircle than the first lobule, and hence $CPEdl^{3rd}$-P should be closer to 1 (between 0.8 and 0.9, in Figure III.32). Cdl^{1st} and $CPEdl^{2nd}$ tendencies matches with the one of $CPEdl^{3rd}$. Charge transfer and diffusion processes, represented by Rct^{3rd} and Wo^{3rd} in the 3rd EEC model, show the highest fitting errors (under 5%), being the causes of the

hysteresys between up and down senses in coloring and bleaching processes, observed in impedance measurements of Figure III.31, related to the hysteresis caused by the extra coloration of the devices for high voltage levels at lasting intervals applied.

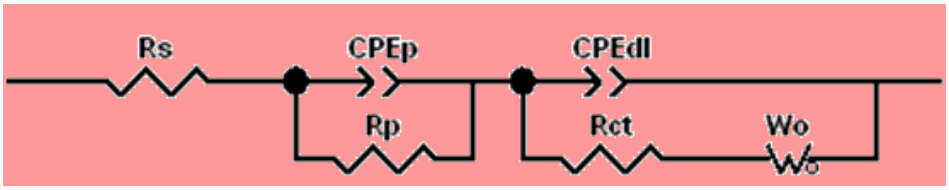

Figure III.30: 3rd proposed EEC model for PEDOT2b and PEDOT3c devices.

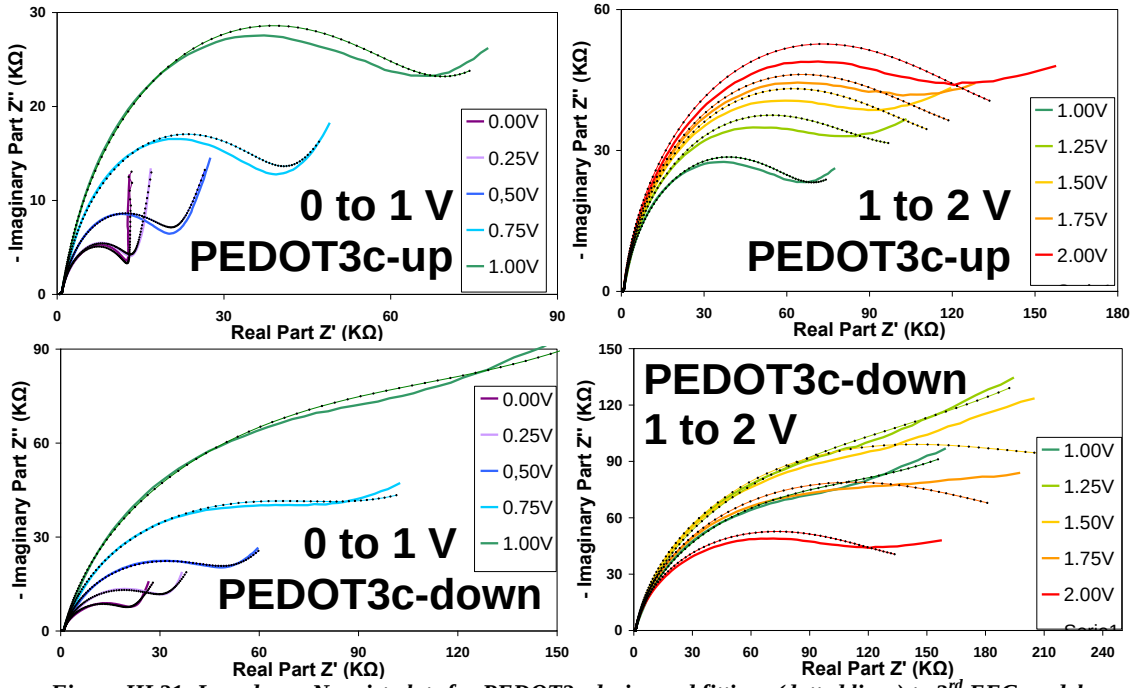

Figure III.31: Impedance Nyquist plots for PEDOT3c device and fittings (dotted lines) to 3rd EEC model for coloring (up) and bleaching (down) processes from 0 to 1 V (left) and from 1 to 2 V (right).

In order to understand the high values of the parameters Wo-T and Wo-R, Figure III.33 shows the simulated Nyquist plot of the open-circuit Warburg impedance element with the obtained parameters Wo-T, for PEDOT3c device, for the coloring and bleaching processes in up and down senses, and for the same frequency range, i.e, from 0.01 Hz to 1 MHz. Same scales in the plots are chosen in order to compare the electrical behavior of Wo at the up and down sense of coloration, which should be related to the hysteresis caused by the extra coloration of the devices for high voltage levels for long intervals applied. Since the Nyquist diagram of a Wo element at high frequencies is an oblique line of 45º slope (Figure III.23), it can be observed in Figure III.33 that the Nyquist diagrams of the simulated Wo from the fitting results would be placed into the high frequency range, and hence the Warburg element could be replaced by a CPE, as it will

be seen below. Also, as it will be observed in the results of viologens based ECDs in the next sections, the influence of the Warburg impedance is negligible at low voltages (i.e, at non coloration levels), being this element deleted from the new EEC model for non coloration voltages (under 1.25 V in the up sense and under 1.00 V in the down sense for PEDOT3c device).

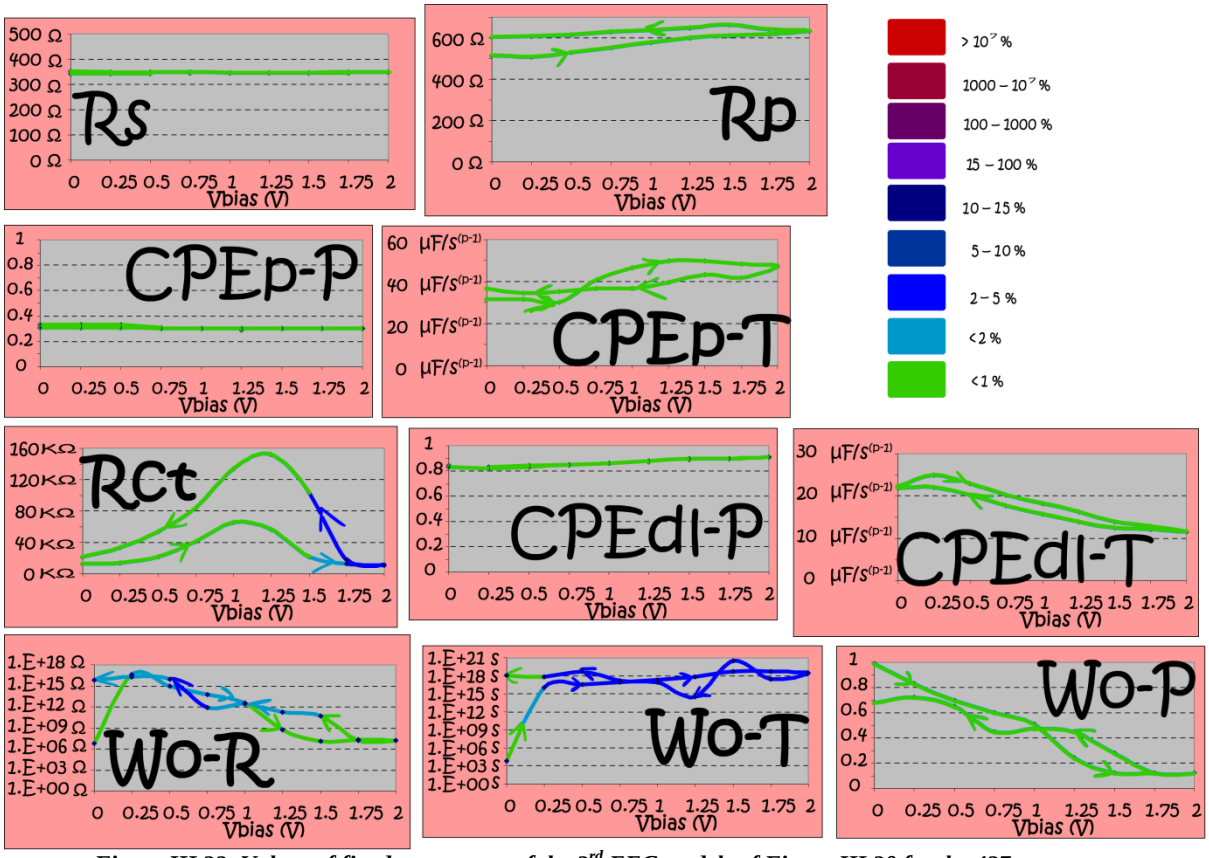

Figure III.32: Values of fitted parameters of the 3rd EEC models of Figure III.30 for the 427 mm² active area 3rd series PEDOT3c device when coloring from 0 to 2 V (up sense) and bleaching from 2 to 0 V (down sense). Fitting errors, indicated with colors, are below 5%.

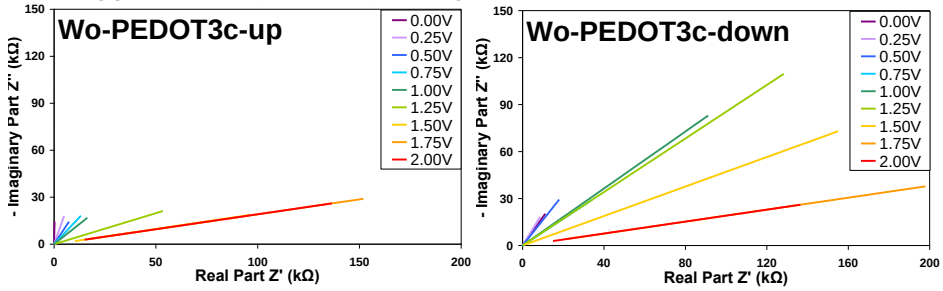

Figure III.33: Simulated open-circuit Warburg impedance element for the obtained values of the parameters Wo-R, Wo-T and Wo-P of Figure III.32 for PEDOT3c device in the frequency range from 0.01 Hz to 1 MHz. (left) up sense (right) down sense.

III.1.4.8 Replacing diffusion open-circuit Warburg by a CPEdiff: 4th EEC model

As it can be observed in Figure III.31, the Nyquist impedance results and the fittings to the 3rd EEC model in the PEDOT3c device show some differences that could be improved by a small change in the 3rd EEC model. In order to choose a Wo or a Ws Warburg elements in the EEC model, despite the oblique line of 45º of a Warburg impedance corresponding to high frequencies (Figure III.34), a tendency of the real part of the impedance to infinite or to zero should be observed in the Nyquist diagram when checking the results of impedance measurements at the lowest frequencies. If no tendency is observed, as it was the case (Figure III.31), it cannot be determined if the length of the diffusion reaches the thickness of the device, being for this frequency range the Nyquist diagram the one of a CPE element, which is called CPEdiff since it stands for the diffusion process.

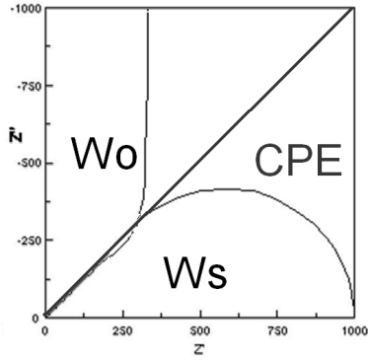

Figure III.34: Using a CPEdiff instead of open-circuit (Wo) or short-circuit (Ws) Warburg impedance element.

Figure III.35 shows a slight modification of the 3rd EEC model of Figure III.30 which will result in a better fitting, decreasing fitting errors to below 2%. The diffusion Warburg element Wo^{3rd} is replaced by a diffusion CPE element in the 4th EEC model, which is called $CPEdiff^{4th}$. Figure III.36 shows the Nyquist impedance results of PEDOT3c device and the fittings to the 4th EEC model of Figure III.35. Figure III.37 shows the values of the obtained parameters and the errors of fittings in colors, below 1% for Rs, Rp, CPEp-T, CPEp-P, CPEdl-T, CPEdl-T, and below 2% for Rct, CPEdiff-T and CPEdiff-P. The evolution of the parameters Rs, Rp, CPEp-T, CPEp-P, CPEdl-T and CPEdl-P are the same for the 3rd and the 4th EEC models. The hysteresis is observed in the Rct^{4th} and $CPEdiff^{4th}$ parameters. Figure III.38 shows the simulation of the $CPEdiff^{4th}$ element for the obtained parameters $CPEdiff^{4th}$-T and $CPEdiff^{4th}$-P of Figure III.37. Same scales than Figure III.33 are chosen for the axes in order to compare the influence of changing the Wo^{3rd} element by a $CPEdiff^{4th}$ element, which could be consider negligible for non coloration voltage levels, as it will be seen in viologens based ECDs. The lower values of $CPEdiff^{4th}$-T parameter result in the higher values of the Nyquist plots. The slope is determined by the $CPEdiff^{4th}$-P parameter.

Figure III.35: 4th proposed EEC model for PEDOT3c device obtained from a slight modification of the 3rd proposed EEC model of Figure III.30.

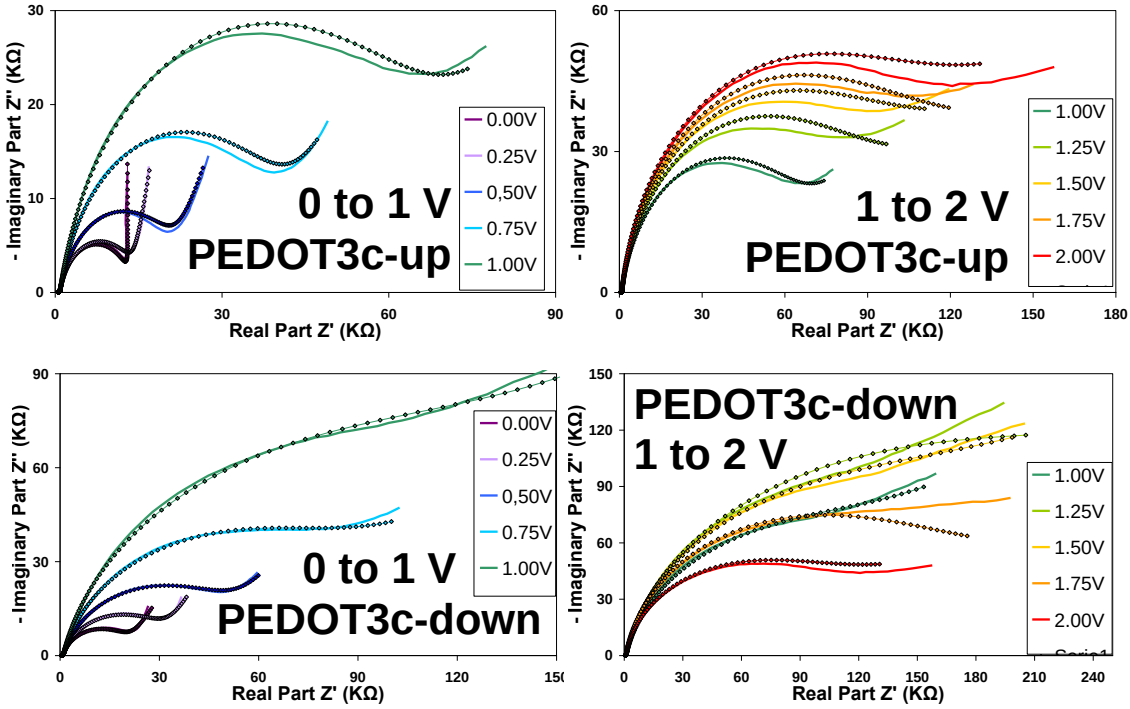

Figure III.36: Impedance Nyquist plots for PEDOT3c device and fittings (dotted lines) to the 4th EEC model of Figure III.35 for coloring from 0 to 1 V (up-left) and from 1 to 2 V (up-right) and for bleaching from 2 to 1 V (down-right) and 1 to 0 V (down-left).

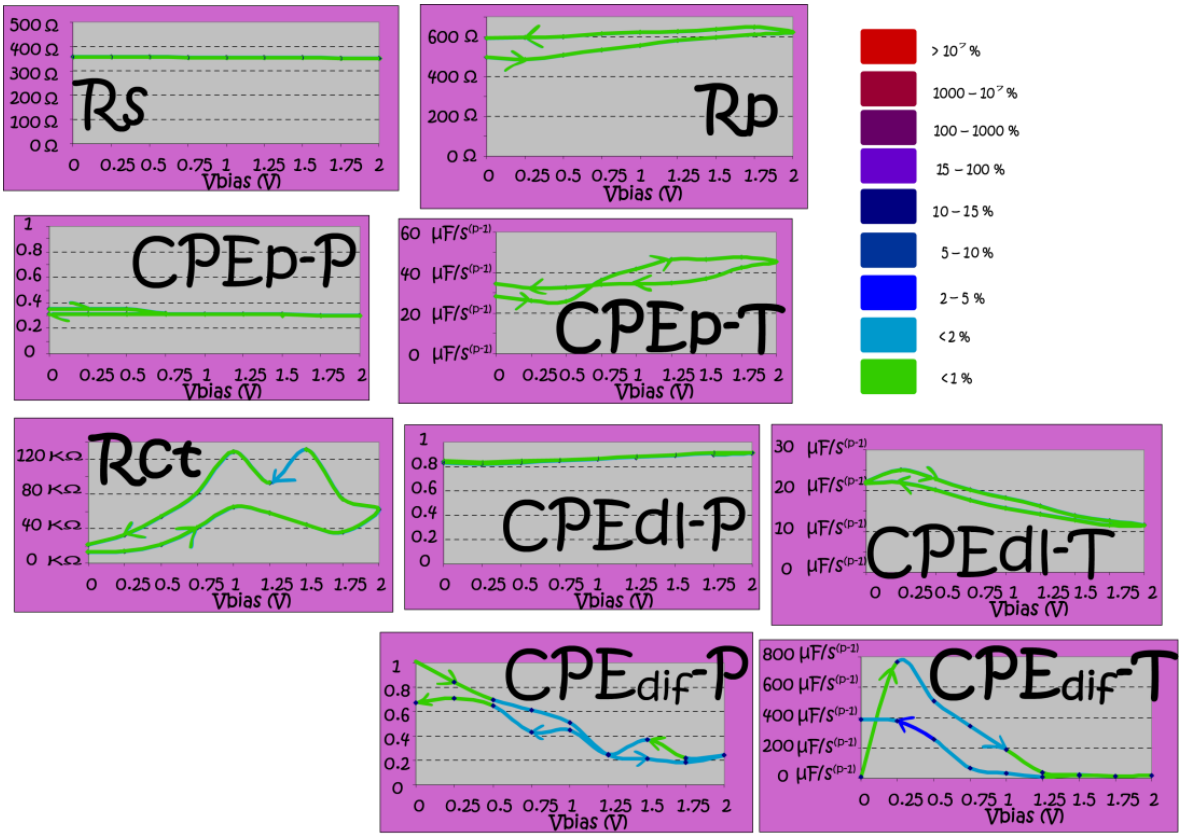

Figure III.37: Values of fitted parameters of the modified 3rd EEC model of Figure III.35 of PEDOT3c device with 427 mm² active area, for coloring and bleaching from 0 to 2 V. Fitting errors are indicated with colors.

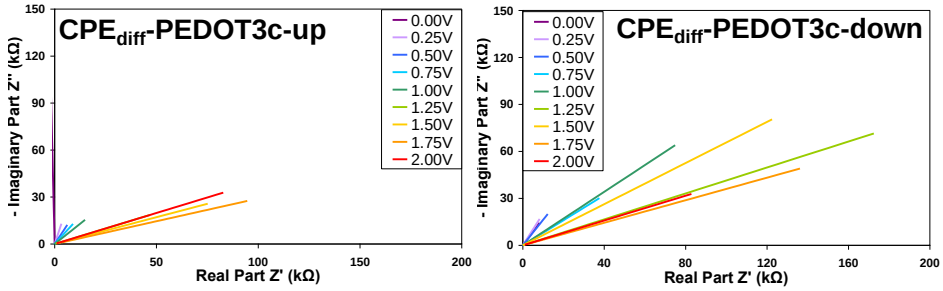

Figure III.38: Simulated open-circuit Warburg impedance element for the obtained values of the parameters CPEdiff-T and CPEdiff-P of Figure III.38 for PEDOT3c device in the frequency range from 0.01 Hz to 1 MHz.

Summarizing, several EEC models were proposed in order to explain the physical behavior of the coloration of two series of PEDOT based ECDs. As conductor polymers, their impedance in the bleached state is smaller than in the colored state. A Randles cell for high frequencies models the problem of sealing and bubbles derived from the manufacturing process. A series resistance standing for the contacts is invariant with the coloration state. As the devices start getting color, the charge transfer resistance increment takes place with a slight decrement of the double layer quasi-capacitive element, which behaves closer to a capacitor for higher colorations. Diffusion effects are almost negligible until coloration appears in the devices, caused by an enough amount of applied potential. Four EEC models were proposed for the impedance behavior of the PEDOT based ECDs when switching from the bleached to the colored states and vice versa, applying different DC bias voltage levels from 0 to 2 V with 0.25 V steps. The evolution of the values of the parameters of the different EEC models with the potential, and hence with the coloration state, was studied.

The 1st EEC model considered two Randles cells in series with a small resistance standing for the contacts. The first Randles cell stands for the sealing problems such as non homogeneities and bubbles inherent to the manufacturing process. The second Randless cell stands for the double layer capacitive and the charge transfer resistive processes. Diffusion process was also represented in the model by means of a short-circuit Warburg impedance element. Fitting errors achieved in some parameters were too high for the model to be validated.

The 2nd EEC model considered the change of the capacitor by a pseudo-capacitive CPE element, decreasing the fitting errors of the parameters of the model to lower than 10%. However, no physically comprehensible values were obtained for some parameters, such as the huge value of the CPE element, of the order of mF.

The 3rd EEC model considered to use the same structure of the 1st EEC model but changing the capacitors by pseudo-capacitive CPE element like the one used in the 2nd EEC model. Short-circuit Warburg impedance element Ws was substituted by an open-circuit one Wo. Fitting errors were decreased to lower than 5% and the evolution of the parameters with the coloration revealed the cause of the hysteresis observed in the impedance measurements between the coloring and the bleaching processes, i.e., the up and down senses, due to diffusion processes.

The 4th EEC model considered the change of the open-circuit Warburg impedance element of the 3rd EEC model by a diffusion CPE element, since impedance measurements did not revealed any tendency at the lowest frequencies. Fitting errors were decreased to lower than 2% in all the parameters of the proposed EEC model.

III.2 New viologen ECDs

Besides the above studied new all-plastic PEDOT based ECDs, another kind of organic EC technology based on bipyridinium salts (also known as viologens) was electro-optically studied. New all-plastic and glass ECDs based on viologen were developed by CIDETEC and described in [Chi07 and Poz08a]. Two different fabrication processes, at high and at room temperatures, were used for manufacturing new samples of three different viologen based ECDs, with plastic or glass supports, leading to different colors obtained for bleached and colored states. Information about the thicknesses of each layer of the ECDs structure was a novelty compared to previous PEDOT based ECDs. A new instrumental for electrochemical measurement was acquired by the research group GDAF, which resulted in the study of new parameters and methods applied to the viologen based ECDs in study. Electrochemical and optical characterizations were carried out in a simultaneous measurement process. T_{600nm} was measured while performing ChrA and CV electrochemical experiments.

III.2.1 Introduction

Figure III.39 shows pictures of the viologen based ECDs in the transparent and colored states, with 0 V or high impedance and with a low DC potential applied respectively. Three samples of viologen based ECDs were developed (Table III.5):

Viologen devices	Name	Area (cm^2)	Work	$\delta_{internal}$
Plastic supported blue device	**PSBD** **PSBD'**	4 4	[Ver08b]	200 µm 300 µm
Glass supported blue device	**GSBD**	20	[Bar08a]	300 µm
Glass supported violet device	**GSVD**	8.5	[Ver09, Bar08c]	300 µm

Table III.5: Viologen based ECDs characterized.

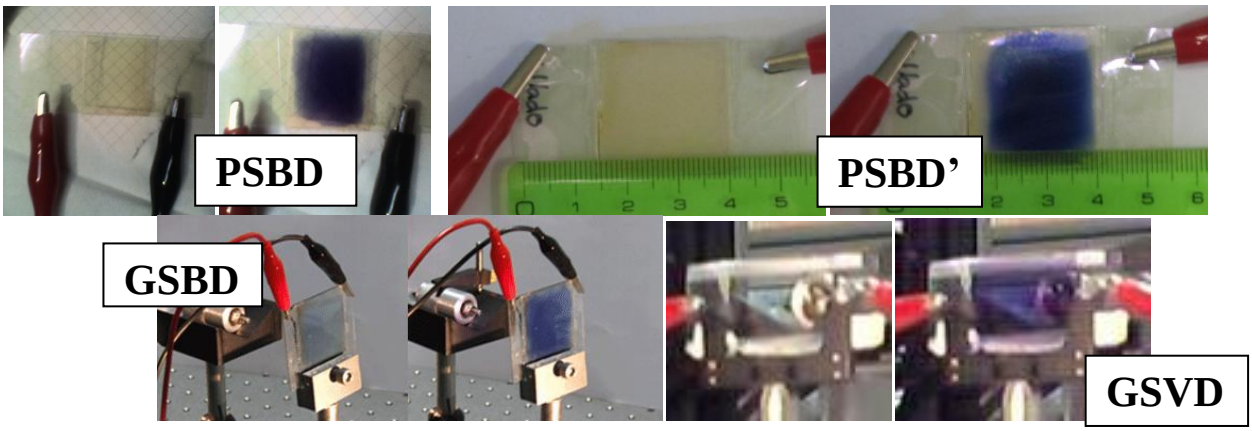

Figure III.39: Viologen based ECDs: Samples PSBD, PSBD', GSBD and GSVD.

The three different samples of ECDs based on a viologen derivate material embedded in a polymeric matrix having ITO coated inner surfaces were prepared by means of different manufacturing methods:

- The first samples of viologen based ECD were fabricated by means of a high temperature process using plastic supports, with a transparent-yellow color for bleached state and dark blue color for colored state [Ver08b]. These samples will be referred as **PSBD** and **PDBD'** (plastic supported blue device).
- The second sample of viologen based ECD was fabricated by means of a high temperature process using glass supports, with a transparent color for bleached state and blue color for colored state [Bar08a]. This sample will be referred as **GSBD** (glass supported blue device).
- The third sample of viologen based ECD was fabricated by means of a room temperature process using glass supports, with a transparent color for bleached state and violet color for colored state [Ver09 and Bar08c]. This sample will be referred as **GSVD** (glass supported violet device).

The samples PSBD and PSBD' are a 4 cm^2 active area and 0.550 and 0.650 mm of total thicknesses respectively, with 175 μm for each ITO + plastic layer and 200 μm the mixture layer thicknesses (300 μm for PSBD'). The samples GSBD and GSVD are a 20 and 8.5 cm^2 area respectively and 2.3 mm of total thickness, with 1 mm each ITO+glass layer and 300 μm the mixture layer thicknesses.

III.2.2 Experimental

The samples PSBD, PSBD' and GSBD were prepared at high temperature following a technology described at [Chi07]. Hence, 0.04 g of ethyl viologen diperchlorate and 0.01 g of hydroquinone were added together with poly(vinylformal) (0.4 g) to propylene carbonate. The melt of the thermoplastic polymer occurs at 70 ºC, therefore the mixture was stirred at 70 ºC for 30 min and deposited on ITO-covered plastic or glass by casting. The ECD was assembled while the mixture was still hot by placing a second layer of ITO plastic or glass on top of the EC layer. A pressure of 50 bars was applied on the device during 10 minutes using a Vogt Labo 200T press. The edges of the devices were sealed using an UV curing epoxi resin ELC2500-clear from Electrolyte. The resin was cured at a UV wavelength of 365 nm during 7 min. and subsequently heated at 80 ºC during 20 min [Sal10].

The sample GSVD was prepared at room temperature as it is indicated in [Poz08a]. A unique EC mixture has been synthesized using a conventional polymeric ionic liquid, a viologen, an electron mediator, such as hydroquinone, and an electrolyte of an ionic liquid, all of them dissolved in a mixture of a high boiling-point polar solvent and acetone. This EC mixture is composed of the electroactive materials required for the

correct functioning of the ECD, and has led to the simplification of the manufacturing process of the final device. Using this method it is possible to perform the synthesis and assembly of the device at room temperature. First, the EC mixture is applied to a transparent conductive substrate using a conventional wet technique, this is then left to dry at room temperature. Subsequently, a second layer of conducting substrate is applied to the dried EC mixture forming a sandwich distribution. Pressure is applied to the device to ensure a constant thickness of the EC mixture between the conductive substrates. Finally, the edges of the device are sealed using epoxy resin.

III.2.3 Optical characterization

The optical characterization of the viologen based ECDs was carried out using the spectrophotometer available at GDAF-UC3M based on the Acton Research monochromator.

III.2.3.1 Spectral transmittance contrast: operation in the visible range

The coloration is produced by reduction from the dication form (of the bleached state) to the radical cation form (of the colored state) of viologen molecules when a low potential is applied [Row02]. Symmetry of the device by construction leads to a redox reaction for both positive and negative voltages. Values of V_{moc} were of 3 V (for sample PSBD) and 2.5 V (for samples GSBD and GSVD) (Figure III.40). GSVD sample was symmetrically tested by applying both polarities voltage levels.

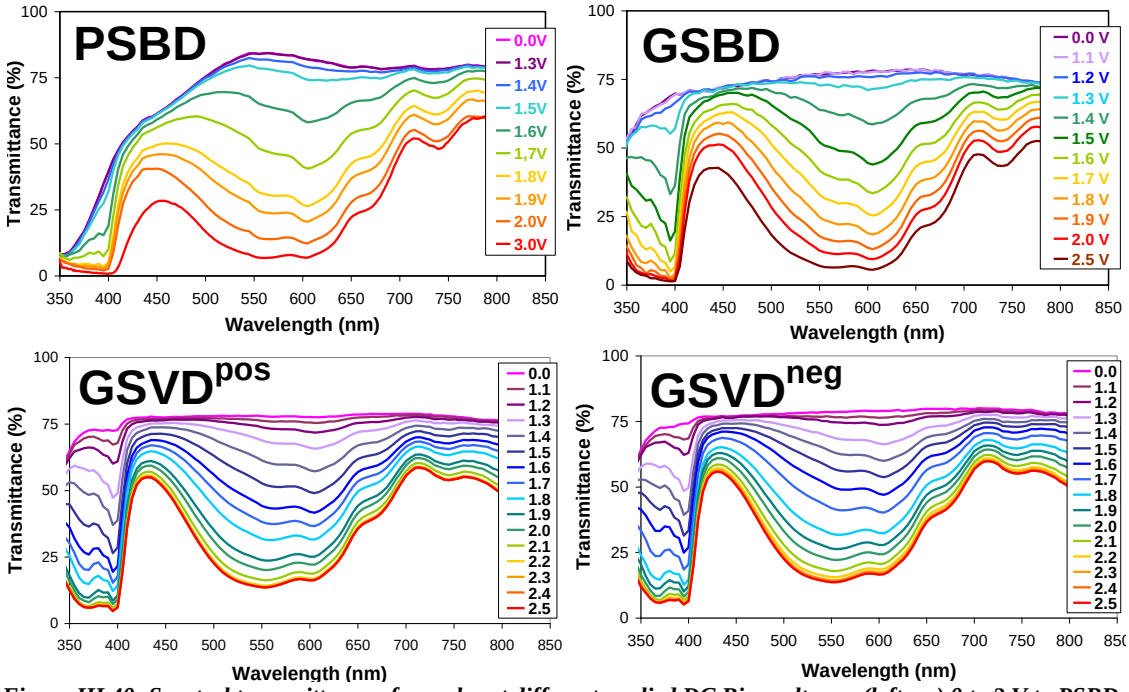

Figure III.40: Spectral transmittance of samples at different applied DC Bias voltage: (left-up) 0 to 3 V to PSBD. (right-up) 0 to 2.5 for GSBD (left-down) 0 to +2.5 V for GSVD (right-down) 0 to -2.5 V for GSVD.

Spectral transmittance from 350 to 850 nm with a 5 nm resolution is obtained. Several transmittance spectra at different applied DC voltages, from 0 V to 3 V for PSBD and from 0 to 2.5 V for GSBD and GSVD, have been measured for the three samples. Results are showed in Figure III.40, with absorption bands corresponding to blue (monomer viologen) and red (dimer viologen) wavelength regions [Mon92, Mon93, Mon98 and Mon99]. Maximum transmittance change wavelength is achieved around 600 nm. The minimum voltage at which coloration starts changing from bleached to colored state can be detected as a threshold value of $V_{TH\text{-}PSBD}$ = 1.4 V for the sample PSBD, $V_{TH\text{-}GSBD}$ = 1.3 V for the sample GSBD and $V_{TH\text{-}GSVD}$ = 1.2 V for the sample GSVD. These values seem independent of the support and are related with the threshold values where the electrical current start being not negligible in voltammograms in next section III.2.4.4 for CV experiments.

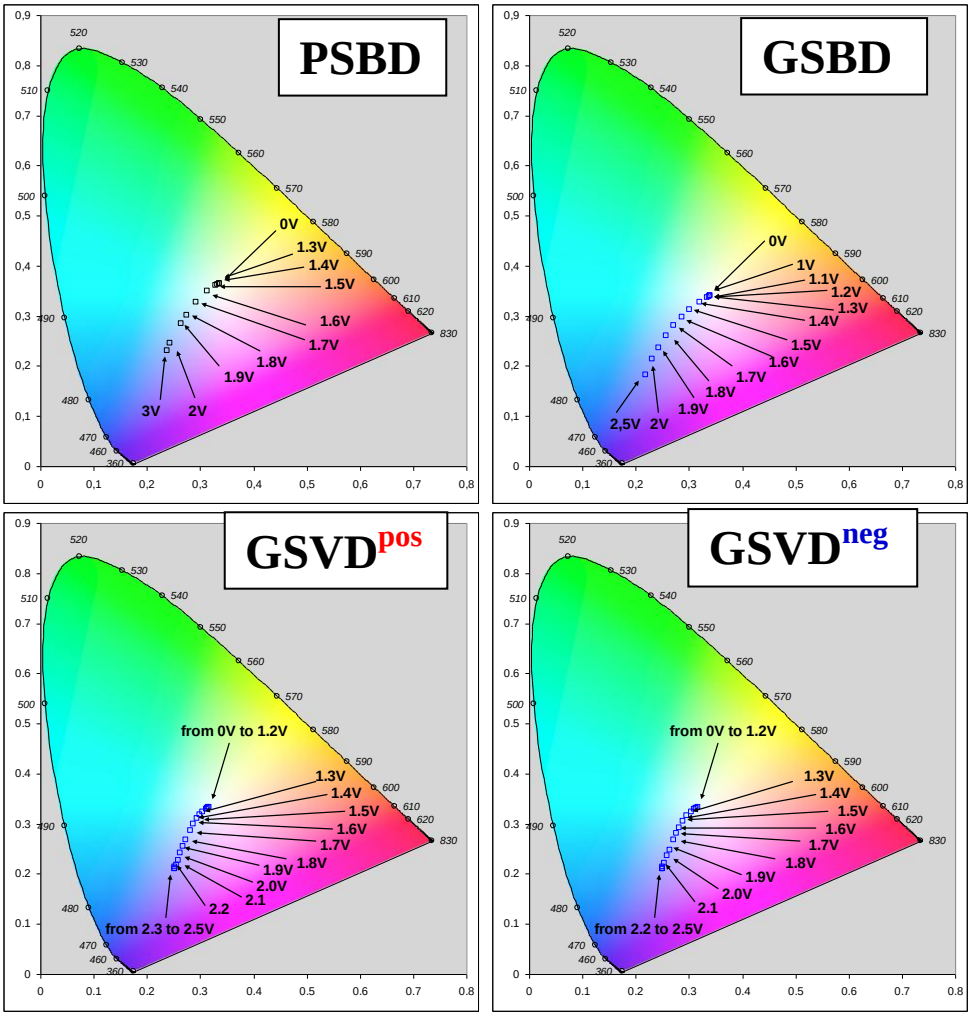

Figure III.41: CIE xy Chromaticity Diagrams at different applied DC bias voltage: (left-up) 0 to 3 V to PSBD, (right-up) 0 to 2.5 V for GSBD, (left-down) 0 to +2.5 V for GSVD (right-down) 0 to -2.5 V for GSVD.

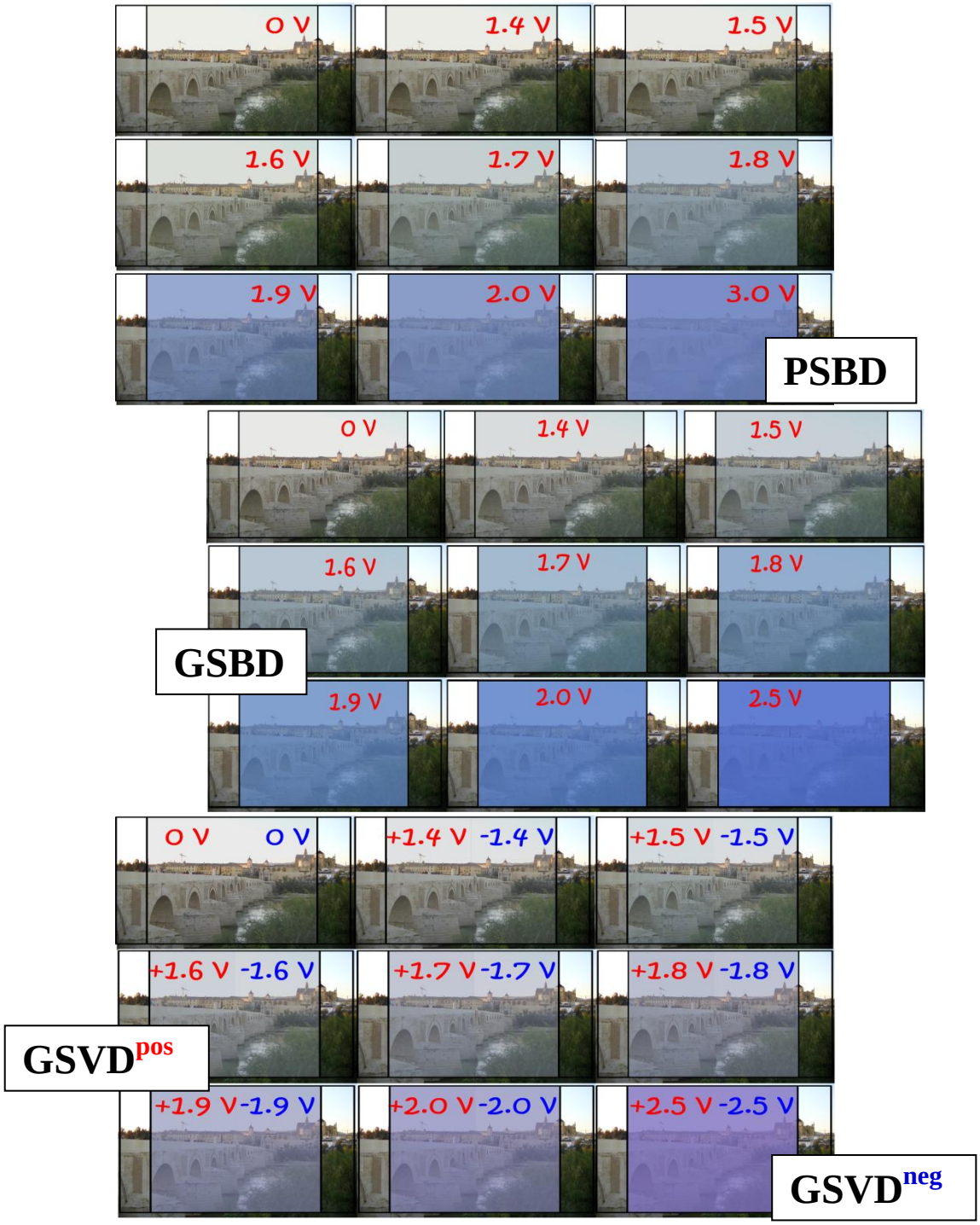

Figure III.42: PSBD (up), GSBD (center) and GSVD-pos/neg (down) simulations over a background photograph of the Mosque of Córdoba (Spain).

CIE xy chromaticity diagrams for each spectral power distribution at different applied voltages are shown in the Figure III.41, covering from pale yellow to blue colorations for PSBD, from uncolored to blue colors for GSBD and from uncolored to violet colors for GSVD. As it can be seen, main changes also take place for coloration from 1.4 V to 3 V for PSBD, from 1.3 V to 2.5 V for GSBD and from 1.2 V to 2.5 V for the GSVD. An average value of the transmittance is calculated with the human eye's sensitive curve for each state of DC bias voltage for each sample. Hence, the real color is simulated with the transparency for each coloration state over the EC samples. Figure III.42 shows the simulated aspect of each viologen device at the different coloration levels for the different potentials applied with a photograph of the Mosque of Córdoba (Spain) at the background.

III.2.4 Electrochemical characterization

Current-time and charge density-time responses for a double-potential step ChrA and ChrC experiments were analyzed. Inversely to ChrA, voltage-time response for a double electrical current step chronopotentiometry (ChrP) experiment was also analyzed. A triangular potential signal with different slopes or scan rates was applied in CV experiments. Additionally, optical transmittance was simultaneously measured in order to relate the electrical current and the optical state of the device. All these measurements and techniques were carried out over the different samples of viologen based ECDs for electrochemical characterization.

III.2.4.1 ChrA, ChrC and chronopotentiometric (ChrP) measurements

Electrical current and charge was measured from the ChrA and ChrC experiments for samples PSBD, GSBD and GSVD. T_{600nm} was also measured simultaneously for samples GSBD and GSVD, in order to obtain some criteria parameters of ECDs from electro-optical characterization. However, electrochemical and optical experiments were not simultaneously measured for sample PSBD. ChrP experiments were carried out for the sample PSBD, in order to compare the measured voltage, for a selected electrical current applied, with the applied voltage, which derive in approximately the same electrical current, obtained from ChrA experiment.

III.2.4.1.1 Sample PSBD

T_{600nm} was measured at different applied square voltage signals for the range between 1.3-2 V for the sample PSBD (Figure III.43-left). Coloring and bleaching times for the sample PSBD are around 13 and 18 seconds respectively at the maximum coloration contrast, appreciated corresponding to 2 V. However, coloring times increase and bleaching times decrease for lower coloration contrast, appreciated with lower voltages. ChrP technique derives the voltage measured in the device when applying a square electrical current of 1, 2 and 3 mA with 10 seconds of period, in Figure III.43-right.

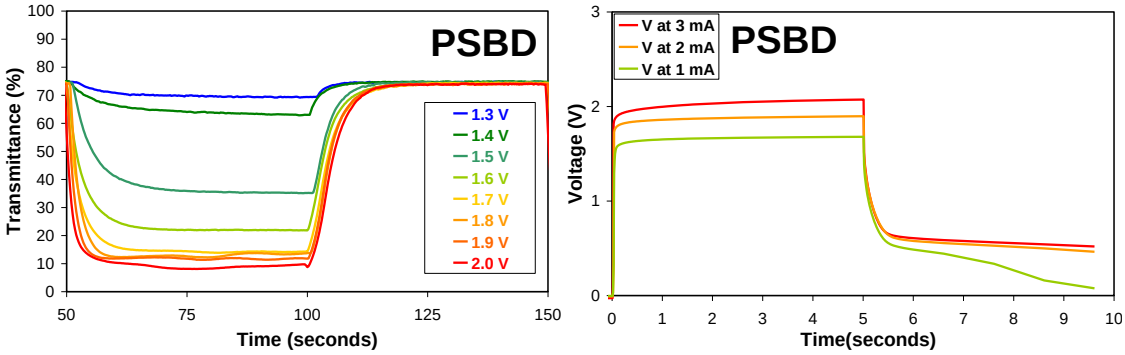

Figure III.43: (left) T_{600nm} for different square voltage signals applied, from 1.25 to 3.00 V with 100 seconds of period. (right) Measured voltage of ChrP experiments compared with the ChrA experiments of Figure III.54.

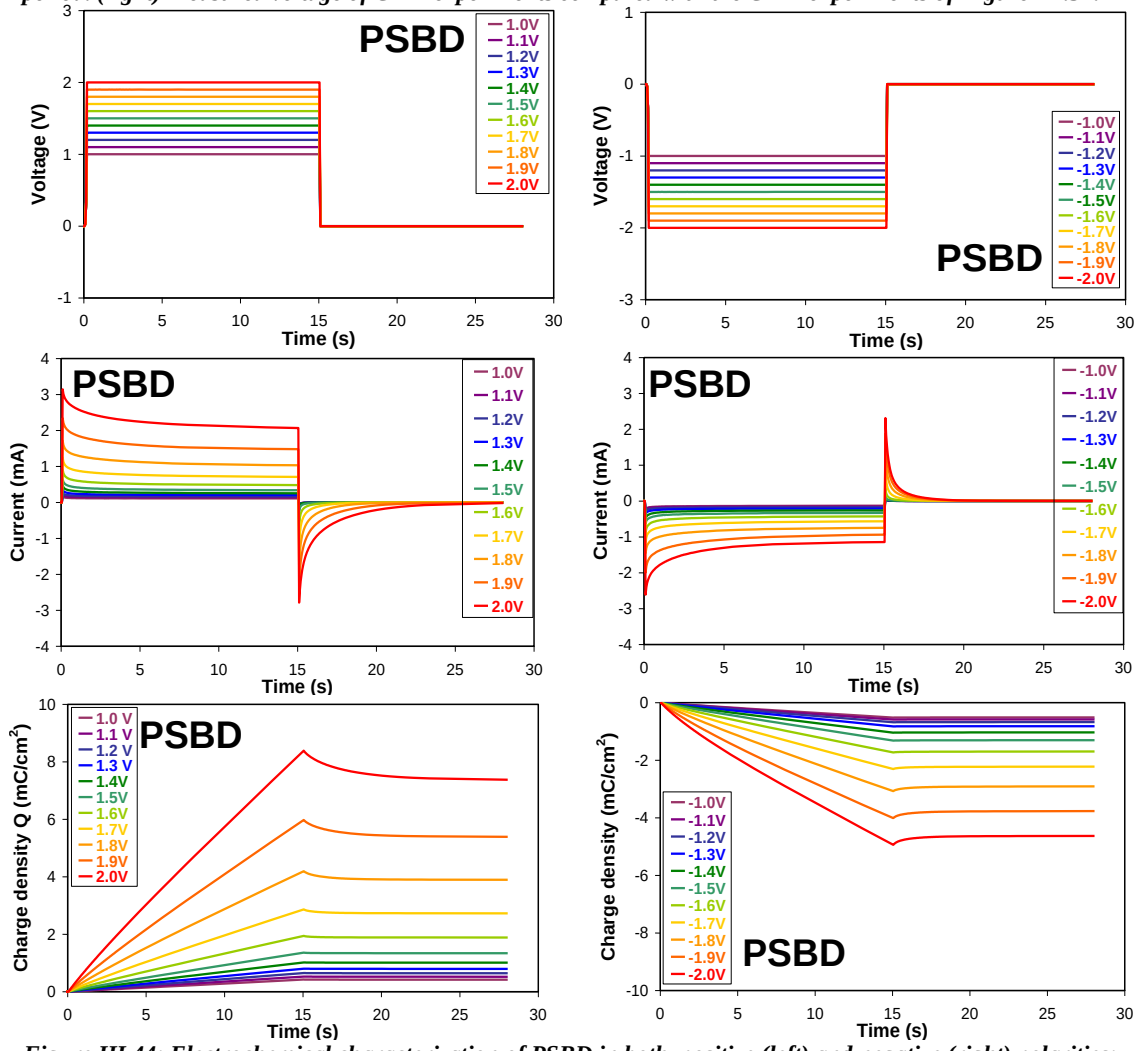

Figure III.44: Electrochemical characterization of PSBD in both, positive (left) and negative (right) polarities: (up) Applied voltage signals, (center) ChrA electrical current and (down) ChrC charge density measured.

Applying different square voltage signals from Vc to 0 V, with 30 seconds of period, being Vc from 1.0 to 2.0 V (Figure III.44-up) with both positive (left graph) and negative (right graph) polarities, electrical current was measured to sample PSBD by means of ChrA technique (Figure III.44-center). For positive polarities (left graph), a small positive peak of current is stabilized to a continuous value after approximately the coloring time. When 0 V is applied at t=15 seconds, a negative peak of current is observed which is stabilized after approximately the bleaching time. For negative polarities (right graph), symmetry is not perfect, which would lead to different coloration states than with positive polarities. However, transmittance was not simultaneously measured for the sample PSBD sample (see GSBD and GSVD samples, below). ChrC technique recorded the charge density (Figure III.44-down). For a constant electrical current signal, from t=0 to t=15 seconds, a ramp electrical charge signal is observed (charge density was computed dividing by the active area of the ECD suitable for coloration). A small decay of charge density is observed at 0 V, for t=15 seconds, derived from the negative electrical current. Since optical transmittance was not measured simultaneously for the sample PSBD, the explanation of the ChrA and ChrC experiments is done after the explanation for the sample GSBD.

Comparing ChrP and ChrA measurements, the electrical current measured for positive polarities in Figure III.44-center-left at t=5 seconds for 2 V applied is related to the voltage measured for 3 mA applied at t=5 seconds in Figure III.43-right. The same proceeding is considered for 1.9 and 1.8 V applied of ChrA experiments in order to relate to 2 and 1 mA applied of ChrP experiments respectively. Further discussion will be done in next section.

III.2.4.1.2 Sample GSBD

By means of ChrA and ChrC experiments, electrical current i, charge density Q and T_{600nm} have been simultaneously measured by applying different square voltage signals with amplitudes between 1 V and 2.5 V for 120 seconds period to the sample GSBD. As it is shown in Figure III.45, the coloring process takes place when applying a potential difference greater than 1.1 V to to the ECD, as it was observed in Figure III.40. Almost a constant electric current is observed for levels between 1 and 2 V. At 2.5 V, a peak current of 9 mA is stabilized to a constant current value after 30 seconds. As it can be observed, a constant value of electrical current is required for the device to maintain the coloration, as it was seen for the solution type I ECDs, described in Chapter I of the current document. The time integral of a constant electric current, i.e., the electrical charge as a temporary ramp, is shown in Figure III.45-down-right. This electric charge increases with time because it corresponds to the electric current flowing through the ECD while it is colored. A small part of this electrical charge is used in the electron transfer reaction of the first reduction process suffered from viologen EC molecules from the dication to the radical cation forms. When the voltage drops to 0 V, according to the

square excitation signal applied to the ECD, small electric charge density ΔQ (mC cm^{-2}) decay can be appreciated. By applying 0 V what it is been doing is short-circuiting the layers of ITO glass. Thus, the small electrical current in opposite sense that it is seen in the Figure III.45 for GSBD sample (Figure III.44 for PSBD sample) should match with the chemical oxidation of the reduced blue chemical compound, which passes back from radical cation form to the dication, while the ECD becomes clearer. I.e., the electrons that joined the molecules in the process of reduction are now released in the process of oxidation. The bleaching process takes place short-circuiting the two ITO layers of the device, applying 0 V. Thus the decrement of the charge density observed at 0 V must be due to the electric charge involved in the redox process and it will be referred as the *effective charge density* ΔQ_{redox} because it is responsible of the change of color of the viologen molecules.

This ΔQ_{redox} is different at each level of coloration. A variation of the charge density Q is not observed after a settling time. The time derivative of a constant electric charge is a null electric current. The higher variation of electric charge matches with the higher coloration of the ECD for the higher applied voltages (Figure III.45-down-left). The charge density used in the reduction process must be equal to the charge density used in the oxidation process, which has been obtained by this procedure.

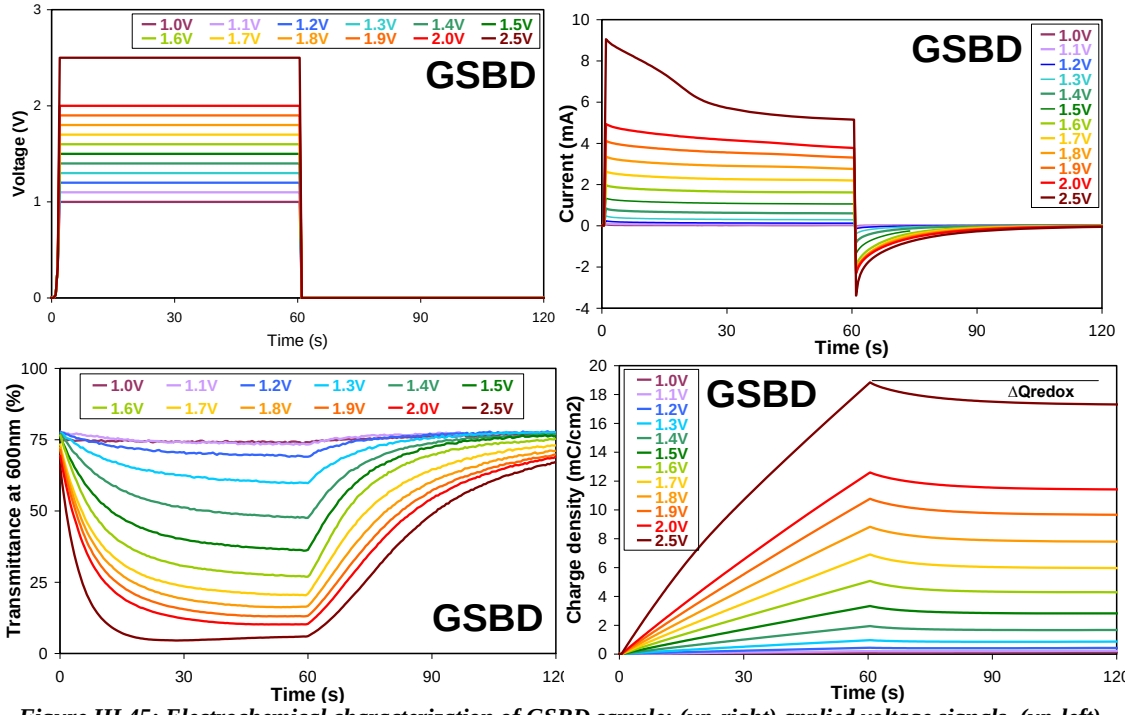

Figure III.45: Electrochemical characterization of GSBD sample: (up-right) applied voltage signals, (up-left) ChrA electrical current, (down-right) ChrC charge density and (down-left) T_{600nm} simultaneously measured.

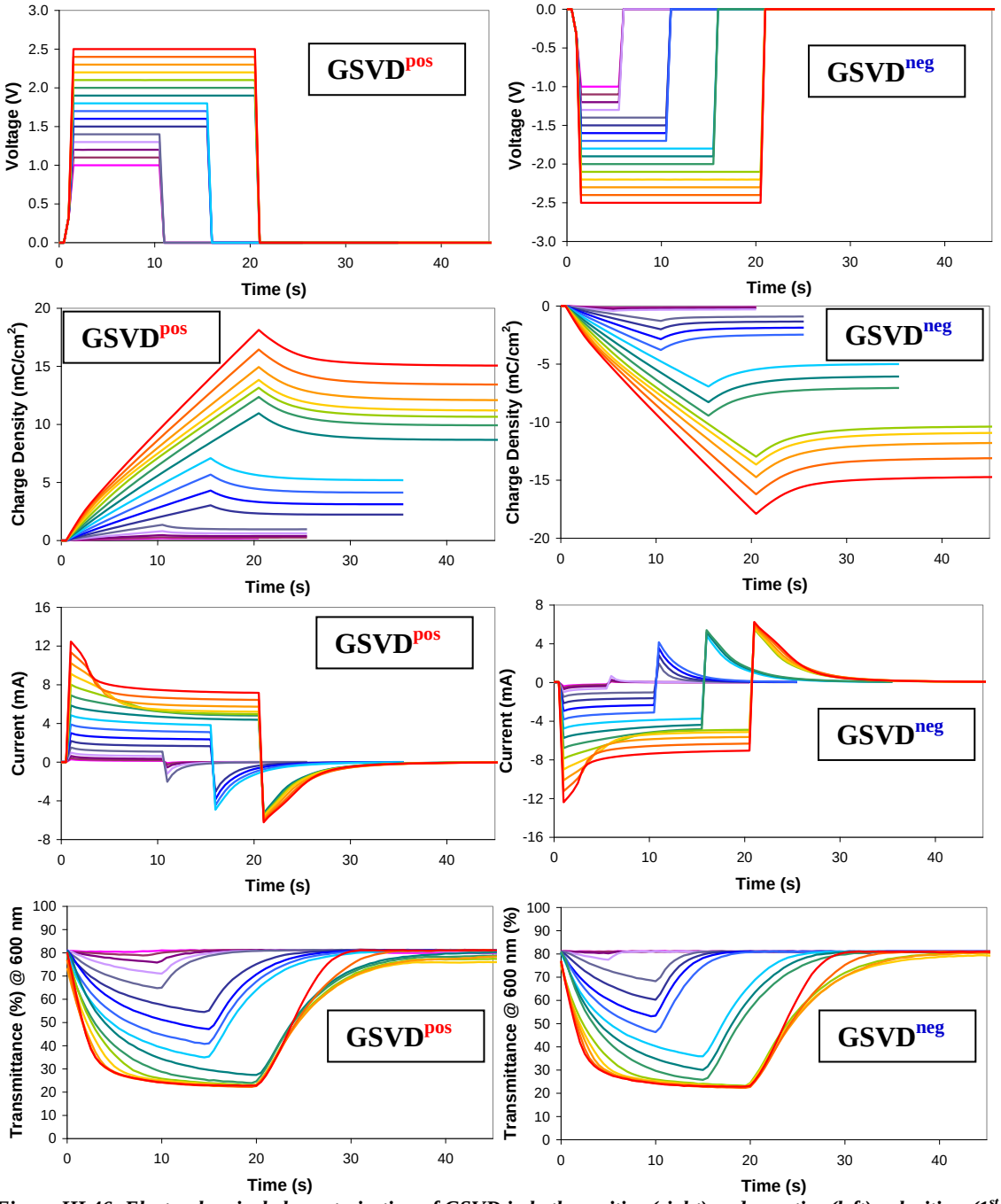

Figure III.46: Electrochemical characterization of GSVD in both, positive (right) and negative (left) polarities: (1st line) applied voltage signals, (2nd line) ChrA electrical current, (3rd line) ChrC charge density and (4th line) T_{600nm} simultaneously measured.

Regarding the sample PSBD, values of ΔQ_{redox}^{PSBD+}=0.94 and ΔQ_{redox}^{PSBD-}=0.23 mC/cm^2 effective charge densities are obtained for positive and negative polarities respectively. Since optical transmittance was not simultaneously measured, not exactly values of coloration can be obtained. However, comparing the values of ΔQ_{redox}^{PSBD+} and ΔQ_{redox}^{PSBD-}, lower coloration should be achieved in the device for negative polarities because of a lower number of color centers should have been formed. A value of ΔQ_{redox}^{GSBD}=1.5 mC/cm^2 at 2.5 V was calculated for the sample GSBD. However, effective charge density of different samples are not related and do not give information about which coloration is the higher. Also, the different internal layer thickness (of 200 and 300 µm for PSBD and GSBD samples respectively) also affects to the color appearance of the different devices. For this task, another parameter such it is the coloration efficiency, is considered as it will be seen in the next pages.

III.2.4.1.3 Sample GSVD

To check the electrical response of the GSVD sample, ChrA experiments were carried out for both, positive and negative polarities. The procedure here was to apply constant voltage level steps in both polarities to the device within the range of 1 to 2.5 V, where the signal is applied for a time t_1 before returning to 0 V (i.e. pulsed signals). The current across the device was measured while the charge density was calculated as the time integral of the current divided by the active area of the GSVD sample (8.5 cm^2). For GSBD, since both ChrA and ChrC experiments were carried out, charge density was calculated from measured electrical charge and then divided by the active area of the GSBD sample (20 cm^2). So as to obtain the complete coloration for each voltage value, t_1 was set to 10 seconds for 1 to 1.4 V, 15 seconds for 1.5 to 1.8 V, and 20 seconds for the rest of the values for positive polarity, while values of t_1 for negative polarity was set to 5 seconds for 1 to 1.3 V, 10 seconds for 1.4 to 1.7 V, 15 seconds for 1.8 to 2 V and 20 seconds for 2.1 to 2.5 V. Figure III.46 presents the results of the charge density for this voltage level step experiment for positive and negative voltage levels. Symmetry has been observed in the results for both polarities steps.

III.2.4.2 Effective charge density

To visualize the relationship between the optical and electrical response, in Figure III.47, a 3D plot is presented showing the relation between the T_{600nm}, the effective charge density ΔQ_{redox} (obtained as explained above) and the voltage applied to both blue and violet glass supports samples GSBD and GSVD, where all of these measurements have been taken simultaneously. As it was used in previous plots, the 600 nm wavelength has been chosen as it displays the maximum optical contrast (λ_{moc}) in the visible light spectrum. In the case of the sample GSVD, both positive and negative voltages were applied, which resulted in a nearly symmetrical behavior, with a small hysteresis for both polarities of current. Electrochemical experiments for both polarities were not

carried out for the sample GSBD because it was degraded after EIS experiments. Both positive and negative voltage scans are plotted for the sample GSVD from the threshold value of 1 V. Neither transmittance change nor charge density is found for lower values, as it was observed in Figures III.45 and III.46. Slight differences are found between both scans, within 0.2 mC/cm^2 charge density and 5% in transmittance. This 3D plot allows the data to be easily interpreted. From 1.2 to 2 V (the section of the curve which corresponds to low charge density required for coloration), T_{600nm} decrement is clearly appreciable, from 70% to 20% in a ΔQ_{redox} from 0.1 to 1 mC/cm^2 for the sample GSBD and from 0.5 to 2.5 mC/cm^2 for the sample GSVD. Regarding the upper part of the plot at the T_{600nm} axis, when the voltage is increased from 2 to 2.5 V, only slight deeper colorations are achieved, being the variation in T_{600nm} in the order of 4 % (from 10 % to 6% for the sample GSBD and from 19 % to 15 % for the sample GSVD) and the ΔQ_{redox} increments by 0.5 mC/cm^2 (from 1.1 to 1.6) and by 1 mC/cm^2 (from 2.5 to 3.5) for both GSBD and GSVD samples respectively.

Figure III.48 shows a linear relation between ΔQ_{redox} and V between 1.3 V and 2.5 V with correlation coefficients of 0.96 and 0.95 and slopes of 0.27 and 0.24 C/V for positive and negative voltage scans of the sample GSVD respectively. However, from 1.3 to 1.7 V, where T_{600nm} decreases rapidly, correlation coefficients improve to 0.99 and 0.98 with slopes of 0.30 and 0.35 C/(V cm^2) for positive and negative scans respectively. A sudden change is observed at 1.8 V ±0.05 V (which is the resolution of the measurement), leading to a different curve that remains linear until the input voltage reaches 2.5 V, the slope in this case is seen to decrease to 0.17 and 0.15 C/(V cm^2) for positive and negative voltage scans, respectively. From this experimental result it is apparent that 1.8 V is a transition voltage where the rate of Q_{redox} is reduced, requiring more input voltage for the same amount of ΔQ_{redox}.

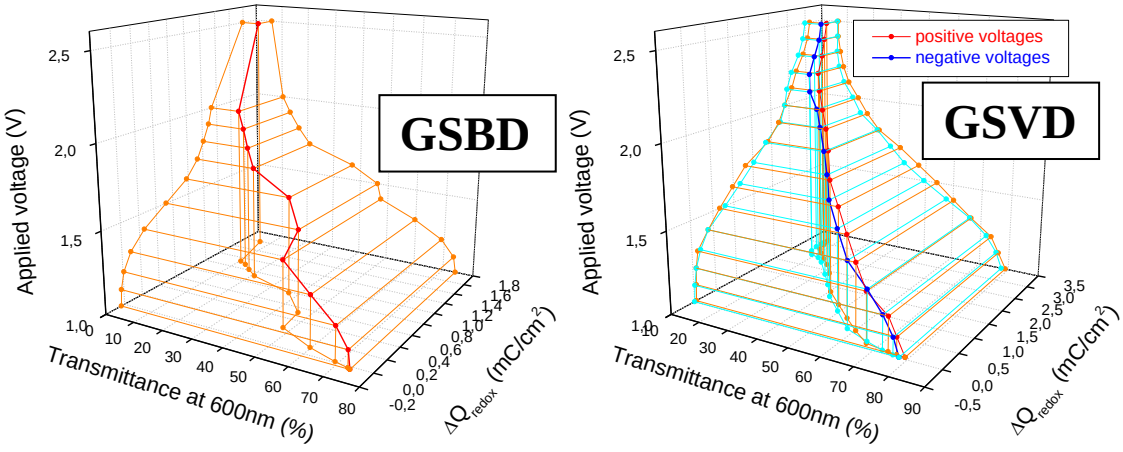

Figure III.47: Effective charge density variation ΔQ_{redox} and optical transmittance of coloration state for applied voltages from 1.0 to 2.5 V for the sample GSBD (left) and for applied bipolar voltages from ±1.0 to ±2.5 V for the sample GSVD (right).

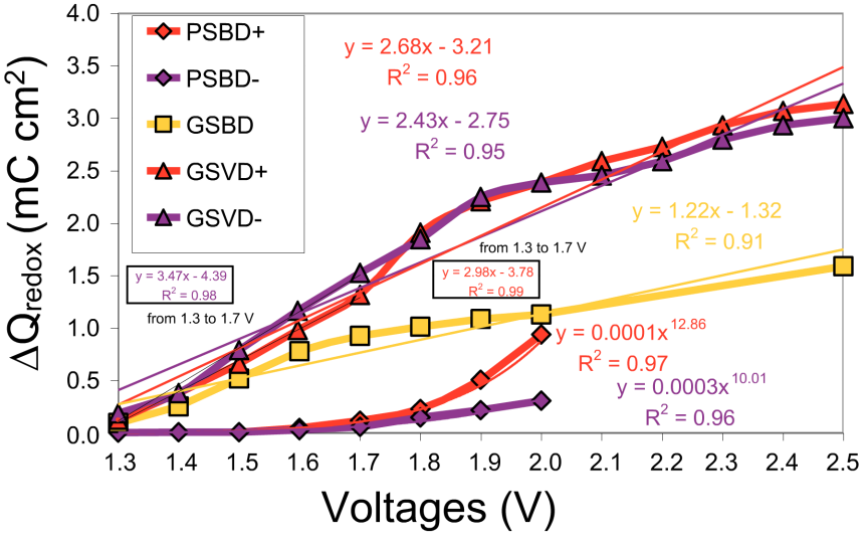

Figure III.48: Charge used for redox reaction as a function of applied voltage for samples GSVD, GSBD and PSBD. Positive and negative values are plotted as absolute values.

The sample GSBD shows a linear relation between ΔQ_{redox} and V with a correlation coefficient of 0.91 and a slope of 122 C/(V cm^2). However, a potential relation instead of a linear relation was used with correlation coefficients of 0.97 and 0.96 for positive and negative voltage scans from 1.3 to 2 V and from -1.3 to -2 V respectively.

III.2.4.3 Criteria and terminology of ECDs operation: Response times, optical density (OD), absorption coefficients, coloration efficiency η (C-E) and write erase efficiency (W-E)

From the results of ChrA and ChrC experiments, simultaneously measured with optical transmittance, several parameters relevant for the criteria and terminology of ECDs operation, such as coloration efficiency η (C-E), write-erase efficiency (W-E), optical density (OD) and absorption coefficients, will be discussed for GSBD and GSVD samples (some of them not for the sample PSBD since optical transmittance was not simultaneously measured with electrochemical ChrA, ChrC or ChrP experiments).

III.2.4.3.1 Sample PSBD

The optical density increment (ΔOD) is defined as the difference of the absorbance observed in the device between the bleached and the colored states. The absorbance A is calculated from the transmittance T% by means of the following expression:

$$A = -\log_{10}\left(\frac{T\%}{100}\right)$$

Response times of 13 seconds for coloring process, where T_{600nm} (%) changes from 74% to 10% (A_{600nm} would change from 0.1308 to 1.001, being ΔOD_{600nm}=0.8702), and 18 seconds for bleaching process, where T_{600nm}(%) changes from 9.04 to 73.36% (A_{600nm} would change from 1.0438 to 0.1345, being ΔOD_{600nm}=0.9093), were observed for this sample at 2 V square voltage signal applied, as it was already described in previous sections. Since the optical transmittance was not measured simultaneously with the electrochemical experiments, only the OD parameter can be detailed for the different voltages, as it is shown in Figure III.49. Main changes of OD are observed at 1.8 V applied. Other parameters will be detailed for PSBD after explanation of GSBD parameters.

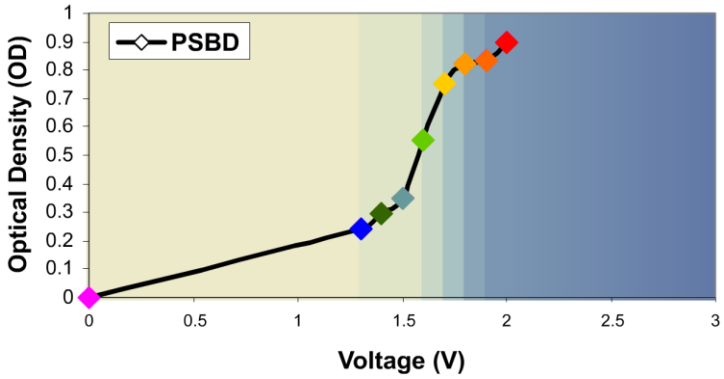

Figure III.49: Optical density increment between the bleached and the colored states.

III.2.4.3.2 Sample GSBD

Regarding the response times of sample GSBD in Figure III.50 it can be observed that coloration times are shorter than bleaching times for applied voltages bigger than 1.6 V and longer for applied voltages smaller than 1.6V. These values have been calculated as the times required for an ECD to change from its bleached to its colored state (or vice versa) in a 10 to 90 percent of the full range. For example, at 1.6V, optical transmittances for bleached and colored states are $T_{bleached}$=75% and $T_{colored}$=26%, being ΔT=75-26=49%. The coloring and bleaching times at 1.6V are $t(T_1)$=29.5 s and $t(T_2)$=30.5 s, being $T_1=T_{colored}+10\%\Delta T$ =26+4.9=30.9% and $T_2=T_{bleached}-10\%\Delta T$=75-4.9=71.1%. It can also be observed that, for applied voltages up to 2V, the bleaching times are higher than 60 seconds and cannot be calculated from data of Figure III.45.

The colored form of the electrochrome is produced by reaction(s) at the electrode. Each redox center of the electroactive species can accept (or donate) an electron at the electrode, one center per *n* electrons, where *n* is usually one or two, according to the balanced redox reaction. Optical density (ΔOD) or increment of absorbance ΔA_{600nm} was calculated from T_{600nm}. Knowing the internal layer thickness, of 300 µm, absorption coefficients α can be calculated (Figure III.51). Let ΔQ be the charge density increment calculated from Figure III.45 at the time required for the ECD to be colored at each

voltage level. For instance, at 2.5 V, the transmittance decreases from 77.10% to 4.72% in 24 seconds, with 8.92 mC/cm^2 of charge density passed in this time. The number of color centers formed is a function of the electrochemical charge passed and it can be quantified by means of the c*oloration efficiency* η and optical absorbance A at a fixed wavelength by Equation III.5. Figure III.52 shows the C-E η and the W-E efficiency for sample GSBD at different levels of coloration.

$$\eta = \frac{\alpha d}{\Delta Q} = \frac{\Delta OD}{\Delta Q} = \frac{\Delta A}{\Delta Q} = \frac{\Delta Log(\frac{I_0}{I})}{\Delta Q} = -\frac{\Delta LogT}{\Delta Q} \qquad \text{(Eq. III.5)}$$

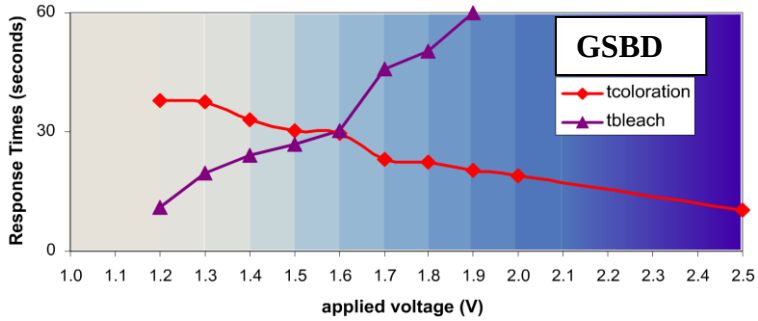

Figure III.50: Responses times for coloration and bleached process of GSBD sample at 600 nm for different applied voltages from 1.2 to 2.5 V.

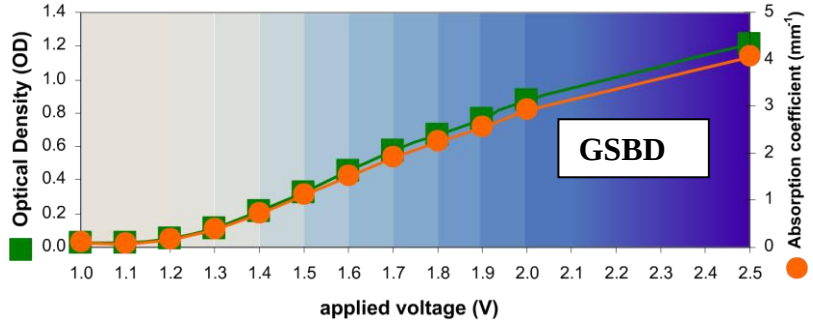

Figure III.51: Optical density and absorption coefficient of GSBD sample at 600 nm for different applied voltages from 1.2 to 2.5 V.

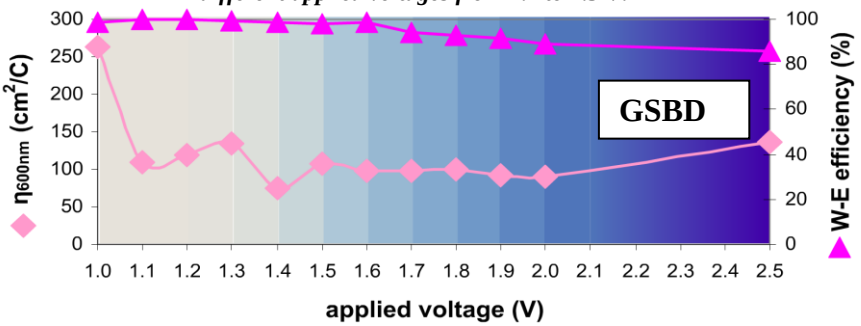

Figure III.52: Coloration efficiency η (C-E) and Write-Erase efficiency (W-E) of GSBD sample at 600 nm for different applied voltages from 1.2 to 2.5 V.

Simulated colors of the visual aspect of the device at the different levels of coloration are at the background of the graphs of Figures III.50, III.50, III.51 and III.52.The coloration efficiency η represents the area of electrochrome, usually expressed in square centimeters units, which color is intensified by unit of absorbance per coulomb of charge that passed. A symmetric optical behavior with positive or negative applied voltages was observed. From 0 to 1.2 V no color change and no charge density are detected. The electrochrome evince a feeble coloration at 1.3V, where the injected charge is more effective, being η_{600nm}= 263 cm^2/C, versus an intense coloration at 2 V being η_{600nm}= 90 cm^2/C. If we increase the applied voltage from 2 V to 2.5 V a more intense color change is detected with shorter coloring time, which derive in an increment of η_{600nm}= 136 cm^2/C.

The Write-Erase efficiency (WE) (fraction of the originally formed coloration that is bleached back in the bleaching process [Mon01]) was computed with T600nm of Figure III.45- down left for t=0, t=60 and t=90 seconds. WE decreases if increasing the applied voltage from 1.6V (94%) to 2.5V (86%). For the sample PSBD, relating T_{600nm} at 2 V of Figure III.43, changing from 73.68 to 9.97%, and checking that coloring time is approximately 13 seconds, the charge density of Figure III.54 at 15 seconds for 2 V applied is 7.35 mC/cm^2. From Figure III.49, an increment of optical density ΔOD=0.897 is obtained, deriving to an absorption coefficient α=4.48 nm^{-1} and a coloration efficiency η=122 cm^2/C. Absorption coefficient values of 4.48 nm^{-1}, obtained for the sample PSBD at 2 V, can be related to the value of 4.05 nm^{-1} obtained for the sample GSBD at 2.5 V.

III.2.4.3.3 Sample GSVD

Same procedure applied to GSBD sample is now applied to GSVD sample, for ±2.5 V. 6.82 and 6.75 mC/cm^2 charge densities are observed at coloring times (7 seconds) in Figure III.46 for positive and negative polarities respectively. Optical densities of 0.551 and 0.548 derived to absorption coefficients of 1.83 and 1.82 mm^{-1}, leading to values of 80 and 81cm^2/C coloration efficiencies respectively.
Table III.6 shows a summary of the parameters calculated for the three samples of viologen devices. The sample GSBD shows the higher values for CE, ΔT and ΔOD, but as a drawback, the worse response times. Even showing lower CE, ΔT and ΔOD, the sample GSVD shows better response times. However, the sample PSBD shows intermediate values between samples GSBD and GSVD regarding to CE, ΔT, ΔOD and response times, but the barely pale yellow appearance of the bleached state could become a problem for some possible applications.

Sample	Potential	ΔT	t_c	t_b	ΔOD	α(nm^{-1})	ΔQ($mCcm^{-2}$)	C-E(cm^2/C)
PSBD	2 V	64.02%	13 s	18 s	0.897	4.48	7.35	122
GSBD	2.5 V	72.38%	24 s	> 60 s	1.2131	4.05	8.92	136
GSVD	+2.5 V	57.20%	7 s	8 s	0.551	1.83	6.82	80
	-2.5 V	57.09%	7 s	8 s	0.548	1.82	6.75	81

Table III.6: Calculated parameters for the viologen based ECDs characterized.

III.2.4.4 Cyclic voltammetry (CV) measurements

Several CV experiments were applied to the samples PSBD, GSBD and GSVD at different scan rates. Voltammograms revealed the potential at which the redox reaction, responsible of coloration changes, takes place. Symmetrical redox reactions were observed for both polarities, positive and negative voltages, in some cases. Symmetry in the optical transmittance, simultaneously measured, will be studied.

A first explanation of the voltammograms obtained for the three samples will be followed by a more detailed description for each sample, with the optical transmittance and different scan rates discussion.

III.2.4.4.1 Samples PSBD, GSBD and GSVD

Figure III.53 shows the voltammograms with embedded areas colored with previously calculated RGB colors for each voltage applied for the samples PSBD, GSBD and GSVD.

For sample PSBD, Figure III.53-up shows the voltammogram of the 3rd cycle of CV experiments at 100 mV/s scan rate. Current peaks in the forward and reverse scans for the redox reaction, from the dicationic viologen form (pale yellow transparent) to a radical cation viologen form (dark opaque blue), take place at ±2.6 V for coloration process (reduction) and at ±2 V for bleaching process (oxidation). From 0 to ±1.3V no color change neither appreciable electrical current occur. At $V_{TH\text{-}PSBD}$=1.4 V, coloration in the device can be appreciable. Both coloration and bleaching peak currents (i_c and i_b) and voltages (E_c and E_b) are observed to be $(E_c, i_c)_{PSBD}$ = (2.6 V, 6.2 mA) and $(E_b, i_b)_{PSBD}$ = (2.0 V, 1.7 mA) in a symmetrical way.

For sample GSBD, Figure III.53-center shows the voltammogram of the 3rd cycle of the CV experiments at 10 mV/s scan rate. A symmetrical optical and electrochemical behavior is observed for positive or negative voltages applied. Current peaks in the forward and reverse scans for the first redox reaction, from the dicationic viologen form (pale transparent white) to a radical cation viologen form (dark opaque blue), take place at ±2.1 V for coloration process and at ±1.9 V for bleaching process. From 0 to ±1.2V no color change neither electrical current occur. At $V_{TH\text{-}GSBD}$=1.3 V, coloration in the device can be appreciable. Both coloration and bleaching peak currents (i_c and i_b) and voltages (E_c and E_b) are observed to be $(E_c, i_c)_{GSBD+}$ = (2.1 V, 6 mA) and $(E_b, i_b)_{GSBD+}$ = (1.8 V, 1.6 mA) for positive polarities, and $(E_c, i_c)_{GSBD-}$ = (-2.2 V, -7 mA) and $(E_b, i_b)_{GSBD+}$ = (-2 V, -2.2 mA) for negative polarities. Asymmetry is observed in the voltammogram. A second peak of current for coloration process and not very pronounced is also observed at ±2.8 V for the sample GSBD. The first one refers to the redox reaction from dication to radical cation forms and the second one may refer to the second redox reaction from

dication to neutral species of viologen materials, being this one a non desired effect for the purpose of a ECD, since a colorless appearance would be observed in the device [Mon98].

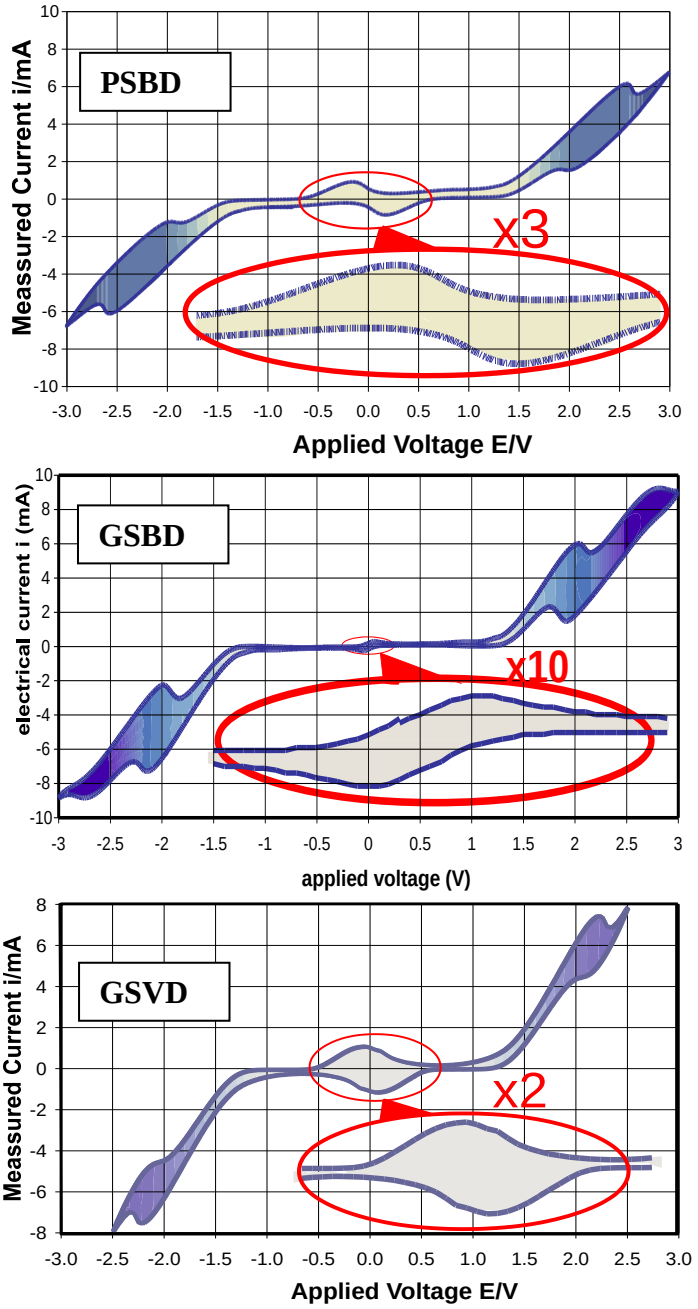

Figure III.53: Voltammograms of the three samples. (up) PSBD at 100 mV/s (center) GSBD at 10 mV/s and (down) GSVD at 100 mV/s scan rates. RGB values colors were derived from the CIE xyY Chromaticity Coordinates.

The peak occurs because at some point the diffusion layer has grown sufficiently above the electrode so that the flux of reactant to the electrode is not fast enough to satisfy that required thermodynamically by the electrochemical equilibrium of the Nernst equation [AJB00 and Ora08]. In this situation the current begins to drop just as it did in the potential step measurements. In fact the drop in current follows the same behavior as that predicted by the Cottrell equation [AJB00 and Ora08].

For the sample GSVD, Figure III.53-down shows the voltammogram of the 3rd cycle of the CV experiments at 100 mV/s scan rate. Electrical current flows when voltage reaches the above mentioned threshold $V_{TH\text{-}GSVD}$ = 1.2 V in both senses. The reason of the coloration changes is the bipolar redox reaction that can be observed for both EC samples in a symmetrical operation. Positive and negative redox reactions appear at the same value of voltages and current. Both coloration and bleaching peak currents (i_c and i_b) and voltages (E_c and E_b) match for positive and negative voltages, regardless the polarities of the current. The values for the sample GSVD are $(E_c, i_c)_{GSVD}$ = (2.3 V, 7.5 mA) at the coloration process and $(E_b, i_b)_{GSVD}$ = (2.1 V, 4.6 mA) at the bleaching process.

The redox reaction observed around zero voltage for the three samples is related to the scan rate used in the CV measurement, since no coloration change appears at this range of potential applied. At very low scan rates this zero voltage reaction is decreased, such as in the case of the GSBD sample, where 10 mV/s, instead of 100 mV/s scan rate, is used.

III.2.4.4.2 Sample PSBD

Three cycles of CV measurements from -3 to +3 V were carried out over PSBD sample at 1, 10, 20, 30, 40 and 100 mV/s scan rates (Figure III.54). A quasi-symmetric redox reaction appears for positive and negative applied voltages. The faster the scan rate, the higher the electrical current consumption. A slight asymmetry is observed between the electrical current with different polarities at some scan rates. The redox reaction appearing at ±0.5 V decreases for lower scan rates.

Simultaneously to the CV experiments at 100 mV/s scan rate, optical T_{600nm} was measured, as it is shown in Figure III.55. Background colors were calculated from CIE Chromaticity coordinates and simulate the optical appearance of the devices switching from colored to bleached states.

The 3D plot of Figure III.56 shows the relation between the electrical current, the applied voltage and the optical transmittance on the device. For a clear visualization, only the projections on the walls are shown. A slight asymmetry of optical transmittance between positive and negative polarities of the voltage applied is observed for the

processes of coloring and bleaching, explained by the arrows of the plot show with colors. Bleaching electrical current show a different behavior than coloring electrical current, as it is shown in the projection wall of the figure.

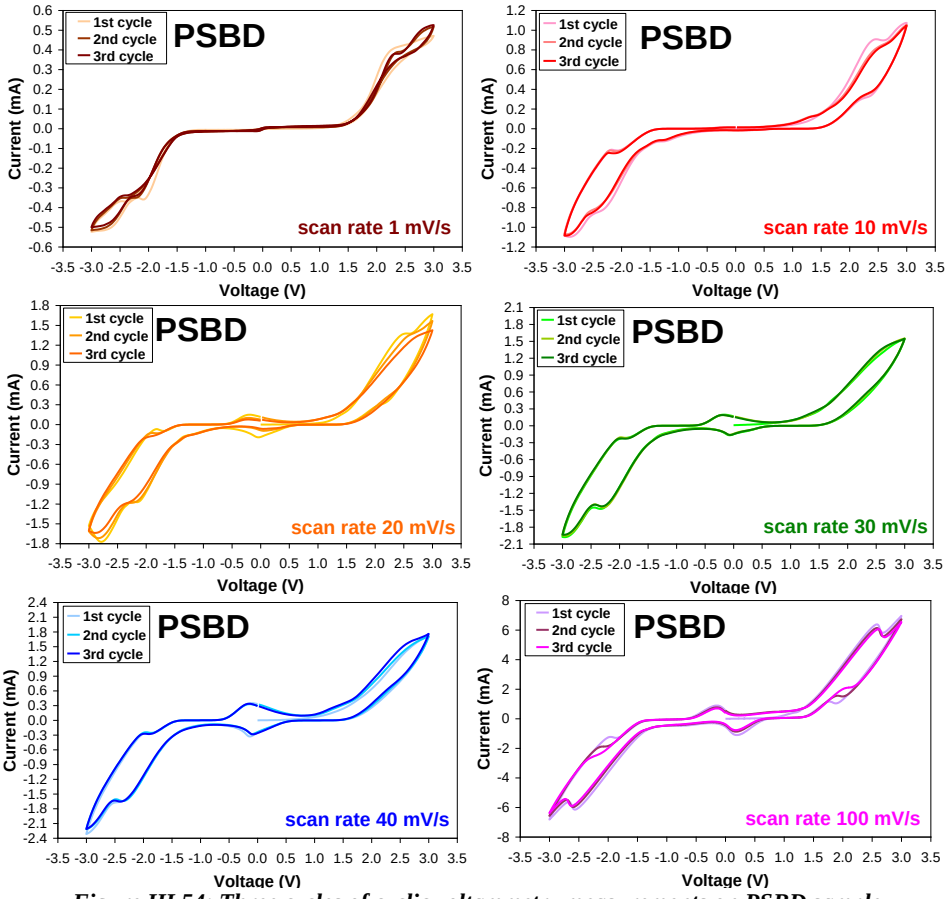

Figure III.54: Three cycles of cyclic voltammetry measurements on PSBD sample from -3 to +3 V at 1, 10, 20, 30, 40, 100 mV/s scan rates.

Current versus voltage (left front wall) is the voltammogram, where a bipolar redox reaction is observed. Transmittance versus voltage (down floor wall) shows the measured optical transmittance versus the applied voltage for the sample PSBD. An asymmetry around zero voltage with different peak width comparing positive and negative sweeps, what denotes a slightly hysteretic behavior and indicates a non symmetric electrode rate, is observed. This could damage the properties of the ECD in time. Current versus transmittance (right side wall) is a new representation where it can be observed a faster decrease of the current for the bleaching process, being almost zero for a 45% value of transmittance. However, a kind of memory effect is observed here when, despite the electrical current reaches zero, the coloration in the device remains decreasing. An asymmetrical shape for different polarities of the current and the

respective peaks of current that do not produce an extra coloration is observed at the lowest values of transmittance.

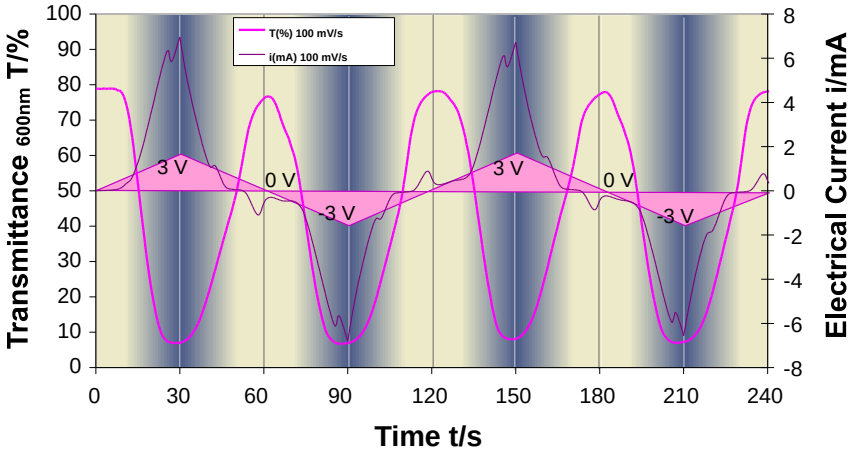

Figure III.55: T_{600nm} simultaneously measured with the electrical current on the sample PSBD while applying three cycles of CV experiment from -3 to +3 V at 100 mV/s scan rate.

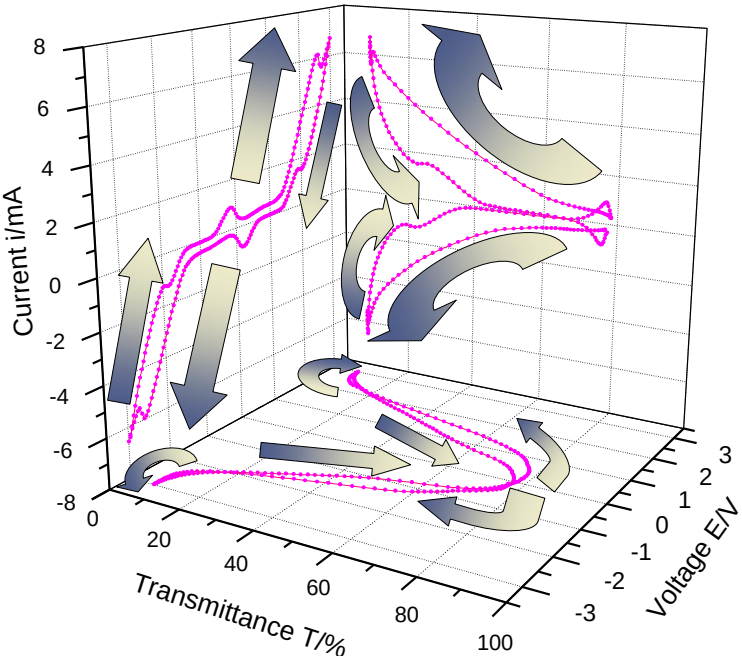

Figure III.56: 3D plot of current, transmittance and voltage for triangular signals of 100 mV/s scan rate for the sample PSBD. The left-up wall of the plot is a voltammogram. Colored arrows indicate coloration and bleaching process.

Voltammograms derived from CV experiments for faster scan rates, from 100 to 900 and from 1000 o 9000 mV/s, are shown in Figure III.57. The bipolar redox reaction, detected at coloration voltages for lower scan rates, disappears and a widening at voltages

between ±0.5 V, not responsible of color change, increases from 100 to 900 mV/s, and stabilizes from 1000 to 9000 mV/s scan rates. The optical transmittance contrast at 600 nm simultaneously measured (Figure III.58) decreases, since the scan rate is faster than the redox reaction. As it can be observed in Figure III.54, for slower scan rates than 100 mV/s, the peaks of current take place at potentials lower than the 2.6 V observed in Figure III.53 left.

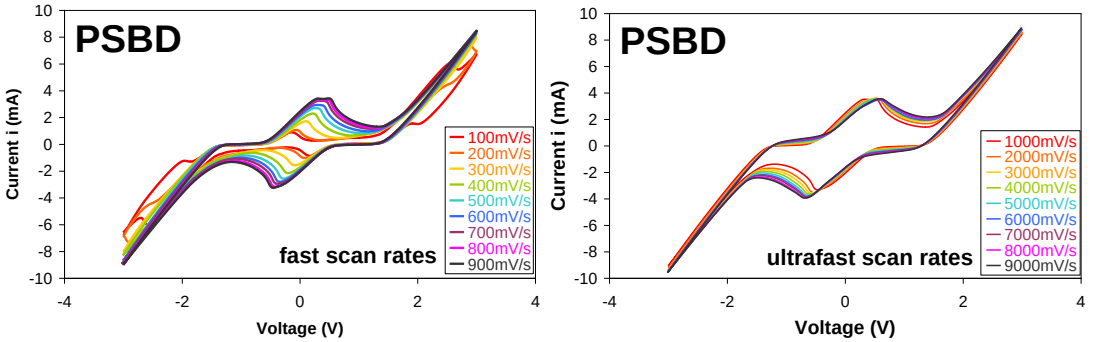

Figure III.57: Voltammograms of sample PSBD at 100-900 (left) and 1000-9000 (right) mV/s scan rates. Released electrons at the bleaching process are observed at non coloration voltage levels for high scan rates because of the rate of the redox reaction.

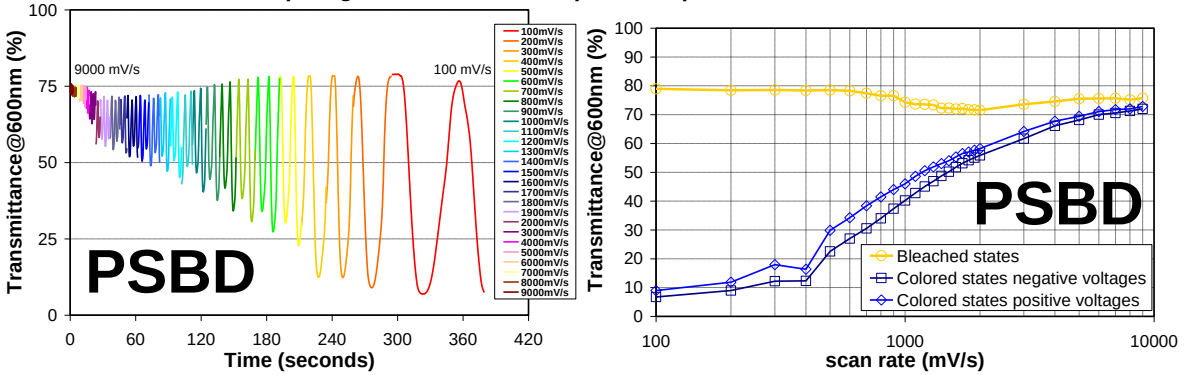

Figure III.58: Transmittance of sample PSBD at 600 nm for fast and ultrafast scan rates, from 100 to 9000 mV/s (left) versus time (right) versus scan rates.

III.2.4.4.3 Sample GSBD

Figures III.59 and III.60 show the measured electrical current while a triangular voltage signal from -3V to 3V at 10 and 100 mV/s scan rate (83.3 mHz triangular signal) is applied to the GSBD sample respectively during three cycles. Simultaneously, T_{600nm} was measured. The current consumption is around 10 mA at ±3V, matching with the highest colored state. An asymmetry is observed in electrical current and T_{600nm} for 100 mV/s scan rate voltammogram. For the ten times slower triangular voltage signal applied, at 10 mV/s scan rate, the symmetry is improved, due to the slow response of the device. However, the bleached state of the device is affected by the longer times of applied voltage at the highest voltage values, which deteriorate its operation. Moreover,

the voltammograms obtained for both scan rates show differences. At the 100 mV/s scan rate, electrical current shows a widening at the range between ±0.5 V, which is not observed at 10 mV/s scan rate. On the other hand, a symmetrical redox reaction is observed in the range from 1.5 to 3 V at 10 mV/s scan rate, which cannot be observed for 100 mV/s scan rate, due to the low response time of coloration process. The widening of the hysteretic electrical current at coloration voltages over the threshold value V_{TH} is explained as the charge and discharge of the ECD, which behaves as a pseudo-capacitor.

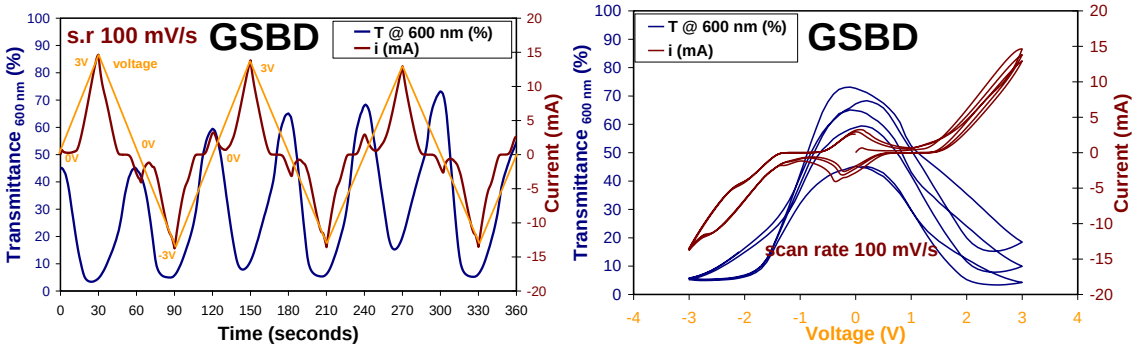

Figure III.59: CV experiment on sample GSBD and 100 mV/s scan rate. T_{600nm} and electrical current (left). Voltammogram (right). An asymmetry is observed for different polarities with different levels of coloration.

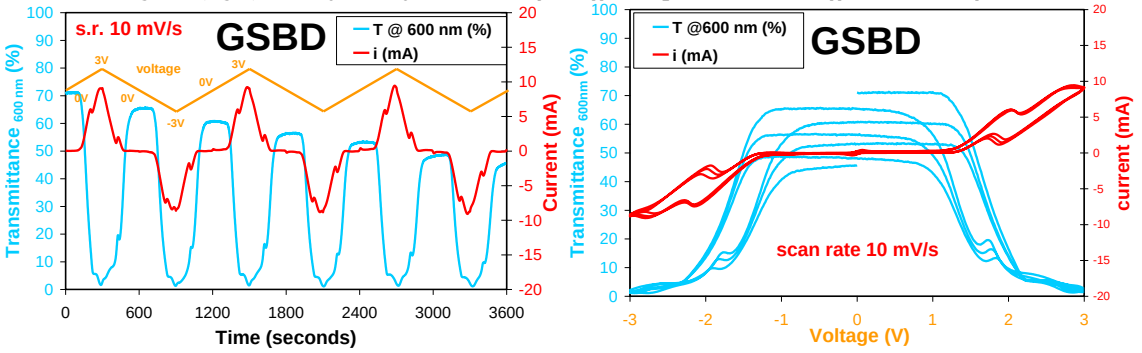

Figure III.60: CV experiment on sample GSBD at 10 mV/s scan rate. (left) T_{600nm} and electrical current (right) Voltammogram. Symmetry is now achieved. However, bleached state gets affected for different cycles.

III.2.4.4.4 Sample GSVD

CV experiments were performed simultaneously with optical transmittance measurements at 600 nm for the sample GSVD. Because of the maximum coloration voltages values, triangular voltages signals from -2.5 V to 2.5 V at 40 mV/s, 60 mV/s, 80 mV/s and 100 mV/s scan rates for the sample GSVD are applied. Simultaneously, electrical current is measured. Figure III.61 shows the measured electrical current and optical T_{600nm} in the time domain for the sample GSVD. Background colors were calculated from CIE Chromaticity coordinates and simulate the optical appearance of the devices switching from colored to bleached states. The lowest values of the

transmittance at the colored states occur for the peaks of electrical current in both polarities. Also, no electrical current consumption is detected for the highest values of the transmittance at the bleached states.

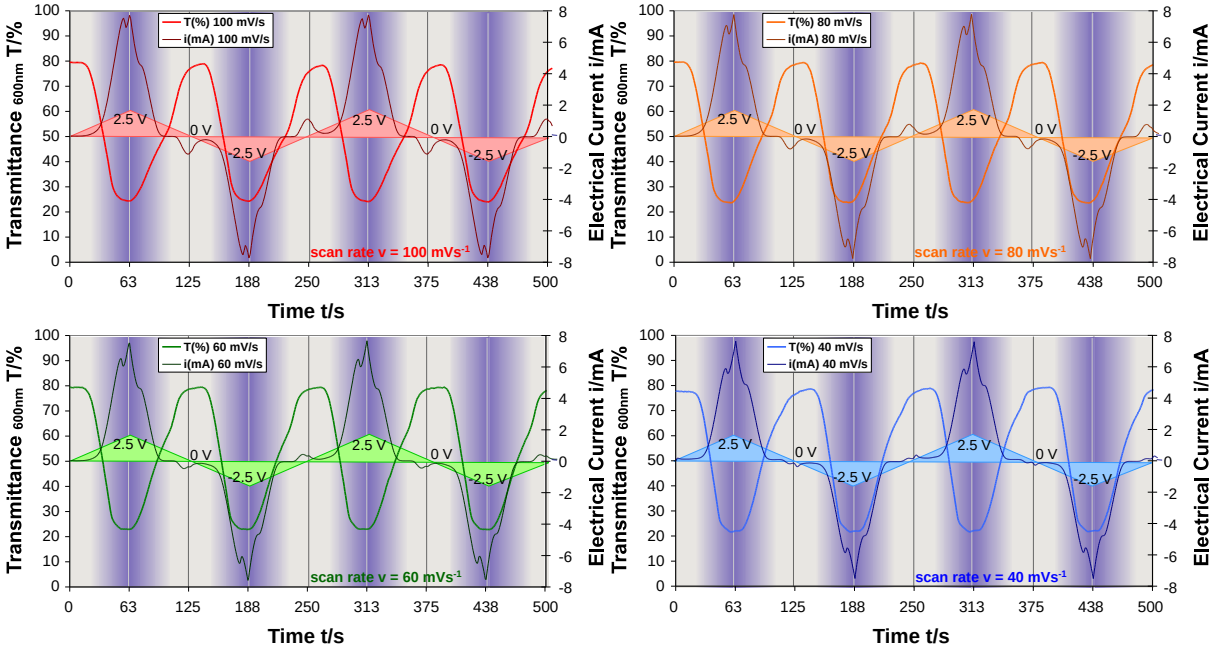

Figure III.61: Current and transmittance results of CV experiment on GSVD sample at 40, 60, 80 and 100 mV/s scan rates. RGB values colors derived from the CIE xyY Chromaticity Coordinates.

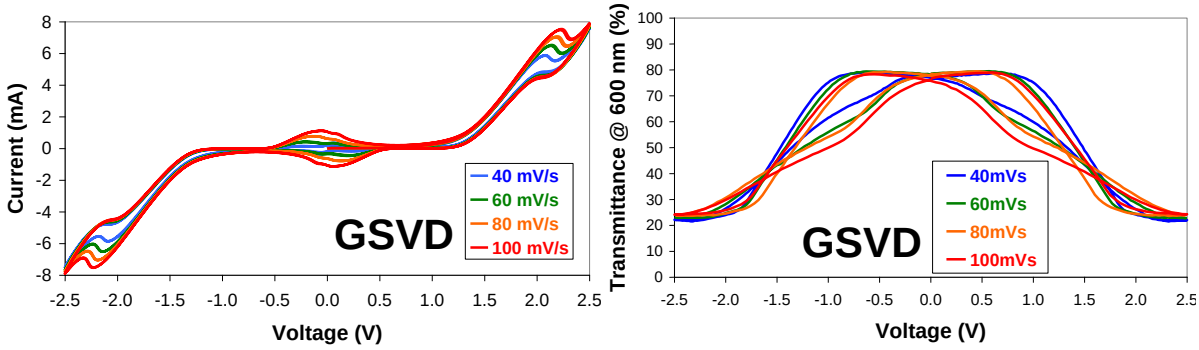

Figure III.62: (left) Voltammogram and simultaneous $T_{600\ nm}$ (right) of sample GSVD at 40, 60, 80 and 100 mV/s.

Figure III.62-left shows different voltammograms for the sample GSVD at 40, 60, 80 and 100 mV/s scan rates. Peak currents of the bipolar redox reaction increase when increasing the scan rate. The zero voltage reaction observed at ±0.5 V is decreasing for the lower scan rates, as with samples PSBD and GSBD. T_{600nm} simultaneously measured is shown in Figure III.62-righ, denoting that the scan rates used in the CV experiments were as slow enough as for reaching the final values of the colored and bleached states.

The 3D plot of Figure III.63 shows the relationship between applied voltage, T_{600nm} and electrical current of sample GSVD at 100, 80, 60 and 40 mV/s scan rate, simultaneously measured during the 3rd cycle of CV experiments. For a clear visualization, only the projections of the curve on the three walls of the graph are plotted.

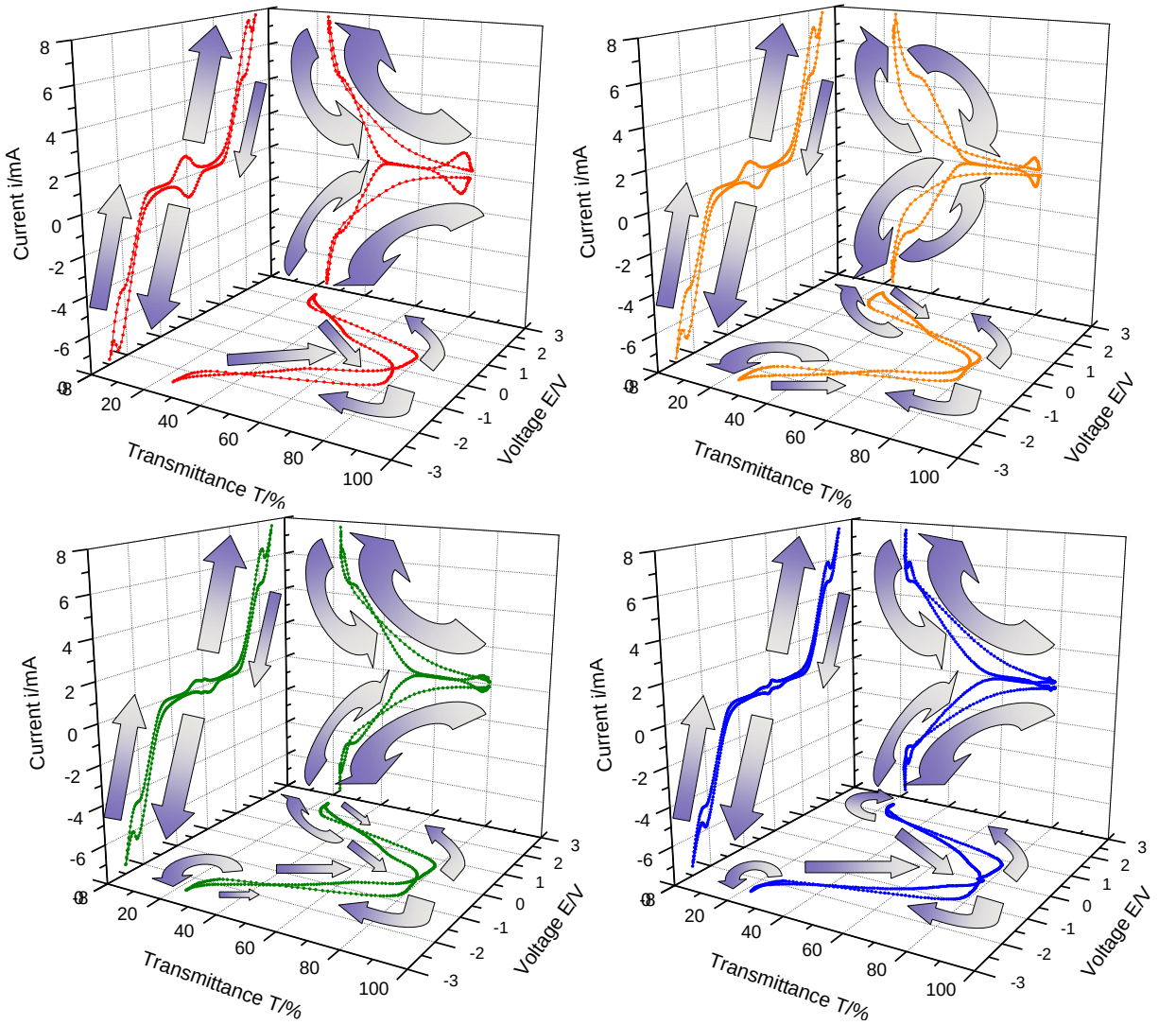

Figure III.63: 3D plot of current, transmittance and potential for triangular voltage signals of 100 (left-up), 80 (right-up), 60 (left-down) and 40 (right-down) mV/s scan rate of CV experiments of the sample GSVD.

Current versus voltage (left front wall) is the voltammogram mentioned in Figure III.61, where a symmetrical redox reaction appears for bigger voltages than $V_{TH\text{-}GSVD}$=1.2 V in both positive and negative voltages. Electrical current is zero for voltages under the threshold value V_{TH}. This behavior could be explained because of a large Rct, observed in this voltage interval, which indicates a slow reaction [Ver09], as it

will be seen in next sections.Transmittance versus voltage (down floor wall) shows how the device gets the colored and bleached states for the triangular or double ramp voltage signal, appearing an hysteresis behavior in the V-shape curve obtained for forward and reverse scans of CV experiments, a characteristic also found in some LC materials studied by the authors' Research Group [Oto04]. The optical response of the device at this scan rate is fast enough to reach the values of 24% and 79% of T_{600nm} for both polarization of electrical current, corresponding to the colored and bleached states of the ECD. The arrows of the plot show the sense of coloration and bleaching processes. Current versus transmittance (right side wall) shows the electrical current crossing the device when it gets colored and bleached. At the lowest transmittance levels, no extra coloration is appreciable for the peaks of current. Electrical current is zero in the bleaching process at a 45% transmittance value, matching with a value of 1 V for triangular applied voltage. Despite no current is flowing, the device state becomes clearer and clearer in the interval from 1.3 V to 0.5 V.

Then, an opposite electrical current, corresponding to the redox reaction appearing at voltages around ±0.5 V in the voltammogram, is observed. This behavior could be represented by the discharge of a CPEdl described in the EEC model of GSVD [Ver09] and PSBD samples [Ver08b]. The difference of electric potential when the triangular signal decreases from 1 V, approaching to a short circuit, causes a change in the structure of the viologen molecules from the dication form to the radical cation form, releasing electrons while the double layer is discharged. The value of transmittance for a zero current at the bleaching process increases to 50, 55 and 60% for 80, 60 and 40 mV/s scan rates respectively.

III.2.4.4.5 Reversible redox reaction

If the electronic transfer at the surface is fast and the current is limited by the diffusion of species to the electrode surface, then the current peak will be proportional to the square root of the scan rate ($i_p \propto \sqrt{v}$), the cathodic and anodic peak current ratio will be equal to unity ($i_p^c/i_p^a=1$) and the cathodic and anodic peak potential separation will be equal to 58 mV ($E_p^c-E_p^a=58$ mV). If $\Delta E_p=E_p^c-E_p^a$ >200 mV, the charge transfer coefficient can be determined:

$$\alpha_c = -2.3\times\frac{RT}{F\times slope_{cathodic}} \qquad \alpha_a = 1-2.3\times\frac{RT}{F\times slope_{anodic}}$$

$$\alpha_{c-pos}=0.46 \quad \alpha_{a-pos}=0.84 \quad \alpha_{c-neg}=0.52 \quad \alpha_{a-neg}=0.83$$

being R the universal gas constant: R = 8.314 472(15) $J K^{-1} mol^{-1}$, T the absolute temperature in Kelvin, F the Faraday constant F = 96490 C mol^{-1} and n the number of electrons involved in the reaction [Bau68, Par79 and Maz09].

III.2.5 Impedance characterization

The electrical characterization of the sample PSBD was made for frequencies from 10 mHz to 10 kHz at different coloration states achieved applying different DC bias voltage levels and scans of a small AC signal with amplitudes of 100 mV. A second sample fabricated as the sample PSBD, with a different optical behavior (Figure III.64), and called PSBD', was also analyzed, in order to compare the EEC parameters. Sample PSBD' showed different optical behavior than PSBD sample, since the potentials required for switching from bleached to dark states were lower than 2 V. The different optical behavior between the samples PSBD and PSBD' may be due to different thicknesses of the internal layer. The impedance analysis of samples PSBD', GSBD and GSVD were made for frequency ranges from 100 mHz to 10 kHz (10 mHz to 10 kHz for sample PSBD) at different coloration states achieved applying different DC bias voltage levels and scans of a small AC signal, with amplitudes of 100 mV for samples PSBD and PSBD', and 50 mV for samples GSBD and GSVD. The different amplitudes of the AC signals were chosen in order to decrease the noisy points of EIS experiments.

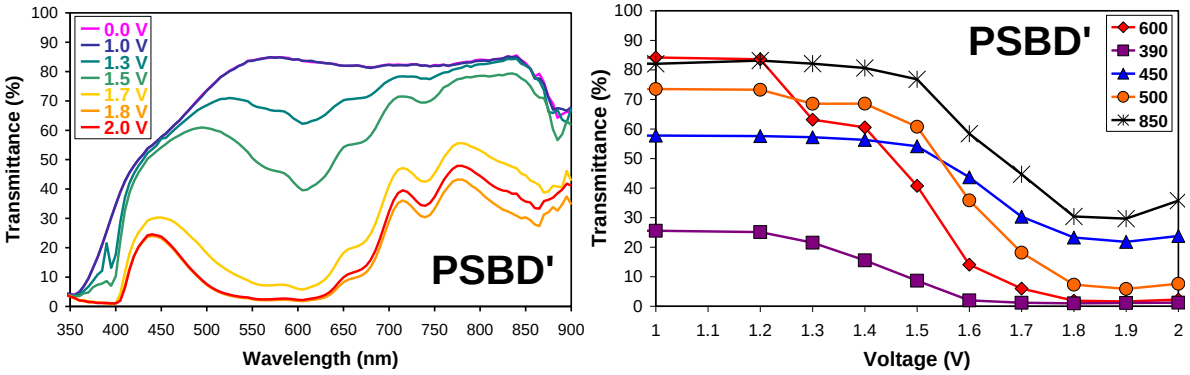

Figure III.64: Transmittance spectra (left) and voltage dependence at different wavelengths (right) from 0 to 2 V.

III.2.5.1 Bode and Nyquist Diagrams

Different DC bias voltage levels, in the up sense or coloring process, and in the down sense or bleaching process, were applied to the different samples analyzed, according to their optical transmittance behavior (Table III.7 and Figure III.65):

Sample	DC bias voltage ranges	steps
PSBD	0 to 3 V	0.25 V
PSBD'	0 to 2 V	0.1 V (0.2 from 0 to 1 V for no coloration)
GSBD	0 to 3 V	0.1 V
GSVD	0 to ±2.5 V	0.1 V (0.5 from 0 to 1 V for no coloration)

Table III.7: DC bias voltage ranges and steps applied to the viologen based ECDs.

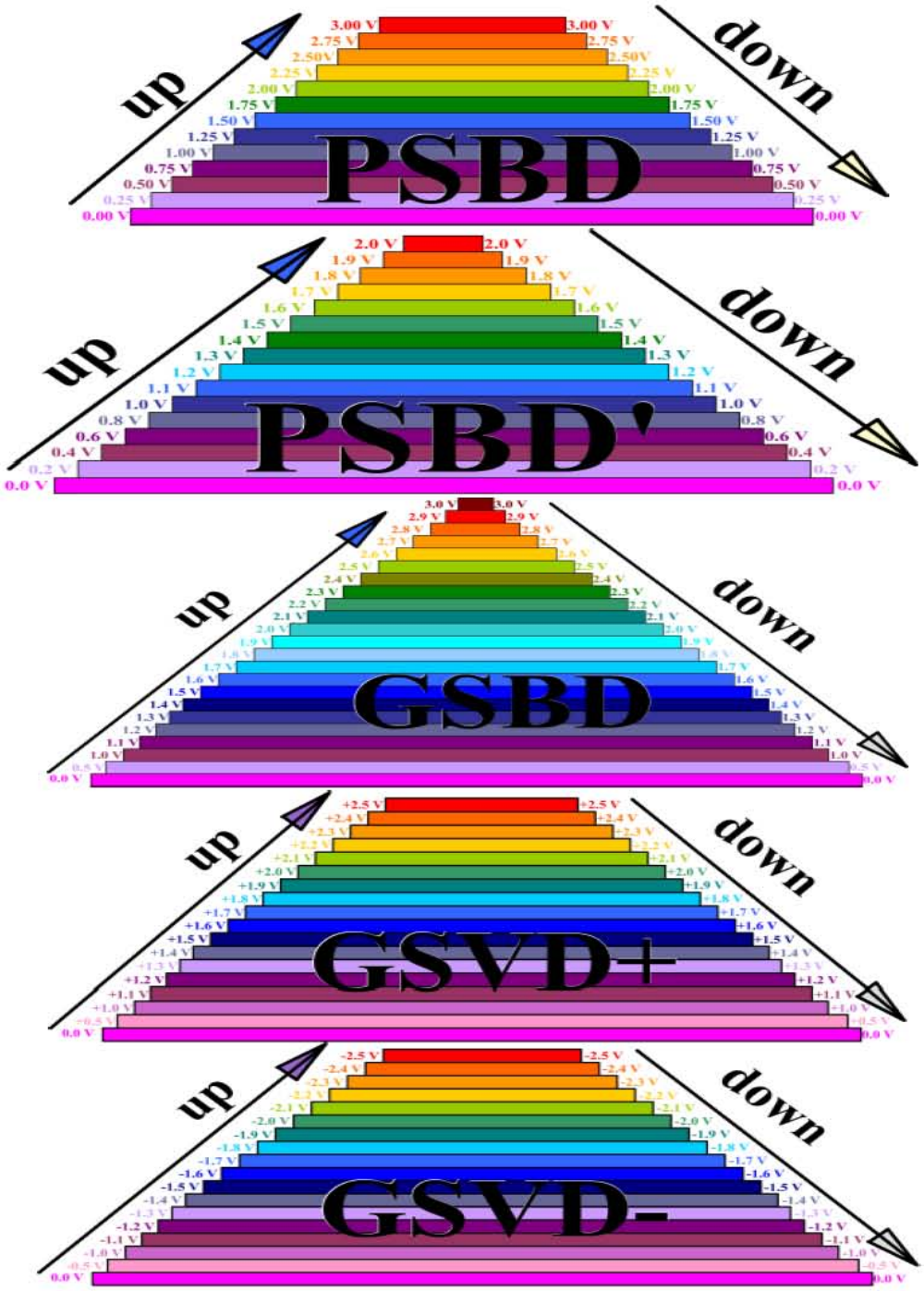

Figure III.65: DC bias voltage signals applied for impedance measurements to each sample.

Figure III.66 shows a 3D plot of the impedance Nyquist diagrams for sample PSBD'. Lowest frequencies lead to higher Z'' (imaginary part of the impedance). Different scales were used in the axis due to the large differences between the magnitudes obtained for the impedance of the samples at the different DC bias voltages applied. Nyquist plot curves are lower as the voltage increases. Impedance is different in the up and down senses, for coloration and for bleaching processes respectively. The hysteresis of impedance is related to the level of coloration acquired depending on if a DC bias voltage is applied from a colored or from a bleached initial state. The noticeable drop of the real and imaginary parts of impedances when increasing the DC bias voltage applied for sample PSBD' is the first eye-catching feature of Figure III.66 [Ver08b]. The first voltages (from 0 to 1 V) show this decay and a quasilinear shape, which stands for a mainly capacitive behavior at the lowest voltages, changing to a diffusion-like behavior. For voltages above 1 V the Figures show clearly two remarkable characteristics: the shape of the curves change, with a branch at low frequencies (on the right side of the curves), standing for a marked charge diffusion effect. At 1.7-1.8 V the decay tendency is broken. Thus, at this voltage the diffusion effect is greatly increased, or a recombination of the charges is produced. As in optical measurements of sample PSBD' (Figure III.64), these voltages seem to be the limit of the device suitable operation. The next efforts are made in order to interpret these data in terms of a model, expressed as an equivalent circuit [EBa05 and Dia11]. The previous experience in interpreting the impedance measurements on simple PEDOT devices [Ver08a] can be used here to derive some properties, regarding the simple structure of the device, in which two contacts sandwich an emulsion with the electrolyte and the EC materials embedded. Nyquist diagrams of Figure III.66 for sample PSBD' from 0 to 2 V in up sense are different from the obtained from 2 to 0 V in down sense. A higher value of impedance may be related to a lower coloration. Hence, at 1.4 and 1.5 V, the sample PSBD' is less colored in the up sense than in the down sense. At 1.6 V, however, the down sense is less colored than the up sense. Different shapes are also observed once the device is acquiring color. The diffusion effect at 1.7-1.8 V is clearly appreciated at low frequencies.

Figure III.67 shows the 3D Nyquist diagrams for the sample PSBD from 0 to 3 V. As it was observed for sample PSBD' at 1.7 and 1.8 V, diffusion effect is here observed but at different voltage range, from 2.25 to 2.50 V. The impedance behavior of sample PSBD is consistent with the peak potentials observed in CV experiments in Figure III.54, in the range between 2 and 2.5 V for the slower scan rates. The diffusion effect, recognized by the tail of the voltammogram at low frequencies, is observed to be higher at voltages related to the peak potentials observed in CV experiments in sample PSBD, for 100 mV/s scan rate. This scan rate is enough for the slow transmittance to reach approximately the fully colored and bleached states.

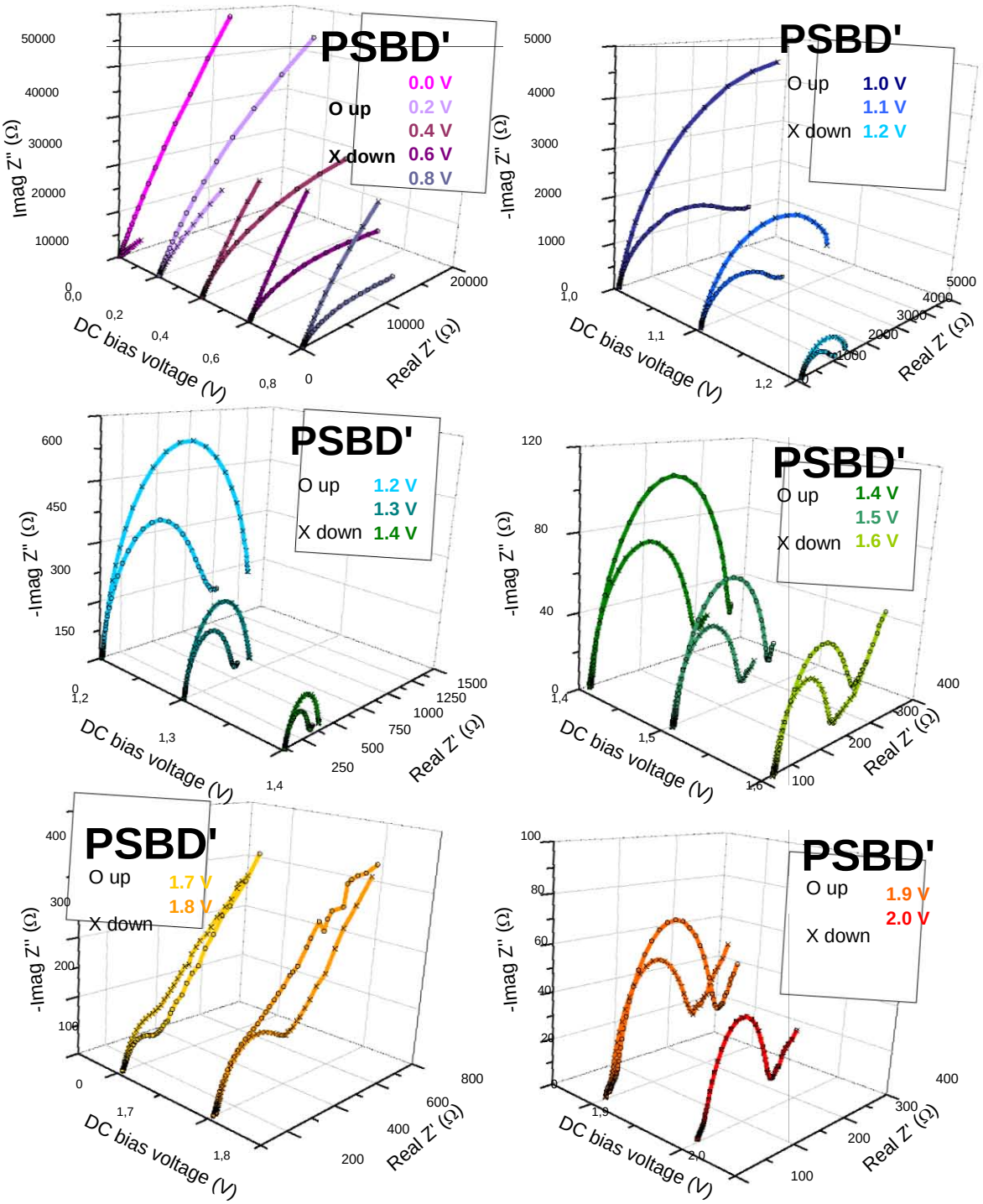

Figure III.66: 3D plot of Nyquist diagrams of sample PSBD' from 0 to 2 V in the up sense of coloration process, and from 2 to 0 V in the down sense or bleaching process.

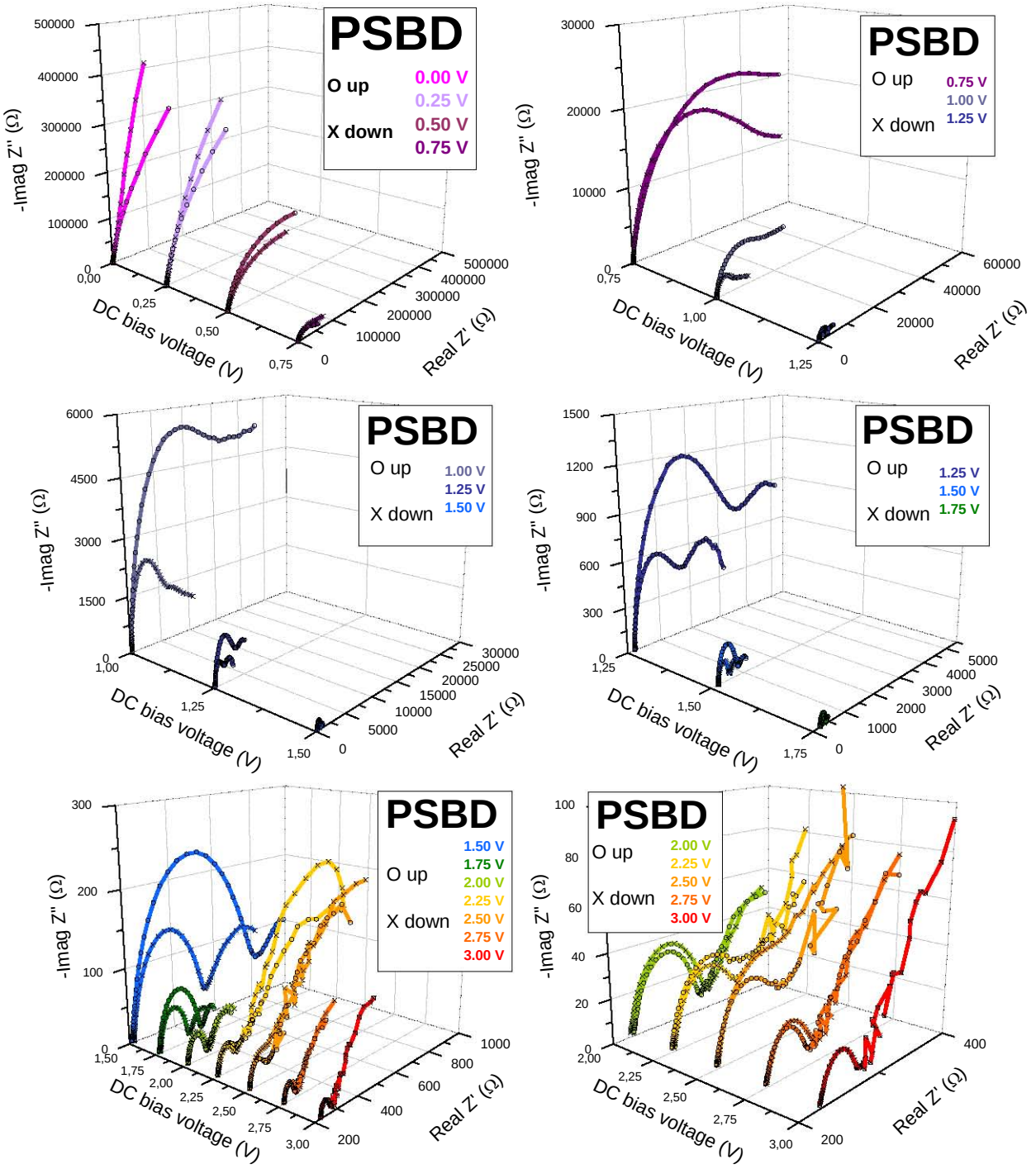

Figure III.67: 3D plot of Nyquist diagrams of sample PSBD from 0 to 3 V in the up sense of coloration process, and from 3 to 0 V in the down sense or bleaching process.

Figure III.68 shows the 3D Nyquist diagrams for the sample GSBD from 0 to 3 V. The diffusion effect here is observed at 1.8 and 1.9 V for the up sense of the DC bias voltage levels applied in the coloration process. Comparing the observed diffusion effect observed with EIS and CV experiments, the values of the peak potentials observed in Figure III.60 for the sample GSBD at 10 mV/s scan rate for positive and negative sweeps are around 2 and 2.1 V respectively. The DC bias voltage levels applied, in Figure III.65 for GSBD sample could be approximated to a triangular signal with a very slow scan rate (≈1 mV/s), since each step last for around 19 minutes (using Solartron 1260, when selecting 100 mHz as the lowest frequency). Considering a much lower scan rate for the CV experiment of GSBD sample, the peak potential should be moved to lower values from the observed around 2 V. Nyquist diagrams for bleaching process (or down sense) are, however, very different from the observed for coloration process (or up sense). As it was observed in Figure III.60, the transmittance recorded for the CV experiment resulted to show a bad reversibility for optical switching, since the sample was not able to reach completely the clear state again when decreasing applied voltage. Depending if an intermediate potential of coloration is applied from a bleacher state or from a darker state, the impedance measured of the device will be different, and hence the coloration achieved.

Figures III.69 and III.70 show the 3D Nyquist diagrams for the sample GSVD from 0 to +2.5 V and from 0 to -2.5 V with 0.1 V step respectively. The peak potentials observed in CV experiments for sample GSVD at the lower scan rate, of 40 mV/s (Figure III.62), are placed around 2 and 2.25 V for both positive and negative polarities of the current. However, it is from 1.9 to 2.0 V for positive polarities GSVD+ (in the up sense of the DC bias voltage levels, in the branch of coloration process) where the diffusion effect is observed in EIS experiments since the diffusion tail is highly relevant. The hysteresis observed in coloration of the device for the down sense or bleaching process is less than for the previous samples PSBD, PSBD' and GSVD, being appreciated as the diffusion effect appearing at 1.9 V. For the negative polarities, the diffusion effect is observed from 1.6 V DC bias applied. The long times of exposition to potentials of coloration levels could have affected the operation of the device during EIS experiments at negative polarities, which should have shown approximately the same Nyquist diagrams than for the positive polarities.

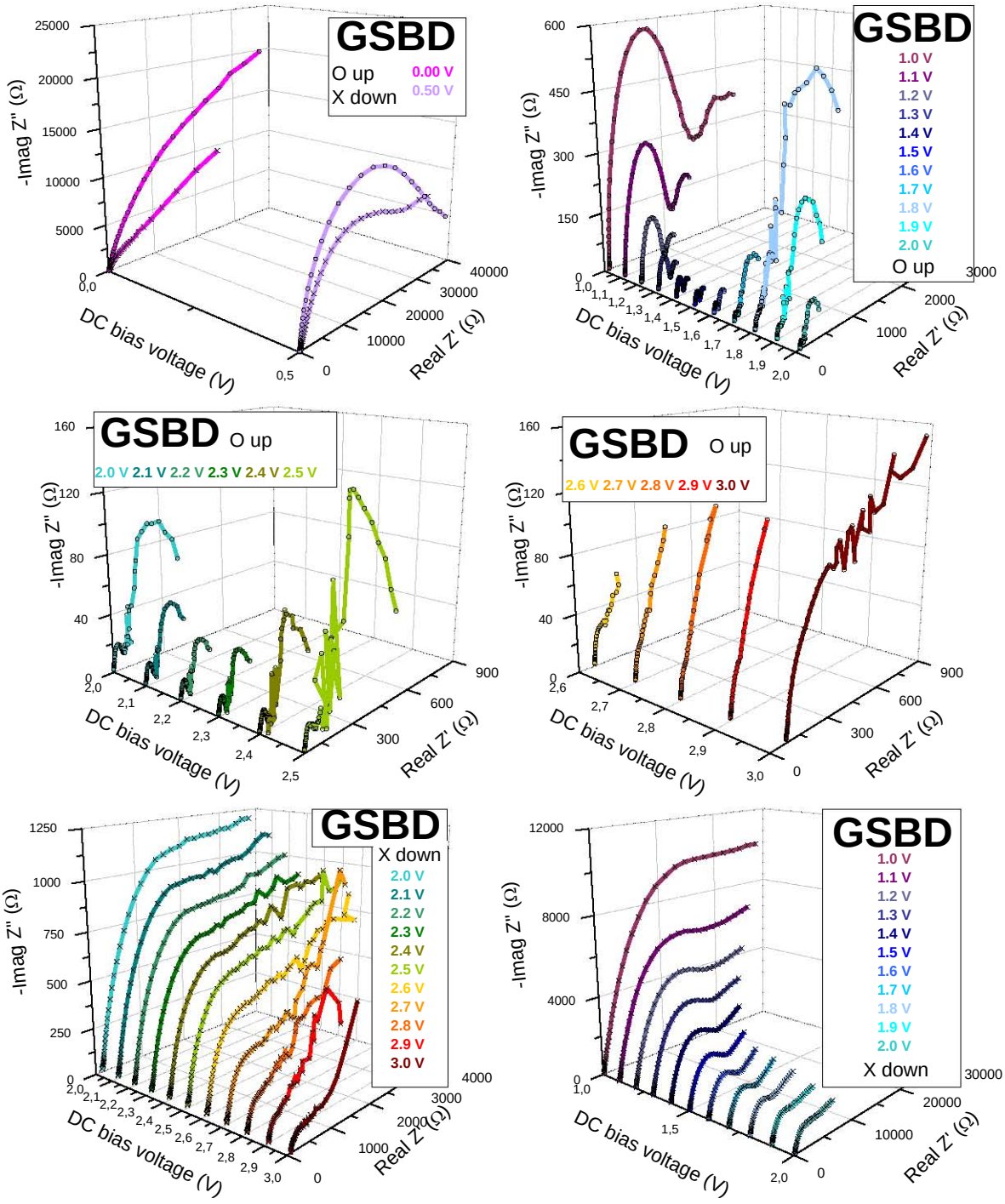

Figure III.68: 3D plot of Nyquist diagrams of sample GSBD from 0 to 3 V in the up sense of coloration process, and from 3 to 0 V in the down sense or bleaching process.

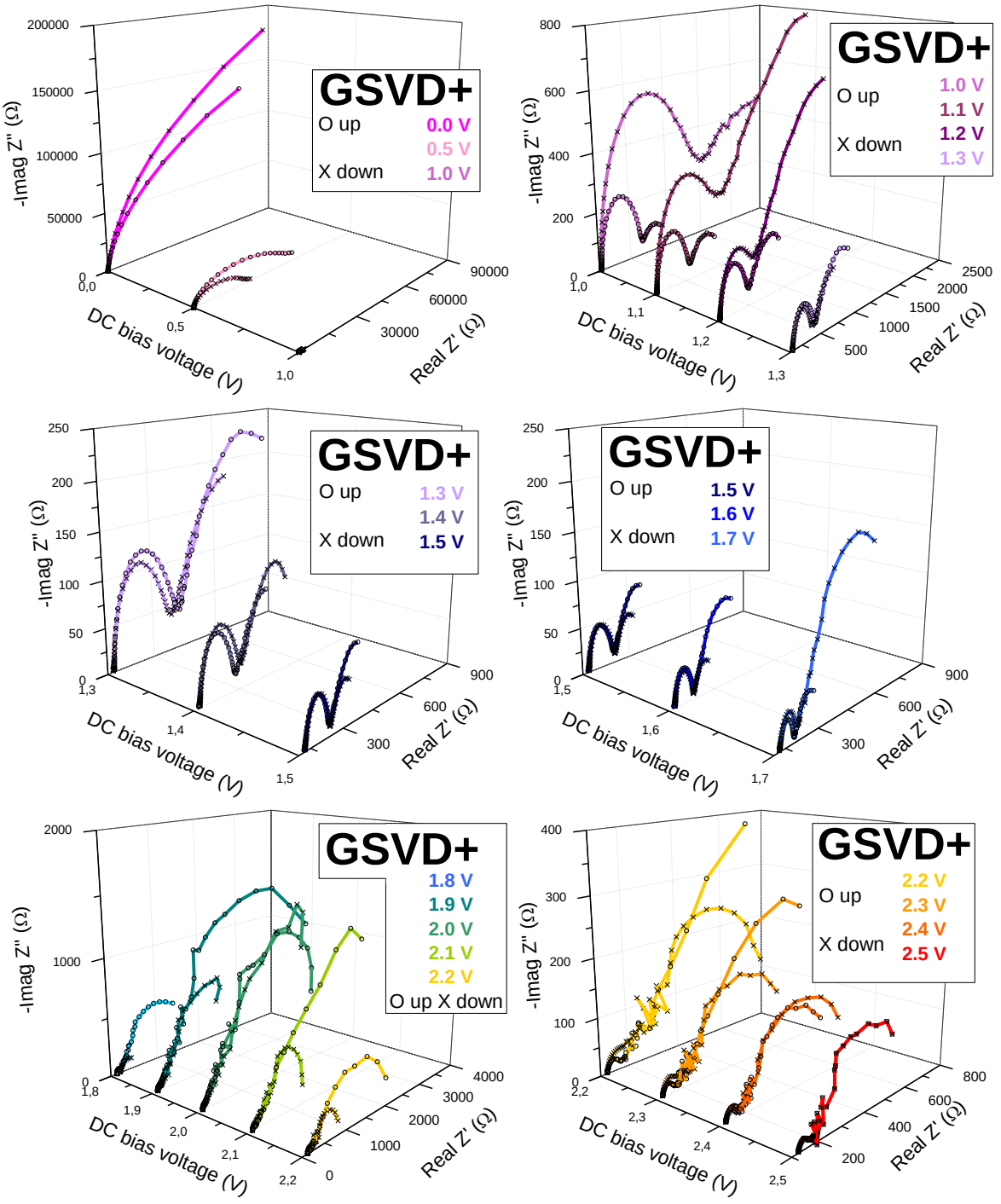

Figure III.69: 3D plot of Nyquist diagrams of sample GSVD from 0 to 2.5 V in the up sense of coloration process for positive polarities, and from 2.5 to 0 V in the down sense or bleaching process.

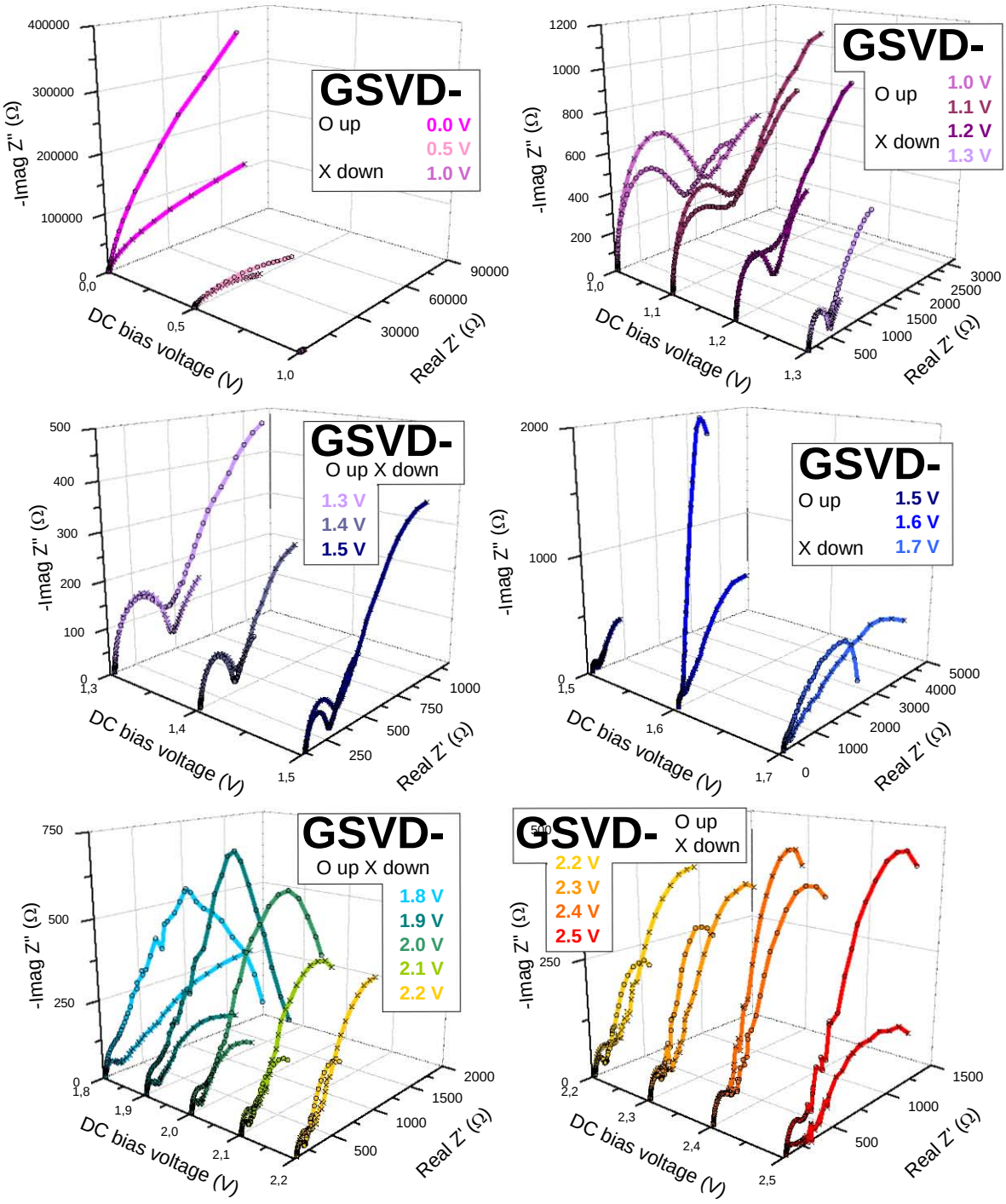

Figure III.70: 3D plot of Nyquist diagrams of sample GSVD from 0 to -2.5 V in the up sense of coloration process for negative polarities, and from -2.5 to 0 V in the down sense or bleaching process.

III.2.5.2 Equivalent electric circuit (EEC) model

As it was used for modeling the PEDOT based ECDs in previous sections, a Randles cell circuit describes the electric behavior of the viologen DC devices samples. It is too simple for devices in which the number of layers and their electrical dynamics are intricate. But it can be guessed at the present devices, paying attention to its simple construction and physical layout. Figure III.95-left shows the main configuration of the model, based on the 3rd EEC model for PEDOT devices of Figure III.37. Thus, a resistance Rs standing for the contacts and electrode impedance is followed by a shunt configuration with a resistance and a CPE. Resistance Rct is the one related with the charge transfer inside the device, so it stands for the resistance at low frequencies, in which capacitive effects are negligible, being CPE an open circuit. The capacitive-like behavior at high frequencies can be achieved with the double-layer CPEdl element, related to the physical layout of the two contacts and the emulsion. The use of a CPEdl element instead of a simple capacitor Cdl, used in the 1st EEC model for PEDOT ECDs (Figure III.25), is due to its frequency trend, more similar to the impedance measurements, and the dynamic behavior of the double layer formed. The shunt parallel CPEp and Rp of Figure III.30, standing for sealing problems and bubbles, has been removed in this EEC model, since the homogeneity problems are avoided due to the improvement in the devices manufacturing process for viologen ECDs samples. The Nyquist diagram of this parallel shunt was observed in Figure III.22 as a very small quasi semicircle appearing at the highest frequencies.

This circuit could be adequate for the lowest voltages, where a mainly capacitive behavior is obtained. But at higher voltages, the Nyquist plot changes its shape and shows the typical diffusion effects of Warburg impedance. Indeed, charges movement can be described as a diffusion process. To represent it, a finite length or short circuit Warburg impedance element Ws is adequate. Depending on the low frequencies behavior, two forms are possible: an open circuit terminus, Wo, if Z'' tends to infinite, or a short-circuit terminus, Ws, if Z'' tends to 0. As the measured impedance result is not clearly divergent at low frequencies, a Ws element is introduced in the EEC [Ver08a]. Since the lowest frequencies of impedance measurements of samples PSBD' and PSBD were 100 and 10 mHz respectively, and checking the behavior at low frequencies for the sample PSBD with decreasing tendencies in Figure III.67, it could be thought that the same decreasing tendencies should be observed for the sample PSBD' if 10 mHz instead of 100 mHz had been selected. The impedance shows two different behaviors at two voltage intervals below and above a threshold value V_{TH} where coloration of the ECD begins to be appreciable, as it was observed for optically characterization in previous sections. The values $V_{TH\text{-}PSBD}$=1.4 V, $V_{TH\text{-}GSBD}$=1.3 V and $V_{TH\text{-}GSVD}$=1.2 V refers to samples PSBD and GSVD respectively. For the sample PSBD', at 600 nm wavelength (absorption band of viologens), a value of $V_{TH\text{-}PSBD'}$=1.3 V is observed in Figure III.64-right.

Figure III.71: Proposed EEC model for PSBD, PSBD', GSBD and GSVD devices for voltage levels without (left) and with (right) coloration changes observed in the devices.

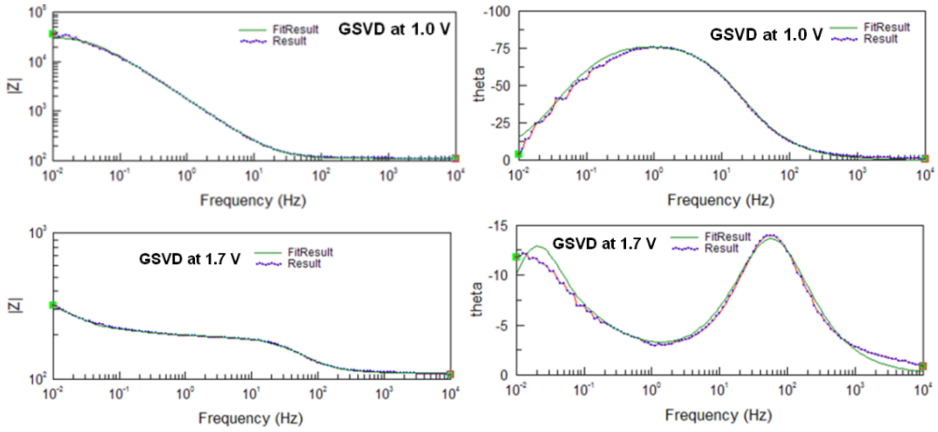

Figure III.72: Impedance magnitude and phase (dotted plots) and EEC fits (continuous lines) from Figure III.71 of sample GSVD for applied bias voltage of 1 V (up) and 1.7 (down).

Figure III.72 shows the magnitude and phase of the sample GSVD and the fitting at two different voltages under and above the threshold value V_{TH} for coloration changes [Ver09]. The fitting is shown as solid lines for magnitude and phase (FitResult). There is strong agreement between the measured data and the data obtained from the EEC models. The dotted line (Result) shown in Figure III.72-up is an experimental Bode plot of the impedance magnitude and phase when 1.0 V is applied to the device. The plot presented in Figure III.72-up, with its corresponding voltage, has been selected as representative of the low voltage input range from 0 to $V_{TH\text{-}GSVD}$. All other plots within this range show similar characteristics. Within this interval the magnitude of the impedance reaches 10^5 Ω at low frequencies and a peak is observed in the phase, which reaches -75 °. Beyond $V_{TH,}$ the magnitude of the impedance decreases to 10^3 Ω and the phase plots present lower angles showing two peaks, one of them at low frequencies, and the second close to 10^2 Hz, where this second peak is seen to decrease as the voltage increases. In Figure III.72-down the dotted line (Result) represents an experimental plot when 1.7 V is applied to the device. In Figure III.72 the solid line shows the fit (FitResult) using the parameters obtained at 1.7 V. It may also be seen that this fit is suitable to describe the features of the system at this input voltage level. Since this element is employed for voltages at and beyond $V_{TH\text{-}GSVD}$=1.2 V, the Warburg effect can be related with the radical cation molecules which move towards the electrodes. This is because it occurs at voltage levels where coloration of the device is produced, as it was observed in previous figures for optical and ChrA characterization of the sample GSVD for voltages greater than 1.2 V.

III.2.5.3 Relevant electric parameters

The next Figures will show the results of the least-squares fitting of the Nyquist plots to the electrical responses of the EEC model of the Figure III.95, leaving all the parameters free except W-P, which is fixed to 0.5, in order to not interfere with the non-capacitive effect of the CPEdl-P parameter. Goodness of fit value will be count by Chi-square (χ^2), the square of the standard deviation between the original data and the calculated spectrum, and the Weighted Sum of Squares, proportional to the average percentage error between the original data points and the calculated values, which is particularly useful when comparing the goodness of fit of two models to a single data set [zview].

III.2.5.3.1 Resistive parameters

The parameters with resistance characteristics are shown in Figure III.73. For samples PSBD' and GSVD, the parameter Rs (Figure III.73-left) hardly varies along the full voltage range being its value around 120 Ω. Contacts should not do it, but in this case, contrary to fluid cases or other device layouts [EBa05], the electrodes are included in the devices, and their resistance should not change during operation. Only a slight hysteresis is shown, a property that will appear in the rest of parameters and is due to the electrical inertia of the system. However, a difference of around 60 Ω with high hysteresis, between the up and down senses of the DC bias voltage levels applied, is observed for the sample GSBD. No explanation to this strange behavior, unless an unlikely electrode degradation, has been found. The evolution of Rct is more interesting, because it can be explained in terms of the redox process. Figure III.73-right is plotted in a logarithmic scale, for the sake of better perception of the evolution. Noticeably, the quick decreasing tendency in samples PSBD' and GSVD, from 1 MHz to 1 kHz, is not broken when switching the model to the above V_{TH} EEC model (Figure III.71), in which the resistance effects could be also immersed in Warburg impedance, which shows the consistency of the model. Clearly, the charge transfer dominates the process.

On the other hand, the huge decreasing is stopped at the voltages in which the optical contrast is seen, from 1.4 to 1.7 V for sample PSBD' (Figure III.73-up-right). At this point the tendency breaks. This result could be interpreted if we think in the charge transfer process: unlike other devices, here it is given mainly by redox hopping [Chi07]. There is no fast translation diffusion in a liquid substrate, but a charge transport into the molecules. This process reduces the impedance associated to charge transfer while the device is in operation. Both the parameters shown are obtained with errors under 1.6% in the whole voltage range in the fitting procedure. High values of Rct or a better fitting without this element, because its error is too high and its absence leads to the same set of the rest of the components, is the meaning of no plotting Rct at some potential levels. Fitting errors are <2% for almost all DC bias voltages applied, except for 1.8 V in the up

sense and 1.7 V in the down sense, reaching around 7%, where the semicircle shape is hardly observed (Figure III.66).

For sample GSBD, from 0 to 2.4 V, the decreasing of Rct is clear (Figure III.73-center-left). Fitting errors are <1% from 0 to 1.6 V, and <4% from 1.7 to 2.4 V, except for 1.8 V where a fitting error of 11.4% is obtained (being the semicircle shape hardly observed in Figure III.68). From 2.5 to 3 V Rct increases, and also the fitting errors, around 25%. This behavior could be explained if the potential applied to the device was close to the undesired second electron transfer reaction observed in viologens materials, from radical cation to neutral species, which appears uncolored. This interpretation could also explain why the Nyquist diagram of Figure III.68 was observed to have very different behavior between the up and down senses of the DC bias voltage levels applied, from 0 to 3 V and from 3 to 0 V respectively. Two redox reactions would occur at the down sense for bleaching process, the first one from neutral species to radical cation form and the second one from dicationic form to radical cation form.

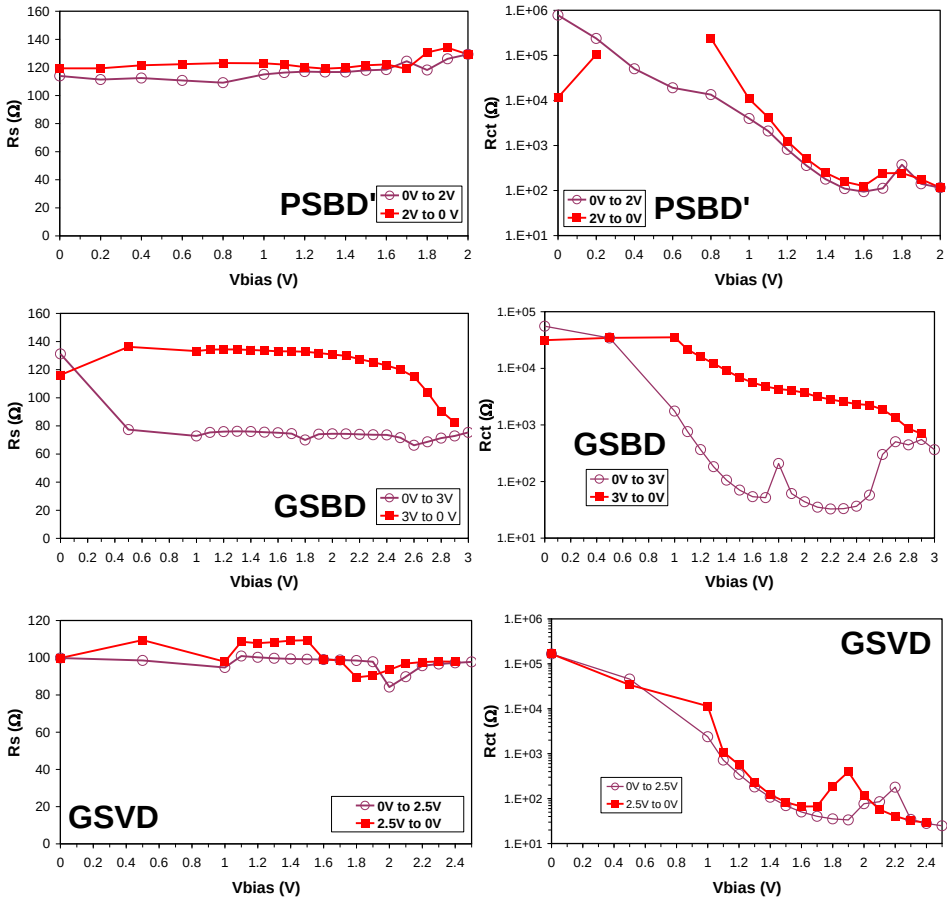

Figure III.73: Evolution of the contacts resistance R_s (left) and the charge transfer resistance R_{ct} (right) in Ω from the fittings of the EEC model of Figure III.95 for the voltage levels of samples PSBD' (up), GSBD (center) and GSVD (down).

For the sample GSVD, Rct decreases once the device starts getting color being the fitting errors <2% from 0 to 1.9 V DC bias voltages in the up sense (Figure III.73-right-down) The peaks observed at 2.2 and 1.9 V, for up and down senses respectively, are accompanied with an increment of the fitting errors, being close to 30% at 2.2 V and 10% for 1.9 V respectively. However, some noisy points are observed at some frequencies of the impedance measurements of Figure III.69. Fitting errors could be decreased by increasing the amplitude of the AC signal used for the EIS experiments carried out.

III.2.5.3.2 Capacitive parameters

Figure III.74 shows the evolution of the double layer CPE element for the samples. No change in the evolution is seen at the change of the EEC model again, from non coloration in the device to a coloration process including Warburg impedance.

For sample PSBD, tendency breaks again at 1.7 V, according to the optical results. The CPEdl-T time constant (Figure III.74-up-left) is lower for the devices during operation, because the movement of charges reduces the static characteristics of the device as a capacitor. The CPEdl-P exponent (Figure III.74-up-right) shows, on the other side, that the set is not so far from a value of 1 (for a pure capacitive structure), being its capacity around the hundreds of microfarad because of the values of CPEdl-T. The values plotted have fitting errors below 1.7% for the sample PSBD', except those near the operation range of the device, between 1.4 V and 2 V, with CPEdl-T reaching an 18.2% of fitting error and CPEdl-P a 3.5% of error at 1.7 V. All the same, the values are reasonably sufficient to consider the EEC model as validated under 1.1 V, because they are under the normal tolerances and errors of commercial circuit elements that will be used in display drivers [Ver08a]. Power consumptions could be computed properly using these values.

For the sample GSBD, in the increasing scan from 0 to 3 V (up), the CPE-P parameter (Figure III.74-center-right) shows a value close to 0.9 and CPE-T parameter (Figure III.74-center-left) indicates a hundred of microfarad, but the same peak than the observed for Rct element is observed at 1.8 V. Fitting errors of parameters CPEdl-T and CPEdl-P are higher in the range from 2.5 to 3 V, which was also observed for Rct, explained by the possible effect of the second successive redox reaction observed in viologens. From 1.7 to 2.5 V, CPEdl-T parameter shows also non negligible fitting errors.

For the sample GSVD, the CPEdl-P parameter (Figure III.74-down-right) shows a value close to 0.9 and a clear decay at 2 V for the increasing voltage scan (0 - 2.5 V) and 1.8 V for the decreasing scan (2.5 - 0 V). Thus, the exponent of CPEdl changes from a value which is close to that of a capacitor to that of a Warburg element. Fitting errors are

higher in the ranges of maximum coloration, in both up and down senses, which correspond to the noisy impedance points of measurements shown in Figure III.69.

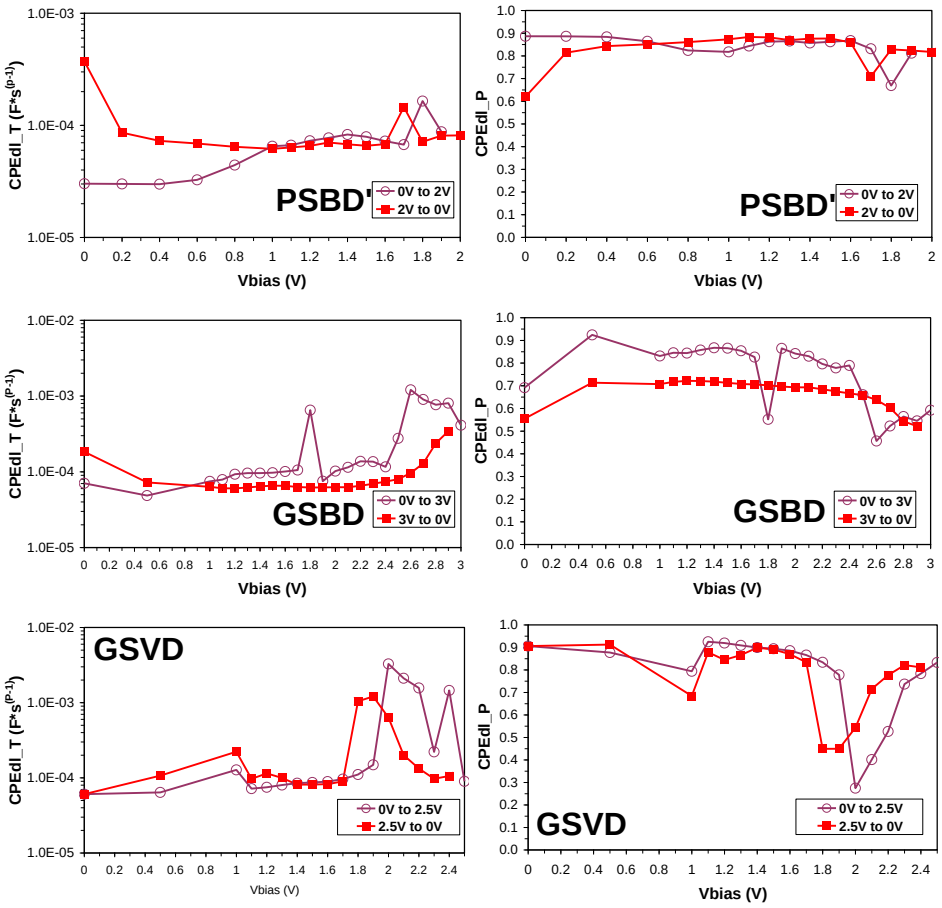

Figure III.74: Evolution of the double layer capacitive parameters CPEdl-T in F•s$^{(P-1)}$ (left) and CPEdl-P exponent (right) from the fittings of the EEC model of Figure III.95 for the voltage levels of samples PSBD (up), GSBD (center) and GSVD (down).

III.2.5.3.3 Diffusion Warburg parameters

The Warburg impedance represents the diffusion of charges: W-R is the electrical resistance opposing the charges, W-P is close to 0.5 for a finite element, and W-T is dependent on the effective diffusion thickness and the effective diffusion coefficients of the particles: a higher W-T represents higher charge diffusion paths. Equation III.6 describes this effect:

$$W-T=\frac{L^2}{D} \quad \text{(Eq. III.6)}$$

Here L is the effective diffusion thickness, and D the effective diffusion coefficient of the particle. The Warburg element describes the solution of the one-dimensional

equation for particle diffusion, and its "finite" characteristic means that charges are able to cross the complete device thickness during the experiment. To consider the equivalent circuit above V_{TH}, we must analyze Warburg impedance results shown at Figure III.75.

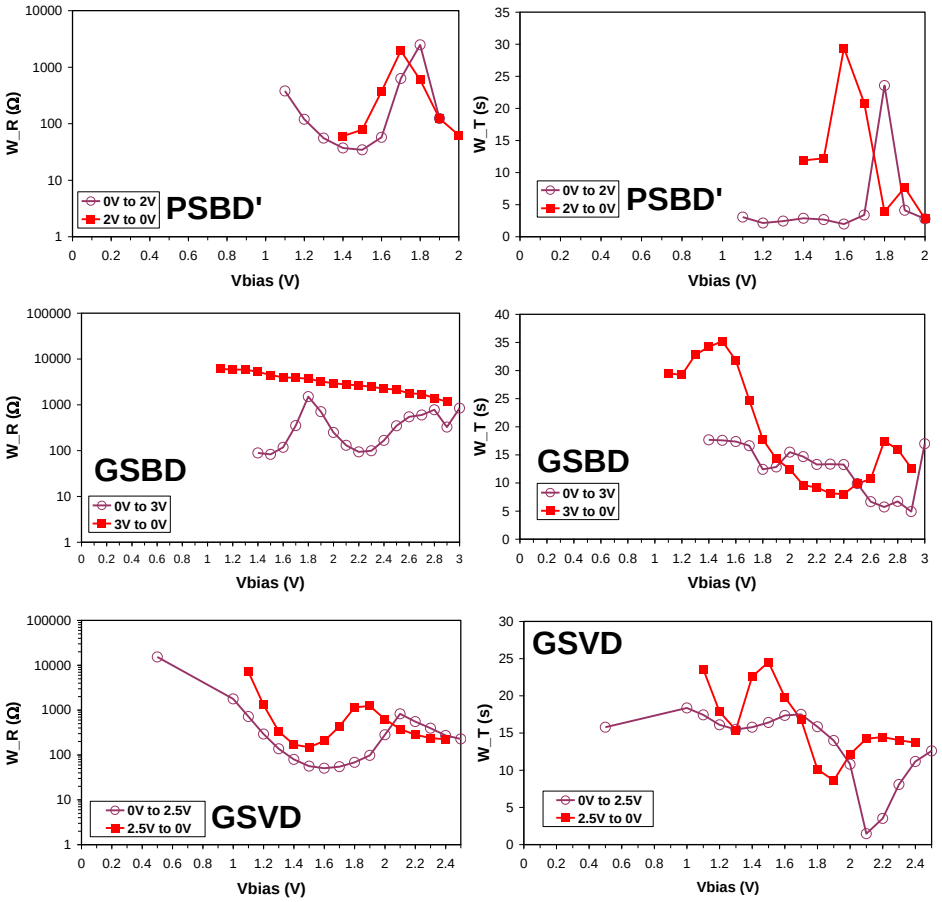

Figure III.75: Evolution of the Warburg impedance free parameters W-R in Ω (left) and W-T in seconds (right) from the fittings of the EEC model of Figure III.95 for the voltage levels of samples PSBD (up), GSBD (center) and GSVD (down).

Figure III.75-up-left shows the Warburg resistance W-R for the sample PSBD' that is decreasing at operation voltages, increasing suddenly at the limiting voltage of 1.7 V obtained at optical measurements. A similar behavior is shown at Figure III.75-up-right for the W-T time constant. Resistance values of the charge diffusion process are paired with the charge transfer one. It is again a result of the limited diffusion process involved in the device, because the charge movement is mainly limited to a redox hopping process. In these parameters, the errors are higher, reaching 9.7% for W-R and 19.2% for W-T at 1.1 V, and decreasing to 3.6% and 6.7% at 1.7 V, respectively. Again there is a gap at 1.8 V, with errors above 100%. A possible explanation for this discrepancy in the fittings at the potential could be related to the substitution of the finite Warburg

impedance element with an infinite Warburg impedance element. I.e., the diffusion length does not reach the internal layer thickness of the device for a determined applied potential. Checking in Figure III.66 at 1.7 and 1.8 V for sample PSBD' it can be observed that the tendency at low frequencies is not clearly decreasing to zero, proper of the Ws. Nevertheless, these errors allow at least the use of the values for Spice simulations to derive power consumption and circuit optimization analysis, which is out of the scope of this work.

For the sample GSBD, in the up sense of DC bias voltage applied, from 0 to 3 V, the parameter W-R (Figure III.75-center-left) shows the peak at 1.8 V also observed in the double layer capacitive and charge transfer resistance plots. Errors of fittings are <5% for voltages lower than 2.5 in the up sense, increasing for the range from 2.5 to 3 V in both, W-R and W-T parameters (Figure III.75-center) reaching at 2.9 V the maximum errors, of around 20 and 30% respectively. Differences between the up and down senses are observed since, for the down sense at the range from 1.5 to 1 V, fitting errors increases for parameters W-T and W-R, this may be due to the short impedance diffusion tails observed in Figure III.68 for this DC bias voltage range. The second redox reaction of viologens could result in a production of neutral species which could modify the EEC model proposed.

For the sample GSVD, the parameters W-R (Figure III.75-down-left) and W-T (Figure III.75-down-right) shows a peak at 2.1 V for the increasing voltage scan (0 - 2.5 V) or up sense, and at 1.9 V for the decreasing scan (2.5 - 0 V) or down sense. However, for the range from 2 to 2.2 V in the up sense, fitting errors for both parameters are >10%, with a maximum error at 2.1 V (46.3% for W-T and 27.5 for W-R). In the down sense, fitting errors are <5% except for 1.9 and 1.8 V (8.1% and 5.3% for W-T and 6.4% and 5.9% for W-R). Noisy impedance points observed in measurements of Figure III.66 for GSVD with positive DC bias voltage levels may be the causes for the highest errors.

III.2.5.3.4 Chi-Square and Weighted Sum of Squares

Considering the fitting results for the impedance measurements of samples PSBD', GSBD and GSVD, and the EEC model proposed, the errors of fittings could help to give a physical interpretation about what is really happening on the devices when they are carried to optical switching, with color changes caused by different electrical potential levels applied. As the redox reaction is induced in the devices, a double layer quasi-capacitive effect is formed between the electrode and the electrolyte (which is the EC mixture) in solution. Since the viologen based ECDs are soluble type I, remaining in the solution during usage, the charge is being transferred between the EC mixture in a dicationic form, releasing an electron once reaching by diffusion the electrode, and diffusing away, in a radical cation form, again into the electrolyte.

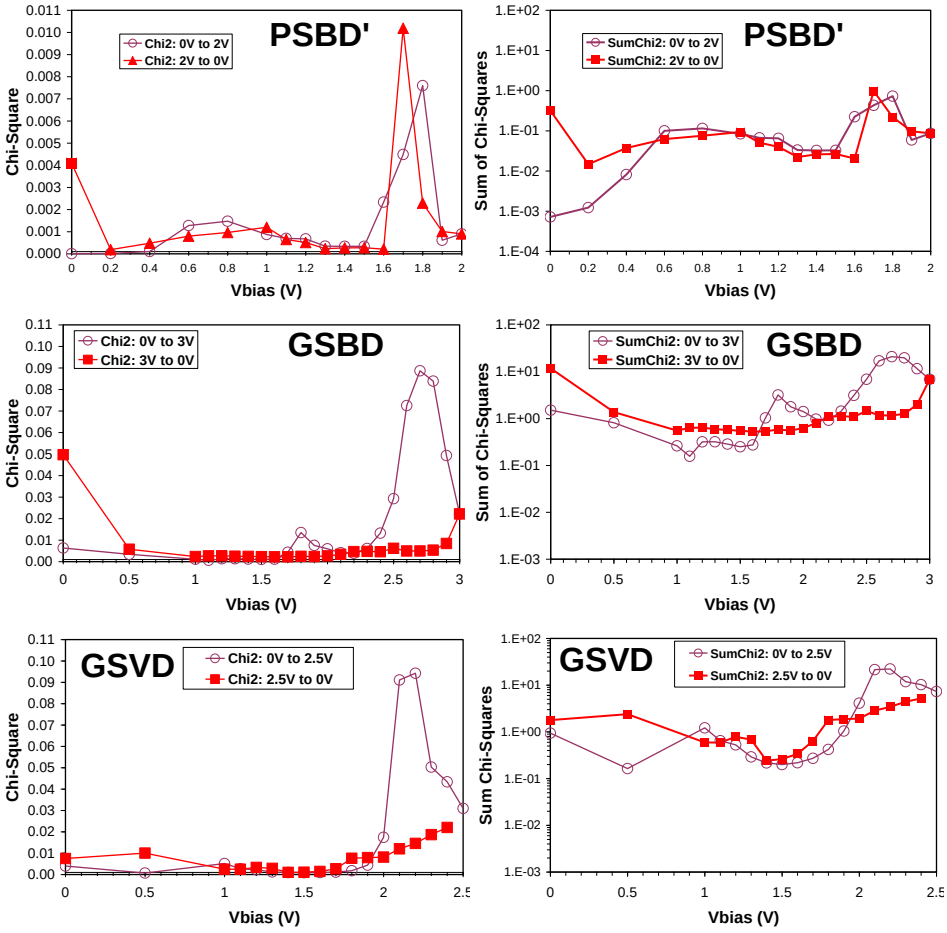

Figure III.76: Evolution of the goodness of the fittings. (left) Chi Square (χ^2). (right)Weighted Sum of Squares of the EEC model of Figure III.95 for the voltage levels of samples PSBD (up), GSBD (center) and GSVD (down).

When the diffusion length is higher than the internal layer thickness of the device, as it is the case of the proposed EEC model for viologens (Figure III.71), the fitting of the parameters should be good, with low values of the square of the standard deviation or Chi-Square parameter and the average percentage error or Sum of Chi-Square parameter (Figure III.76). However, a diffusion length shorter than the internal layer thickness, as it could be the case of the sample PSBD' for 1.7 and 1.8 V (Figure III.76-up), the goodness of the fitting is worse. If the potential applied is higher than the needed for the first electron transfer redox reaction of viologens, a second redox reaction, undesired from the point of view of reversible coloration changes, could result into the increase of the neutral viologen molecules population, as it could be the case of the sample GSBD at the potential range from 2.5 to 3 V in the up sense, where the values of Chi^2 and Sum of Chi^2 are higher (Figure III.76-center). The sample GSVD from 2 to 2.5 V in the up sense

shows highest values for Chi^2 and Sum of Chi^2, which could be due to the use of the infinite instead of the finite Warburg impedance element (Ws instead of Wo). Some noisy points could have been observed for the EIS experiments, appearing at low frequencies in some cases, especially if a low value of AC is selected in the measurements. For the sample GSVD a value of 50 mV was used, being possible that a value of 100 mV could have resulted in a decrement of the fitting errors (Figure III.76-down).

Summarizing, from the errors obtained in the fitting EEC model proposed it can be concluded that for the sample PSBD' it behaves like a Randles cell up to 1.8 V, voltage in which no optical enhancement contrast is achieved. The diffusion effects appear while the coloration in the device is observed. For the sample GSBD a DC bias voltage level up to 2.5 V could have resulted in better fittings since no neutral species should be present. For sample GSVD the model does not accommodate at high input voltage values, as in this case the diffusion lengths are shorter and the EEC model may derive to Warburg infinite elements, as most of the charges cannot cross the complete device. However, another explanation for such effect is the one previously seen for PEDOT devices, as the change of the Wo by a CPEdiff element at the 3rd and 4th proposed EEC models in Figures III.30 and II.35. Slower diffusion of charges at the DC bias voltage levels matching with the potential peaks observed in CV experiments lead to impedance Nyquist plots where the tendency of the low frequencies Warburg diffusion tail is not clearly divergent. Also, a continuous electrical current observed in ChrA experiments should indicate a resistive behavior of the ECD once coloration is stabilized in the device, leading to the use of short-circuit Ws, instead of an open-circuit Wo Warburg impedance. Parameter W-R, in series with Rct and Rs would form the resistive circuit, as it will be seen in the next section. Nevertheless, simulation of EEC models for higher voltages is not strictly required; it has been observed from experimental results (see Figure III.40-down and Figure III.47-right) that this voltage interval is not of major interest for the coloration process.

III.3 Dependence on thickness of new viologen ECDs

The thickness of the internal layer of new glass supported viologen based ECDs is a parameter that can be modified for achieving the best performance of the ECDs, according to the parameters used in the evaluation criteria such as transmittance contrast, response times, optical density, injected charge density, coloration efficiency, write-erase efficiency or effective charge density.

III.3.1 Introduction

Several viologen ECDs with different thicknesses on glass substrates were constructed, using a mixture of 4,4'-bipyridine and 1-bromoethane. The thickness of each device was fixed using a thermoplastic spacer. The devices were electrochemically tested with optical and impedance analysis. The range of the transmittance change is highly dependent on thickness. Optical measurements, ChrA, ChrC, CV and EIS were the techniques used for characterization. Coloration properties such as switching times for coloring and bleaching processes, coloration efficiency and effective charge density, previously studied for samples PSBD, GSBD and GSVD with a unique thickness, are now obtained for several samples with different thicknesses of a single device type. Dependence on thickness in the response times and in voltage dependent parameters of the EEC model, such as Warburg diffusion, double layer capacitance or charge transfer resistance, obtained with EIS, are related with the coloration properties and their dependence on the thickness obtained by the above mentioned ChrA and CV characterization. The electrical behavior of the material and the physical and chemical characteristics are derived from the proposed EEC model. A simple Randles circuit including a Warburg diffusion impedance element, a charge transfer resistance and a double layer capacitive CPE is proposed for the fittings process. Variations on thickness of internal layer of devices lead to use a short or an open circuit Warburg element. A threshold potential, from which the device is colored, indicates the charge diffusion effects.

Figure III.77: Viologen based ECD of 230 µm thickness and 3 x 2 cm^2 effective area in the bleached (left) and colored (right) states for 0 and 2.5 V respectively.

III.3.2 Experimental

III.3.2.1 Materials

4,4'-Bipyridine (98%) and 1-bromoethane (98%) were purchased by Aldrich and used without further purification. Hydroquinone (99.5%) was obtained from Riedel-de-Haën and 1-butyl-3-methylimidazolium tetrafluoroborate (99%) was obtained from Solvionic. Extra pure solvents (N,N-dimethylformamide, ethyl acetate and propylene carbonate) were supplied by Scharlau. Surlyn® 1702 (thickness 50 μm) was purchased by DuPontTM. Amosil 4H and Amosil 4R were obtained from Solaronix. ITO-coated glass slides (glass thickness: 1.1 mm; ITO thickness: 100 nm; R = 30-50 Ω/□) were a gift from Solems.

III.3.2.2 Methods

The fabrication of the devices was done by CIDETEC by synthesizing the EC mixture and following a process for the devices construction.

III.3.2.2.1 Synthesis of 1,1'-diethyl-4,4'-bipyridilium dibromide

The synthesis was carried out according to the procedure reported in [Bru77] with some slight modifications. A mixture of 4,4'-bipyridine (1g, 0.0064 mol) and 1-bromoethane (2.8 g, 0.0256 mol) in 10 mL of DMF was refluxed while stirring for 3 hours. The precipitate was filtered off and the crude product was washed with hot ethyl acetate several times, to yield a yellow solid (2.3 g, 95% yield).
1H NMR (DMSO-d6, 500 MHz): δ = 9.48 (d, 4H, bipyridine, J = 6.5 Hz), 8.85 (d, 4H, bipyridine, J = 6.5 Hz), 4.77 (m, 4H, N-CH2), 1.60 (t, 6H, CH3, J = 7.3 Hz).

III.3.2.2.2 Preparation of the EC mixture and devices construction

1,1'-diethyl-4,4'-bipyridilium dibromide (0.01g, 0.027 mmol), hydroquinone (0.003 g, 0.027 mmol), 1-butyl-3-methylimidazolium tetrafluoroborate (1.6 g) and propylene carbonate (2 g) were mixed for 1 hour at room temperature.

ITO coated glass slides (3 x 2 cm^2) were washed subsequently with water, acetone and isopropanol and dried with nitrogen stream. ITO/glass cells were prepared by joining two slides through a thermoplastic spacer (Surlyn ® 1702) placed along the whole perimeter, but with an opening (1 mm wide) in one corner. The spacer becomes sticky after heating at 130 ºC for a few minutes. In order to prepare devices of different thicknesses different number of Surlyn layers (from 1 to 5) were applied. Thicknesses of 50, 100, 150, 200 and 250 μm should thus have been obtained. However, according to the measurements made with a micrometer, the real final thicknesses were 50, 90, 130, 180 and 230 μm. The cell was evacuated in a vacuum chamber. Then it was dipped in the EC mixture and filled by the opening introducing Argon into the vacuum chamber.

Once filled with the EC mixture, the edges of the cell were sealed with a mixture of Amosil 4H (45% wt) and Amosil 4R (55% wt), being allowed to cure at room temperature overnight.

III.3.2.2.3 Characterization setup

Spectral optical transmittance of these ECDs was measured using an Ocean Optics USB2000+ spectrometer in the 400 to 800 nm range. EIS was the tool used with the different ECDs for electrical characterization. Bode impedance magnitude and phase plots as well as Nyquist or Cole-Cole plots were obtained by means of the impedance gain – phase analyzer Solartron 1260 with frequency sweeps from 0.01 Hz to 1 MHz of 100 mV amplitude AC signals and different DC bias voltages. The obtained impedance results were used for fitting to an electrical equivalent circuit (EEC) model by the least squares method (Levenberg-Marquardt).

III.3.3 Results

III.3.3.1 Optical measurements

Figure III.78-left shows a 3D plot of the $T_{spectral}$ dependence with the thickness of the internal layer of the ECDs. The thicker the internal layer, the higher number of color centers formed, and hence the darker the colored state. Bleached state with 0 V is highly transparent, with values of T close to 78% at 600 nm. No variation of T is observed until a threshold DC bias voltage value of 1.5 V is reached (1.25 V for 230 μm), appearing a blue coloration due to an absorption band at wavelengths near the red interval of the optical spectrum. Figure III.78-right shows the thickness dependence of the ChrT600nm measured while applying a square voltage signal from V1 to 0 V with 120 seconds of period and varying V1 from 1.25 to 2.5 V with 0.25 V steps. The voltage level for maximum coloration is observed to be 2.50 V for the thinner devices (from 60 to 130 μm). No appreciable changes in the transmittance are observed applying potentials higher of 2.25 and 2.00 V to the thicker devices of 180 and 230 μm thicknesses respectively.

III.3.3.2 Electrochemical measurements from ChrA and ChrC experiments

Figure III.79 shows the current density J (mA/cm^2) and charge density Q (mC/cm^2) measured from ChrA & ChrC experiments for the different potential signals observed in Figure III.78-right for the simultaneous $ChrT_{600nm}$. Current and charge densities plots show two different behaviors, from 0 to 30 seconds and from 30 to 60 seconds, related to coloration and bleaching processes respectively. A peak of current is observed to increase with the thickness and the potential level applied in the coloration process (Figure III.79-left). After several seconds, related with the coloring times, the current is stabilized to a constant value which is required for the ECD coloration maintenance.

When 0 V is applied, needed for the bleaching process (at t=60 s), a negative peak of current is observed in the devices, which is stabilized to zero after several seconds, related to the bleaching time. This negative current is due to the release of the electrons of the radical cation (colored state) to the dicationic (bleached state) of viologen forms.

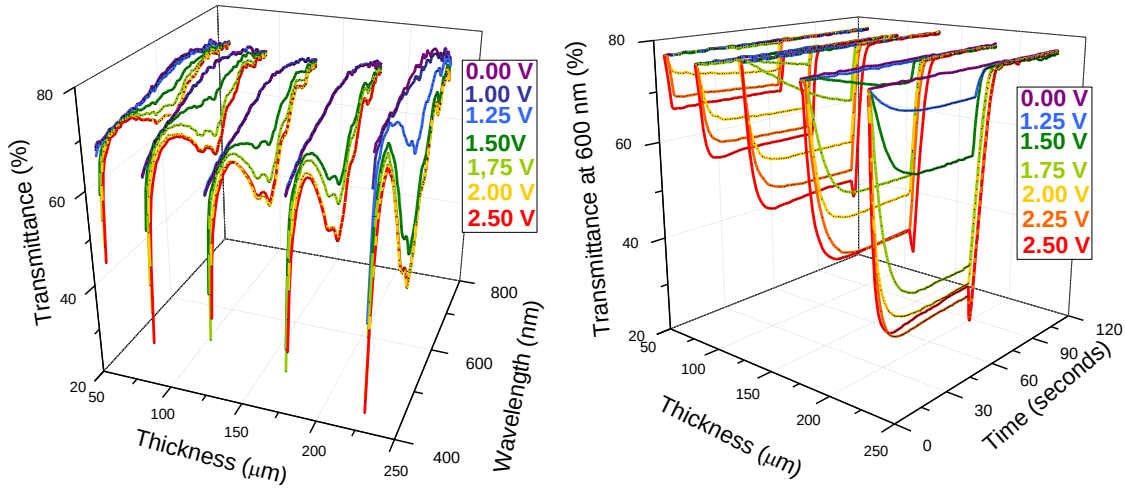

Figure III.78: Thickness dependence spectral $T_{spectra}$(%) (left) and time domain $ChrT_{600nm}$(%) (right) transmittances.

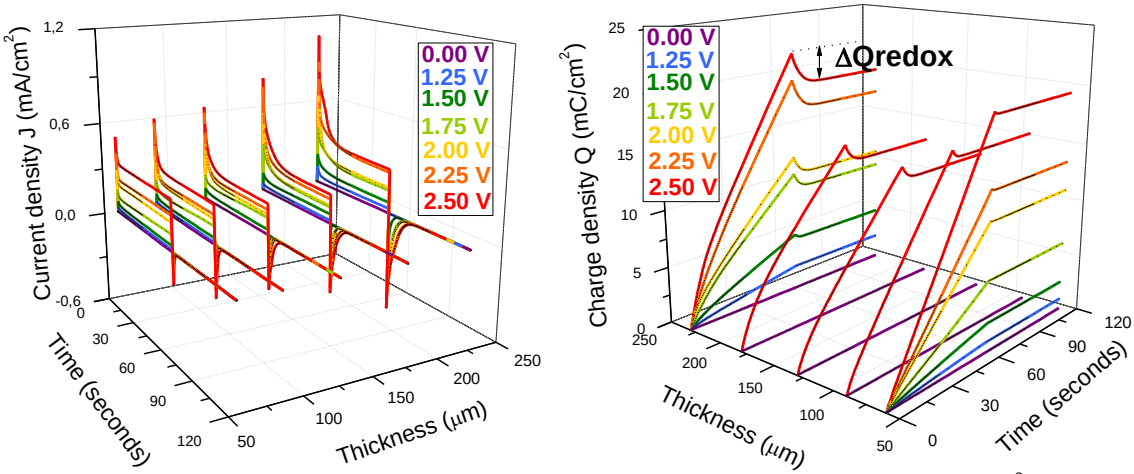

Figure III.79: Thickness dependence current (left) and charge (right) densities J (mA/cm^2) and Q (mC/cm^2) results derived from ChrA and ChrC experiments.

Time integral of a constant current density signal is a ramp charge density signal, which slope increases with the potential level (Figure III.79-right). Short-circuiting the contacts of the ECDs (at t=60 s) causes a negative current density and a decrement of the charge density. The effective charge density, parameter referred as ΔQredox, is calculated as the difference of the charge density between the dark and the bleached states in the

bleaching process [Ver09], as it was seen in section III.2.4.2. Related with the amount of color centers (as it will be detailed in the discussion section), ΔQredox increases with the coloration, which depends on the thickness and on the potential. For a clear visualization of Figure III.79-right, only 0.00 and 2.50 V cases are plotted for 180, 130 and 90 μm thicknesses.

III.3.3.3 Electrochemical measurements from CV experiments

Figure III.80 shows the current density J (mA/cm^2) and the optical cyclic transmittance at 600 nm (CT_{600nm}) thickness dependence. The results are obtained from the 3rd cycle of CV experiments at 25 mV/s scan rate from -2.5 V to +2.5 V. A symmetrical redox reaction (Figure III.80-left) is observed due to the symmetry of construction of the solution type I viologen based ECDs. As it will be detailed in the discussion next section, the area of the voltammogram is related with the coloration contrast observed in the devices (Figure III.80-right).

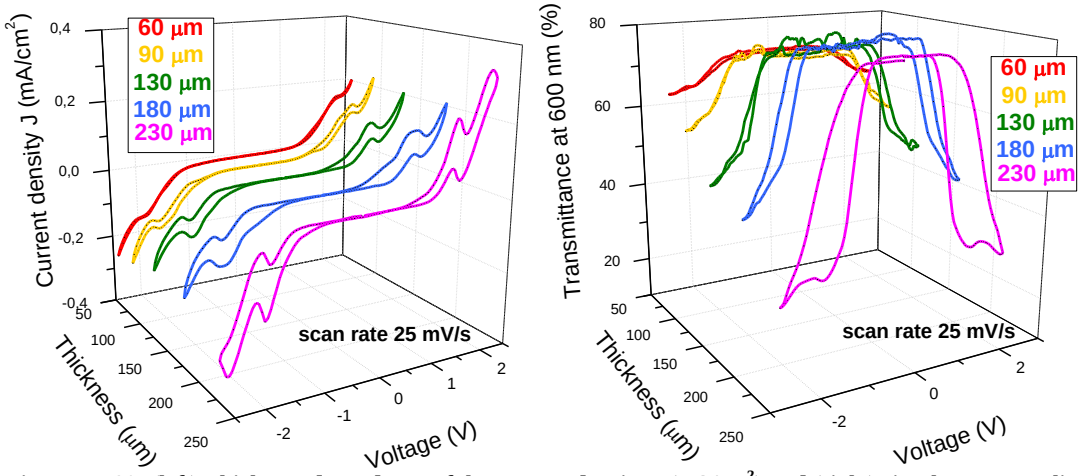

Figure III.80: (left) Thickness dependence of the current density J (mA/cm^2) and (right) simultaneous cyclic transmittance at 600 nm CT_{600nm}(%) from the 3rd cycle of CV experiments at 25 mV/s scan rate.

Slight differences in the voltammograms of the thicker devices were observed at around ±0.5 V for faster scan rates. In particular, these effects were observed for the device of 230 μm at 50 mV/s scan rate (Figure III.81) and for the devices of 180 and 230 μm at 100 mV/s scan rate (Figure III.82). The rate of the reaction seems to be slower as the thickness increases, being not fast enough for the 230 μm thickness device at 100 mV/s scan rate since CT_{600nm} does not completely recover the bleached state.

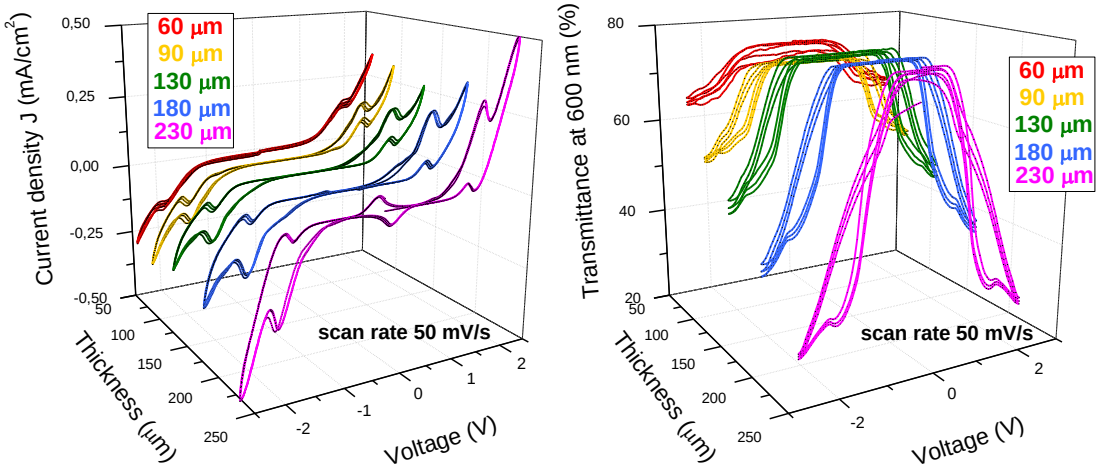

Figure III.81: (left) Current density J (mA/cm^2) and (right) simultaneous cyclic transmittance at 600 nm CT_{600nm}(%) from 3 cycles of CV experiments at 50 mV/s scan rate.

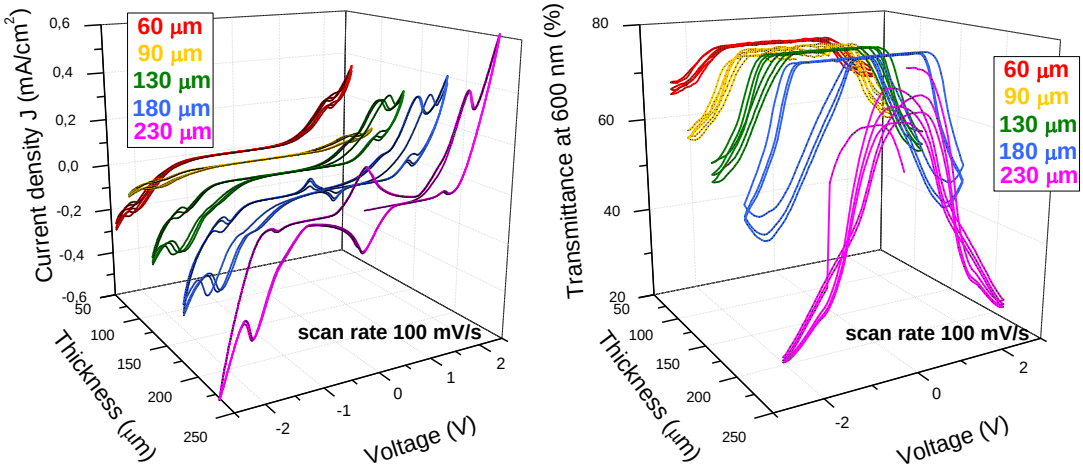

Figure III.82: (left) Current density J (mA/cm^2) and (right) simultaneous cyclic transmittance at 600 nm CT_{600nm}(%) for 3 cycles of CV experiments at 100 mV/s scan rate.

III.3.3.4 Electrochemical measurements from EIS experiments

Figure III.83 shows the Nyquist diagrams of the impedance measurement of the five devices at the different DC bias voltage levels from 0 to 2.5 V with 0.25 V steps. Logarithmic scales were used for plots of imaginary versus real parts for a complete visualization due to the big differences of magnitudes between the bleached and the colored states of the devices. Impedance decrement behavior is observed for the five devices in the coloration process. Linear scale, instead of logarithmic scale, will be used at the discussion section for the Nyquist diagrams visualization, useful for deriving the EEC model at the relevant DC bias voltage levels applied.

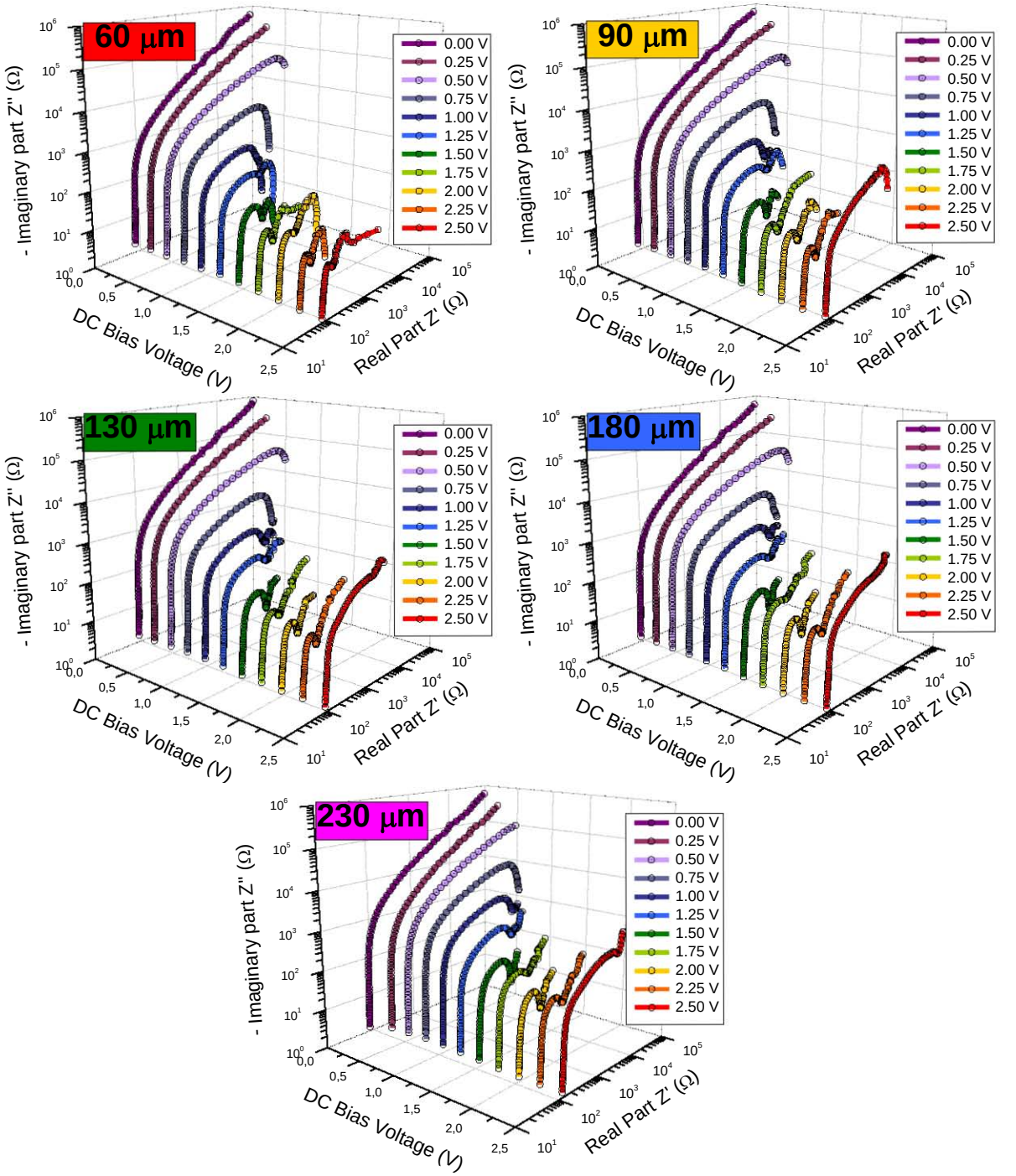

Figure III.83: Nyquist impedance diagrams for different coloration levels and thicknesses of devices.

III.3.4 Discussion

III.3.4.1 Optical measurements

Figure III.84-left shows the transmittance contrast at 600 nm (ΔT_{600nm}) dependence with the thickness at 2.5 V DC bias voltage levels applied. Defined as the difference between the maximum and the minimum optical transmission, for the bleached and darken states respectively, ΔT_{600nm} depends clearly on the thickness of the devices. The background color, calculated from the spectral transmittance applying the CIE Yxy chromaticity and luminance coordinates and the XYZ to sRGB color space conversion matrix, simulates the color appearance in the different devices. The thickness dependence of the response times, calculated from 10 to 90% of the final value, is shown in Figure III.84-right. At 2.5 V, coloring times t_c are approximately equal to bleaching times t_b for the thinner devices (being t_c=4,9, and 15 and t_{tc}=5, 9 and 16 seconds for 60, 90 and 130 µm respectively). Slight differences are observed for the thicker devices of 180 and 230 µm thicknesses.

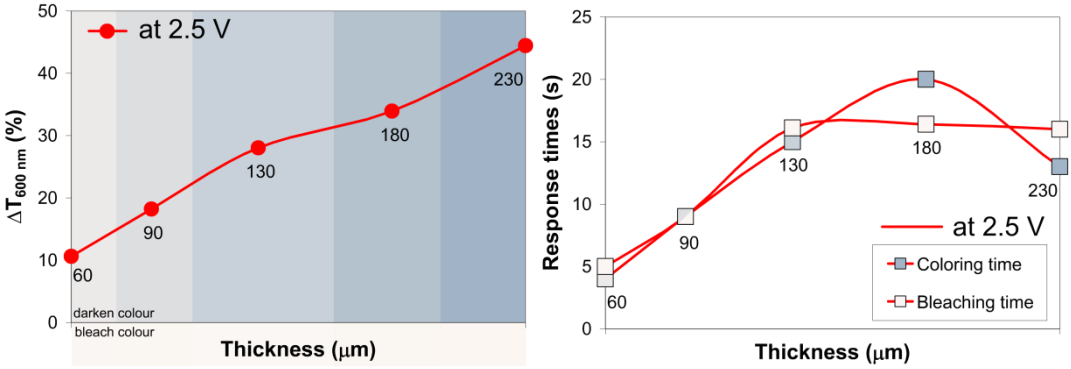

Figure III.84: Thickness dependences: (left) Transmittance contrast at 600 nm (ΔT_{600nm}) and simulated background color. (right) Response times (coloring and bleaching).

III.3.4.2 Electrochemical measurements from ChrA and ChrC experiments

Figure III.85-left shows the current and charge measurements obtained with ChrA and ChrC experiments when applying 2.5 V (from 0 to 60 seconds) and 0 V (from 60 to 120 seconds) to the 230 µm thickness device. For 2.5 V applied, a peak of current is observed at the first 30 seconds which is stabilized to a constant value. Then, a negative peak current appears when short-circuiting the device, resulting in a decrease of the charge from t=60 to t=90 seconds. This decrement, divided by the effective area, is the effective charge density ΔQ_{redox} used in the reduction from viologen bleached dicationic form to viologen colored radical cation form [Ver09]. Figure III.85-right shows a 3D plot relating the applied potential levels, ΔQ_{redox} and $ChrT_{600nm}$ at t=30 s for the colored state of the different thickness devices. Increasing over 2.25 V (2.00 for 230 mm) resulted into no appreciable coloration change in the devices.

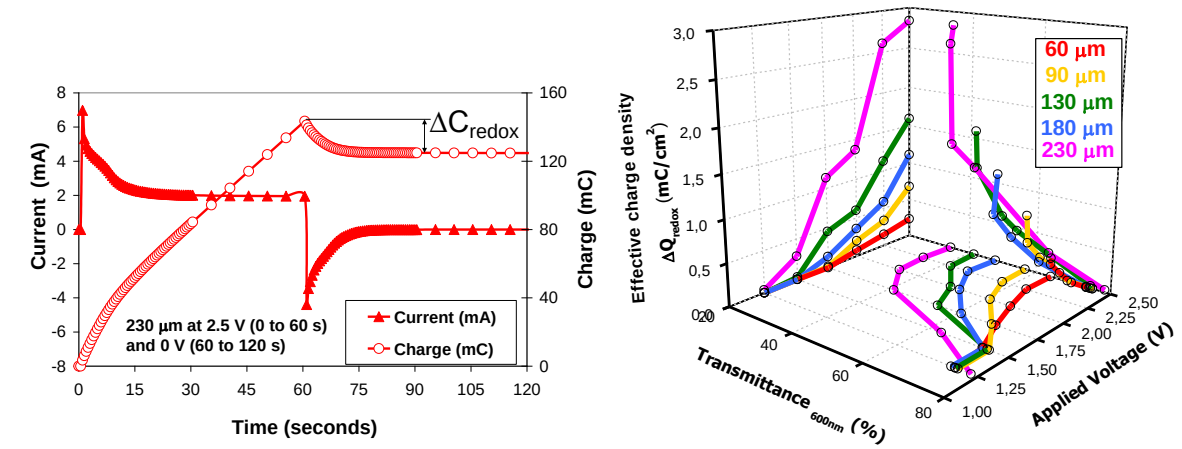

Figure III.85: (left) Current and charge measurements of ChrA & ChrC experiments at 2.50 V for the 230 µm thickness device. (right)Thickness dependence effective charge density variation ΔQ_{redox} and optical transmittance of coloration state for applied voltages from 1.00 to 2.50 V. Only projections over the walls are plotted for a better visualization.

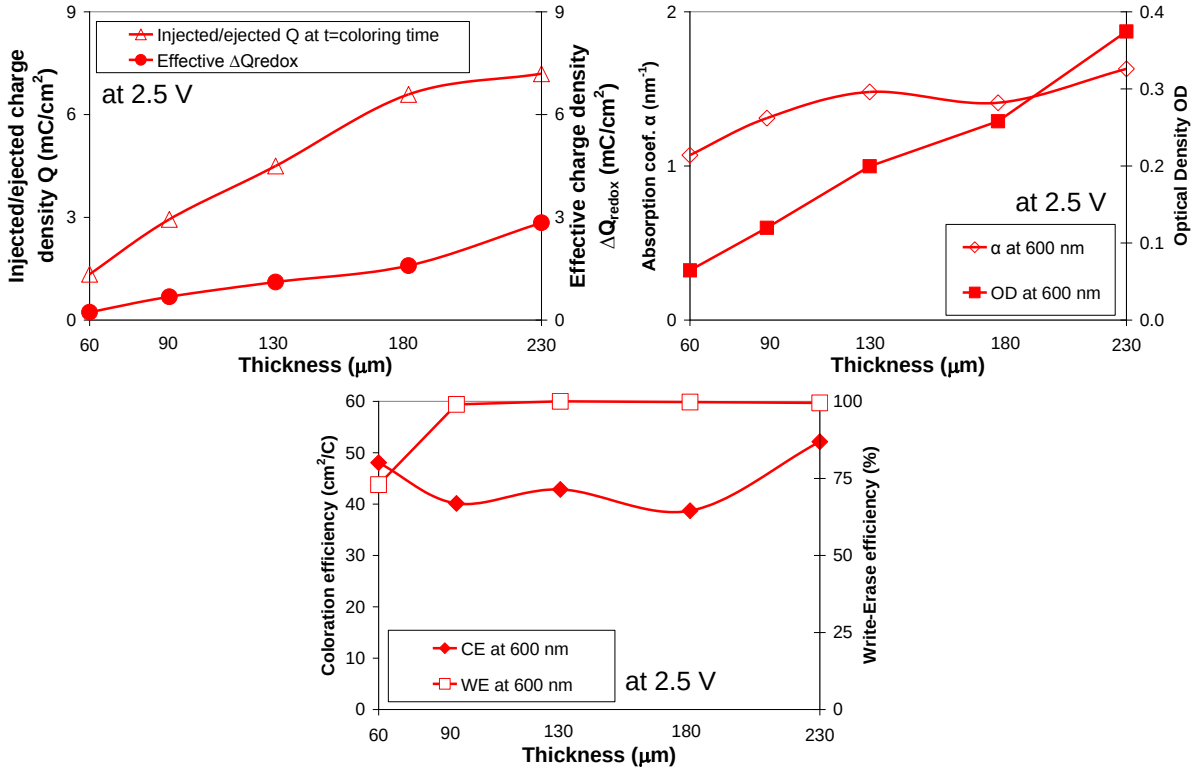

Figure III.86: Thickness dependences: (left) Injected/ejected and effective charge densities. (right) Absorption coefficient and optical density. (down) Coloration and Write-Erase efficiencies (CE and WE).

Figure III.86-left shows a relation between the injected/ejected Q and the effective ΔQ_{redox} charge densities of the different devices. Only a part of the injected/ejected charge Q is used to reduce the viologen molecules. Figure III.86-right shows similar absorption coefficients at 2.50 V for 130 and 230 μm thickness devices with different optical densities. The write-erase efficiency (WE) is defined as the fraction of the originally formed coloration that may be subsequently electrobleached. Figure III.86-down shows the thickness dependence of the CE and the WE parameters at 2.5 V applied. A maximum of 52 cm^2/C of CE is observed for the 230 μm thickness device. A CE value of 136.6 cm^2/C was obtained on other thicker viologen ECDs developed following similar manufacturing process [Poz09]. WE is around 100% at 2.5 V in the case of the four thicker devices, being 72% in the case of 60 μm. However, a maximum value of 2.25 V is observed for a $WE_{60\mu m}$ around 100% (Figure III.78-right).

III.3.4.3 Electrochemical measurements from CV experiments

The 3rd cycle of CV experiments at 25 mV/s scan rate of Figure III.80-left show a shift in the cathodic peak potentials V_{pc} from 1.74 to 2.09 V when decreasing the thickness of the device from 230 to 60 μm (Figure III.87-left). The charge capacity of the CV experiments, calculated as the area containing each voltammogram divided by the scan rate, is related to the coloration observed in the devices. The transmittance contrast at 600 nm for CV experiments ($\Delta T_{CV\text{-}600nm}$) is calculated from the simultaneous T_{600nm} thickness dependence of Figure III.80-right-down. Figure III.87-right shows that, for the devices characterized in this work, the thicker the device, the higher the $\Delta T_{CV\text{-}600nm}$, which is related to the charge capacity parameter. It is expected that thicker devices than 230 μm should show an increment of $\Delta T_{CV\text{-}600nm}$ until a maximum value corresponding to an optimum thickness. Higher thicknesses over the optimum value would result into a decrement of $\Delta T_{CV\text{-}600nm}$, for a higher absorption.

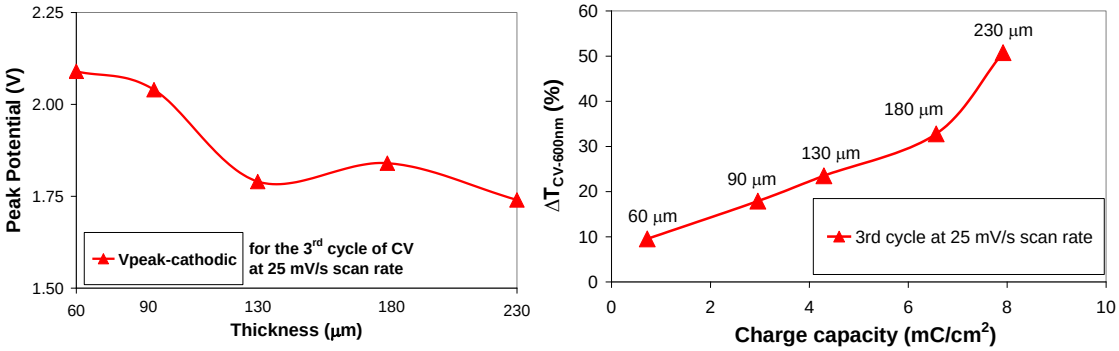

Figure III.87: (left) Thickness dependence cathodic peak potentials for positive polarity. (right) Transmittance contrast at 600 nm versus charge capacity.

III.3.4.4 Electrochemical measurements from EIS experiments

Figure III.88 shows the Bode magnitude (up-left) and phase (up-right) and the Nyquist diagrams of the impedance dependence with thickness of the internal layer of the ECDs in bleached (down-left) and darken (down-right) optical states with 0 and 1.75 V DC bias applied respectively.

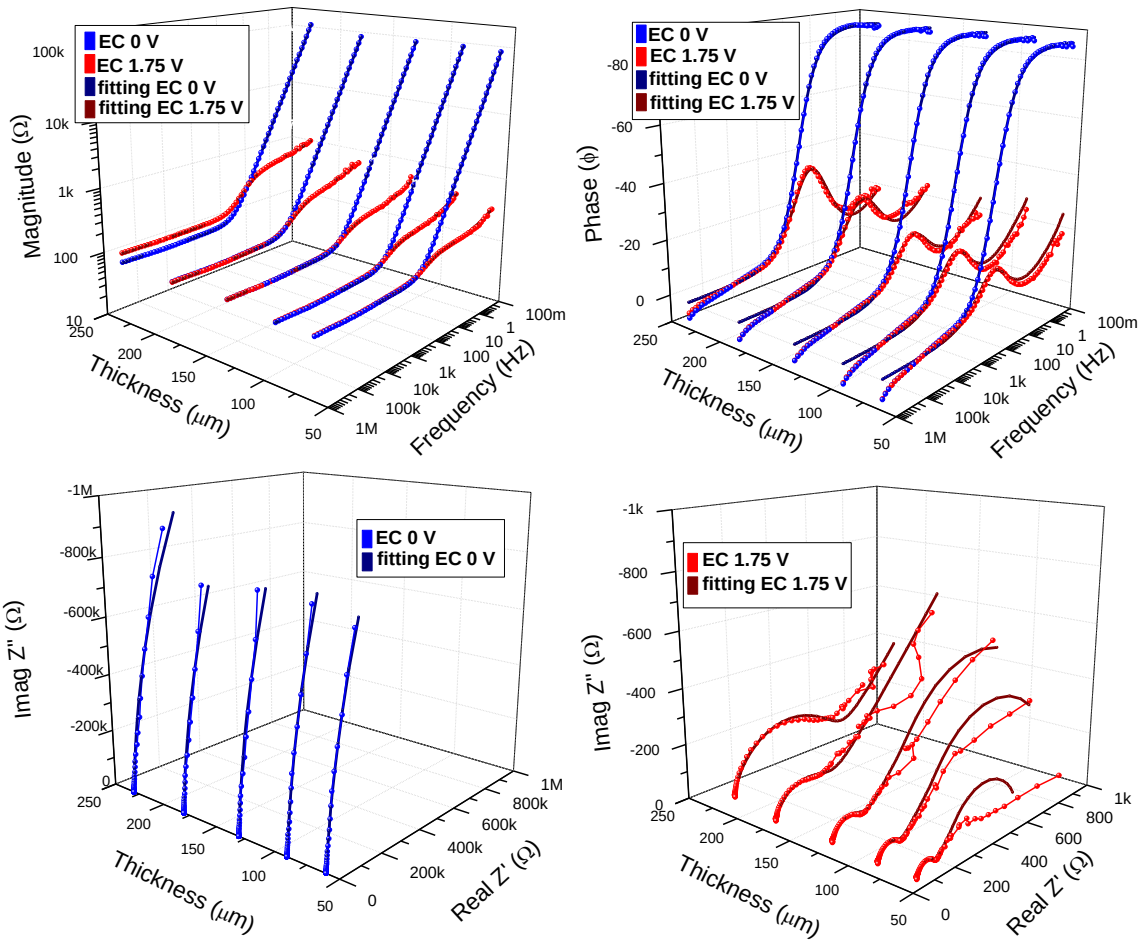

Figure III.88: Bode magnitude (up-left) and phase (up-right) and Nyquist impedance thickness dependence at 0 V for bleached state (down-left) and at 1.75 V for colored state (down-right).

The main differences of magnitude (in logarithmic scale) and phase, between bleached and darken states, take place at frequencies under 1 kHz (Figure III.88-up). The bleached state at 0 V shows a capacitive behavior with phase near 90 degrees and a logarithmic decrement of the magnitude, from around 1 MΩ to around 1 kΩ for a frequency change from 0.1 to 1 Hz. Hence, the behavior of the bleached state of the devices is very similar to a capacitor, with slight differences between the magnitude and phase impedance

results for the different thicknesses. On the other hand, the darken state at 1.75 V shows a decrement of both magnitude and phase with respect to the bleached state. Magnitude increases with thickness. Phase is independent of thickness at frequencies higher than 1 kHz, appearing at mean frequencies a peak increasing with the thickness. Hence, the electrical properties of the darken state depend on the thickness. A resistive behavior with phase near 0 degrees and almost constant impedance logarithmic magnitude value of around 100 Ω is observed at frequencies over 1 kHz for both optical states.

Nyquist diagrams are shown in Figure III.88-down. Linear scales up to 1 MΩ is used for visualizing the bleached state and up to around 1 kΩ for the darken state. Nyquist diagrams of the devices at the bleached state with 0 V seems the one of a capacitor while at the darken state with 1.75 V shows a semicircle at high frequencies and a line at low frequencies. The diameter of the semicircle increases with the thickness, an effect hardly observed in the plots with logarithmic scales of Figure III.83. Impedance plots at 1.75 V were fitted to the EEC model shown in Figure III.89 [Bar11a, Bar11b, Bar11c and Bar12a]. This EEC model was proposed in other works with viologen [Ver08b, Ver09 and MMa07] and also inorganic WO_3 (EC layer) and V_2O_5 (counter electrode) ECDs [PBa91]. Wo was substituted by a Ws for the thinner ECDs because the effective diffusion length of the charges seems to be higher than the active layer thickness of the ECD.

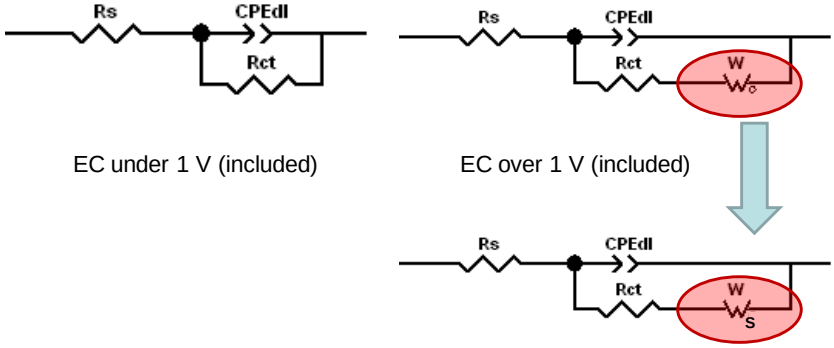

Figure III.89: EEC model for ECDs under (left) and over (right) a threshold value of 1 V DC bias voltage. Wo must be replaced by Ws for thinner devices (right-down).

The fittings to this EEC model are plotted together with the measurements in Figure III.88 with higher deviation at lower frequencies of darken state, where the diffusion process takes place. A χ^2 value under 0.02 was obtained for fittings, being under 0.01 at 60 μm thickness and higher at 230 μm. The fittings errors for parameters were under 10% except for Rct at low voltages and thicknesses (where Rct is around MΩ) and for Warburg impedance parameters at higher thicknesses. Hence, Wo instead of Ws was used for 180 and 230 μm thicknesses in order to decrease the fitting errors from over 200% to around 20%, improving χ^2 in an order of magnitude. Low frequency Z" behavior at Nyquist plot of Figure III.88-right tending to increase or to zero is explained by using Wo or Ws, as it was seen in Figure III.22.

Figure III.90 shows the retrieved parameters and their dependence with voltage and thickness. Values of Rs around 80 Ω (120 Ω for 230 μm) are constant with voltage as expected. Values of Rct have an exponential decay from 0 to 1.5 V, stabilizing at values between 100 and 700 Ω for the optically detected as redox voltage (1.75 V), where anodic and cathodic potential peaks of CV experiments should take place. W-R and W-T are jumping just at 1.75 V, but only for 180 and 230 μm thicknesses, when Ws is replaced by Wo. CPE-P shows a behavior close to a capacitor response only differing at darken states. Changes in CPE appear at 1.25 V matching with the coloration on the device and the accumulation of charges of redox reaction. CPE-T is constant at bleached states and increases at darken states to values among 20 and 100 $\mu F/s^p$. The electrical behavior of the bleached state from 0 to 1.25 V is the one of a CPE (being CPE-P≈0.95) in series with Rs, which is mainly a capacitor, as it is observed in Figure III.88-left (since the high Rct neglects the shunt parallel circuit).

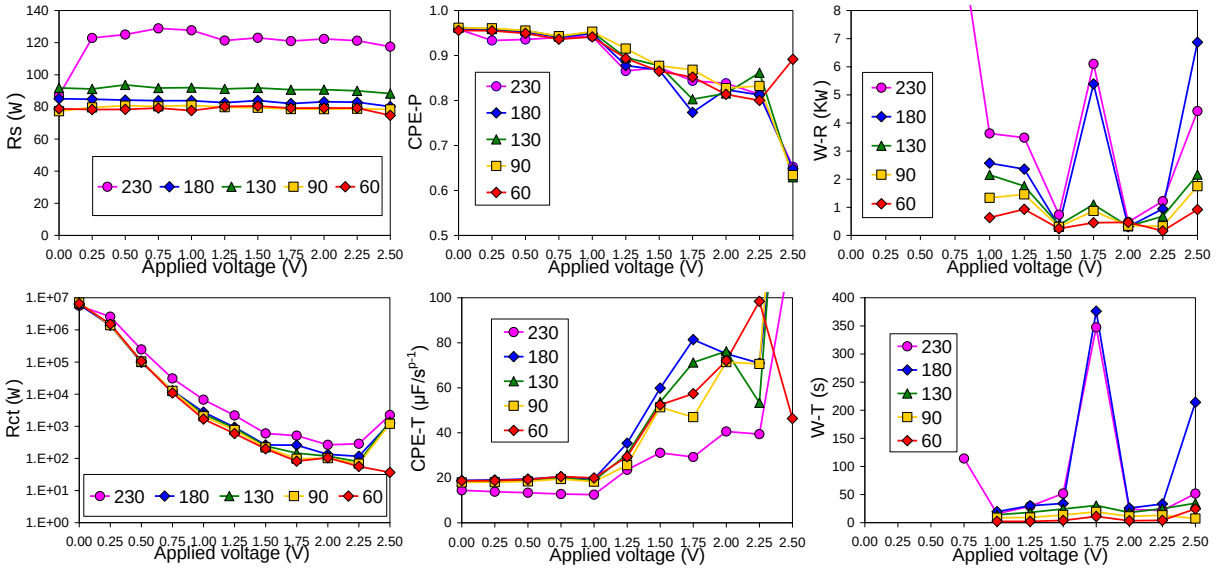

Figure III.90: Thickness and applied voltage dependence of the parameters of the EEC model.

Relevant information about diffusion effects is derived from Figure III.91, which shows the Nyquist diagrams of the Warburg impedance elements simulated from the W-R and W-T parameters of Figure III.90 for the frequency range from 10 mHz to 1 MHz. For the five thicknesses studied, a high value of the Warburg impedance magnitude is observed at potentials of non coloration in the devices (1.00 and 1.25 V), decreasing at 1.5 V, which corresponds to the threshold DC bias voltage of Figure III.78. The diffusion Warburg behavior follows with an increment observed at 1.75 V for a new decreasing at 2.00 V (2.00 and 2.25 V for the 60 μm case, which could be related to the shift on the peak potentials of CV experiments of Figure III.87-left).

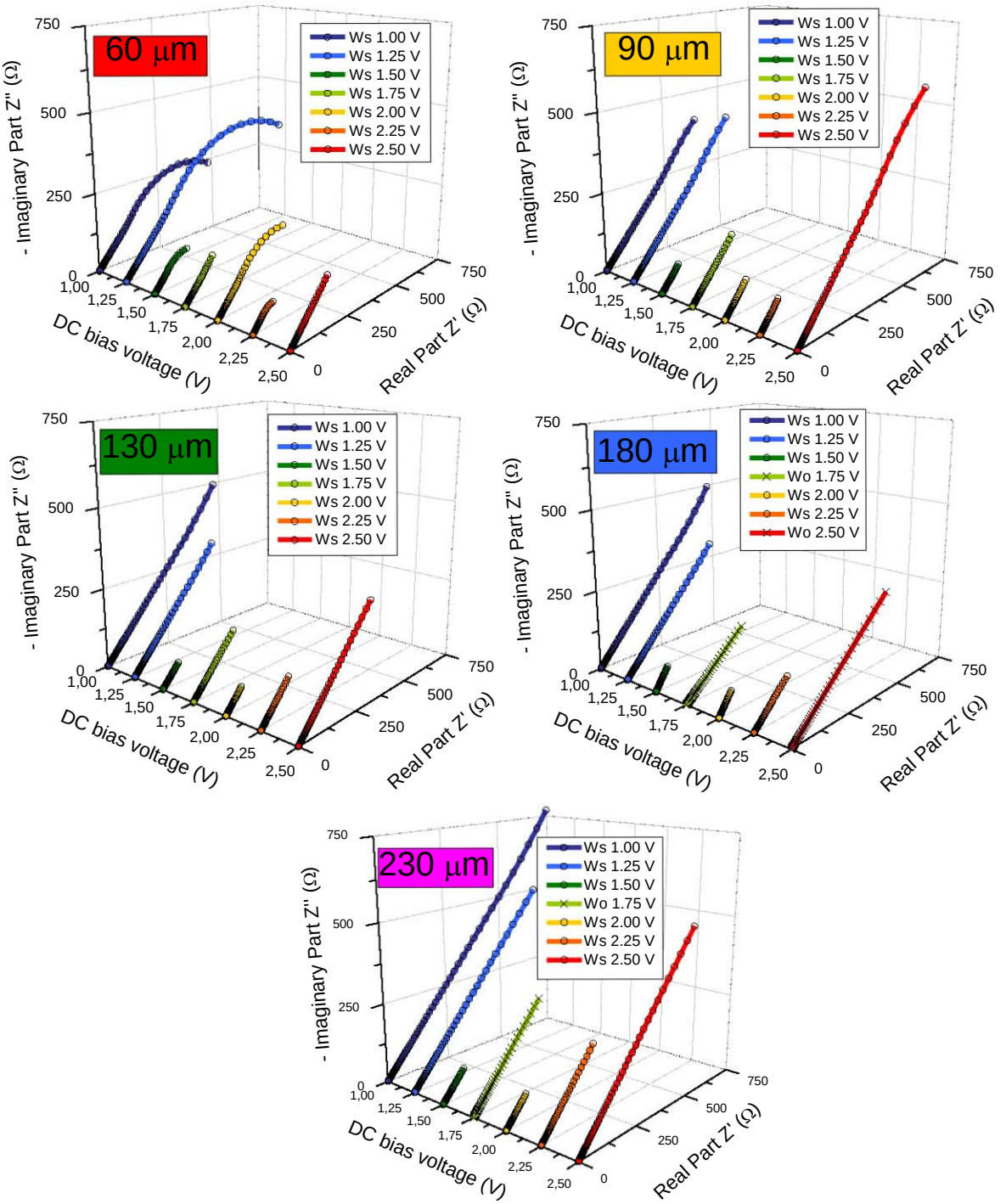

Figure III.91: Nyquist diagram of the Warburg impedance element for different potentials and thicknesses.

III.3.4.5 Relating electrochemical measurements from EIS and from ChrA & ChrC and CV experiments

Short-circuit Ws Nyquist impedance at low frequencies is the right side of a semicircle which matches with the one of a simple Randles cell. For the lowest frequency (close to a DC signal), the imaginary part Ws" tends to zero and the real part Ws' tends to the parameter Ws-R (Rs+Rct in a Randles cell). Hence, in Figure III.91, diffusion effect on 60 μm thickness device seems to be faster at 2.00 V than at 1.75 V for the other four devices, since their data exhibit only the high frequency trend (45 degree slope). From CV experiments (Figures III.80, III.81 and III.82), the rate of the reaction seemed to be slower as the thickness increased. On the other hand, since from ChrA experiments (Figure III.85-left), a continuous electrical current was observed once coloration process stabilized, the fitting to the EEC model should be in all cases using a Ws and not a Wo (even though the fittings improvements), since Wo" at low frequencies tends to infinite (i.e. an open circuit) and no electrical current consumption should be observed. For a perfect fitting, perhaps new components should be added to the proposed EEC model for simulating the effects of the second redox reaction observed in viologen forms, from radical cation (colored state) to neutral species (undesired state for switching). Figure III.92-left shows the variation of the magnitude of the Warburg impedance $|Z_W|$ observed in Figure III.91, at the lowest frequency 10 mHz, with the different DC bias voltage levels, for the five different thicknesses. The jump observed in EIS experiments at 1.75 V (2.00 V for 60 μm) is related to the cathodic potential peaks V_{pc} observed in CV experiments at 25 mV/s scan rate of Figure III.87-left. Figure III.92-right shows the voltammograms of the 3rd cycle of the positive sweeps for CV experiments for the different thicknesses. New measurements at DC bias voltage levels between 1.75 and 2.25 V with 0.05 V steps, or even lower (instead of 0.25 V) could derive to a better concordance of both EIS and CV experiments in order to obtain a relation between the redox reaction cathodic potential peaks Vpc and the diffusion process. Also, as with the charge capacity of Figure III.87-right, the area containing the voltammograms are directly related with coloration contrast in the devices.

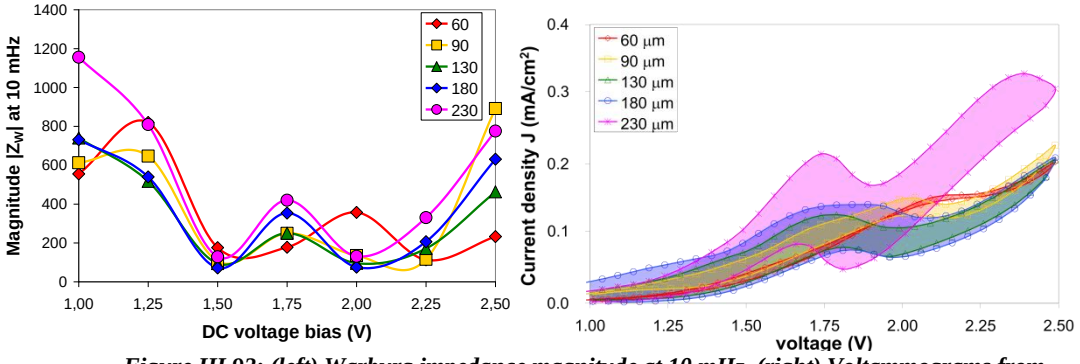

Figure III.92: (left) Warburg impedance magnitude at 10 mHz. (right) Voltammograms from the 3rd cycle of CV experiments at 25 mV/s scan rate.

III.3.5 Conclusions

The increment of ΔT, between bleached and darken states of the studied viologen based ECDs is achieved by increasing the thickness of their internal layer, which results into the increments of the effective charge density and the charge capacity. The parameters of the EEC model depend on the thickness and on the DC bias voltage levels, being directly related to the coloration states (Table III.8). The increment of the diffusion length for thicker devices has been determined by the behavior of the fitted Warburg impedance.

Thickness of film internal layer (μm)	**230**	**180**	**130**	**90**	**60**
Active area (cm^2)	6.56	6.79	6.96	6.35	6.44
Transmittance contrast (%)	44.43	33.92	28.03	18.20	10.61
Coloring time (s)	13	20	15	9	4
Bleaching time (s)	16	16	16	9	5
Injected electrical Charge Density (mC/cm^2)	7.19	6.59	4.50	2.94	1.34
Optical Density (ΔOD)	0.3744	0.2579	0.1995	0.1197	0.0644
Absorption coefficient α (nm^{-1})	1.63	1.41	148	1.31	1.07
Coloration efficiency CE (cm^2/C)	52.15	38.71	42.82	40.12	48.07
Write-Erase efficiency WE (%)	99.49	99.76	100	99.02	72.94
Effective Charge Density ΔQ (mC/cm^2)	2.84	1.59	1.11	0.68	0.23

Table III.8: Parameters obtained from ChrC and T_{600nm} measurements and 2.5 V.

Following the same procedure as in Figure III.42, the real color is simulated with the transparency for each coloration state over the different thicknesses of the viologen based ECDs. Figure III.93 shows the simulated aspect of each thickness of the viologen device at the different coloration levels for the different potentials applied with a photograph of the Mosque of Córdoba (Spain) at the background. Tables III.9 and III.10 show the fitted values of the parameters of the EEC model of Figure III.89 and the fitting errors obtained for the different thicknesses and the different DC bias voltage levels. Two cases are studied, depending on the selection of a Ws (left part) or using Wo (right part). In the case of the 60 μm thickness only the Ws based EEC model was considered, since not a good approximation was achieved with the Wo based EEC model. The thicknesses of 60, 90 and 130 mm are shown in Table III.9, where Ws fits better to the impedance results. For the thicker devices, of 180 and 230 μm, the substitution of Ws by Wo at some DC bias voltage levels (1.75 and 2.50 V for 180 μm and 1.75 V for 230 μm, red and green numbers) improves the fitting errors and chi^2 parameter (Table III.10).

Figure III.93: Visual aspect of the ECDs for the different thicknesses (columns) and the different DC bias voltage applied (rows) with a background of the Mosque of Córdoba.

	60 um	with Ws						with Wo					
voltage	0.00	1.25	1.50	1.75	2.00	2.25	2.50	1.25	1.50	1.75	2.00	2.25	2.50
Rs	78.85	80.24	80.54	79.22	79.30	79.26	74.70						
CPE-T	18.65	29.38	52.37	57.35	72.04	98.39	46.36						
CPE-P	0.96	0.89	0.86	0.85	0.81	0.80	0.89						
Rct	6586500	592	198.2	81.82	104.6	56.24	36.62						
W-R		929.2	241.4	450.8	463.6	159.4	919.9						
W-T		2.17	3.89	11.09	3.40	4.13	24.53						
W-P	0.5	0.5	0.5	0.5	0.5	0.5	0.5						
Rs err	0.36	0.39	0.47	1.47	0.56	0.46	3.56						
CPE-T err	0.41	3.68	6.76	38.79	13.81	16.06	187.34						
CPE-P err	0.12	0.67	1.25	6.64	2.48	2.87	28.02						
Rct err	12.17	1.42	1.46	6.14	3.01	2.41	27.04						
W-R err		1.42	2.16	4.69	1.43	1.63	14.53						
W-T err		3.33	5.12	9.67	3.26	3.79	28.10						
W-P err													
chi2	0.011445	0.0073861	0.013219	0.10711	0.013269	0.012144	0.65233						

	90 um	with Ws						with Wo					
voltage	0.00	1.25	1.50	1.75	2.00	2.25	2.50	1.25	1.50	1.75	2.00	2.25	2.50
Rs	77.30	79.83	79.44	78.63	78.58	78.85	78.44	78.93	79.07	78	77.84	77.85	76.8
CPE-T	17.93	25.62	51.33	46.96	71.39	70.58	249.56	2.99E-05	5.80E-05	4.76E-05	9.98E-05	9.61E-05	3.68E-04
CPE-P	0.96	0.92	0.88	0.87	0.83	0.83	0.63	0.89	0.86	0.87	0.78	0.79	0.57
Rct	7081100	762.6	219.7	97.83	101.8	68.49	1201	830.4	229.1	97.16	110.7	73.32	2291
W-R		1461	303.7	869.4	344.5	326.7	1750	4298	796.3	2489	982.5	965.6	2574
W-T		9.23	13.69	19.15	11.16	13.16	7.40	92.7	96.96	137.5	93.13	111.4	87.36
W-P	0.5	0.5	0.5	0.5	0.5	0.5	0.5	0.5	0.5	0.5	0.5	0.5	0.5
Rs err	0.37	0.43	0.40	1.06	0.50	0.67	0.76	1.12	0.71	1.60	1.09	1.25	1.08
CPE-T err	0.42	3.22	5.07	25.05	10.70	19.23	5.21	7.93	8.64	38.23	21.75	34.12	4.30
CPE-P err	0.12	0.60	0.95	4.22	1.95	3.35	1.50	1.53	1.67	6.43	4.26	6.31	1.59
Rct err	12.61	1.09	0.99	4.26	1.76	2.74	5.81	2.69	1.68	6.68	3.82	5.21	5.77
W-R err		1.78	2.48	3.95	1.93	2.53	4.17	22.15	19.78	40.64	19.11	26.67	50.88
W-T err		3.76	5.03	7.45	3.92	5.00	8.23	47.53	43.14	83.30	40.93	56.25	113.72
W-P err													
chi2	0.012504	0.0084989	0.010069	0.05018	0.012301	0.022953	0.013743	0.052228	0.028998	0.11033	0.050167	0.070277	0.023581

	130 um	with Ws						with Wo					
voltage	0.00	1.25	1.50	1.75	2.00	2.25	2.50	1.25	1.50	1.75	2.00	2.25	2.50
Rs	91.78	91.22	91.82	90.68	90.75	90.03	88.32	90.99	91.71	90.63	90.45	89.72	88.39
CPE-T	18.31	30.44	53.70	71.25	76.23	53.34	247.23	3.14E-05	5.49E-05	6.53E-05	8.53E-05	5.18E-05	2.43E-04
CPE-P	0.96	0.90	0.88	0.80	0.82	0.86	0.63	0.89	0.87	0.82	0.80	0.87	0.63
Rct	6726600	880.5	243.8	145.6	117.6	78.41	1394	896.8	245.7	141.5	121	77.39	1370
W-R		1753	371.1	1100	323.4	679.9	2163	4327	870.1	2607	823.1	1758	3884
W-T		18.23	24.35	30.57	18.09	24.78	34.51	101.2	117.3	149	107.2	143.2	91.04
W-P	0.5	0.5	0.5	0.5	0.5	0.5	0.5	0.5	0.5	0.5	0.5	0.5	0.5
Rs err	0.32	0.44	0.36	0.74	0.40	0.88	0.59	0.66	0.48	0.93	0.70	1.20	0.57
CPE-T err	0.37	3.12	4.47	14.19	8.15	25.92	3.23	4.69	6.04	18.47	14.00	36.09	3.21
CPE-P err	0.11	0.61	0.87	2.71	1.55	4.40	1.02	0.93	1.17	3.45	2.73	6.08	1.00
Rct err	10.66	1.04	0.85	2.76	1.29	3.82	2.75	1.58	1.17	3.61	2.28	5.41	2.74
W-R err		2.46	3.06	4.04	2.16	4.11	6.54	16.10	19.29	29.19	17.75	34.77	15.50
W-T err		4.68	5.61	7.15	4.12	7.49	11.46	34.73	41.38	59.86	38.10	71.24	34.75
W-P err													
chi2	0.010219	0.0091031	0.0089521	0.021931	0.0087808	0.041281	0.0090386	0.02015	0.015823	0.035088	0.025121	0.075745	0.0084277

Table III.9: Values and errors of the fitted parameters of the EEC model of Figure III.89 for 60, 90 and 130 μm.

	180 um	with Ws						with Wo					
voltage	0.00	1.25	1.50	1.75	2.00	2.25	2.50	1.25	1.50	1.75	2.00	2.25	2.50
Rs	85.05	82.63	83.95	82.08	83.17	82.95	80.20	82.71	83.94	82.12	83.07	82.94	80.28
CPE-T	18.81	35.34	59.82	81.40	75.09	70.94	200.12	3.46E-05	5.95E-05	7.96E-05	7.65E-05	6.51E-05	1.95E-04
CPE-P	0.96	0.88	0.87	0.77	0.82	0.81	0.65	0.88	0.87	0.78	0.82	0.82	0.65
Rct	6108700	936.1	262.1	257.9	133.4	116.2	1278	924.5	261.7	255.8	134.1	113.2	1245
W-R		2359	331	5387	305.9	945.3	6870	4409	714.9	2885	731.6	2153	3551
W-T		30.11	34.11	376.10	25.80	33.19	214.10	88.92	136.3	106	128.3	150.9	50.34
W-P	0.5	0.5	0.5	0.5	0.5	0.5	0.5	0.5	0.5	0.5	0.5	0.5	0.5
Rs err	0.34	0.59	0.37	0.82	0.40	0.61	0.71	0.56	0.41	0.81	0.55	0.76	0.69
CPE-T err	0.39	3.93	4.17	10.69	7.02	12.70	4.08	3.80	4.65	10.71	9.63	16.47	4.04
CPE-P err	0.11	0.79	0.83	2.20	1.35	2.35	1.19	0.76	0.92	2.19	1.85	2.99	1.17
Rct err	10.54	1.38	0.81	2.83	1.12	2.26	3.11	1.36	0.93	2.84	1.57	2.94	3.06
W-R err		4.44	4.85	261.30	3.01	3.54	70.26	11.12	24.70	16.06	20.94	24.52	7.93
W-T err		7.79	8.46	524.33	5.44	6.23	139.82	24.29	52.05	34.11	44.15	50.03	15.93
W-P err													
chi2	0.010683	0.015026	0.0095662	0.022243	0.0093429	0.015198	0.012173	0.013446	0.011433	0.021962	0.01692	0.024241	0.011428

	230 um	with Ws		with Ws				with Wo					
voltage	0.00	1.25	1.50	1.75	2.00	2.25	2.50	1.25	1.50	1.75	2.00	2.25	2.50
Rs	87.10	121.30	123.00	121.00	122.30	121.20	117.50	121.4	123.1	121.1	122.2	0.75833	117.6
CPE-T	14.43	23.56	31.10	29.22	40.56	39.39	124.66	2.33E-05	3.07E-05	2.86E-05	4.16E-05	1.14E+01	1.21E-04
CPE-P	0.96	0.87	0.87	0.84	0.84	0.81	0.65	0.87	0.88	0.85	0.83	2.15	0.66
Rct	5649900	2177	598.8	511.9	265.5	286.1	2231	2164	595.8	507.8	267.5	2.286	2167
W-R		3476	734.5	6102	474.7	1218	4421	6816	1404	3136	1131	11.494	7622
W-T		29.08	51.86	347.40	23.74	21.42	51.72	93.62	167.1	88.38	118.2	24.834	130.8
W-P	0.5	0.5	0.5	0.5	0.5	0.5	0.5	0.5	0.5	0.5	0.5	0.5	0.5
Rs err	0.35	0.51	0.28	0.66	0.33	0.75	0.90	0.50	0.28	0.64	0.47	0.76	0.90
CPE-T err	0.39	2.83	2.48	6.96	4.83	11.09	4.66	2.79	2.56	6.86	6.82	11.43	4.94
CPE-P err	0.11	0.59	0.49	1.33	0.92	2.10	1.37	0.58	0.50	1.30	1.30	2.15	1.42
Rct err	7.67	1.14	0.53	1.60	0.82	2.19	3.44	1.15	0.56	1.59	1.18	2.29	3.82
W-R err		4.40	6.15	191.18	2.53	3.53	14.36	12.70	25.79	11.39	17.05	11.49	39.91
W-T err		7.83	10.36	384.17	4.66	6.39	24.08	28.04	52.81	24.84	36.45	24.83	85.52
W-P err													
chi2	0.0099007	0.010622	0.0046972	0.017088	0.0062097	0.021515	0.019665	0.0099683	0.0048393	0.016417	0.011973	0.021787	0.019626

Table III.10: Values and errors of the fitted parameters of the EEC model of Figure III.89 for 180 and 230 μm.

References

[AJB00] Allen J. Bard & Larry R. Faulkner, "Electrochemical Methods: Fundamentals and Applications" (2nd ed.) Wiley (2000). ISBN 0471043729.

[Bar05] David Barrios, Ricardo Vergaz, José M. Sánchez-Pena, Carmen Vázquez, Miguel Ángel Jurado, "Estudio Comparativo de Tecnologías basadas en Materiales Electroópticos para Aplicaciones en Ventanas Inteligentes", 4ª Reunión Española de Optoelectrónica, (2005) Elche (Spain).

[Bar07] David Barrios, Ricardo Vergaz, José M. Sánchez-Pena, Cristina Pozo-Gonzalo, José A. Pomposo, "Propuesta de un nuevo circuito eléctrico equivalente para dispositivos electrocrómicos", 5ª Reunión Española de Optoelectrónica, Bilbao (Spain) (2007).

[Bar08a] David Barrios, Ricardo Vergaz, J.M. Sánchez-Pena, Cristina Pozo, "Coloration, Voltage and Charge Density Relation of Viologens Based Electrochromic Devices", Proceedings of CIE Expert Symposium on Advances in Photometry and Colorimetry, Turin (Italy) (2008).

[Bar08b] David Barrios, A.F.P. Román, Ricardo Vergaz, J.I. Santos, J.M. Sánchez-Pena, "Chromatic Characterization of a RGB-LED Backlight System for an Antiferroelectric LC", CIE Expert Symposium on Advances in Photometry and Colorimetry, Turin (Italy) (2008).

[Bar08c] David Barrios, Ricardo Vergaz, J.M. Sánchez-Pena, Cristina Pozo-Gonzalo, "Relating Cyclic Votammetry and Impedance Analysis in a Viologen Electrochromic Device", 8th International Meeting on Electrochromism I.M.E.8, Seoul (South Korea) (2008).

[Bar11a] David Barrios, Ricardo Vergaz, Juan Calos Torres, J. M. Sánchez-Pena, Cristina Pozo-Gonzalo, Ana Vinuales and Maitane Salsamendi , "Dependence on the Parameters of the Equivalent Electrical Circuit Model with the Thickness of Viologen-based Electrochromic Mixture on Glass Substrate Devices". Symposium H: Electrochromic Materials and Devices, Materials Research Society MRS, San Francisco (USA) (2011).

[Bar11b] David Barrios, Ricardo Vergaz, Juan Carlos Torres, José-Manuel Sánchez-Pena, Ana Viñuales, M. Salsamendi, "Dependence on the parameters of the equivalent electrical circuit model with the thickness of viologen-based electrochromic mixture on glass substrate devices", Proceedings of MRS, DOI: 10.1557/opl.2011.1305 (2011).

[Bar11c] David Barrios, Ricardo Vergaz, Juan Carlos Torres, Cesar Vega, José Manuel Sánhez-Pena, Ana Viñuales, "Thickness-dependent coloration properties of glass substrates viologen-based electrochromic devices". Symposium G: New trends in chromogenic materials and devices, European Materials Research Society EMRS, Warsaw (Poland) (2011).

[Bar12a] David Barrios, Ricardo Vergaz, Juan Carlos Torres, Cesar Vega, José Manuel Sánhez-Pena, Ana Viñuales, "Thickness-dependent coloration properties of glass substrates viologen-based electrochromic devices". IEEE Photonic Journal (to be sent).

[Bau68] Henry H. Bauer, "The electrochemical transfer-coefficient", Journal of Electroanalytical Chemistry and Interfacial Electrochemistry 13 (3) (1968) 419-432.

[Bru77] J. Bruinink, C. G. A. Kregting, and J. J. Ponjeé, "Modified Viologens with Improved Electrochemical Properties for Display Applications", Journal of The Electrochemical Society 124(12) (1977) 1854-1858.

[Chi07] G. Chidichimo, M. De Benedittis, J. Lanzo, B.C. De Simone, D. Imbardelli, B. Gabriele, L. Veltri, G. Salerno, Chem. Mat., 19, (2007) 353-358.

[CV93] D.K. Gosser, Cyclic Voltammetry, Simulation and Analysis of Reaction Mechanisms, VCH Publishers, USA (1993).

[Dia11] J.-P. Diard, B. Le Gorrec, C. Montella, "Handbook of Electrochemical Impedance Spectroscopy. Diffusion Impedances", bio-logic (2011).

[EBa05] E. Barsoukov, J.R. Macdonald (Eds.), "Impedance Spectroscopy: Theory, Experiment, and Applications", Wiley Interscience, Amsterdam, ISBN 0471647497, 2005.

[gam] Basics of Electrochemical Impedance Spectroscopy, Gamry Instruments. http://www.gamry.com/assets/Application-Notes/Basics-of-EIS.pdf

[Lam98] Carl M. Lampert, "Smart switchable glazing for solar energy and daylight control", Solar Energy Materials & Solar Cells 52 (1998) 207-221.

[Mar06] Rebeca Marcilla, Francisco Alcaide, Haritz Sardon, Jose A. Pomposo, Cristina Pozo-Gonzalo, David Mecerreyes,"Tailor-made polymer electrolytes based upon ionic liquids and their application in all-plastic electrochromic devices",Electrochemistry Communications 8 (2006) 482–488.

[Maz09] Mohammad Mazloum-Ardakani, Zahra Taleat, "Investigation of Electrochemistry Behavior of Hydroxylamine at Glassy Carbon Electrode by Indigocarmine", International Journal of Electrochemical Science 4, (2009) 694 - 706.

[Mec04] D. Mecerreyes, R. Marcilla, E. Ochoteco, H. Grande, J.A. Pomposo, R. Vergaz and J.M. Sánchez-Pena, "A Simplified All-Polymer Flexible Electrochromic Device". Electrochimica Acta 49 (2004) 3555-3559.

[MMa07] Matthias Marescaux, Filip Beunis, Filip Strubbe and Kristiaan Neyts, "Electrochromic materials for electronic paper", 8th FIRW PHD Symposium, Ghent Belgium (2007).

[Mon92] P. M. S. Monk, N.M. Hodgkinson, "Charge-transfer complexes of the viologens: effects of complexation and the rate of electron transfer to methyl viologen", Electrochimica Acta 43 (1997) 245-255.

[Mon93] P.M.S. Monk, R.D. Fairweather, M.D. Ingram and J.A. Duffy, "Pulsed electrolysis enhancement of electrochromism in viologen systems: Influence of comproportionation reactions", Journal of Electroanalitical Chemistry 259 (1993) 301-306.

[Mon98] P. M. S. Monk,Comment on: 'Dimer Formation of Viologen Derivatives and their Electrochromic Properties', Dyes and Pigments 39 (2) (1998) 125-128.

[Mon99] Paul M.S. Monk, Neil M. Hodgkinson, Saika A. Ramzan, "Spin pairing (`dimerisation') of the viologen radical cation: kinetics and equilibria", Dyes and Pigments 43 (1999) 207-217

[Ora08] M. E. Orazem and B. Tribollet, Electrochemical Impedance Spectroscopy, John Wiley & Sons (2008).

[Oto04] J.M. Otón, X. Quintana, P.L. Castillo, A. Lara, V. Urruchi, and N. Bennis, "antiferroelectric liquid cristal display", Opto-electronics Review 12(3) (2004) 263-269.

[Pao99] M.A. De Paoli, G. Casalbore-Miceli, E.M. Girotto, and W.A. Gazotti, All polymeric solid state electrochromic devices, Electrochim Acta 44 (1999) 2983-2991.

[Par79] Roger Parsons, "Electrode reaction orders, transfer coefficients and rate constants. Amplification of definitions and recommendations for publication of parameters", International Union of Pure and Applied Chemistry (IUPAC), Physical Chemistry Division, Commission on electrochemistry, Pure & appi. Chern 52 (1979) 233-240.

[PBa91] Paul Baudry, Michel André Aegerter, Daniel Deroo and Bruno Yalla , "Electrochromic Window with Lithium Conductive Polymer Electrolyte", Journal of Electrochemical Society 138 (2) (1991) 460-465.

[Poz06] C. Pozo-Gonzalo, D. Mecerreyes, J.A. Pomposo, M. Salsamendi, R. Marcilla, H. Grande, R. Vergaz, D. Barrios, J.M. Sánchez-Pena, "All-plastic electrochromic devices based on PEDOT as switchable optical attenuator in the near IR", 7th International Meeting on Electrochromism I.M.E.7 Istanbul (Turkey) (2006).

[Poz08a] C. Pozo-Gonzalo, J. Pomposo, H. Grande, M. Salsamendi, R. Marcilla, "Composiciones electrocrómicas basadas en viológenos, formulables y aplicables a temperatura ambiente", Patent P200800258 (2008).

[Poz09] Cristina Pozo-Gonzalo, Maitane Salsamendi, Ana Viñuales, Jose A. Pomposo, Hans-Jürgen Grande, "Highly transparent electrochromic plastic device that changes to purple and to blue by increasing the potential", Solar Energy Materials & Solar Cells 93 (2009) 2093-2097.

[Row02] Natalie M. Rowley and Roger J. Mortimer, "New electrochromic materials", Science Progress 85(3) (2002) 243-262.

[Sal10] M. Salsamendi. "Síntesis de materiales electrocrómicos orgánicos y desarrollo de dispositivos electroópticos". Ph.D. Thesis. Universidad País Vasco (2010).

[Sek09] N. A. Sekushin, "Equivalent Circuit of Warburg Impedance", Russian Journal of Electrochemistry Elektrokhimiya 45(7) (2009) 889-894.

[Ver03] R. Vergaz, J.M. Ollero, J.M.S. Pena, D. Mecerreyes, H. Grande, J.A. Pomposo, "Preliminary Characterization of Novel Electrochromic Devices for Domotics", 3ª Reunión Española de Optoelectrónica, Leganés (Spain) (2003).

[Ver04a] R. Vergaz, J. M. S. Pena, A. B. Gonzalo, J. M. Ollero, C. Vázquez, J. A. Pomposo, H. Grande and D. Mecerreyes, "Characterization of novel all-plastic electrochromic devices: electro-optic and voltammetric response", Optical Engineering 43 (12) (2004) 2967.

[Ver04b] R. Vergaz, J. M. S. Pena, D. Barrios, C. Vázquez and D. Mecerreyes, "Spectral and Time Responses of New All-plastic Electrochromic Devices". 6th International Meeting on Electrochromism I.M.E.6 Brno, (Czech Republic) (2004).

[Ver04c] R. Vergaz, J. M. S. Pena, D. Barrios, C. Vázquez and D. Mecerreyes, "AC Impedance Spectroscopy Analysis of New All-plastic Electrochromic Devices". 6th International Meeting on Electrochromism I.M.E.6 ,Brno (Czech Republic) (2004).

[Ver05] R. Vergaz, J.M.S. Pena, D. Barrios, C. Vázquez, C. Pozo, D. Mecerreyes, J. Pomposo, "Variable Optical Attenuator based on Organic Electrochromic Materials", Microtechnologies for the New Millennium 2005 Symposium: Photonics and Optoelectronics (SPIE) Seville (Spain) (2005).

[Ver06a] R. Vergaz, J. M. S. Pena and D. Barrios, "Microcontrolled electrooptic system for online light transmission control of novel electrochromic devices". Microwave and Optical Technology Letters 48(8) (2006) 1572-1574.

[Ver06b] R. Vergaz, J. M. S. Pena, D. Barrios and C. Vázquez, "Electrical Analysis of New All-Plastic Electrochromic Devices", Optical Engineering 45 (11) (2006).

[Ver06c] Ricardo Vergaz, David Barrios, J.M.S. Pena, Cristina Pozo-Gonzalo, Jose A. Pomposo, Maitane Salsamendi, "Electro-optical Analysis of PEDOT Symmetrical Electrochromic Devices", 7th International Meeting on Electrochromism I.M.E.7, Istanbul (Turkey) (2006).

[Ver07a] R. Vergaz, D. Barrios, J. M. S. Pena, C. Pozo and J. A. Pomposo, "Electrical Characterization of New Electrochromic Devices". Proceedings of 6th Spanish Conference on Electronic Devices. El Escorial (Spain) (2007).

[Ver08a] R. Vergaz, D. Barrios, J. M. S. Pena, C. Marcos, C. Pozo and J. A. Pomposo, "Electro-optical Analysis of PEDOT Symmetrical Electrochromic Devices". Solar Energy Materials and Solar Cells 92 (2008) 107-11.

[Ver08b] Ricardo Vergaz, David Barrios, José M. Sánchez-Pena, Cristina Pozo-Gonzalo, Maitane Salsamendi, José A. Pomposo, "Impedance Analysis and Equivalent Circuit of an All-plastic Viologen Based Electrochromic Device", Displays 29 (2008) 401-407.

[Ver09] Ricardo Vergaz, David Barrios, José-Manuel Sánchez-Pena, Cristina Pozo-Gonzalo, Maitane Salsamendi, "Relating Cyclic Votammetry and Impedance Analysis in a Viologen Electrochromic Device", Solar Energy Materials and Solar Cells 93 (2009) 2125-2132.

Chapter IV: Suspended particle devices (SPDs)

A detailed optical and electrical characterization of three similar samples of SPD devices supplied by the company CRICURSA (Cristales Curvados SA, Barcelona, Spain) was carried out. CRICURSA is a Licensee of Research Frontiers for the SPDs. As it was described in previous sections, SPD technology principle is shown in the Figure IV.1. When no voltage is applied, the suspended particles are arranged in random orientations and tend to absorb light, so that the glass panel looks dark (or opaque), blue or, in more recent developments, grey or black color. When voltage is applied, the suspended particles align and let light pass. SPDs can be dimmed, and allow instant control of the amount of light and heat passing through.

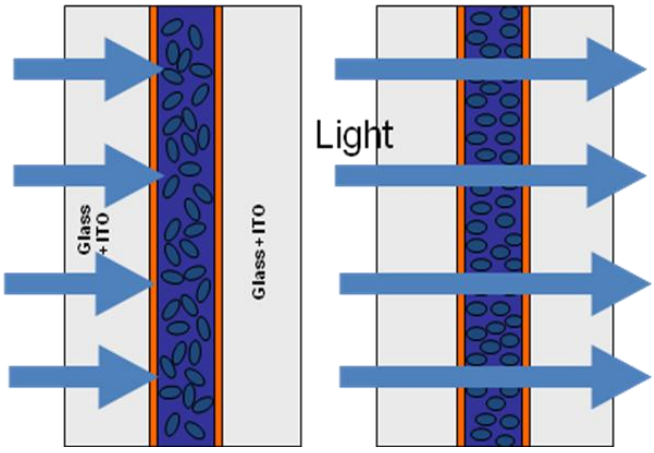

Figure IV.1: Working principle of a suspended particle device.
(left) OFF state: Operation with no applied voltage. Particles are in random positions and light is absorbed.
(right) ON state: Operation with applied voltage. Particles aligned and light is transmitted.

In the SPD, there are a large number of black, light absorbing, suspended particles (SP) within a polymeric film placed between two glass layers equipped with electrical contact layers. The particles are polyiodide (polyhalide crystals) [Cha02] and exhibit a large optical anisotropy, being heraphatite (quinine bisulphate polyiodide) [Kah09] used on polarizers and other optical devices of previous works [Kno09]. The optical anisotropy of heraphatite has been studied in detail in [LLi09]. Other related compounds have been used for SPDs [Tak97 and Sax03]. The size of the particles should be lower than 200 nm in order to minimize light scattering and avoid a non desired haze effect.

For optical characterization, the transmittance was measured at the visible wavelength range, when applying different values of AC potential to the SPD samples, which lead to different levels of optical transmission. Haze and light scattering of the SPD samples were determined by measuring the total and diffuse components of the transmittance and reflectance. Extensive scattering and absorption optical coefficients (S & K) are derived

from measurements of direct and diffuse optical transmittance (T_{dir} and T_{diff}) and specular and diffuse optical reflectance (R_{spec} and R_{diff}). These coefficients make possible to model the optical properties of devices, depending on design parameters such as the thickness. Measurements were carried out in the solar wavelength range of frequencies, in order to study if solar heat gain can be controlled with the characterized samples. Impedance Bode (magnitude and phase) and Nyquist diagrams were obtained with EIS method. Impedance analysis shows similar characteristics to those of a Randles circuit. An EEC model is proposed and experimentally validated.

IV.1 Introduction

The three SPD samples used in this work (SPD1, SPD2 and SPD3), all of them with an active area of 28 cm x 22 cm and a thickness (δ) of 300 µm, are a CriRegulite device type supplied by CRICURSA (Cristales Curvados SA, Barcelona, Spain) [cri]. Cri-Regulite is a trade mark of CRICURSA, a Licensee of Research Frontiers [RFr] for the SPDs. The work of the Research Frontiers' emulsion makers produces the basic chemicals (particles) and the special polymers that work in conjunction with those particles.

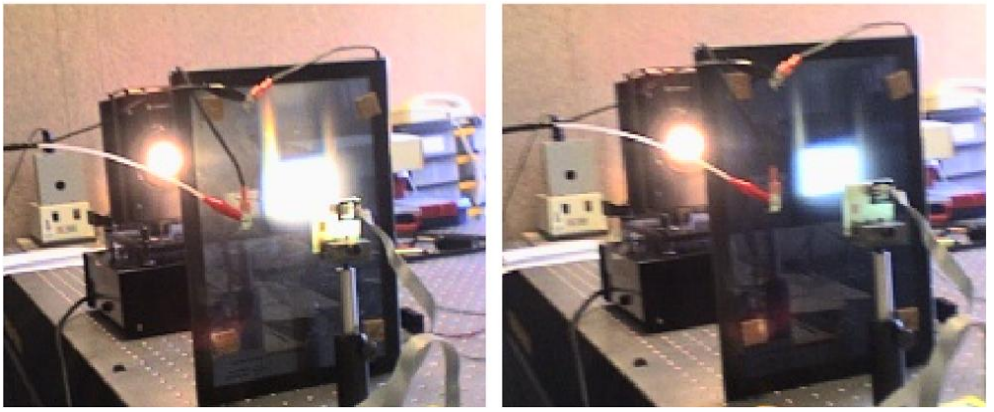

Figure IV.2: Photograph of the sample SPD2 for the bleached and dark states. (left) With applied voltage. (right) Without applied voltage.

Figure IV.3: Photograph of the sample SPD3 for bleached and dark states. (a) With applied voltage. (b) Without applied voltage.

Intermediate levels of transmittance are obtained applying different AC voltage levels, which were achieved using a variable AC transformer (commonly known as Variac) for the first SPD sample, a customized field programmable gate array (FPGA)-based electrical circuit, for the second SPD sample, and a function generator in series with a broadband linear amplifier for the third SPD sample. Finally, measurements are taken to check the applicability of the SPD device and control system in smart glazing or photonic applications.

V.2 Experimental

The SPD samples supplied by Cricursa included a data sheet which specified the following features (Table IV.1):

Maximum size: 1200 x 2800 mm	**Light transmission: minimum <1% maximum 57%**
Admitted electrical current: 80-220 Vac, 50-60 Hz	**Rise time < 0.5 second**
Power consumption < 5 watt/m^2	**Fall time < 1 second**
Number of cycles > 1×10^6	**Minimum thickness 300 µm**
Operation temperature range: -30 to 90 ºC.	**Connectors Fast-on**

Table IV.1: Datasheet of the SPD samples supplied by Cricursa.

The film was made according [Cha02], by means of a cross-linked polymer matrix having droplets of polyhalide particles suspended in a liquid suspension distributed in it. The emulsion was spread over an indium tin oxide-coated glass plate using a wire-wound glass rod and exposed to UV radiation for 30 seconds in order to cure it. Curing was carried out with a second indium tin-oxide coated glass plate on top of the emulsion. The droplet and the matrix components refractive indices of the film matched within 0.005 and the droplets were around 1 µm size; both items configure a low-scattering and blue-tone device, as can be seen in Figures IV.2 and IV.3.

Optical response of the samples SPD1 and SPD2 was measured during switching using the spectrophotometer based on Acton Research monochromator available at GDAF-UC3M lab. Total reflectance and transmittance (R_{tot} and T_{tot}), as well as diffuse reflectance and diffuse transmittance (R_{diff} and T_{diff}) were measured for sample SPD3 in the $0.3 < \lambda < 2.5$ µm wavelength range by use of a double beam Perkin-Elmer Lambda 900 spectrophotometer equipped with an integrating sphere available at the Ångström Laboratory of Uppsala. The recordings of reflectance and transmittance were performed at normal incidence with 5 nm resolution and the diffuse components represented the light that was not specularly reflected or transmitted through the sample, as shown in Figure II.4-left.

Impedance analysis was made by using two different impedance/gain phase analyzers. A Hewlett Packard 4194A available at GDAF-UC3M lab was used for the first sample

SPD1. The reduced capabilities of this analyzer for this purpose with frequency and magnitude ranges from 100 Hz to 40 MHz and 0.1 Ω to 1.6 MΩ, was an obstacle to find the EEC model since lower frequencies and higher magnitudes were required. A Solartron 1260 analyzer, later available at GDAF-UC3M, was used for the sample SPD2. The frequency and magnitude ranges from 0.5 mHz to 32 MHz and magnitude higher than 100 MΩ were enough impedance data to satisfy the requirement for fitting results to an equivalent electrical circuit model. Finally, the same Solartron 1260 instrumental, but now available at Ångström Laboratory of Uppsala (Sweden), was used to characterize the third sample SPD3. The electrical current during switching of the sample SPD3 was measured with a digital multimeter model Keithley 197A (Figure II.17-left in Chapter II).

Three different ways for electrically feeding the SPD samples were used. A single phase autotransformer or variac (model Verilec) supplying intermediate AC sinusoidal voltage signals from 0 to 220 V rms and 50 Hz, was used to optically characterize the sample SPD1 while switching (Figure II.18-left). Since a higher clearance was expected for a higher applied voltage, measurements were carried out at the maximum voltage. Unfortunately, despite the datasheet of the samples included as electrical current admitted from 80 to 220 V rms AC, 50 Hz, the sample SPD1 stopped its optical switching after no more than 50 cycles. Due to the short lifetime of the first sample, and the possible peaks of voltage that could damage the optical operation of the SPD devices when using the variac for electrical feeding, other options were taken into account in order to switch the rest of SPD samples.

A FPGA-based customized electronic driver was designed and implemented for addressing the sample SPD2 (Figure II.18-right). This driver could be used, in principle, with devices of arbitrary size, except for the output power stage which largely depends on panel consumption. This has been measured to be about 5 Wm^{-2} in our current working conditions. Since none appreciable extra bleaching was observed for applied voltage signals higher than 100 V peak, a function generator (model HP33120A/001, available at GDAF-UC3M, and model GX240 ITT Metrix, in Figure II.19-left and available at Ångström Laboratory) in series with a broadband linear amplifier, model F10A of FLC Electronic AB (Figure II.19-right, available at both GDAF-UC3M and Ångström Laboratory) with an amplification of 10 times and maximum input voltage of ±10 V, were used for the samples SPD2 and SPD3 in order to achieve electrical control signals, of 50 Hz frequency with amplitude values from 0 to 100 V peak.

IV.3 Optical characterization

Spectral measurements were carried out in the visible and in the solar wavelength range, from 300 to 900 nm and from 300 to 2500 nm respectively.

IV.3.1 Spectral measurements: Visible wavelength range

Figure IV.4-up shows the spectral transmittance of the sample SPD1 at the wavelength range from 300 to 900 nm for the bleached state, with 220 V_{rms} AC 50 Hz sinusoidal applied signal, and the dark state, with 0 V applied, or also in the state of high impedance (HZ), showing a 30% of transmittance change between both states at 600 nm.

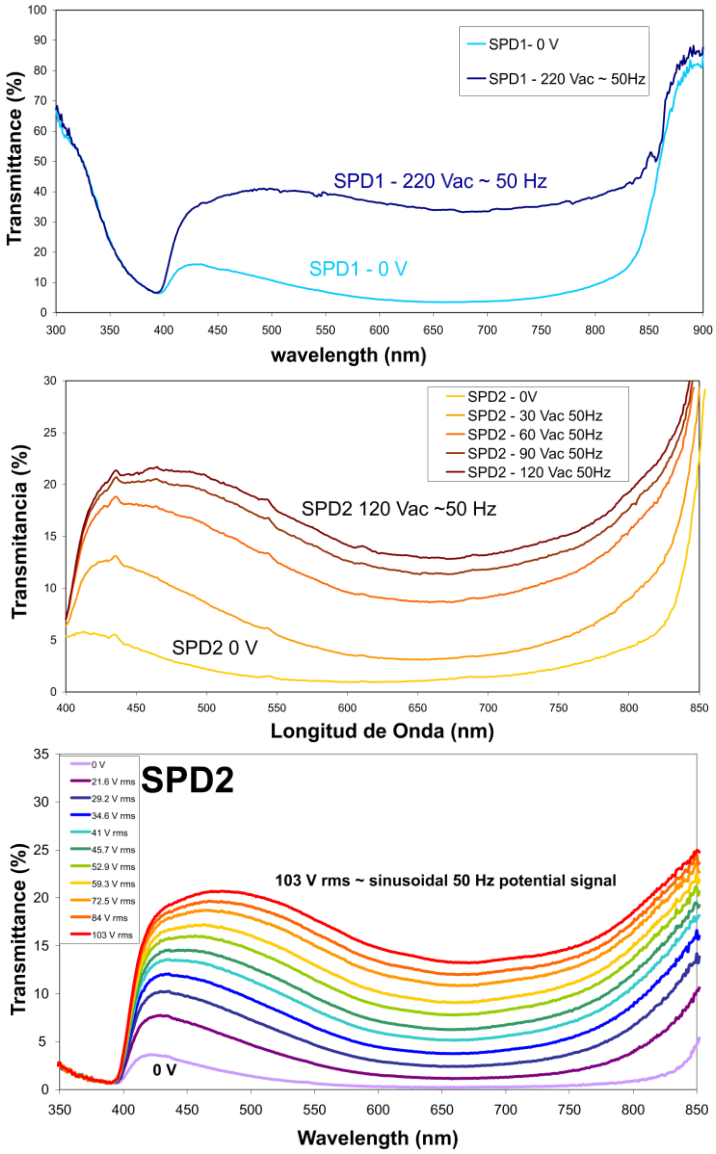

Figure IV.4: Transmittance spectra of the devices SPD1 at 0 and 220 Vrms (up) and SPD2 at 0, 30, 60, 90 and 120 Vrms (center) AC 50 Hz sinusoidal voltage signal applied by means of a variac and SPD2 (down) at the different tested FPGA voltage levels from 0 (lower plot) to 103 V rms.

Figure IV.4-center shows the spectral transmittance of sample SPD2 at the wavelength range from 300 to 900 nm for intermediate states between the bleached and the darker one, at 0, 30, 60, 90 and 120 V_{rms} AC 50 Hz sinusoidal signals supplied by the variac. In order to compare when electrically feeding the sample SPD2 with a different instrumental, Figure IV.4-down shows spectral transmittance at ten different levels from 0 to 103 Vrms (0, 21.6, 29.2, 34.6, 41, 45.7, 52.9, 59.3, 72.5, 84 and 103 Vrms) supplied by the FPGA + actuator set-up. Optical direct transmission in the bleached state of the sample SPD2, less than 25%, is still poor for many photonic applications. The best contrast in wavelength can be seen at around 480 nm. The dark-colored state is a result of the low transmittance, but diffuse radiation is not measured. The different ratio between the blue and the red intervals of the spectrum, defined at 440-490 and 600-700 nm respectively, makes a bluer coloration, especially at low or no applied voltages (ratios of 9:1 in the integrated mean transmittance). Increasing the transmittance in the whole spectrum with higher voltages makes the device more transparent [Ver07b and Ver08d].

IV.3.2 Switching times measurements

T_{600nm} was measured at different applied steps voltage signals for the range between 80 to 200 V rms and from 0 and 103 V rms for the samples SPD1 and SPD2 respectively. Only a small change, of 5% of T_{600nm}, is achieved in Figure IV.5 when increasing from 80 to 200 V rms the applied voltage supplied by a variac for the sample SPD1 (30 % of $T_{600\ nm}$ for 80 Vrms at 30 seconds and 35% of $T_{600\ nm}$ for 200 Vrms at 355 seconds).

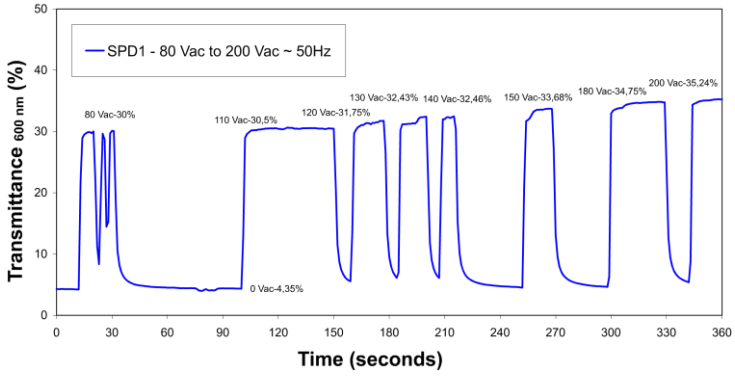

Figure IV.5: T_{600nm} of the sample SPD1 for different steps voltage signal for the range between 80 a 200 V rms supplied by a variac.

A measurement of the transmittance change for SPD2 at 600nm with the applied voltage is shown in Figure IV.6-left, in which a quadratic relationship can be established between both magnitudes, with a correlation coefficient higher than 0.99. Rise and fall times of 2.61 and 2.65 seconds respectively were measured for the sample SPD2 applying a step signal from 0 to 70.71 V rms (100 V peak) as it is shown in the Figure IV.6-right. These times disagree with the data sheet supplied from the manufacturer in the Table IV.1 (rise time less than 0.5 second and fall time less than 1 second).

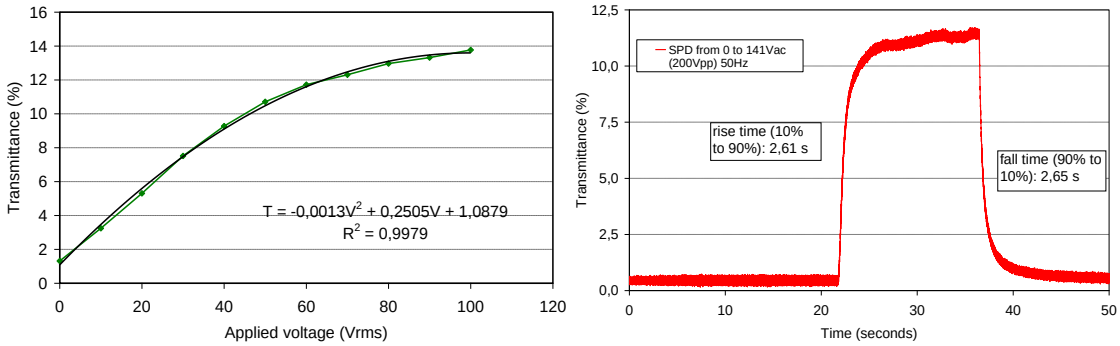

Figure IV.6: (left) Transmittance measured at 600 nm for the sample SPD2 as a function of the applied rms voltage (dots). Line and inset: least squares fit to a quadratic relationship between both magnitudes. (right) Rise and fall times.

Figure IV.7 shows the transmittance results when different shape signals from 0 to 100 V rms are applied using a variac for electrically driving the sample SPD2. Slight hysteresis is observed for the transmittance states depending on the previous state. Previous results of Figure IV.4-down at 600 nm match with the ones obtained when ten square pulses with different amplitude from 0 to 103 V rms of voltage were applied with the implemented FPGA electronic driver for the sample SPD2, which lead to ten different levels of T_{600nm}, shown in the Figure IV.7-down.

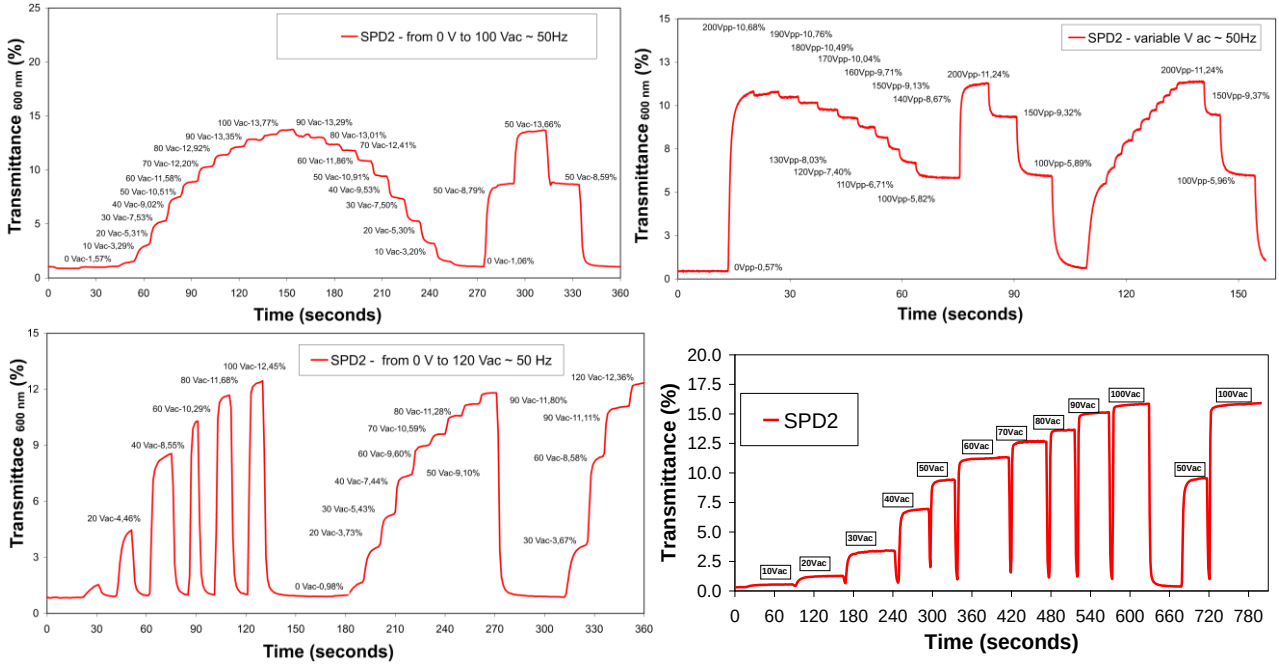

Figure IV.7: T_{600nm} of the sample SPD2 between 0 and 103 V rms for several shapes of voltage signals supplied by a variac and for different square pulses supplied by FPGA driver.

IV.3.3 Spectral measurements: Operation in the solar range

IV.3.3.1 Transmittance and reflectance

A function generator in series with a broadband amplifier was used for electrical feeding of the sample SPD3 and measuring the optical properties (Figure IV.8). In many plots of this section, transmittance and reflectance will be plotted not as a percentage, but from 0 to 1. The SPD3 states for 0 V and 100 V_{peak} 50 Hz sinusoidal applied voltage signal are denoted "off" and "on", respectively. The value of 100 V peak was chosen as the maximum voltage applied for SPD3 since applying higher voltages could be the reason of the stop of switching for the samples SPD1 and SPD2, being also this value the maximum voltage reached with the system function generator + amplifier. Figure IV.8-left-up shows the direct and diffuse transmittance of the SPD device for applied voltages of 0 and 100 V.

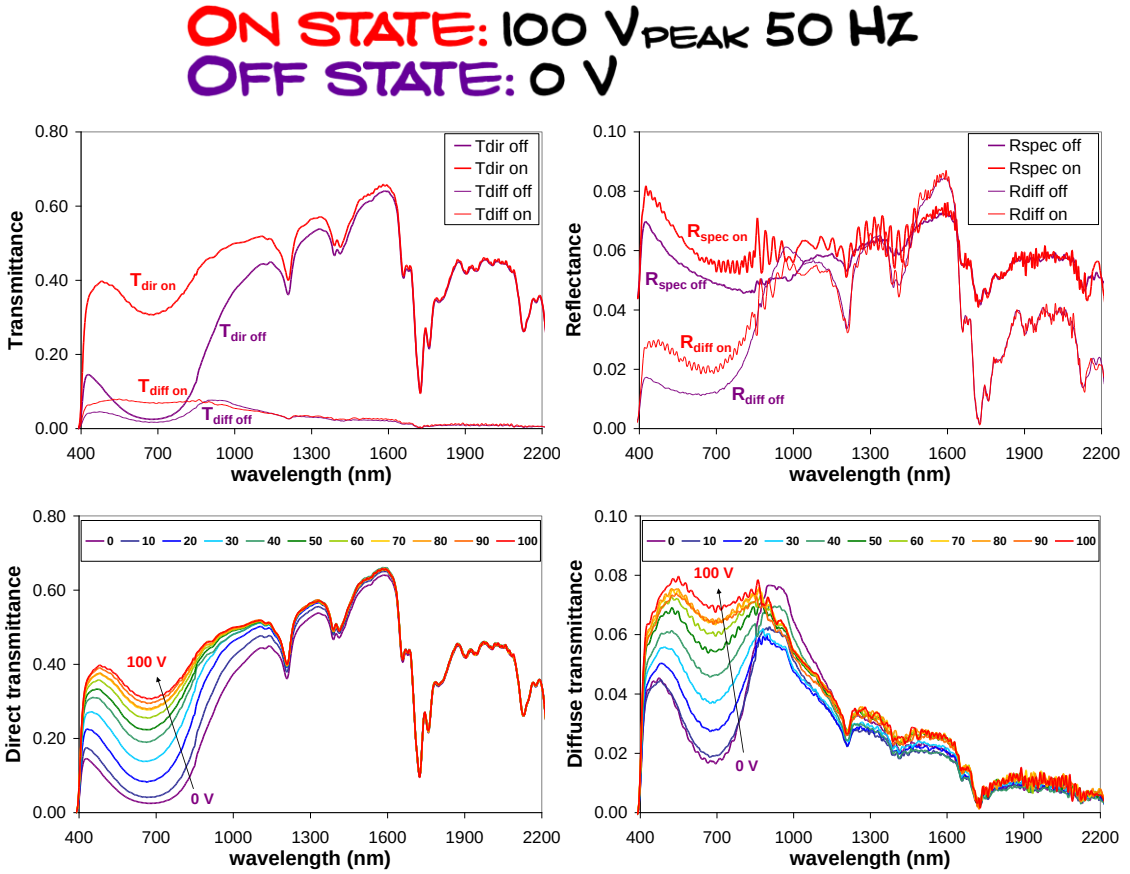

Figure IV.8: Direct and diffuse components of transmittance and reflectance of sample SPD3. (up) T_{dir} and T_{diff} (left) and R_{spec} and R_{diff} (right) in colored (off) and bleached (on) states. (down) T_{dir} (left) and T_{diff} (right) for different applied voltages from 0 to 100 V.

In the SPD3 sample, visible transmittance changes between approximately 0.05 and 0.4. However no change in NIR transmittance above a wavelength of about 1600 nm is observed. A significant T_{diff} (always below 0.1) that causes a non desired scattering effect in the bleached state is observed. R_{tot} was around 0.1 in the whole wavelength range. R_{spec} and R_{diff} are shown in Figure IV.8-right-up, for the dark and bleached states. Ten different levels of T_{dir} and T_{diff}, obtained by varying the applied voltage in steps of 10 V, are shown in the Figures IV.8-left-down and IV.8-right-down respectively.

IV.3.3.2 Dependence of incidence angle

T_{tot} spectra in the $0.3 < \lambda < 1.1$ μm wavelength range were recorded using the integrating sphere setup detailed in [Nos99] and explained in this work in section II.1.4. The measurements were carried out with different incidence angles from 0º to 60º with 15º intervals. A quartz crystal polarizer located in front of the experimental assembly was used for obtain s or p polarized light. The transmittance value was calculated as the average of both polarization measurements [Bar09].

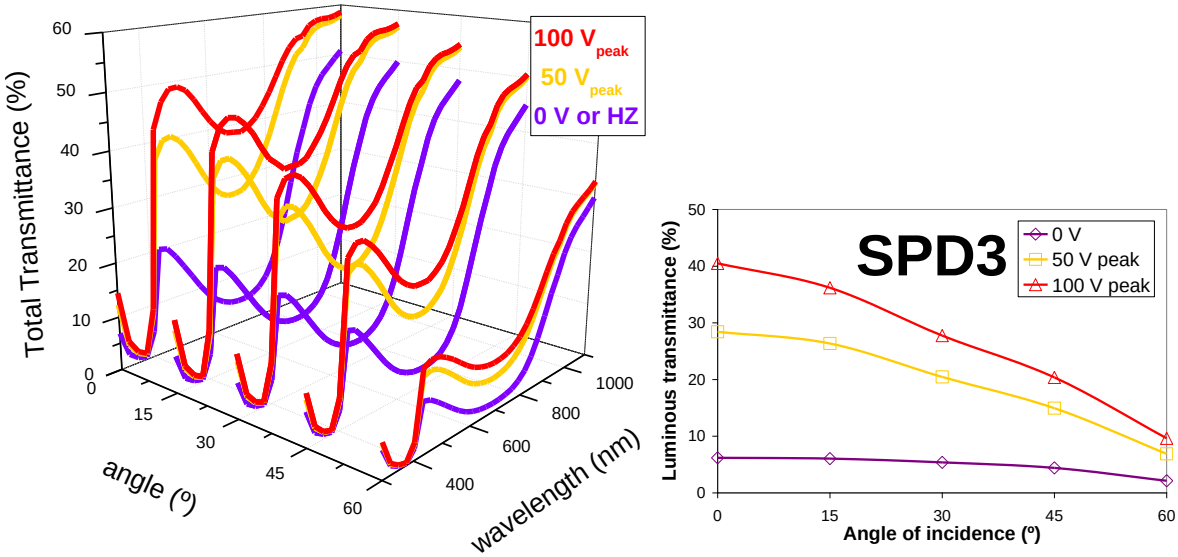

Figure IV.9: T_{tot} for different incidence angle of incidence from 0 to 60º with 15º steps for sample SPD3 at three applied 50 Hz sinusoidal signal voltages: 0, 50 and 100 V peak [Bar09]. (left) Spectral (right) Luminous value.

Figure IV.9-left shows T_{tot} spectra in the bleached, half bleached and dark states for a number of incidence angles of the light. T_{tot} in the bleached state decreases as the angle of incidence becomes larger. This is expected because the light has to travel a longer path through the sample in the case of a large angle of incidence. The transmission of the bleached state is markedly more dependent of the incidence angle than that of the dark state, as the luminous transmittance trend shows (Figure IV.9-right).

IV.3.3.3 Determination of absorption and scattering coefficients

Determining intrinsic scattering and absorption coefficients (α & β) from experimental spectral transmittance and reflectance measurements in light scattering media is a difficult problem [Rod00], which equations are described in the four flux model [MLG84, MLG86 and Var98]. Nevertheless, knowing the value of the separated α & β coefficients (which sum is denoted as the extinction coefficient) of a film of a determined thickness exhibiting R_{spec} and R_{diff} as well as T_{dir} and T_{diff} is a powerful tool in order to predict the value of these optical properties for different thicknesses of the same film. Equations of four flux model includes parameters such as collimated interface reflectance for collimated R_{spec} and T_{dir} components, and forward scattering ratios (FSR), average crossing parameter (ACP) and diffuse interface reflectances for diffuse R_{diff} and T_{diff} components [Var98]. Since these diffuse equations include α & β parameters separately, decoupling extinction coefficient into scattering and absorption coefficients is a required task. However, inverting diffuse equations in order to obtain the value of these parameters from the experimental measurements seems a very difficult problem, being advanced fitting methods like the spectral projected gradient method the only option applied for such problem [Cur02].

Two flux models [MLG86] are another simpler but approximated option of determining the parameters associated to diffuse light, being the conditions of applicability studied in detail [Var97a, Var97b and Var99]. Levinson et al. considered that total components R_{tot} and T_{tot} can be determined by two flux models when the scattering is weak and R_{spec} and T_{dir} are close to the total R_{tot} and T_{tot} components respectively (which is traduced directly to a spectral value of ACP close to 1, as in non scattering media) [Lev05]. As it will be detailed below, the process of determination and decoupling the extensive scattering and absorption coefficients (S & K) of the SPD sample consists on several steps, including the spectral interface reflectance to collimated light r_c obtained by a fitting process using four flux collimated equations, from which it can be derived the spectral refractive index n of the film, which is used for computing the spectral interface reflectance to diffuse light r_d, which together with the spectral diffuse fractions of light determined at the top and the bottom interfaces allow to obtain the spectral total interface reflectance also at the top and bottom interfaces of the SPD sample (being the top interface the closer to the spectrometer illuminant). Equations of two flux model are then used for total components once knowing the total interface reflectances. The change of the refractive index at each interface was taken into account by using the Saunderson correction. Finally, S & K are determined by a fitting process, once the values of these parameters have been previously obtained.

Once S & K are obtained by the below detailed method, the predicted optical properties T_{dir}, T_{diff}, R_{spec} and R_{diff} were simulated for several thicknesses of the internal layer of the SPD sample different than the 300 μm of the film of the constructed device.

IV.3.3.3.1 Four flux theory

The geometry of the SPD sample has been modeled as a simple glass/SPD/glass stack [Bar12b]. Since the refractive indices of glass, plastics and the SPD layer are close, all reflections were neglected except the air/glass and glass/air interfaces. This approximation is necessary since the refractive indices of the intermediate layers of the SPD sample are unknown.

Four flux model considers two collimated (I_c and J_c) and two diffuse (I_d and J_d) light beams [Var97b and MLG84]. The scattering and absorption coefficients α & β are the intrinsic values. Equation IV.1 shows that downwelling collimated intensity I_c is decreased by scattering and absorption. Equation IV.2 shows that upwelling collimated intensity is enhanced by scattering and absorption. Equation IV.3 shows that downwelling diffuse intensity I_d is decreased by absorption and I_d backscattering ((1-FSR) α) but enhanced by the scattering of I_c and the backscattering of J_d and J_c. Equation IV.4 shows that upwelling diffuse intensity J_d is enhanced by absorption and J_d backscattering but decreased by the scattering of J_c and the backscattering of I_d and I_c. Figure IV.10 shows a schematic of the four flux model.

$$\frac{dI_c}{dz} = -(\alpha + \beta) I_c \qquad \text{(Eq. IV.1)}$$

$$\frac{dJ_c}{dz} = (\alpha + \beta) J_c \qquad \text{(Eq. IV.2)}$$

$$\frac{dI_d}{dz} = -ACP \cdot \beta \cdot I_d - ACP \cdot (-FSR_d)\alpha \cdot I_d + ACP \cdot (-FSR_d)\alpha \cdot J_d + FSR_c \cdot \alpha \cdot I_c + (-FSR_c)\alpha \cdot J_c$$

(Eq. IV.3)

$$\frac{dJ_d}{dz} = ACP \cdot \beta \cdot J_d + ACP \cdot (-FSR_d)\alpha \cdot J_d - ACP \cdot (-FSR_d)\alpha \cdot I_d - FSR_c \cdot \alpha \cdot J_c - (-FSR_c)\alpha \cdot I_c$$

(Eq. IV.4)

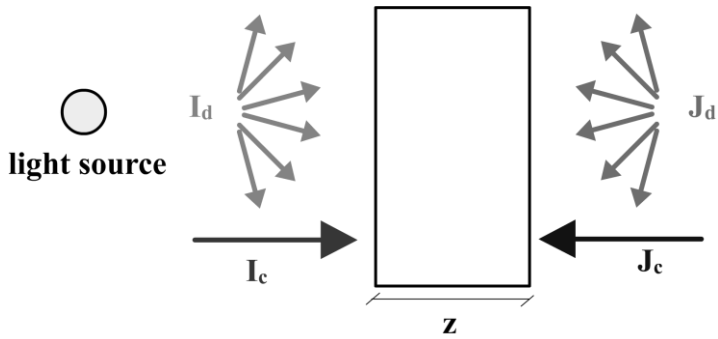

Figure IV.10: Four flux model. Downwelling (I) and upwelling (J) collimated ($_c$) and diffuse ($_d$) intensities.

The parameter ACP is equal to 1 for totally collimated beam (i.e. in a medium without scattering), being equal to 2 for a totally diffuse beam (i.e. in a completely scattering medium). The parameter FSR can vary from 0 to 1 depending on the proportion of forward and backward scattering. Using Equations IV.3 and IV.4 it is sometimes assumed that $FSR_c=FSR_d$, i.e. the parameter FSR is equal for collimated and for diffuse light beams.

Equations IV.5 and IV.6 are obtained from collimated four flux equations for T_{dir} and R_{spec} respectively [MLG84], neglecting multiple reflections since the reflectances are small (Figure IV.8-up-right).

$$T_{dir} = (1-r_c)^2 \cdot e^{-(\alpha+\beta)\delta} \qquad \text{(Eq. IV.5)}$$

$$R_{spec} = r_c + r_c \cdot (1-r_c)^2 \cdot e^{-2(\alpha+\beta)\delta} \qquad \text{(Eq. IV.6)}$$

Being δ the thickness, r_c the collimated interface reflectance (which for most glass and polymer materials is around 0.04, corresponding to a refractive index of 1.5). Extinction coefficient $E= \alpha+\beta$ and r_c are obtained solving these two equations (slightly different than the obtained following the formula $E=(1/\delta)*\ln[(1-R_{spec})/T_{dir}]$ for strong absorbing films [WuQ89]). Figure IV.11-left shows the extinction coefficients of the SPD3 sample in the "OFF" and "ON" states. The extinction is much higher in the visible and part of the NIR range for the absorbing OFF state, showing a pronounced peak around 700 nm. Figure IV.11-right shows the collimated interface reflectance r_c in both "OFF" and "ON" states. For r_c, a value slightly higher than 0.04 is obtained, corresponding to a refractive index of the film between 1.5 and 1.7, which varies with wavelength as it is seen in Figure IV.11-left. In order to determine both scattering and absorption coefficients, T_{diff} and R_{diff} must be considered. However, the four flux expressions for the diffuse parts are too complicated to be inverted and contain too many free parameters. Instead the two flux theory was used, as explained below.

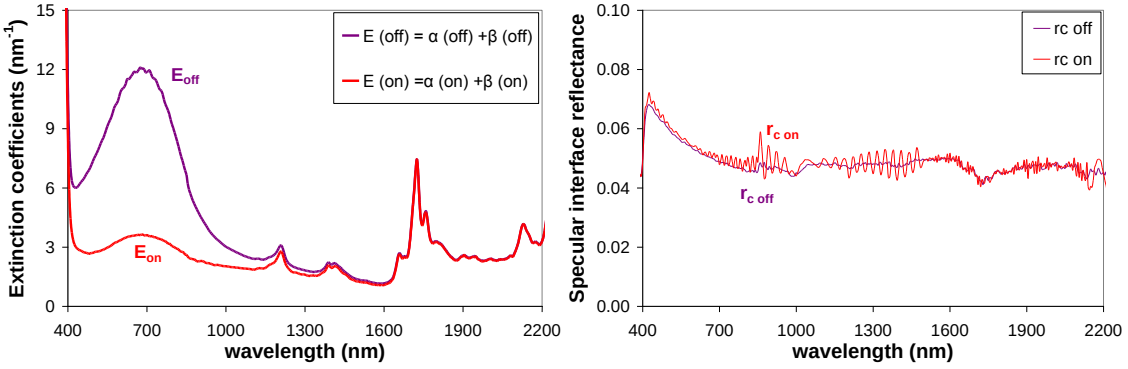

Figure IV.11: (left) Extinction (intrinsic absorption + scattering) coefficients and (right) specular interface reflectance r_c as a function of wavelength, for a SPD sample in the OFF and ON states.

IV.3.3.3.2 Two flux theory

Two flux model considers two collimated and diffuse (I and J) light beams [Lev05]. The scattering and absorption coefficients S & K are the extensive values. Equation IV.7 shows that downwelling intensity I is decreased by scattering and absorption and enhanced by upwelling intensity J backscattering. Equation IV.87 shows that upwelling intensity J is enhance by scattering and absorption and decreased by downwelling intensity I backscattering. Figure IV.12 shows a schematic of the two flux model.

$$\frac{dI}{dz} = -(S + K)I + S \cdot J \qquad \text{(Eq. IV.7)}$$

$$\frac{dJ}{dz} = (S + K)J - S \cdot I \qquad \text{(Eq. IV.8)}$$

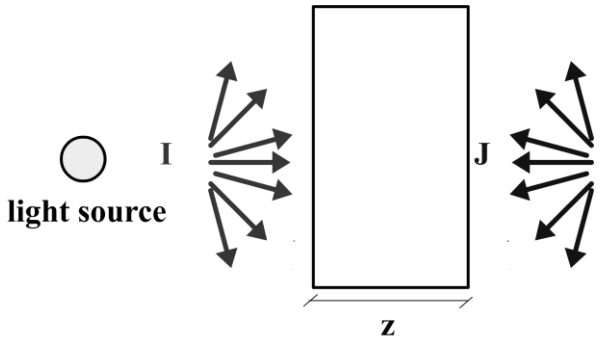

Figure IV.12: Two flux model. Downwelling (I) and upwelling (J) collimated and diffuse (total) intensities.

Two flux model developed by Levinson et al. obtain approximated values for T_{tot} and R_{tot}, assuming semi-isotropic diffuse light and equal value of ACP for diffuse and collimated light. This is an assumed error since in the SPD sample there is a mix of diffuse and collimated light. Since the relations between intrinsic and extensive scattering and absorption coefficients are [Var99]:

$$\beta = \frac{K}{ACP} \qquad \text{(Eq. IV.9)} \qquad \alpha = \frac{S}{ACP \cdot (1 - FSR)} \qquad \text{(Eq. IV.10)}$$

The relationship between intrinsic and extensive coefficients E= α+β = S+K is only true when ACP=1 and FSR=0, i.e. in a non scattering medium and when scattering is small and in a backward direction.

The Kubelka-Munk approximation is considered for R_{tot} and T_{tot} neglecting interface reflections are given by [Kub48 and MLG86] and assuming that incident light passes to a medium of the same refractive index (CRI standing for continuous refractive index):

$$R_{CRI} = \frac{1 - R_g (a - b\coth bS\delta)}{a - R_g + b\coth bS\delta} \qquad \text{(Eq. IV.11)}$$

$$T_{CRI} = \frac{b(1 - R_g)}{(a - R_g)\cdot \sinh bS\delta + b\cosh bS\delta} \qquad \text{(Eq. IV.12)}$$

Here R_g is the reflectance of the background, i.e. where the transmitted radiation exits the sample. Since no background is placed at the back interface, R_g is the interface reflectance due to the change of the refractive index between the sample and the surrounding medium [Mol99]. The derivation of these equations for R and T is detailed in Appendix A of the present work. The parameters a and b are given by:

$$a = 1 + \frac{K}{S} \qquad \text{(Eq. IV.13)} \qquad\qquad b = (a^2 - 1)^{1/2} \qquad \text{(Eq. IV.14)}$$

The change of the refractive index at the interfaces is considered by the Saunderson correction [Sau42].

Here S and K are the effective scattering and absorption coefficients defined in the two flux Kubelka-Munk (KM) model [Lev05]. In order to take into account the reflections at the front surface, it was used the procedure introduced by Saunderson [Sau42] for the "observed" reflectance and the correction procedure of Levinson [Lev05] for the "observed" transmittance:

$$R_f = \omega_i + \frac{(1 - \omega_i)\cdot(1 - \omega_j)\cdot R_{CRI}}{1 - \omega_j R_{CRI}} \qquad \text{(Eq. IV.15)}$$

$$T_f = \frac{(1 - \omega_i)\cdot T_{CRI}}{1 - \omega_j R_{CRI}}. \qquad \text{(Eq. IV.16)}$$

These corrections are due to the change in refractive index at the air-SPD interfaces in the model of the SPD sample. Here ω_i and ω_j denote the reflectance of the front interface to the incident light from the outside and from the inside of the layer, respectively. The parameter ω_i is the reflectance of the incident collimated light at the front interface and is equal to r_c. The parameters ω_j and R_g are approximated as described below. The parameter ω_j is the partly diffuse reflectance at the front interface to the radiation coming from inside the film. Specular radiation would exhibit a reflectance equal to r_c, while totally diffuse one would have a high reflectance (r_d) of 0.6 or even higher [Gio56] mainly because of total internal reflection at high angles. Hence the fractions of diffuse light at the interfaces of the film are derived from the optical measurements by the

methods developed in sect. 2.6 in Levinson [Lev05]. The following relations for the diffuse light fractions in the film at the top interface (q_δ) and at the bottom interface (q_0) were obtained after some algebra:

$$q_0 = \frac{(T_{tot} - T_{dir}) \cdot (1 - r_c)}{T_{tot}(1 - r_c) - T_{dir}(r_d - r_c)} \qquad \text{(Eq. IV.17)}$$

$$q_\delta = \frac{(R_{tot} - R_{spec}) \cdot (1 - r_c)}{R_{tot}(1 - r_c) - R_{spec}(r_d - r_c) + r_c r_d - r_c} \qquad \text{(Eq. IV.18)}$$

The calculations proceed as follows:

(1) The effective refractive index n of the films (Figure IV.13-left) is obtained from the collimated interface reflectance r_c (Figure IV.11-right) by means of Equation V.19 for perfectly collimated light:

$$r_c = \omega_{c,n_0 \to n_1} = \left(\frac{n_1 - n_0}{n_1 + n_0} \right)^2 \qquad \text{(Eq. IV.19)}$$

Here, n_0 and n_1 are the refractive index of the different layers. For downwelling (upwelling) light at the top (bottom) interface, n_0 is the refractive index of air and n_1 is the refractive index of SPD. For downwelling (upwelling) light at the bottom (top) interface, n_0 is the refractive index of SPD and n_1 is the refractive index of air.

(2) The diffuse interface reflectance r_d is computed by averaging the Fresnel reflection coefficients over all angles of incidence. Equations V.20 and V.21 [Lev05] are used to obtain the diffuse interface reflectance, which depends on whether the light is passing from a medium of low index to a medium of high index ($n_0 < n_1$), or vice versa ($n_0 > n_1$).

$$r_d = \omega_{d,n_0 \to n_1} = \begin{cases} f\left(\frac{n_1}{n_0}\right), & n_0 < n_1 \\ 1 - \left(\frac{n1}{n0}\right)^2 \left[1 - f\left(\frac{n_0}{n_1}\right)\right], & n_0 > n_1 \end{cases} \qquad \text{(Eq. IV.20)}$$

$$f(m)=\frac{1}{2}+\frac{(m-1)(3m+1)}{6(m+1)^2}+\left[\frac{m^2(m^2-1)^2}{(m^2+1)^3}\right]\ln\frac{m-1}{m+1}$$

being $$-\frac{2m^3(m^2+2m-1)}{(m^2+1)(m^4-1)^2}+\left[\frac{8m^4(m^4+1)}{(m^2+1)(m^4-1)}\right]\ln m \qquad \text{(Eq. IV.21)}$$

Figure IV.13-right shows the obtained diffuse interface reflectance for upwelling and downwelling light at the top and bottom interfaces of the sample SPD3 in OFF and ON states. Hence, diffuse interface reflectance $\omega_{d,0}^{j}$ is referred to the upwelling flux (j) at the bottom interface (z=0), $\omega_{d,0}^{i}$ is referred to the downwelling flux (i) at the bottom interface (z=0), and $\omega_{d,\delta}^{j}$ is referred to the upwelling flux (j) at the top interface (z=δ). Note that since the beam generated by the spectrometer is collimated, the downwelling flux (i) at the top interface (z=δ) interface reflectance $\omega_{d,\delta}^{i}$ is considered zero. The parameter r_d of Equations IV.17 and IV.18 are equal to the diffuse interface reflectances $\omega_{d,0}^{i}$ and $\omega_{d,\delta}^{j}$ with a value close to 0.6.

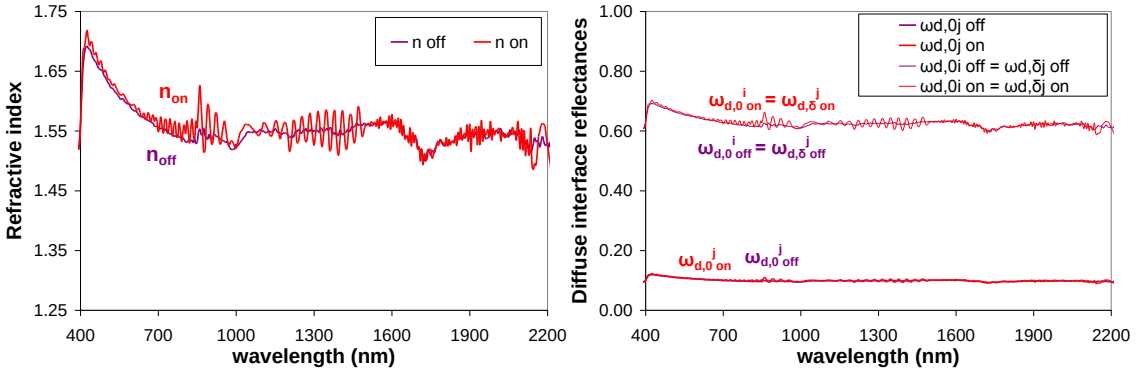

Figure IV.13: (left) Refractive index and (right) diffuse interface reflectances $\omega_{d,0}^{i}=\omega_{d,d}^{j}$ (upper curves) and $\omega_{d,0}^{j}$ (lower curves) for a SPD sample in the OFF and ON states.

Figure IV.14 shows a scheme of the interface reflectances at the top (δ) and bottom (0) interfaces for downwelling (I) and upwelling (J) light beams. The approximation was done neglecting the layers of glass and TCs. Note that for a constant value of the refractive index n=1.5 (instead of the fitted spectral value), values of r_c=0.04 and $\omega_{d,0}^{i}=\omega_{d,\delta}^{j}$=0.6 for collimated and diffuse interface reflectances for radiation coming from inside the film would be obtained. In case of considering more interfaces, without neglecting glass and TCs layers, partly diffuse upwelling light J at the bottom interface (0) should be considered, and hence its interface reflectance, which would be partly diffuse and different from r_c. For the case of SPD-air interface, with a constant refractive index n=1.5, $\omega_{d,0}^{j}$=0.09. For the present case, $\omega_{d,0}^{j}$ was spectrally calculated but not required to be used in the formulation

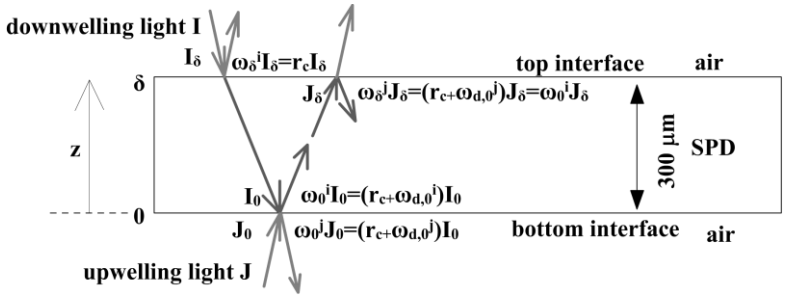

Figure IV.14: Scheme of the approximation used with downwelling and upwelling radiations at the top and bottom interfaces.

(3) The fractions of diffuse light close to the interfaces of the SPD sample are obtained from Equations IV.17 and IV.18 (Figure IV.15-left). The diffuse fraction of downwelling light striking the air-SPD interface at $z=\delta$ is $q_d^i=0$ because the spectrometer illuminates the SPD sample with a collimated light. The initially collimated beam generated by the spectrometer is partially diffuse when passing through a scattering medium such the sample SPD. Since the SPD-air interface preferentially reflects diffuse light, the upwelling light striking the SPD-air interface at the top of the SPD will be almost perfectly diffuse unless the scattering is very weak.

(4) The interface reflectances ω_j and R_g are obtained by averaging the specular and diffuse interface reflectances over the diffuse fractions by means of Equation IV.22. They are depicted in Figure IV.15-right for the SPD device in dark and clear states. It is realized that the light at the upper interface is mainly diffuse ($q_d^j \approx 1$) and that leads to a value of ω_j of the order of 0.6 to 0.7. At the bottom interface the light has a significant diffuse component in the visible range leading to quite large interface reflectance. However, the light is mainly collimated at wavelengths larger than 1200 nm, and R_g approaches r_c. I.e. at these wavelengths, the parameter R_g, which is the interface reflectance of downwelling light at the bottom interface of the SPD sample, is approximately equal to its collimated interface reflectance r_c, since the diffuse fraction q_0^i is closer to zero.

$$\omega_{n_0 \to n_1}(q) = (1-q) \cdot \omega_{c,n_0 \to n_1} + q \cdot \omega_{d,n_0 \to n_1} \qquad \text{(Eq. IV.22)}$$

The phenomenological scattering and absorption coefficients can now be readily obtained by numerical inversion of Equations IV.11 to IV.16. The values of S and K obtained from the best fits, for both ON and OFF states, are plotted in Figure IV.16-left.

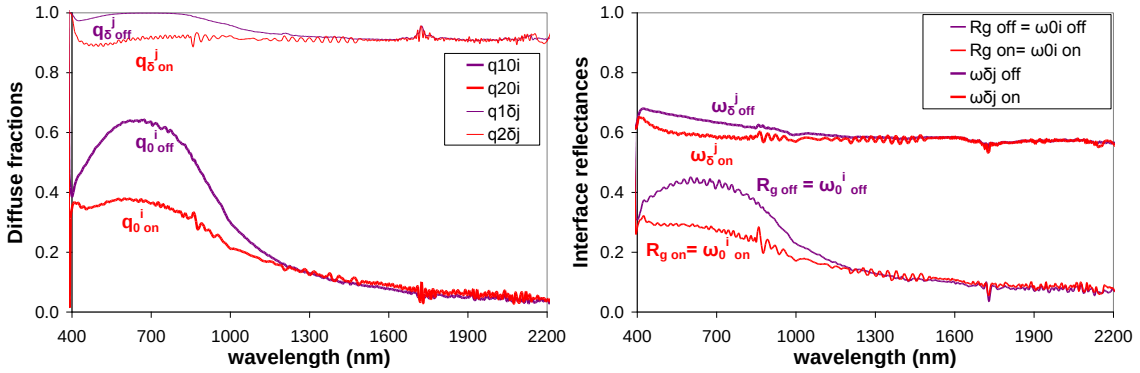

Figure IV.15: (left) Diffuse fractions q_0^i and q_δ^j and (right) interface reflectances ω_j (upper curves) and R_g (lower curves) for a SPD sample in the OFF and ON states.

The visible scattering coefficient S is very low when particles (or dipoles) are aligned with the applied field in the ON state and higher when dipole orientations are random in the OFF state. Figure IV.16-right shows the absorptance A of the SPD in OFF and ON states (computed as $A=1-R_{tot}-T_{tot}$) and the absorptance contrast observed between both states $\Delta A=A^{OFF}-A^{ON}$ While A^{OFF} and A^{ON} are referred to all the layers of the SPD device, i.e. including the glass, transparent conductor and SPD film, ΔA is only referred to the SPD layer, since no changes of A take place in the other layers between OFF and ON states. The absorption in the visible range is much higher in the OFF state as expected. It exhibits a pronounced peak at a wavelength of about 650 nm in both states. A peak in the mid-visible is a characteristic of the optical properties of polyiodide materials [LLi09]. The sharp structures in the NIR are probably related to absorption in the polymer matrix rather than the particles.

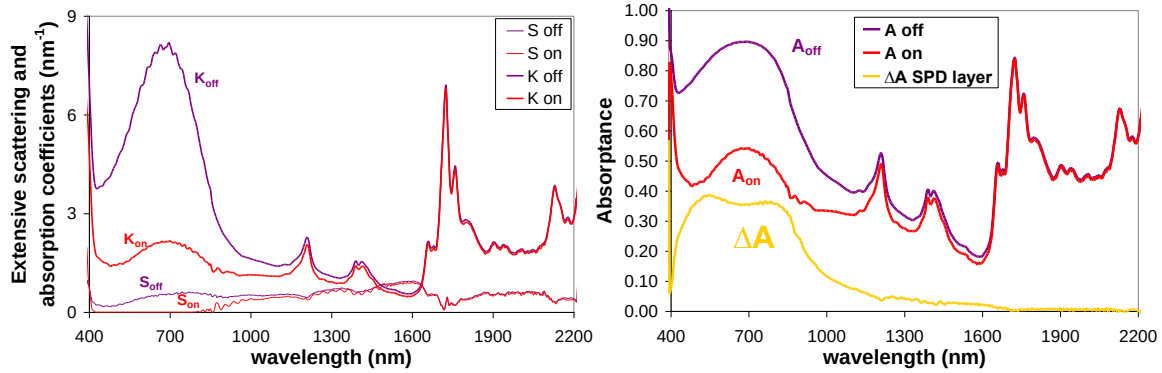

Figure IV.16: Extensive scattering (S) and absorption (K) coefficients at "on" and "OFF" states.

The procedure for fitting S & K of the SPD device could be also used in other materials. For instance, for solar absorbing paints. A previous work in this topic used Equations IV.11 and IV.15 only for R_{tot} component [Crn97]. However, some arrangements, such as a layer of the paint with the same thickness over glass than over aluminum would be needed since this procedure would also require transmittance components.

IV.3.3.3.3 Comparison of measurements with two flux computations

Because the two flux theory was used in this work considering several approximations, it is important to check its consistency with the measured R_{tot} and T_{tot} for the SPD3 device, serving also as a check on the consistency of the calculated values of S and K. Figure IV.17 depicts a comparison of our measured data with two flux computations for R_{tot} and T_{tot} in the ON and OFF states. A very good agreement is observed. The only discrepancy is a slight underestimation of the reflectance for the ON state in the visible wavelength range. The deviation from measured and fitted values is negligible in the visible wavelength when scattering coefficients have a negative small value (see Figure IV.16-left), which is not possible. The differences between R_{tot}^{ON} and R_f^{ON} could be due to:

- The K-M model applied to light that is partially collimated and partially diffuse tends to overestimate both (a) attenuation by absorption and scattering and (b) intensification by opposite-beam scattering [Lev05].
- The approximation of using an unique refractive index for all layers of the sample SPD, including the two external glasses, two transparent conductor layers, and the internal layer containing the suspended particles.

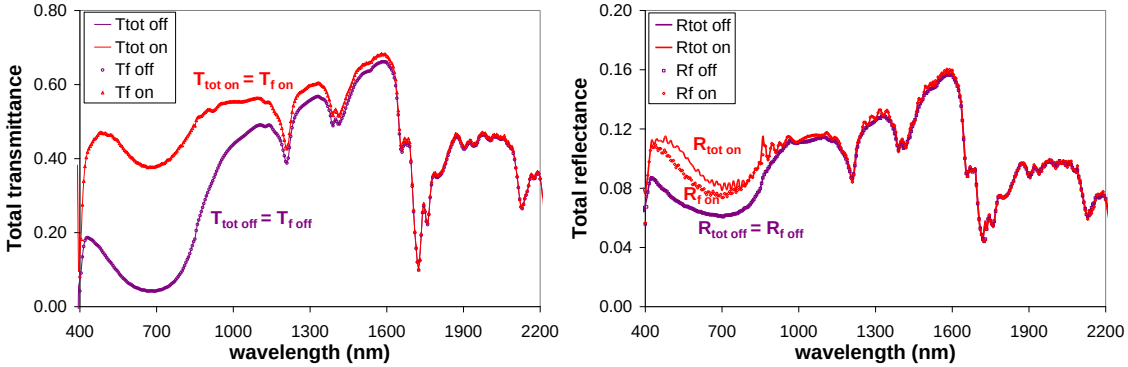

Figure IV.17: Total reflectance and transmittance from experiments compared to two-flux computations (T_f and R_f) using the parameters given in Figures IV.11 to IV.14.

Hence these calculations show an overall consistency of the two flux model, using our derived S and K parameters, with the experimental data.

IV.3.3.4 Luminous and solar integrated values of transmittances and haze

Solar and luminous transmittances are computed for the different levels of applied voltage, from 0 to 100 V_{peak} with 10 V steps in Figure IV.18. Solar transmittance is calculated using the solar irradiance spectrum (Figure II.1) for air mass 1.5 (the sun standing 37º above the horizon) [ASTM08]. Luminous transmittance is calculated using the eye sensitivity curve, which is the y curve of chromaticity 1931 coordinates (Figure I.1 and Figure II.2-right). Haze is a parameter that can be calculated from diffuse and total components of the transmittance as T_{diff}/T_{tot}.

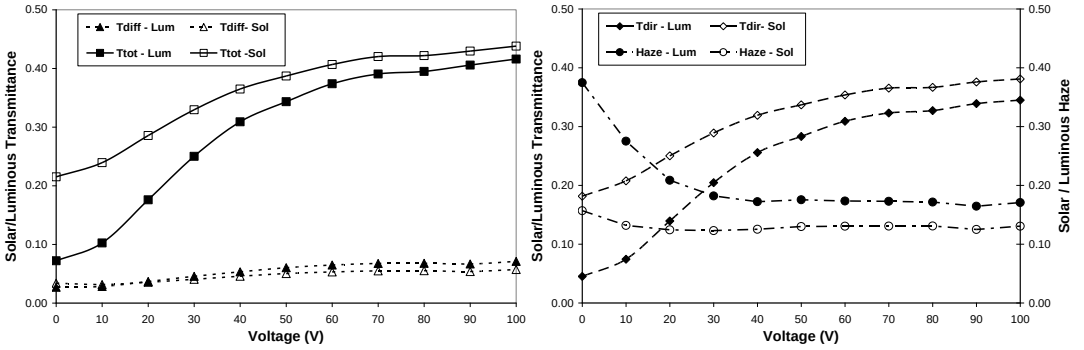

Figure IV.18: Voltage dependence of the luminous and solar values of the total and diffuse transmittance (left) and the haze and the direct transmittance (right).

IV.3.3.5 Predicted transmittance and reflectance computed backwards for different thicknesses of the internal active layer

Once obtained the values of *S* and *K* corresponding to the sample SPD3, the optical properties have been predicted for a variety of internal layer thicknesses δ of the sample SPD3, from 100 μm to 800 μm, in Figure IV.19. T_{dir}, and R_{spec} were calculated using r_c and E=(α+β). Ttot and Rtot were calculated using $\omega_i=r_c$, $\omega_j=r_d$ and R_g. T_{diff} and R_{diff} were calculated from T_{tot}-T_{dir} and R_{tot}-R_{spec}. Increments of T_{dir} and R_{spec} are observed when decreasing the thickness (Figure IV.19-up). For thinner thicknesses than 300 μm (actually the thickness of the SPD3 sample), a higher contrast of T_{dir} is observed at 200 μm, with higher values for OFF and ON states in the visible wavelength range. However, non desirable increments of R_{spec} are also observed, leading to a more transparent but also more reflective device. Regarding to R_{diff} and T_{diff} (Figure IV.19-center), there is an appreciable decrement of T_{diff} at 200 μm accompanied with the increment of the R_{diff}, aggravating the haze of the SPD3 which could appears as a diffuse mirror-like. R_{tot} and T_{tot} show a clear decrement at the visible range for thicker devices (Figure IV.19-down).

Figure IV.20 shows thickness dependence of the luminous (up) and solar (down) integrated values of transmittance (left) and reflectance (right) in both OFF and ON states, computed from the expected T_{tot}, T_{dir} and T_{diff} and R_{tot}, R_{spec} and R_{diff} components of Figure IV.19 obtained from the calculated S & K coefficients of Figure IV.16-left. For a better visualization between OFF and ON states, Figure IV.21 shows the luminous and solar transmittance (left) and reflectance (right) contrast. Although the maximum ΔT_{tot} and ΔT_{dir} are observed for 200 μm thickness (for both luminous and solar parameters), the undesired high value of $R_{tot,lum}$ for this thickness value (Figure IV.20-righ-up) of 9.5% and 10.7% for OFF and ON states respectively, can be decreased to 7.9% and 9.7% when increasing the thickness to 300 μm. Another relevant parameter in order to choose the optimum thickness is the haze (Figure IV.22), for both transmittance (left) and reflectance (right), as a ratio between the diffuse and the total component.

Thus, the best thickness could be thought to be 200 µm, since luminous transmittance haze should be decreased with a slight increment of the reflectance as a drawback.

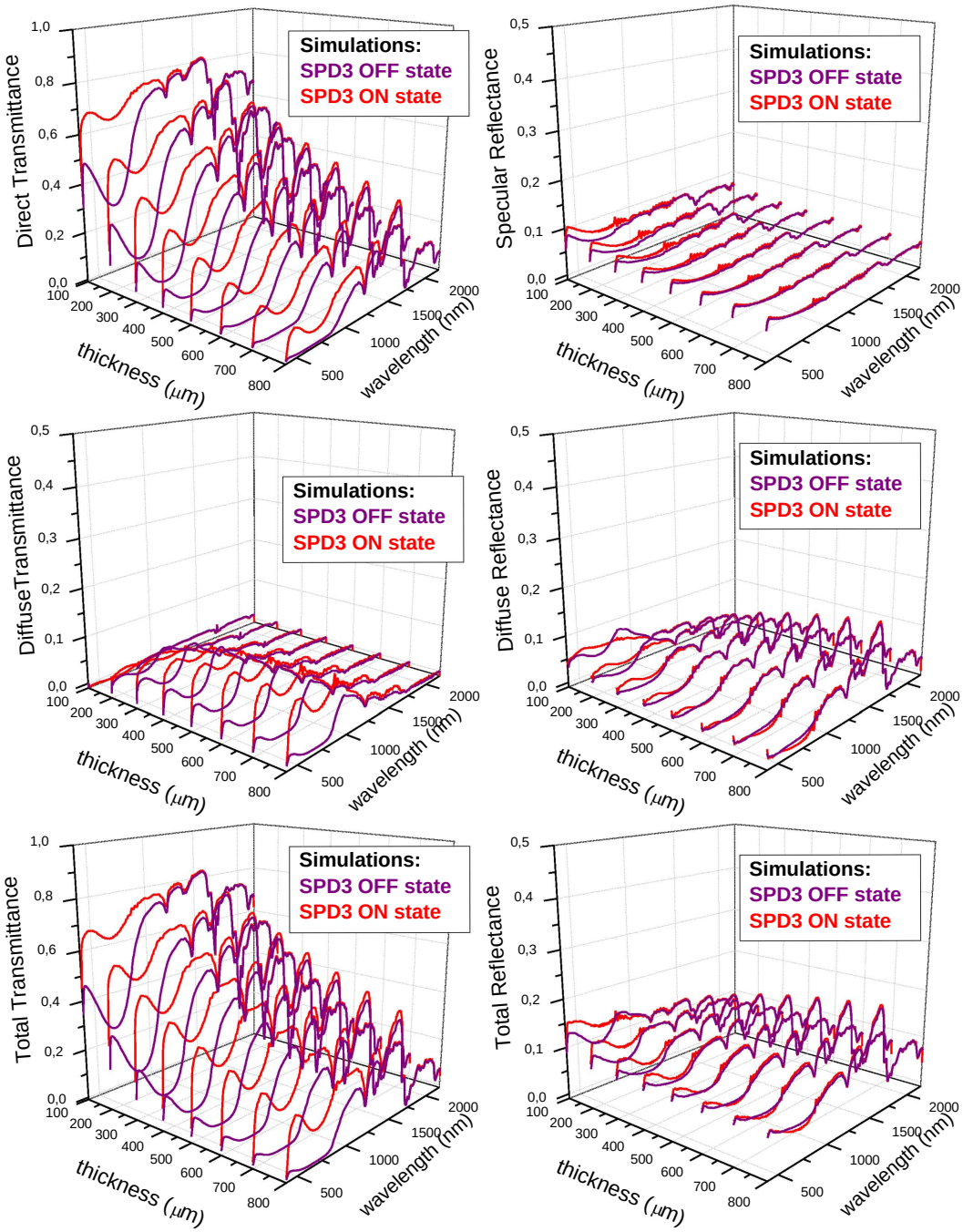

Figure IV.19:"Observed" transmittance (left) & reflectance (right) of sample SPD3 simulated for different thicknesses. (up) Direct T & Specular R, (center) Diffuse T & R and (down) Total T & R.

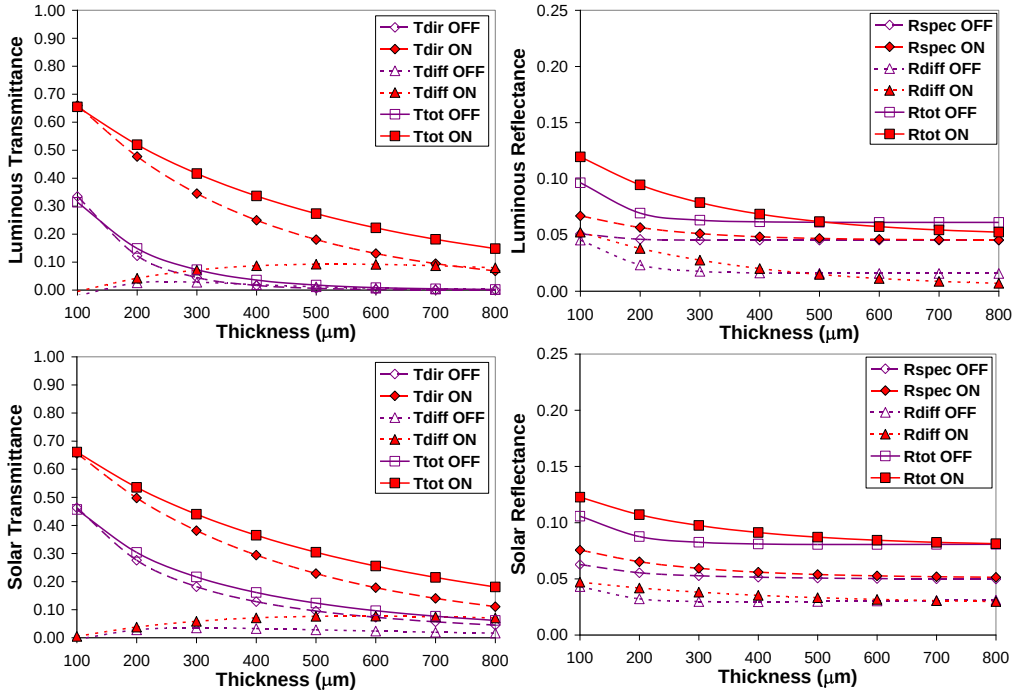

Figure IV.20: Thickness dependence of luminous (up) and solar (down) of expected transmittances (left) and reflectances (right) derived from the calculated scattering S and absorption K coefficients.

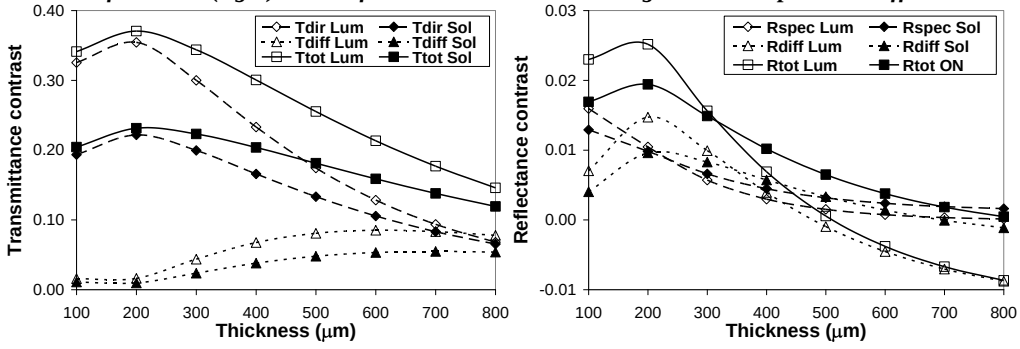

Figure IV.21: Thickness dependence of luminous and solar transmittance (left) and reflectance (right).

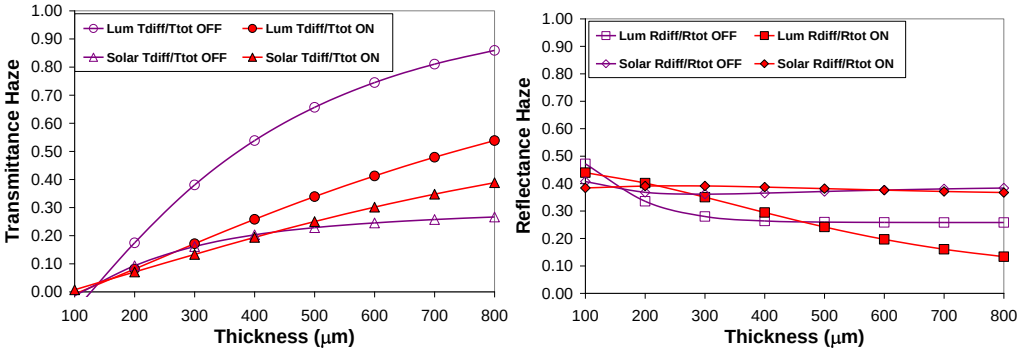

Figure IV.22: Thickness dependence of luminous and solar transmittance (left) and reflectance (right) haze.

IV.3.4 Comparison of the three SPD samples

Figure IV.23 shows a plot comparing the optical spectrums of the direct transmittance observed for the three characterized SPD samples for different amplitudes of the feeding signals supplied by different instrumentals: SPD1 from 0 to 220 V supplied using a variac (Figure IV.4-up), SPD2 from 0 to 120 V supplied using the set-up consisting of a FPGA + actuator, with ten levels (Figure IV.4-down), and SPD3 from 0 to 100 V supplied using a function generator and a linear amplifier (Figure IV.8). Figure IV.24 shows the CIE 1931 chromaticity diagram for each SPD sample in the different levels of coloration. Note the bluish coloration of the SPD samples in the darken state without applied voltage, which changes to a close to white chromaticity uncolored bleached state. In a three dimensional view of these CIE 1931 xy plots, imaging an axis perpendicular to the paper plane, a quasi-cone shaped with a black peak (for a luminance of 0%) would be placed at the deepest down peak, being the colors of the diagram observed at the base of the quasi-cone placed at the top plane of the paper (for a luminance of 100%). Since luminance is lower in the darken state than in the bleached state, the plots should be interpreted as a deeper darkness at 0 V than the obtained when the voltage is applied.

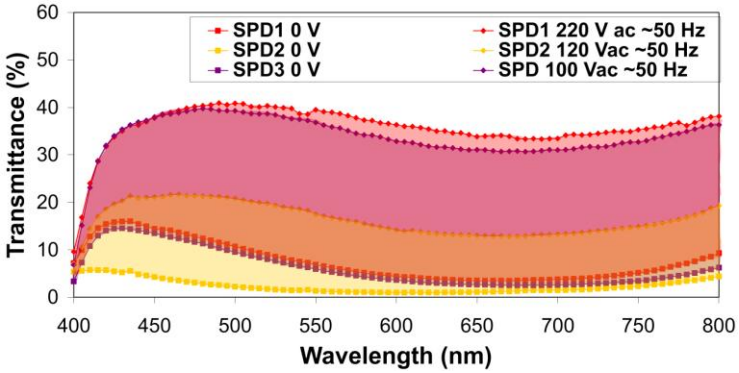

Figure IV.23: Spectral transmittance for samples SPD1, SPD2 and SPD3 showing different contrast.

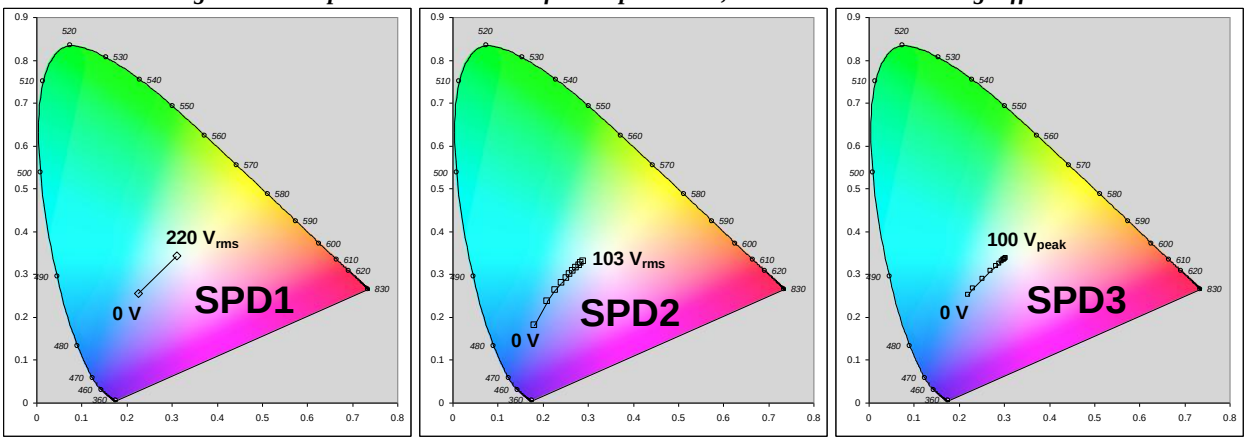

Figure IV.24: CIE 1931 color space chromaticity diagram for 2 degree observer and D65 illuminant for the samples SPD1 (left), SPD2 (center) and SPD3 (right) in both darken and bleached states [Bar07].

Figure IV.25 shows a simulated appearance of the three samples SPD1, SPD2 and SPD3 for the different applied voltages. Colors are obtained from the CIE chromaticity coordinates and the conversion matrix from XYZ to RGB values. An average value for the transparency has been calculated over the human eye sensitivity curve in order to simulate the different levels of transparencies observed.

Figure IV.25: Simulated appearance of the samples SPD1, SPD2 and SPD3 for different levels of applied voltage over a photograph of the Mosque of Cordoba at the background.

Figure IV.26 shows the differences between the measured T_{tot} using Perkin Elmer Lambda 900 (each 5 nm, but sampled to each 25 nm) and the measured at 0º of angle of incidence using the angle dependence spectrometer setup of section II.1.4, for 0, 50 and 100 V applied to sample SPD3. These differences have been taken into account for simulation of the optical appearance in Figure IV.27 of the SPD3 sample at different angles of incidence (from transmittance data of Figure IV.9). A correction factor was also considered since the RGB and T_{lum} values are derived from T_{dir}, and not T_{tot}. Spectral transmittances were also measured at different wavelength steps, 5 and 25 nm.

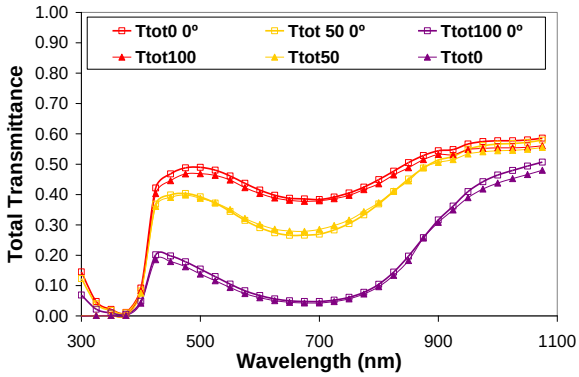

Figure IV.26: Differences between total transmittance measured with Perkin Elmer Lambda 900 and the angle dependence spectrometer setup at 0º of angle of incidence, for 0, 50 and 100 V applied.

Figure IV.27: Simulated appearance of the sample SPD3 for 0, 50 and 100 V_{peak} applied voltage at different angles of incidence (Figure IV.9), from 0 to 60º with 15º steps, over a photograph of the Mosque of Cordoba at the background.

Figure IV.28 shows the simulation of the SPD3 sample in both OFF and ON states from the expected T_{dir} for different thicknesses of the internal layer from 100 to 800 μm, (Figure IV.19-up-left). Decreasing from 300 μm, the fabricated thickness, results into a more transparent bleached and darken states. On the contrary, increasing the thickness, more opaque states are achieved. From these plots, the optimum thickness for higher contrast is visually between 200 and 300 mm, as it was concluded from Figures IV.20, IV.21 and IV.22. Reflectance and scattering of the SPD3 sample have been neglected for these simulations and those of Figures IV.25 and IV.27.

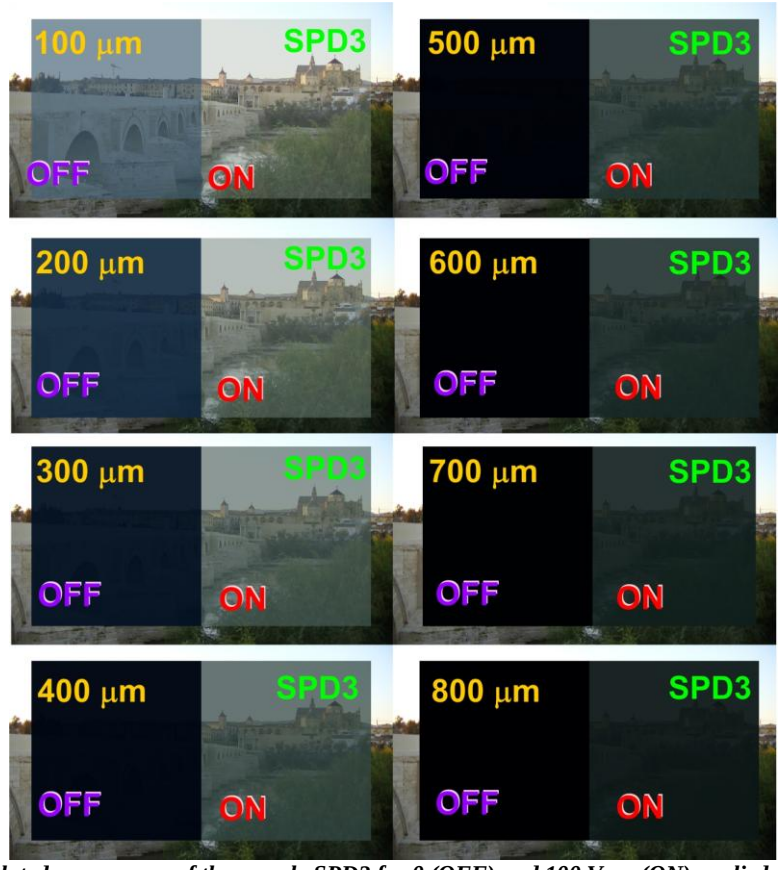

Figure IV.28: Simulated appearance of the sample SPD3 for 0 (OFF) and 100 V_{peak} (ON) applied voltage for the different thicknesses, from 100 to 800 μm (Figure IV.19-up-left), over a photograph of the Mosque of Cordoba at the background.

IV.4 Impedance characterization

Impedance spectroscopy is the main tool used to obtain information about the electrical response of this kind of device. According to the structure of the sample SPD, the EEC model that can reproduce electrical behavior of the sample SPD2 in real operation conditions is supposed to be based on a regular Randles cell but including a diffusion Warburg impedance in series with the parallel charge transfer resistance Rct [Ver07b, Ver08c, Ver08d].

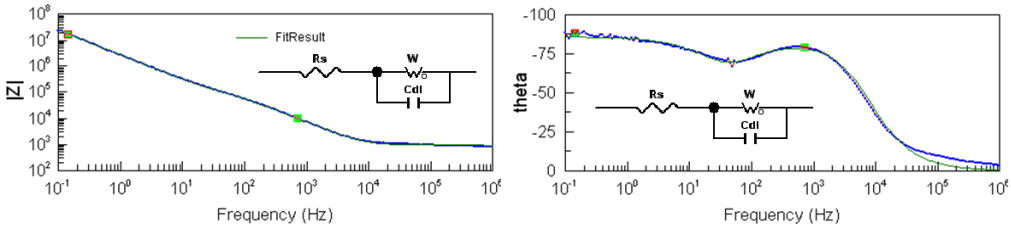

Figure IV.29: Bode plots of the magnitude |Z| in Ω (left) and phase theta in degrees (right) of the impedance (solid lines) and best fitting (dashed lines) for the proposed EEC model of the sample SPD2 (insets).

The proposed EEC model made for our test SPD samples is shown in Figure IV.29, inset. Each electrical element accounts for some parameter involved in the fabrication of the SPD samples: even being not shown since it was suppressed in the final EEC model proposed, the resistance (Rct), in the EEC model reflects the charge transfer insertion reaction, and is paired in parallel with a capacitor that stands for the double-layer capacitance (Cdl) associated with the interfaces between charged zones. These elements are the main parts of the usual Randles circuit. The resistance (Rs) usually corresponds to the resistive effect of electrical contacts and it is in series with the rest of the set. But there is also a diffusion of charges in our devices, and hence a Warburg impedance (W) should be added in series with Rct. As it can be observed, Rct was suppressed in the analysis because of its poor results in comparison with the rest of the components in the EEC: errors in Rct higher than 100% in the fit, and variations under 1% in the rest of the components if Rct is suppressed, lead to its elimination. The Warburg impedance thus absorbs the charge transfer resistance effect. Cdl is transformed into a simple capacitor.

Physico-chemical considerations lead us to interpret Rs as the resistance of the contacts-droplets set, Cdl as the capacitance formed by the contacts-emulsion set, and W–R, W–T and W–P as the parameters involved in the charge movement inside the droplets. Cdl is, therefore, a simple capacitance because the device is as simple as that from a global electrical point of view. The analysis of the parameters retrieved by fitting the impedance measurements to this circuit through an inversion least-squares method can serve as a way to make a manufacturing feedback improving process. Figure IV.29 shows a plot of the magnitude and phase impedance. The decay in magnitude, mainly logarithmic for low frequencies, and the phase curling around -90º, shows a clear

capacitive effect coming from the Cdl capacitance. Nevertheless, the clearly bi-lobular phase shape also shows the effect predicted by the Warburg element.

The fitted data for this device have the magnitudes (data and errors) shown in Table IV.2. W–R, W–T and W–P are parameters of the Warburg impedance element, a resistance, time constant and power exponent respectively, as it was seen in Chapter II. Warburg impedance stands for diffusion of charges; W–R is the electrical resistance seen by these charges, W–P is near 0.5 for a finite element, and W–T is dependent on effective diffusion thickness and the effective diffusion coefficients of the particles. Errors in retrieved parameters are not higher than 4%. This is a permissible error, because components used in electronic driving circuits usually have tolerances of 5%, and power consumptions that can be computed with these data can reach up to an 8% error. Thus, the model can be considered as consistent with the acquired experimental data.

Equivalent Circuit	Rs	Cdl	W-R	W-T	W-P
Values	919 Ω	20.5 nF	401610 Ω	0.013 s	0.465
Errors (%)	0.5	0.7	3.3	4.2	0.4

Table IV.2: Best fitting values and mean relative errors for the proposed EEC model for the SPD2.

A capacitance of 21.8 nF was obtained by using a LCR 400 Precision LCR Bridge of Thurlby Thandar Instruments, being this value very close to the double layer capacitance Cdl retrieved by this fitting. Figure IV.28 shows a plot comparing the impedance measured over the three SPD samples. The measurements were carried out by using Solartron 1260 (the one available at the lab of the Ångström Laboratory of Uppsala for sample SPD3 and the one available at the lab of GDAF-UC3M for sample SPD2) and Hewlet Packard 4194A (for sample SPD1, since the sample stopped the optical switching before the impedance analyzer Solartron 1260 was available at the lab of GDAF-UC3M). The magnitude plot (Figure IV.30-up) shows two inset plots as a zoom in order to appreciate the behavior for different frequencies ranges from 100 mHz to 1 MHz for samples SPD2 and SPD3, and from 100 Hz to 1 MHz for sample SPD1. The comparison of the results of the three samples (SPD1, SPD2 and SPD3) shows a similar impedance magnitude and phase but different optical behavior. A 35% of ΔT_{600nm} is observed in Figure IV.23 for the sample SPD3, with a lower potential applied, of 100 V_{peak} (a 32% for sample SPD1 with the maximum potential applied of 220 V_{rms}). Due to the similarity of the electrical impedance of the three SPD samples studied, it could be concluded that the sample SPD3, supplied by CIDETEC, shows better optical transmittance contrast with lower potential consumption.

Figure IV.31-left shows the simulated diffusion Warburg impedance from the fitted parameters of Table IV.2 (Wo-R, Wo-T and Wo-P). At 50 Hz, the frequency of operating, the phase is -44º and the magnitude is 189 KΩ. The higher frequencies show lower impedance, which should favored the bleached state. However, as it will be seen

in next figures, no appreciable improvement of the transmittance contrast is achieved by increasing the frequency of the applied AC signal.

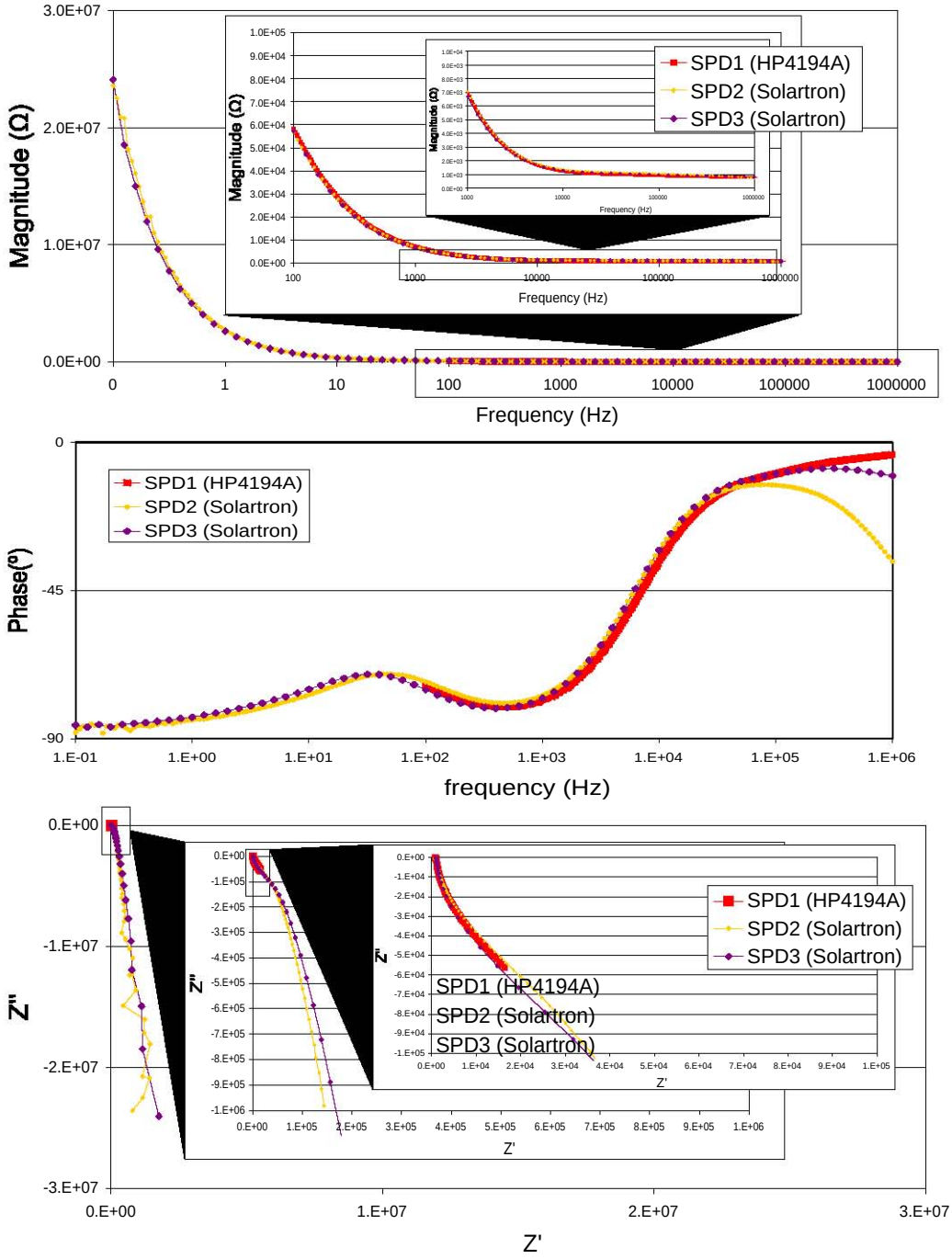

Figure IV.30: Results of 3 SPD samples: Impedance Bode magnitude (up) and phase (center) plots and Nyquist plot (imaginary versus real parts) (down).

IV.5 Power consumption

Figure IV.31-right shows the relation between T_{600nm}, electrical current drawn and applied RMS voltage to the SPD device. The electrical current through the device was less than 700 µA rms. The maximum value was measured for the clear state.

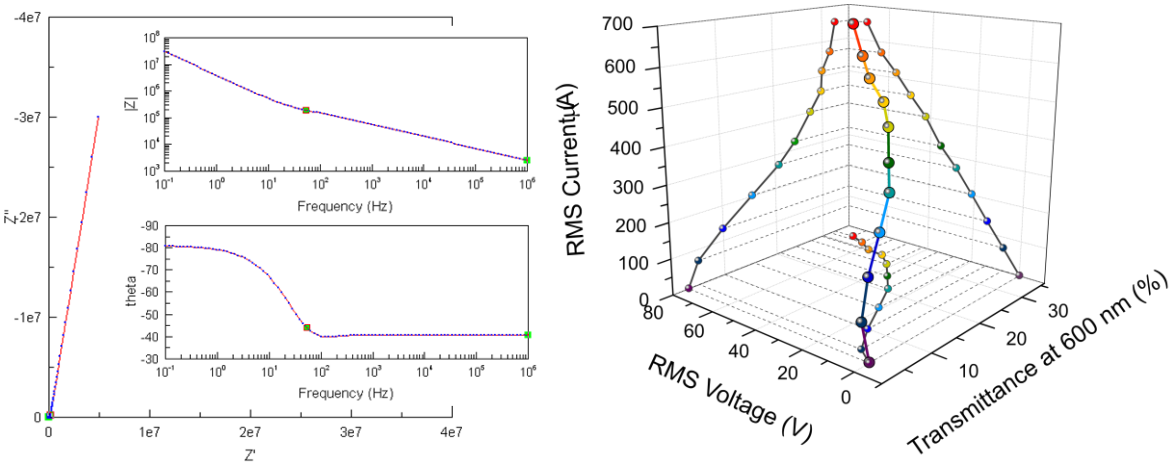

Figure IV.31: (left) Nyquist and Bode magnitude and phase impedance of the simulated Warburg impedance Wo from fitted parameters of Table IV.2 (Wo-R, Wo-T and Wo-P). (right) Electrical current and T_{600nm} for the different applied voltage levels to the SPD3 device.

IV.6 Operation at different frequencies

Finally, transmittance spectra and T_{600nm} were measured on the sample SPD3 using the spectrophotometer based on a monochromator available at GDAF-UC3M for 100 V_{peak} at different frequencies, higher than 50 Hz, with the electrically feeding system based on the function generator and the linear amplifier, in order to observe if some improvements in the transmittance contrast could be achieved. However, no appreciable changes with respect to the 50 Hz frequency applied were seen. Undesired oscillations were observed for frequencies higher than 1 kHz (Figure IV.32).

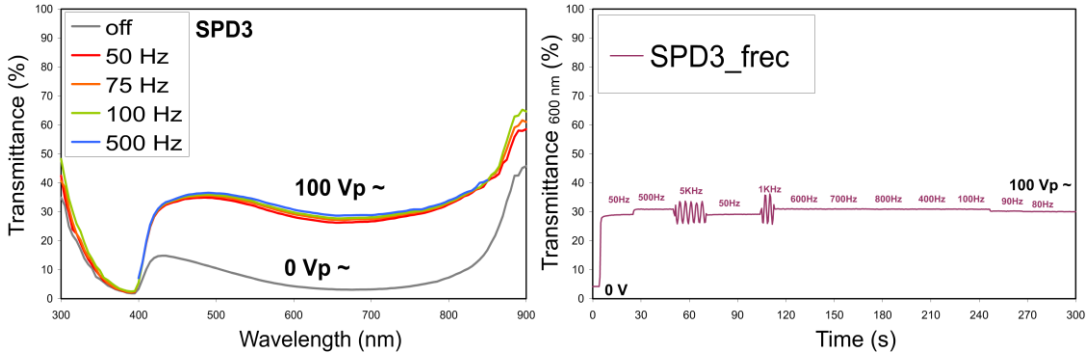

Figure IV.32: (left) Optical spectral transmittance of the SPD3 for 100 V_{peak} applied and different frequencies, from 50 to 500 Hz, sinusoidal signals. (right) T_{600nm} for 100 V_{peak} and different frequencies from 50 to 5 kHz to the SPD3.

IV.7 Conclusions

Three SPD samples were electro-optically characterized, showing different optical appearance for darken and bleached states when applying 50 Hz AC sinusoidal voltage signals with different amplitudes. Optical transmittance was seen to be independent of frequencies of the applied voltage higher than 50 Hz. The samples behave different than the expected by the datasheet, regarding the amplitude of the feeding signal. Different transmittance contrast were observed for the three samples, which also show different darken OFF states without applied voltage. The sample SPD2 shows the darkest OFF state and the lowest transmittance contrast (ΔT_{lum}=13.18%, $T_{lum\text{-}0V}$=3.16% and $T_{lum\text{-}103Vrms}$=16.34%). The samples SPD1 and SPD3 show approximately the same transmittance contrast (ΔT_{lum}=30%) with different applied voltage signals, being the luminous transmittance in both darken and bleached states $T_{lum\text{-}0V}$=6.80% and $T_{lum\text{-}120Vrms}$=36.80% for sample SPD1and $T_{lum\text{-}0V}$=4.51% and $T_{lum\text{-}100Vpeak}$=34.50% for sample SPD3. The different optical behavior between the samples SPD3 and SPD1, with a 30% of transmittance contrast, and the sample SPD2, with a 13%, could be caused by a different concentration of the suspended particles of the active layer. Thus, the concentration of suspended particles in the sample SPD2 should be larger, leading to a darker appearance and lower transmittance contrast.

A new method for deriving the optical scattering and absorption coefficients, based in two-flux and collimated equations of four-flux models, was developed and applied to the SPD3 sample measurements. The method use fittings by least squares for achieving the refractive index of the SPD film. Then, interface reflectance of each layer is spectrally determined by computing the diffuse fractions of light at the top and bottom interfaces. A correction due to the refractive index discontinuities is also applied. Extensive scattering and absorption coefficients are derived by fittings to total components of the measured transmittance and reflectance. The expected direct and diffuse transmittances and specular and diffuse reflectances for different thicknesses of the internal active layer can be computed from the scattering and absorption coefficients. The optimum thickness of the film for a determined optical behavior can be predicted. The method can be applied to any scattering surface.

References

[Bar07b] D. Barrios, R. Vergaz, J.M.S. Pena, P. Contreras, J.C. Torres, "Control de cromaticidad de dispositivos de particulas suspendidas", en actas de VIII Congreso Nacional de Color, Madrid (Spain) (2007).

[Bar09] David Barrios, Ricardo Vergaz, José Manuel Sánchez-Pena, Gunnar Niklasson, Claes Göran Granqvist, "Diffuse optical reflectance and transmittance spectra of a suspended particle device", 6ª Reunión Española de Optoelectrónica, Málaga (Spain) (2009).

[Bar12b] David Barrios, Ricardo Vergaz, Jose M. Sánchez-Pena, Claes G. Granqvist, Gunnar A. Niklasson, "Towards a quantitative model for suspended particle devices: Optical scattering and absorption coefficients", Solar Energy Materials and Solar Cells (in press).

[Cha02] S. Chakrapani, S.M. Slovak, R.L. Saxe, B. Fanning, SPD films and light valves comprising same, Research Frontiers-US Patent 6416827, 2002. See /http://www.patentstorm.us/patents/6416827-description.html.

[cri] http://www.cricursa.com

[Crn97] Zorica Crnjak Orel, Marta Klanjsek Gunde, Boris Orel, "Application of the Kubelka-Munk theory for the determination of the optical properties of solar absorbing paints", Progress in Organic Coatings 30 (1997) 49-66

[Cur02] F. Curiel, W.E. Vargas, R.G. Barrera, "Visible spectral dependence of the scattering and absorption coefficients of pigmented coatings from inversion of diffuse reflectance spectra Applicability conditions of the Kubelka-Munk theory", Applied Optics 41 (2002) 5969-5978.

[Gio56] R.G. Giovanelli, "A note on the coefficient of reflection for internally incident diffuse light", Optica Acta 3 (3) (1956) 127-130.

[Kah09] B Kahr, J. Freudenthal, S Philips, W Kaminsky, "Herapathite", Science 324 (2009) 1407.

[Kno09] K.M. Knowles, "Commentary: Herapathite – the first man-made polarizer", Philosophical Magazine Letters, 89 (2000) 745-755.

[Kub48] P. Kubelka," New contributions to the optics of intensely light-scattering materials. part I.", Journal of the Optical Society of America 38 (1948) 448-457.

[Lev05] Ronne Levinson, Paul Berdahl, Hashem Akbari, "Solar spectral optical properties of pigments – Part I: model for deriving scattering and absorption coefficients from transmittance and reflectance measurements", Solar Energy Materials & Solar Cells 89 (2005) 319-349.

[LLi09] Lei Liang, Paul Rulis, Bart Kahr, W.Y. Ching, "Theoretical study of the large linear dichroism of herapathite", Physical Review B80, 235132-1-5 (2009).

[Nos99] P. Nostell, A. Roos, D. Ronnow, D. Ronnow, "Single-beam integrating sphere spectrophotometer for reflectance and transmittance measurements versus angle of incidence in the solar wave length range on diffuse and specular samples", Review Of Scientific Instruments 70 (1999) 2481-2494.

[MLG84] B. Maheu, J.N. Letoulouzan, G. Gouesbet, “Four-flux models to solve the scattering transfer equation in terms of Lorenz-Mie parameters”, Applied Optics 23 (1984) 3353-3362.

[MLG86] B. Maheu and G. Gouesbet, “Four-flux models to solve the scattering transfer equation: special cases”, Applied Optics 25 (1986) 1122-1128.

[Mol99] Molenaar R, ten Bosch JJ, Zijp JR., "Determination of Kubelka-Munk scattering and absorption coefficients by diffuse illumination." Applied Optics 38(10) (1999) 2068-77.

[Sau42] J.L. Saunderson, “Calculation of the color of pigmented plastics”, Journal of the Optical Society of America 32(12) (1942) 727-736.

[RFr] http://www.refr-spd.com/

[Rod00] J. Rodriguez, M. Gomez, J. Ederth, G.A. Niklasson, C.G. Granqvist, “Thickness dependence of the optical properties of sputter deposited Ti oxide films”, Thin Solid Films 365 (2000) 119-125.

[Sax03] Robert L. Saxe, Barry Fanning, Steven M. Slovak, Robert I. Thompson, Jean Thompson, "Polyhalide particles and light valves comprising same", US patent No. 6517746 (2003).

[Tak97] H. Takeuchi, A. Usuki, N. Tatsuda, H. Tanaka, A. Okada, K. Tojima, Material Research Society Symposium Proceedings 424 (1997) 317-322.

[Var97a] William E. Vargas and Gunnar A. Niklasson, “Applicability conditions of the Kubelka-Munk theory”, Applied Optics 36 (1997) 5580-5586.

[Var97b] William E Vargas and Gunnar A Niklasson, "Forward-scattering ratios and average pathlength parameter in radiative transfer models", Journal of Physics: Condensed Matter 9 (1997) 9083–9096.

[Var98] William E. Vargas, “Generalized four-flux radiative transfer model” Applied Optics 37 (1998) 2615-2623.

[Var99] William E. Vargas, “Two-flux radiative transfer model under nonisotropic propagating diffuse radiation”, Applied Optics 38(7) (1999) 1077-1085.

[Ver08c] R. Vergaz, J.M.S. Pena, D. Barrios, I. Perez, J.C. Torres, “Electrooptical behaviour and control of a suspended particle device”, Opto-electronic review 15(3) (2008) 154-158.

[Ver08d] R. Vergaz, J.M.S. Pena, D. Barrios, C. Vazquez, P. Contreras-Lallana, “Modelling and electro-optical testing of suspended particle devices”, Solar Energy Materials and Solar Cells 92 (2008) 1483-1487.

[WuQ89] Wu Qi Hong, “Extraction of extinction coefficient of weak absorbing films from special absorption”, Journal of Physics D: Applied Physics 22 (1989) 1384-1385.

Chapter V: Polymer dispersed liquid crystals (PDLCs)

As it was seen in Chapter I, PDLC devices consist of a thin film of a polymer matrix containing micro-sized droplets of a LC. In order to fabricate PDLC devices, the mixture is usually laid between two transparent substrates coated with a conductive layer, usually of ITO [DKY06]. Previous works of GDAF group on PDLC devices can be found in electro-optic applications such as smart windows [San02] or variable optical attenuators (VOAs) [Jur05]. Other applications of PDLCs, such as projection displays, have been also been found in the literature [Cro90]. As it was described in Chapter I, PDLC technology principle is shown in Figure V.1. When no voltage is applied (OFF state), the LCs are arranged in random orientations and tend to scatter light, so that the glass panel looks translucent. The LC dipoles align and let light pass when an AC potential signal is applied (ON state). The refractive index of the isotropic polymer and the ordinary refractive index of the LCs are similar [Ram03 and Drz95]. This is the normal mode of operation of PDLC devices. PDLC devices with a reverse mode of operation, i.e., transparent state is obtained without applied potential (OFF state) which becomes translucent when applying an AC potential signal (ON state), were also developed. Capabilities of EC and PDLC devices have been combined in a new tandem device (Figure V.2). A glass with conductor on both sides is used as support to one EC viologen device on one side, and a PDLC device on the other one.

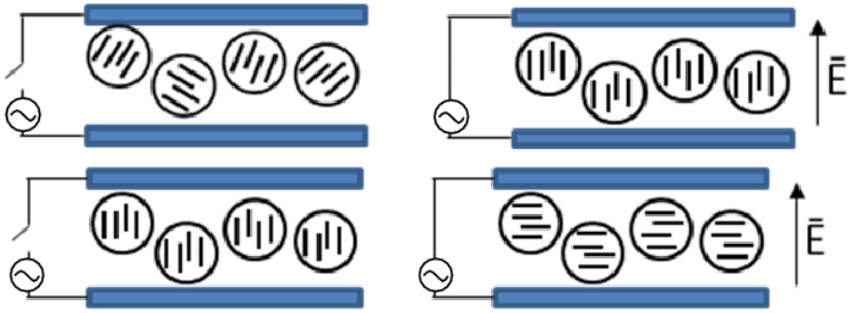

Figure V.1: Liquid crystals orientation in PDLC technology for both operation modes [Bar10]. (up) Normal mode: (left) Translucent OFF state (right) transparent ON state. (down) Reverse mode: (left) Transparent OFF state (right) translucent ON state.

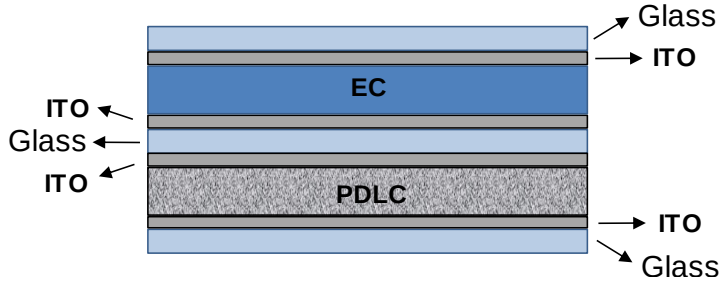

Figure V.2: Tandem device manufactured. Glasses coated with ITO are supports [Bar10]. The inner glass is covered with ITO on both sides. Viologen EC mixture at the top and PDLC at the bottom of the device.

A full optical and impedance characterization has been made, to extract two equivalent circuits for both parts of the device. Selecting the suitable frequency range for the operation of PDLC devices is a matter of simplifying their response. A low frequency electric field can induce degradation of the LC material due to the adsorption of ion charges and generation of strong electric field on the electrode layers [Thu84 and Per96]. The main applications could be found on smart windows on buildings, cars or planes, adding privacy and in some cases illumination control (depending on the values of T_{tot} in both OFF and ON states respectively).

Reverse mode PDLC (RM_{PDLC}) devices:

Reverse mode PDLC (RM_{PDLC}) devices are of interest in some applications, such as windows, where most of the time they are required to be in the transparent state [YDM90]. RM_{PDLC} devices are constructed by using LCs with negative dielectric anisotropy, which tend to orient perpendicular to the electric field in the ON translucent state. The initial homeotropic alignment of normal mode PCLC (NM_{PDLC}) devices (Figure V.1-up-left) can be achieved polymerizing the matrix while applying to the cell either a magnetic field [Nic99] or another force field in order to suitably align the LC directors. A method for preparing RM_{PDLC} devices without forcing the initial homeotropic alignment and using LC with positive dielectric anisotropy has been described in the literature. However, it requires the use of a LC polymer matrix and a planar pre-alignment of the material employing rubbed surfaces or dual frequencies of operation [Yam97 and Mac00]. Using the same composition in both, NM_{PDLC} and RM_{PDLC} devices, and a LC with positive dielectric anisotropy, a different degree of scattering in the OFF state was achieved by modifying the polymerization conditions. A possible explanation to the behavior of the RM_{PDLC} devices could be the high LC content [Hik90]. On the other hand, using LC with negative dielectric anisotropy, a self-adjusting light control PDLC device was developed by aligning homeotropically the LCs by means of a rough surface [Cup09]. The mixture also contains a dispersion of photoconductive molecules in ionic liquid. Applying an electric field just below the threshold one, the LC molecules can be reoriented scattering the incident light and switching the RM_{PDLC} device towards the translucent state.

Tandem EC – PDLC device:

Some attempts to join PDLC and EC technologies in a single device are found in the literature, being its interest the mixed control of privacy and illumination in a single device and in some cases the custom control of heat transmission by the right election of the EC material. The efforts in this research have been made mainly by the group of Chidichimo and coworkers. The first attempt tried to use a PDLC device that hosted viologen EC molecules [Nic05], obtaining variations between 10 and 40% in transmittance at 632.8 nm by the EC molecules and 0 to 80% by PDLC structure. Nevertheless, a PDLC needs high AC voltage and EC needs low DC voltage to switch. Since LC devices tend to degrade with DC voltage application, in order to not degrade the electro-optical response of the PDLC part, the mixture should not have excessive

number of EC molecules. Other attempts have been oriented to study the intrinsic nature of the electrolyte-LC dispersions to exhibit also EC effect when there is formation of complexes at the cathode, between the positive ions of electrolyte and LC dispersed in the matrix [Cup06]. Different kinds of commercial LCs gave rise to yellow or green colorations, with changes in optical absorption mainly at 400 - 450 nm range. In fact, studies on the EC blue shift inherent to PDLC cells as a function of applied electric field have been also made [Ram04], being it dependent on the droplet size and LC confinement degree. None of these attempts can achieve the full skills of both kinds of materials separately because of their mixture nature. The tandem PDLC-EC device developed and characterized in this work required some manufacturing efforts, such as using the same conductive support for both part of the device, without decreasing the transmittance at the bleached states of each part separately. The more transparent state of the tandem device, achieved with the EC part in the OFF state and the PDLC part in the ON state, is mostly limited by the non negligible and undesired scattering effect observed in the developed PDLC devices in the more transparent state.

V.1 Introduction

A detailed optical and electrical characterization of three series of samples of PDLC devices fabricated by CIDETEC is performed:

- The 1st series of PDLCs devices consists of four samples of the same size (1.3 x 1.3 cm^2) with two different operation modes and two different internal layer thicknesses (Figure V.3).
    - Normal mode (PDLCn) and reverse mode (PDLCr) operations.
    - Samples PDLC-20 and PDLC-50 with internal layer thicknesses of 20 and 50 microns respectively.

- The 2nd series of normal mode operation PDLCs devices consisting of eight samples of two different sizes and four different internal layer thicknesses (Figure V.4):
    - Sizes of 3.5 x 2.7 cm^2 (PDLCa) and 3.3 x 1.8 cm^2 (PDLCb).
    - Samples internal layer thicknesses of 25, 50, 75 and 100 microns (PDLC-25, PDLC-50, PDLC-75 and PDLC-100 respectively).

- The 3rd series is a tandem PDLC-EC device of 3.5 x 1.8 cm^2 active area size and 50 and 300 μm internal active layers thicknesses for the PDLC and EC parts respectively (Figure V.5). A glass with conductor on both sides is used as support for one EC viologen device on one side, controlling the chromaticity of the device between the bleach uncolored state and a deep blue colored state, and a LC device on the other side, controlling the level of scattering between the transparent and the translucent states.

Figure V.3: Photograph of the samples PDLCn-20 (left) and PDLCr-20 (right) at OFF and ON states respectively with translucent and transparent appearances.

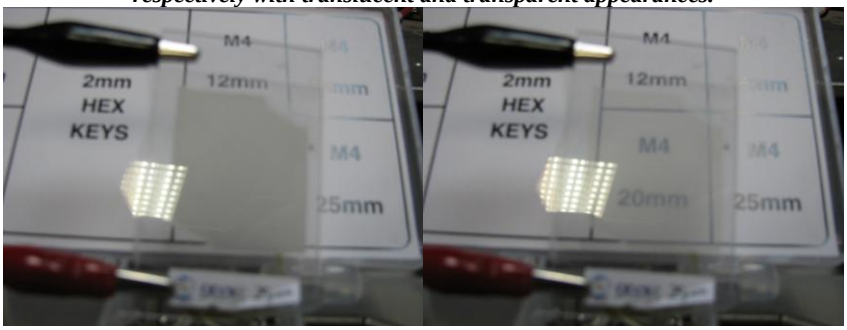

Figure V.4: Photograph of the sample PDLC25a at OFF and ON states with translucent and transparent appearances [Bar11d].

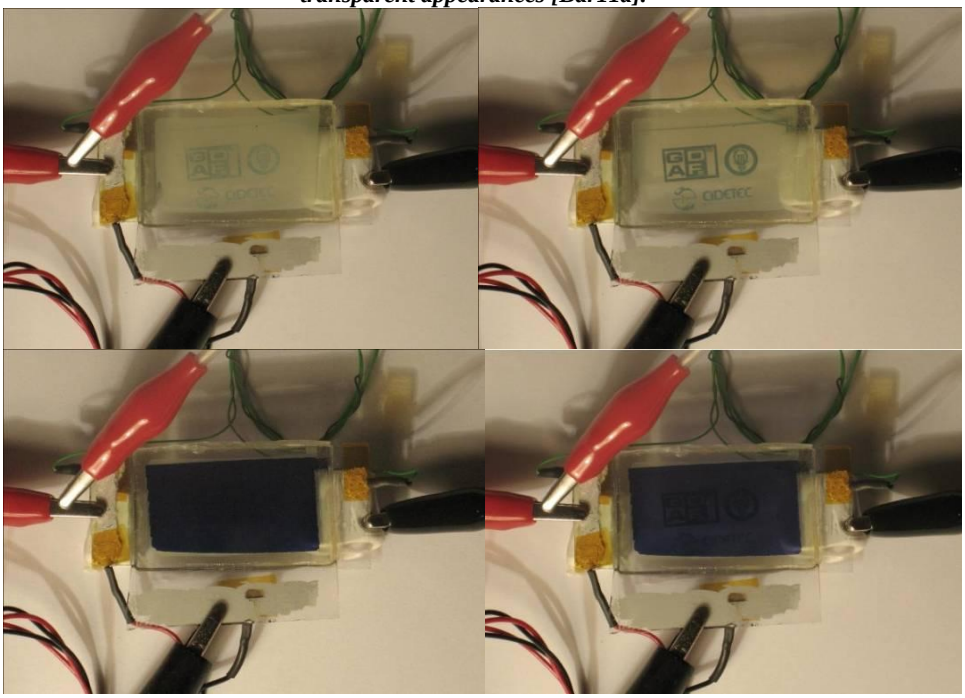

Figure V.5: Photographs of the tandem PDLC – EC device in the four possible states [Bar10]:
(left) PDLC part in OFF translucent state with 0 V applied.
(right) PDLC part in the ON transparent state with 100 V_{peak} 1.8 kHz square signal applied.
(up) EC part in the clear uncolored OFF state with 0 V applied.
(down) EC part in the deep blue colored ON state with 2 V DC applied.

V.2 Experimental

The 3 series of PDLC devices were manufactured by CIDETEC using the following methods:

1st and 2nd series: NM_{PDLC} and RM_{PDLC}:

A homogeneous mixture of 20 wt% of a UV curable matrix (Bisphenol A glycerolate diacrylate from Aldrich) and 80 wt% of an eutectic nematic LC mixture (E7 from Merck) consisting mostly of 4-pentyl-4'-cyanobiphenyl, with positive dielectric anisotropy was used for the normal mode operation PDLC devices. A 2 wt% of a photoiniciator was added to another similar mixture, also with positive dielectric anisotropy, for the reverse mode operation PDLC devices. Different effective sizes of glass cells with ITO coated inner surfaces with different internal gaps were filled by capillarity with the mixtures. PDLC was formed by polymerization induced phase separation (PIPS) method, exposing the cell to a 365 nm light for 10 minutes. In the case of the normal PDLC devices the irradiation was carried out at 65ºC. The reverse PDLC devices (PDLCr-20 and PDLCr-50) were irradiated at room temperature. A Leica DM 4000M optical microscope with cross polarizers was used to study the morphology of the composites. Microphotographs in Figure V.6 show the structure of the polymer and PDLC dropplets (<1 μm diameter for PDLCn-20 and a mean of 50 μm for PDLCr-20).

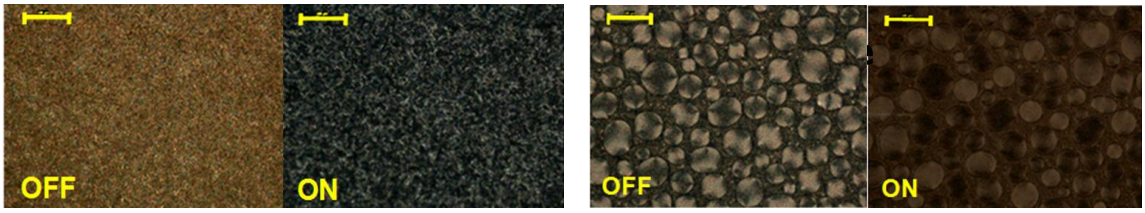

Figure V.6: Micro-textures of the droplets morphologies of the PDLC films under cross polarizers at 20x magnification (the scale bar corresponds to 100 μm). PDLCn-20 (left) and PDLCr-20 (right) in the OFF and ON states with 0 and 24 V_{rms} applied.

Tandem EC-PDLC device

Construction of the tandem device was carried out as follows: First a PDLC device was manufactured from an homogeneous mixture of the photocurable polymer NOA-65 (Norland Products) and a eutectic nematic LC mixture (E7 from Merck) consisting mostly of 4-pentyl-4'-cyanobiphenyl, at a weight ratio of 1.6:1 NOA-65: E7. The mixture was introduced by vacuum between two glass substrates coated with ITO, one of them on both sides. The thickness was fixed using a thermoplastic spacer (DuPontTM surlyn®1702, 50 μm thick). PDLC was formed by polymerization induced phase separation (PIPS) method, exposing the cell to a 365 nm light for 15 minutes. Afterwards, another glass substrate was placed on the two-face coated glass side, using a 240 μm thermoplastic spacer. This cell was vacuum-filled with a viologen-based EC mixture consisted of ethyl viologen perchlorate, 1-butyl-3-methylimidazolium tetrafluoroborate, poly(1-vinyl-3-ethylimidazolium tetrafluoroborate) and hydroquinone, dissolved in DMF. The final device was sealed with NOA-65. The active area was 3.5x1.8 cm.

V.3 Optical characterization

In this section, the optical behavior in the visible and the solar spectrum ranges of the different PDLC devices in study will be discussed:

- Optical diffuse and direct transmittances of PDLCn-50 and PDLCr-50 devices in the visible range measured using the UV-Vis-NIR Jasco V 570 double beam spectrophotometer equipped with an integrating sphere available at CIDETEC (see Chapter II).

- Optical total and direct transmittances of PDLCn-20 and PDLCr-20 devices in the visible range measured using the Ocean Optics USB2000 spectrometer and FOIS-1 integrating sphere, available at GDAF-UC3M lab. Optical direct transmittance of PDLCn-20 and PDLCr-20 varying the distance to the illuminant, which stands for the objects behind the PDLC device, using the spectrophotometer equipped with an Acton Research monochromator available at GDAF-UC3M lab.

- Optical diffuse and direct transmittance and diffuse and specular reflectance of two sizes, (a and b) and four thicknesses, (25, 50, 75 and 100 microns) devices: PDLCa-25, PDLCa-50, PDLCa-75, PDLCa-100, PDLCb-25, PDLCb-50, PDLCb-75 and PDLCb-100 using Lambda 900 spectrophotometer equipped with an integrating sphere available at Ångström Laboratory of Uppsala University.

- Optical direct transmittance of the tandem PDLC-EC device using the spectrophotometer based on a monochromator available at GDAF-UC3M lab.

V.3.1 Spectral measurements: Visible wavelength range

The total transmitted light through the normal and reverse operation modes PDLC devices in OFF and ON states, as well as the direct and diffuse parts of transmittance, and the dependence on the direct transmittance with the distance to the illuminant, i.e., the visual aspect of the the objects behind the PDLC sample, as it happens in the case of a fog, are described below in the visible wavelength range from 300 to 900 nm.

V.3.1.1 PDLCn-50 and PDLCr-50 devices

Despite both PDLCn-50 and PDLCr-50 devices show a very similar total transmission in OFF and ON states, with 0 V and 24 V_{rms} applied, with values $Ttot_{lum}^{OFF}$=74.56% and $Ttot_{lum}^{ON}$=77.73% (Figure V.7-up), their transparent and translucent states can be distinguished when this total transmission is decoupled into direct and diffuse components (Figure V.7-center and VI.7-down). However, both states are not ideals, since the transparent state has a component of the diffuse transmission and vice versa. This could be interpreted as one state is more transparent and the other state is more

translucent. This is more evident in the case of the sample PDLCr-50, where sharpness of objects placed behind would appear quite similar in both states. A slight improvement on the definition would be appreciated in the OFF state. The differences observed between Tdir and (Ttot-Tdiff), are due to the different distance at which is placed the sensor from the PDLC device. For a device with a weak scattering, these two measurements should be equals. However, for the measured PDLCn-50 and PDLCr-50 devices, these two plots are different since the sensor is placed at different positions when measuring Tdir than when measuring, by using the integrating sphere, both Ttot and Tdiff components.

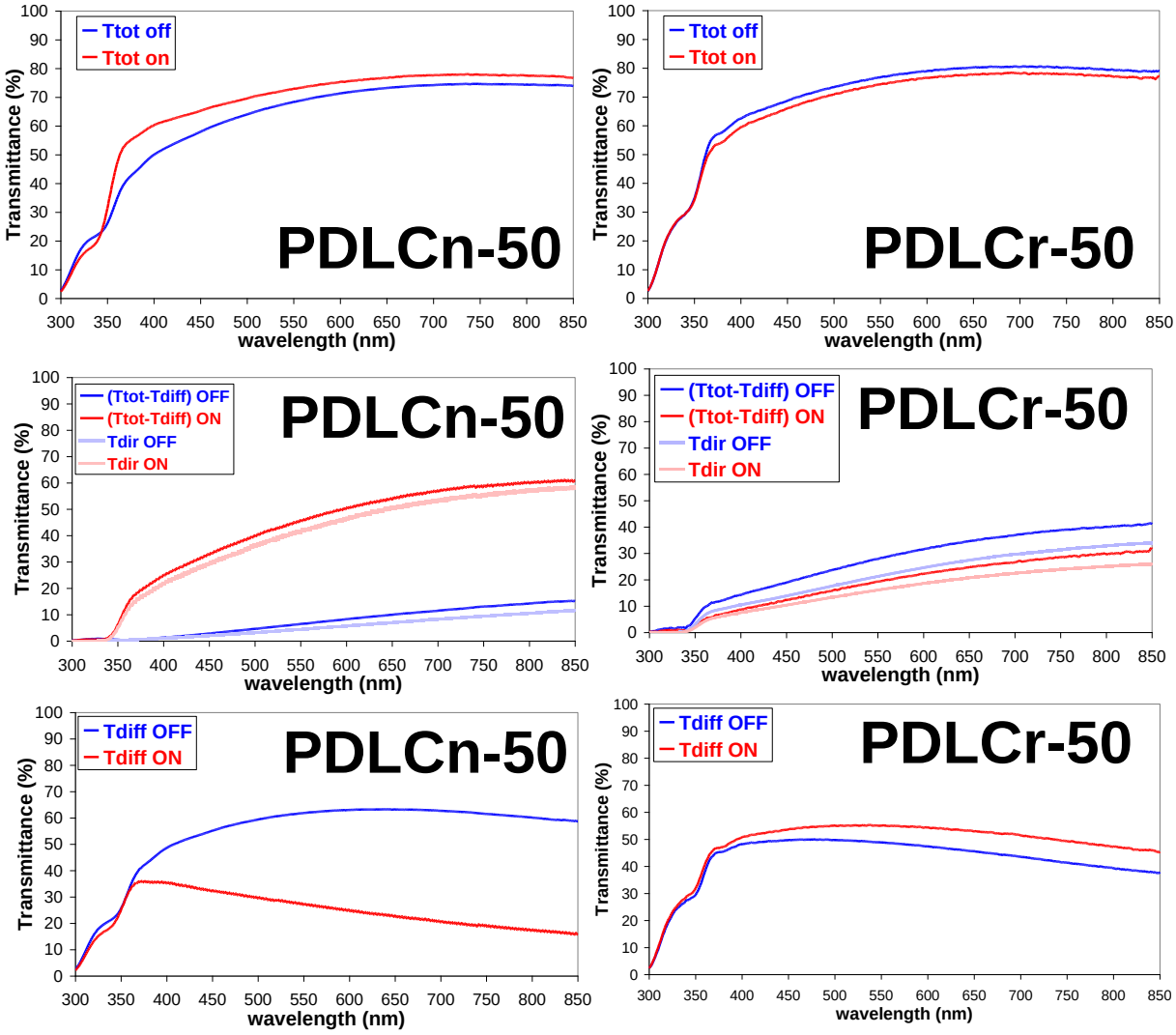

Figure V.7: Total (up), direct (center) and diffuse (down) transmittance of PDLCn-50 (left) and PDLCr-50 (right) devices for O V (OFF state) and 24 V_{rms} 50 Hz sinusoidal voltage signal (ON state) applied using UV-Vis-NIR Jasco V 570 double beam spectrophotometer equipped with an integrating sphere available at CIDETEC.

V.3.1.2 PDLCn-20 and PDLCr-20 devices

The similar potential than for PDLCn-50 and PDLCr-50 devices is applied for PDLCn-20 and PDLCr-20 devices, i.e. 50 Hz 24 V_{rms}. However, as it will be seen in the next section, square instead of sinusoidal voltage signal is used. A different spectrometer than the used for PDLCn-50 and PDLCr-50 devices was used in this case. Since FOIS-1 integrating sphere featured only one input port for measuring Ttot component, the diffuse component Tdiff was computed as the difference between the Ttot and Tdir.

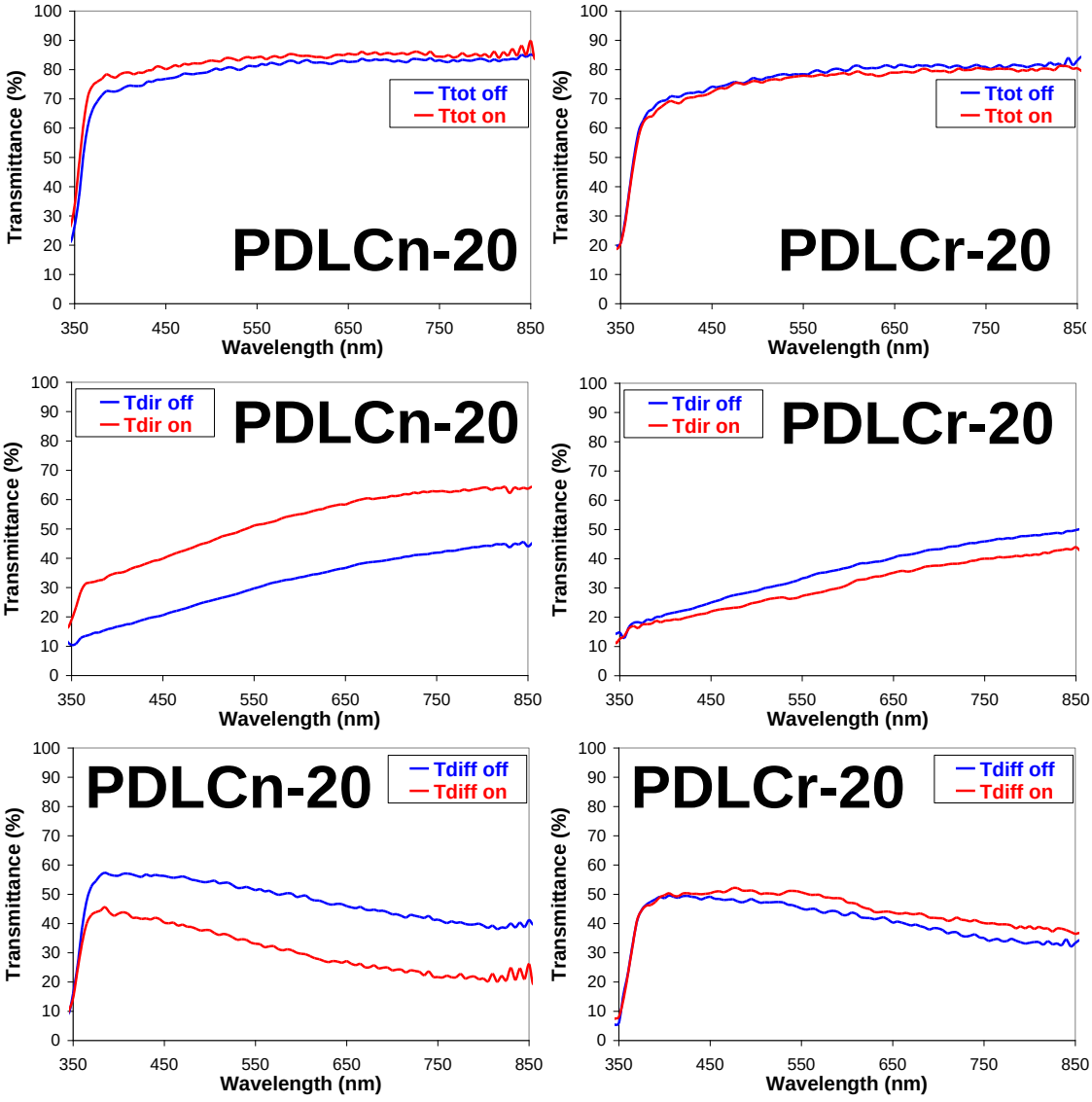

Figure V.8: Total (up), direct (center) and diffuse (down) transmittance of PDLCn-20 (left) and PDLCr-20 (right) devices for 0 V (OFF state) and 24 V_{rms} 50 Hz sinusoidal voltage signal (ON state) applied using the spectrophoto-meter Ocean Optics USB2000 + fiber optic integrating sphere (FOIS-1) available at GDAF-UC3M lab.

The direct transmittance in the visible range was measured for samples PDLCn-20 and PDLCr-20 varying the distance from the illuminant to the PDLC device, maintaining as a constant the distance between the illuminant and the observer or sensor (Figure V.9).

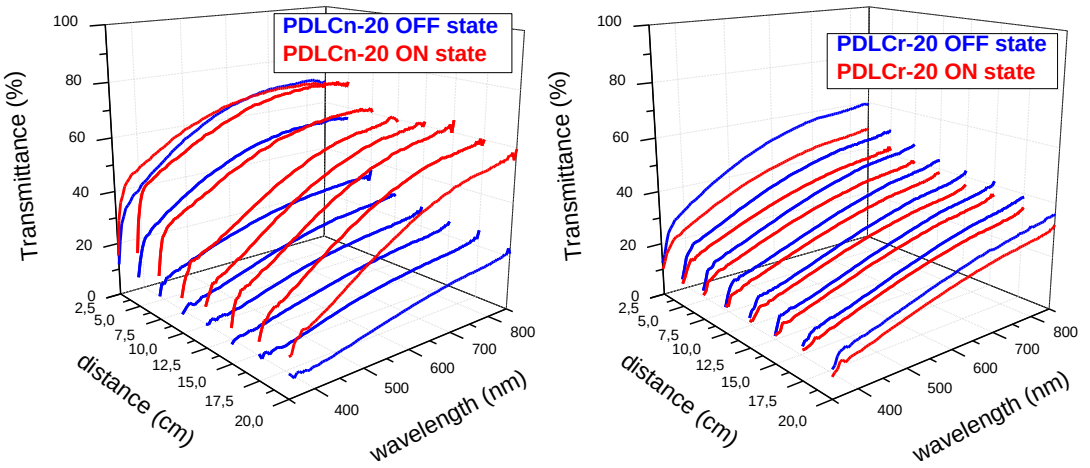

Figure V.9: Direct transmittance varying the distance between the illuminant and the PDLC device, being 25 cm the constant distance between the illuminant and the observer. (left) PDLCn-20 (right) PDLCr-20.

Hence, it could be interpreted that objects behind the PDLC device must be at a sufficient distance to be scattered in the translucent state. However, the transparent state is not appreciably affected. Numerically, averaging the direct transmittance plots to the human-eye sensitivity curve ($Tdir_{lum}$), the PDLCn-20 device, the transmittance $Tdir_{lum}$ at 2.5 cm of distance is 70% and 69% for both ON and OFF states respectively. However, at 20 cm of distance, the transmittance $Tdir_{lum}$ is 55% and 20% for ON and OFF states respectively. I.e. the more translucent state (OFF) shows a 49% of transmittance $Tdir_{lum}$ change between objects placed 2.5 cm and 20 cm behind the PDLCn-20 device, being around 15% for the case of the more transparent state (ON). In the case of the PDLCr-20 device, at 2.5 cm, the transmittance $Tdir_{lum}$ is 58% and 47% for OFF and ON states respectively. However, at 20 cm of distance, the transmittance $Tdir_{lum}$ is 33% and 28% for OFF and ON states respectively. I.e. the more transparent state (OFF) shows a 25% of transmittance $Tdir_{lum}$ change between objects placed 2.5 cm and 20 cm behind the PDLCr-20 device, being around 19% for the case of the more translucent state (ON). The differences of the transmittance with the distance are related with the scattering in the medium. The more transparent the device, the lower change of transmittance between objects placed far and close, and hence the lower diffuse parts. The more translucent the device, the lower direct parts of transmittance, and hence the higher difference of transmittance between far and close objects. Nevertheless, Ttot must remain constant with the thickness.

In Figure V.8, Tdir was measured at 30 cm of distance between the PDLC device and the illuminant.

V.3.2 Switching times measurements

Two different AC potential signals of 50 Hz and 24 V_{rms}, sinusoidal and square, modulated with a square signal of 10 seconds of period, were applied to both PDLCn-20 and PDLCr-20 devices in order to check the optical stabilization of ON and OFF states (Figure V.10). Direct T_{600nm} was measured. Transparent state for square signal seems to be more stable than for the sinusoidal one for the PDLCn-20 device since a curling in the temporal transmittance is observed, with a 1.2% of transmittance variation with oscillation periods of 3 seconds. Switching times of 0.3 seconds from translucent to transparent state, and 2.5 s vice versa are observed for PDLCn-20 device. For PDLCr-20 device, a symmetrical switching time of 0.5 s is observed between both states.

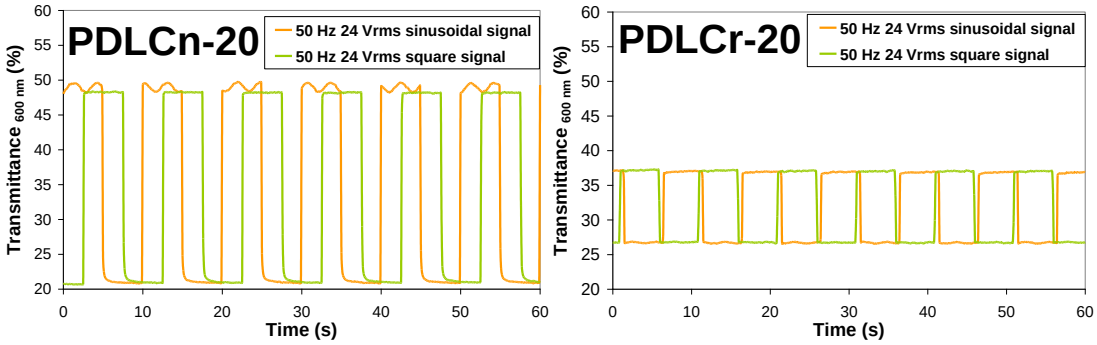

Figure V.10: T_{600nm} for two different AC potential signals, sinusoidal and square, of 50 Hz and 24 V_{rms}, modulated with a square signal of 10 seconds of period. (left) PDLCn-20 (right) PDLCr-20.

V.3.3 Spectral measurements: Operation in the solar range

Spectral absorptance, calculated from the energy conservation equation applied to an electromagnetic radiation, i.e. A=1-Rtot-Ttot, is plotted in Figure V.11 for the eight samples of PDLC of the second series, of two active area sizes and four different internal layer thicknesses. Total transmittance and reflectance plots of PDLC samples with two different sizes of 3.5 x 2.7 cm^2 and 3.3 x 1.8 cm^2 (named a and b respectively) and four internal layer thicknesses (25, 50, 75 and 100 μm) operating in a normal mode are shown in Figure V.12. A small difference between states ON and OFF (referred as 1 and 2 respectively, with 0 and 24 V_{rms} 50 Hz square voltage signal applied) in total transmittance is observed mainly in the visible range, which is explained since both transparent and translucent states let light to be transmitted in direct or diffuse modes. However, the devices reflect practically equal for both ON and OFF states. Devices with lower internal layer thickness show a higher total transmission and a small appreciable total reflection. Oscillations in transmittance with wavelength are due to the thickness of the internal layer. Decoupled direct and diffuse transmittance from the total one, as well as decoupled specular and diffuse reflectance from the total one, are also plotted in Figures V.13 and V.14 respectively. Comments of these plots will be covered in next section.

V.3.3.1 Absorptance

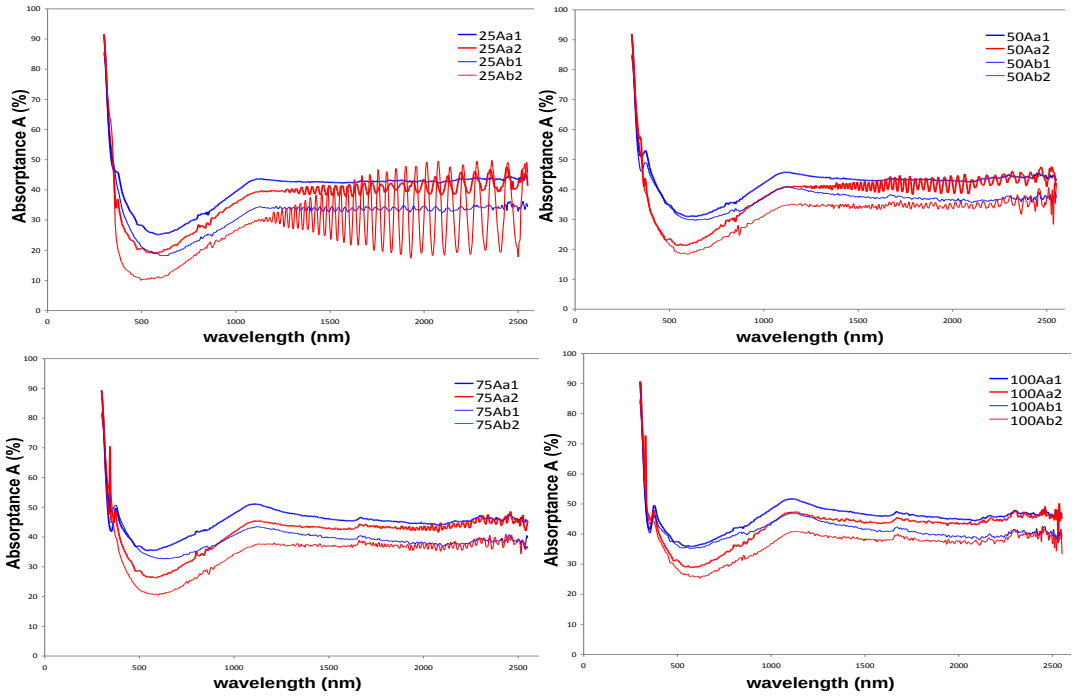

Figure V.11: Absorptance of the 2nd series of PDLC devices, for 25, 50, 75 and 100 µm of internal layer thickness and two sizes, a (3.5 x 2.7 cm^2) and b (3.3 x 1.8 cm^2).

The differences in the absorptance A plots between OFF and ON states are better visualized over the thicker device of 100 µm thickness, since the thinner one of 25 µm thickness shows interferences in the IR region in the ON state (Figure V.13). In the four cases, A is lower in the smaller effective area devices. The absorption bands appear in the visible range, with a flat spectrum at the IR region, except for the interferences previously cited, which are higher for the thinner of the larger effective area devices (PDLC25a). A peak is observed in the UV region, which is due to the reflectance components. Small differences between the OFF and ON states are observed in the T_{tot} and R_{tot} (Figure V.12), excepting the IR oscillation in the ON state and a slightly higher T_{tot} in the ON state. When decoupling into T_{dir} and T_{diff} (Figure V.13), higher differences are observed, with a higher T_{dir} contrast observed for PDLC25b, followed by 25a, 50a, 50b, 75b, 75a, 100a and 100b. T_{diff} show differences between sizes a and b, which decreases for the thicker devices, i.e. for the lower T_{dir} cases. IR interferences are due to T_{dir} and R_{spec} components. A higher R_{diff} than R_{spec} is observed in the eight cases.In Figure V.14 it can be observed the peak appearing at the UV region, being more noticeable for R_{diff} than for R_{spec}.

V.3.3.2 Total transmittance and reflectance

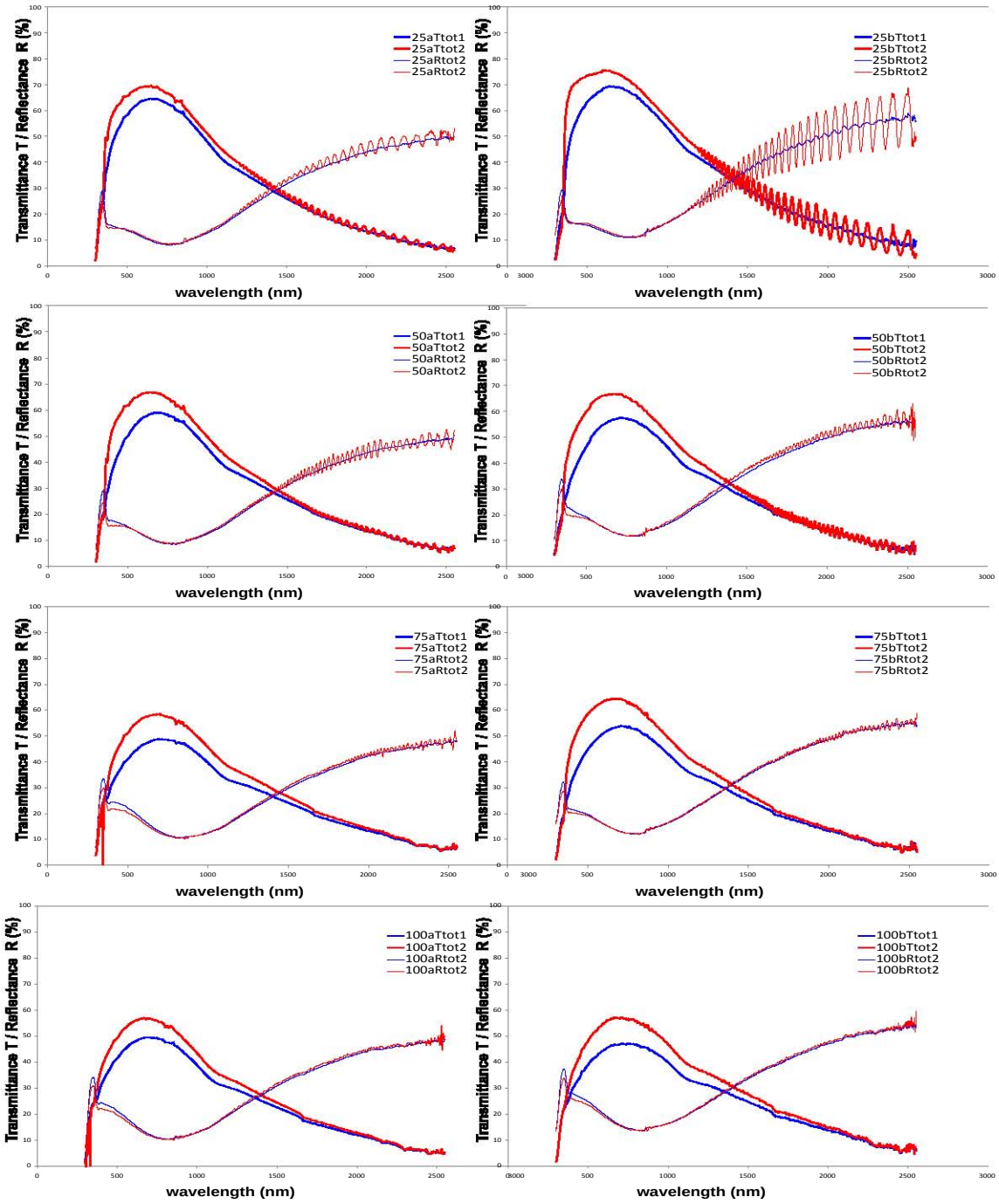

Figure V.12: Total transmittance and reflectance of the 2nd series of PDLC devices, for 25, 50, 75 and 100 µm of internal layer thickness and two sizes, a (3.5 x 2.7 cm^2) and b (3.3 x 1.8 cm^2).

VI.3.3.3 Direct and diffuse transmittance

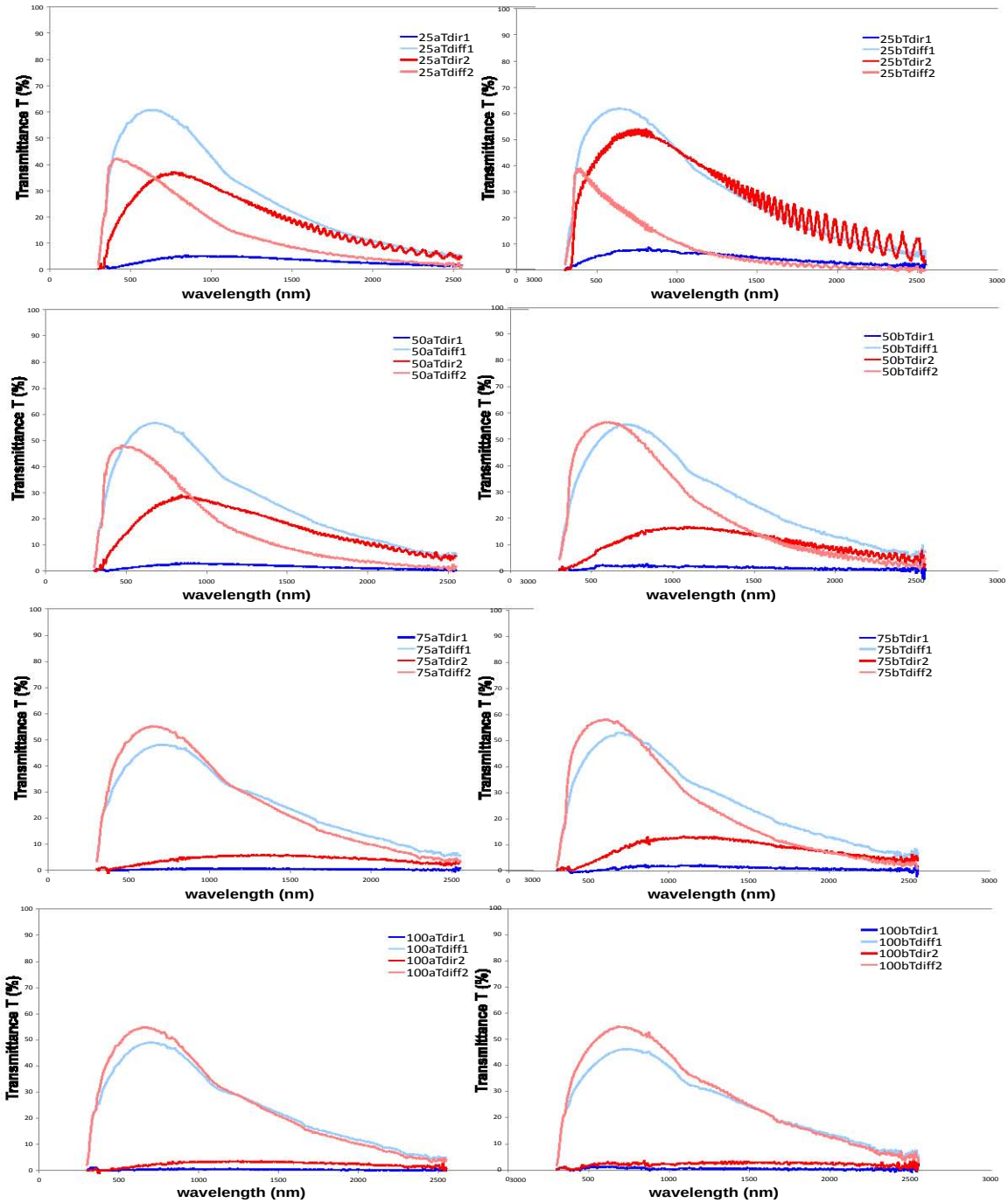

Figure V.13: Direct and diffuse transmittance of the 2nd series of PDLC devices, for 25, 50, 75 and 100 µm of internal layer thickness and two sizes, a (3.5 x 2.7 cm^2) and b (3.3 x 1.8 cm^2).

V.3.3.4 Specular and diffuse reflectance

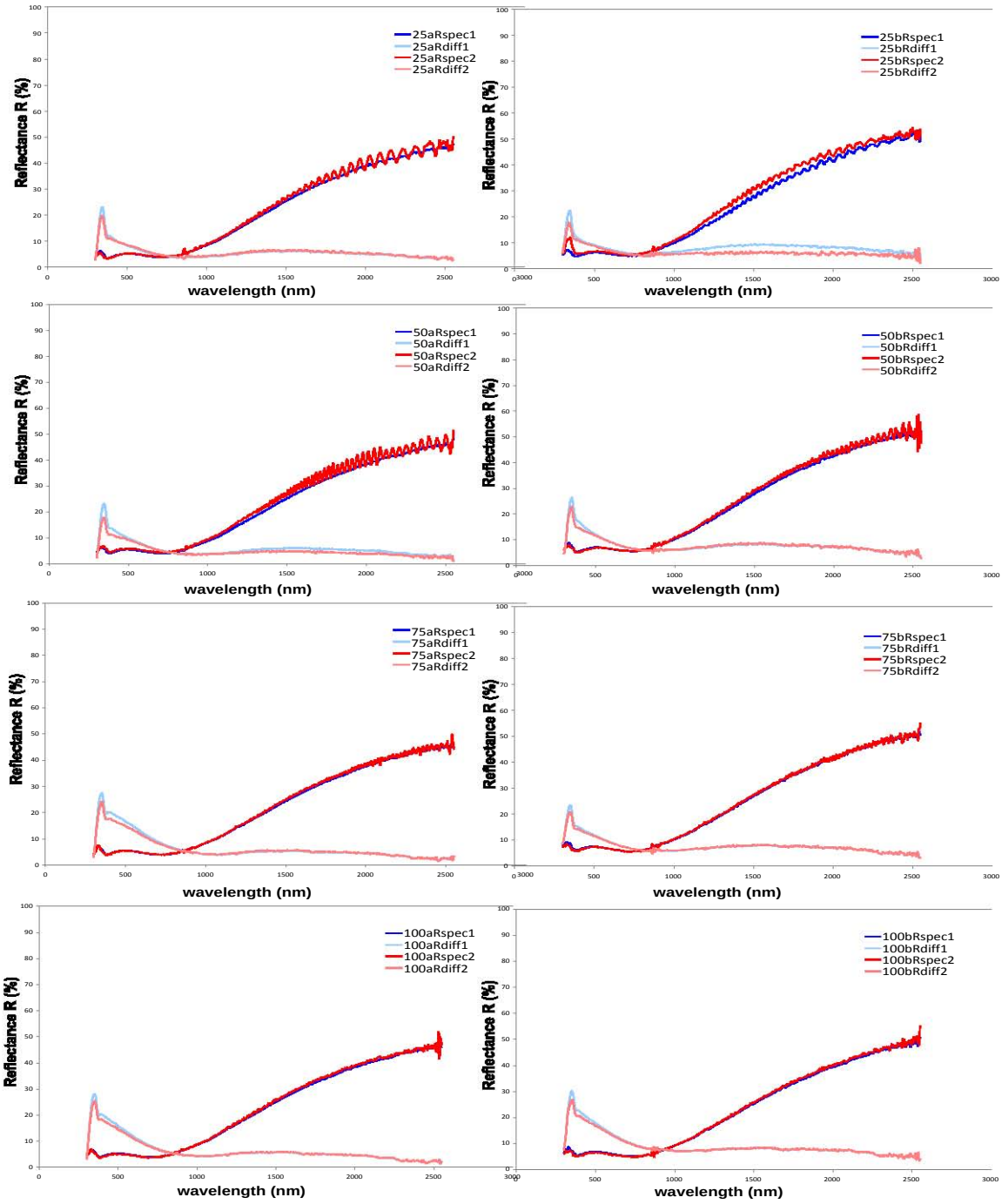

Figure V.14: Specular and diffuse reflectance of the 2nd series of PDLC devices, for 25, 50, 75 and 100 µm of internal layer thickness and two sizes, a (3.5 x 2.7 cm^2) and b (3.3 x 1.8 cm^2).

V.3.3.5 Optical measurements compared at different thicknesses and areas

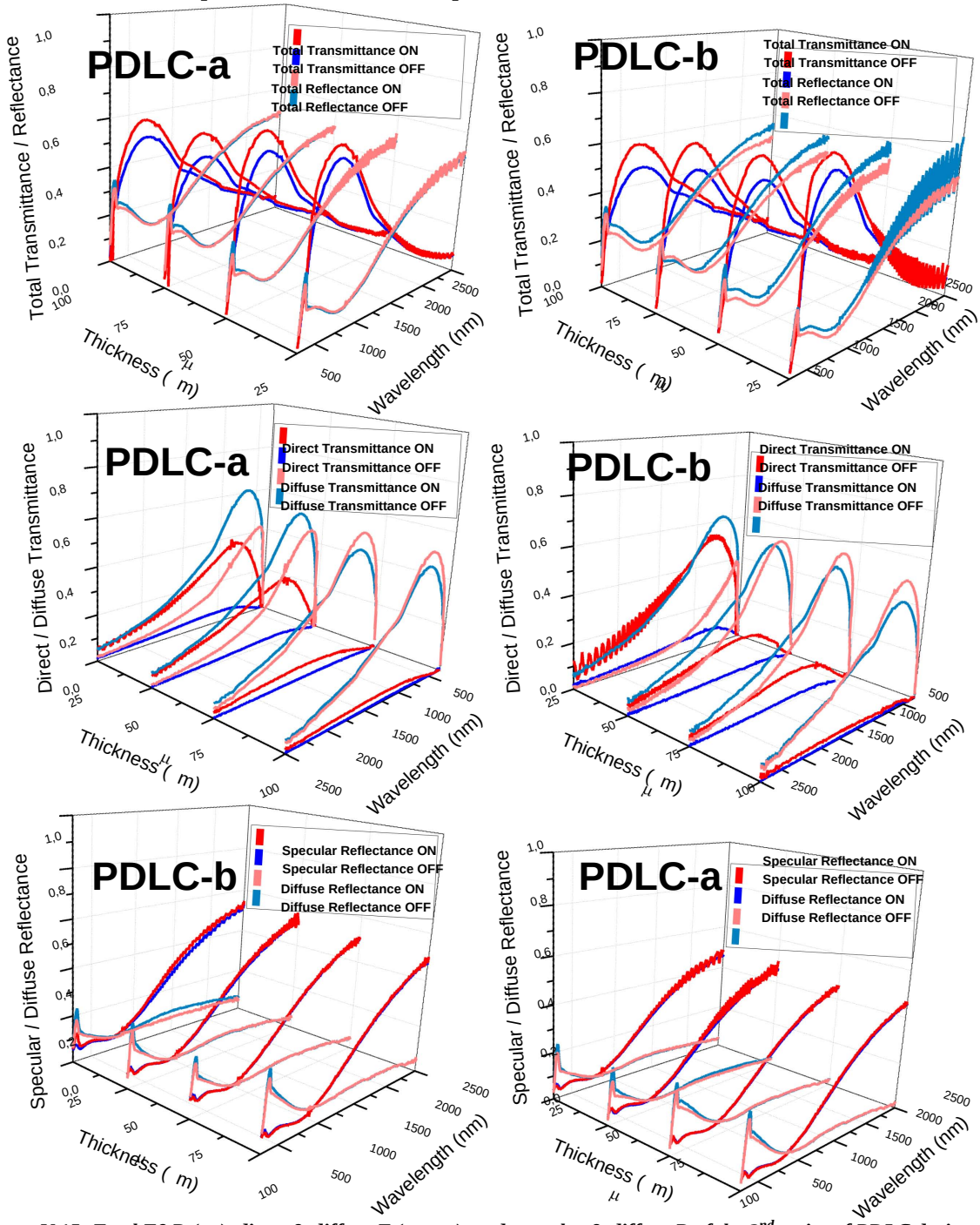

Figure V.15: Total T&R (up), direct & diffuse T (center), and specular & diffuse R of the 2nd series of PDLC devices, for 25, 50, 75 and 100 µm of internal layer thickness and two sizes, a (3.5 x 2.7 cm^2) & b (3.3 x 1.8 cm^2) [Bar11d].

Figure V.15 shows the data of Figures V.12, V.13 and V.14 in three dimensional plots for a thickness dependence comparison. Note that, for a better visualization, the order of the axes is not the same in all plots. Total transmission of the eight PDLC samples looks to be slightly higher in the transparent ON state than the total transmission in the translucent OFF state. The difference does not exceed 10% of the total transmittance between OFF and ON states at visible wavelength, which means that the PDLC samples totally transmit a similar amount of light. However, differentiating the total transmitted light from directly and diffusely transmitted light, the difference increases to 40% in direct transmittance between OFF and ON states of 25 microns internal active layer thickness PDLC devices, being this contrast slightly higher for the lower active area one (PDLC25b). The direct transmittance contrast decreases by increasing the thickness of the internal active layer, being barely noticeable to a thickness of 100 μm.

Figure V.18 shows thickness dependence of the luminous integrated values of transmittance (left) and reflectance (right) of the PDLC-a (up) and PDLC-b (down) different size devices, in both OFF and ON states, computed from the expected Ttot, Tdir and Tdiff and Rtot, Rspec and Rdiff components of Figure V.15. The differences between OFF and ON states observed in Ttot-lum (continuous lines) are smaller than the observed for Tdir-lum (dashed lines) or Tdiff-lum (dotted lines) only for thinner devices, i.e. for 25 μm and 50 μm (Figure V.16-left). Smaller size PDLC-B device shows better contrast than higher size PDLC-A. Ttot decreases for thicker devices of both sizes. The clear increase of Tdir in the ON states when decreasing the thickness to values lower than 50 μm is accompanied with a non desirable increase of Tdir in the OFF states, which can be easily observed as the difference of Ttot-Tdiff. The differences between Tdir and Tdiff in the ON states are higher for the smaller devices. In the case of the reflectances, no noticeable differences are observed between the OFF and the ON states. For the thicker and higher devices, Rdiff is clearly higher than Rspec (Figure V.16-right). Figure V.17 shows the solar integrated values. Differences between Tdir and Tdiff in the ON states decrease with respect to luminous values for the thinner devices of 25 and 50 μm. Bigger size PDLC-a devices are around 10% less transmissive than smaller size PDLC-b devices, which are around 10% less reflective.

Relevant information can be deduced from Figure V.18 regarding to haze. Note that in these plots the ideal case would be 0% for transparent ON states and 100% for translucent OFF states. However, the best results for luminous transmittance haze are obtained for the thinner device of 25 μm with a 31% and 89% for the bigger size, and 24% and 88%, for the smaller size, in ON and OFF states respectively. Figure V.19 shows the transmittance and reflectance contrast, defined as the difference between the measured in the ON and in the OFF states. Total transmittance contrast and all reflectance contrasts are negligible, being only noticeable the Tdir and Tdiff contrasts for 25 μm in the case of luminous values, and for 25 and 50 μm in the case of solar values.

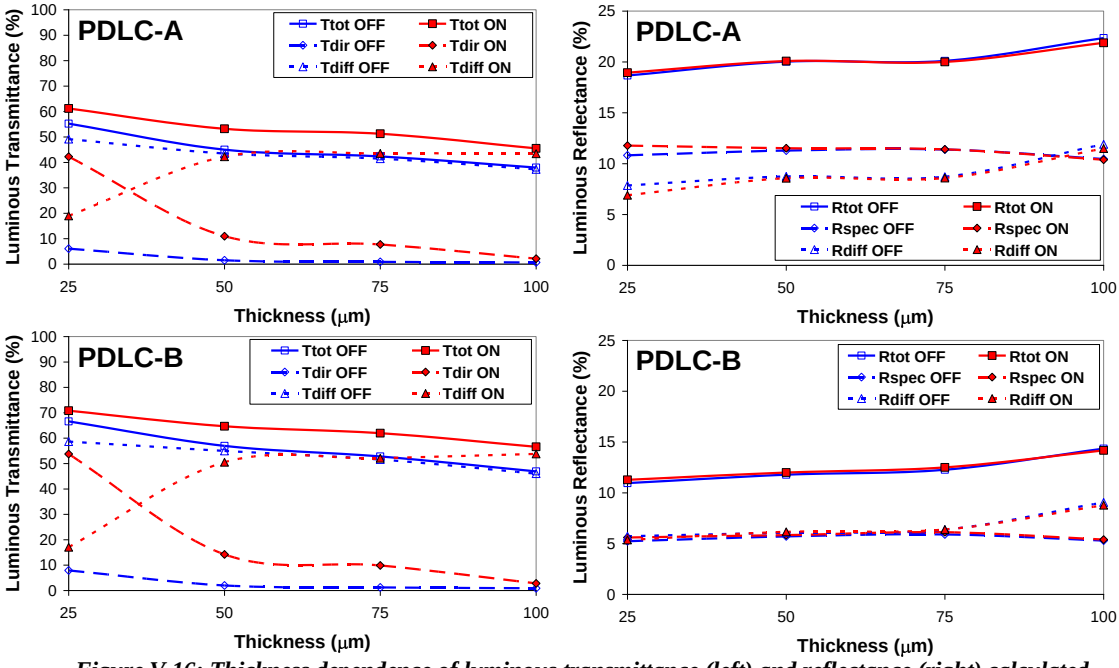

Figure V.16: Thickness dependence of luminous transmittance (left) and reflectance (right) calculated from the measurements over the PDLC-A (3.5 x 2.7 cm^2) devices (up) and PDLC-B (3.3 x 1.8 cm^2) devices (down) in both OFF and ON states.

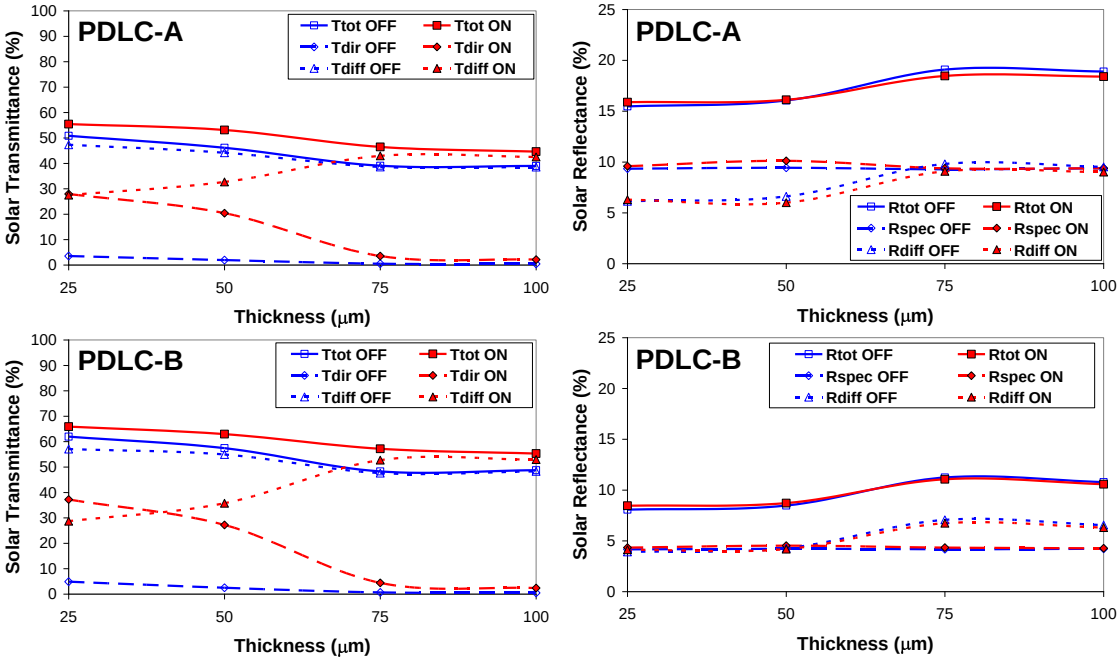

Figure V.17: Thickness dependence of solar transmittance (left) and reflectance (right) calculated from the measurements over the PDLC-A (3.5 x 2.7 cm^2) devices (up) and PDLC-B (3.3 x 1.8 cm^2) devices (down) in both OFF and ON states.

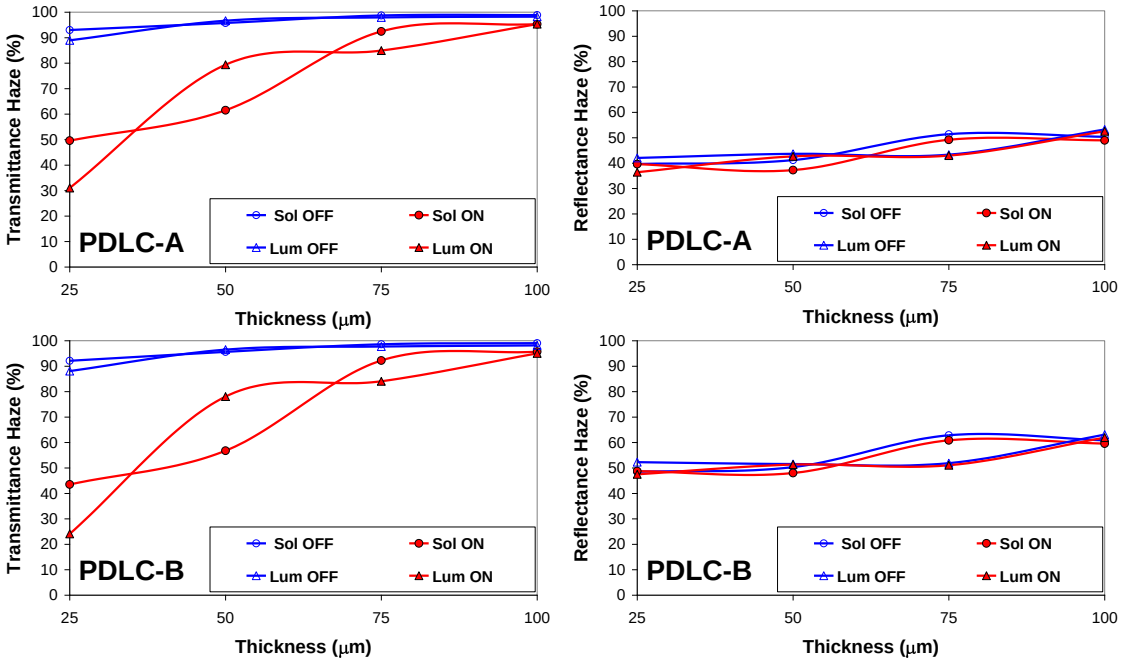

Figure V.18: Thickness dependence of luminous and solar transmittance (left) and reflectance (right) haze of the PDLC-A (3.5 x 2.7 cm^2) devices (up) and PDLC-B (3.3 x 1.8 cm^2) devices (down) devices (down) in both OFF and ON states.

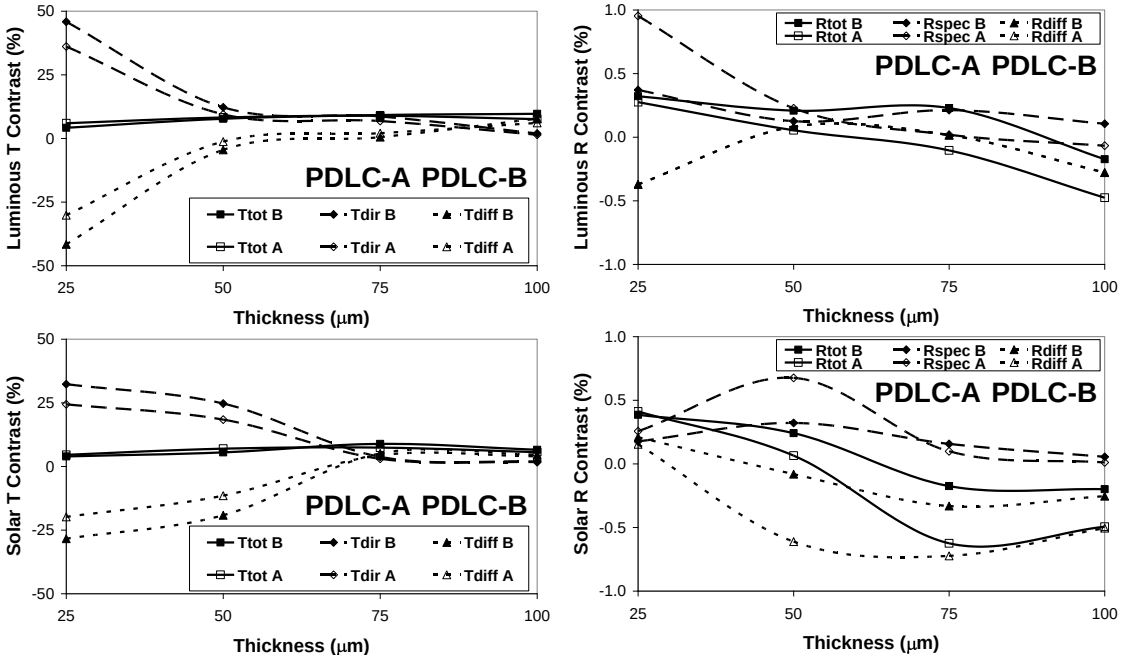

Figure V.19: Thickness dependence of luminous (up) and solar (down) transmittance (left) and reflectance (right) contrast of the PDLC-A (3.5 x 2.7 cm^2) devices and PDLC-B (3.3 x 1.8 cm^2) devices.

Figure V.20 shows the simulation of the PDLC devices with sizes "a" and "b" and thicknesses 25, 50, 75 and 100 μm, in both, OFF and ON states, with a background placed more than 20 cm of distance from the PDLC devices. The appearance of the PDLC devices was simulated by computing the sRGB coordinates by means of the CIE Yxy chromaticity and luminance coordinates, using the direct transmittance measurements. The transparency and scattering appearance of each PDLC device was simulated by three steps: (1) An average value of the Tdir for the human eye sensitivity curve was computed and applied as the first transparency property "alpha1", being alpha1=Tdir-lum. (2) The diffuse component was simulated by applying a second transparency property "alpha2" over the sRGB results obtained in (1), being alpha2=Tdir-lum/Ttot-lum. (3) The dependence with the distance is considered by using the Tdir-eye at 2.5 cm and Tdir-eye at 20 cm values observed in Figure V.9. Since the Ttot is decoupled into a Tdir and Tdiff, and depending on the distance "d" of objects placed behind the PDLC, Tdir and Tdiff change. If "d" decreases, Tdir increases and Tdiff decreases, while Ttot remain constant. Comparing Tdir of Figure V.9 and Ttot of Figure V.12, for PDLCn-20 and PDLC25a, respectively, it could be deduced that the measurements obtained by using Perkin Elmer Lambda 900 spectrometer are related with the obtained with the Acton Research monochromator spectrometer of GDAF-UC3M at 2.5 cm of distance. Hence, a third transparency property "alpha3" over the sRGB results obtained in (2) is applied, being alpha3=alpha2 x $T_{dir\text{-}eye}^{20cm}/T_{dir\text{-}eye}^{2.5cm}$. As it was expected and visually experimented, OFF states for all PDLC thicknesses and areas show a highly diffuse state. Figure V.21 shows the simulations of the PDLC devices over a closer background placed at 2.5 cm of distance. In this case, the procedure is the same than the followed in Figure V.20 excepting the step (3). Diffuse OFF state of PDLC25 devices shows the main differences between Figures V.20 and V.21. Transparent ON states are also different, but not as much as in the OFF states.

Summing up, from the eight PDLC samples characterized with two different sizes and four different thicknesses, it seems that the thinnest devices, i.e. PDLC25a and PDLC25b, show the best results since the luminous Tdir contrast is the higher, with 36% and 23% respectively. However, values of 24% and 31% of luminous transmittance haze in the transparent ON state are the main problem for these developed PDLC samples.

Combining the PDLC behavior, switching between transparent and translucent states, with the EC behavior, switching between bleached and colored states, could derive to a tandem PDLC-EC device with four different states, i.e. transparent bleached, translucent bleached, transparent colored and translucent colored.

Figure V.20: Simulated appearance of PDLC devices with 25, 50, 75 and 100 μm of thickness, with active areas "a" and "b", in both OFF and ON states, over a photograph of the Mosque of Cordoba at the background (objects placed at 20 cm of distance or more).

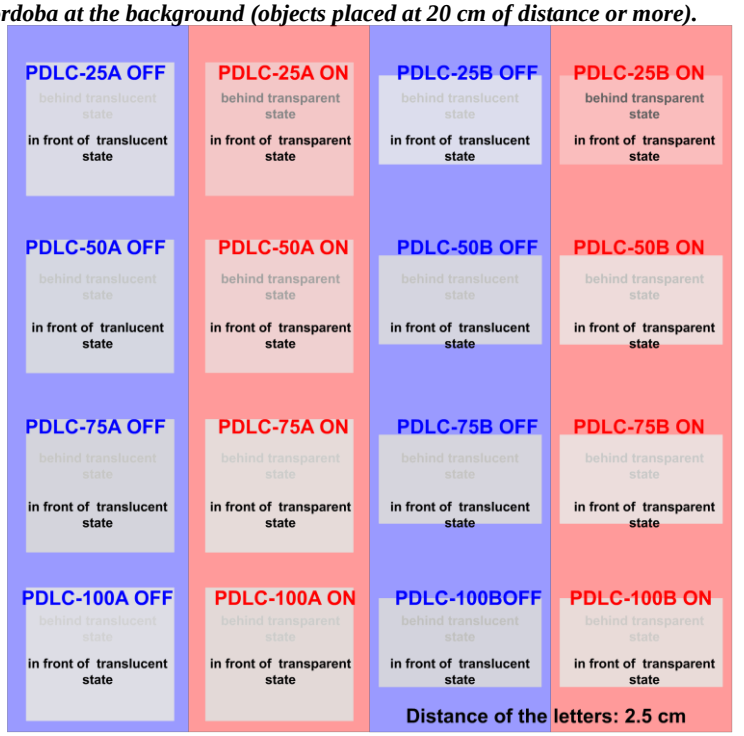

Figure V.21: Simulated appearance of PDLC devices with 25, 50, 75 and 100 μm of thickness, with active areas "a" and "b", in both OFF and ON states, over a background placed at 2.5 cm of distance [Bar11d].

V.3.4 Tandem PDLC-EC device: Spectral measurements at the visible range

Figure V.22 shows the transmittance of the tandem PDLC-EC device for the different states of the PDLC and the EC parts [Bar10]. The transparent-uncolored state is observed to reach around 60% of T_{600nm}, shown in Figure V.22-left-up for 0 V applied to the EC part and 100 V_{peak} to the PDLC part. An optical contrast of 25% between the transparent uncolored and the translucent uncolored states is observed. For 1 V applied to the EC part in Figure V.22-right-up, the optical contrast increases to a 30%, with a slight bluer transparent to translucent appearance observed in the device.

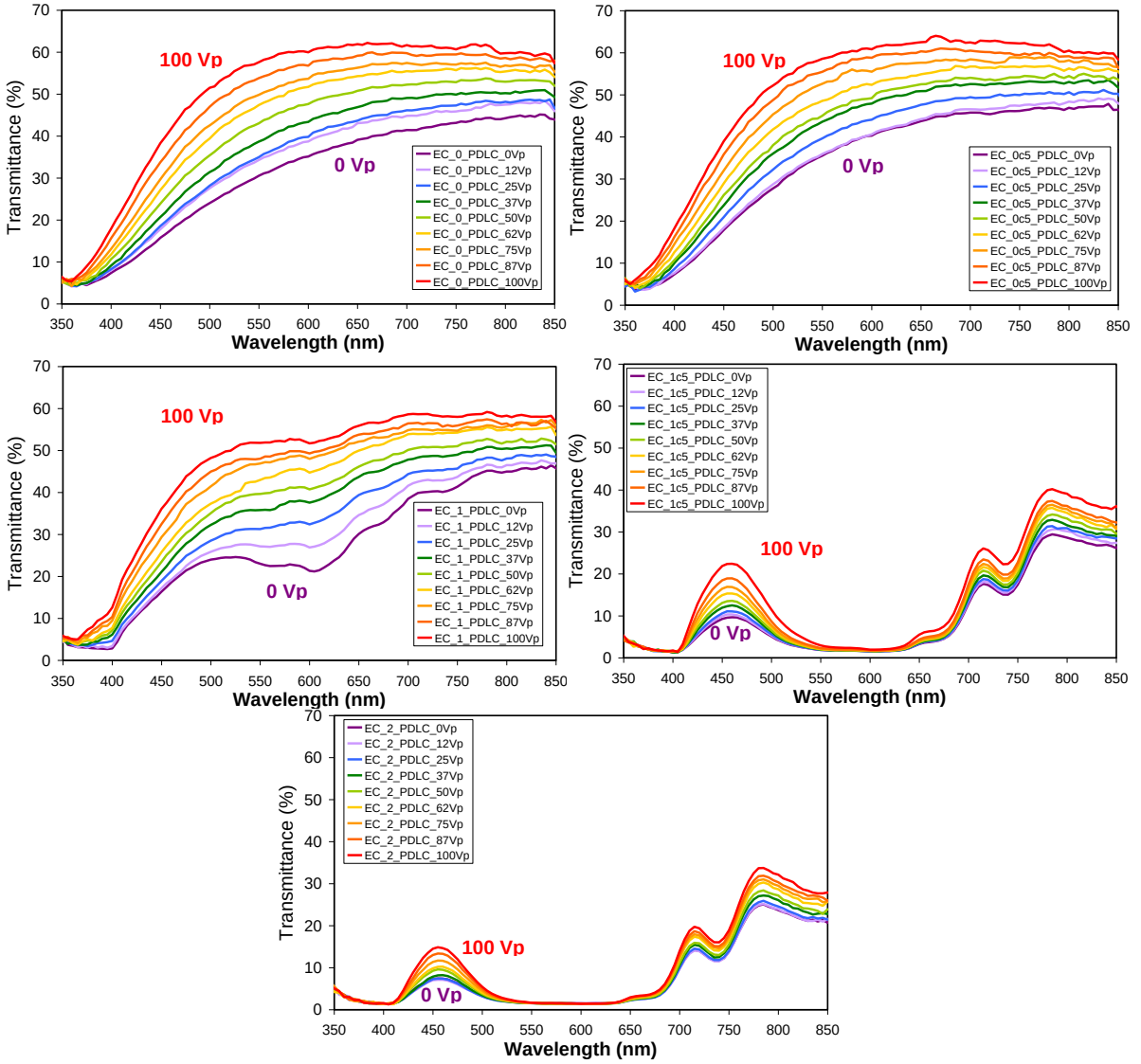

Figure V.22: Direct transmittance of the tandem PDLC-EC device for 0, 1, 1.5 and 2 V applied to the EC part and 0, 12, 25, 37,50,62,75, 87 and 100 V_{peak} 1.8 kHz square voltage signal [Bar10].

For 1.5 V applied to the EC part in Figure V.22-left-down, the optical contrast at 600 nm is negligible. However, the absorption bands are now observed at around 460 nm, with a 23% of optical contrast in the direct transmittance, and at around 720 nm, with a 9% of optical contrast. The device shows blue-transparent and blue-translucent appearances. For 2 V applied to the EC part in Figure V.22-right-down, the optical contrasts at 460 nm ad 720 nm decrease to an 8 and 6% respectively.

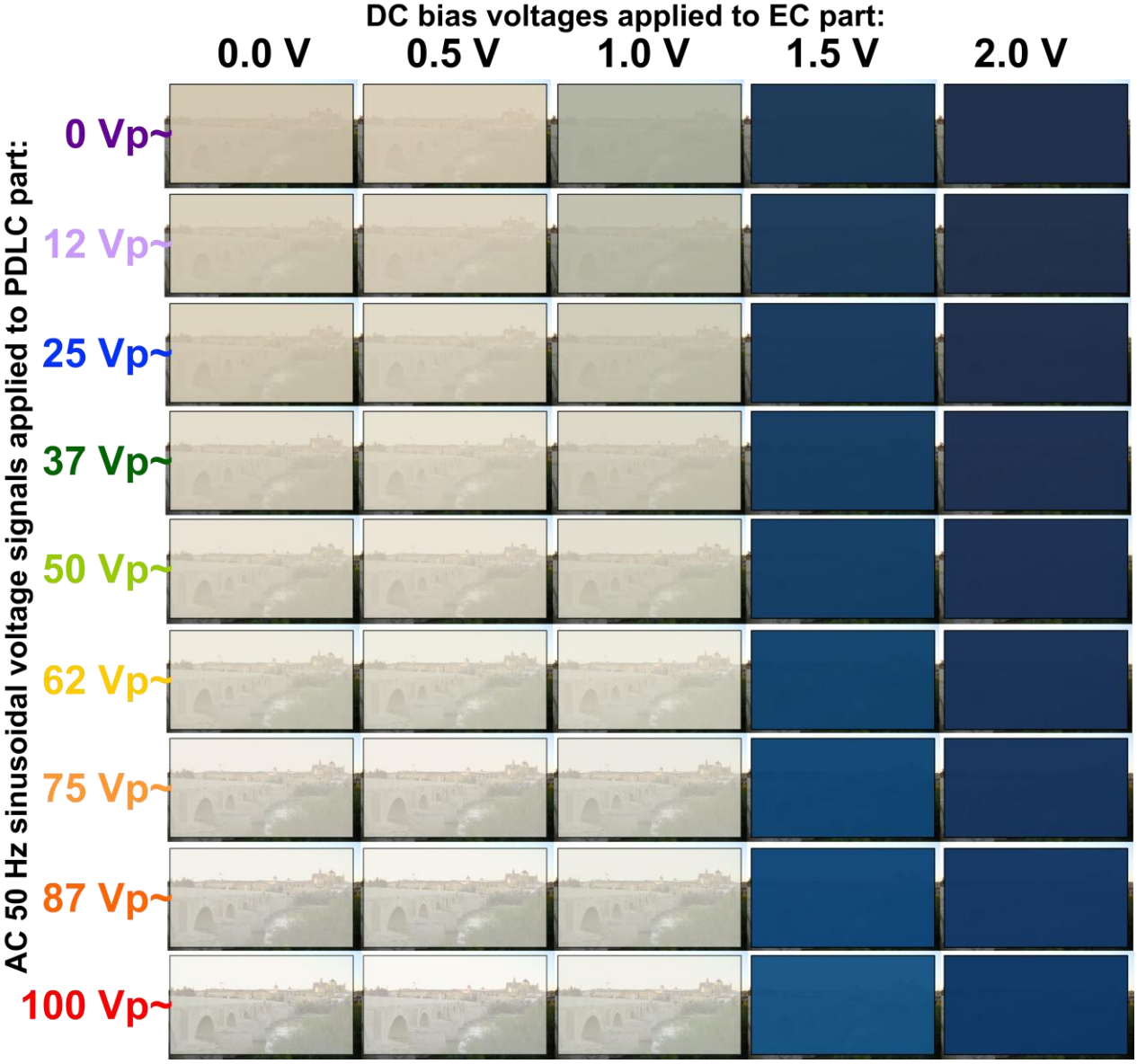

Figure V.23: Simulated appearance of the Tandem device for different DC bias voltage levels applied to the EC part (columns) and different AC amplitude signals at 50 Hz applied to the PDLC part (rows) over a photograph of the Mosque of Cordoba at the background (objects placed at 20 cm of distance or more).

Figure V.23 shows the simulation of the appearance of the Tandem device for different DC bias voltage applied to the EC part, from 0 to 2 V with 0.5 V steps, and different amplitudes of the 50 Hz AC square voltage signal applied to the PDLC part. The PDLC part requires a higher potential for optically switching than the PDLC devices. Values of amplitudes are now applied up to 100 Vp for PDLC part of the Tandem device, instead of 24 V_{rms} applied for previous PDLC devices studied.

V.4 Impedance characterization

In this section, the electrical properties such as the model of the EEC of the different devices in study, as well as the dependence on the variation of the parameters of the EEC with the thickness of the internal active layer, will be discussed. Impedance measurements were carried out using the gain/phase impedance analyzer Solartron 1260 available at GDAF-UC3M lab:

- Complex impedance in the frequency range from 100 mHz to 10 MHz to devices PDLCn-20 and PDLCr-20.

- Complex impedance in the frequency range from 1 Hz to 1 MHz to devices PDLCa-25, PDLCa-50, PDLCa-75, PDLCa-100, PDLCb-25, PDLCb-50, PDLCb-75 and PDLCb-100.

- Complex impedance in the frequency range from 100 mHz to 100 kHz to the tandem PDLC-EC device.

V.4.1 Complex impedance of normal and reverse mode PDLC devices

Bode magnitude and phase and Nyquist impedance plots of PDLCn-20 and PDLCr-20 devices are shown in Figure V.24. Impedance magnitude is linearly decaying and impedance phase is constant and close to -90 degrees in the range between 1 kHz and 1 MHz. These impedance results can be interpreted as both PDLC devices look like a simple capacitor Cdl in series with a resistance standing for contacts. The behavior at low frequencies, where accumulation of ionic charges does occur near the electrodes and also in the interfaces between polymeric matrix and LC dropplets, is modeled by the insertion of a new resistance of charge transfer in series with a CPE, standing for that accumulation, in a shunt configuration with the previous capacitor. The EEC model of Figure V.25 is proposed for PDLC devices. A series resistance Rs reflects the resistive behavior of the contacts of ITO glass. Two parallel branches, one for the low frequencies and the other for the high ones, reflect the electrical behavior of the rest of the device. The resistive behavior at low frequencies is mainly due to the molecular orientation of LC droplets, represented electrically by a resistance to displacement of the dipoles Rd in series with a CPE reflecting the accumulation of ions, and whose electrical impedance is described in Equation III.3 in Chapter III.

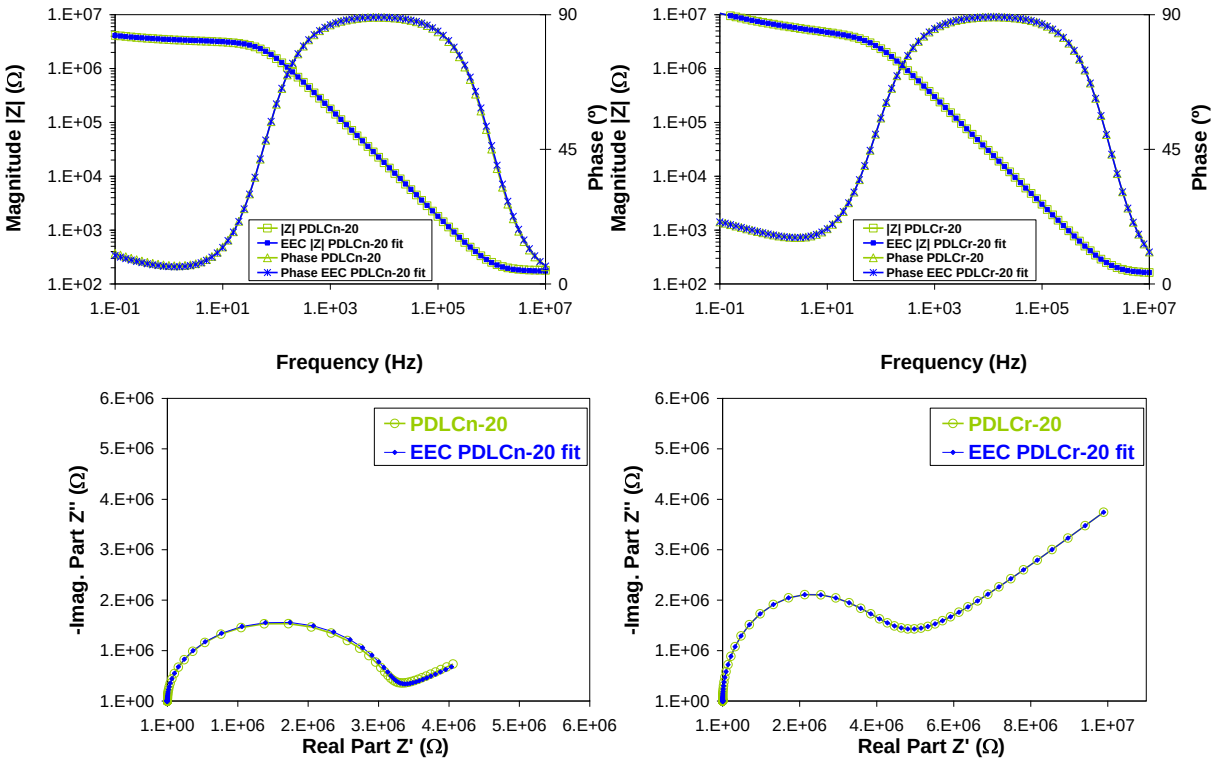

Figure V.24: Bode magnitude and phase (up) and Nyquist (down) impedance measurements and fittings of the proposed EEC model for the samples PDLCn-20 (left) and PDLCr-20 (right).

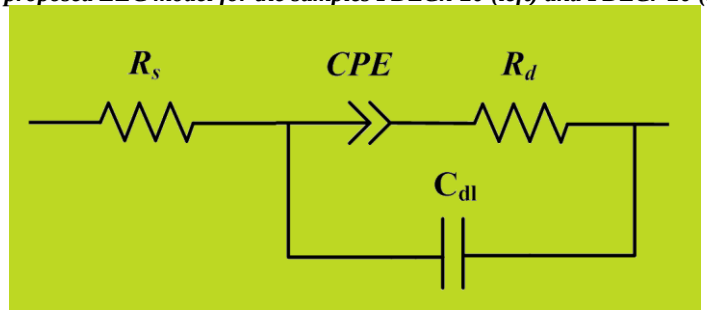

Figure V.25: Proposed EEC model for PDLC devices.

Device:	PDLCn-20		PDLCr-20	
Parameter:	Value	Error (%)	Value	Error (%)
Rs (Ω)	172	2.3	160	2.9
Rd (MΩ)	3.03	1.5	3.38	2.4
CPE-T (nFs^{P-1})	984	8.8	155	3.0
CPE-P	0.373	10.6	0.329	3.3
Cdl (nF)	0.883	1.1	0.527	1.1
Chi^2 (Sum Chi^2)	0.040647 (6.5442)		0.038817 (6.2496)	

Table V.1: Values of parameters and fitting errors of the EEC model for PDLCn-20 and PDLCr-20 devices.

The capacitive behavior at high frequencies is represented in this case by the double layer capacitor Cdl caused by the movement of ions, resulting in an accumulation of ionic charges near the electrodes and the interfaces of LC droplets and polymer matrix. Figure V.24 also shows the fittings to the EEC model proposed for PDLC devices. Table V.1 shows the values of the parameters of the EEC model and the fitting errors. Slight differences are observed in the Nyquist diagrams at low frequencies for PDLCn-20 device, which are the causes of the fitting errors obtained for CPE element.

V.4.2 Complex impedance dependence with the area and thickness

The results of the impedance measurements in the Bode plots of magnitude and phase and Nyquist diagrams for the different sizes and thickness of PDLC devices, in their translucent OFF states, are shown in Figure V.26, including the fittings to the EEC model of Figure V.25 [Bar11d].

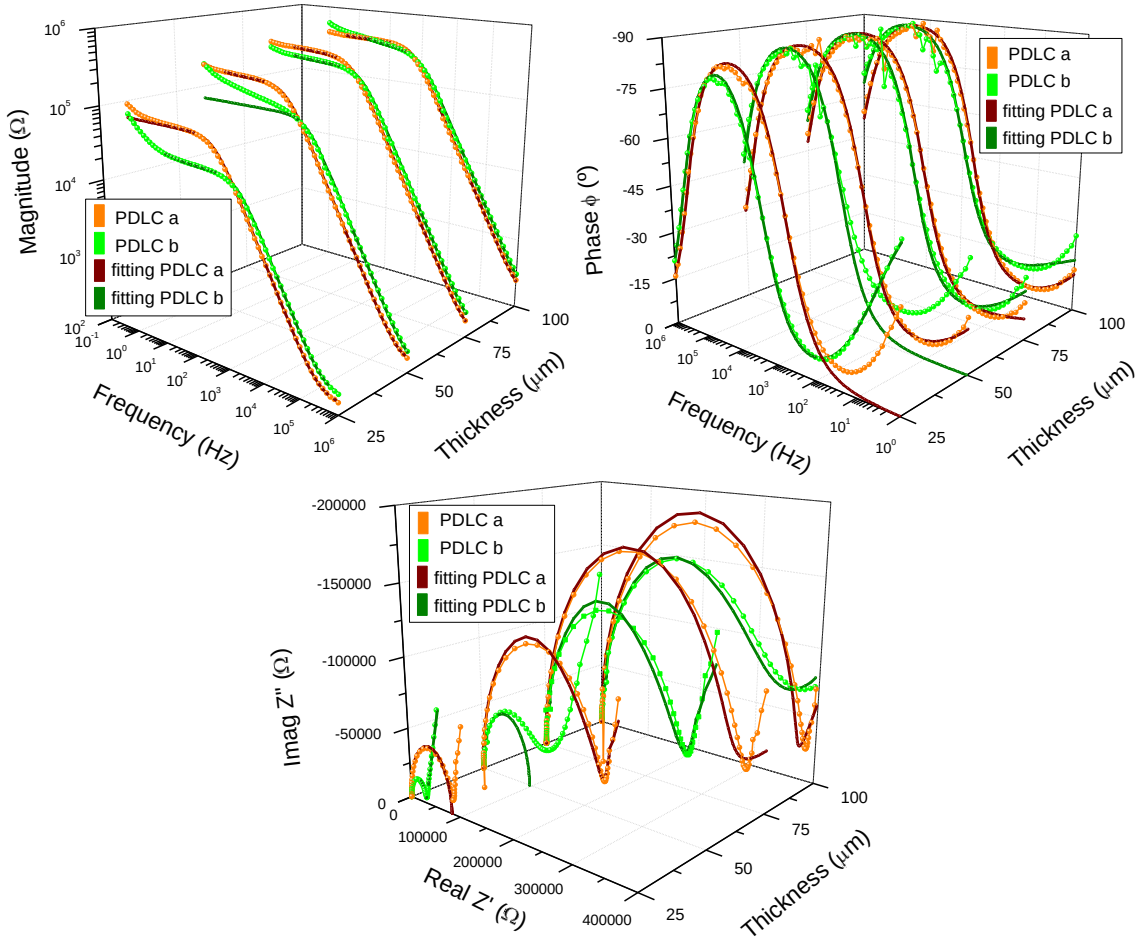

Figure V.26: Bode magnitude & phase and Nyquist impedance diagrams of 2nd series of PDLC devices.

Bode magnitude and phase impedance plots of Figures V.26 and V.24-up show the same tendency with the frequency, i.e. at high frequencies, from 1MHz to 1kHz, a double layer capacitive effect is clearly observed. At low frequencies the dipolar resistance and the accumulation of ionic charges are distinguished in the Nyquist impedance plots. Dependence with the effective area and with the internal layer thickness, of the parameters obtained in the ECC model, is observed in Figure V.27. The small variations observed in the contacts resistance Rs should indicate a lower resistive value of the bigger size devices. Differences could be related to the fitting process. The displacement resistance Rd evolution shows that, the thicker the internal layer, or the larger the effective area, the higher the Rs parameter. Accumulation of ionic charges, modeled by the CPE element, is observed to increase with the effective area of the PDLC devices, and also a slight decrement with the internal layer thickness. The double layer capacitive effect is clearly dependent on the thickness and the area, in such way that the thinner or larger the PDLC device, the higher the Cdl value obtained, as it is expected in a capacitor-like component. Finally, electrical current consumption shows that the smaller size and thickness device, i.e. PDLC25b, requires the greater value of current, lower than 1 mA rms, to switch from translucent to transparent state.

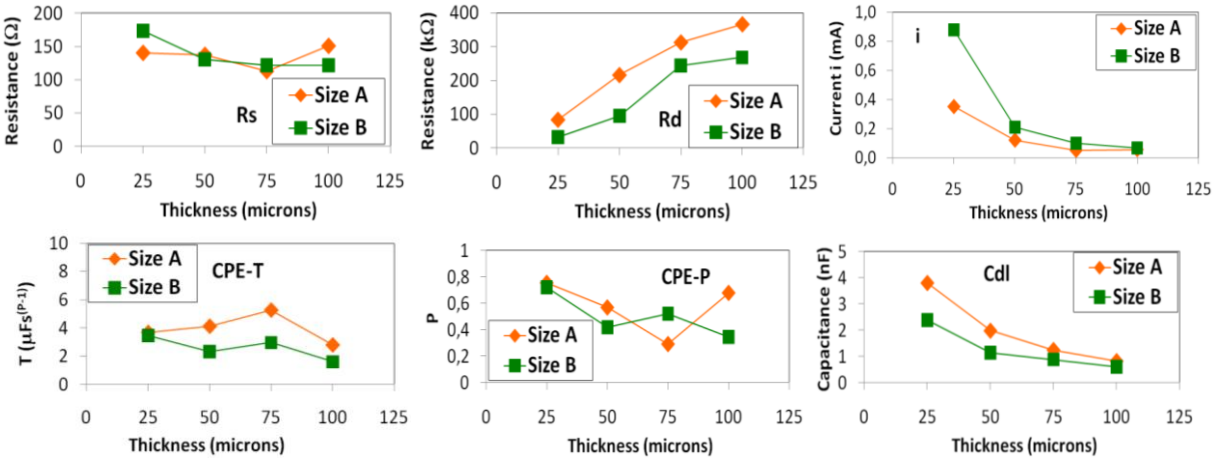

Figure V.27: Dependence on the area and thickness of the parameters Rs, Rd, CPE-T, CPE-P and Cdl of the EEC model of PDLC devices and electrical current consumption.

V.4.3 Complex impedance of the tandem PDLC-EC device

Figures V.28 and V.29 show the Bode magnitude and phase and the Nyquist impedance plots measured over the PDLC and EC parts of the tandem device separately. For the EC part, impedance was measured for the different coloration states, from 0 to 2 V DC bias voltages. For the PDLC part, the impedance was measured only for the translucent state, due to the impedance analyzer (Solartron1260) limitations for measuring impedance of a sample when a high AC signal is simultaneously applied [Bar10].

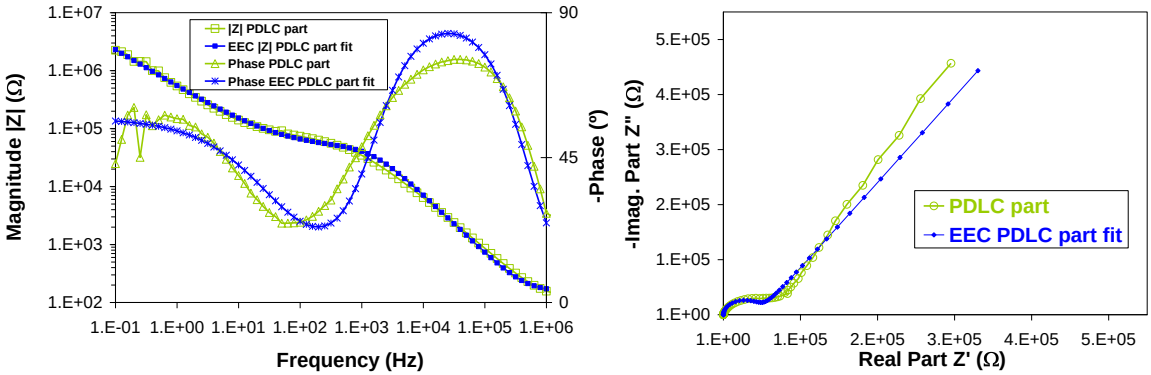

Figure V.28: (left) Bode magnitude (square symbol) and phase (triangle symbol) impedance plots and (right) Nyquist impedance plots for the PDLC part of the Tandem device at the frequency range of 100 mHz to 1 MHz, and fittings to the EEC model.

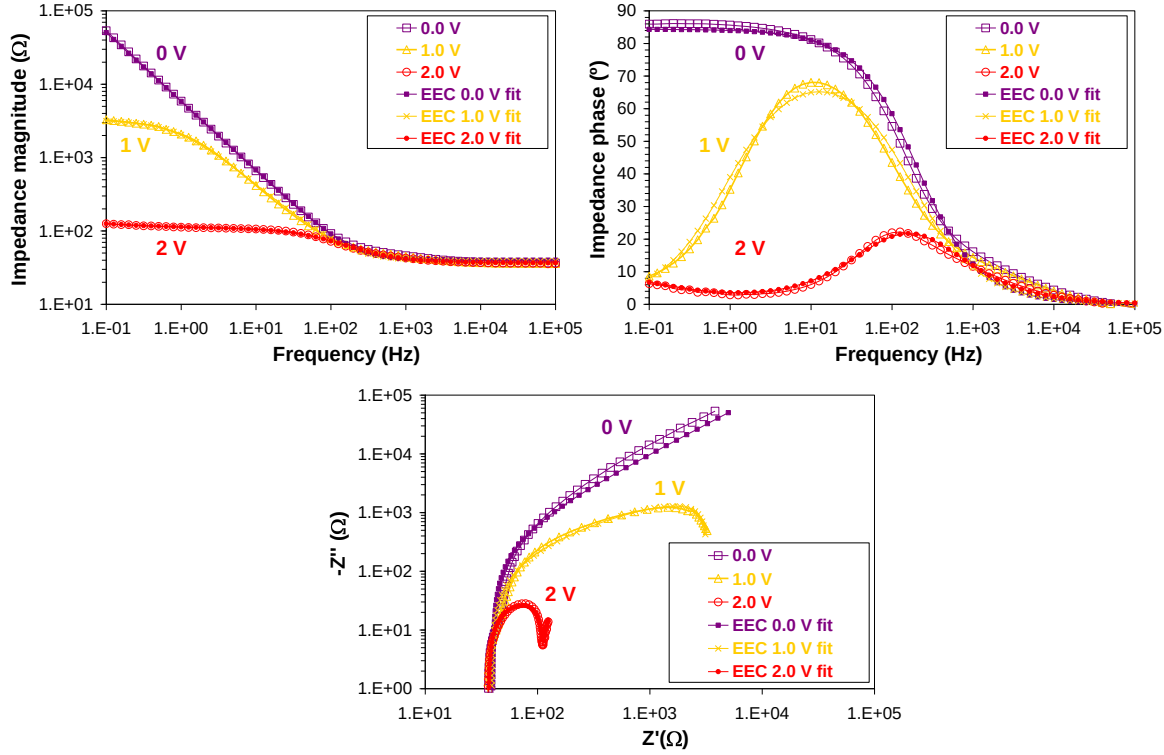

Figure V.29: (up) Bode magnitude (square symbol, left) and phase (triangle symbol, right) impedance plots and (down) Nyquist impedance plots for the EC part of the Tandem device for three DC bias voltage levels (of 0, 1 and 2 V) at the frequency range of 100 mHz to 100 kHz, and fittings to the EEC model.

The EEC model observed in Figure V.30 for the PDLC and EC parts respectively are the same than the previously obtained for each device type separately (Figure V.25 and III.89 respectively). Tables V.2 and V.3 show the values of the parameters of the EEC model and the fitting errors, which show a large value for Wo parameter, since the diffusion tail

observed in the impedance Nyquist plots at low frequencies was not clearly appreciated for the frequency range used in the measurements.

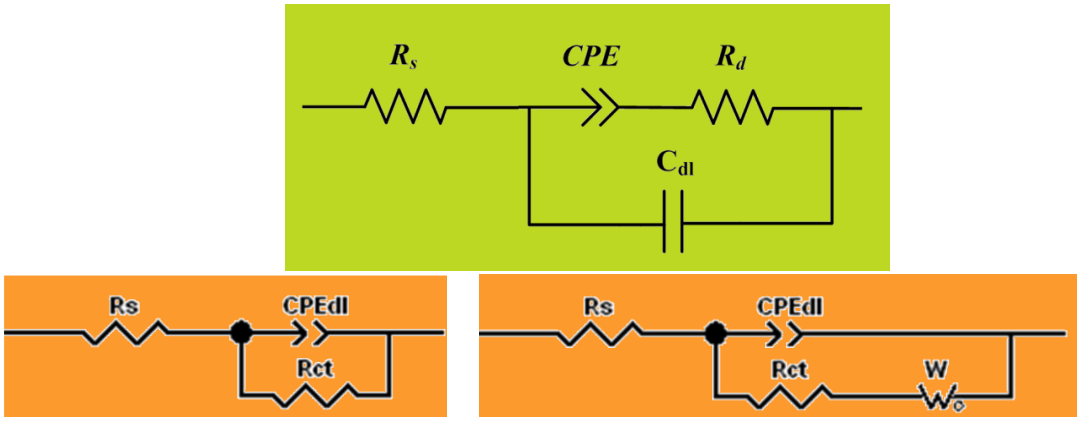

Figure V.30: EEC model for PDLC part (up) and EC part (down) for non coloration (left) and coloration observed (right) in the tandem PDLC-EC device.

Device:	Tamden (PDLC part)	
Parameter:	Value	Error (%)
Rs (Ω)	156	5.6
Rd (Ω)	48693	4.1
CPE-T (nFs^{P-1})	587	3.2
CPE-P	0.636	1.7
Cdl (nF)	2.22	2.2

Table V.2: Values of parameters and fitting errors of the EEC model for the PDLC part.

Device:	Tamden (EC part)				
Parameter:	0.0 V	0.5 V	1.0 V	1.5 V	2.0 V
Rs (Ω)	40	40	39	37	36
Rct (Ω)		126910	3241	122	73
CPE-T (μFs^{P-1})	30.6	34.2	67.4	100.1	100.1
CPE-P	0.937	0.927	0.855	0.803	0.788
Wo-R(Ω)				48.8	58.18
Wo-T (s)				13.18	11.51
Wo-P				0.5	0.5
Errors (%)	0.0 V	0.5 V	1.0 V	1.5 V	2.0 V
Rs (Ω)	1.08	1.07	1.06	0.54	0.37
Rct (Ω)		10.16	1.92	0.78	0.59
CPE-T (μFs^{P-1})	1.42	1.52	2.7	4.79	4.42
CPE-P	0.36	0.39	0.65	0.93	0.81
Wo-R(Ω)				38.9	12.6
Wo-T				85.01	28.12
Wo-P					

Table V.3: Values of parameters and fitting errors of the EEC model for the EC part for 0.0, 0.5, 1.0, 1.5 and 2.0 V DC bias voltage levels applied.

References

[Bar10] David Barrios, Ricardo Vergaz, Juan Carlos Torres, José-Manuel Sánchez-Pena, Cristina Pozo-Gonzalo, Ana Viñuales, M. Salsamendi,"Tandem Polymer-Dispersed-Liquid-Crystal – Electrochromic Device", 9th International Meeting on Electrochromism I.M.E.9, Bordeaux (France) (2010).

[Bar11d] David Barrios, Juan Carlos Torres, Carlos Marcos, Plinio J. Pinzón, Ricardo Vergaz, José-Manuel Sánchez-Pena, Ana Viñuales, "Dependence on the thickness and area of the parameters of equivalent electrical circuit model for devices in polymer dispersed liquid crystal on glass substrate", 7ª Reunión Española de Optoelectrónica, Santander (Spain) (2011).

[Cro90] P. P. Crooker and D. K. Yang, "Polymer-dispersed chiral liquid crystal color display", Applied Physics Letter 57 (1990) 2529-2531.

[Cup06] D. Cupelli, G. De Filpo, G. Chidichimo, F. P. Nicoletta, "The electro-optical and electrochromic properties of electrolyte-liquid crystal dispersions", Journal of Applied Physics 100 (2006) 024515.

[Cup09] D. Cupelli, F. P. Nicoletta, S. Manfredi, M. Vivacqua, P.Formoso, G. De Filpo, G. Chidichimo, "Self-adjusting smart windows based on polymer-dispersed liquid crystals", Solar Energy Materials and Solar Cells 93 (2009) 2008-2012.

[DKY06] D.-K. Yang and S.-T. Wu, "Fundamentals of liquid crystal devices," John Wiley & Sons, Ltd., (2006).

[Drz95] P.S. Drzaic, "Liquid Crystal Dispersions", World Scientific Publishing Co. Pte. Ltd. Singapore (1995).

[Hik90] R.A.M. Hikmet, "Electrically induced light scattering from anisotropic gels", Journal of Applied Physics 68 (1990) 4406.

[Jur05] M. A. Jurado, C. Vázquez, J. M. Sánchez, D. S. Montero, P. C. Lallana, "Variable Optical Attenuator for Perfluorinated Gradual Index Polymer Optical Fiber using a Polymer Dispersed Liquid Crystal Cell", SPIE International Congress on Optics and Optoelectronics, Proceedings of SPIE 5947, 5940H (2005).

[Mac00] M. Macchione, D. Cupelli, G. De Filpo, F.P. Nicoletta, G. Chidichimo, "Rough surfaces for orientation control in reverse mode polymer dispersed liquid crystal films", Liquid Crystals 27 (2000) 917-920.

[Nic99] F.P. Nicoletta, G. De Filpo, J. Lanzo, G. Chidichimo, "A method to produce reverse-mode polymer dispersed liquid cristal shutters" Applied Physics Letter 74 (46) (1999) 3945-3947.

[Nic05] F. P. Nicoletta, G. Chidichimo, D. Cupelli, G. De Filpo, M. De Benedettis, B. Gabriele, G. Salerno, A. Fazio, "Electrochromic Polymer-Dispersed Liquid-Crystal Film: A New Bifunctional Device". Advanced Functional Materials 15 (2005) 995-999.

[Per96] S. H. Perlmutter, D. Doroski and G. Moddel, "Degradation of liquid crystal device performance due to selective adsorption of ions", Applied Physics Letter 69 (1996) 1182.

[Ram03] R. A. Ramsey, S. C. Sharma, R. M. Henry, and J. B. Atman, “Electro-optical Properties and Interfacial Charges in Polymer-Dispersed Liquid Crystal Devices”, Material Research Society Symposium Proceedings 771 (2003) 339-344.

[Ram04] R. A. Ramsey and S. C. Sharma, “Electrochromic blueshift in polymer-dispersed liquid-crystal cells”, Optical Letter 29 (19) (2004).

[San02] J. M. Sanchez, C. Vazquez, I. Perez, J. M. Otón, I. Rodriguez, “Electro-optic system for online light transmission control of polymer-dispersed liquid crystal windows”, Optical Engineering 41 (7) (2002) 1608-1611.

[Thu84] R. N. Thurston, J. Cheng, R. B. Meyer and G. D. Boyd, “Physical mechanisms of dc switching in a liquid-crystal bistable boundary layer display“, Jorunal of Applied Physics 56 (1984) 263.

[Yam97] R. Yamaguchi, Y. Waki, S. Sato, “Reverse-mode and wide view angle properties in polymer dispersed liquid crystal cells prepared using a UV curable liquid crystal”, Japanese Journal of Applied Physics 36 (1997) 2771-2774.

[YDM90] Y. D. Ma, B.G. Wu, “Reverse-mode microdroplet liquid crystal display”, Proceedings SPIE 1257 (1990) 46-57.

Chapter VI: Developed applications

Four different developed applications will be detailed in this Chapter, in order to apply the studied chromogenic technologies to the real world. New glasses with for people with low vision and variable optical attenuators were studied as applications using the EC devices developed by CIDETEC. A domotic system for transparency local and remote (Internet) control of smart windows of PDLC technology was also developed. Finally, a prototype of electro-optical characterizer for EC devices was developed using a National Instrument data acquisition card.

VI.1 New glasses with EC filter for people with low vision

This application is dedicated for people who need a total blockade of the blue light which is caused by the majority of diseases affecting the retina or those who require extra protection for the development of their daily activities. Eyeglasses with spectral filters are recommended as an ophthalmological solution to help and protect the eyes of patients with low vision symptoms by blocking the ultraviolet (UV) to blue spectrum of light [You94]. Many patients with retinopathies, mainly in retinal inherited eye diseases [Adr77], complain about symptoms which vary from glare to photophobia. Past studies of tinted lenses and low vision have assessed effects on visual acuity (VA), grating acuity, contrast sensitivity (CS), visual field, adaptation time, glare, photophobia and TV viewing [Lea94, YZR00, Epe04]. Optical filters which block visible wavelength intervals, mainly in the blue part of the spectrum, may reduce these symptoms [Cro97]. These lenses are light spectral selective filters capable of varying the light intensity and color that reaches the eye. Depending on the environmental light conditions, the eye adaptation can be improved using a different filter [Epe03]. The main disadvantage here is that patients usually require carrying two sets of filters, a dark set which is used in bright environments and a clear set for indoor activities such as reading. To change from one set of filters to another can be a waste of time and uncomfortable process. Usual photochromic lenses are not suitable in severe changing light conditions, as the chemical reaction involved can be a matter of minutes, not fast enough to prevent retinal adaptation [Epe03]. These disadvantages have motivated an innovative research as the work presented in this paper, where a single filter has been developed that changes its color or optical transmittance according to the requirements of the user and/or the low-vision practitioner. Several materials which optical properties can be tuned by applying current could be used for this application, for instance, LCs, electrophoretic particles in SPDs and devices based on EC materials. Smart EC sunglasses developments have been attempted [CMa08], even a failed commercial one (Nikon in the last decade), with transmittance ranging from 10 to 60 %, but there are not applications specifically oriented to low vision patients.

The main objective of this application was to design and implement a new technical aid for patients with low vision using new EC materials controlled by a full-custom electronic driver. The specific objectives were to create an electronic circuit capable of driving EC devices, and to construct a stylish spectacles prototype which can be straightforward useful, with low power consumption and portable and easily programmable by the low-vision practitioner. These glasses should vary from clear to a fixed maximum dark state to cover the needs of all patients. As with all the EC devices characterized in this document, CIDETEC, the Research Centre for electrochemistry at San Sebastián, Spain, developed the new EC materials and devices used for this application. The EC used for this purpose is a new viologen based EC sample called GSBD' (glass support blue device), similar to the sample GSBD analyzed in Chapter III [Bar08a], but in this case EC mixture being prepared at room temperature [Poz08a] instead (GSBD mixture was prepared at high temperature). A change in the appearance from transparent to dark blue for an input voltage signal ranging between 0 V and 2 V was observed in the GSBD' sample.

The IOBA, a health and research institution at the University of Valladolid, Spain, stated the spectral and temporal characteristics that should be reached by the device, in order to be viable for patients with low vision. The spectral requirements of the filters are based on its adequacy to the current prescribed market filters (curves will be shown in the next section), and the temporal requirements of the electro-optic system are designed to adapt to the temporal answer of the filter, slow enough for the eye to achieve adaptation and quick enough for the patient to avoid glare (from 2 to 10 seconds). The optical characterization of the combination of the EC device with different ophthalmologic filters, along with the design and development of the electronic circuits and software required for efficient operation, was developed by GDAF.

Three prototype electronic controlled spectacles using EC filters were designed to be used as a novel customized light filter, a valuable tool for a wide range of visual tasks and eye protection for patients with low vision symptoms. Since they use the EC technology, these devices are able to modify the transmittance and the spectral characteristics of light in function of the electrical voltage applied to the combination EC device + ophthalmologic photochromic filter. The combination of blocking and EC filters achieved a wide range of predetermined colorations and transmittances (Figure VI.1), thus reducing the number of pairs of glasses required by a single patient. The simulated colors have been obtained from CIE chromaticity coordinates and the XYZ to RGB matrix conversion.

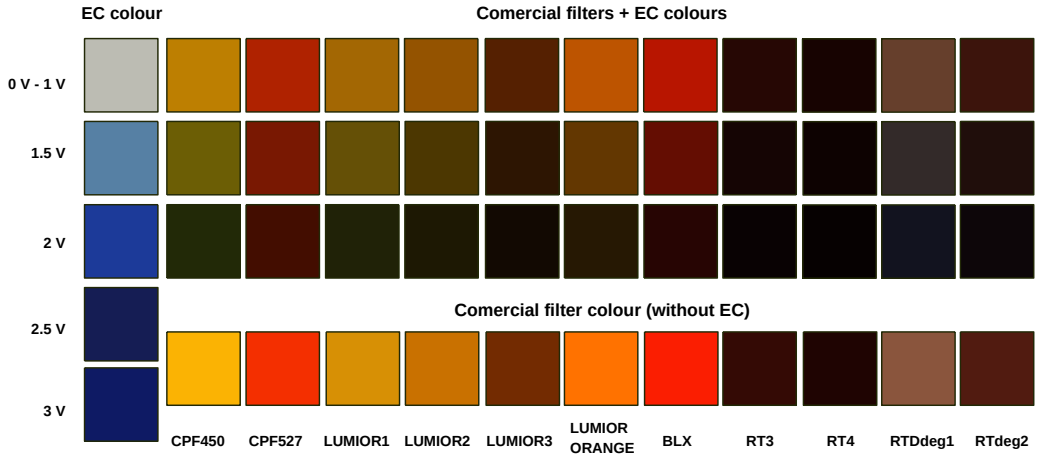

Figure VI.1: Simulated colors of the combined photochromic filters with the EC device switching from 0 to 2 V (up) and without the EC device (down) for the different ophthalmologic filters analyzed.

Figure VI.2: Three prototypes of EC glasses developed by GDAF. First (up) and second (down-left) prototypes used manual control by means of a variable resistance. Third prototype (down-right) included the possibility of an automatic control by means of a microprocessor and photodiodes.

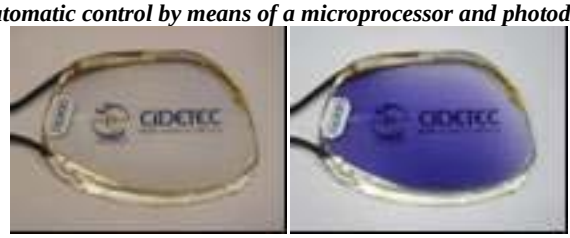

Figure VI.3: EC devices developed by CIDETEC for the glasses.

Figure VI.4: Ophthalmologic photochromic Corning filters, from left to right, CPF 450, CPF 450XD, CPF 511, CPF 527, CPF 550 and CPF Glarecutter.

The characterization of the set EC + filters was carried out with the purpose of being implemented in the EC glasses prototypes of Figure VI.2 [Veg10]. A complete circuit which controls the maximum and minimum voltages was developed in a first prototype (based in previous works [Cha07, Cer08, Alb08 and Gut08]), being located in the sidepiece of the glasses. A variable resistance allows the control of the coloration appearance of the glasses. A second prototype, with the complete circuit placed in the center of the glasses (Figure VI.2-right-down) included a system with photodiodes which allow the possibility of an automatic control of the state of the glasses, depending on the outside light. Custom-designed software was developed to program the voltage levels required by the EC filters for each patient and can be operated using a conventional PC. The viologen based EC devices prepared by CIDETEC were modeled as the normal lenses used for glasses (Figure VI.3). The photochromic filters used to combine with the EC device are the Corning series provided by IOBA (Figure VI.4). As photochromic, these filters change their appearance by a light stimulus. However, the times required for optically switching are in the order of 30 minutes. The improvement of the developed application is to reduce this time by using EC devices. Color appearance of the photochromic filters in lightened and darkened states is shown in Figure VI.5.

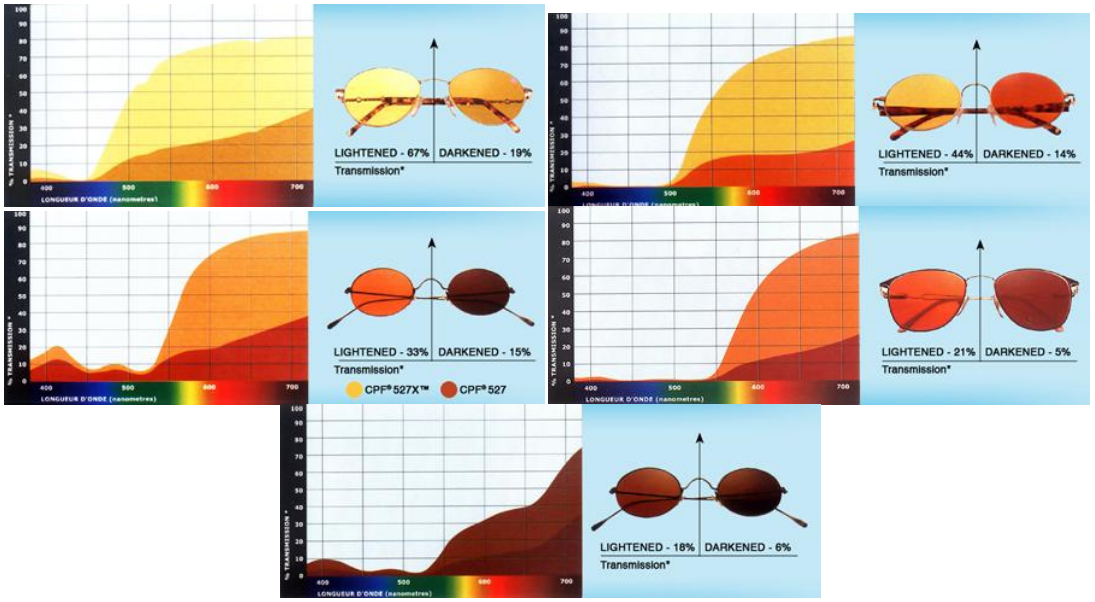

Figure VI.5: Lightened and darkened states of photochromic ophthalmologic filters Corning CPF 450 (left-up), CPF 511 (right-up), CPF 527 (left-center), CPF 550 (right-center) and CPF GlareCutter (down).

Figures VI.6, VI.7 and VI.8 show photographs of three different combinations of filters and EC device for bleach and dark states, with 1 and 2 V applied respectively. From all the possibilities of achieved colors obtained from Figure VI.1, and according to the specifications detailed from IOBA, patients with low vision would prefer an EC filter switching from a yellow color to a green color, as it is the case of CPF450 (Figure VI.6)

or Lumior 1 (Figure VI.7). Other possibilities such as switching from orange to brown colors, for instance for filter BLX (Figure VI.8), could be also considered.

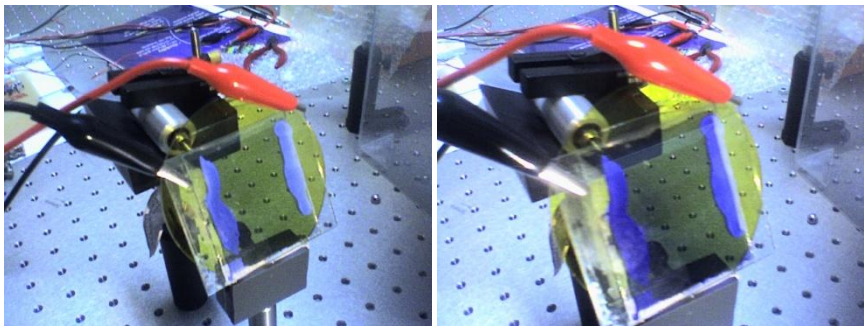

Figure VI.6: CPF450+EC at 1 V and at 2 V.

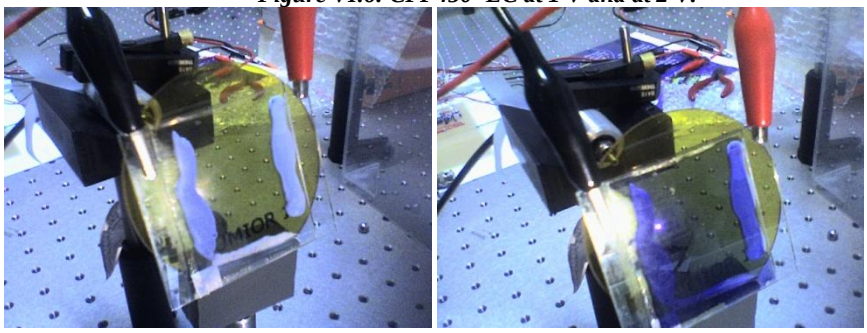

Figure VI.7: Lumior1+EC at 1 V and at 2 V.

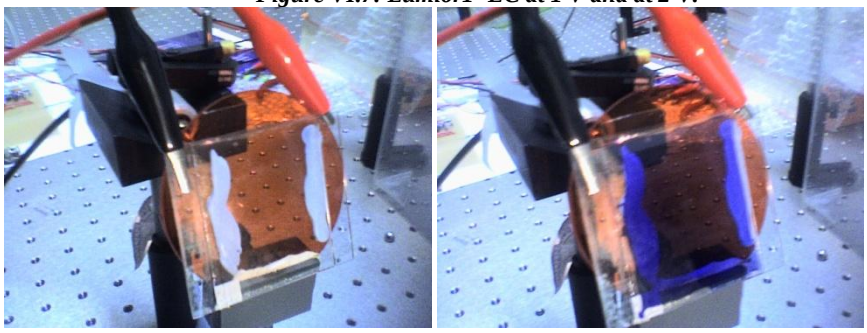

Figure VI.8: BLX+EC at 1 V and at 2 V.

Figures VI.9, VI.10 and VI.11 show the transmittance of each studied filter and the transmittance of the EC device at each different voltage level applied from 0 to 2 V with 0.1 V steps. The left figures show the transmittance of both the photochromic filter and the EC device separately, and the right figures show the transmittance of the photochromic filter and the EC device joined. A comparison with Figure VI.5 shows that the complete control of the spectra is achieved. The photochromic lenses are not changing in these measurements, being in the bleached state. Approximately the results are close to the obtained by multiplying both transmittance spectrums, but interface reflectances cause slight differences.

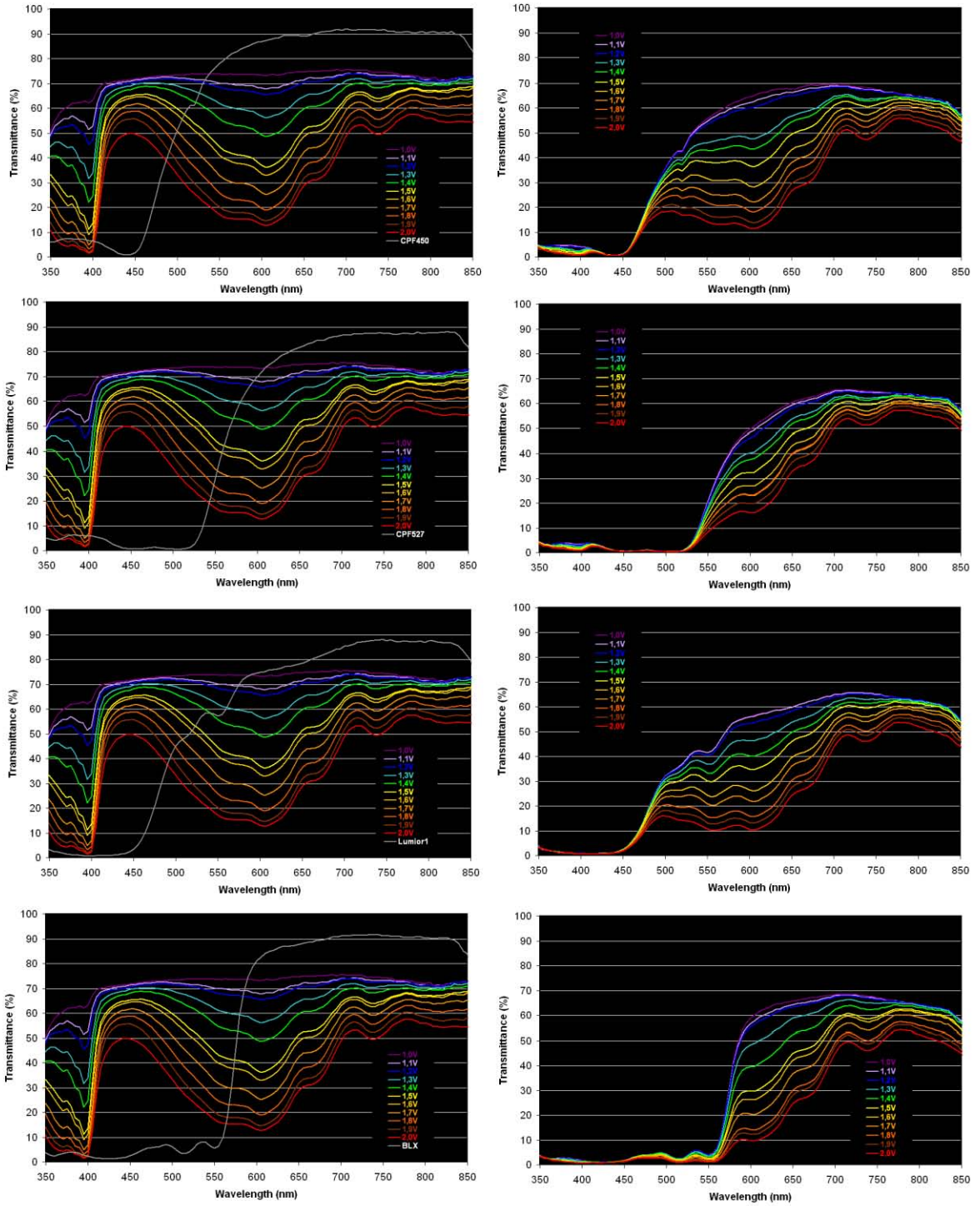

Figure VI.9: Spectral transmittance of filters and GSBD' measured separately (left) and together (right). CPF 450, CPF 527, Lumior 1 and BLX (from up to down)

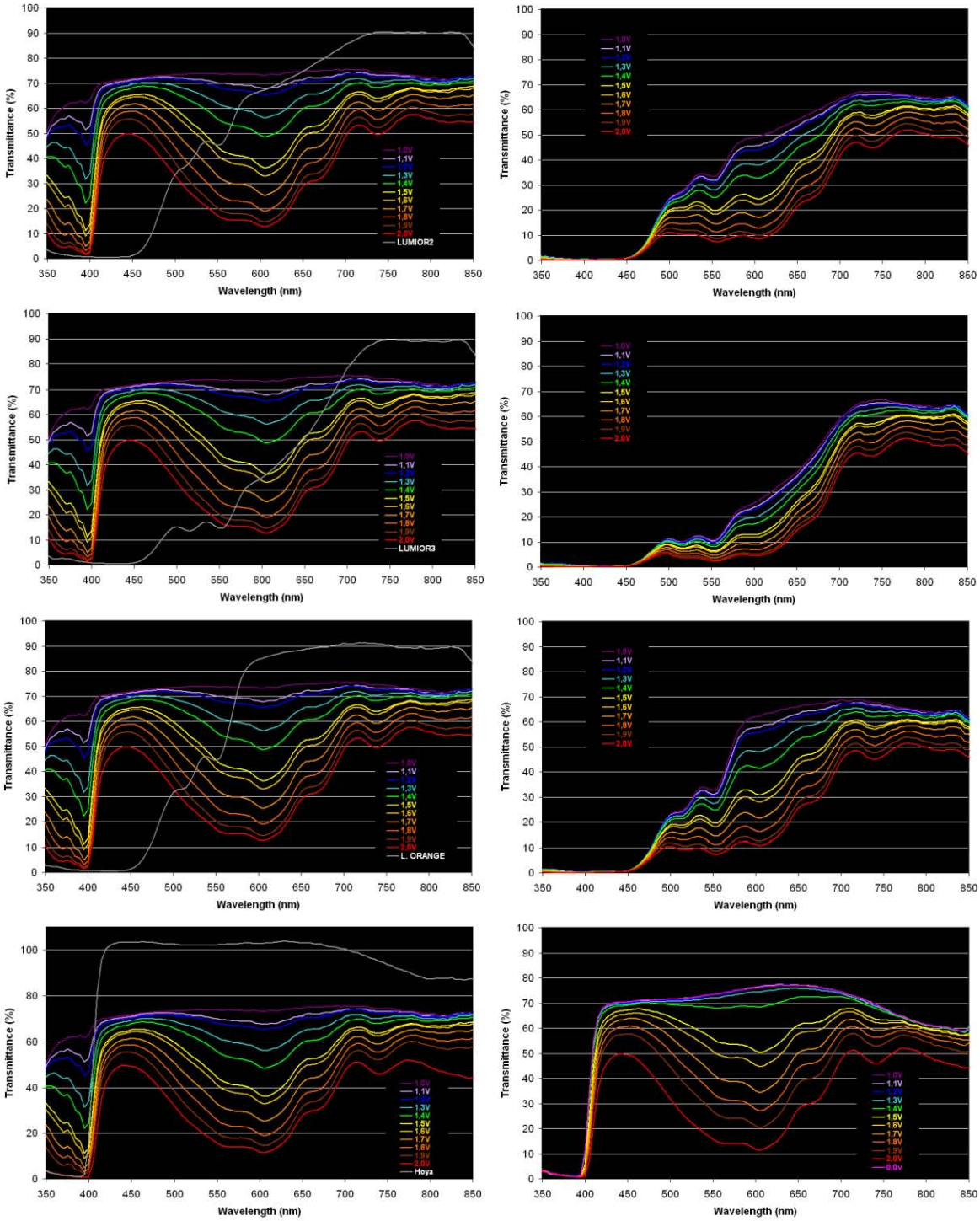

Figure VI.10: Spectral transmittance of filters and GSBD' measured separately (left) and together (right). Lumior 2, Lumior 3, L. Orange and Hoya (from up to down).

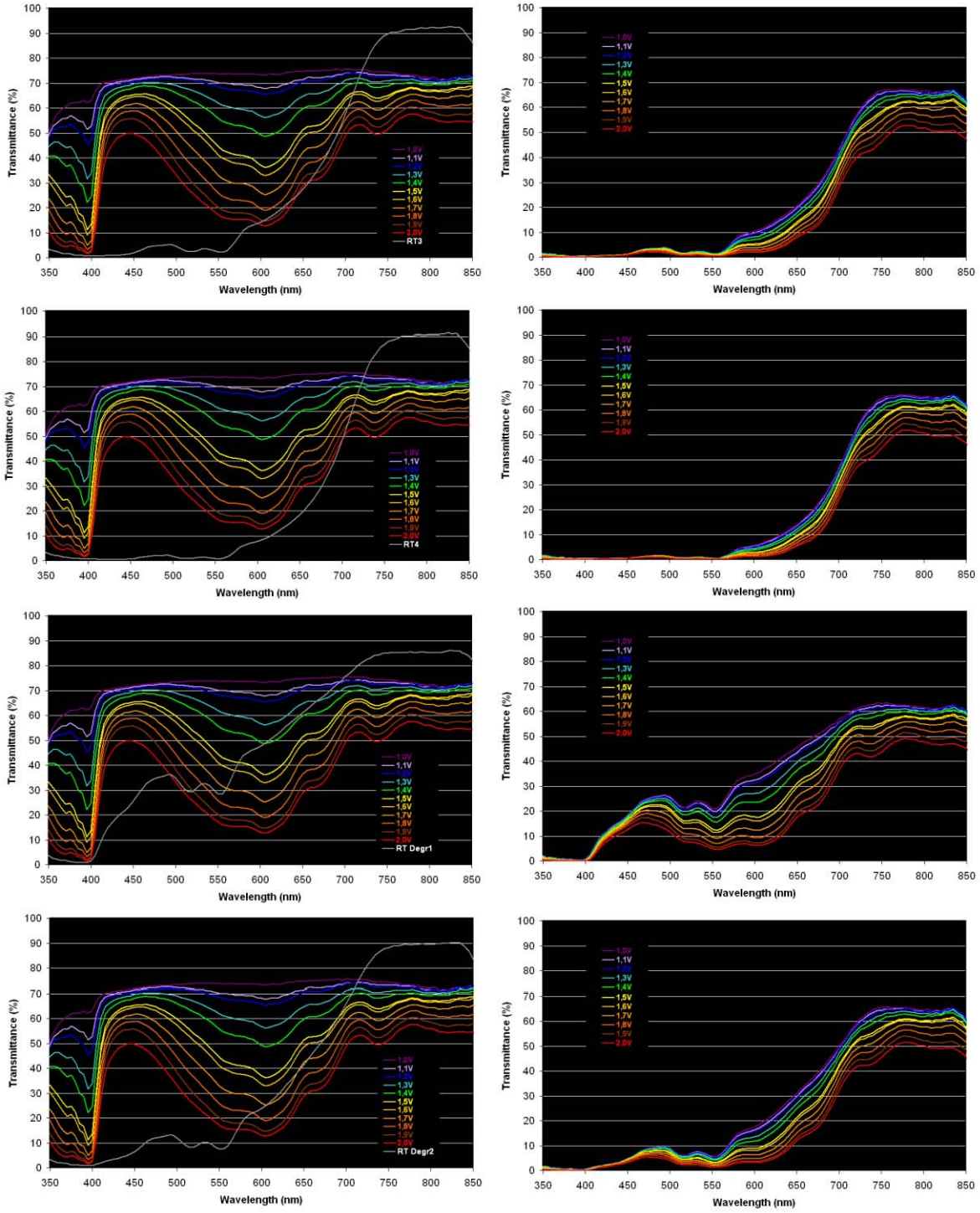

Figure VI.11: Spectral transmittance of filters and GSBD' measured separately (left) and together (right). RT3, RT4, RT Degr. positions 1 and 2(from up to down).

VI.2 Variable optical attenuator (VOA) using EC devices

A variable optical attenuator (VOA) acts as a component in advanced telecommunication systems, such as wavelength division multiplexing networks for equalizing the different channels by dynamically reconfigure the optical amplifiers' gain [Lou03], or in line VOA crossconnects, and add/drop multiplexer [Gil99], etc. Commercial VOAs are optomechanical or thermooptic. Another kind of solutions based on the voltage-controlled transmittance changes in several kinds of materials has been provided for the VOA application. Among these materials, PDLC [Lou03, Jur05] and EC [Bri99, Ver05b, Poz08b] devices can be found. Electrochromic variable optical attenuators (ECVOAs) have received limited attention traditionally. The major drawbacks of the EC devices that can be detrimental for their good performance in optical communications and signal processing are the high response times and the low transmittance range. The former is caused by the times needed to produce an electrochemical reaction (from several seconds to minutes); as opposed to this, the simple movement of a molecule around its axis is several orders of magnitude faster (some miliseconds). The latter is caused by the absorption in the IR region of the different non-active layers present in the devices, such as substrates and contacts. Especially in the former effect, liquid crystals are the best candidates for VOAs. But there are important reasons to press the idea of ECVOAs, because there are some advantages compare to liquid crystal devices: they can be switched at very low DC voltages, simply 0 to 3 V; they can be made on simple and thin flexible sandwiches, especially if we are searching polymer materials; the EC could have memory effect, i.e., once the device is switched on, the applied voltage can be removed and the coloration obtained can be maintained; they can be easily integrated in optical fiber networks; and they can reach to a linear control of the transmitted light power crossing them by means of a simple feedback configuration. Several attempts have been made; the first were using inorganic materials such as IrO_x, Ta_2O_5 and WO_3 over silicon [Bri99], some reflective devices were obtained with a good performance at the 1200-2000nm range, a 15dB dynamic range and 5dB/sec of switching response. Molybdenum redox reactions were the key to obtain another kind of ECVOA with a 50dB attenuation range [Cow01], with ITO as contacts; although the optical attenuation was good, the response time was in the order of minutes. Works of Wang and coworkers have migrated from the ruthenium [YHQ02] to PEDOT [JDZ04]. This last material, compared to metal oxides, can show a faster response time and the possibility of integration in flexible devices. But the absorption coefficients of organic EC materials are far from the operation required for a VOA device in terms of its dynamic attenuation range. Besides, the low quality of the transparent conductor layer onto plastic substrates is still a major drawback, and some of the results that are usually shown have removed its important contribution to the attenuation to improve the bleached state properties. As it was seen in Chapter III, PEDOT is colored in transparent-blue when oxidized and in dark-blue when reduced. Other works oriented the research on PEDOT devices towards the improvement of their transmissive characteristics in the bleached state. After the first work on an all-polymeric

device [Arg03], that removed the contact layer to make the most of the PEDOT conductive properties, another kind of devices were made [Mec03, Mec04] that improve the manufacturing process by the use of a reduced number of layers, using PEDOT playing the role of contacts, as it was seen in Chapter III (Figure III.1).

Two different kinds of approaches have been used to construct EC devices for this work [Ver05b]. In the former one, commercial PEDOT foils were used. In the latter, PEDOT foils were synthesized completely in the laboratory through oxidative polymerisation. For the sake of simplicity, we will mention the first kind of devices as EC A and the second one as EC B. Figure VI.12 shows their appearance for the bleached state. Both are mainly blue, being EC B quite darker than EC A. Both are approximately square, and with an active area of 420 mm^2; both switch properly when voltages from 0 to 3V are applied. And mainly, both are avoiding the use of contacts, one of the major drawbacks for the infrared performance of the devices, because they use the conductive properties of PEDOT to make it play the double role of contact and active layer. The devices have been tested in a VOA configuration as it is described in Figure VI.13. A laser diode (Advanced Fiber Solutions ©) emitting at 850 and 1300 nm is used as source, and the EC device is inserted in the optical path. The transmitted light is focused on the entrance of the power meter Equitel© 201 for both wavelengths. We have stressed those wavelengths, but the results are expected to improve in the 1500 nm band, according to the usual spectra of PEDOT absorption ranges.

The operation of these devices in the optical transmission windows (850, 1310 and 1550 nm) are of interest for ECVOA applications. Attenuation in the NIR range is measured for the device focusing on the 1310 nm second transmission window. The transmittance was obtained by dividing the measured power with the EC device by the measured power without the EC device. No appreciable transmittance change (around 1.6%) was observed for EC A, with values of 28.5 and 26.9% measured for bleached and colored states respectively. For EC B, a 26% of transmittance contrast is observed at 1310 nm wavelength, with values of 17.8 and 43.9 % of transmittance for bleached and colored states respectively (Figure VI.14-left) was observed, with insertion loss is of 3.6 dB. The results depend strongly on the cycling process. The maximum and minimum transmittance changes are obtained when applying to the EC device a square voltage signal from 0 to 3 V with 40 seconds of period and sampled each 20 seconds. Colored state stabilizes after 8 cycles. Bleached state stability is not appreciated since the device shows an increment in transmittance for the first 8 cycles and a decrement of transmittance after the eighth cycle. The evolution of the transmittance at 1310 nm for different voltages shows an almost linear dependence from 0 to 1.5 V (Figure VI.14-right), being not necessary to switch the EC device further from 1.5 to 3 V. Also, it is possible to obtain a linear control of the transmittance, profitable for VOAs. Further voltages could result in stresses in the charge interchanging process, and the quick degradation of the material. These results are still not sufficient to be a good VOA in an optical fiber network, but different manufacturing process could lead to improvements in

the transmittance contrast and stability in NIR wavelength range. Further research showed a 44% of transmittance contrast at 1971 nm and 50.5% in the visible wavelength range when IL-BF_4^- family was used in the electrolyte [Poz08b].

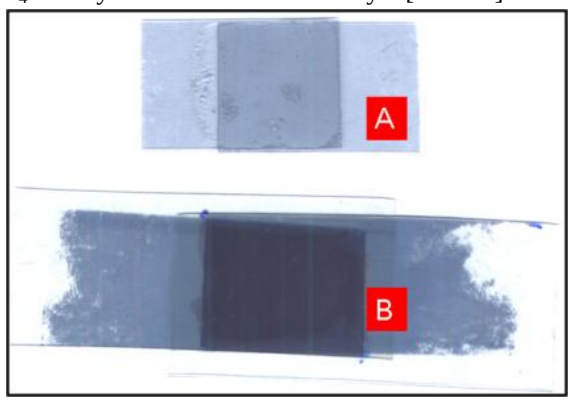

Figure VI.12: Developed PEDOT EC devices, shown in their bleached state. EC A devices, manufactured starting from AGFA's Orgacon films. EC B new oxidized all-polymeric devices.

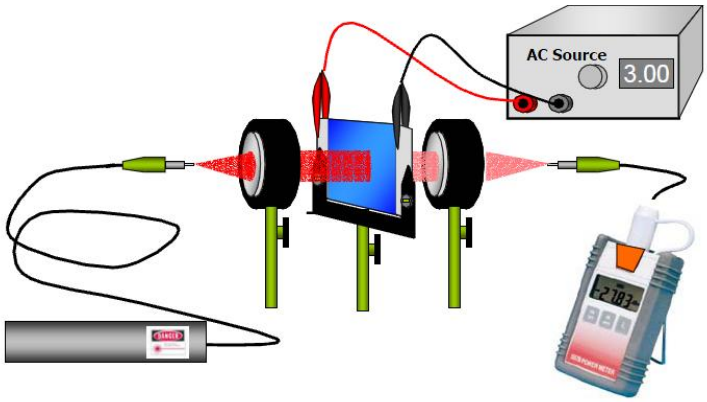

Figure VI.13: Experimental set-up for the VOA. A laser diode is used as source, and the EC device is inserted in the optical path. The transmitted light is focused in the entrance of the power meter.

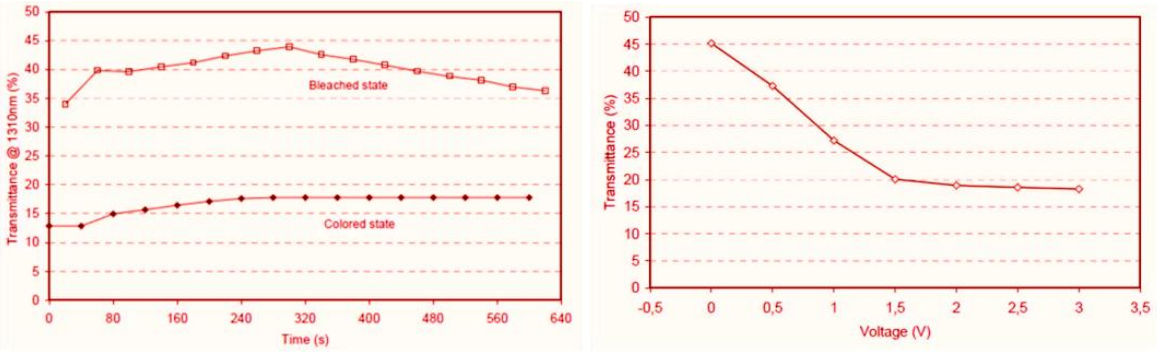

Figure VI.14: (left) Transmittance at 1310 nm observed in the EC device when applying a square voltage signal from 0 to 3 V with 40 seconds of period and sampled each 20 seconds. (right) Transmittance at 1310 nm evolution with the DC potential applied.

VI.3 Transparency domotic control of PDLC based smart windows

As it was described in Chapters I and V, polymer dispersed liquid crystal (PDLC) smart window technology allows to electrically switch optical appearance of a window from a translucent state to a transparent state by applying an AC sinusoidal potential signal. A remote and local control of a domotic net was developed by Ruben Gomez-Chacón [Gom07], a student of UC3M which project was supervised by J.M. Sánchez-Pena and David Barrios, using Crossbow wireless WSN-PRO2400CA Professional kit consisting on a net of sensors with transmission standard IEEE 802.15.4/ZigBee. Remote control is made by a Web browser, such as Internet Explorer, which allows checking and also modifying the state of the PDLC windows by a logged user. An automatic control is also available, by using a light sensor, in order to maintain a determined level of lightness as the user desires.

This remote control system consists of a client-server application communicated by sockets, with a Macromedia Flash programmed client, based on the project of David Barrios when being student of University of Córdoba [Bar02, Bar02b, Tho], with a domotic control system using EIB (European Installation Bus) standard instead of Crossbox Zigbee. NesC (C programming for embedded system), JSP (Java Server Pages), Servlets and a Tomcat Apache Web server were used for the server application, which also communicates with also communicates with a MySql managed database of users with access to the net.

The local control system consist of an actuator circuit developed by Sergio Martinez, a student of UC3M, which project was supervised by Carmen Vazquez and M.A. Jurado, based on a programmable logic device (PLD) programmed in VHDL which also includes an interface with a transmission node for remote control. This system was also used lately for electrically feeding a suspended particle device (SPD), as it can be seen in Chapter II (Figure II.18-right). Figure VI.15 shows the experimental setup using a purchased PDLC sample over a carton and placing inside the optical sensor node of Figure VI.16. When the user wants to switch the state of the PDLC in the manual mode or the lightness changes in the automatic mode, the sensor node communicates with the base station, which communicates with the actuator node, which communicates with the actuator circuit for electrically feeding or for stopping feeding the PDLC sample in both transparent and translucent states, respectively. The user can also check values given by the sensor node such as the level of illuminance, temperature, humidity, pressure, states of the batteries of sensor and actuator nodes or switch from manual to automatic modes. Figure VI.17 shows a screenshot of the Flash developed control software appearance. Other application using the Crossbow Zigbee standard was further developed by other members of GDAF for a network of sensors for fiber optic applications [Cha11, SMo11].

Figure VI.15: Experimental setup of a PDLC in a carton placing sensor nodes inside.

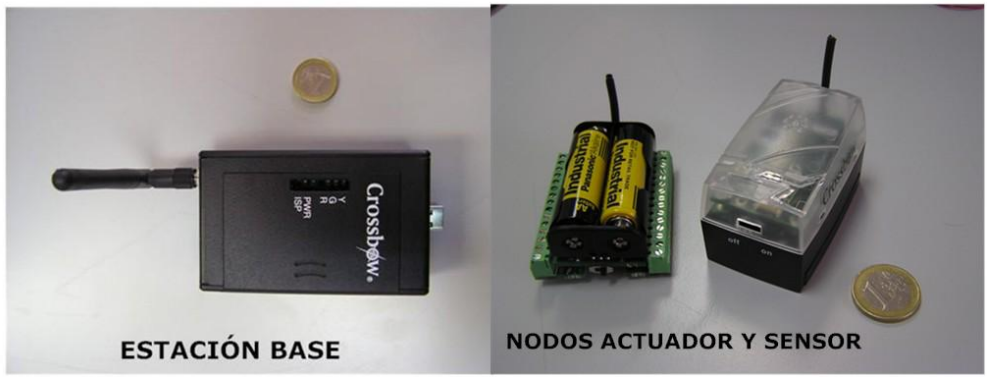

Figure VI.16: Crossbow Zigbee base station (left) and actuator and sensor nodes (right).

Figure VI.17: Screenshot of the developed control software appearance [Gom07].

VI.4 Electro-optic Characterizer of Electrochromic Devices (CEODEC)

A prototype of electro-optic characterizer for EC devices (named CEODEC) was developed by a Victor Montero [Mon11], a student of the UC3M which project was supervised by David Barrios, using a National Instrument NI USB 6009 data acquisition (DAQ) card, two RGB photodiodes (which measured signals were amplified by a designed processing signal module) for performing simultaneous electrical current and optical transmittance when different potential signals are applied to the EC device by a developed software programmed in Labview (Figure VI.18).

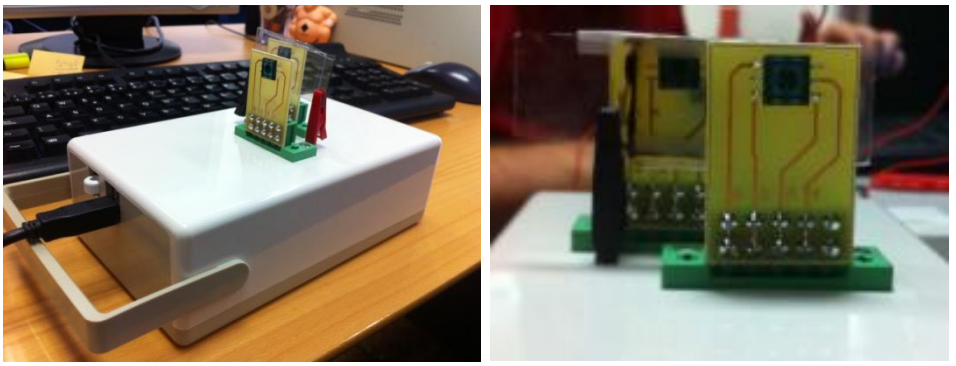

Figure VI.18: Photographs of CEODEC characterizer introduced in a PVC box and placing the photodiode connectors over the surface of the box [Mon11].

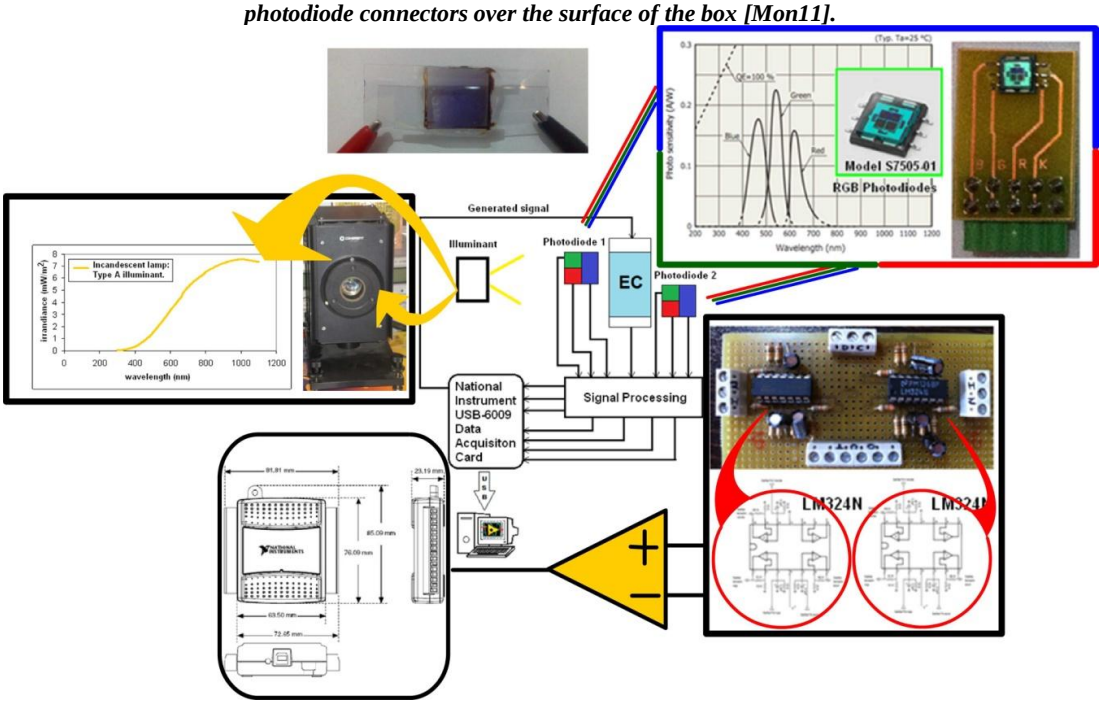

Figure VI.19: General scheme of CEODEC: Illuminant, EC device, pair of RGB photodiodes, signal processing module and NIUSB-6009 DAQ card.

The general scheme is shown in Figure VI.19. CEODEC uses two RGB photodiodes for measuring, simultaneously, the optical transmittance in three different peak wavelengths (660, 540 and 460 nm for red, green and blue respectively). The photodiodes are placed one in front and the other behind the EC device. A correction constant, due to the different distance from the illuminant to both photodiodes, is applied for achieving a 100% of transmittance without the EC device. The signals captured by the pair of photodiodes are amplified by a processing signal module including two LM324N operational amplifiers (OA) fed by the NI USB-6009 DAQ card with 5 V, which also applies different forms of potential signals to the EC device by means of the crocodile connectors, simultaneously measuring the electrical current and the optical transmittance vs. time. Triangular, square or sinusoidal signals are the three different options for cyclic voltammetry (CV), chronoamperometry (ChrA) and electrochemical impedance spectroscopy (EIS) measurements fully developed by the authors. CEODEC includes Labview programmed software developed for monitoring the measurement process. First and second step potential values and the times in both levels of potentials are selected by the user for ChrA experiments, scan rate and minimum and maximum potential values for CV experiments, and frequency signal and DC bias voltage applied for EIS experiment. Hence, with the values of the potentials of each photodiode, T_R, T_G and T_B are computed. A variable color block shows in real time the color appearance of the device, computed by the RGB values of the transmittances of the pair of photodiodes. Measurements of electrical current were carried out by a resistive circuit of Figure VI.20, once knowing the value of the small resistance R (around 100 Ω).

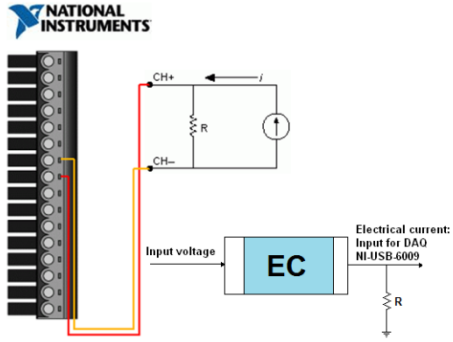

Figure VI.20: Scheme of the electrical current measurement.

Previous works for this characterizer can be found in [Cab05], where the signals of the photodiodes are read by a C8051 microprocessor after being amplifier by AD620 OAs, in order to save the data in a file by RS232 series communication for simultaneously measuring of T_R, T_G and T_B. The substitution of the microprocessor by the parallel port of a PC, including a Labview programmed software for monitoring the results which are also saved to excel file was carried out in [Mer08]. A system for measuring CV experiments was developed by using a microprocessor which generated the ramp potential signals and saved the data of electrical current in a file by RS232 series communication [Gon09]. *Arduino Duemilaove* DAQ card was originally thought to be

used for the present characterizer, but it was rejected since the no availability of the analog outputs. Finally, the NI USB-6009 DAQ card was selected. All the system was packaged in a PVC box of 11x18x6 cm^3 size. The photodiodes are placed in the proto board and fixed to the PVC box by two connectors model Phoenix DFK-MSTB 2,5/5-G as it is shown in Figure VI.19. The system is then connected to a laptop by a USB cable which electrically feeds the EC devices for optical switching (by the different potential signals) and also read the measured electrical current and amplified potential signals from the photodiodes.

Figure VI.21 shows the T_R, T_G and T_B results for the CV (left figures) and for the ChrA (right figures) experiments. Amplified potential signals for each photodiode are also observed in the figures, as well as the color resulted from the RGB space color (horizontal color block, with violet and pink colors in left and right figures).

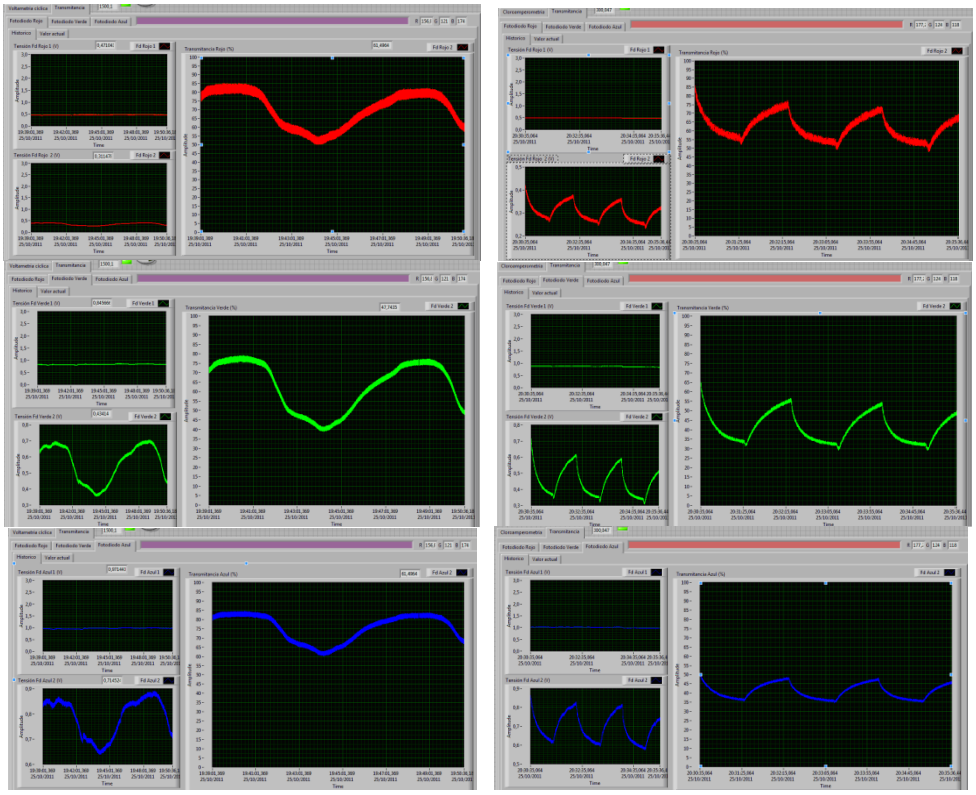

Figure VI.21: Optical transmittances T_R, T_G and T_B computed by the potential signals two RGB photodiodes paced at the front and behind the characterized EC device.

Figures VI.22, VI.23 and VI.24 show the applied potential signals and the measured electrical current for CV, ChrA and EIS experiments. Some improvements could be carried out for future versions of this characterizer, such as higher amplification of electrical current and varying frequency scans for EIS experiments, or digital signal

processing for computing EC devices parameters such as coloring and bleaching times, transmittance contrast or coloration efficiency. Chronocoulometry (ChrC) experiments could be also added to the system by integrating the measured electrical current of ChrA experiments.

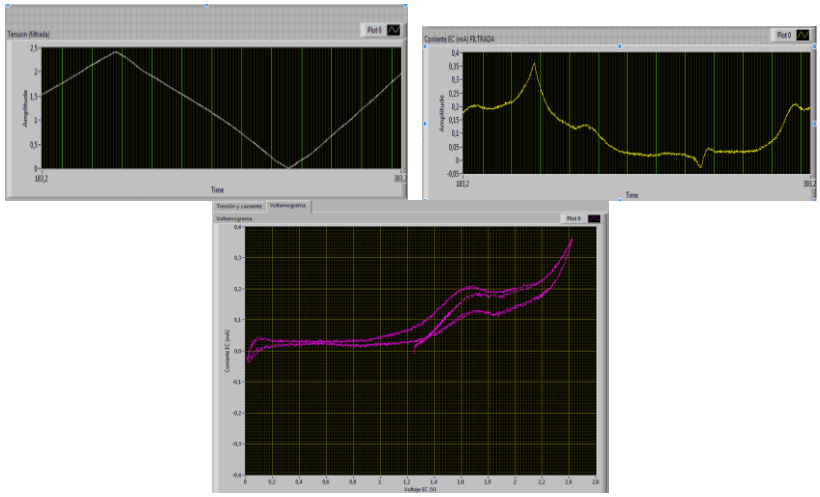

Figure VI.22: Triangular potential signal applied to the EC device (left), electrical current measured (right) and voltammogram obtained in real time (down) for CV experiment carried out by using CEODEC.

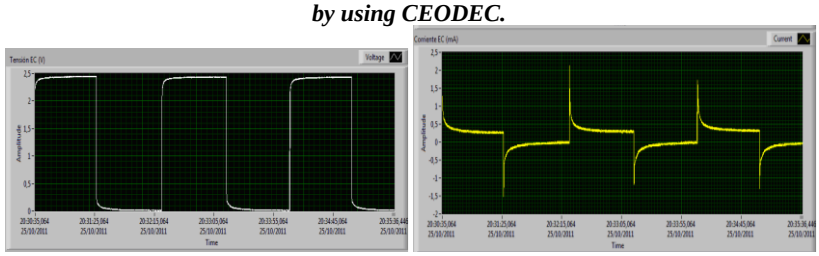

Figure VI.23: Square potential signal applied to the EC device (left) and electrical current measured (right) for ChrA experiment carried out by using CEODEC.

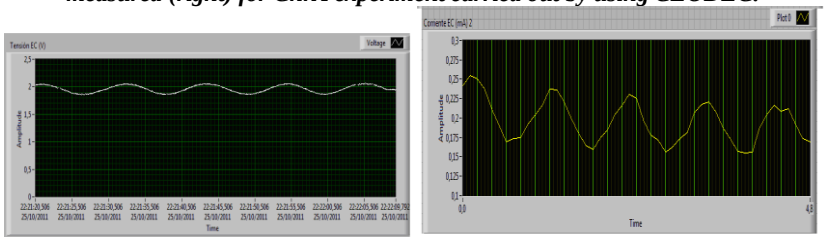

Figure VI.24: Sinusoidal potential signal over a DC bias voltage level applied to the EC device (left) and electrical current measured (right) for EIS experiment carried out by using CEODEC.

References

[Adr77] W. Adrian, R.W. Everson, I. Schmidt, "Protection against photic damage in retinitis pigmentosa", Advances in Experimental Medicine and Biology 77, (1977) 233- 47.

[Arg03] A.A. Argun, A. Cirpan, J.R. Reynolds, "The first truly all-polymer electrochromic devices" Advanced Materials 15, 1338-1341, 2003.

[Alb08] Javier Alba Sastre "Illumination detector system for electrochromic glasses", Project of Engineering, Electronic Technology Department, University Carlos III of Madrid (2008). Supervisor: Ricardo Vergaz Benito.

[Bar02] David Barrios Puerto, Aurelio José Urbano Burgueño, "EIBUCO (European Installation Bus for University of Córdoba)", Project of Engineering of Systems and Automatic Engineering Department, University of Córdoba (2002). Supervisor: Cristóbal Romero Morales http://www.uco.es/~p42bapud/proyecto.html

[Bar02b] David Barrios Puerto, Aurelio José Urbano Burgueño, Cristóbal Romero Morales, "EIBUCO, EIB system - Internet control software", El mundo de la domótica 38 (6) (2002) http://www.uco.es/~p42urbua/eibuco.pdf

[Bar08] David Barrios Puerto "Characterization of new electrochromic devices based on viologen materials", Master diploma (2008). Electronic Technology Department, University Carlos III of Madrid (2010). Supervisor: Ricardo Vergaz Benito.

[Bri99] N.A. Brien, N.A., Mathew, J.G.H., Hichwa, B.P., "An electrochromic variable optical attenuator (ECVOA)", Optical Fiber Communication Conference and the International Conference on Integrated Optics and Optical Fiber Communication. OFC/IOOC '99. PD26/1-PD26/3 (1999).

[Cab05] Jesus Ramiro Caballero Diaz, "Measurer of optical transmittance for electrochromic devices", Project of Engineering, Electronic Technology Department, University Carlos III of Madrid (2005). Supervisor: Ricardo Vergaz Benito.

[Cha07] Mercedes Chaparro de la Peña, "Integration and miniaturization of a driver circuit for electrochromic devices", Project of Engineering, Electronic Technology Department, University Carlos III of Madrid (2007). Supervisors: Juan Carlos Torres Zafra and Carlos Marcos Lucas.

[Cha11] Mercedes Chaparro de la Peña, "Wireless Zigbee technology based plastic fiber optic sensors network", Project of Engineering, Electronic Technology Department, University Carlos III of Madrid (2011). Supervisor Carmen Vázquez García.

[Cer08] Abraham Cerro Sánchez, "Improvement of a controller circuit for electrochromic devices and development of a software tool for users" Project of Engineering, Electronic Technology Department, University Carlos III of Madrid (2008). Supervisors: Juan Carlos Torres Zafra and Carlos Marcos Lucas.

[CMa08] C. Ma, M. Taya, C. Yu. "Smart sunglasses based in electrochromic polymers". Polymer Engineering Science 48 (2008) 2224 – 2228.

[Cow01] Cowin, M.A., Varrazza, R., Morgan, C., Penty, R.V., White, I.H., McDonagh, A.M., Bayly, S., Riley, J., Ward, M.D., McCleverty, J.A., "Low power electrochromic variable

optical attenuator with 50dB attenuation range". Optical Fiber Communication Conference and Exhibit 3 (2001). WR6-1- WR6-3.

[Cro97] P. Croughs. "Filtering lenses in retinopathy". Bulletin de la Societe Belge d Ophthalmologie 264 (1997) 119 - 24.

[Epe03] F. Eperjesi, "Non-optical assistive devices in low vision". Optometry Today 12 (2003) 36-38.

[Epe04] F. Eperjesi, C.W. Fowle, B.J. Evans. "Effect of light filters on reading speed in normal and low vision due to age-related macular degeneration". Ophthalmic and Physiological Optics 24 (1), (2004) 17 – 25.

[Gil99] C. R. Giles, V. Aksyuk, B. Barber, R. Ruel, L. Stulz, and D. Bishop. A Silicon MEMS Optical Switch Attenuator and Its Use in Lightwave Subsystems. IEEE Journal of Selected Topics in Quantum Electronics 5(1) 1999.

[Gom07] Ruben Gomez-Chacón Camuñas, "Remote control of a PDLC based smart window", Project of Engineering, Electronic Technology Department, University Carlos III of Madrid (2008). Supervisors: José Manuel Sanchez-Pena and David Barrios Puerto.

[Gon09] Iván Andrés González García, "Cyclic voltammetry measurer for controllable transmittance devices", Project of Engineering, Electronic Technology Department, University Carlos III of Madrid (2009). Supervisor: Ricardo Vergaz Benito.

[Gut08] David Gutiérrez Salto "Control introduction in a electrochromic glasses for low vision people" Project of Engineering, Electronic Technology Department, University Carlos III of Madrid (2008). Supervisor: Ricardo Vergaz Benito.

[JDZ04] Ji Dong Zhang, Hong An Yu, Xian Guo Wu, Zhi Yuan Wang. Towards the improvement of attenuation range and response time of electrochromic polymer-based variable optical attenuators. Optical Materials 27 (2004) 265–268.

[Jur05] Miguel Angel Jurado Pontes, Carmen Vázquez, J.M. Sánchez-Pena, David Sánchez Montero, Pedro Contreras Lallana, "Variable optical attenuator for perfluorinated gradual index polymer optical fiber using a polymer dispersed liquid crystal cell ", SPIE International Congress on Optics and Optoelectronics, Warsaw (Poland) 2005.

[Lea94] S.J. Leat, A. Fryer, N. J. Rumney. "Outcome of low vision aid provision: the effectiveness of a low vision clinic". Optometry and Vision Science 71(3), (1994) 199 – 206.

[Lou03] T. Loukina, R. Chevallier, J. L. de Bougrenet de la Tocnaye, and M. Barge. "Dynamic spectral equalizer using free-space dispersive optics combined with a polymer-dispersed liquid-crystal spatial light attenuator" Journal of Lightwave Technology 21(9) 2003.

[Mar06] Sergio Martínez García, "Development of electronics of PDLC based variable optical control for plastic optical fibers nets", Project of Engineering, Electronic Technology Department, University Carlos III of Madrid (2006). Supervisors: Carmen Vázquez García and Miguel Angel Jurado Pontes

[Mec04] D. Mecerreyes, R. Marcilla, E. Ochoteco, H. Grande, J. A. Pomposo, R. Vergaz and J. M. Sánchez Pena, "A simplified all-polymer flexible electrochromic device", Electrochimica Acta 49 (21) 3555-3559, 2004.

[Mec03] D. Mecerreyes, J. A. Pomposo, H. Grande, Spanish patent P200301884. 2003

[Mer08] Fernando Merino Lozano, "Optical cyclability measurer for electrochromic devices", Project of Engineering, Electronic Technology Department, University Carlos III of Madrid (2008). Supervisor: David Barrios Puerto.

[Mon11] Victor Montero Burgos, "Electro-optical characterizer for electrochromic devices (CEODEC)", Project of Engineering, Electronic Technology Department, University Carlos III of Madrid (2011). Supervisor David Barrios Puerto.

[Poz08b] C. Pozo-Gonzalo, D. Mecerreyes, J.A. Pomposo, M. Salsamendi, R. Marcilla, H. Grande, R. Vergaz, D. Barrios, J.M. Sánchez-Pena, "All-plastic electrochromic devices based on PEDOT as switchable optical attenuator in the near IR", Sol. En. Mat. Sol. Cells, 92(2), (2008) 101–106.

[Tho] http://www.michael-thomas.com/tech/flash/flash5socket/index.htm

[SMo11] D.S. Montero, M. Chaparro de la Peña, C. Vázquez, J. Zubia, "Wireless mesh network applied to polymer optical fibre-based sensors", in Proc. 20th International Conference on Plastic Optical Fibers (ICPOF) 547-552 Bilbao (Spain).

[Veg10] César Vega Colado, "Electrochromic glasses feedback control system", Master diploma, Electronic Technology Department, University Carlos III of Madrid (2010). Supervisor: Ricardo Vergaz Benito.

[Ver05b] Ricardo Vergaz, David Barrios, Jose M. Sanchez-Pena, and Carmen Vazquez, Cristina Pozo-Gonzalo, David Mecerreyes, and Jose Pomposo , "Variable optical attenuator made by using new electrochromic devices", Proceedings SPIE 5840, 389 (2005); doi:10.1117/12.608391

[Ver08a] R. Vergaz, D. Barrios, J. M. S. Pena, C. Marcos, C. Pozo and J. A. Pomposo, "Electro-optical Analysis of PEDOT Symmetrical Electrochromic Devices". Solar Energy Materials & Solar Cells 92, (2008) 107-11.

[YHQ02] Y.H. Qi, P. Desjardins, X.S. Meng, Z.Y. Wang. Electrochromic ruthenium complex materials for optical attenuation. Opt. Mater. 21 255–263. 2002.

[You94] R.W. Young. "The family of sunlight-related eye diseases". Optom Vis Sci. 71(2), (1994) 125 – 44.

[YZR00] Y.Z. Rosenblum, P.P. Zak, M.A. Ostrovsky, I.L. Smolyaninova, E.V. Bora, U.V. Dyadina, N.N. Trofimova, A. G. Aliyev. "Spectral filters in low-vision correction". Ophthalmic Physiol Opt. 20(4), (2000) 335 – 341.

Chapter VII: Brief discussion and conclusions

Several conclusions are derived from this work according to the different electrically controllable transmittance technology studied. In this chapter, the first section will show short discussions summarizing the results and conclusions presented in the previous chapters, grouped by the technology. The second section will outline the opened research branches that may follow the present work.

VII.1 Conclusions

VII.1.1 Electrochromic (EC) devices

o New organic EC devices developed by CIDETEC were characterized, based on PEDOT and viologen materials. The spectrometer based on an Acton Reseach monochromator and a Hamamatsu photomultiplier was used for optical characterization. Hewlet Packard 4194A and Solartron 1260 impedance analyzers were used for electrical impedance characterization by means of EIS experiments for PEDOT and viologen based EC devices. A Gamry FAS2 potentiostat was used for electrochemical characterization by means of ChC, ChrA and CV experiments only for viologen based EC devices.

VII.1.1.1 New all-plastic PEDOT EC devices

o Optical and electrical impedance characterization of three series of new all-plastic PEDOT devices of different active areas was carried out. The devices, developed by CIDETEC, have a sandwich structure with lower number of layers than the traditionally used, with PEDOT avoiding the contact layers and playing the role of electrochromic and counter electrode layers. The PEDOT EC devices switched optically from a slightly blue transparent bleached state, without applied voltage, to a darker blue less transparent colored state, with a small DC bias voltage applied.

o A small transmittance contrast at 600 nm (ΔT_{600nm}), reaching a maximum of 20%, was observed at the different applied DC bias voltage levels. Optical behavior of the devices was determined for both positive and negative polarities of the applied voltage, testing their quasi-symmetrical performance. The coloring and bleaching times (t_c and t_b) were 9 and 4 seconds respectively.

o The 1st series of PEDOT based EC devices shows a decrement of the impedance when coloring. On the contrary, the 2nd and 3rd series of PEDOT based EC devices show an increment of the impedance when coloring, since PEDOT is a conducting polymer in the bleached state that becomes less conductive when colored. Ionic liquids used in the

electrolyte of 1st series are basically the main differences from the 2nd and 3rd series and must be the cause for this behavior.

- Different EEC models were derived from the Nyquist diagrams obtained from electrical impedance characterization by means of EIS method, being some of these models a new contribution to the state of the art. Evolution of the parameters of the circuit with the applied DC bias voltage was studied for up and down voltage senses, corresponding to coloration and bleaching processes respectively. The hysteresis observed in impedance results, and hence in the fitted parameters, was related to the different evolution of the coloration state of the devices when coloring and bleaching.

- The 3rd EEC model showed the best fitting and consistency with the impedance measurements and the physical and chemical interpretation of the system. It consists of a resistance Rs standing for the contacts, in series with a CPEp||Rp shunt standing for sealing problems and bubbles, which is placed in series with a double layer CPEdl in parallel with a charge transfer resistance Rct and an open circuit Warburg diffusion impedance.

- Since the open circuit Warburg impedance Wo fittings only operated at high frequencies, it was substituted by a diffusion CPE in the 4th EEC model.

- The series resistance Rs standing for the contacts showed a constant behavior, independent from the coloration evolution, with a fitted value of approximately 350 Ω and errors lower than 1%.

- The parallel shunt CPEp and Rp standing for sealing problems and bubbles showed also a constant behavior, consistent with their physical meaning, independent from the coloration evolution, with values of approximately 600 Ω for Rp and 40 $\mu F/s^{(P-1)}$ for CPEp-T with a CPEp-P of 0.3, far from a capacitive feature.

- The double layer capacitive element CPEdl shows a decrement with the coloration of the CPEdl-T parameter, from 20 to 10 $\mu F/s^{(P-1)}$ being its behavior very close to a capacitor, with CPEdl-P varying from 0.8 to 0.9. Fittings errors are < 1%.

- The charge transfer resistance Rct shows an increment with the coloration. The hysteresis observed between bleaching and coloring processes could be due to deterioration of the device, maybe due to the introduction of spurious water molecules during the manufacturing process. Fitting errors in the 3rd EEC model using Wo are lower than 1%, except for higher voltages (from 1.5 to 2 V), being lower than 5%. The 4th EEC model improves the fitting errors to lower than 1%.

- Diffusion impedance (represented by Wo or CPEdiff elements in the 3rd and the 4th EEC models respectively) is negligible for DC bias voltage levels of non coloration appearance in the devices, since no diffusion process is taking place. Low diffusion impedance favors the redox reaction at coloration DC bias voltage levels.

VII.1.1.2 New viologen based EC devices

- Electro-optical characterization was carried out on new plastic and glass supported viologen based EC devices manufactured by CIDETEC at room and high temperatures processes. The glass supported devices switched from the uncolored states of dicationic viologen molecules form when no voltage was applied, to the colored states in the radical cation form of viologen molecules when applying a DC bias voltage. The colors are deep blue for those manufactured at high temperature and violet for those manufactured at room temperature. The plastic supported devices switched from pale transparent yellow bleached state to deep blue colored state. The devices were called PSBD, GSBD and GSVD according to the plastic (P) or glass (G) supports and their blue (B) or violet (V) colored states of the devices (D).

- Two samples on plastic supports, PSBD and PSBD' with internal layer thicknesses of 200 and 300 μm respectively, and two samples on glass supports, GSBD and GSVD, with internal layer thicknesses of 300 μm, were studied.

- The effective charge density (ΔQ_{redox}) defined as the electrical charge per unit of area used in the redox reaction, and the coloration efficiency (CE), defined as the colored area per unit of increment of absorbance and one coulomb of injected electrical charge, were determined by means of electrochemical characterization using ChrA and ChrC methods, simultaneously measured with optical transmittance at 600 nm for samples PSBD, GSBD and GSVD. The increment of coloration in the devices, due to an increase of the applied potential, is accompanied with an increment of the ΔQ_{redox}, since the higher number of color centers formed requires more electrical charge consumed. ΔT_{600nm} and times t_c and t_b were measured. The absorption coefficient at 600 nm (α_{600nm}) was determined from the optical density (ΔOD) calculated from the absorbance, neglecting the scattering effect.

- From the three characterized viologen based EC devices, the higher ΔQ_{redox} value, 8.92 mC/cm^2, was observed for the GSBD sample at 2.5 V, which can be explained since its CE at 600 nm of 136 cm^2/C was also the higher observed. I.e., the more electrical charge consumed is required for the more color centers formed with a deeper coloration, showing a ΔT_{600nm} of 72.38% and α_{600nm} of 4.08 nm^{-1}, with t_c and t_b of 24 and more than 60 seconds respectively.

- The sample GSVD was operated for positive and negative voltages, showing a quasi-symmetrical electro-optical behavior for spectral and T_{600nm}simultaneously measured with ChrC and ChrA experiments. ΔQ_{redox} of 6.82 and 6.75 mC/cm^2 and CE of 80 and 81 cm^2/C were obtained for +2.5 and -2.5 V, respectively. ΔT_{600nm} of 57.20% and 57.09 %, α_{600nm} of 1.83 and 1.82 nm^{-1} and same t_c and t_b of 7 and 8 seconds respectively, were the other parameters symmetrically observed for both polarities.

- With the thinner 200 μm internal layer, the sample PSBD showed comparative better results, since a ΔQ_{redox} of 7.35 mC/cm^2 and a CE of 122 cm^2/C were obtained with lower DC bias voltage, 2 V instead of 2.5 V. ΔT_{600nm} was 64.02%, and t_c and t_b, 13 and 18 seconds respectively. Since scattering in this sample could not be negligible, the absorption coefficients α_{600nm} of 4.48 nm^{-1} are different than the extinction coefficients. It was observed that ΔT_{600nm} increases to more than 80% for PSBD' sample, with 300 μm of internal layer.

- The quasi-symmetrical optical behavior for both polarities voltages was also tested by measuring the optical T_{600nm}, simultaneously with the CV experiments at low scan rates, in a range from negative to positive voltages.

- Threshold value V_{TH}, voltage from which the coloration starts changing in the EC device, were observed at 1.4 V, 1.3 V and 1.2 V for samples PSBD, GSBD and GSVD, respectively.

- Both coloring and bleaching peak currents (i_c and i_b) and voltages (E_c and E_b) were determined using the voltammograms. (E_c,i_c) and (E_b,i_b) were observed symmetrically for sample PSBD. For sample GSBD, a clear asymmetry was observed in the voltammograms. However, symmetrical peaks were observed for sample GSVD.

- Electrical impedance characterization of the devices showed a high decrement of the impedance increasing the level of coloration, from several kΩ to a few Ω. An EEC model was proposed from EIS method, with several improvements. No sealing problems and bubbles were determined from the Nyquist diagrams, which were reflected in the EEC model by avoiding the Rp||CPEp shunt in parallel previously observed in the EEC model for PEDOT devices. Two different circuits, one for no coloration change and another for coloration change appearing in the devices, were considered. The only difference between both of them was the Warburg impedance, standing for diffusion process, at voltages where coloration change is observed. The open circuit Warburg diffusion impedance Wo was substituted by a short-circuit one Ws.

- Diffusion tail of Nyquist diagrams at different DC bias voltage levels were related to the peaks of potential observed in CV experiments. The diffusion effect

increases at potentials higher than the peak potentials detected with CV experiments, causing a decrement of the electrical current. The increment of the diffusion impedance, represented by the Warburg element in the EEC model, is modeling such decrement of the electrical current.

VII.1.1.3 Dependence on thickness of new viologen EC devices

- Electro-optical characterization was carried out on several viologen based EC devices manufactured by CIDETEC on glass substrate supports, varying the thickness of the internal active layer from 50 to 250 μm with 50 μm intervals, using a thermoplastic spacer. The EC mixture was prepared at room temperature. The final thicknesses of the devices were 60, 90, 130, 180 and 230 μm.

- ΔT_{600nm} varied from 10%, for the thinner device of for 60 μm, to 45% for the thicker device of 230 μm. The higher the thickness, the higher the amount of color centers formed and hence the higher the coloration appearance. The response times t_c and t_b, with similar values for coloring and bleaching processes for 60, 90 and 130 μm, showed a quasi-linear behavior increasing with the thickness from 5 to 16 seconds. For 180 and 230 this tendency is broken, since t_b remains 16 seconds and t_c increases to 20 seconds for 180 μm and decreases to 13 seconds for 230 μm.

- CV experiments and optical T_{600nm} were simultaneously measured at different scan rates. Transmittance contrast at 600 nm was related with the redox reactions observed by means of the charge capacity, a parameter calculated by dividing the area enclosed in the voltammogram by the scan rate. The higher the area, the higher the charge capacity and the higher the transmittance contrast. The tendency of this plot showed that the thickness of the devices could be increased over 230 μm in order to achieve a higher transmittance contrast, as it was the case of the 300 μm previously studied.

- EIS experiments were carried out on PSBD, PSBD', GSBD and GSVD samples, with different DC bias voltage levels applied.

- Regarding the electrical impedance behavior, a first approach of EEC model was derived from Nyquist diagrams, revealing that the thicker devices showed a better fitting process by using an open-circuit Warburg impedance element Wo for the lowest frequencies of the EIS experiments. On the contrary, a short-circuit Warburg impedance element Ws fitted better for the thinner devices. However, ChrA experiments revealed a constant electrical current consumption at the colored states, which suggested the use of a Ws element instead of a Wo element. At the lowest frequency, Ws" tends to zero and

Ws' tends to Ws-R. Hence, electrical current could be obtained by applying Ohm law $i=V_{DC\text{-}bias}/(Rs+Rct+Ws-R)$.

- Relating EIS and CV experiments, the rate of the reaction seems to be slower as the thickness increases. Nyquist diagrams of Warburg impedance elements derived from fittings of the EEC model show high values of the magnitude for potentials of non coloration in the devices. The diffusion Warburg impedance follows an increment around the peak of potential observed in the voltammograms, and a decreasing after the peak potential. Nyquist diagrams also show that data corresponding to lower frequencies of the simulated Warburg impedance elements look similar to the Nyquist diagram of a CPE, i.e. the tendency at high frequencies range, for the thicker devices. Only for the thinnest device it shows a behavior corresponding to lower frequencies different from the one of a CPE.

VII.1.2 Suspended particle devices (SPDs)

- Three commercial samples of SPD, with 12 x 28 cm^2 active area and 300 μm of internal layer thickness, were electro-optically characterized. A new method for determining the scattering and absorption coefficients from experimental diffuse and total transmittance and reflectance measurements was developed based in two and four flux models.

- The three samples of SPD showed different optical behavior in both darken (or OFF) and bleached (or ON) states. Different intermediate levels of transmittance were observed by varying the amplitude of the applied AC signals. High impedance (HZ) operation (or open-circuit), i.e., without applied potential, showed the same optical results than OFF state, with 0 V applied (or short-circuit). The measured transmittance was different than the detailed in the datasheet (from <1% to 57%).

- The power electrical signals were applied using three different systems: a variac from 0 to 220 V_{rms} 50 Hz, a FPGA + actuator setup from 0 to 103 V_{rms}, and a function generator in series with a broadband amplifier, from 0 to 100 V_{peak} at 50 Hz. The operation of the SPD samples at higher frequencies did not show relevant changes.

- Luminous transmittance (T_{lum}), calculated as the integral of the transmittance spectrum over the human eye sensitivity curve, was used for comparing the three SPD samples.

- A 30% of T_{lum} contrast (ΔT_{lum}) was observed for the sample SPD1, using the variac. A 13% of ΔT_{lum} was observed for SPD2 using the FPGA. A 34% for SPD3 by using the function generator and the broadband amplifier.

- Rise and fall times of 2.61 and 2.65 seconds were observed in sample SPD2 for bleaching and darkening processes respectively. The response times were different than the detailed in the datasheet (0.5 and 1 seconds).

- The samples SPD1 and SPD2 stopped switching. The number of cycles was lower than the detailed in the datasheet ($1x10^6$). The sample SPD3 currently keeps switching optically.

- Total and diffuse transmittance and reflectance were measured in both darken and bleached states, with 0 and 100 V_{peak} 50 Hz respectively (OFF and ON states). Ten different levels of the direct and diffuse transmittance were measured from 0 to 100 V_{peak}, with 10 V_{peak} intervals.

- Luminous values of Ttot, Tdir, Tdiff, Rtot, Rspec and Rdiff are specified in Table VII.1 for OFF and ON states of the SPD3 sample. Luminous transmittance haze ($Haze_{Tlum}$), defined as the ratio between $Tdiff_{lum}$ and $Ttot_{lum}$, was observed to decrease from 37.5%, in the OFF state, to 17.1%, in the ON state. The main changes in $Haze_{Tlum}$ are found from 0 to 30 V_{peak}, being stabilized from 30 to 100 V_{peak}. Luminous reflectance haze ($Haze_{Rlum}$), defined as the ratio between $Rdiff_{lum}$ and $Rtot_{lum}$, was observed to increase from 27.4% in the OFF state, to 33.2%, in the ON state.

SPD3	$Ttot_{lum}$(%)	$Tdir_{lum}$ (%)	$Tdiff_{lum}$ (%)	$Rtot_{lum}$ (%)	$Rspec_{lum}$ (%)	$Rdiff_{lum}$ (%)
OFF	7.21	4.51	2.70	6.46	4.69	1.77
ON	41.60	34.50	7.10	7.91	5.28	2.62

Table VII.1: Luminous values of Ttot, Tdir, Tdiff, Rtot, Rspec and Rdiff.

- Solar values of Ttot, Tdir, Tdiff, Rtot, Rspec and Rdiff are specified in Table VII.2 for OFF and ON states of the SPD3 sample. Solar transmittance haze ($Haze_{Tsol}$), defined as the ratio between $Tdiff_{sol}$ and $Ttot_{sol}$, was observed to decrease from 15.7%, in the OFF state, to 13.1%, in the ON state. The main changes in $Haze_{Tsol}$ are found from 0 to 20 V_{peak}, being stabilized from 20 to 100 V_{peak}. Luminous reflectance haze ($Haze_{Rsol}$), defined as the ratio between $Rdiff_{sol}$ and $Rtot_{sol}$, was observed to increase from 23.2% in the OFF state, to 28.7%, in the ON state.

	$Ttot_{sol}$(%)	**$Tdir_{sol}$ (%)**	**$Tdiff_{sol}$ (%)**	**$Rtot_{sol}$ (%)**	**$Rspec_{sol}$ (%)**	**$Rdiff_{sol}$ (%)**
OFF	21.52	18.15	3.38	6.46	4.69	**1.77**
ON	**43.81**	**38.09**	**5.72**	**7.91**	**5.28**	**2.62**

Table VII.2: Solar values of Ttot,Tdir, Tdiff, Rtot,Rspec and Rdiff.

- A 30% of direct transmittance contrast ($\Delta Tdir_{lum}$) is observed between 0 and 100 V_{peak}, being the main changes taking place from 0 to 70 V_{peak}, with a 28% of $\Delta Tdir_{lum}$. For solar values, a 20% $\Delta Tdir_{sol}$ is observed from 0 to 100 V_{peak}, being 18% from 0 to 70 V_{peak}.

- The optical total transmittance dependence with the angle of incidence (from 0º to 60º with 15º intervals) of the sample SPD3 in three different states (0 V, 50 V_{peak} and 100 V_{peak}) was characterized in the visible wavelength region. The darkest state shows a low dependence of the angle of incidence and the clearest state shows a higher dependence (see Table VII.3).

SPD3	0º	15º	30º	45º	60º
0 V	6.18	6.04	5.38	4.41	2.13
50 V_{peak}	28.42	26.35	20.46	14.94	6.89
100 V_{peak}	40.48	36.19	27.74	20.38	9.64

Table VII.3: Total transmittance dependence with the angle of incidence for SPD3 sample at 0, 50 and 100 V_{peak} applied.

- The extensive scattering and absorption coefficients (S & K) of the SPD3 in the OFF and ON states were approximated by the development of a new method, by means of fitting to Tdir & Rspec and Ttot and Rtot measurements. The SPD sandwich structure was approximated to a single SPD film due to the consideration of matching the refractive index values of the different layers. The method followed different steps for fitting and computing several intermediate parameters:

    - The refractive index "n" of the SPD was derived from Fresnel reflection coefficient for normal incidence, which is the collimated interface reflectance "r_c" obtained by fitting of the Tdir and Rspec to the collimated equations of 4 flux model.

    - Once "n" is known, the diffuse interface reflectances for downwelling and upwelling lights, ωd^i and ωd^j respectively, are obtained by averaging the Fresnel reflection coefficients over all angles of incidence, for radiation flowing inward and outward of the SPD.

    - Diffuse fractions of light at the top and bottom interfaces are obtained from collimated and diffuse interface reflectances and the measured Ttot, Tdir, Rtot and Rspec.

    - Extensive (S & K) are obtained by fittings to Kubelka-Munk (KM) equation for Ttot and Maheu-Letouzoulan-Gouesbet (MLG) derived equation

for Rtot, after the application of the Saunderson correction. From the obtained S & K, the optical behavior can be predicted for different thickness simulating Ttot, Tdir & Tdiff and Rtot, Rspec & Rdiff components.

- In the case of the sample SPD3, the best optical behavior observed from simulations was determined for 200 μm and 300 μm, being this one indeed the constructed thickness of the sample.

- The computed Ttot and Rtot from the values of S & K obtained by the developed method showed a slight discrepancy for the Rtot fitting in the visible wavelength region corresponding to the ON state of the sample SPD3 ($Rtot_{visON}$). The differences between the fitted and the measured $Rtot_{visON}$ could be saved by using small but negative values of S (which is physically impossible, but as an artifact it works properly). Due to the approximation of a single layer, instead of a multilayer system, and considering that KM is not an exact method, since it considers some small errors, the method shows consistency and it can be used for other kind of devices showing scattering effect.

- The electrical impedance characterization was carried out for the three samples SPD1, SPD2 and SPD3. An EEC model was obtained. A series resistance Rs standing for the contacts is placed in series with a shunt of a double layer capacitance Cdl in parallel with an open-circuit Warburg diffusion impedance Wo. Values of 919 Ω and 20.5 nF are obtained for Rs and Cdl respectively. The simulated Warburg impedance showed at 50 Hz values of 189 kΩ for magnitude and -44º for phase. Higher frequencies would decrease the magnitude and the phase.

- The power consumption of the SPD3 reached the maximum value close to 0.7 mA for the higher amplitude of 100 V_{peak} AC signal applied.

- Slight improvements of the spectral ΔT were observed increasing the frequency of the sinusoidal signal from 50 Hz to 500 Hz, which could be related with the decrease of the simulated diffusion Warburg impedance obtained by fitting to the EEC model. However, undesired oscillations were observed increasing the frequency of the feeding signal over 1 kHz.

VII.1.3 Polymer dispersed liquid crystals (PDLCs)

- Three series of PDLC devices developed by CIDETEC on glass + ITO substrates were electro-optically characterized. The PDLC devices switched between a more translucent optical state, without applied voltage, to a more transparent state, when applying an AC voltage signal of different amplitudes.

- The 1st series of PDLC devices were 4 samples, of 1.3 x 1.3 cm^2 active area, with two different internal layer thicknesses, of 20 and 50 μm respectively, and two different operation modes, normal and reverse, being called PDLCn-20, PDLCr-20, PDLCn-50 and PDLCr-50 respectively.

- The devices PDLCn-50 and PDLCr-50 were optically characterized for two different optical states, without applied voltage (at 0V or short-circuit, showing the same appearance than at open circuit or HZ) and when applying 24 V_{rms} 50 Hz sinusoidal signal (called OFF and ON states, respectively). An integrating sphere based spectrometer was used for measuring Ttot and Tdiff components. The component Tdir was measured without the use of the integrating sphere and compared with the subtractions Ttot-Tdiff. The differences were due to the different distance of the sensor in both measurements, and affecting because of the high scattering observed. The luminous values are shown in Tables VII.4 and VII.5 for PDLCn-50 and PDLCr-50 devices respectively.

PDLCn-50	Ttot (%)	Tdiff(%)	Ttot(%)-Tdiff(%)	Tdir(%)
OFF	74.56	60.88	13.68	10.01
ON	77.73	18.52	59.21	56.56

Table VII.4: Luminous values of Ttot, Tdiff, Ttot-Tdiff and Tdir of sample PDLCn-50.

PDLCn-50	Ttot (%)	Tdiff(%)	Ttot(%)-Tdiff(%)	Tdir(%)
OFF	79.94	40.97	39.67	32.20
ON	77.66	48.17	29.49	24.55

Table VII.5: Luminous values of Ttot, Tdiff, Ttot-Tdiff and Tdir of sample PDLCr-50.

- The results of the luminous values for the different measured transmittances showed a better, but still poor, behavior of the PDLCn-50 device, with values of transmittance hazes $Haze_{Tlum}^{OFF}$=81.7% and $Haze_{Tlum}^{ON}$=23.8%, versus the values obtained for PDLCr-50 device, $Haze_{Tlum}^{OFF}$=50.4% and $Haze_{Tlum}^{OFF}$=62.0%. For an ideal PDLC device, these values should be 100% and 0% for OFF and ON states in normal operation mode, and vice versa for reverse operation mode.

- The devices PDLCn-20 and PDLCr-20 were optically characterized in OFF and ON states using an integrating sphere based spectrometer, for measuring Ttot components. Tdir was measured without the integrating sphere. Tdiff was obtained from Ttot-Tdir. The luminous values are shown in Tables VII.6 and VII.7 for PDLCn-20 and PDLCr-20 devices respectively.

PDLCn-20			
OFF	83.32	42.92	40.40
ON	85.59	62.87	22.72

Table VII.6: Luminous values of Ttot, Tdir and Tdiff (Ttot-Tdir) of sample PDLCn-20.

PDLCn-20	Ttot(%)	Tdir(%)	Tdiff(%)=Ttot(%)-Tdir(%)
OFF	81.01	47.02	33.99
ON	80.23	40.56	39.67

Table VII.7: Luminous values of Ttot, Tdir and Tdiff (Ttot-Tdir) of sample PDLCr-20.

- The results of the luminous values for the different measured transmittances showed a better, but still poor, behavior of the PDLCn-20 device, with the values off transmittance hazes $Haze_{Tlum}^{OFF}$=48.5% and $Haze_{Tlum}^{ON}$=26.5%, versus the values obtained for PDLCr-20 device, with $Haze_{Tlum}^{OFF}$= 42.0% and $Haze_{Tlum}^{OFF}$=49.4%. For an ideal PDLC device, these values should be 100% and 0% for OFF and ON states in normal operation mode, and vice versa for reverse operation mode.

- The dependence of the direct transmittance with the distance of the PDLC device to the illuminant was measured, for PDLCn-20 and PDLCr-20 devices. The spectrums were quantified by the luminous direct transmittance ($Tdir_{lum}$).

- For PDLCn-20 at 2.5 cm of distance, $Tdir_{lum}^{OFF}$=69% and $Tdir_{lum}^{ON}$=70%, varying to $Tdir_{lum}^{OFF}$=20% and $Tdir_{lum}^{ON}$=55%, for 20 cm of distance. The luminous direct transmittance contrast observed for different distances are $\Delta Tdir_{lum}^{OFF}$=49% and $\Delta Tdir_{lum}^{ON}$=15%.

- For PDLCr-20 at 2.5 cm of distance, $Tdir_{lum}^{OFF}$=58% and $Tdir_{lum}^{ON}$=47%, varying to $Tdir_{lum}^{OFF}$=33% and $Tdir_{lum}^{ON}$=28%, for 20 cm of distance. The luminous direct transmittance contrast observed for different distances are $\Delta Tdir_{lum}^{OFF}$=25% and $\Delta Tdir_{lum}^{ON}$=19%.

- Switching times of 0.3 and 2.5 seconds from 'translucent' OFF state to 'transparent' ON state were observed for PDLCn-20 device, and symmetrical 0.5 seconds for transitions between both states are observed for PDLCr-20 device.

- Square AC signal, instead of sinusoidal AC signal, avoided an undesired curling of transmittance observed in the ON state of PDLCn-20 device.

- The 2nd series of PDLC devices were 8 samples of normal mode operation, of two different sizes "a" and "b" of active areas (3.5 x 2.7 cm^2 and 3.3 x 1.8 cm^2, respectively), and four different internal layer thicknesses (of 25, 50, 75 and 100 μm

respectively), being called PDLC25a, PDLC50a, PDLC75a & PDLC100a and PDLC25b, PDLC50b, PDLC75b & PDLC100b respectively.

- The 2nd series of PDLC devices were optically characterized by means of an integrating based spectrometer. Total and diffuse transmittance and reflectance were measured in the 'translucent' OFF and 'transparent' ON states, with 0 and 24 V_{rms} sinusoidal signal applied. Direct transmittance and specular reflectance were obtained by subtractions of the total and diffuse components.

- Bigger size PDLC-a devices showed around 10% less transmissive behavior than smaller size PDLC-b devices, which showed around 10% less reflective behavior than them.

- Thinner devices PDLC25 showed the best results for luminous transmittance haze, with values of $Haze_{Tlum}^{OFF}$=31% and $Haze_{Tlum}^{ON}$=89% for bigger size "a" and values of $Haze_{Tlum}^{OFF}$=24% and $Haze_{Tlum}^{ON}$=88% for smaller size "b".

- The best results from the 8 samples of PDLC devices studied for the applied voltage levels was the PDLC25b, since a lower luminous reflectance, of 10% and 11% for OFF and ON states, respectively, and higher ΔT_{lum}, of 44%, was observed.

- The 3rd series of PDLC devices is a tandem PDLC-EC device, with 3.5 x 1.8 cm^2 active area, and 50 μm and 300 μm of internal layer thicknesses for PDLC and EC parts respectively, in order to achieve different levels of coloration in the tandem device. The EC part (viologen) was switched from 0 to 2 V with 0.5 V intervals. The PDLC part was switched from 0 to 100 V_{peak} sinusoidal signals at 1.8 kHz with 12.5 V_{peak} intervals, in order to achieve different levels of scattering in the tandem device.

- Four differentiate states are mainly observed in the PDLC-EC tandem device: A translucent uncolored state (with both PDLC and EC parts in OFF states with 0 V applied), a transparent uncolored state (with the EC part in the OFF state and the PDLC part in the ON state), a translucent colored state (with the EC part in the ON state and the PDLC part in the OFF state), and a transparent colored state (with both PDLC and EC parts in the ON states, with 100 V_{peak} AC and 2 V DC applied respectively).

- The 60% of direct T_{600nm} for the most transparent state can be considered the drawback of this device, since a higher value should be necessary for smart windows applications. A 25% of direct transmittance contrast was observed for the uncolored translucent and transparent states.

- Intermediate values between 1 and 1.5 V are required to apply to the EC part for differentiate the transparent colored and the translucent colored states.

- Bode magnitude and phase and Nyquist impedance diagrams were obtained for PDLCn-20 and PDLCr-20 devices. An EEC model was proposed for the both devices, consisting on a series resistance Rs, standing for the contacts of ITO glass, with a value of 172 Ω and 160 Ω for PDLCn-20 and PDLCr-20 respectively, in series with two parallel branches, one for the low frequencies and the other for the high frequencies. A double layer capacitance with values of 0.883 and 0.557 nF for PDLCn-20 and PDLCr-20 respectively, represents the behavior of the devices at high frequencies. A resistance of the displacement of the dipoles Rd due to the molecular orientation of the LC droplets, with values of 3.03 and 3.38 MΩ for PDLCn-20 and PDLCr-20, respectively, is placed in series with a CPE reflecting the accumulation of ions for the low frequencies behavior.

- The EEC model is used for the 2^{nd} series of PDLC devices, deriving relevant information of the operation behavior for the different active area sizes and internal layer thicknesses, like the dependence of parameter Rs on areas and thicknesses, remaining with a low value. On the other hand, the parameter Rd shows a clear increment with the area and the thickness of the PDLC device. Capacitive Cdl parameter can be related to the configuration of two parallel plates of area A separated by a distance d. Hence, the capacitance increases with the area and decreases with the thickness of the PDLC devices. The behavior of the CPE is appearing at the lowest frequencies.

- The electrical current consumption of the 8 samples showed that a clear increment of the amplitude of the AC signals is required for the thicker and larger areas PDLC device in order to switch them optically.

- The EEC model used for the tandem PDLC-EC device was a combination of the EEC model used for the PDLC devices of the 1^{st} and 2^{nd} series, with values of Rs=156 Ω, Rd=48.7KΩ, Cdl=2.22nF and CPE-T=587 $nFs^{(P-1)}$ being P=0.386. The EC part was fitted by using the EEC model used for the viologen based EC devices, with two different circuits, one for no coloration change and another for coloration change appearing in the devices. The EC diffusion process was represented by the open circuit Warburg diffusion impedance. Fitting errors are high for Wo parameter, which could be required to switch with a short-circuit Ws parameter.

VII.1.4 EC, SPD and PDLC devices compared

- Repeated for the three technologies studied in this work, simulations of the different appearance observed at the different levels of voltage applied are obtained from

chromaticity CIE Yxy coordinates, which have been derived from transmittance measurements in the visible wavelength range and the eye sensitivity curve.

- From the three ‘smart’ windows technologies studied in this work, it could be concluded that there are advantages and drawbacks for each one.

- Regarding EC devices, the advantages are related to the high transparent state that can be achieved (more than 80% of luminous transmission), being this state observed without applied voltage and hence without electrical current consumption. Deep colored states are also possible to observe, being possible to choose the color by choosing different EC materials. No scattering effect is usually observed. However, the long response times required for switching from bleached to colored states, for large areas of EC windows, and the repeatability of the transmission states of the windows, after several cycles, are the main current drawbacks for the new technology tested. The different coloration and bleaching processes in the center and the corners of the EC windows are also a significant disadvantage. Light and heat control possibility would reduce the electric energy by using EC energy saving ‘smart’ windows in buildings, although the EC samples studied in this work showed main transmission changes in the visible wavelength region.

- The fast response times, of the order of 2.5 seconds for both bleaching and darkening processes, and the large areas possibilities of the SPD ‘smart’ windows, are the main advantages of this technology. A bluish-black color achieved for the darken state, attractive for windows applications, is the optical state without applying voltage. Thus, electrical current consumption is required, in a continuous way, for the clear state. Additionaly, the main problems of this technology are the low transmission level that can be achieved for the clear state (around 40% of T_{lum} in the case of the SPD samples in this work) and the undesired scattering effect observed in both OFF and ON states. Another drawback is the high undesired observed reflectance (from 6% to 8% of total luminous reflection in darken and bleached states of the SPDs studied in this work). Different thicknesses of the internal layer would result into a variation of these parameters, which could be predicted by the method for determining the scattering and the absorption coefficients detailed in this work.

- ‘Smart’ windows PDLC technology shows the same advantages than SPD windows regarding the response times and large area possibilities, but also the same problems regarding the electrical current consumption in the clear ON state and, in a lesser extent, the scattering of the bleached state. The white ‘milky’ appearance of the PDLC devices at the translucent OFF state, limits the applications to inner privacy windows for offices or for bathroom showers. The tandem PDLC-EC device could have

some advantages by mixing energy saving and privacy ‘smart’ window applications, but only after solving the problem of the transparency of the clear state.

VII.1.5 Developed Applications

- Combining EC technology with different ophthalmologic filters could be a good solution for people with problems of low vision and glare. The best combination from those studied in this work was using a viologen based EC device together with a yellow filter in order to achieve an optical switching from yellow to green colorations states.

- A 26% of transmittance contrast, achieved in this work for EC devices at 1310 nm wavelength, with values of 17.8 and 43.9 % of transmittance for bleached and colored states respectively (with insertion loss is of 3.6 dB), is still a low value for EC VOA application used in optical telecommunication systems. Faster response times should also be needed.

- A domotic network using PDLC ‘smart’ windows technology was described in this work, as an example of electrically controllable transmittance devices application, allowing a local and remote control by means of a programmed tool for Internet control.

- A prototype of electro-optical characterizer for EC devices, based on a data acquisition card, was designed and constructed, for RGB transmittance and electrical current simultaneous measurements for developing fast CV and ChrA experiments.

VII.2 Future research lines

Finally, several issues related to the results reported in this work, according to the different electrically controllable transmittance technology studied, can be considered as future works.

VII.2.1 Electrochromic (EC) devices

- Electro-optical characterization of new organic viologen based EC devices developed by CIDETEC, with bigger internal layer thicknesses than the studied in section IV.3, should be carried out in order to establish the limits of the thickness, according to the maximum transmittance contrast that can be achieved, and taking into account the evolution of the response times for coloring and bleaching processes. The possible decrease of the level of transparency of the bleached state should also be studied for large thicknesses.

- Although scattering effect is negligible for the viologen based EC devices, increasing the thickness of the internal layer could derive to an increment of both diffuse transmission and total reflectance. Total and diffuse transmittance and reflectance measurements of the devices would be necessary to carry out in case that scattering effect in the thicker devices could not be negligible or in case that showing high reflectance increment.

- Electro-optical characterization of inorganic tungsten and nickel oxides (WO_3 and NiO) based EC devices, developed by Boris Orel research group "Laboratory for Spectroscopy of Materials" at the National Institute of Chemistry of Slovenia (Ljubljana) will be carried out since the research collaboration established last year, being the author of this work in a research stay at their labs.

- Cathodic and anodic WO_3 and NiO EC materials change, upon an electrical current application, to deep blue and brown colorations, respectively. However, when both materials are used together in a device, a grey coloration is observed at the colored state. Figure VII.1 shows a simulation of the color appearance obtained for different hypothetic devices with the same thicknesses for WO_3 and NiO of layers. The simulation was approached neglecting scattering effect and interface reflectances of the different layers of the final device and taking as inputs the direct transmittances (Tdir) of separated WO_3 and NiO single layers (x1) of the same thicknesses (in solution, but not in a device), at two different coloration states, +3 V and -3 V, respectively. Figure VII.2 show the simulation of the color appearance for different thicknesses hypothetic devices. This approach is a first step for predicting the final appearance of the devices with different thicknesses (as a first approach, since $T_{12}=T_1T_2/(1-R_1R_2)$ and $R_1=R_2=0$, $T_{12}=T_1T_2$). Scattering and absorption coefficients of separated WO_3 and NiO layers will be studied from total and diffuse transmittance and reflectance measurements of glass supported inorganic EC devices in a second step, for prediction of the thickness dependence in the optical appearance of bleached and colored states. Refractive index of glass, ITO and electrolyte will be considered into the computations.

Figure VII.1: Simulations of color appearance of WO_3 and NiO layers separated and joined in a device (NiO&WO_3), from one to four layers of same thicknesses.

Figure VII.2: Simulations of color appearance of WO_3 & NiO EC device with different combinations thicknesses, from one to four layers.

VII.2.2 Suspended particle devices (SPDs)

- Rtot and Ttot fittings were used for obtaining the extensive scattering and absorption coefficients (S & K) computed from the two flux method. However, this is an approximated method and several improvements could be carried out with diffuse transmittance and reflectance fittings for obtaining the intrinsic scattering and absorption coefficients (α & β) following the four flux method. Two additional parameters, forward scattering ratio (FSR) and average crossing parameter (ACP) are also involved in this method. Future works on the fitting program will be carried out for the difficult task of decoupling α & β, instead of S & K, being the sum α + β the extinction coefficient of Lambert-Beer law.

- Some model calculations of the S & K coefficients will be studied considering the geometry of the particle and the optical constants of herapathite, in a research stay for the summer of 2012 at the Angstrom Laboratory, in order to find the useful performance limits on SPD devices.

VII.2.3 Polymer dispersed liquid crystals (PDLCs)

- Since the transmittance contrast observed in the PDLC devices of different active areas and internal layer thicknesses depends on the amplitude of the applied AC voltage signal, a study for different amplitudes than the already used in Chapter VI (24 V_{rms}) on the 8 samples of PDLC, with two different sizes ("a" and "b") and four different thicknesses (25, 50, 75 and 100 μm), will be carried out in order to determine the maximum optical direct and diffuse transmittance contrast.

- S & K of the 8 samples of PDLC will be studied, for the new values of amplitude voltages previously mentioned, in a research stay for the summer of 2012 at the Angstrom Laboratory. Relationships between the values of the fitted parameters of the EEC model, such as the dipolar displacement resistance Rd, and the achievable direct and diffuse transmittance contrast, should be searched.

- Diffuse and total transmittance and reflectance measurements are required for completing the optical characterization on the tandem PDLC-EC device at the four different states, with the EC part in bleached or colored states, and the PDLC part in translucent or transparent states.

VII.2.4 Solar absorbers

- Prediction of the optimum thickness for maximizing the solar absorbance (a_S) and minimizing the thermal emittance (e_T) will be carried out by means of the study of the S & K coefficients on spectrally selectable black coatings used for solar absorbers applications and researched by Boris Orel group of Ljubljana.

VII.2.5 Temperature dependence

- Dependence on the temperature is well known in competing technologies, as the photocromatic one. Electrochromic are supposed to be less temperature dependent, but nevertheless the study of the transmittance and electrical properties with temperature is a mandatory task to be fulfilled before any commercial application can arise to the market.

VII.2.6 Waveforms for signals

- The EC devices are traditionally powered by a square signal of very low frequency. But in fact, both the maintaining of the coloration by a voltage under the one used to switch, and the aid for the contrary reaction that can be derived by the application of reverse voltages until bleaching, are necessary to be studied. Several waveforms must be tested in order to match the electrical optimal consumption with the optical one.

Appendix A

Two flux transmittance and reflectance equations

Propagation of light in scattering and absorbing media is described by the general radiative transfer theory. One of the earliest solutions of this theory was developed by Kubelka and Munk (KM) in 1931, who proposed a model of two light fluxes traveling in the forward and backward directions. Although KM has been extensively used, this two flux method is only approximated and shows some limitations, since its solution describes the experimental results adequately only if the illumination provided by a light source is diffuse or if the medium is such scattered that the light is perfectly diffuse distributed. Hence, the KM method is applicable when all light in the medium is diffuse, either because the film is diffusely illuminated (which is not the present case since the spectrometer illuminates the films with collimated light) of because the film is strongly scattering (which is neither the present case since the SPD sample shows a weak scattering) [Ish99]. In spite of being a non accurate method for the case of the SPD, since collimated T_{dir} and R_{tot} measured components in the sample cannot be neglected, the KM model was used in this work as an approximated method for obtaining consistent and reliable values of the phenomenological scattering and absorption coefficients S & K.

In order to obtain the formulas for the transmittance and reflectance in the KM model, Figure IV.12 in Chapter IV of the present work must to be observed. Considering diffuse fluxes I and J travelling in the forward and backward directions respectively, within a differential distance *dz*, the forward flux (I) decreases due to absorption (K) and scattering (S) in the backward direction, but increases due to scattering (S) in the backward direction of the backward flux (J). Similarly, for differential equation is found for backward flux (J):

$$\frac{dI}{dz} = -(S+K)\cdot I + S\cdot J \qquad \frac{dJ}{dz} = (S+K)\cdot I - S\cdot J \qquad \text{(Eq.A1)}$$

Solutions to previous equations are obtained by assuming an exponential dependence exp(αz) for I and J. Then, by doing d/dz=α:

$$[\alpha + (K+S)]I - SJ = 0 \qquad SI + [\alpha + (K+S)]J = 0 \qquad \text{(Eq. A.2)}$$

To obtain nonzero solutions for I and J the determinant of the coefficients in previous equations must be zero:

$$\begin{bmatrix} \alpha + (K+S) & -S \\ S & \alpha - (K+S) \end{bmatrix} = 0$$

From which two values for α are obtained (positive and negative of the square root):

$$\alpha_{\pm} = \pm\sqrt{K(K+2S)}$$

For each value of α, the ratio of I and J is given from the one of the Equations A.2:

$$A_{+} = \frac{J}{I} = \frac{\alpha_{+} + (K+S)}{S} = -\frac{S}{\alpha_{+} + (K+S)} \text{ for } \alpha_{+}$$

$$A_{-} = \frac{J}{I} = \frac{\alpha_{-} + (K+S)}{S} = -\frac{S}{\alpha_{-} + (K+S)} = \frac{S}{\alpha_{+} + (K+S)} = \frac{1}{A_{+}} \text{ for } \alpha_{+}$$

Since $A_{+} \cdot A_{-} = 1$ then $A_{+} - A_{-} = \frac{2b}{S}$ and $A_{+} + A_{-} = \frac{2(K+S)}{S} = 2a$

The complete expression for I and J is a linear combination of two solutions for $\alpha_{+}=b$ and $\alpha_{-}=-b$:

$$I(z) = C_1 e^{bz} + C_2 e^{-bz} = C_1[\sinh(bz) + \cosh(bz)] + C_2[\cosh(bz) - \sinh(bz)] =$$
$$= (C_1 + C_2)\cdot\cosh(bz) + (C_1 - C_2)\cdot\sinh(bz)$$
$$J(z) = C_1 A_{+} e^{bz} + C_2 A_{-} e^{-bz} = C_1 A_{+}[\sinh(bz) + \cosh(bz)] + C_2 A_{-}[\cosh(bz) - \sinh(bz)] =$$
$$= (C_1 A_{+} + C_2 A_{-})\cdot\cosh(bz) + (C_1 A_{+} - C_2 A_{-})\cdot\sinh(bz)$$

where C_1 and C_2 are unknown coefficients to be determined by the boundary conditions. The simplest boundary conditions are that at z=0 the positive flowing flux (I) is equal to the given incident flux I_0, and at z=δ, although there is no backward flux J incident upon the slab, for the CRI (continuous refractive index) formulae, the interface reflectance R_g is considered:

$$I(0) = C_1 + C_2 = I_0 \qquad J(\delta) = R_g I(\delta)$$

$$J(\delta) = C_1 A_{+} e^{b\delta} + C_2 A_{-} e^{-b\delta} = C_1 R_g e^{b\delta} + C_2 R_g e^{-b\delta}$$
$$C_1 (A_{+} - R_g)\cdot e^{b\delta} + (I_0 - C_1)\cdot(A_{-} - R_g)\cdot e^{-b\delta} = 0$$
$$C_1[(A_{+} - R_g)\cdot e^{b\delta} + (A_{-} - R_g)\cdot e^{-b\delta}] = -I_0 (A_{-} - R_g)\cdot e^{-b\delta}$$
$$\boxed{C_1 = -I_0 \cdot \frac{(A_{-} - R_g)\cdot e^{-b\delta}}{[(A_{+} - R_g)\cdot e^{b\delta} + (A_{-} - R_g)\cdot e^{-b\delta}]}}$$

$$(I_0 - C_2)\cdot(A_+ - R_g)\cdot e^{b\delta} + C_2(A_- - R_g)\cdot e^{-b\delta} = 0$$

$$I_0(A_+ - R_g)\cdot e^{b\delta} = C_2\left[(A_+ - R_g)\cdot e^{b\delta} - (A_- - R_g)\cdot e^{-b\delta}\right]$$

$$\boxed{C_2 = I_0 \cdot \frac{(A_+ - R_g)\cdot e^{b\delta}}{\left[(A_+ - R_g)\cdot e^{b\delta} - (A_- - R_g)\cdot e^{-b\delta}\right]}}$$

The denominator can be written in usual hyperbolic notation:

$$\Delta = (A_+ - R_g)\cdot e^{b\delta} - (A_- - R_g)\cdot e^{-b\delta} = (A_+ - A_-)\cosh(b\delta) + (A_+ - A_- - 2R_g)\sinh(b\delta) =$$

$$= \frac{2b}{S}\cosh(b\delta) + 2\left(\frac{K+S}{S} - R_g\right)\sinh(b\delta)$$

Transmittance:

$$T = \frac{(1-R_g)\cdot I(\delta)}{I_0} = \frac{(1-R_g)\cdot\left(C_1 e^{b\delta} + C_2 e^{-b\delta}\right)}{I_0} =$$

$$= \frac{(1-R_g)\left(-I_0\cdot\frac{(A_- - R_g)\cdot e^{-b\delta}}{\Delta}e^{b\delta} + I_0\cdot\frac{(A_+ - R_g)\cdot e^{b\delta}}{\Delta}e^{-b\delta}\right)}{I_0} =$$

$$= (1-R_g)\frac{-(A_- - R_g) + (A_+ - R_g)}{\Delta} = (1-R_g)\cdot\left[\frac{\left(\frac{2b}{S}\right)}{\Delta}\right] = \frac{(1-R_g)\cdot\frac{b}{S}}{\frac{b}{S}\cosh(b\delta) + \left(\frac{K+S}{S} - R_g\right)\sinh(b\delta)}$$

$$\text{If } \frac{b}{S} = \tilde{b} = \sqrt{a^2 - 1} = \sqrt{\left(\frac{K+S}{K}\right)^2 - 1}$$

$$\boxed{T = \frac{(1-R_g)\cdot\tilde{b}}{\tilde{b}\cosh(\tilde{b}S\delta) + (a - R_g)\sinh(\tilde{b}S\delta)}} \text{ (Eq. A.3)}$$

Reflectance:

$$R=\frac{J(0)}{I_0}=\frac{(C_1A_+ + C_2A_-)}{I_0}=\frac{\left(-I_0\cdot\frac{(A_- - R_g)\cdot e^{-b\delta}}{\Delta}A_+ + I_0\cdot\frac{(A_+ - R_g)\cdot e^{b\delta}}{\Delta}A_-\right)}{I_0}=$$

$$=\frac{(1-R_gA_-)\cdot e^{b\delta}-(1-R_gA_+)\cdot e^{-b\delta}}{\Delta}=\frac{R_g(A_+ - A_-)\cosh(b\delta)-(2-R_gA_- - R_gA_+)\sinh(b\delta)}{\Delta}$$

$$=\frac{R_g\frac{2b}{S}\cosh(b\delta)-\left(2-R_g\frac{2(K+S)}{S}\right)\sinh(b\delta)}{\frac{2b}{S}\cosh(b\delta)+2\left(\frac{K+S}{S}-R_g\right)\sinh(b\delta)}=\frac{R_g\frac{b}{S}\cosh(b\delta)-\left(1-R_g\frac{(K+S)}{S}\right)\sinh(b\delta)}{\frac{b}{S}\cosh(b\delta)+\left(\frac{K+S}{S}-R_g\right)\sinh(b\delta)}$$

$$R=\frac{R_g\tilde{b}\cosh(\tilde{b}S\delta)-(1-R_ga)\sinh(\tilde{b}S\delta)}{\tilde{b}\cosh(\tilde{b}S\delta)+(a-R_g)\sinh(\tilde{b}S\delta)}=\frac{R_g\tilde{b}\coth(\tilde{b}S\delta)-(1-R_ga)}{\tilde{b}\coth(\tilde{b}S\delta)+(a-R_g)}=$$

The equation used for reflectance expressed in terms of S, K and d is:

$$R=\frac{1-R_g\left[a+\tilde{b}\coth(\tilde{b}S\delta)\right]}{a-R_g+\tilde{b}\coth(\tilde{b}S\delta)+}= \quad \text{(Eq. A.4)}$$

Assumed error:

For the measurements of transmittance and reflectance performed to the SPD sample by using the spectrometer Perkin Elmer Lambda 900 (available at the Angstrom Laboratory of Uppsala), the initially collimated light provided by the light source is diffused when crossing the SPD sample, being the scattering of the SPD is not as strong to consider diffuse illumination. As it was mentioned before, the phenomenological (also called extensive values) scattering and absorption coefficients (S & K) are properly calculated by the two flux KM model when all light in the film is perfectly diffuse, which is not the present case in the SPD sample. Hence in this case it should be necessary to apply the use of four flux theory, but equations of diffuse components include new unknown parameters, making more difficult to accurately find the values of the scattering and absorption coefficients. On the other hand, Maheu, Letoulouzan and Gouesbet (MLG) established in 1984 the formulas for transmittance and reflectances of a four flux model [MLG84] (two fluxes travelling in the forward direction and two fluxes travelling in the backward direction, being one collimated and one diffuse in each direction, Figure IV.10 of Chapter IV of the present work). The scattering and absorption coefficients appearing in the MLG model (α & β) are nonphenomenological or also called intrinsic values. Four flux model requires the introduction of two new parameters, the average path parameter

or average crossing path parameter (ACP) and the forward scattering ratio (FSR). It must be noted that, contrary to the equation of the reflectance, the equation of the transmittance was not originally proposed in the KM model, being possible to find in a later study of special cases of MLG [MLG86]. In this work Equations A.3 and A.4 have been applied for T_{tot} and R_{tot} respectively, even when collimated components T_{dir} and R_{spec} are not negligible. The error of the applied approximation is below calculated.

Knowing that the relationship between the intrinsic and the extensive scattering and absorption coefficients are [Var97b]:

$$\boxed{\beta = \frac{K}{ACP}} \qquad \boxed{\alpha = \frac{S}{ACP \cdot (1 - FSR)}}$$

The four flux MLG equations for collimated light beams can be expressed as:

$$\left(\frac{dI_c}{dz}\right)_{MLG} = -(\alpha + \beta) \cdot I_c = -\left(\frac{S}{ACP \cdot (1 - FSR)} + \frac{K}{ACP}\right) \cdot I_c = -\frac{1}{ACP}\left(\frac{S}{(1 - FSR)} + K\right) \cdot I_c$$

$$\left(\frac{dJ_c}{dz}\right)_{MLG} = (\alpha + \beta) \cdot J_c = \left(\frac{S}{ACP \cdot (1 - FSR)} + \frac{K}{ACP}\right) \cdot J_c = \frac{1}{ACP}\left(\frac{S}{(1 - FSR)} + K\right) \cdot J_c$$

In the same way, the four flux MLG equations for diffuse light beams can be expressed as:

$$\left(\frac{dI_d}{dz}\right)_{MLG} =$$

$$= -ACP \cdot \beta \cdot I_d - ACP \cdot (1 - FSR_d) \cdot \alpha \cdot I_d + ACP \cdot (1 - FSR_d) \cdot \alpha \cdot J_d + FSR_c \cdot \alpha \cdot I_c + (1 - FSR_c) \cdot \alpha \cdot J_c =$$

$$= -(K + S) \cdot I_d + S \cdot J_d + \frac{1}{ACP} \cdot \left(\frac{FSR \cdot S}{1 - FSR}\right) \cdot I_c + \frac{1}{ACP} \cdot S \cdot J_c$$

$$\left(\frac{dJ_d}{dz}\right)_{MLG} =$$

$$= ACP \cdot \beta \cdot J_d + ACP \cdot (1 - FSR_d) \cdot \alpha \cdot J_d - ACP \cdot (1 - FSR_d) \cdot \alpha \cdot I_d - FSR_c \cdot \alpha \cdot J_c - (1 - FSR_c) \cdot \alpha \cdot I_c =$$

$$= (K + S) \cdot J_d - S \cdot I_d - \frac{1}{ACP} \cdot \left(\frac{FSR \cdot S}{1 - FSR}\right) \cdot J_c - \frac{1}{ACP} \cdot S \cdot I_c$$

However, if the two flux KM equations are used with total light beams (collimated and diffuse) instead of only the diffuse light beams, their equations can be expressed as:

$$\boxed{\frac{d\left(I_c+I_d\right)}{dz}=\left(\frac{dI}{dz}\right)_{KM}=-\left(S+K\right)\cdot I+S\cdot J=-\left(S+K\right)\cdot\left(I_c+I_d\right)+S\cdot\left(J_c+J_d\right)}$$

$$\boxed{\frac{d\left(J_c+J_d\right)}{dz}=\left(\frac{dJ}{dz}\right)_{KM}=\left(S+K\right)\cdot I-S\cdot J=\left(S+K\right)\cdot\left(J_c+J_d\right)-S\cdot\left(I_c+I_d\right)}$$

Hence, applying the above two flux KM model instead of the below four flux MLG model in the case of the SPD sample assumes an error. The equations below would not makes the approximation error, but include ACP and FSR unknown parameters.

$$\left(\frac{d\left(I_c+I_d\right)}{dz}\right)_{MLG}=\frac{dI_c}{dz}+\frac{dI_d}{dz}=$$

$$=-\frac{1}{ACP}\left(\frac{S}{1-FSR}+K\right)\cdot I_c-\left(K+S\right)\cdot I_d+S\cdot J_d+\frac{1}{ACP}\cdot\left(\frac{FSR\cdot S}{1-FSR}\right)\cdot I_c+\frac{1}{ACP}\cdot S\cdot J_c=$$

$$=-\left(K+S\right)\cdot I_d+S\cdot J_d+\frac{1}{ACP}\cdot\left(\frac{FSR\cdot S}{1-FSR}-\frac{S}{1-FSR}+K\right)\cdot I_c+\frac{1}{ACP}\cdot S\cdot J_c=$$

$$=-\left(K+S\right)\cdot I_d+S\cdot J_d-\frac{1}{ACP}\cdot\left(\frac{S\cdot\left(1-FSR\right)}{1-FSR}+K\right)\cdot I_c+\frac{1}{ACP}\cdot S\cdot J_c$$

$$\boxed{\left(\frac{d\left(I_c+I_d\right)}{dz}\right)_{MLG}=-\left(K+S\right)\cdot I_d+S\cdot J_d-\frac{1}{ACP}\cdot\left(S+K\right)\cdot I_c+\frac{1}{ACP}\cdot S\cdot J_c=}$$

$$\left(\frac{d\left(J_c+J_d\right)}{dz}\right)_{MLG}=$$

$$\frac{dJ_c}{dz}+\frac{dJ_d}{dz}=\frac{1}{ACP}\left(\frac{S}{1-FSR}+K\right)\cdot J_c+\left(K+S\right)\cdot J_d-S\cdot I_d-\frac{1}{ACP}\cdot\left(\frac{FSR\cdot S}{1-FSR}\right)\cdot J_c-\frac{1}{ACP}\cdot S\cdot I_c=$$

$$=\left(K+S\right)\cdot J_d-S\cdot I_d+\frac{1}{ACP}\left(\frac{S}{1-FSR}-\frac{FSR\cdot S}{1-FSR}+K\right)\cdot J_c-\frac{1}{ACP}\cdot S\cdot I_c=$$

$$=\left(K+S\right)\cdot J_d-S\cdot I_d+\frac{1}{ACP}\left(\frac{S\cdot\left(1-FSR\right)}{1-FSR}+K\right)\cdot J_c-\frac{1}{ACP}\cdot S\cdot I_c$$

$$\boxed{\left(\frac{d\left(J_c+J_d\right)}{dz}\right)_{MLG}=\left(K+S\right)\cdot J_d-S\cdot I_d+\frac{1}{ACP}\left(S+K\right)\cdot J_c-\frac{1}{ACP}\cdot S\cdot I_c=}$$

The assumed error of applying the previous equations is the difference between the two flux and the four flux models:

$$\left(\frac{dI}{dz}\right)_{KM} - \left(\frac{d\left(I_c + I_d\right)}{dz}\right)_{MLG} = \left(1 - \frac{1}{ACP}\right) \cdot \left(S + K\right) \cdot I_c + \left(1 - \frac{1}{ACP}\right) \cdot S \cdot J_c$$

$$\left(\frac{dJ}{dz}\right)_{KM} - \left(\frac{d\left(J_c + J_d\right)}{dz}\right)_{MLG} = \left(1 - \frac{1}{ACP}\right) \cdot \left(S + K\right) \cdot J_c - \left(1 - \frac{1}{ACP}\right) \cdot S \cdot I_c$$

Since two flux KM model considers diffuse illumination, with ACP=2 and FSR=0, the scattering coefficient S is here completely backscattered. The previous equations show the difference of applying two flux KM model with diffuse downwelling I_d and upwelling J_d with respect to total downwelling $I=I_c+I_d$ and upwelling $J=J_c+J_d$. This means that the solution found for S & K is overestimated, i.e., attenuated by scattering and absorption but intensified by scattering of the backward light beam [Lev05].

References

[Ish99] Akira Ishimaru, "Wave Propagation and Scattering in Random Media", IEEE Press Series on Electromagnetic Wave Theory Series, Wiley, John & Sons (1999).

[Lev05] Ronne Levinson, Paul Berdahl, Hashem Akbari, “Solar spectral optical properties of pigments – Part I: model for deriving scattering and absorption coefficients from transmittance and reflectance measurements”, Solar Energy Materials & Solar Cells 89 (2005) 319-349.

[MLG84] B. Maheu, J.N. Letoulouzan, G. Gouesbet, “Four-flux models to solve the scattering transfer equation in terms of Lorenz-Mie parameters”, Applied Optics 23 (1984) 3353-3362.

[MLG86] B. Maheu and G. Gouesbet, “Four-flux models to solve the scattering transfer equation: special cases”, Applied Optics 25 (1986) 1122-1128.

[Var97b] William E Vargas and Gunnar A Niklasson, "Forward-scattering ratios and average pathlength parameter in radiative transfer models", Journal of Physics: Condensed Matter 9 (1997) 9083–9096.